IMAGE-BASED HIGH-THROUGHPUT PHENOTYPING FOR ESTIMATING SORGHUM STALK THICKNESS WITH AN ELECTRIC HIGH-CLEARANCE VEHICLE

A Dissertation

by

MARIO ALBERTO MÉNDEZ DORADO

Submitted to the Office of Graduate and Professional Studies of
Texas A&M University
in partial fulfillment of the requirements for the degree of

DOCTOR OF PHILOSOPHY

Chair of Committee,	J. Alex Thomasson
Committee Members,	Stephen W. Searcy
	Yufeng Ge
	William L. Rooney
Head of Department,	John C. Tracy

December 2020

Major Subject: Biological and Agricultural Engineering

ABSTRACT

This research presents the development of two imaging systems capable of estimating stalk thickness of sorghum plants as well as the design, validation, construction and testing of an electric ground phenotyping vehicle (EGPV) able to carry sensors aimed at high-throughput phenotyping (HTP) on mature energy sorghum and corn. The first imaging system was developed with a low-cost RGB camera with an integrated infrared time-of-flight sensor to measure distance. The system captured images of eight energy sorghum plants on a weekly basis for six weeks under greenhouse conditions. The images were postprocessed off-line with *k*-means and minimum distance classification methods and visually inspected. The user then manually selected the stalk center, an image-processing algorithm was used to estimate stalk thickness, and estimates were compared to manual caliper measurements. The best estimates were found based on the *k*-means classification method and explained 70% of the variability in the caliper data, with a root mean squared error (RMSE) of 3.19 mm. The second imaging system was developed with a high-precision stereo camera (STR) and mounted on a high clearance vehicle to record video images of mature sorghum plants under field conditions. The STR images were postprocessed to compute depth maps. The user then selected two locations on the stalk in the images, another image-processing algorithm was used to estimate stalk thickness, and estimates were again compared to manual caliper measurements. The STR estimates explained 81% of variation in the caliper data, with an RMSE of 1.87 mm.

The EGPV was designed and constructed in order to clear 3-m tall mature energy sorghum plants, planted at 76.2-cm or 101.6-cm furrow spacing. The design was validated with finite element analysis, assuming a factor of safety of 4.0 or higher, corresponding to the design of static structures or machine elements under dynamic loading with significant uncertainty in the stress analysis relative to the application. The maximum theoretical speed of the vehicle was found to be 6 km/h, falling in the range of 5 to 9 km/h of most agricultural machinery operations. The vehicle's minimum turning radius during testing at 3 m was measured.

In summary, two imaging systems were designed and tested for estimating stalk thickness of energy sorghum plants. One performed reasonably well under greenhouse conditions, and the other, a stereo-camera system, performed well under field conditions. The stereo vision system was tested on a high clearance vehicle, and it is ultimately intended to be integrated with the EGPV (autonomous high-clearance phenotyping vehicle) as a semiautomatic tool for HTP under field conditions, specifically for assessing biomass content in sorghum or corn plants, and eliminating the tedious tasks of measuring and registering by hand.

DEDICATION

To the memory of my father, Manuel Méndez, a hardworking man who taught me to try harder; to my lovely mother, Alejandrina Dorado, who always missed me when I was in the USA; and to my brothers, Manuel and Miguel, who encouraged me to continue my studies.

ACKNOWLEDGEMENTS

My gratitude goes to my God and His only son, Jesus Christ, for his salvation and grace. I am grateful for the opportunity to study in this great Country, at Texas A&M University and its prestigious Department of Biological and Agricultural Engineering (BAEN).

I thank Dr. Alex Thomasson, my main advisor and committee chair, for accepting me as his graduate student in the construction of the phenotyping platform and the development of the plant stalk identification vision system. His guidance and advice came always at the right moment, and in that patient and friendly manner that characterizes him. He motivated me to continue to improve my research skills.

I thank Dr. Stephen Searcy, one of my committee members, who motivated me to apply to the BAEN program when I first visited Texas A&M in December 2011. He offered invaluable council as my advisor during the first two semesters of my studies, always challenging me to search for solutions to agricultural problems relevant to my home country.

I thank Dr. Yufeng Ge, one of my committee members, who first invited me to be part of the BAEN robotics team. He helped me to develop the skills needed to construct robots for the ASABE robotics student competition in 2013, and later invited me to be part of the phenotyping team to develop the actual electric ground phenotyping vehicle (EGPV), reported in this dissertation.

I thank Dr. William Rooney, one of my committee members, for sharing his knowledge about the sorghum varieties and for providing the appropriate sorghum varieties for the field experiment.

I thank Jose Batz, research fellow and friend, for his friendship during my stay as a graduate student sharing the same office, for his collaboration in developing vision systems and collecting data in the field. And especially, for helping me to better understand the English language.

I thank Richard Epting, technical machine shop coordinator, for providing safety training to use the machine shop equipment and for his experience and supervision during the purchasing of components and construction of the EGPV.

I thank Cody Garret, and DJ Forest, student workers. Cody for his ability to weld aluminum and steel, needed to construct the chassis of the EGPV. And DJ for his ability to assemble the chassis, suspension, wheels and transmission of the EGPV.

I thank Zikun Guo, research fellow, for his help and knowledge in connecting and testing the electric and electronic components and developing the control systems of the EGPV.

I thank Dr. John Mullet, professor; and Brock Weers, research assistant scientist, both from the Department of Biochemistry and Biophysics at Texas A&M University and AgriLife Research, for providing, growing, and maintaining sorghum plants under greenhouse conditions, and allowing us to collect images of sorghum stalks.

I thank Dr. Seth Murray, associate professor of the Department of Soil and Crop Sciences at Texas A&M University, for his knowledge in corn breeding and genetics, for suggesting important ideas to develop the EGPV, and for providing funding for the construction of the vehicle.

I thank Stephen Labar, research assistant, for coordinating planting, irrigation, and fertilization activities to maintain sorghum plants in the field and allowing us to collect images of sorghum stalks.

I thank Cody Bagnall and Farzad Hosseinali, research fellows, for their collaboration in tagging and collecting stalk diameter hand measurements in the sorghum field.

I thank Colby Ratcliff, a student worker, for driving the phenotyping vehicle and helping me mount the camera to collect images of sorghum in the field.

I also thank all faculty and staff members of the Department of Biological and Agricultural Engineering for their assistance during my studies and research activities at Texas A&M University.

CONTRIBUTORS AND FUNDING SOURCES

Contributors

Part 1: faculty committee recognition

This work was supervised by a dissertation committee consisting of Professor J. Alex Thomasson (chair), Professor Stephen W. Searcy, and Professor Yufeng Ge of the Department of Biological and Agricultural Engineering; and Professor William L. Rooney of the Department of Soil and Crop Sciences.

Part 2: student/collaborator contributions

The work of sorghum stalk thickness estimations in the greenhouse, reported in Section 3, was already published in a scientific journal article (2016) in collaboration with José Batz and J. Alex Thomasson, as listed in the References Section.

All other work conducted for the dissertation was completed independently by the student.

Funding Sources

The Mexican National Council of Science and Technology (CONACYT), and its local office in the state of Coahuila (COECYT), which provided financial aid during the four years of my studies at Texas A&M.

The *Universidad Autónoma Agraria Antonio Narro (UAAAN)* and its faculty training program, which allowed me to study abroad, and granted me the salary of a leave of absence during the four years of my studies at Texas A&M.

The Texas A&M AgriLife Research, which provided the funding for the construction of the electric ground phenotyping vehicle and purchase of components for the vision system.

NOMENCLATURE

(Acronyms and abbreviations)

2D/2d	Two-dimensional
3D/3d	Three-dimensional
ASL	Above the sea level
ATV	All-terrain vehicle
BAEN	Biological and Agricultural Engineering
CAD	Computer Aided Design
CAL	Caliper
CMOS	Complementary metal-oxide semiconductor
EGPV	Electric Ground Phenotyping Vehicle
FEA	Finite Element Analysis
FOV	Field-of-view
FPS	Frames per second
GPV	Ground Phenotyping Vehicle
IR	Infrared
KMS	*k*-means single-window
KMD	*k*-means double-window
MD	Minimum distance
MDS	Minimum distance single-window
MDD	Minimum distance double-window
PVC	Polyvinyl chloride
RGB	Red, green, blue

RMSE	Root mean square error
STR	Stereo
TAMU	Texas A&M University
TIG	Tungsten Inert Gas
ToF	Time-of-flight
TX	Texas State
USA	United States of America
USB	Universal seral bus

(Math Romans/Romans)

A	Input matrix (image)
b	Baseline (distance between stereo cameras), damping coefficient
B	Output matrix (image)
c	Caliper-measured stalk thickness
d	Distance
D	Disparity matrix
DM	Disparity map matrix
E	Modulus of elasticity
f	Conversion factor, focal length
G	Shear modulus
H	Hat matrix
h	Element of the hat matrix
J	Polar moment of inertia
k	Number of clusters, number of classes, spring constant, kilo

l	Length
m, m	Number of rows, mean, mass, meters, milli
n	Number of columns, angular velocity in rpm
N	Newtons
p	Pixel or point in an image
P	Point in world coordinates
$\mathbb{R}$	Real number
r	Radius
R	Gear ratio
R^2	Coefficient of determination
$\mathbb{R}^3$	Vector of three real elements
s	Sample standard deviation
T	Torque
u	Coordinate u of an image
v	Coordinate v of an image, velocity
X	Coordinate X of the world frame, design matrix
x	Coordinate x of the local frame, estimated stalk thickness
Z	Coordinate Z of the world frame
z	Coordinate z of the local (camera) frame, suspension position
$\dot{z}$	Velocity of z
$\ddot{z}$	Acceleration of z

(Math Greeks)

γ	Shear strain

κ	Kinetic energy
ν	Poisson ratio
ϕ	Angular deflection
Σ	Coordinate frame
σ	Normal stress
$\hat{\sigma}$	Sample standard deviation
τ	Shear stress
θ	Leaf angle
ε	Relative error
$\hat{\varepsilon}$	Raw residual
$\tilde{\varepsilon}$	Studentized residual
ξ	Damping ratio
ω	Angular velocity in rad/s

(Math Operators)

$\in$	Element of
$\Vert \ \Vert$	Euclidian norm
$\geq$	Greater or equal than
$>$	Greater than
$\leq$	Less or equal than
$<$	Less than
Log	Logarithm
max	Maximum
$\times$	Times

$\rightarrow$	Vector

(Sub-indices)

1, 2	One, two
i	i-th element
j	j-th element
l	left
Lim	Limit or permissible
max	Maximum
min	Minimum
p	Road profile
r	Right
v	von Mises
xy	On x-face in direction y

TABLE OF CONTENTS

Page

LIST OF FIGURES

LIST OF TABLES

1. INTRODUCTION

1.1. Food and Energy Needs

Two of today's most pressing problems are the insufficient supplies of food and energy (Nature, 2010; Otsuka, 2013; Li, 2015; Bortolamedi, 2015). Though there is limited availability of raw and healthy food products and a shortage of non-renewable energy sources for an increasing demand, much of the food and energy processing industry does not see these problems as critical from a technological perspective (Shetty, 2015; Mei et al., 2015).

Population growth is the main factor in food and energy shortages, having consequences like depletion of fresh water and arable land, environmental pollution, and unpredictable climate change (Constant et al., 2014; Hayashi et al., 2013; Shane et al., 2000). Any solution should consider the high probability that the current population of 7.7 billion in 2019 (United Nations, 2019) will increase anywhere from 33% to 70% before it plateaus around the end of the century (Gerland et al., 2014), challenging those responsible for producing more and better food and energy products.

1.2. Sources of Food and Energy

Plants and animals are the primary sources of food for humans, but because plants are the primary source of food for animals involved in meat production, plants are more important in the analysis of food shortages.

The main sources of energy are non-renewables such as oil, natural gas, mineral coal, and uranium (Tatar & Popescu, 2015). Uncertain timelines for discovery, extraction, and depletion of these sources threatens the population growth to come. In addition, fossil fuels generate CO_2 and contribute to climate unpredictability (Chapman et al., 2012). One solution to future energy shortages is renewable energy including solar, wind, biomass, biogas, and water dynamics (Laihanen et al., 2016).

Research in plants has the potential to mitigate both food and energy demands due to their primary raw food value and their biomass contents for bioenergy production. Research efforts must find the best crop or variety for a given application. C_4 plants can accumulate biomass rapidly, suggesting that crops like sorghum, maize, or sugar cane could be used for both food and energy purposes. Impending shortages will require C_4 plants to produce even higher yields, leading to a need for collaborative, multidisciplinary research on genotyping and phenotyping techniques and the discovery of higher potentials for food and energy production.

1.3. Phenotyping as a Solution for Food and Energy Needs

Crop cultivation has been studied and improved since it began. Empirical observation revealed that plant seeds can inherit desired traits, and thus production of fruits and vegetables exhibiting those traits was implemented through plant breeding. Maximizing production and improving adaptation to adverse conditions like nutrient and water stresses, illnesses, pests, or climate changes in new plant varieties comes as a result of plant breeding. Genetically, each individual or group of individuals can be analyzed according to two sets of characteristics: (1) genotypes and (2) phenotypes. Genotypes are hidden in the plant DNA while many phenotypes can be identified by human senses and are intimately related to genotypes, since a phenotype is a physical response of a genotype under specific environmental conditions. Because plant improvement is expressed physically, phenotyping is of high interest for producing more and better food and bioenergy.

Phenotyping was established long ago (Johannsen, 1911), but the process still requires plant breeding experience and time. Breeding the best-adapted organisms to some specific condition requires testing several individual genetic lines through several generations. Additionally, if a phenotyping experiment compares multiple varieties of a specific crop under different environmental conditions, the breeding process is time consuming and labor intensive, especially if it involves tracking traits that are vital to plant growth and development along the crop's lifecycle, requiring data collection in appropriate temporal and spatial scales, that motivate the development of HTP approaches that are still under development (Roitsch et al., 2019).

Breeding processes under the controlled conditions of greenhouses can be easier to carry out than field-oriented phenotyping since there is less variability of soil, temperature, water, nutrients, and light. Because this variability is lower, collected data can be more easily correlated to assess crop improvement. However, when considering mass production of food and energy, field-oriented phenotyping is a necessary approach since the limitations of reduced space, unrealistic environmental conditions, and greenhouse costs do not apply (Montes et al., 2007). Additionally, when plants have been improved by testing under natural, realistic environments, the results are more predictive of expectations for farmers and agronomists. Nonetheless, greenhouses are useful to determine the response of genotypes to the environment, and the results could have similarities to field-based results if light, plant density, soil, and temperature are similar (Poorter et al., 2016; Roitsch et al., 2019).

Although field-based phenotyping more accurately portrays the relationship between plant traits and their environments, it also presents some difficulties (Munns et al., 2010). For example, measuring traits with electronic sensing equipment or sensor platforms can produce reading errors due to uncontrolled temperature and humidity conditions: heavy rain and muddy soil can limit access to crop fields; large plots and fields can make data collection time consuming, especially with high temporal frequency; some sensors are affected by excessively bright or dim light conditions; and some crops grow tall enough that sensing platforms cannot reach parts of them for measurement. Results of experiments in greenhouses can be translated to field conditions if growing conditions are similar to those in the field (Poorter et al., 2016).

In summary, field-based phenotyping can contribute to meeting food and energy demands, but suitable crops, techniques and technologies must be identified in both greenhouses and field conditions.

1.4. High-Throughput Phenotyping for Maize and Energy Sorghum

Two important crops in the future of bioenergy production are maize and sorghum. The so-called “energy sorghum” is a rapidly growing lignocellulosic feedstock with a long breeding history and a wide collection of germplasm (Rooney et al., 2007; Yuan et al., 2008). These attributes make it suitable for phenotyping and developing varieties with high yield, drought tolerance, and high nitrogen-use efficiency; maize has similar attributes. While phenotyping is a straightforward concept, some basic measurement challenges arise when high-throughput phenotyping is applied to a field-based experiment, especially with high-clearance crops like sorghum and maize. The main traits that breeders consider when breeding energy sorghum are stalk diameter (where most of the biomass and sugar accumulate) (Rooney et al., 2007), tillering ability, and plant height. However, stalk thickness is considered the most important trait for estimating sorghum biomass (Mullet, 2014; Rooney, 2016, personal communication).

1.4.1. Phenotyping and Precision Agriculture

One of the challenges of high-throughput phenotyping involves measuring and tracking the effects of environmental variation on numerous plants. Understanding the relationships of genotype × environment × management requires the use of sensor-based plant phenotyping approaches (Roitsch et al., 2019). For instance, mass trait analysis requires technologies capable of quickly and reliably screening and storing information without using destructive methods (Busemeyer et al., 2013; Svensgaard et al., 2014). Field phenotyping requires georeferencing to assess spatial variability, which underpins precision agriculture, defined as the use of sensed information to aid decision making related to crop management at specific locations (CACYSSF, 1997; Brase, 2006). Historically, a specific area of interest in precision agriculture has been defined as a homogeneous management zone within an agricultural production field, but in phenotyping for breeding, the area must be more precise, ranging from small plots to individual plants. Thus, sensors that measure plant traits must be accurate and precise. Some sensing technologies involved in phenotyping include artificial vision, robotics, and computing systems (Furbank & Tester, 2011). Together these tools must be reliable for quantitative measurement and for understanding the molecular networks that control complex traits and interactions between organisms (USDA & NSF, 2011). Beyond simply replacing the need for human observation, breeding process time can be significantly reduced with automated phenotyping technologies (Montes et al., 2007) because many more genotypes can be measured in a given season.

1.4.2. Image Analysis as a Sensing Technique

Human observation has been historically used in measuring phenotypic traits such as color, size, shape, and texture. Artificial vision can be used to mimic human vision, integrating cameras, algorithms, and computers to measure traits that can be used to improve food and energy production. Recent studies in HTP suggest a trend towards including image systems to collect plant phenotypes related to morphology, physiology, development and postharvest measurements (Jiang and Li, 2020). Image sensors can extract plant information such as color, temperature, shape, or size and relate these to phenotyping traits useful to differentiate some plants from others in terms of important characteristics like drought tolerance and yield.

1.4.3. Related Work

Some phenotyping systems have shown potential to automatically collect, record, process, and analyze high-throughput phenotyping data. These systems have provided ideas for designing sensing platforms able to recognize stalk diameter, a critical parameter in tall crops like sorghum and maize.

1.4.3.1. Push Carts

Collecting multiple data measurements simultaneously is important to increase efficiency and reduce labor requirements. A low-cost solution was proposed by White and Conley (2013), who constructed a proximity-sensing vehicle by connecting two bicycle frames with square steel tubing. The resulting chassis was able to integrate monochrome cameras, ultrasonic sensors, radiometers, infrared thermometers (IRT), and a global position system (GPS) to gather information at different plant growth stages in wheat, barley, camelina, and cotton, at a sampling rate of 5.0 Hz, with an average speed of 0.36 m-s^{-1}. Inspired in this platform, Bai et al (2016) constructed a similar cart easily moved by two operators to cover a maximum of 0.2 ha/h. The phenotyping platform included four sets of different sensors to assess five canopy traits at a row or plot scale: height, NDVI, temperature, reflectance spectra, and green pixel fraction with RGB images. Each sensor set consisted of an ultrasonic sensor, an NDVI sensor, a thermal infrared radiometer, a portable spectrometer, and an RGB camera. Additionally, the platform included an environment sensing module in the middle of the cart that included an up-looking Normalized Difference Vegetation Index (NDVI) sensor, a GPS receiver, and an air temperature and relative humidity sensor. Similarly, but with the idea of having a narrower vehicle, Crain et al. (2016) developed a portable field-phenotyping system to estimate wheat yield, utilizing only the rear half of a bicycle, accommodating a GreenSeeker (Trimble Agricultural Division, Westminster, CO, USA), sensor to measure NDVI, a color web cam to estimate canopy coverage, an IRT to measure canopy temperature, and a GPS to register location. This platform reduced data collection time to around a third compared to individual handheld devices, and increased about six times the travel speed (up to 2.0 m-s^{-1}) of the first platform. However, since both used human effort, the working time, payload, and consistency of speed are limited. Additionally, these platforms require frame modifications to measure tall crops or growth stages of plants that are higher than 1.0 m.

1.4.3.2. Tractor-Based Platforms

A solution to increase working time and sensor payload while maintaining a more stable speed of travel on phenotyping platforms is by using tractors or sprayers. The works of Lan et al. (2009) and Montes et al. (2011) show that tractors can carry more sensors compared to the two previously cited cart-type platforms. Lan et al. added some sensors such as leaf area index analyzers to measure biomass, hyper-spectral radiometers to measure crop stress, and multispectral cameras to measure vegetation indices and perform plant-background segmentation. The platform of Montes et al. accommodated four sets of light curtains and spectral reflectance sensors to estimate maize biomass of four maize rows simultaneously.

The platform of Lan et al. was superior in travel speed, driving at 0.45 m-s^{-1}, but its data acquisition frequency was once every 1.2 s, while that of Montes et al. was driven at 0.28 m-s^{-1}, had four sets of sensors, and had higher efficiency overall, not to mention that in future work it could be expanded to cover eight or twelve maize rows.

One limiting factor when using conventional tractors is clearance. With the platforms of Lan et al. and Montes et al., the use of mini-tractors limited the clearance to 1.1 m, suggesting that taller vehicles are needed for taller crops or later growth stages. However, the work of Salas-Fernandez et al. (2017), overcame the clearance limitation by using a John Deere 1026R subcompact utility tractor (Deere & Company World Headquarters, Moline, IL, USA) with a mounted tubular structure to hold cameras and be able to image sorghum plants up to 3-m tall. The tractor navigated in the middle of two contiguous plots and imaged the plants laterally with two sets of stereo cameras viewing the plants laterally from the left and right sides of the structure. The tractor was able to travel at the minimum speed of 0.3 m/s (1.1 km/h) needed to activate an autosteering system linked to an RTK GPS system, and it was able to collect data at an approximate area-coverage rate of 0.5 ha/h.

1.4.3.3. Sprayer-Based Vehicles

More recently, an improvement for measuring taller plants and crop stages while maintaining payload and consistent speed came with the adaptation of hydraulic-booms type sprayers as phenotyping vehicles. A good example is the phenotyping platform developed by Andrade-Sanchez et al. (2014), who adapted a LeeAgra 3434 DL open-rider sprayer (LeeAgra, Lubbock, TX, USA), mounting sonars to measure height, multi-spectral sensors to measure NDVI, and an IRT to measure temperature over cotton or other crops shorter than 1.93 m. The sampling rate was 2.0 Hz, limited by the response time of the IRT, and the system measured four rows simultaneously while traveling at 0.75 $m \cdot s^{-1}$, covering 8,400 m^2 per hour. Similarly, Barker III et al. (2016) used a Bowman Mudmaster agricultural sprayer (Bowman Manufacturing Co. Inc., Newport, Arizona, USA) and mounted ultrasonic sensors, IRTs, spectrometers, and laser sensors to measure height, temperature, vegetation indices, and distances, respectively. The system was used on wheat and soybeans in three plots simultaneously and had a sampling rate of 10.0 Hz and traveled at speeds from 0.89 to 1.11 $m\text{-}s^{-1}$. The sprayer-based phenotyping vehicle of Barker III had higher data sampling rates than that of Andrade-Sanchez, but its crop clearance was 33 cm less. The literature does not include examples of a phenotyping platform with clearance over 1.93 m, which would be required to work with the later stages of corn or sorghum. This shortcoming brings about the idea of designing higher clearance vehicles while incorporating the ideas of the lightweight construction of the push carts to minimize soil compaction, the self-propelled capabilities of tractors or sprayers, and minimizing the complexity in design and construction.

1.4.3.4. Suspended Systems and UAVs

Suspended phenotyping systems mounted on cranes (gantry) or unmanned aerial vehicles (UAV) are used to take RGB, NIR, thermal, or LiDAR data. Their main advantage is the ability to take images from above the crops, overcoming some limitations of the previously mentioned ground phenotyping platforms, such as measuring traits of high-clearance crops like sorghum, maize, or sugar cane, and accessing the crops in muddy soils or in dense vegetation. One example of suspended systems is the Field Scanalyzer (Virlet et al., 2017). This fully automated phenotyping platform consisted of a metal structure mounted on rails to slide horizontally in one direction. The overhead gantry carries a camera box that holds all image sensors on it. The platform can move in cartesian coordinates *XYZ* to cover a plot area of 115.8 m × 11.3 m with a height of 4.1 m, suitable to work with high-clearance crops. The phenotyping platform has a high resolution RGB camera, a thermal infrared camera, two 3D laser scanners, a multispectral camera, an NDVI sensor, and a chlorophyll sensor to assess green pixel fraction (canopy cover), soil and canopy temperature, canopy fluorescence, plants height, and quantification of wheat ears. Advantages of this platform are its ability to perform high spatial and temporal resolution sensing and work 24 hours/day.

Another example is the cable suspended phenotyping system named NU-Spidercam (Bai et al., 2019). The sensing platform consisted of a multispectral camera, a thermal IR camera, a spectrometer, and a 3D LiDAR, able to take images from above the crops. The phenotyping system also integrated an anemometer, a GPS and an optical fiber to measure incident illumination from the sky. The platform consisted of four poles (27 m) located at the corners of the study area (60 m × 67 m), and cables pulled by winches were connected to the poles. The system had a vertical working range from 0 to 9 m, and the XYZ accuracy was ±5 cm. The system measured canopy temperature (R^2 = 0.93, *RMSE* = 1.84 °C) and plant height (R^2 = 0.97, *RMSE* = 3 cm) in soybean accurately when compared to ground truth data. The system also demonstrated its capability to measure canopy temperature, soil temperature, air temperature and photosynthetically active radiation continuously during 6 hours in a single day, presenting the potential to acquire data in high spatial and temporal resolutions. However, in both examples of gantry and suspended phenotyping platforms is the cost of all the infrastructure and the limited area in which they can perform their phenotyping tasks, providing UAVs an advantage in covering much larger areas using similar sensors, but with the drawback of lower resolution and lower dwell time. For example, Maimaitijiang et al. (2020) estimated plant height and leaf area index (LAI) in two fields of sorghum using an RGB camera and a LiDAR sensor mounted in a DJI Matrice 600 Pro hexacopter (DJI Technology Co. Ltd., Shenzhen, China) flying at 65 m above ground level (AGL). Their results for canopy height using RGB photogrammetry showed an $R^2 = 0.873$, with an $RMSE = 0.118$ m, while estimates for LiDAR showed an $R^2 = 0.975$, with an $RMSE = 0.052$ m, when compared to ground truth data. These results favored the LiDAR technology over RGB photogrammetry, but with a resolution of 20 cm at the given AGL, stalk thickness cannot be measured, not to mention that stalk thickness data cannot be recorded from above. Similarly, Malambo et al. (2018) used a Professional UAV (Phantom 3, Shenzhen, Guangdong, China) with a mounted RGB camera to compute structure from motion in Pix4D software (Pix4D SA, Lausanne, Switzerland) to determine plant height on sorghum and maize in a field of 1.5 ha. Their results showed correlations ranging from $R^2 = 0.41$ to 0.91 with *RMSEs* from 0.11 m to 0.19 m for maize, and $R^2 = 0.61$ to 0.85 with *RMSEs* from 0.12 m to 0.24 m for sorghum, when compared to terrestrial laser scanner data. Even taking the best correlations, the point cloud resolutions are too low to see details enabling stalk thickness estimations. At this stage, it is important to mention that ground vehicles still represent the best potential to mount sensors or cameras to estimate plant stalk thickness at a millimetric resolution (proximal sensing).

1.4.3.5. Using Vision

As mentioned in Subsection 1.4.1, artificial vision can measure plant traits effectively (Furbank & Tester, 2011), and the trend to use it in HTP is increasing (Jian and Li, 2020). Phenotyping systems should thus be able to identify plant forms through artificial vision. Although in previously cited works some cameras were mounted (White and Conley, 2013; Crain et al, 2016; and Lan et al., 2009), their relevance was focused on their capacity to record reflection intensity of crops rather than their spatial feature extraction and recognition capabilities. However, the focus here is on vision and optical sensing capabilities. For instance, Comar et al. (2012) developed a system to measure wheat canopy structure and leaf chlorophyll index over the course of the growing season. Along with four fiber-optic spectrometers, they used two RGB cameras with flash lighting to compute green fraction from two different angles over micro-plots of $5 \times 2\ m^2$, while a separate device measured the incoming photosynthetically active radiation (PAR), useful in computing the diffuse fraction and performing radiometric adjustments. Other vision-based platforms have avoided radiometric corrections by enclosing the vision systems to minimize the variable effects of sunlight. For example, Busemeyer et al. (2013) used a multi-optical-sensor platform to measure plant height, tiller density, moisture content, and nitrogen status of triticale and other small grains. The vision system consisted of two 3D time-of-flight (ToF) cameras, a color camera, three laser distance sensors, a hyper-spectral imaging camera, and two light curtains. Another similar enclosed vision system was presented by Svensgaard et al. (2014), who used a phenotyping system called PhenoField (Videometer A/S, Herley, Deenmark). This platform uses a 5MP monochrome camera to image an area of 1x1 m^2, illuminated with multispectral LEDs in nine bands (from 465 to 850 nm) within 1.0 s. After data collection image stacking was performed with VideometerLab (Videometer A/S, Herley, Deenmark). The system was able to measure vegetation indices and canopy texture. The image-analysis system performed supervised binary classification between green leaf and soil with the classification-tree algorithm, but no morphological feature extraction was performed.

The vision systems in the literature worked with radiometric properties and computed green fraction, LAI, or NDVI. The closest work to morphological feature extraction was presented by McCarthy et al. (2010), who developed a vision system and a vehicle able to detect internode length in cotton plants for the study of water and nutrient stresses. This vision system integrated a video camera, a transparent enclosure, and a set of movable links with three degrees of freedom (DoF) that allowed targeting of plants at a specific location such as an internode. Additionally, the platform was a self-propelled vehicle driven by windshield-wiper motors and powered with a 12V car battery and a solar panel to operate manually or automatically at a speed of 0.2 m-s^{-1} over plants shorter than is 0.9 m. The system was capable of measuring an average of 12 out of 100 plant internodes with overhead sunlight, and 64 out of 100 for vigorous plants with perpendicular sunlight to the view angle of the camera. This system provided a clear example of morphological feature extraction, but it could not be used to measure stalk thickness, because it first detected the main stem and candidate plant branches, showing them as lines to later compute length, while the width of the stalk was lost in the process. This shortcoming highlights the need to develop stalk-thickness extraction algorithms for crops like sorghum, for which stalk thickness can be an important metric.

Closely related work was presented by Atefi et al. (2020), where a vision system and a robot manipulator were used to measure stems of maize and sorghum in a greenhouse environment. Their measuring system included a ToF camera (Model: SR4500, Mesa Imaging Inc., Zürich, Switzerland), which was used to image the plants. The data were later analyzed with a convolutional neural network (CNN) to distinguish the stems from other parts of the plants. During the experiment, plants were placed manually at approximately 40 cm from the camera, an appropriate distance to use the camera's ToF ability to provide position coordinates, and instruct a 4-DoF robot manipulator (Model: MICO2, KINOVA Inc., Boisbriand, QC, Canada) to grasp the stems in an adequate location with a gripper on the end effector. The gripper had a linear potentiometer (Model: LP804-03, OMEGA Engineering Inc., Norwalk, CT, USA) attached to it that was able to measure the maize and sorghum plant stalks with a high correlation ($R^2 = 0.98$ and 0.99, with $RMSE = 1.0$ and 1.2 mm, respectively) compared to manual measurements made with a caliper. The overall process to get one stem measurement took an average of 45 s, as compared to a manual measurement that required about 10 s. The tasks of identifying and measuring stems were relatively fast, but most of the time was spent in grasping, with an approximate time of 42 s, representing an area of needed improvement.

In another closely related work (Salas-Fernandez et al., 2017), stereo cameras (Model: GRAS-20S4C-C, Point Grey, Ludwigsburg, Germany) were used to image sorghum plants laterally and estimate two traits linked to biomass, height and stem diameter. Two different semiglobal block matching methods, DenS-Di and IpaS-Di, were used for 3D reconstruction of stereo images, and the results for diameter were correlated to manual measurements with R^2 values ranging from R^2 = 0.56 to 0.89 for a subset of 20 genotypes, measured at two different growing stages.

Another related vision system (Xiang et al., 2019) focused on plant height, stem diameter, leaf angle, and leaf area, which were correlated to ground truth values measured manually by using a measuring tape, a caliper, a protractor, and a LI-3000C Area Meter (LI-COR, Lincoln, Nebraska, USA). They also estimated the stem volume and total leaf area to correlate them with wet and dry biomass. The vision system was mainly integrated by an RGB plus ToF camera (Kinect 2, Microsoft Corporate, California, USA) and a linear actuator that moved the camera vertically to take multiple images along the height of each plant. For the experiment, four varieties of sorghum plants with eight replications were grown in a growing chamber (a total of 32 plants) and sampled at three different growing stages. The sampling process consisted of manually placing each potted plant approximately 90 cm away from the imaging system, while maintaining the widest side of the canopy perpendicular to the camera’s view. The imaging acquisition (per plant) started by taking a picture each second from the base up to the top of the plant, moving the linear actuator at a speed of 40 mm/s, which allowed 90% overlap between two consecutive pictures. The image processing consisted of point cloud preprocessing, stem and leaf segmentation, and morphological trait extraction, to finally evaluate the performance. The results showed that the estimated and measured stem diameter values were highly correlated, and the coefficient of determination was R^2 = 0.86, with an *RMSE* of 1.61 mm, leading to the conclusion that their point cloud processing method is accurate for measuring sorghum stem diameters.

1.5. Importance of Developing a Phenotyping Platform for High-Clearance Crops

Time is one of the key aspects in plant breeding. Breeders want to reduce the phenotyping process time and thereby include much more genetic diversity in their studies (Passioura, 2012; Montes et al., 2007). In addition to measuring a large variety of traits with multiple sensors, measurement repetition with different types of sensors can provide data verification (Munns et al., 2010). Furthermore, White et al. (2012) suggest that a useful phenotyping platform should carry sensors able to measure multiple traits in multiple plots on a regular basis along each growth stage of the crop, even in diurnal time.

A major gap in current research on high-throughput phenotyping platforms is the lack of a high-clearance system for tall crops like sorghum and maize. Some tractor- and sprayer-based phenotyping platforms can work with young sorghum and maize plants, but fields with mature plants would be difficult to access (White et al., 2012; Cobb et al., 2013). For these crops, platforms with a 3.0 m clearance need to be developed (Crain et al., 2016) to traverse the field during the later crop stages, when biomass accumulation is particularly important.

Another important gap in high-throughput phenotyping platforms is a lack of automation. Current systems are either manually propelled or IC-engine propelled and manually driven. Electric propulsion would contribute to automatic navigation, as it affords easy integration of navigation systems that the next generation of phenotyping platforms must include (Comar et al., 2012) to reduce human labor and time (von Mogel, 2013).

As a summary, basic requirements of a high-throughput phenotyping platform are (a) measuring traits over large plant populations, (b) carrying multiple sensors to measure various traits (e.g., plant height, LAI, number of nodes, biomass content, and chlorophyll content), and (c) measuring traits frequently to track plant development over time. Thus, an autonomous, high-clearance, multi-sensor phenotyping platform could provide fast, accurate, and precise plant-trait information and inform decision making when selecting the best cultivars.

1.6. Objectives

1. Develop an imaging system to measure reliably stalk thickness in sorghum under
    a. controlled environmental conditions.
    b. field conditions.

    The standard by which stalk-thickness estimates were to be evaluated was manual measurement with calipers. Preliminary and postliminary data indicated that caliper measurements on sorghum stalks had maximum absolute errors near 1.0 mm, with root mean square error of less than 0.4 mm. Error values for sensor-based estimates reported in recent literature ranged from 1.2 to 1.6 mm. Because the research reported herein was focused on HTP, both in the greenhouse and the field, a compromise between accuracy and speed was reasonable. Therefore, an error level roughly in line with recent reports in the literature – i.e., something under 2.0 mm – was deemed acceptable.

2. Design, validate, construct, and test a phenotyping platform with the following capabilities:
    a. accommodates multiple sensors.
    b. enables integration of an image-based sorghum stalk-thickness measurement system.
    c. is electrically propelled for fully autonomous operation.
    d. has adequate clearance for mature corn and sorghum.

For objective 2, in addition to designing the phenotyping platform to fulfill all the above requirements, including clearing 3-m tall plants, the machine should withstand loads with a factor of safety near 4.0 or higher, adequate for a machine constructed of ductile materials under static loading with uncertainties about dynamic loading, material properties and environmental conditions. The phenotyping platform must also be tested in the field for functionality and its ability to enter in a single turn to a set of four furrows after a headland (2.29 m of turning radius for furrows of 76.2 cm, and 3.05 m of turning radius for furrows of 101.6 cm, after skipping a working width of four furrows), for an average speed necessary to perform image recordings (2.9 km/h, estimated from the stereo vision experiment) and for a maximum speed for navigating in the roadway (6 km/h).

2. PART I: VISION SYSTEMS: MATERIALS AND METHODS*

2.1. Greenhouse and Field Conditions

2.1.1. Greenhouse Conditions

The first of two experiments involved growing sorghum plants under the guidance of Dr. John Mullet's research team. The plants were planted in black plastic pots placed inside a greenhouse located in the Norman Borlaug Institute for International Agriculture at Texas A&M University (TAMU), College Station, TX, USA. Environmental conditions were monitored with a Tinytag® data logger (Gemini Data Loggers, Chichester, West Sussex, UK). The average daily minimum and maximum temperatures were 24.1 ºC (±1.1 ºC) and 32.2 ºC (±1.8 ºC), respectively. The average daily minimum and maximum relative humidities were 36.0% (±14.0%) and 69.9% (±11.3%).

2.1.2. Field Conditions

The second of two experiments was conducted on field plots of sorghum plants grown by Dr. William Rooney's research team. These plants were planted on a rectangular field area covering an area of 1.8 × 225.0 m^2, where a Belk clay soil predominates. The field is located on the Texas A&M University Farm, falling within the opposite corner points: 30º32'13" N, 96º25'10" W; and 30º32'19" N, 96º25'5" W (see Figure 2.1). Based on

* Part of the data reported in this section is reprinted with permission from "Imaging for High-Throughput Phenotyping in Energy Sorghum" by Jose Batz, Mario A. Méndez-Dorado and J. Alex Thomasson, 2016, *Journal of Imaging*, 2 (4), 1-12, Copyright 2016 by MDPI.

Google Earth data, both corners of the northeast side had an elevation of 66 meters above sea level (MASL), while the two corners of the south east side had an elevation of 67 MASL.

2.2. Vegetative Materials

2.2.1. Plant Varieties for the Greenhouse

Two energy sorghum varieties, R07019 (variety A) and R07007 (variety B), were grown in a greenhouse under the guidance of Dr. John Mullet's research team. Both varieties are known to rapidly accumulate biomass in the stalk, so their stalk thickness (effective diameter) is an excellent trait to record and correlate with biomass. On May 17, 2015, two plants of the same variety were planted per pot, with four pots containing Variety A and four containing Variety B. By June 30, 2015, one plant was removed from each pot to facilitate the imaging process of a single stalk. All plants were supplied with 17 g of Osmocote® 14-14-14 slow release fertilizer (The Scotts Company LCC, Marysville, Ohio, USA), and periodic irrigation to maintain their health and growth.

Figure 2.1 Location for field experiment enclosed by the rectangular area marked in white lines, within the Texas A&M Farm, Caldwell, Texas, USA. Non up to date photography taken from Google Earth.

2.2.2. Plant Varieties for the Field

Varieties A and B were also planted in a field on April 7, 2016, with a John Deere 7100 planter (Deere & Company, Moline, IL, USA) equipped with Almaco cone type seed meters (Almaco, Iowa, IA, USA). A post planting herbicide treatment of 3.5 L/ha of Atrazine plus 1.75 L/ha of S-metolachlor was applied, followed by 146 mL/ha of Sharpen® (Saflufenacil) herbicide on April 11, 2016. Additionally, a side dress application of 150 units of nitrogen, applied as urea ammonium nitrate (UAN) was applied with a single shank knife, placed approximately 8 cm deep and 25 cm to the side of the seedbed. A pre-plant application of 168 kg/ha of 11-37-0 (N-P-K) and 4.5 kg/ha of Zn was knifed about 15 cm below the seedbed in February. No irrigation was needed due to sufficient rainfall of 673 mm. Three contiguous rows of each variety were planted along a straight line of 225 m, creating thirty-two 4.6-m long micro plots, with six furrows each, and alleys of 2.6 m between micro plots (Figure 2.2).

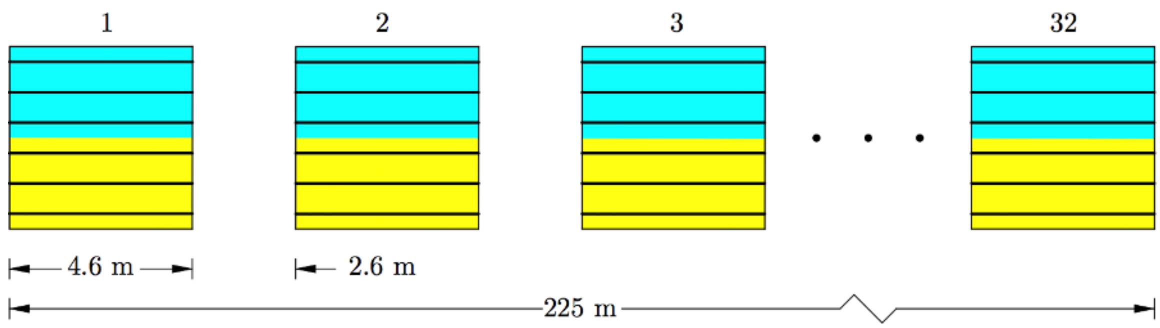

Figure 2.2 Micro plots with six furrows, blue areas containing three furrows of Variety A, and yellow areas containing three furrows of Variety B.

2.3. Vision Systems Materials

2.3.1. Camera for the Greenhouse

A Creative Senz3D web camera (Figure 2.3), model VF0780 (Creative Technology Ltd, Milpitas, CA, USA), was used to capture images of sorghum plants in the greenhouse. The dual-mode camera was composed of a conventional red-green-blue (RGB) sensor, able to collect color images with a pixel resolution ranging from 320 × 240 to 1,280 × 720; and an infrared (IR) 3D sensor (SoftKinetic Inc., Sunnyvale, CA, USA), capable of collecting depth information by computing the time-of-flight (ToF) between the laser IR emitter and the CMOS array receiver, at 320 × 240 pixel resolution. The RGB sensor field-of-view (FoV) has a fixed lens focusing with a diagonal FoV of 73º, while the 3D sensor has an ultra wide lens with a diagonal FOV of 87º. The operating range for this camera is 15 to 100 cm.

Figure 2.3 Creative Senz3D web camera used in the vision system for the greenhouse (reprinted from Creative Technology Ltd., 2020).

2.3.2. Imaging Chamber for the Greenhouse

A 56 × 107 × 207 cm box-shaped chamber was built to facilitate sorghum plant feature extraction (Figure 2.4). The frame was made of polyvinyl chloride (PVC) pipe (48 mm diameter), and a thick black cotton cloth covered the chamber’s top, back, left, and right faces. The cloth was used to create a high-contrast background and to block direct sunlight coming into the windows in the greenhouse that might interfere with the camera’s IR receiver. The chamber allowed natural sunlight to enter only through the front face (Figure 2.4), and no additional illumination was required for imaging since data were collected between 10:00 A.M. and 12:00 P.M. on the given dates.

Figure 2.4 Imaging chamber for the greenhouse to help blocking undesired infrared sunlight. Inside the chamber a plant to measure, and outside the tripod holding the camera.

2.3.3. Camera for the Field

A stereo camera, model DUO MC (DUO3D™ Division, Code Laboratories Inc., Henderson, NV, USA), was used to record video of sorghum plants in the field (Figure 2.5). The camera consists of two monochrome camera sensors with seven resolution configurations varying from 320 × 120 to 752 × 480 pixels and 6.0 × 6.0 µm pixel size; Each sensor is behind a 170º wide-angle lens and enclosed in a compact aluminum case

(57.0 × 30.5 × 14.7 mm). The stereo camera has a baseline (distance between lenses) of 30.0 mm and a focal length between 2.0 and 2.1 mm. The camera was designed for detailed depth accuracy of 127 μm within a range of 7.7 to 190.5 cm. The camera has a Micro-B USB 2.0 port and a 40-cm cable to connect to a computer. It uses the DUO Dashboard software (DUO3D™ Division, Code Laboratories Inc., Henderson, NV, USA). A 3-m long super speed USB 3.0 type A male to female extension cable (Cable Matters Inc., Southborough, MA, USA) was added to accommodate the sensor at the correct position on the field machine. The software stores video from the stereo camera at 56 to 360 frames per second (FPS), with a global shutter varying from 0.3 μs to 10 s. The output-storage format is Audio Video Interleave (AVI).

Figure 2.5 Stereo camera DUO MC used to take sorghum images in the field (reprinted from Code Laboratories Inc., 2020).

2.3.4. Enclosure and Bracket for the Stereo Camera

An enclosure was designed and 3D-printed in Acrylonitrile Butadiene Styrene (ABS) material to affix the stereo camera onto a field phenotyping machine. The enclosure consists of a box-like shape as shown in Figure J.26. In addition, an aluminum sheet metal bracket was manufactured to provide an extension arm that supported the plastic bracket at the correct height with respect to the ground and at the correct position with respect to the vehicle and sorghum plants. A drawing is shown in Figure J.26; the whole assembly of the 3D-printed enclosure and bracket is shown in Figure 2.6.

Figure 2.6 Stereo camera mounts, consisting of two aluminum brackets, a camera enclosure, and a lamp bracket. All attached to the maroon GPV.

2.4. Equipment and Software

2.4.1. Calipers and Rulers

A 10 cm long digital caliper (Model CD-4” ASX, Mitutoyo Corporation, Takatsu-ku, Kawasaki-shi, Kanagawa, Japan) and a 10 cm long analog caliper (Blackface Machinist Grade model, Fowler High Precision, Newton, MA, USA) were used to manually measure sorghum stalk thickness. In the greenhouse, a 1.0 m long aluminum ruler was used to measure the distance from the camera to the sorghum plants.

2.4.2. Phenotyping Vehicle for the Field

A custom-made ground phenotyping vehicle (GPV) (Wildcat Manufacturing, Tahoka, TX, USA) was used to carry the stereo camera alongside the sorghum plants for stalk thickness measurements in the field (Figure 2.7). The GPV includes a frame consisting of 15.2 × 10.2 cm steel square tubing, providing a fixed width of 229 cm between wheels and vertical crop clearance of 272 cm. Two rear hydraulic motors powered with an 18-kW diesel engine propel the GPV, while a hydraulic piston steers the front wheels. The GPV speed and steering are controlled by manually controlled valves located in the driver’s cabin.

Figure 2.7 Ground Phenotyping Vehicle (Wildcat Manufacturing, 2015).

2.4.3. MATLAB®

MATLAB® (Academic Student Version 9.1, R2016b, The MathWorks, Inc., Natick, MA, USA) was used as the programming platform to develop vision algorithms. To develop the stereovision systems, the Image Processing and the Computer Vision System toolboxes were installed in MATLAB®.

2.5. Methods for the Vision Systems

2.5.1. RGB Image Representation for the Camera used in the Greenhouse

In computer graphics, a gray scale image can be represented as an $m \times n$ rectangular array of square pixels, where m denotes the number of rows and n denotes the number of columns. Each pixel, denoted as $p_{ij} \in R$, contains a single brightness value ranging from black to white (0 to 1). For color images, the representation typically includes three brightness values representing the visual tristimulus colors of red, green, and blue (RGB). In this way, the two-dimensional $m \times n$ rectangular array becomes a three-dimensional array with RGB bands (layers), as shown in Figure 2.8. Consequently, each color pixel, also denoted as $p_{ij} \in R^3$, will have three values arranged in a three-dimensional vector. This image representation and pixel notation will be used to describe the following vision methods.

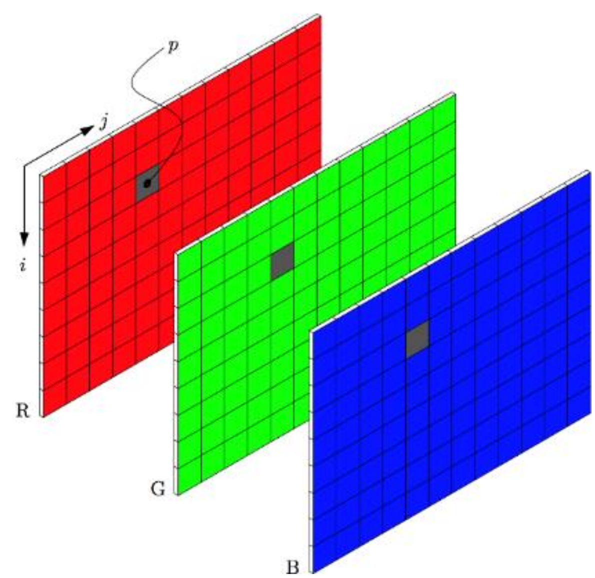

Figure 2.8 RGB image model with three staked planes: red, green, and blue. Each pixel *p*, located by its Cartesian coordinates *i* and *j*, has three values, one for each color.

2.5.2. Minimum Distance Image Classification for the Greenhouse Images

Minimum distance (MD) classification of images is a well-known supervised classification method that requires the user to select pixel samples of visually identified informational classes in the image (Ghimire, 2012; AnnRose, 2014). For each pixel in an RGB image, the algorithm computes Euclidean distances between the RGB pixel values and the mean RGB values of the samples (Campbell and Wynne, 2011). Once the distances are computed, the shortest distance to a sample class indicates that a given pixel belongs to that sample class. The following methodology is explained graphically in a simplified way in Appendix A.

The first picture taken in the experiment (Figure 2.9) was selected as a training image, and similar spectral values were assumed for the following images due to the controlled conditions of the greenhouse. This procedure was chosen to reduce the number of supervised processes in sampling subsequent images in order to test the robustness of the method. Three samples of each class $k = 1, 2, 3, 4$ – background, green plant, soil, and stalk (Figure 2.9) – were manually selected and served as references for their respective class. Each sample included rectangular areas of representative pixels.

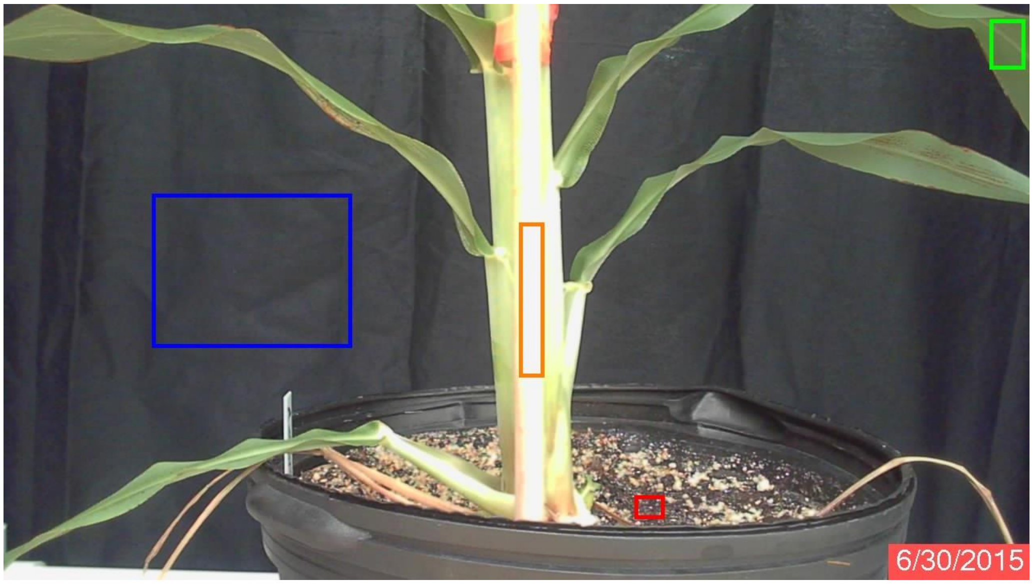

Figure 2.9 Sorghum plant image, corresponding to Plant A1 on June 30. The colored rectangles enclose the approximate locations where the samples were taken. The color samples correspondence are blue = background, orange = bright stalk, green = plant leaf, and red = soil.

Figures 2.10 and 2.11 show the distribution of pixel values with RGB frequency histograms that plot the number of pixels *vs.* color intensity, along with corresponding means and standard deviations (for scripts, see Appendix B.1 and B.2). For each sample class, a vector of RGB intensity means and a vector of standard deviations, denoted as $m_k \in \mathbb{R}^3$ and $s_k \in \mathbb{R}^3$, respectively, were computed and used for comparison with the pixels of other images. For classification, each image pixel $p_{ij} \in \mathbb{R}^3$ was compared against the four vectors of sample means m_k and classified to the corresponding class with the shortest Euclidian distance. However, a distance of two standard deviations of the maximum value of the three RGB elements of s_k was defined as a threshold to assign a pixel to an "unknown" category. Also, the minimum and the average of s_k were computed for each class, but a visually better image classification was obtained when the maximum value of s_k was used. So, if the minimum distance was

$$d_{min} = \left\| m_k - p_{ij} \right\| \geq 2 \max s_k \in \mathbb{R},$$

a new pixel $p_{ij} = 0$ was assigned to "unknown". If otherwise, $d_{min} < 2 \max s_k$, then the pixel $p_{ij} \in \mathbb{R}^3$ was converted to a new pixel $pij = \frac{k}{N} \in (0, 1]$, belonging to class k. For this case, $N = 4$ was the number of classes defined. Therefore, an "unknown" class and four defined classes were considered, so the classified images had five possible brightness values of 0.00, 0.25, 0.50, 0.75, and 1.00. Algorithm 1 shows the minimum distance classification implementation (see also the minimum distance coding for MATLAB® in Appendix B.3).

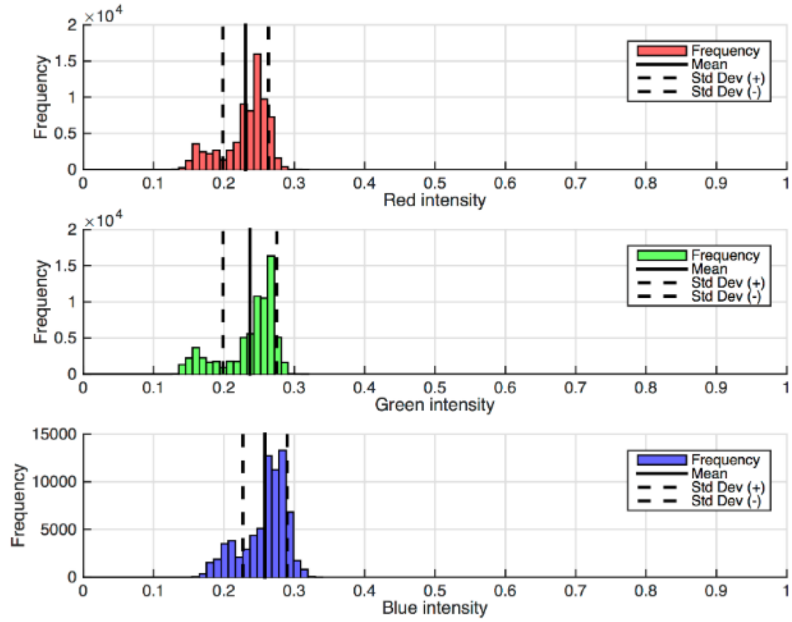

(a)

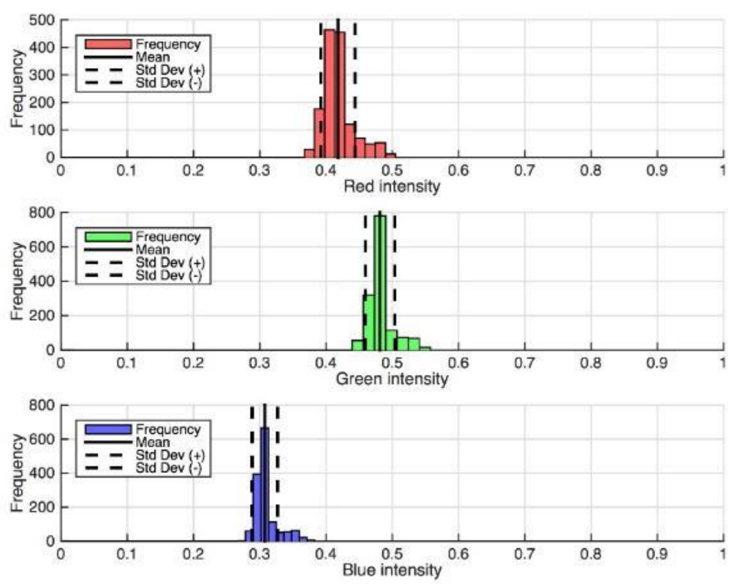

(b)

Figure 2.10 Frequency histograms of the RGB values of the training samples corresponding to background and plant leaf. A vertical solid line at each histogram indicates the location of the mean, while a vertical dashed line indicates the location at two times the standard deviation. The histograms correspond to (a) background, and (b) plant leaf.

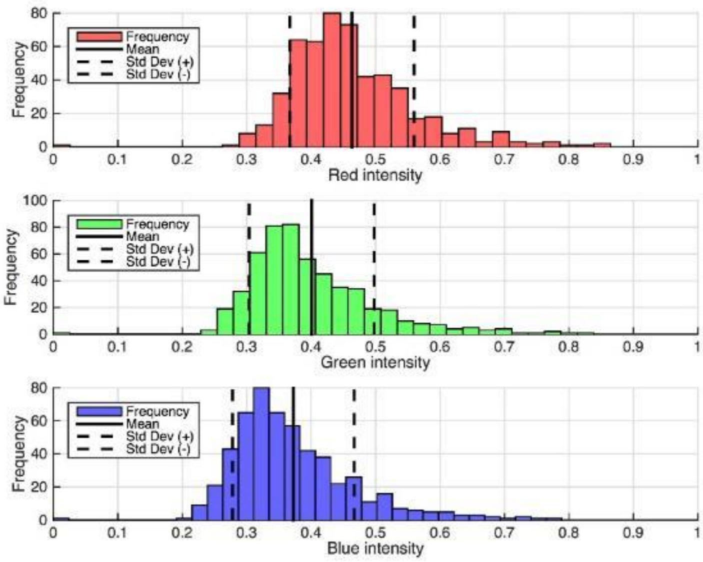

(c)

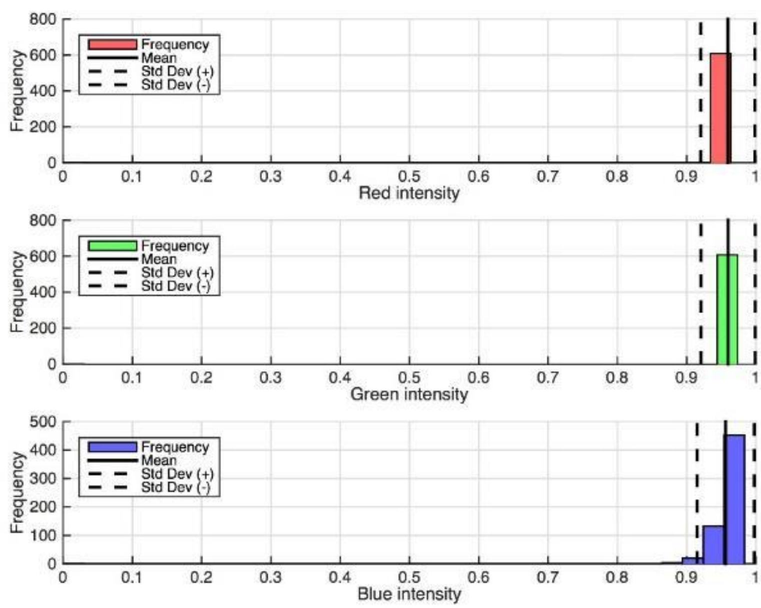

(d)

Figure 2.11 Frequency histograms of the RGB values of the training samples corresponding to soil and bright stalk. A vertical solid line at each histogram indicates the location of the mean, while a vertical dashed line indicates the location at two times the standard deviation. The histograms correspond to (c) soil, and (d) bright stalk.

Data: Input RGB image, $(A)_{ij}$
Result: Output classified image, $(B)_{ij}$
initialization with $(B)_{ij}$ as a matrix of zeros;
for $i = 1$ *to* m **do**
  for $j = 1$ *to* n **do**
    for $t = 1$ *to* N **do**
      $d_{\min} = D_t$;
      for $k = 1$ *to* N **do**
        if $||\boldsymbol{m}_k - \boldsymbol{p}_{ij}|| < d_{min}$ **then**
          $d_{\min} = ||\boldsymbol{m}_k - \boldsymbol{p}_{ij}||$;
          $(B)_{ij} = k/N$;
        end
      end
    end
  end
end

Algorithm 1. Minimum distance classification. Where $(A)_{i,j}$ is a matrix containing the original RGB values; while $(B)_{i,j}$ is the classified image with new pixel values in gray scale (script in Appendix B.3).

After classification, a post classification was performed by combining stalk, leaf, and unknown as plant, while background and soil were combined as background. The steps of the classification process are shown in Figure 2.12.

Figure 2.12 Original RGB, minimum distance classified with five classes, and binary images of the sorghum plant A1. RGB image taken on 30 June 2015,during the third week of growth.

2.5.3. K-means Clustering Image Classification for the Greenhouse Images

The *k*-means clustering algorithm groups *n*-dimensional points in an image into *k* clusters or classes. An *n*-dimensional center point is estimated to define each cluster; then, each *n*-dimensional point in the image is assigned to the closest center point and associated cluster. Once all points in the image are classified, *k* new center points are computed from the *k* cluster means, and an iterative process is performed until the resulting classification is satisfactory to the user, usually defined by some maximum number of iterations or some minimal change per iteration (Corke, 2011). For this image classification process, the points were 3-dimensional pixels, corresponding to points in the RGB images, and the *k*-means algorithm used was adapted from Peter Corke's Computer Vision library, which receives an RGB image, the user-selected *k* number of clusters and the allowed number of iterations. The algorithm maps each pixel RGB value into *xy*-chromaticity coordinates, then it randomly (or according to user input) locates the *k* cluster centers to later compute the Euclidian distances of each pixel against the *k* center points, choosing the smallest distance as an indication of cluster membership. Finally, the algorithm stops the iterative process when it reaches a prescribed number of iterations and gives an output image classified with *k* classes.

Each sorghum plant image was classified into ten spectral classes. From a sample of ten images; the user visually inspected the five classes that almost exclusively contained plant matter. The center points (means) of these five were stored in a text file for later use as input for classifying the image into only five classes. After classification, a process of noise removal and consolidation was implemented including morphological opening with a 9×9 kernel and class combination to achieve two image classes of plant and background. The binary image was then post-processed with area opening to remove small artifacts, and finally morphological closing with a 5×5 kernel was performed to attenuate apparent plant lesions and small stalk deformities (Batz, et al, 2016).

2.5.4. Stalk Thickness Estimation and Calibration in Images of the Greenhouse

“Single-window” and “double-window” algorithm modes were implemented to estimate stalk thickness. In single-window mode, the user identified the stalk and manually picked its center by clicking on the image. Then, a sweep of a 3×3-pixel window automatically searched for the stalk edges, moving horizontally from the stalk center. The width in pixels was computed by subtracting the left edge coordinate from the right edge coordinate. In double-window mode, the user again identified the stalk center, but this algorithm identified upper and lower bounds (16 pixels from the center each) to compute the stalk thickness, averaging the upper and lower coordinates of the right and the left stalk edges and then calculating the difference between the right and left averages.

For calibration, a conversion factor was developed by imaging a 47.6 mm PVC pipe at different distances. Figure 2.13 shows the regression line relating the number of pixels associated with the external diameter of the pipe to depth. As expected, the plot shows that the conversion factor increases linearly from a value close to 0.0 mm/pixel up to a value close to 1.0 mm/pixel for depth values ranging from 0 to 100 cm. The linear equation was then

$$f = 0.0098\, d - 0.0097, \tag{2.1}$$

where f is the conversion factor in mm/pixel, and d is the depth in cm from the camera to the center of the sorghum stalk. In this way, a correlation between the size of a stalk and its distance to the camera was determined by estimating the pixel size at a specific distance. For the PVC pipe, equation 3.1 had an adjusted coefficient of determination $R^2 = 0.997$ and $RMSE = 0.013$. See Appendix B.4 for script details.

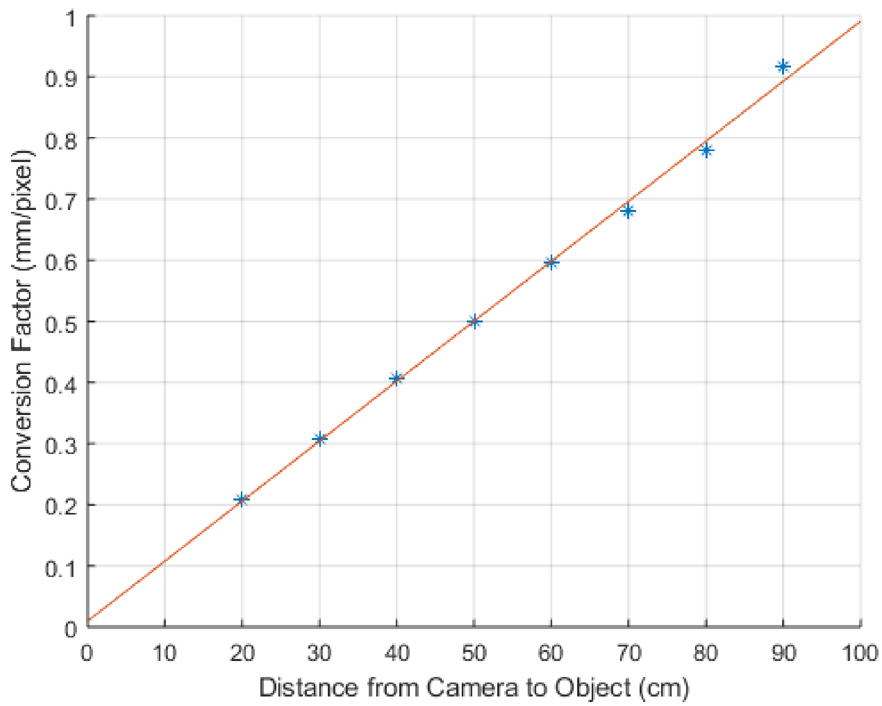

Figure 2.13 Linear regression for depth measurements calibration. Caliper measurements of a PVC pipe divided by its width in number of pixels *vs.* the camera distance computed by its IR sensor.

2.5.5. Depth from Camera to Stalks in the Greenhouse

For every sorghum-plant image collected in the greenhouse, a manual measurement of the distance between the camera and the plant stalk was recorded to the nearest half centimeter with an aluminum ruler. These distances were taken to validate the depth measurement precision of the IR depth camera. Since the IR depth camera images presented some erroneous depth values, 3 × 3 depth-pixel windows of two representative stalk areas were used. The average of the 18 depth values was used as the camera's measured distance between camera and stalk. The computed depth distances were compared to the manual measurements with linear regression (see Appendix B.5).

2.5.6. Geometry of Stereo Vision for Stalk Estimation in the Field

The depth camera used in the greenhouse employs an infrared laser to measure depth, but solar radiation can interfere with depth detection. Therefore, a stereovision camera was used to measure the depth from the camera to the stalks in the field experiment, enabling better estimation of stalk diameter in sorghum plants in the field.

A single camera image is a two-dimensional (2D) projection of an original three-dimensional (3D) scene. In the projection, the depth dimension is lost. However, the 3D information can be recovered if at least two images contain the same scene viewed from two different perspectives; then a 3D reconstruction can be performed by triangulation. A simplified stereovision scenario, with two central-projection camera models (Corke, 2011) is shown in Figure 2.14, where point P is viewed in two distinct image planes. By projecting rays from point P to the frames Σ_l and Σ_r, it is possible to find intersections p_1 and p_2 with the two image planes. Assuming that both image planes are coplanar and share the same focal length, the depth information can be easily retrieved by using similar triangles. Thus, for the left camera $X/Z = x_1/f$, while for the right camera $(X - b)/Z = x_2/f$; where X and Z are distances measured in the world coordinate frame in their respective directions x_w and z_w, x_1 is the distance measured from the local left coordinate frame Σ_l in the x_l direction, x_2 is the distance measured from the local right coordinate frame Σ_r in the x_r direction, f is the focal length, and b is the baseline between cameras. Now, by solving for X in both triangular relationships, and substituting the values of X, the resulting relationship is

$$\frac{Zx_1}{f} = \frac{Zx_2}{f} + b.$$

Finally, by solving for Z, the depth information is recovered as

$$Z = \frac{bf}{x_1 - x_2},$$

and X can be solved by substituting the Z value in any of the two triangular relationships.

Note that the denominator is the disparity between images, which is the difference of a horizontal distance of the projected points p_1 and p_2, and it is usually computed from stereo images, and expressed in pixel values as $u_1 - u_2$. However, in the actual image application, it is common to have a disparity map that shows the pixel differences for all the pixels in the image. For this experiment, the disparity maps were computed with the MATLAB® Computer Vision System and Image Processing toolboxes, assuming rectified images. Then the disparity maps expressed in pixel values were converted to real world coordinate depth values, expressed in millimeters for the purpose of measuring and comparing stalk thickness values with hand measurements made with calipers.

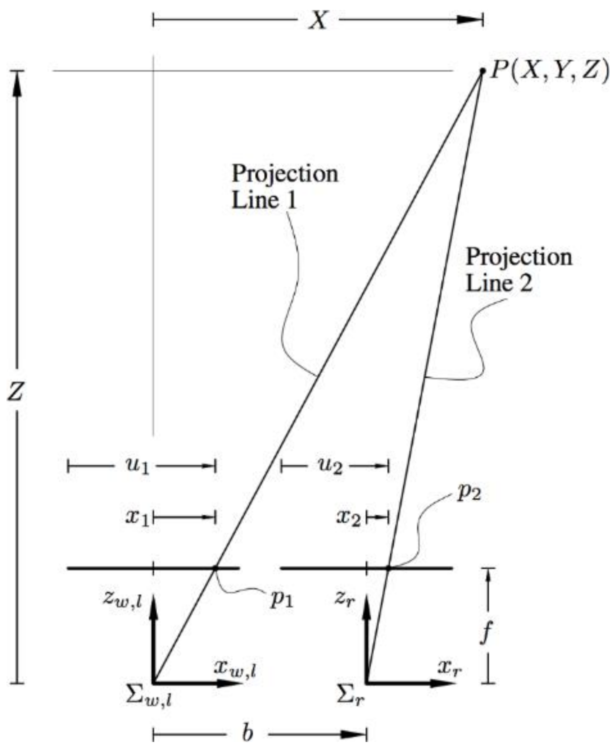

Figure 2.14 Stereovision geometry using two-dimensional central projection camera models.

2.5.7. Video Reading, Storage, and Image Extraction for Stalk Estimation in the Field

The video for Variety A was read and stored as an object variable with a script code in MATLAB® (see 'video_reader.m' in Appendix B.8). From the video object, it was possible to manually explore each image (frame) individually. Visual inspection was the means to detect and record the frame numbers of images where labeled sorghum stalks were clearly seen without being occluded by other plants. For each of these images, a disparity map was computed with the disparity function of the Computer Vision Toolbox in MATLAB®. Of the two possible methods of this disparity function, block matching was preferred over semi-global, because block matching can compute disparities with a smaller root mean square error (*RMSE*) and achieve pixel matching percentages above 87% on Brodatz's textured images (Sabater, et al, 2011). Block matching parameters were left as default, because trial and error tests showed visual similarity between disparity maps generated with various combinations of parameter values. Default parameters were block size = 15 pixels; contrast threshold = 0.5, a scalar value within the (0, 1] interval, defining the acceptable range of contrast values (increasing this parameter results in fewer pixels being marked as unreliable); a uniqueness threshold = 15, a non-negative integer defining the minimum value of uniqueness; distance threshold = [] (disabled), a non-negative integer of the maximum distance for left-right checking; and texture threshold = 0.0002, a scalar within the [0, 1) interval, defining the minimum texture. More detailed information can be found in the MATLAB® help for the disparity map function or in the Appendix B.17.

2.5.8. Supervised Stalk Identification and Thickness Estimation for the Field Images

As the stereo camera baseline and focal length were known, a depth map image containing depth values in millimeters was computed with the following formula

$$D_{ij} = \frac{bf}{DM_{ij}};$$

where $D \in \mathbb{R}^{m \times n}$ is the depth map matrix expressed in mm, $b \in \mathbb{R}$ is the baseline distance between image sensors expressed in mm (b = 30 mm), $f \in \mathbb{R}$ is the focal length expressed in pixels (350 pixels = 2.1 mm), $DM \in \mathbb{R}^{m \times n}$ is the disparity map matrix of the left image expressed in pixels, $m \times n$ is the pixel size (dimension) of the image, and the subindices i and j denote the corresponding row and column position of the ij element of each matrix.

Then the depth map matrix was expressed as a gray-scale image and overlaid with the leftward gray-scale image to create a two-band false color image. Two image points were selected on this false color image with the mouse pointer, locating the left and right sides of a sorghum stalk at approximately the same location as the caliper measurement, a method that follows a similar approach to the DenS-Di method (Salas-Fernandez et al., 2017). The false color image was used to aid in locating these points on homogeneous colors on the stalk to obtain consistent depth values.

Then the pixel values from the two image points were mapped into world coordinate system units (mm) with the procedure explained in Subsection 2.5.6 and implemented in the MATLAB® script 'wcsys.m' (Appendix B.9). The Euclidian distance between them was then computed with the script 'euclidian.m' (Appendix B.10) and displayed over the left image with the script 'imagediam.m' (Appendix B.11), which also shows the image coordinates of the two points selected along with their corresponding world coordinates. A difference in depth of 20 mm between the left and right points used to estimate thickness was considered a maximum to allow reliable selection of the points. This value was selected as follows. A sorghum stalk cross-section was approximated as an ellipse (Figure 2.15), and an average of all measured plants suggested the minor axis could be assumed to be 25.6 mm and the major axis 1.32 times greater and, in the worst case, rotated 60° with respect to the horizontal. Thus, if the depth difference was greater than 20 mm (see Figure 2.15) due to an abrupt change in depth values (Figure 2.16), the points were assumed to be not on the same stalk, so the user had the option to repeat the point selection process until obtaining a smaller depth difference value. After point selection, the image number (video frame), pixel coordinates (rounded up to the next integer), and real world coordinates in mm, were stored in a new line of a text file. Each line of the text file was used as input to a custom computer script that automatically generated a left image with all the thickness estimation and coordinate data overlaid. This process was performed on those images where a clear and non-occluded sorghum stalk with a paper label (Subsection 2.7.2) was visually identified. The process of displaying, selecting, and storing these image points was aided by the script 'point_identification_gui.m' (Appendix B.12).

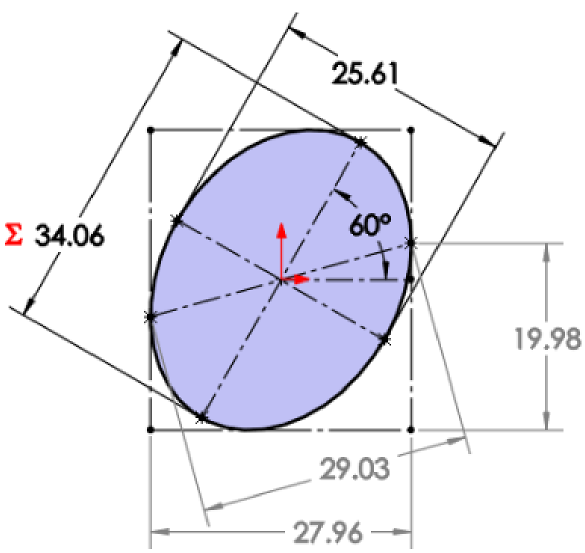

Figure 2.15 Sorghum cross-section approximated to an ellipse.

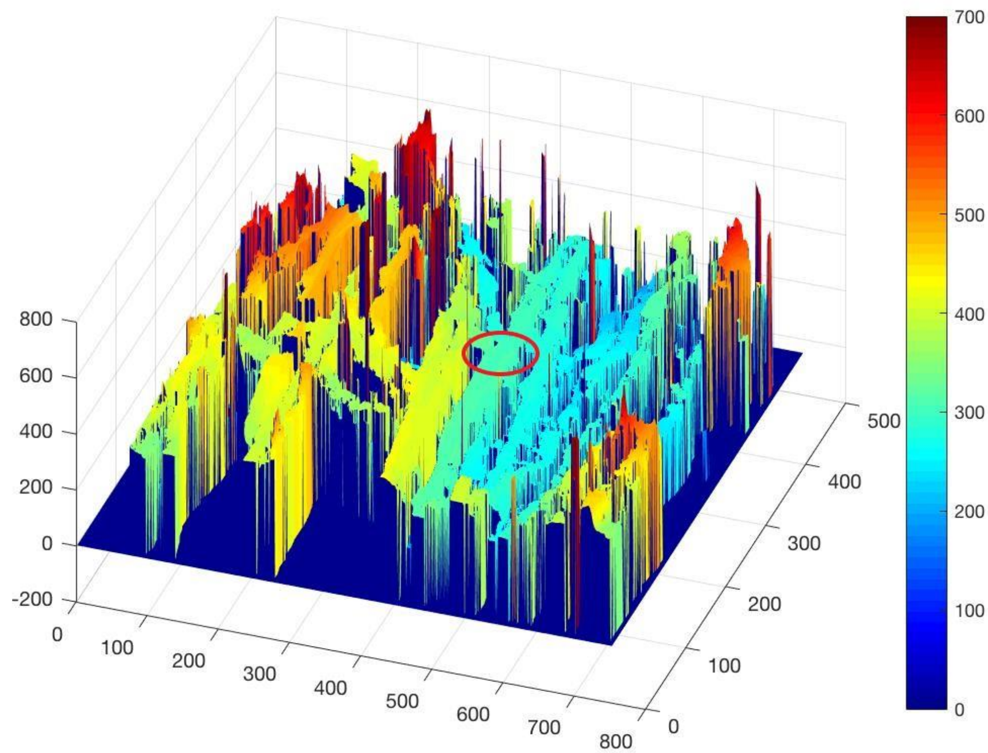

Figure 2.16 Depth map of the left image on Plant A1. The red circle shows the abrupt depth value changes in the limits of the stalk with the blue background. The vertical axis and colored scale show depth values in millimeters, while the other two axes show pixel units.

A total of 100 images (video frames) were identified in the video, and the text file containing the image number and the pixel coordinates were used to estimate the stalk thickness in each image. The results of the estimation were overlaid with text on the corresponding image (left side of the stereo image) with the script 'results_images.m' (Appendix B.13).

To estimate plant leaf angle, three points were selected instead of two. The computation of the angle between two lines formed by the first and second points and second and third points was computed with the formula

$$\theta = \cos^{-1} \frac{\vec{u} \cdot \vec{v}}{||\vec{u}|| \, ||\vec{v}||}$$

where θ is the leaf angle, $\vec{u}$ and $\vec{v} \in R^3$ are vectors of the first and second line, respectively, expressed in mm within the world coordinate system, with respect to the leftward camera. This formula was implemented in 'angle3.m' (Appendix B.14) and displayed on the leftward image of the stereo image pair with 'imageangle.m' (Appendix B.15). Leaf angle estimation was not a critical feature of this research, so no ground truth data were collected for validation.

2.6. Data Collection in the Greenhouse

2.6.1. Imaging Location and Orientation

The data collection was performed on roughly a weekly basis over a period of ten weeks. Due to issues with direct sunlight, image collection events were conducted before noon, and the imaging chamber (described in Subsection 2.3.2) was oriented to avoid IR interference with the depth camera. The eight plants grown in black pots were transported one by one to the imaging chamber (Figure 2.4). According to the recommendations of Dr. William Rooney, Texas A&M University, sorghum stalk diameter and biomass exhibit high correlation if diameter is measured at the third, fifth, or seventh internodes during the later plant growth stages (Rooney, 2015). Thus, the camera and tripod were placed in front of each plant at the height of the third internode. However, at early plant growth stages, the plants did not exhibit visible internodes, so a 7-cm distance above the pot soil was used to measure stalk thickness until approximately the sixth week, when internodes began to be defined. Because sorghum stalks exhibit an approximately elliptical cross-section, all the plants were oriented with their cross-sectional major axis perpendicular to the camera's viewing direction. To keep the same imaging orientation at each data collection visit, a plastic marker was placed in the pot for future placement reference.

2.6.2. IR Camera Settings

The camera was mounted on a conventional tripod (Figure 2.3) and connected to a laptop computer via a USB 2.0 high-speed port, and the RGB and depth images were recorded with Creative Live!® and DepthSense® (SoftKinetic Inc. San Jose, CA, USA) software, respectively. During the first image captures, the resolution of both image types was set to match at 320 × 240 pixels, but the different field of view and offset of the sensors prevented complete image overlap (Figure 2.3). Thus the RGB and IR layers could not be stacked into one composite image with 4 bands, so the IR layer was disregarded for the purposes of measuring stalk thickness with smaller pixels, so the RGB sensor resolution was increased to the maximum resolution of 720 × 1280 for a more precise stalk thickness estimation, working with only RGB bands for image classification.

2.6.3. Diameter and Depth Manual Measurements

For each imaged plant, on each data collection date, the stalk diameter was manually measured with a digital caliper at the plant's major and minor axes at a height of 7 cm during the early growth stages. After the sixth week the manual measurements were taken immediately above third internode. Along with the diameter measurements, the horizontal distance between the camera and the center of each plant stalk was measured with an aluminum ruler and rounded up to the next half centimeter.

2.7. Data Collection in the Field

2.7.1. Stereo Camera Location and Orientation

Following the previously mentioned recommendations of Dr. William Rooney (2015), the stereo camera was placed at 69 cm above ground when data were collected to estimate sorghum stalk thickness (Figure 2.6). The camera was aligned with respect to the furrow valley, i.e. it was offset 38 cm from the plants, and it was oriented perpendicular to the vertical. The stereo camera was attached with the 3D-printed camera case and an aluminum bracket to the right-side frame of the GPV underneath the driver's seat (Figure 2.6).

Figure 2.17 Sorghum plants on 5 August 2016, after taking the video recordings. The plants have labels on them. Plants recorded on videos were those of the fourth row to the right (marked red).

2.7.2. Labels for Sorghum Plants

A total of 100 paper labels were created to tag 100 sorghum plants on Variety A. The labels were 2.3 cm wide and 18.7 cm long, printed with bold Calibri (Body) font size 50. Variety and plant number were repeated five times along the tag to facilitate reading it on the captured video. On August 5, 2016, each label was stapled around a sorghum plant at about 69 cm above the ground in an attempt to place it immediately next to a node. The time to complete the tagging task was around 45 minutes, followed by caliper hand measurements that lasted about 15 minutes. Two people, each with one of the calipers, performed the measurements. One person measured plants A1 to A25 using the analog caliper (CV = 16.8%), while a second person measured plants A26 to A50 with the digital caliper (CV = 15.8%), then the second person measured plants A51 to A75 with the analog caliper (CV = 17.6%), while the first person measured plants A76 to A100 with the digital caliper (CV = 13.9%). The measurements were taken immediately above the tags, in the direction perpendicular to the camera view.

2.7.3. Stereo Camera Video Recording

After tagging, time was spent evaluating camera setting functions in the stereo camera's software package (DUO Dashboard App, DUO3D™ Division, Code Laboratories Inc., Henderson, NV, USA) such as Exposure, that automatically updates the exposure parameters on the camera, resulting in higher exposure; Gain, that automatically updates the gain parameters on the camera, resulting in brighter images; Resolution, that set the image size; and recording speed in frames per second (fps), while keeping other parameters as default. Recording started at 12:30 P.M. on the sunny day of Friday, August 5th, 2016 (Figure 2.17), traveling from NE to SW, and the camera facing to the NW (see Figure 2.1 for orientation). After preliminary visual testing, the camera software was used to set the camera with the following parameters: exposure of 1%, gain of 0%, recording speed of 15 fps, and resolution of 752 × 430 pixels.

2.8. Data Analysis for the Stalk Thickness Estimations

2.8.1. Relative Error Between Caliper and Imaging Measurements

In both greenhouse and field experiments the image stalk thickness estimations were compared to those taken manually with a caliper. The relative error (ε_r) at the i-th data pair was estimated as

$$\varepsilon_{r_i} = \frac{x_i - c_i}{c_i},$$

where x_i is the estimated stalk thickness, and c_i is the manually measured thickness.

2.8.2. Linear Regression

Linear regression was performed, and caliper measurements were plotted against results from each imaging method used to estimate stalk thickness. Coefficient of determination (R^2) and root mean square error (*RMSE*) were computed for each method to determine the methods with the best accuracy.

2.8.3. Residual Analysis, Logarithmic Data Transformation, and Outliers

Once the method with the lowest RMSE was identified, the results with that method were visually interpreted. Some points on the greenhouse-data plots of estimated vs. actual stalk width deviated significantly from the regression line. As a means to identify outliers appropriately, the following procedure (adapted from Neter et al, 1996; and Cline, 2015) was implemented: (1) Residuals were plotted against caliper measurements. (2) The data were observed to be heteroscedastic, so both estimated and caliper data were transformed by taking their logarithms. Log(Caliper) and Log(Estimated) were regressed linearly against each other, and residuals were again plotted against caliper measurements. It was apparent that the log transformation had mitigated the heteroscedasticity. (3) Studentized residuals of the Log-transformed data were calculated, and their distribution was determined. Those data points that were likely outliers (*i.e.*, studentized residual greater than 2.0) were left out of the analysis after visual inspection of the images determined these data points included major sources of measurement error. The studentized residuals were calculated with the following formula:

$$\tilde{\varepsilon}_i = \frac{\hat{\varepsilon}_i}{\hat{\sigma}\sqrt{1 - h_{ii}}} \tag{2.1}$$

where $\tilde{\varepsilon}_i$ is the i-th studentized residual; $\hat{\varepsilon}_i$ is the i-th raw residual; $\hat{\sigma}$ is the sample standard deviation of the set of raw errors; and the h_{ii} is the diagonal element of the *hat matrix* $H = X(X^T X)^{-1} X^T$, where $X \in R^{n\times 2}$ is the *design matrix*, the first column of which has the value 1 in each of its elements, and the second column contains the predicted diameter values.

2.8.4. Confidence Interval for an Individual Response in a Linear Regression

To estimate the confidence interval (*CI*) of any predicted stalk thickness value (*x*), equation (2.2) was used (Cline, 2015):

$$CI = \hat{Y} \pm t_{\alpha/2,\mathrm{df}} \times \sqrt{MS_{Error} + \widehat{SE}(\hat{\mu}_Y(x))^2}, \tag{2.2}$$

where the prediction $\hat{Y}$ is computed from the estimated regression; *t* is the random variable that has Student's *t*-distribution evaluated at a significance level α (typically 0.05) with the degrees of freedom of the error (df); MS_{Error} is the mean square for error, and the estimated standard error, $\widehat{SE}$, is computed with equation (2.3):

$$\widehat{SE}(\hat{\mu}_Y(x)) = \hat{\sigma}\sqrt{\frac{1}{n} + \frac{(x - \bar{X})}{(n-1)S_X^2}}, \tag{2.3}$$

where $\hat{\mu}_Y(x)$ is the estimated average at a value x, found with the regression equation; $\hat{\sigma}$ is the estimated standard deviation of the errors (or *RMSE*), n is the number of sample observations; $\bar{X}$ is the average of the predictor variable; and S_X^2 is the sample variance of the predictor variable.

3. VISION SYSTEMS: RESULTS AND DISCUSSION*

3.1. Stalk Thickness Measurements and Estimations in the Greenhouse

3.1.1. Manual Measurements

The caliper measurements of the major and minor axes (Table 3.1) were recorded, and differences between varieties during the growing season were noted. The average value on the major axis for the entire season was 29.7 mm and 24.4 mm for the minor axis, with an average ratio of 1.21. Both varieties presented higher ratios (Figure 3.1) from June 30 to July 14 (4^{th} to 6^{th} week of growth), averaging 1.32 for Variety A and 1.25 for Variety B. This increased ratio was due to the leaves growing near to the base of the plants that thickened the major axis at early stages.

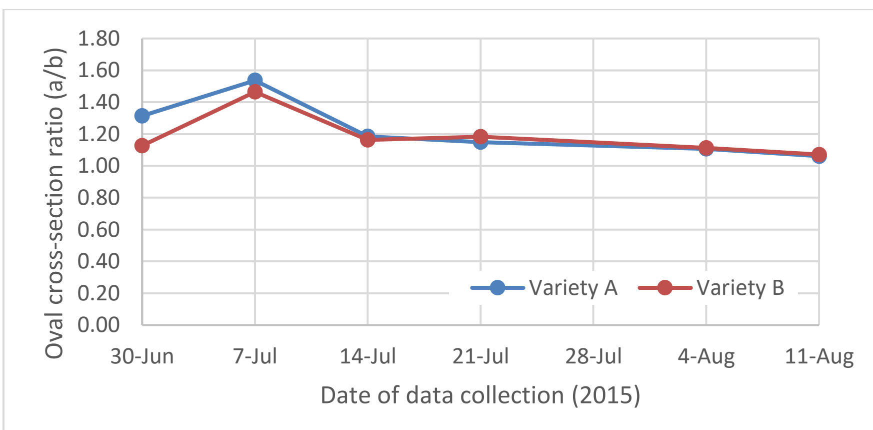

Figure 3.1 Average ratios of major (a) and minor (b) axes per variety of sorghum along the data collection period.

---

* Part of the data reported in this section is reprinted with permission from "Imaging for High-Throughput Phenotyping in Energy Sorghum" by Jose Batz, Mario A. Méndez-Dorado and J. Alex Thomasson, 2016, *Journal of Imaging*, 2 (4), 1-12, Copyright 2016 by MDPI.

Table 3.1 Manual measurements of major and minor axes and their ratio.

Date	Plant ID	Major Axis (mm)	Minor Axis (mm)	Plant Height (cm)	Ratio
30-Jun	1A	32.46	25.58	-	1.27
	2A	33.17	22.08	-	1.50
	3A	30.82	27.08	-	1.14
	4A	32.59	24.23	-	1.35
	1B	29.75	27.84	33	1.07
	2B	28.61	24.89	41	1.15
	3B	29.90	27.76	40	1.08
	4B	25.62	21.14	31	1.21
7-Jul	1A	40.81	28.13	38	1.45
	2A	48.14	25.98	38	1.85
	3A	34.91	28.61	38	1.22
	4A	44.34	27.35	36	1.62
	1B	38.35	26.04	57	1.47
	2B	32.73	26.12	79	1.25
	3B	38.23	29.09	81	1.31
	4B	47.65	26.21	76	1.82
14-Jul	1A	36.54	30.61	73	1.19
	2A	36.04	28.72	78	1.25
	3A	35.38	30.31	69	1.17
	4A	33.68	29.93	63	1.13
	1B	36.68	28.38	123	1.29
	2B	34.51	32.29	124	1.07
	3B	25.19	22.22	150	1.13
	4B	37.28	32.25	156	1.16
21-Jul	1A	20.45	19.67	106	1.04
	2A	25.51	23.29	100	1.10
	3A	25.17	22.29	100	1.13
	4A	34.26	25.70	97	1.33
	1B	21.01	19.25	183	1.09
	2B	24.75	21.60	157	1.15
	3B	25.70	21.67	208	1.19
	4B	29.97	22.89	218	1.31
4-Aug	1A	21.01	19.92	140	1.05
	2A	25.22	22.50	146	1.12
	3A	25.58	22.39	152	1.14
	4A	27.03	24.34	145	1.11
	1B	20.45	18.50	300	1.11
	2B	23.02	22.93	350	1.00
	3B	22.26	20.36	350	1.09
	4B	26.22	21.00	400	1.25
11-Aug	1A	24.23	23.99	152	1.01
	2A	25.23	24.00	164	1.05
	3A	24.25	22.05	169	1.10
	4A	26.13	24.11	155	1.08
	1B	19.14	17.57	350	1.09
	2B	20.31	18.75	300	1.08
	3B	21.19	21.06	400	1.01
	4B	21.68	19.59	450	1.11

3.1.2. Image Classification

Two subsets of images classified with the minimum-distance method are shown in Figures 3.2 and 3.3 as samples of image-classification results. For visual comparison, both sets of images include the original RGB image, the classified image with five classes, and the post processed binary image that isolates plants from the rest of the scene. The classified images have a color code corresponding to the pixel sampling described previously in Subsection 2.5.2 and are defined as follows: green = fresh leaf, yellow = bright stalk, red = soil, blue = background, and black = unknown; while the binary images show sorghum plants in green and everything else in blue. With a representative image for each date, the first subset (Figure 3.2) contains the classified images for which the thickness estimations were the closest to the hand measurements. Similarly, the second subset (Figure 3.3) shows the images for which the most inaccurate estimations from the hand measurements were found. The remaining classified images are shown in Appendix C.

In general, the resulting binary images in Figures 3.2 and 3.3 show the ability to classify plants from the rest of the objects in the scenes, but some portions of soil, plastic pots and PVC frame were occasionally misclassified as plant. In the case of soil, the misclassification probably was due to its texture and spectral heterogeneity, difficult to represent with the rectangular sampling method used and the nature of the classification technique that works better with normally distributed samples; the distribution of pixels of soil samples (Figure 2.11c) had heavy tails to the right. In the case of bright stalks, Figure 2.11d shows pixel values close to 1.0, similar to those of the PVC pipes, meaning PVC pipes are sometimes misclassified as sorghum stalks. Even though these

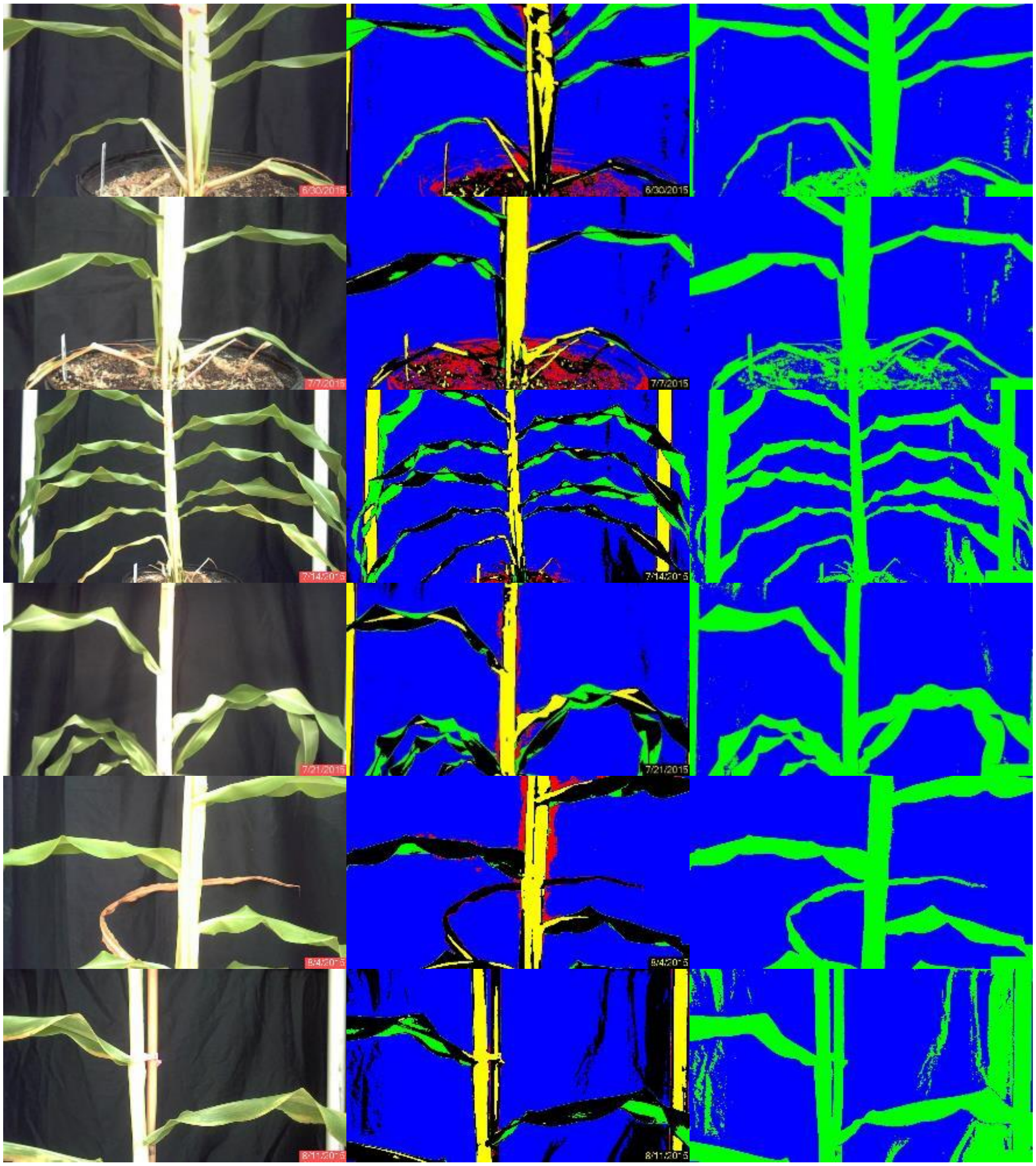

Figure 3.2 Minimum distance classified images selected according to the most accurate stalk diameter estimation per date. From top to bottom, plants 1B, 3B, 2B, 3A, 4A, and 2B, corresponding to the dates 6/30/15, 7/7/15, 7/14/15, 7/21/15, 8/4/15, and 8/11/15, respectively.

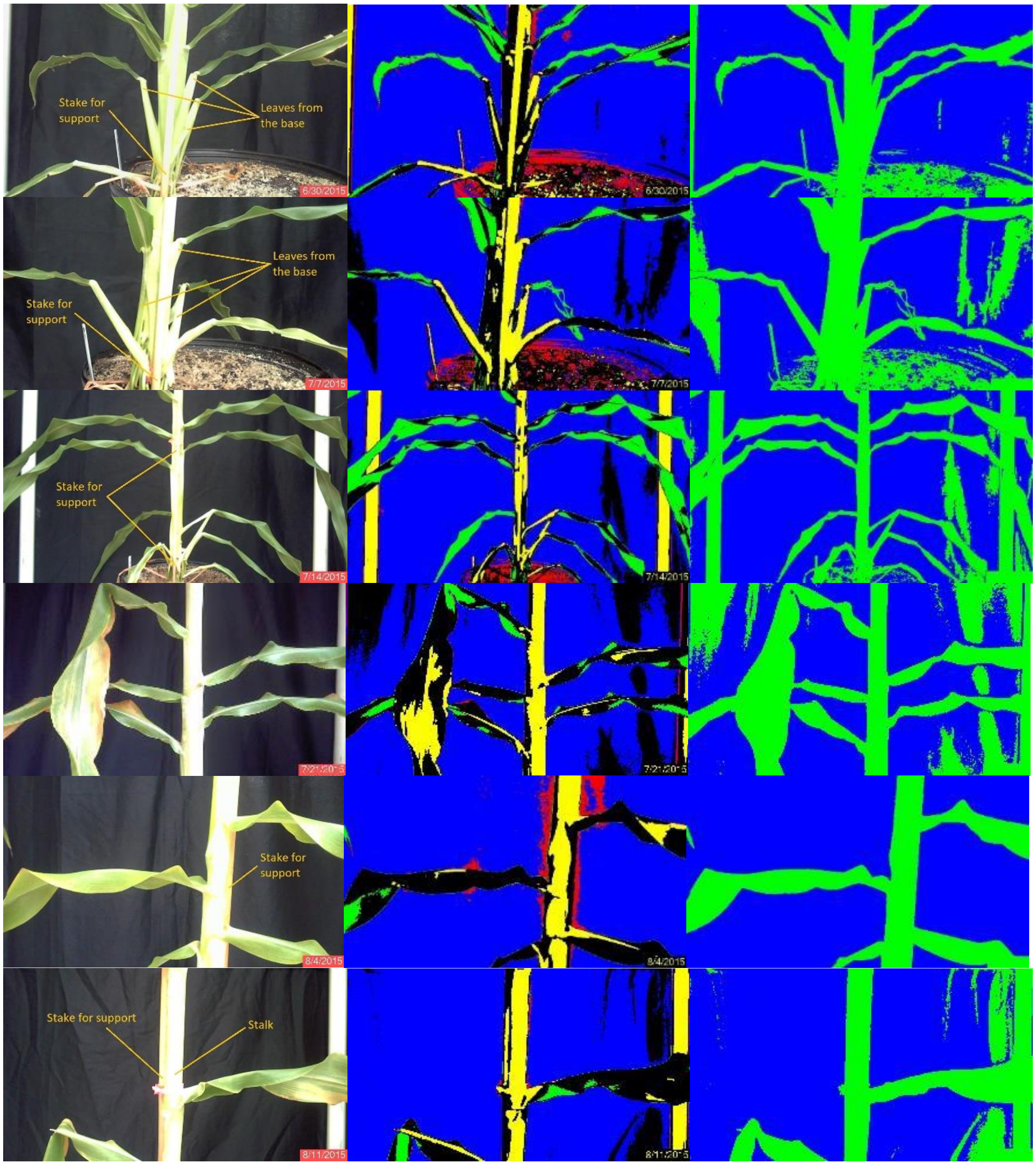

Figure 3.3 Minimum distance classified images selected according to the least accurate stalk diameter estimation per date. From top to bottom, plants 4B, 4B, 3B, 3B, 2B, and 3B, corresponding to the dates 6/30/15, 7/7/15, 7/14/15, 7/21/15, 8/4/15, and 8/11/15, respectively.

misclassifications were present, they did not affect the middle section of the scenes where the stalk needs to be differentiated clearly, and where manual pointer selection was performed to estimate the stalk thickness.

By visual inspection of Figure 3.2, it is noticeable that the best classified images were those of plants that had a well-differentiated stalk. In comparison, the images of Figure 3.3 exhibited occluded stalks due to multiple leaves coming from the stalk base or added width due to supporting stakes and had the most erroneous stalk thickness estimations, especially at the earlier dates of June 30, and July 7, 2015. Denser and widely open leaves at early stages seems to be a phenotype expression of Variety B, since mainly this variety presented difficulty in measuring the stalk and it had the four most erroneous estimations.

3.1.3. Depth Camera Accuracy

Table 3.2 shows the depths measured from the camera to the center of the sorghum stalks. As a means to judge depth camera accuracy, a linear regression shown in Figure 3.4a compares the manual measurements to the estimations by the IR camera, displaying a linear correlation with an adjusted $R^2 = 0.876$ and $RMSE = 4.53$ cm. After visual inspection of the graph, it was seen that two data points corresponding to plants 1A and 3B on July 7 and 21, respectively, displayed a considerable difference from the trend in the rest of the data. The camera-plant distance value for plant A1 on July 7 was measured as 60.0 cm *vs.* an estimated ToF distance of 45.8 cm; for plant 3B on 21 July, the measured value was 61.0 cm *vs.* a ToF value of 46.6 cm (see Table 3.2). These two data points were determined to be outliers according to equation (2.2), and it is likely a transcription mistake was made when recording the values in a notebook (Heiberger, R.M., 2015). A second linear regression after removing the outliers is shown in Figure 3.4b and had an adjusted R^2 = 0.978 and *RMSE* = 1.97 cm. For script details see Appendix B.5.

3.1.4. Stalk Thickness Analysis

Stalk thickness estimations from image analysis were compared with the caliper hand measurements. Table 3.2 shows the caliper-measured values (CAL), and the estimated stalk diameters based on the four imaging methods used as well as percent relative errors (absolute values) during eight weeks of the growing season. Diameters in pixel units obtained from the four image methods were multiplied by the conversion factor from equation (2.1), and the estimates were reported in millimeters (Figure 2.13). Averaging relative errors per method, the values obtained were 27.9% for K-means with double-window stalk thickness estimation (KMD), 19.5% for minimum distance with double-window stalk thickness estimation (MDD), 16.0% for K-means with single-window stalk thickness estimation (KMS), and 16.7% for minimum distance with single-window stalk thickness estimation (MDS). Based on the percent relative error, KMS represents the best imaging method among the four for estimating stalk thickness.

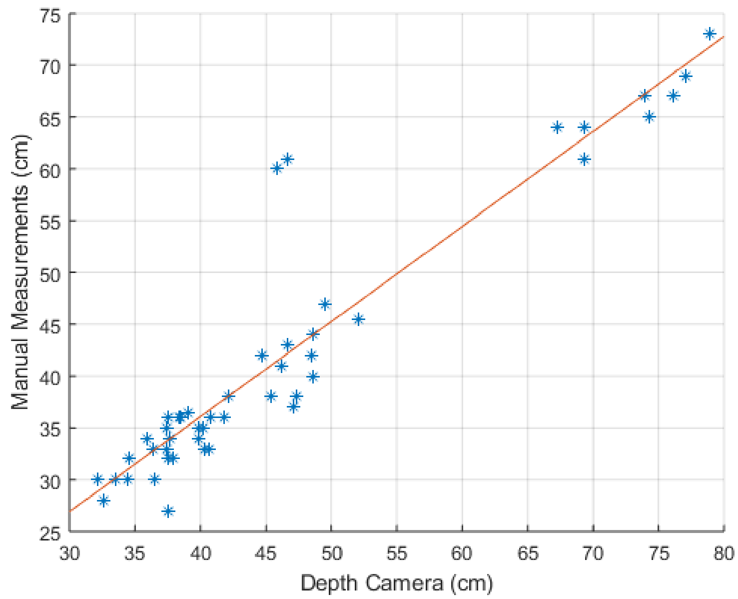

(a)

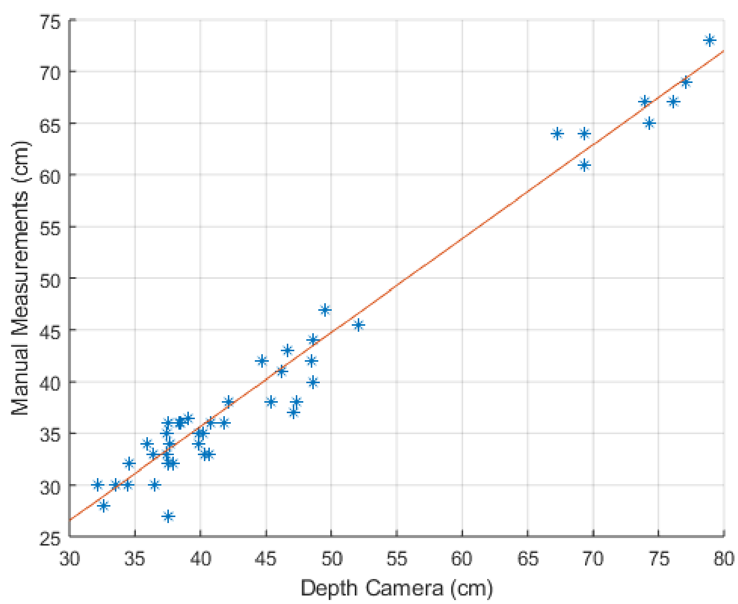

(b)

Figure 3.4 Linear regressions for depth distances of manual measurements *vs.* IR camera values. (a) Regression with all the depth values of the dataset, and (b) regression without the two outliers corresponding to plants 1A and 3B of 7 and 21 of July.

Figure 3.5a shows a scatter plot of the CAL measurements versus KMS estimations and a linear regression with a coefficient of determination of $R^2 = 0.28$, which means that KMS accounts only a 28% of the variability in the caliper measurements, while the linear fit has an $RMSE$ = 6.27 mm. Figure 3.5b shows a scatter plot of the CAL measurements versus KMS estimation with no outliers. A detailed inspection of Figure 3.5a showed that some data pairs might be outliers; thus, the additional scatter plot of the residuals (row error) of Figure 3.6a was performed to observed heteroscedasticity and later apply the method described earlier in subsection 2.8.3. The outliers were identified to correspond to plants 4B of 7 July (Figure 3.3), this mainly due to multiple leaves coming from the stalk base, and 1A, 3B and 4B of 21 July (Figures 3.3 and C.4), due to supporting stakes that are close to the plant stalks.

Additionally, pair values from rows 10 to 13 of Table 3.2, corresponding to plants 2A, 3A, 4A, and 1B of 7 July were identified as outliers by the studentized residual analysis, and it was clear that these plant stalks were not well defined in the images due to multiple leaves coming from the base of those plants (Figure C.2). These data points were left out of the final analysis because the leaves of these plants occluded the stalks at the fourth week of growing season, suggesting that image-based measurements may be particularly error-prone at certain growing stages.

All the removed outliers and values, which belonged to occluded stalks, are indicated in bold in Table 3.2. Thus, a linear regression of the new dataset was performed and shown in Figure 3.5b, resulting in a better fit with a coefficient of determination R^2 = 0.70, meaning that KMS estimations accounted for 70% of the caliper measurements' variability, with an *RMSE* = 3.19 mm. The new residuals versus caliper measurements without outliers are also shown in Figure 3.6b, where heteroscedasticity is seen to be mitigated. From this last residual analysis, a general overestimation in the stalk thickness by KMS is evident, as the residuals were defined as the difference between caliper measurements and the estimations by the linear regression. For more information about the script details, see Appendix B.6.

As a general result, individual stalk estimates were found to have a mean bias of 1.3 mm, relative to the average caliper measurements (27.8 mm), and a 95% confidence interval of 29.1±6.5 mm, as computed with equation (2.2).

Table 3.2 Measured stalk thickness with caliper and camera-stalk distance with ruler; and estimated thickness and error by method. Notes: *the best estimate of the corresponding date, **the worst estimate of the corresponding date for KMS, and outliers are in bolds.

	Plant	**Caliper Reading**	**Estimated Value (mm)**				**Percent Relative Error (%)**				**Depth (cm)**	
Date	**ID**	**(mm)**	**KMD**	**MDD**	**KMS**	**MDS**	**KMD**	**MDD**	**KMS**	**MDS**	**Ruler**	**IR Camera**
30-Jun	1A	25.58	24.12	32.27	28.47	27.47	5.71	26.17	11.29	7.41	36.0	37.5
	2A	33.17	28.96	40.13	30.15	29.18	12.69	20.98	9.12	12.04	42.0	44.7
	3A	30.82	31.18	31.41	28.25	26.88	1.17	1.91	8.32	12.77	30.0	32.1
	4A	32.59	35.75	35.11	32.85	27.31	9.70	7.74	0.80	16.20	34.0	35.9
*	1B	29.75	21.84	30.62	29.65	31.45	26.59	2.92	0.35	5.70	36.0	38.4
	2B	28.61	27.57	37.41	34.60	32.96	3.64	30.78	20.95	15.19	42.0	44.7
	3B	27.76	21.65	26.22	27.49	25.36	22.01	5.56	0.96	8.65	36.5	39.0
**	4B	25.62	60.49	39.14	32.77	26.98	136.10	52.79	27.90	5.29	32.0	34.5
7-Jul	1A	40.81	19.07	58.85	45.05	49.09	53.27	44.20	10.38	20.28	60.0	45.8
	2A	48.14	34.41	41.70	36.72	38.83	28.52	13.38	23.73	19.34	45.5	52.1
	3A	34.91	20.73	35.05	26.69	26.85	40.62	0.40	23.55	23.08	35.0	40.2
	4A	44.34	29.50	36.88	33.76	34.52	33.47	16.82	23.86	22.15	41.0	46.2
	1B	38.35	15.44	31.84	26.24	29.48	59.74	16.97	31.58	23.13	38.0	45.4
	2B	32.73	21.52	32.23	31.33	29.43	34.25	1.51	4.29	10.07	33.0	40.6
*	3B	29.09	25.07	30.90	27.86	30.43	13.82	6.22	4.23	4.61	34.0	37.7
**	**4B**	47.65	20.16	28.48	28.80	29.31	57.69	40.23	39.56	38.49	28.0	32.6
14-Jul	1A	36.54	35.44	34.25	38.05	32.10	3.01	6.27	4.13	12.16	64.0	67.3
	2A	36.04	40.80	40.50	34.42	32.92	13.21	12.38	4.51	8.64	64.0	69.4
	3A	35.38	41.10	41.98	37.50	36.87	16.17	18.65	5.99	4.22	61.0	69.3
	4A	33.68	41.59	35.09	37.14	36.47	23.49	4.20	10.27	8.29	65.0	74.3
	1B	36.68	35.40	36.81	32.76	31.55	3.49	0.37	10.69	14.00	67.0	74.0
*	2B	34.51	31.20	36.08	34.98	35.55	9.59	4.54	1.36	3.00	73.0	78.9
**	3B	22.22	35.39	38.57	29.83	30.71	59.27	73.59	34.23	38.23	69.0	77.1
	4B	37.28	44.04	34.63	34.32	31.37	18.13	7.11	7.94	15.85	67.0	76.1
21-Jul	**1A**	20.45	28.60	31.55	32.77	31.88	39.85	54.29	60.24	55.91	43.0	46.7
	2A	25.51	22.77	25.98	27.00	26.77	10.74	1.84	5.82	4.94	44.0	48.6
*	3A	25.17	24.36	26.34	24.41	24.77	3.22	4.65	3.04	1.59	47.0	49.5
	4A	34.26	31.41	32.74	32.10	32.20	8.32	4.43	6.32	6.01	42.0	48.5
	1B	21.01	16.10	57.74	18.67	17.11	23.37	174.8	11.16	18.58	38.0	47.3
	2B	24.75	37.99	25.20	26.23	27.25	53.49	1.83	5.98	10.11	40.0	48.6
**	**3B**	25.70	43.96	39.39	44.28	44.75	71.05	53.28	72.30	74.13	61.0	46.6
	4B	22.89	37.24	36.41	38.16	38.99	62.69	59.07	66.71	70.32	36.0	40.8
4-Aug	1A	21.01	24.12	23.31	24.66	23.14	14.80	10.97	17.35	10.12	35.0	39.8
	2A	25.22	28.96	29.13	32.09	32.09	14.83	15.50	27.24	27.24	36.0	38.5
*	3A	25.58	31.18	26.33	27.66	26.99	21.89	2.94	8.13	5.51	33.0	37.4
	4A	27.03	35.75	24.83	29.06	29.70	32.26	8.15	7.49	9.88	36.0	41.8
	1B	20.45	21.84	21.55	23.79	23.54	6.80	5.39	16.31	15.11	32.0	37.6
**	2B	23.02	27.57	27.43	30.18	30.48	19.77	19.17	31.08	32.41	30.0	36.5
	3B	22.26	21.65	21.28	24.46	25.90	2.74	4.42	9.88	16.33	27.0	37.5
	4B	26.22	60.49	22.49	24.16	24.31	130.70	14.21	7.88	7.29	30.0	33.5
11-Aug	1A	24.23	19.07	23.31	23.55	23.64	21.30	3.78	2.83	2.42	37.0	47.1
	2A	25.23	34.41	29.13	29.12	27.96	36.39	15.46	15.42	10.81	35.0	37.4
	3A	24.25	20.73	26.33	22.87	21.86	14.52	8.59	5.69	9.86	33.0	36.4
	4A	26.13	29.50	24.83	31.99	30.26	12.90	4.99	22.43	15.80	34.0	39.8
	1B	19.14	15.44	21.55	17.32	17.40	19.33	12.60	9.51	9.07	33.0	40.3
*	2B	20.31	21.52	27.43	20.13	20.32	5.96	35.07	0.91	0.02	38.0	42.1
**	3B	21.19	25.07	21.28	27.78	28.26	18.31	0.41	31.08	33.38	32.0	37.9
	4B	21.68	20.16	22.49	20.80	20.96	7.01	3.76	4.06	3.34	30.0	34.4

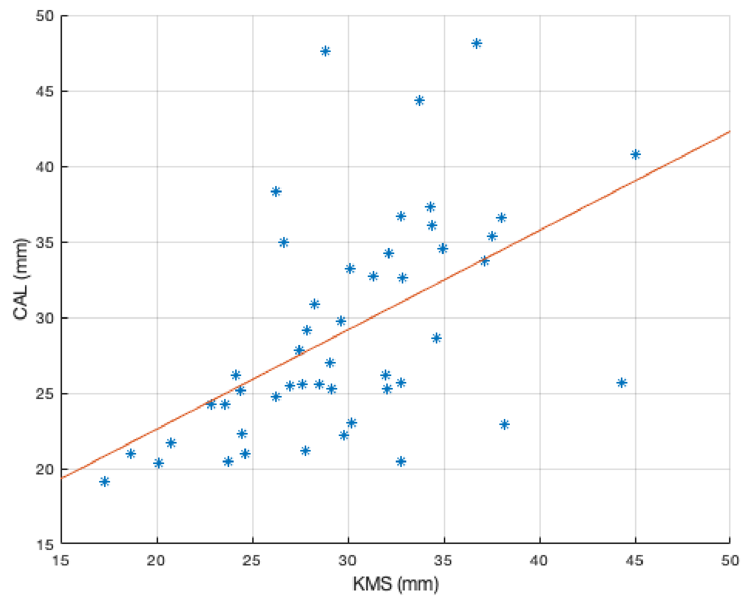

(a)

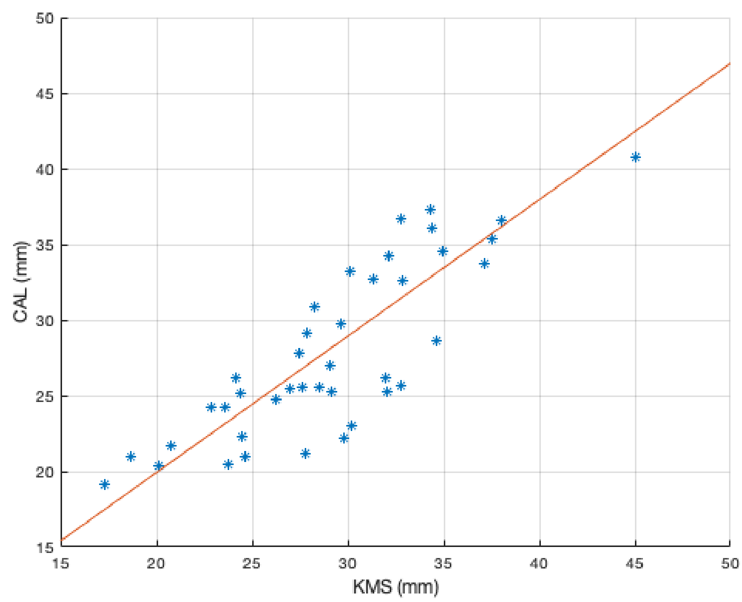

(b)

Figure 3.5 Scatter plots and linear regressions for stalk thickness caliper measurements *vs.* *k*-means single-window stalk thickness estimations. (a) Regression without removing outliers, and (b) regression after removing outliers.

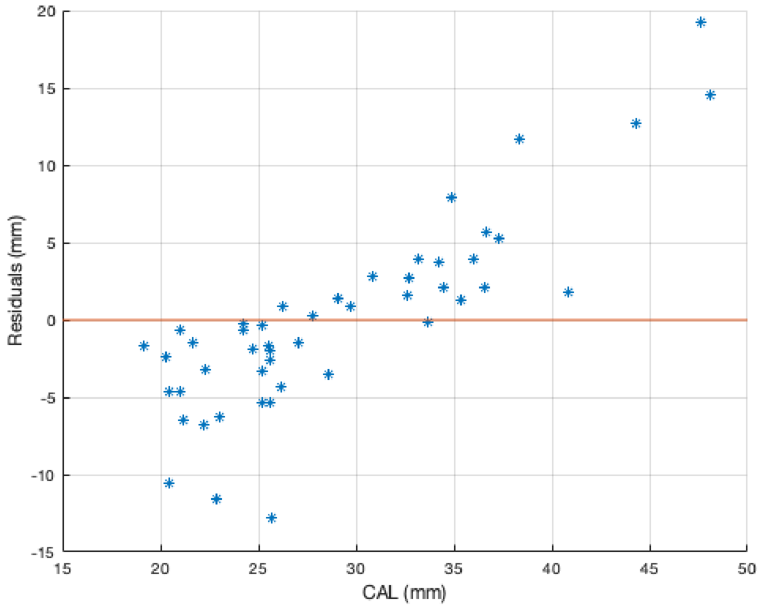

(a)

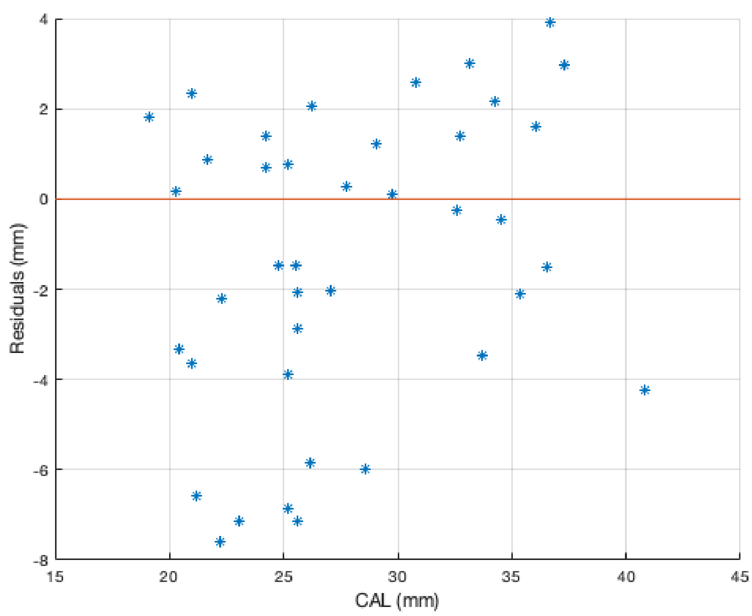

(b)

Figure 3.6 Scatter plots of residuals for linear regressions. (a) Residuals without removing outliers, showing heteroscedasticity; and (b) residuals after removing outliers without heteroscedasticity.

3.1.5. Error in Thickness Estimations per Variety of Sorghum

On Figure 3.7, average relative percent errors of the thickness estimations are displayed along the growing season. In general, the stalk estimations of variety B have higher relative error values than those on variety A, with global averages of 11.10% and 9.28%, respectively. Also, note that only for the week on July 7, the relative error for variety A (10.38%) was higher than for variety B (4.26%), where three plants of that variety presented stalks occluded by leaves and were considered outliers.

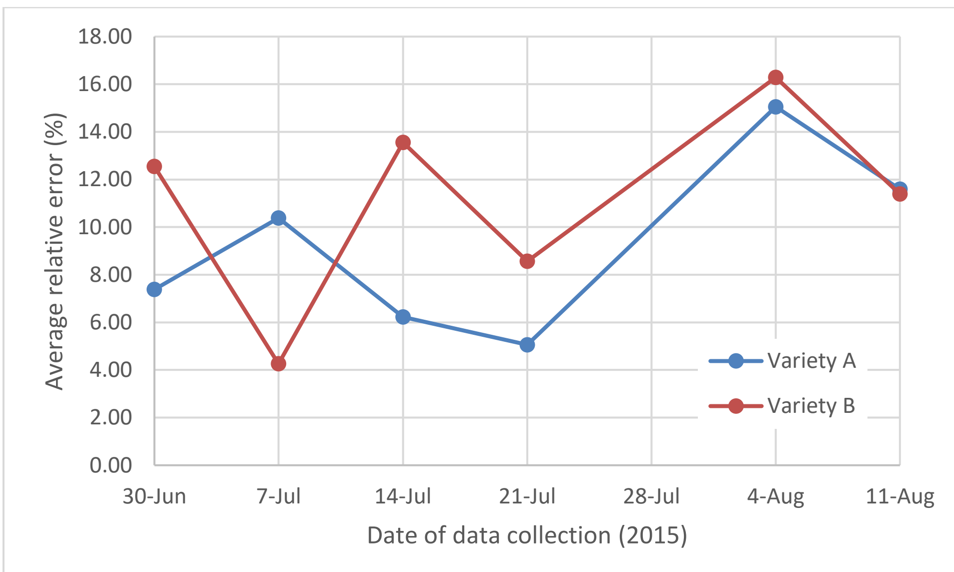

Figure 3.7 Thickness average relative error per variety of sorghum during the growing season (no outliers).

Linear regressions (without outliers) performed for each variety independently show differences in the coefficients of determination and the RMSEs. Figure 3.8a shows the regression for variety A, which had an $R^2 = 0.76$ and an $RMSE = 2.63$ mm. Figure 3.8b displays the regression for variety B, which had an R^2 = 0.59 and an $RMSE$ = 3.52 mm. Variety A had a mean value estimated with KMS of 30.8 mm, while variety B had a mean of 27.5 mm, with corresponding caliper measurements means of 29.4 mm and 26.2, respectively. If both means and their respective 95% confidence intervals (computed form equation 2.2) are considered, it can be seen that variety A has values in the range of 30.8±6.0 mm, and variety B has values in the rage of 27.5±8.0 mm, with overlap in some values due to the random and standard errors. Similar research by Xiang et al. (2019) showed higher correlation between the estimated stalk diameter and the caliper measurements, with values of R^2 = 0.86 and $RMSE$ = 1.61 mm, when performing point cloud data analysis of ToF images. It is important to note that Xiang et al. (2019) averaged the major and minor axes of the elliptical cross-section of the stalks, which is different to the approach in the research herein, which only considered the major axis. Another related experiment in a greenhouse with sorghum plants, presented by Atefi et al. (2019), showed an R^2 = 0.99, and a $RMSE$ = 1.2 mm between 48 estimates with a potentiometer mounted in a gripper and caliper measurements, suggesting that physically measuring stalk diameters by touching them is more accurate than imaging or point cloud analysis. However, even with the errors in our system estimations, the KMS method would be useful for breeders in determining that variety A presented larger stalks than variety B. On the other hand, determining whether the sorghum variety had an impact on the precision of the estimations would require further research. Data from the earlier growth stages when leaves sometimes occluded the stalks and the stalks cross sections were more elliptical, as in the fourth to sixth weeks (Figure 3.1), should be avoided.

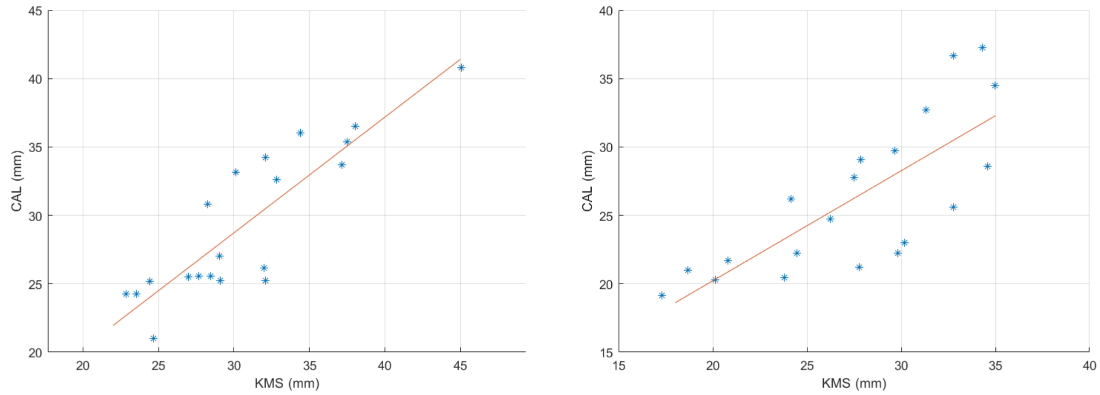

(a) (b)

Figure 3.8 Scatter plots and linear regressions of caliper measurements *vs.* *k*-means single-window (no outliers). (a) Regression on variety A, and (b) regression on variety B.

3.2. Stalk Thickness Estimation in the Field

3.2.1. Depth Maps

Depth maps were computed as described in Subsection 2.5.8. On the right-hand side of Figures 3.9 and 3.10, two subsets that led to the four most accurate and the four least accurate stalk thickness estimations, respectively, are shown. On the left-hand side of Figures 3.9 and 3.10, the original left images of the stereo camera are displayed as a visual aid to qualitatively compare with the depth maps. Depth maps have a color scale ranging from 0 mm (dark blue) to 700 mm (dark red).

In general, depth maps show sorghum stalks visibly differentiated from the background and leaves (see also Appendix D for the full set of images). Assuming sorghum plants were planted precisely, and the camera mounted on the GPV was placed 381 mm away from the plants (half the row distance), the stalks of interest should have distance values around 381 mm, corresponding to the light green color in the depth scale.

3.2.2. Stalk Thickness Estimations

The average absolute deviation of all the 100 stalk thickness estimations listed in Tables 3.3 and 3.4 and shown in the figures of Appendix D was 2.11 mm, corresponding to an average absolute relative error of 7.97%. On Figure 3.9, there is a subset of the four most accurate estimations, corresponding to plants A92, A97, A65, and A67, indicated with an asterisk (*) in Tables 3.3 and 3.4. On average, these four estimations have an absolute deviation of 0.07 mm and absolute relative error of 0.24%. As shown in Figure 3.9, all the stalks of interest are well defined in the depth maps, and the measuring points correspond to the edge of the stalks, right above the identification labels, approximately where the caliper measurements were taken previously for validation.

In contrast, Figure 3.10 displays the four least accurate estimations, corresponding to plants A37, A83, A10, and A49, indicated with double asterisk (**) in Tables 3.3 and 3.4, with an average absolute deviation of 10.72 mm, or an average absolute relative error of 38.59%. Additionally, the stalk of plant A83 is blurry and was difficult to locate precisely. The stalk of plant A37 is occluded and the estimation had to be taken offset from the hand-measured location. The stalk thickness estimations of plants A10 and A49 could be highly erroneous because their depth maps do not look well defined and they have non-homogeneous colors due to many leaves.

These most and least accurate cases represent the range of stalk-measurement situations encountered during estimation of stalk thickness. However, a more objective comparison was performed by excluding those images where occluded or blurry stalks were identified visually. From the inspection, images of plants A35 and A37 were

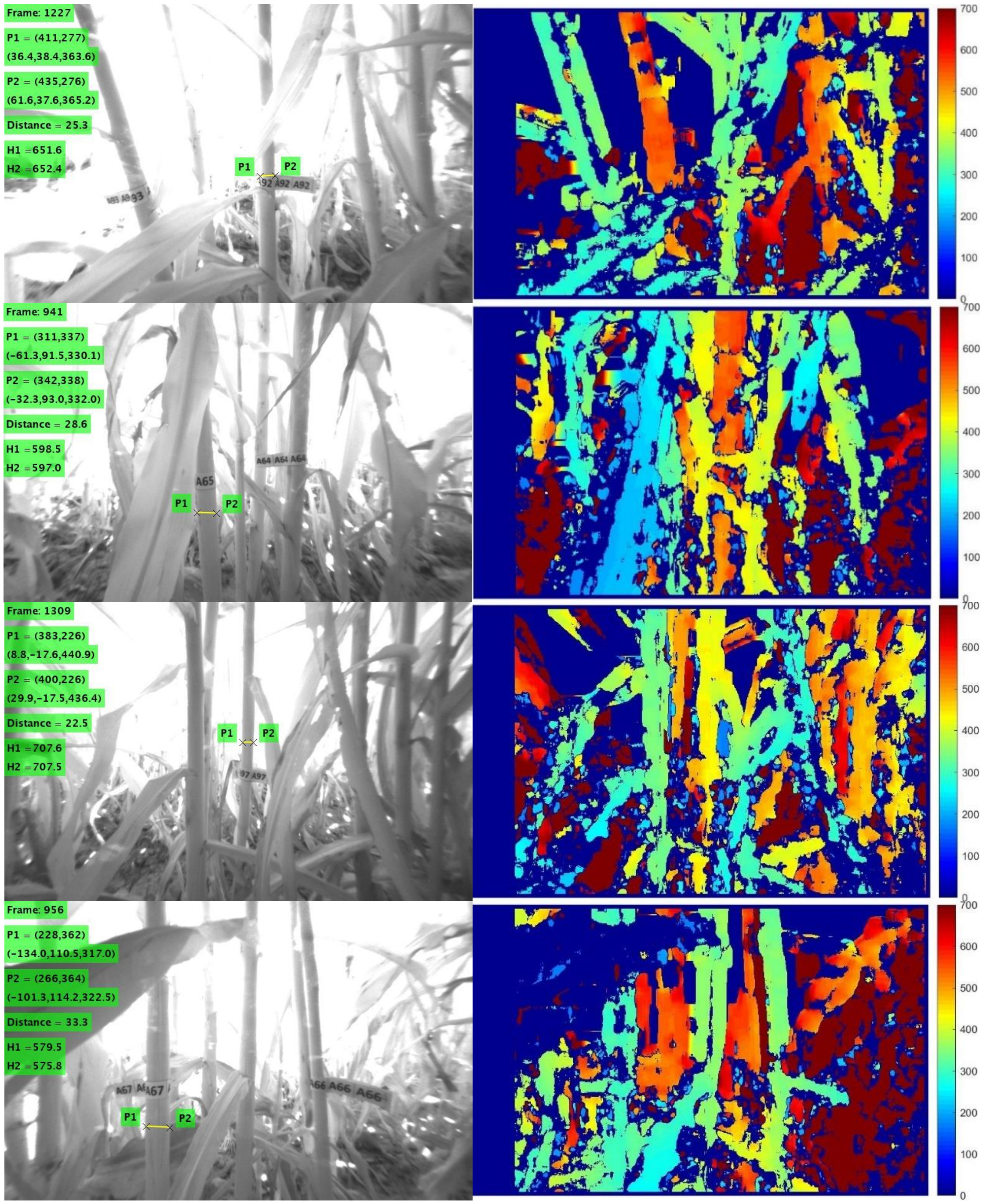

Figure 3.9 The four most accurate stalk thickness estimations using stereovision for plants A92, A97, A65 and A67. On gray scale, the left hand side images of the stereo camera; overlaying frame number, pixel and world coordinates of the two points (P1, P2), distance (stalk thickness) between the two points, and their height from the ground (H1, H2). On color, the corresponding depth maps with a scale bar in millimeters.

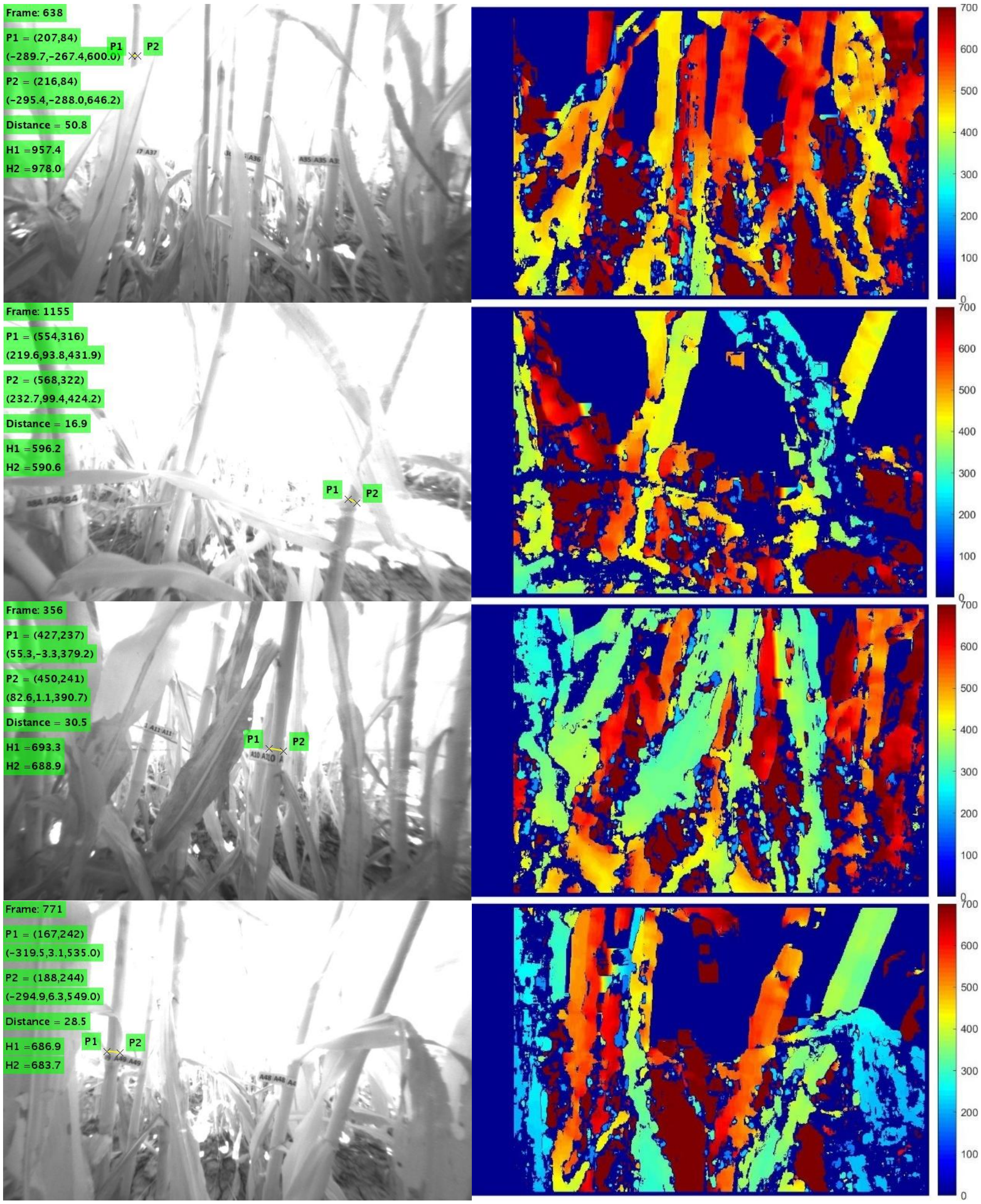

Figure 3.10 The four least accurate stalk thickness estimations using stereovision for plants A37, A83, A10, and A49. On gray scale, the left hand side images of the stereo camera; overlaying frame number, pixel and world coordinates of the two points (P1, P2), distance (stalk thickness) between the two points, and their height from the ground (H1, H2). On color, the corresponding depth maps with a scale bar in millimeters.

identified as occluded (see Figures D.9 and D.10), while images of plants A31, A45, A47, A52, A83, and A94 were identified as very bright because the plants were located at the beginning of the plots were sunlight penetrated more in the scene (see Figures D.8, D.12, D13, D.21, and D.24). The excluded images were marked with the “Plant ID” within square brackets in Tables 3.3 and 3.4. Estimates from the subset of the 94 images had an average absolute deviation of 1.70 mm, corresponding to an average absolute percent error of 6.59%. In Figure 3.11a, a scatterplot with a simple linear regression line of the caliper measurements *vs*. estimates was analyzed, giving an adjusted coefficient of determination R^2 = 0.712, and $RMSE$ = 2.07 mm (see Appendix B.16).

By close inspection of the residuals plotted in Figure 3.12a and by computing their studentized values, it was possible to identify four data points as potential outliers (studentized residual values $\geq$ 2.5, according to Cline (2015)). These outliers corresponded to plants A10 and A49 (Figures D.3 and D.13), with depth maps that do not present homogeneous colors on the stalk areas, and A57 with a depth map that does not have homogeneous colors in the stalk areas where its thickness was measured. Thus, the point pair had to be taken offset from the caliper measurement location, leading to a thickness underestimation of 24.43 mm, where the caliper measurement was 30.33 mm (see Table 3.4). It is also possible that transcription errors occurred when when recording these data (Heiberger, 2015). The remaining subset of 89 of the 100 estimations presented an average absolute deviation of 1.53 mm, corresponding to an average absolute percent error of 5.98%, while the regression-fitting curve of the caliper-measured values (CAL) *vs.* the stereo vision (STR) measurements (Figure 3.11b) had an adjusted coefficient of determination, R^2 = 0.81, and *RMSE* = 1.89 mm. Also, the residuals, after removing outliers, appear to be evenly distributed (see Appendix B.16). Individual stalk estimates were found to have a mean bias of 0.98 mm relative to the average caliper measurements (25.36 mm), and a 95% confidence interval of 24.34±3.74 mm. The coefficient of determination (R^2 = 0.809) is higher than the one reported by Salas Fernandez et al. (2017), who used a similar stereo system method and reported an R^2 = 0.764 for stem diameter estimations of sorghum plants between 63 to 75 days after planting in the field, and lower than the R^2 = 0.99 with *RMSE* = 1.2 mm, reported by Atefi et al., (2020).

Saturated images encountered in the field experiment for this research represent 6% of the data. These erroneous images can be eliminated if the system avoids capturing images near the edges of the plots, where sunlight penetrates the canopy cover, and plants would not grow at optimum conditions anyway. A proposed solution to avoid bright images is to mount the stereo system in the developed autonomous vehicle (Part II of this dissertation report) and program routes that use the GPS signal to avoid collection data near plot edges. For the 2% of cases in which stalk occlusion was encountered, some potential solutions are reducing the travel speed of the phenotyping vehicle, or increasing the number of fps of the sensor, or using a faster camera, allowing the camera to capture more frames of the same plant, options that could also avoid blurriness. These three potential practical solutions could avoid rejecting about 8% of the whole data set.

Table 3.3 Stalk thickness estimations for plants A1 to A50. Notes: ** are the four worst estimates, plant IDs enclosed in brackets are erroneous estimations, and plant IDs enclosed in parenthesis are outliers.

Plant	Caliper	Frame	Point 1		Point 2		Estimate	Absolute Deviation	Abs. Relative Error
ID	(mm)	Number	u_1	v_1	u_2	v_2	(mm)	(mm)	(%)
A1	15.32	229	434	269	450	269	14.39	0.93	6.07
A2	29.92	229	222	232	249	237	30.96	1.04	3.48
A3	28.65	238	207	201	233	203	27.72	0.93	3.25
A4	29.24	252	350	147	369	147	25.67	3.57	12.21
A5	26.7	256	205	219	222	219	23.61	3.09	11.57
A6	20.02	276	362	202	377	203	17.90	2.12	10.59
A7	33.73	284	313	307	336	301	30.86	2.87	8.51
A8	21.49	304	574	253	589	253	23.90	2.41	11.21
A9	30.23	346	292	240	314	244	26.30	3.93	13.00
(A10)**	23.32	356	427	237	450	241	30.47	7.15	30.66
A11	28.91	356	233	187	248	192	25.39	3.52	12.18
A12	30.48	368	167	195	199	195	29.82	0.66	2.17
A13	27.53	381	426	237	445	236	27.75	0.22	0.80
A14	27.46	388	311	241	330	241	26.06	1.4	5.10
A15	19.69	409	450	130	464	126	20.26	0.57	2.89
A16	32.79	413	311	253	332	256	34.27	1.48	4.51
A17	28.19	421	239	211	261	213	26.28	1.91	6.78
A18	21.74	427	323	208	340	208	21.29	0.45	2.07
A19	26.44	433	390	209	416	205	25.30	1.14	4.31
A20	32.59	481	380	208	409	218	30.53	2.06	6.32
A21	25.53	485	283	201	304	204	25.22	0.31	1.21
A22	28.83	497	403	210	423	212	29.26	0.43	1.49
A23	24.13	507	459	129	475	131	26.10	1.97	8.16
A24	28.63	516	298	259	318	259	30.15	1.52	5.31
A25	25.22	526	327	212	343	212	22.94	2.28	9.04
A26	19.43	537	412	276	430	276	20.04	0.61	3.14
A27	22.3	543	383	65	402	67	23.81	1.51	6.77
A28	25.26	552	418	280	443	279	26.51	1.25	4.95
A29	25.87	555	386	237	412	236	24.55	1.32	5.10
A30	31.23	555	203	246	228	248	32.01	0.78	2.50
[A31]	28.33	609	480	242	500	247	23.15	5.18	18.28
A32	22.43	611	363	258	385	260	20.61	1.82	8.11
A33	21.32	616	431	225	445	228	20.00	1.32	6.19
A34	25.55	624	254	156	276	158	24.45	1.1	4.31
[A35]	25.5	634	382	196	393	196	19.09	6.41	25.14
A36	18.52	640	428	250	438	251	17.82	0.70	3.78
[A37]**	30.53	638	207	84	216	84	50.78	20.25	66.33
A38	22.49	654	386	223	404	220	21.62	0.87	3.87
A39	27.08	661	374	276	388	276	26.83	0.25	0.92
A40	32.27	671	409	258	433	258	29.95	2.32	7.19
A41	26.31	676	369	219	386	217	23.20	3.11	11.82
A42	23.22	683	296	285	319	285	23.52	0.3	1.29
A43	23.1	689	274	305	296	306	22.27	0.83	3.59
A44	26.17	696	371	257	393	260	25.91	0.26	0.99
[A45]	27.65	700	351	277	367	274	22.18	5.47	19.78
A46	31.17	747	549	219	568	225	29.13	2.04	6.54
[A47]	32.93	741	71	198	102	200	37.21	4.28	13.00
A48	28.37	771	455	282	473	286	27.74	0.63	2.22
(A49)**	29.29	771	164	260	188	261	36.35	7.06	24.10
A50	24.45	782	412	258	428	258	25.66	1.21	4.95

Table 3.4 Stalk thickness estimations for plants A51 to A100. Notes: * are the four best estimates, ** are the four worst estimates, plant IDs enclosed in brackets are erroneous estimations, and plant IDs enclosed in parenthesis are outliers.

Plant	Caliper	Frame	Point 1		Point 2		Estimate	Absolute Deviation	Abs. Relative Error
ID	(mm)	Number	u_1	v_1	u_2	v_2	(mm)	(mm)	(%)
A51	32.13	783	292	270	309	270	30.32	1.81	5.63
[A52]	31.88	798	459	233	474	232	28.75	3.13	9.82
A53	26.82	803	267	252	285	250	25.61	1.21	4.51
A54	31.17	821	115	315	146	315	27.72	3.45	11.07
A55	19.23	886	395	210	411	212	18.53	0.7	3.64
A56	28.73	891	365	205	389	206	28.16	0.57	1.98
(A57)	30.33	893	304	204	318	205	24.43	5.9	19.45
A58	24.69	900	340	236	357	238	24.96	0.27	1.09
A59	26.09	909	360	250	375	251	21.90	4.19	16.06
A60	24.79	916	314	172	336	167	23.18	1.61	6.49
A61	24.69	922	493	253	510	253	26.73	2.04	8.26
A62	18.59	925	411	242	426	241	17.11	1.48	7.96
A63	20.7	926	297	164	312	160	18.47	2.23	10.77
A64	31.14	937	283	228	304	225	25.98	5.16	16.57
A65*	28.5	941	311	337	342	338	28.56	0.06	0.21
A66	18.77	956	495	283	514	284	17.47	1.3	6.93
A67*	33.4	956	228	362	266	364	33.28	0.12	0.36
A68	26.42	1016	511	271	526	276	26.28	0.14	0.53
A69	27.97	1017	461	248	482	257	26.54	1.43	5.11
A70	24.94	1017	287	215	300	215	22.88	2.06	8.26
A71	25.65	1029	373	248	388	249	26.00	0.35	1.36
A72	18.08	1034	424	240	437	241	17.27	0.81	4.48
A73	23.47	1039	417	241	434	240	22.72	0.75	3.20
A74	23.5	1046	435	285	454	286	24.17	0.67	2.85
A75	22	1046	249	274	267	272	23.40	1.4	6.36
A76	27.13	1054	318	275	343	276	31.36	4.23	15.59
A77	18.03	1061	324	311	338	310	20.07	2.04	11.31
A78	22.45	1071	404	287	416	288	21.11	1.34	5.97
A79	23.71	1075	337	146	355	142	20.89	2.82	11.89
A80	23.44	1082	435	264	450	260	22.69	0.75	3.20
A81	20.41	1085	329	307	343	307	20.99	0.58	2.84
A82	30.23	1102	350	306	372	307	29.55	0.68	2.25
[A83]**	25.29	1155	554	316	568	322	16.88	8.41	33.25
A84	25.86	1158	273	329	297	328	27.98	2.12	8.20
A85	23.5	1166	361	266	378	265	21.07	2.43	10.34
A86	21.25	1169	287	327	307	325	21.59	0.34	1.60
A87	24.04	1179	363	236	383	235	23.56	0.48	2.00
A88	22.49	1187	256	227	273	225	20.73	1.76	7.83
A89	28.73	1206	266	281	298	272	30.68	1.95	6.79
A90	26.57	1210	122	307	152	302	24.10	2.47	9.30
A91	31.99	1222	525	305	570	293	36.78	4.79	14.97
A92*	25.3	1227	411	277	435	276	25.34	0.04	0.16
A93	27.97	1231	437	330	467	323	30.96	2.99	10.69
[A94]	29.58	1289	556	240	594	244	31.06	1.48	5.00
A95	26.87	1291	308	307	333	302	27.08	0.21	0.78
A96	24.92	1302	617	288	654	289	28.41	3.49	14.00
A97*	22.45	1309	383	226	400	226	22.50	0.05	0.22
A98	22.95	1316	310	255	331	257	25.82	2.87	12.51
A99	19.57	1325	351	272	367	273	20.47	0.9	4.60
A100	22	1337	543	234	569	239	22.28	0.28	1.27

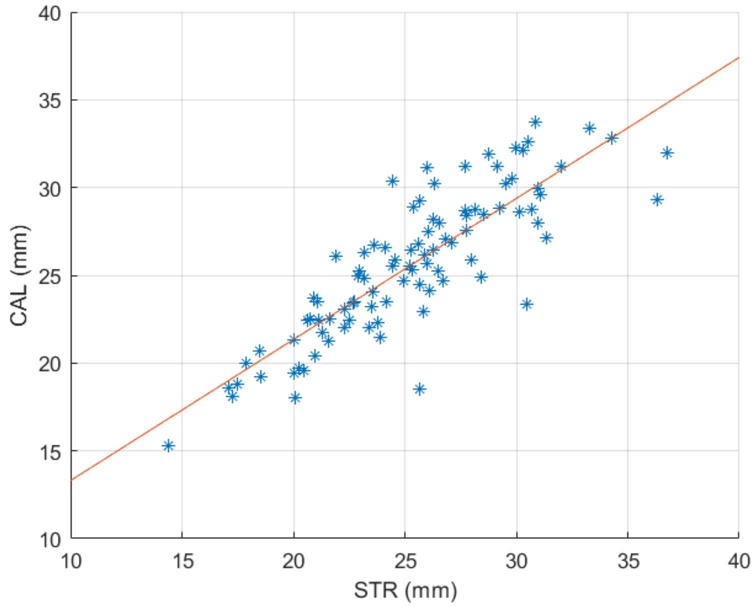

(a)

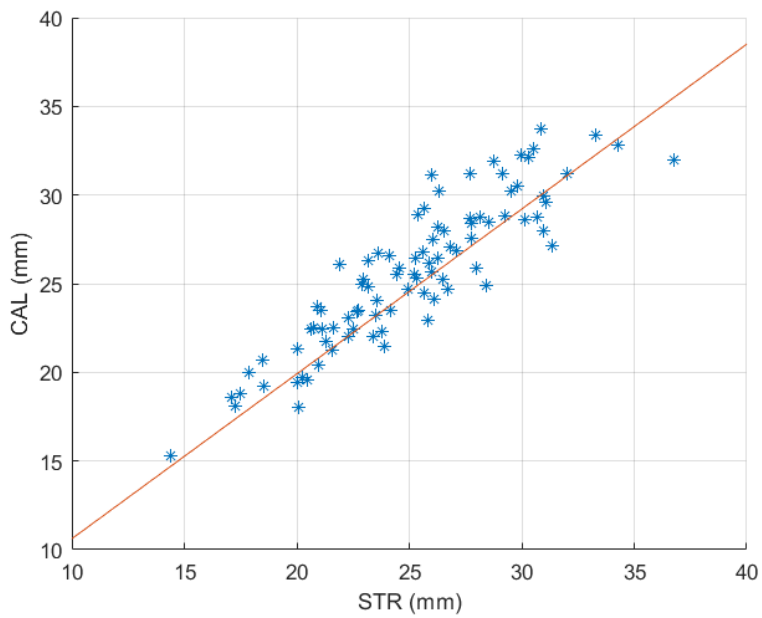

(b)

Figure 3.11 Scatter plots and linear regressions for stalk thickness caliper measurements *vs.* stereovision (STR) stalk thickness estimations. Data from images where points were selected at visible labels: (a) regression without removing outliers, and (b) regression after removing outliers.

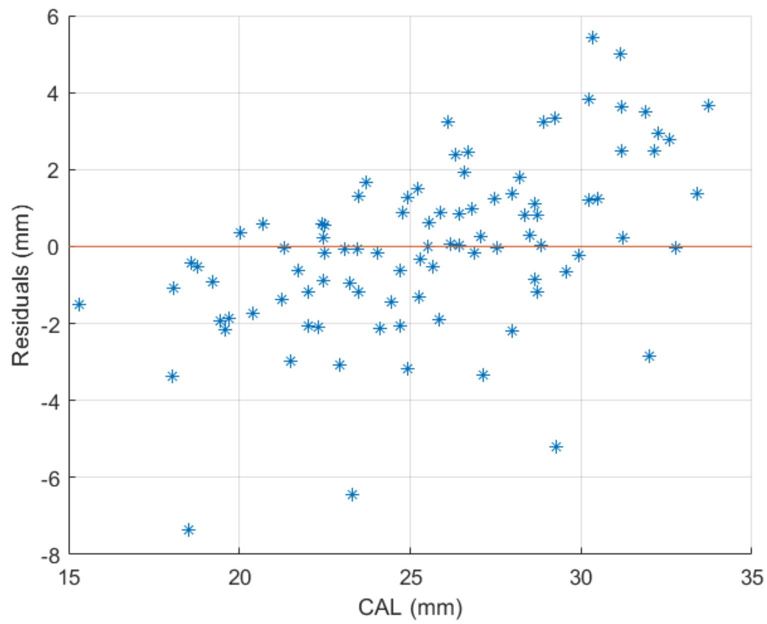

(a)

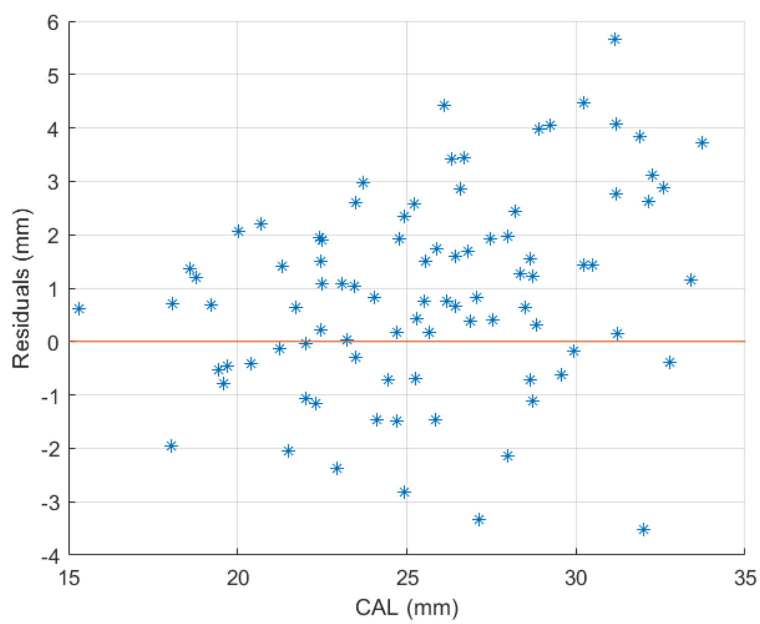

(b)

Figure 3.12 Scatter plots of STR residuals for linear regressions *vs*. caliper measurements. (a) Residuals without removing outliers, and (b) residuals after removing outliers.

3.3. Comparison Between KMS and STR Stalk Thickness Measuring Methods

The *k*-means single-window (KMS) image classification method used in the greenhouse experiment was compared to the stereovision (STR) method of the field experiment. Table 3.5 summarizes the comparison. The STR method seemed to be superior, with a better coefficient of determination and RMSE. Comparing the means of CAL (caliper measurements) with both methods, STR had a smaller difference, 0.48 mm, while KMS had a difference of 1.37 mm. However, the two methods were used under the evidently different conditions of the greenhouse and the field. In the greenhouse, background and plant location were manually set to take pictures, while in the field these parameters were not controlled by humans. With respect to the plants varieties, plant size, and plant number, in the greenhouse, two sorghum varieties (A and B) were planted and measured during five sessions within a period of six weeks with different growing stages and a total of 48 plants, while in the field only one variety (A) was measured and imaged in one session when the sorghum was mature, and 100 plants were sampled. Additionally, since each experiment used a different camera model with different sensors, then further research should be made under the same conditions to assess a better comparison between methods.

Table 3.5 Comparison summary between *k*-means image (KMS) and the stereo vision (STR) methods, after removing outliers.

	Means		**Adjusted Coefficient**	***RMSE***
Method	**CAL**	**Method**	**Determination (R^2)**	**(mm)**
KMS	27.83	29.20	0.70	3.19
STR	25.43	24.95	0.81	1.87

4. PART II: ELECTRIC GROUND PHENOTYPING VEHICLE: METHODS AND MATERIALS

4.1. Methods of Design and Construction

The main design requirements of the EGPV were its high clearance of 3.15 m, and its capability to work with two planting widths of 76.2 and 101.6 cm, allowing the vehicle to perform phenotyping in mature sorghum and corn at speeds lower than 8 km/h, especially using cameras to image plant stalks and estimate their thickness as done in Part I of this dissertation. Other design considerations were to provide two lateral trusses for mounting cameras and other sensors that would be able to sense in opposite directions and take information of four rows of plants in a single transit of the vehicle (Figure 4.1). The trusses were also intended for attaching the structures that carry the motors, batteries and suspension systems at the lower third of the height of the vehicle in order to keep the center of gravity as low as possible (about 1 meter from the ground). A wheelbase of two furrows (1524 mm) was thus considered an appropriate minimum distance that yet provides stability for the following reasons: 1) Murphy, et al (1985) reported a reference turn over limit of 25-degree slope (excessive slope) for a similar vehicle (tractor with a wheel base of 1630 mm and two-wheel drive system); and 2) the projection of the center of gravity out of the wheels of the vehicle (support polygon) can cause a roll over laterally if the EGPV is tilted to an extreme condition of 37-degree slope in static conditions. Another design consideration was to develop the EGPV to minimize soil compaction, so it was decided to construct its structures primarily from aluminum 6061-T6, with some steel brackets.

The design of the EGPV was an iterative process, in which structural parts were refined according to the requirements of sorghum and corn working conditions previously described and to match with the dimension of the purchased components. Selection of common machine components (gearboxes, electric motors and controllers, batteries, shock absorbers, and rubber bushings), raw material (tubing and plates), and manufacturing equipment used (metal inert gas welding (MIG) and tungsten inert gas welding (TIG) for aluminum and steel, and a horizontal band saw) were made by consensus of the design team.

MATLAB® (Academic Student Version 9.1, R2016b, The MathWorks, Inc., Natick, MA, USA) was used as the programming platform to compute mechanical design parameters. Additionally, Simulink® Version 8.8, embedded in MATLAB® version, was used to compute the energy requirements to design the EGPV and impact forces for the suspension system.

SolidWorks® (Student Edition, Academic Year 2016-2017, Dassault Systèmes Americas Corp. Waltham, MA, USA) was used to design and analyze the proposed vehicle components, creating single parts, assemblies and drawings. Additionally, to validate the EGPV design, the SolidWorks Simulation® and SolidWorks Motion® add-ins were used to perform finite element analysis (FEA) on the parts and trusses and kinematic analysis on mobile assemblies. For the FEA analyses, mesh density was computed automatically by SolidWorks® within the continuous interval ranging from “Coarse” to “Fine” and varied from part to part. Convergence estimations were made by manually dividing the coarse-fine interval to get five different element sizes and compare whether stress and deformation converged to a specific number when changing mesh sizes. As recommended by Lee (2004), global settings for stress and strain in the FEA were set to nodal mode. Main mesh parameters were set to Curvature based mesh, as recommended by Kurowski (2004), because second-order curvature elements can better simulate curved shapes such as holes, rounds or other cylindrical surfaces; Maximum (for boundaries with lowest curvature) and Minimum (for boundaries with highest curvature) element sizes set to be as default; Minimum number of elements in a circle set to be 12; and Element size growth ratio set as 1.5 (default), which starts to grow from the regions of high curvature to all directions. Advanced option of Jacobian points, that sets the number of integration points to be used in checking the distortion level of tetrahedral elements was set as default with 4 points. Finally, the failure criteria were selected to be mainly Maximum von Mises stress $\sigma_v < \sigma_{Lim}$, and Maximum Shear Stress (Tresca) $\tau_{max} < \frac{\sigma_{Lim}}{2}$, especially for round tubes, with the intent to have a minimum factor of safety (FOS) near 4.0 or greater, adequate for a machine constructed of ductile materials under static loading with uncertainties about dynamic loading, material properties and environmental conditions (R. L. Mott, 2004).

4.1.1. Vehicle's Top Structure

The vehicle's top structure was designed and constructed to give a wheel-to-wheel width of 152.4 or 203.2 cm to allow travel around furrows of 76.2 or 101.6 cm of interspacing, respectively (Figure 4.1, top blue structure). The top structure was designed to be lightweight to avoid a high center of gravity. Torsion between left and right frames was expected to be the main loading mode. After analyzing the option of having an adaptable top structure to enable both widths, it was decided that two rigid interchangeable upper beams were best to provide structural rigidity. Thus, two top beams were constructed, one of 152.4 cm width and another of 203.0 cm width.

A cylindrical component is the most efficient at withstanding torsion (Norton, 2014), so each top structural member was made of 6061-T6 aluminum round tube and two circular plates (Figure 4.4), both with 12.7 mm thickness (Metals Depot International, Winchester, KY, USA). To estimate the maximum torque at extreme conditions, the maximum kinetic energy of the vehicle was considered. The EGPV mass was assumed to be 2,000 kg, taking into account that the all-terrain vehicle (ATV) used as a reference for the suspension system (subsection 4.1.2) has a mass of 400 kg with a passenger, the initial estimated size of the EGPV was to be two times the size of the ATV, the vehicle was going to be a dynamic body, and a minimum factor of safety of 2.0 was required. Thus, the kinetic energy was computed as

$$\kappa = \frac{1}{2} m v^2, \tag{4.1}$$

where κ is the kinetic energy of the vehicle, m its mass, and v its velocity. The velocity was taken as 2.2 m/s, a design requirement of the project sponsor, Dr. Seth Murray. The calculated energy value was assumed to be transferred as a static torsion load over the round tube. Substituting values into equation (4.1), the kinetic energy was 4928.4 N-m.

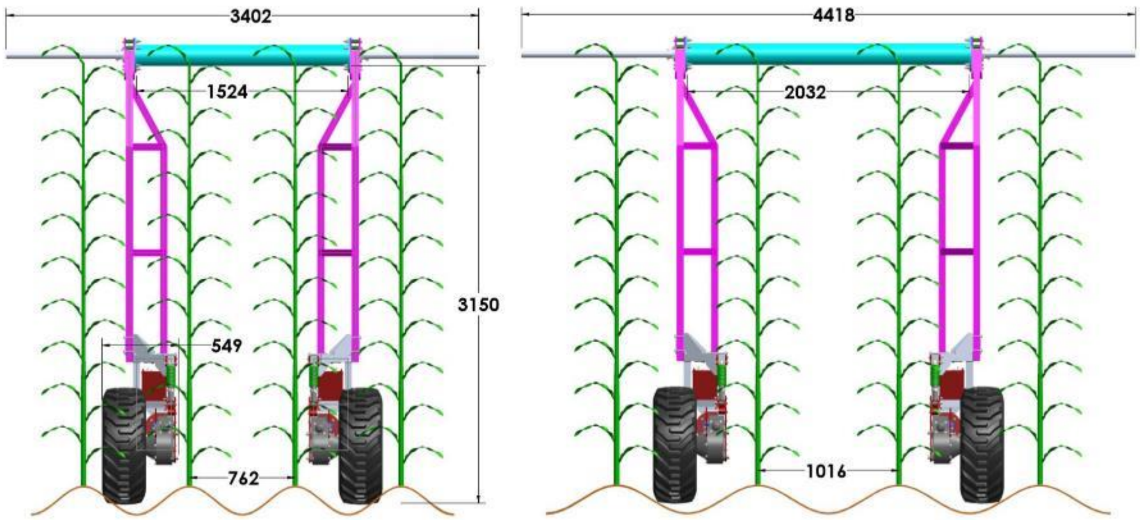

Figure 4.1 Main dimensions in millimeters of the two width configurations of the EGPV, allowing two furrow spacing options of 762 and 1016 mm (30 and 40 in.). Design shown at its final design stage.

To compute the maximum shear stress, angular deformation, strain, and factor of safety (FOS) on the two round tubes of 1524 and 2032 mm, two methods were used: (a) an analytical method on the tubes only; and (b) finite element analysis (FEA) on the tubes, the circular plate and whole welded assemblies.

For the analytical solution, the following equation was used to determine the maximum shear stress

$$\tau_{max} = \frac{Tr}{J}, \tag{4.2}$$

where T is the torque applied, r is the external radius, and J is the polar area moment of inertia (Norton, 2014). This last parameter can be calculated with

$$J = \frac{\pi}{2}(r_2^4 - r_1^4), \tag{4.3}$$

where r_1 is the minor radius and r_2 is the major radius (Norton, 2014). The maximum angular deformation was obtained with

$$\phi = \frac{Tl}{JG}, \tag{4.4}$$

where ϕ is the angular deflection, l is the length of the tube, and G is the shear modulus (Norton, 2014), which can be computed as

$$G = \frac{E}{2(1+\nu)}, \tag{4.5}$$

where E is the modulus of elasticity of the material, and ν is Poisson's ratio of the material (Norton, 2014). As the manufacturer does not provide the modulus of elasticity nor Poisson's ratio for the aluminum 6061-T6, these properties were taken from Hibbeler (2014) for a generic aluminum alloy: $E = 68.9$ GPa, and $\nu = 0.35$. The strain values can be calculated with the following equation

$$\gamma_{xy} = \frac{\tau_{xy}}{G}, \tag{4.6}$$

where γ_{xy} is the strain on the x-face in direction y of an infinitesimal cube element, and τ_{xy} is the shear stress of a cubic element on the x-face in direction y (Lee, 2014).

A finite element analysis (FEA) was performed for both tube lengths of 1524 and 2032 mm, maintaining the mentioned mesh parameters of Section 4.1. To set adequate boundary conditions, the ends of the tubes were divided to have external cylindrical surfaces of 12.7 mm length to simulate the contact areas of the welding beads where fixtures and loading were applied as shown in Figure 4.2. Details of the meshes used in the FEA are shown in Appendix G.

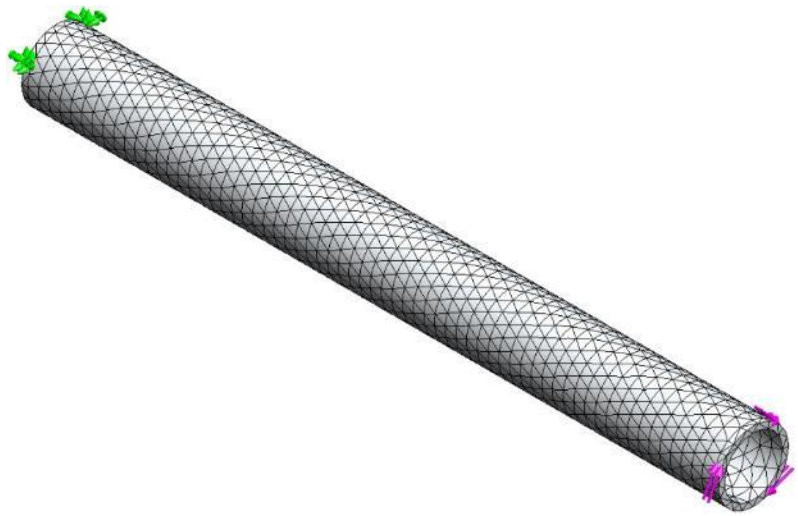

Figure 4.2 Boundary conditions of FEA on round tubes. On green, all nodes of the external cylindrical surface were fixed; while in magenta, all nodes of the external cylindrical surface were twisted clockwise with respect to the longitudinal axis of the tube (see Figure G.1).

Although the round tube is the main component of the top structure, it was necessary to weld a circular plate at the end of each round tube. This circular plate was designed to attach to a lateral truss with eight bolts of 12.7 mm diameter. The four plates were later water-jet cut from 6061-T6 aluminum plate of 12.7 mm thickness (Second Generation Arc ‘N Spark, Bryan, TX, USA). The FEA was performed on the designed plate (Figure 5.3), maintaining the mesh parameters mentioned in Section 4.1. Two scenarios of FEA were assumed to set the appropriate boundary conditions: (1) the annular planar welding surface was rigidly fixed, while the torsion load was applied on the cylindrical external surface of the round plate as shown in Figure 4.3a, and (2) the eight cylindrical holes of the bolts were rigidly fixed, while the torsion load was applied in an annular planar surface that simulated 12.7 mm of welding bead at the intersection of the round tube with the circular plate as shown in Figure 4.3b. Details of the meshes used in the FEA for each scenario are shown in Tables G.2 and G.3.

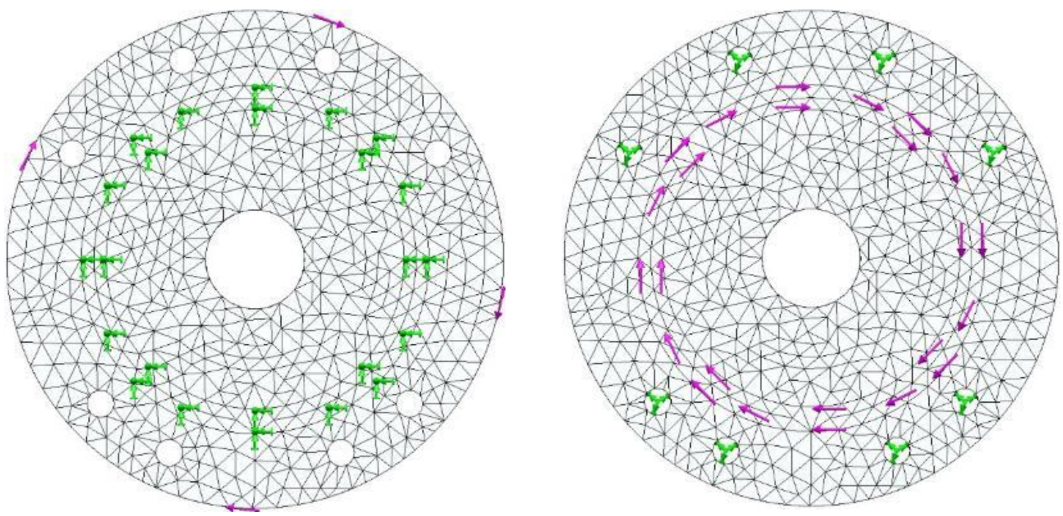

(a) (b)

Figure 4.3 Boundary conditions of FEA on the circular plate. (a) First scenario, on green, all nodes of the annular planar welding surface were fixed; while in magenta, all nodes of the cylindrical external surface of the circular plate were twisted clockwise with respect to the axis of the plate (see Figure G.2); and (b) second scenario, on green, all nodes of the cylindrical surfaces of the bolt holes were fixed; while in magenta, all nodes of the planar annular welding surface were twisted clockwise with respect to the axis of the plate (see Figure G.3).

Additionally, since each top structure was designed and built of three welded parts, only the longest whole assembly was evaluated with FEA due to its maximum deformation, maintaining the mesh parameters of Section 4.1, and assuming the eight cylindrical surfaces of the bolts of one end were rigidly fixed, while applying the torsional force on the external cylindrical surface of the circular plate at the other end as shown in

Figure 4.4. Details of the meshes used in the FEA for each scenario are shown in Table G.4.

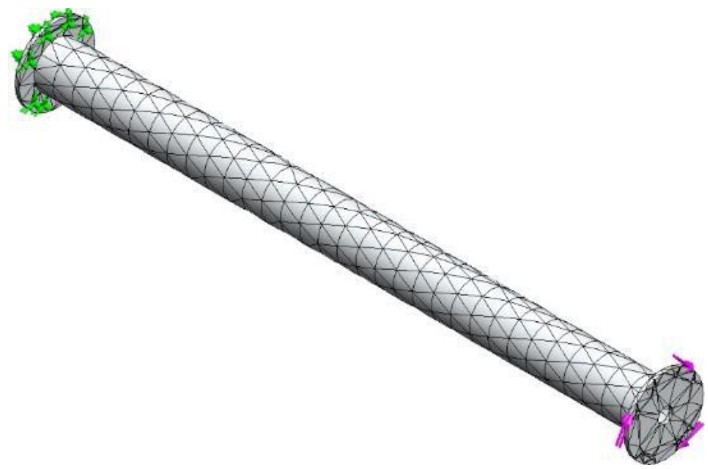

Figure 4.4 Boundary conditions of FEA on the top structure welded assembly of 2032 mm long. On green, all nodes of the cylindrical surfaces of the bolt holes were fixed; while in magenta, all nodes of the cylindrical outer surface were twisted clockwise with respect to the axis of the tube.

4.1.2. Suspension System

According to recommendations by Richard Epting, Technical Laboratory Coordinator in Biological and Agricultural Engineering at Texas A&M University, (Personal Communication, 2016), the suspension system of the EGPV was designed considering an ATV, an example of which was found at a local motorcycle dealership. By comparing weight capacity and size of shock absorbers on different brands and models, it was determined that the most similar suspension system to that required for the sorghum field conditions was that of the 2016 Brute Force® 300 ATV (Kawasaki Motors Corp., Santa Ana, CA, USA) (specs in Appendix E.2).

The analysis of the suspension dynamics was performed with a quarter car suspension model (Yang, Li, Fang, & He, 2014; Preda, 2016), as shown in Figure 4.5. This system of lumped parameters assumes that the first body, on top, represents one quarter of the total mass of the vehicle, while the second body at the bottom concentrates the mass of the wheel and tire, including moving parts of the suspension. This simplified model has two sub-actuated degrees of freedom, since there are no actuators directly driving these mass bodies. However, their dynamics depend on the height of the ground profile (Figure 4.5), with the assumption that there are no horizontal forces acting on the suspension. Another assumption is that the tire stiffness and damping coefficient can be modeled with spring and damper components.

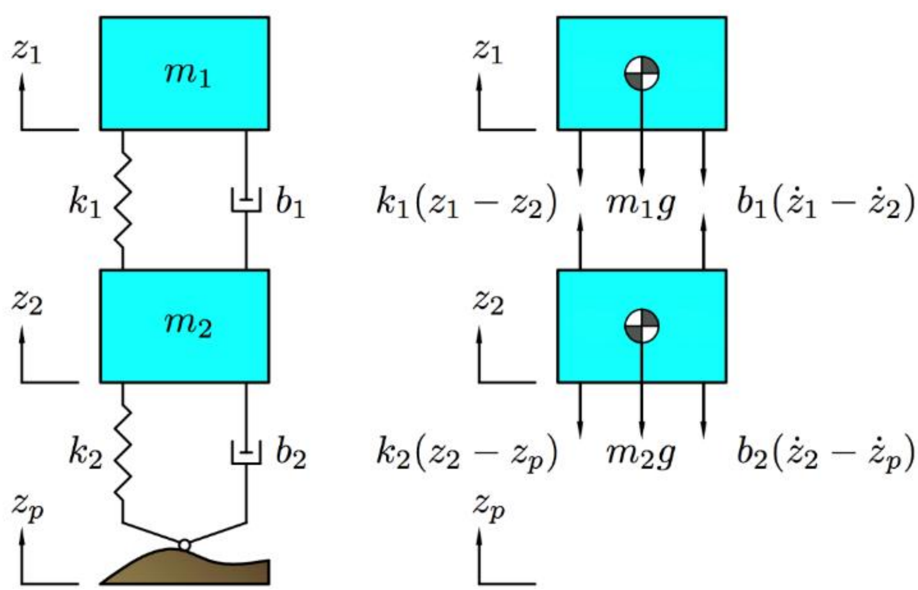

Figure 4.5 One-quarter suspension model with its free body diagrams.

The suspension model was derived with Newton's Second Law ($F = ma$) with the visual help of two free body diagrams (Figure 4.5). The mathematical model was written with a set of two equations, one for each degree of freedom (DoF), such that the first is the movement caused by the force moving mass 1 (m_1) along the DoF z_1, while the second is caused by the force needed to move mass 2 (m_2) along the DoF z_2. Thus,

$$m_1\ddot{z}_1 = -k_1(z_1 - z_2) - b_1(\dot{z}_1 - \dot{z}_2) - m_1 g, \tag{4.7}$$

$$m_2\ddot{z}_2 = k_1(z_1 - z_2) + b_1(\dot{z}_1 - \dot{z}_2) - k_2(z_2 - z_p) - b_2(\dot{z}_2 - \dot{z}_p) - m_2 g, \tag{4.8}$$

where m_i is the mass of the body i, k_i is the stiffness coefficient of the spring i, and b_i is the viscous friction coefficient of damper i, g is the acceleration due to gravity, while z_i, $\dot{z}_i = dz_i/dt$, and $\ddot{z}_i = d^2z_i/dt^2$ are the position, velocity, and acceleration of the body i, respectively. In this case, body 1 is the quarter mass of the vehicle, body 2 is the wheel and tire, and body p is the ground (profile).

From the mathematical model, it is seen that the most difficult parameter to estimate is the damping coefficient. However, according to Preda (2016), the damping coefficients can be estimated with the equation

$$\xi = \frac{b}{2\sqrt{km}}; \tag{4.9}$$

where ξ is the damping ratio, b is the damping coefficient, k is the spring constant, and m is the mass of the body (in this case one quarter of the total vehicle's mass). Now, knowing that sport vehicles have damping ratios commonly between 0.8 and 0.9 (Milliken & Milliken, 1995; Preda, 2016), the damping coefficient can be computed as

$$b = 2\xi\sqrt{km}. \tag{4.10}$$

With the damping ratios suggested, the stiffness constants described below in Subsection 4.3.5, and an estimated mass assuming the half weight of the ATV, m = 167 kg (Appendix E), the damping coefficient was found using equation (4.10) in an interval as follows:

$$b = \left[2(0.8)\sqrt{45533(167)},\ \ 2(0.9)\sqrt{52538(167)}\right] = \ [4412,\ \ 4739] \text{ Ns/m.}$$

For the tire stiffness coefficient, the average of the tire load capacity divided by the difference between the unloaded and loaded tire radii was calculated on three tire types under several working conditions as shown in Table 4.1. The resulting average tire coefficient used was 209,943 N/m; while the tire friction coefficient was assumed to be one tenth of the average of the shock absorber damping coefficient, as used in Preda (2016). Thus, the average damping coefficient for the tires was 458 N·s/m.

Table 4.1 Summary of tire parameters to estimate their stiffness coefficients, rounded up to the next integer. A = Firestone Super All Traction II 23º, 250/85D16.5; B = Michelin Multibib XM108, 320/65 R16; and C = BKT AT-621, 12.5/70-16. See Appendix E.3 for data sheets.

Tire	Load Condition	Load (kg)	Overall Diameter (mm)	Loaded Radius (mm)	Stiffness Coefficient (N/m)
A	Load Index: 92	630	838	378	150,693
	Max. Load (ML)	850	838	378	203,316
B	10 kph @ 0.6 bar	630	844	375	131,456
	10 kph @ 1.0 bar	885	844	375	184,664
C	8 kph @ 2.6 bar, ML	1645	855	385	379,589

For purposes of computer simulation, one quarter of the vehicle's mass was estimated to be $m_1 = 165.61$ kg, while the suspension mass was estimated to be $m_2 = 116$ kg. The shock absorber spring constant was set to be the average of its specifications:

$k_1 = 49$ kN/m; while its damping coefficient was set as the average of equation 2.12: $b_1 = 4.6$ kN·s/m. The tire coefficients were set to be the average of Table 4.1: $k_2 = 210$ kN/m, and $b_2 = 458$ N·s/m.

A short MATLAB® script called 'suspension_parameters.m' (Appendix F.2) was written with the previous parameters, while Simulink® was configured to solve the system of equations with the default following settings: solver: ode45 (Dominant-Prince), type: variable-step, and relative tolerance: 10^{-6}. The simulation was set to have all initial conditions of displacement and velocity as zero, while the only input to the system is a step function (variable z_p in Figure 4.5), simulating an abrupt change in the road as high as 30 cm. The simulation solved simultaneously the pair of equations for a period of 1 second, when the peak body positions, velocities, and inertial and spring forces were simulated. This simulator is shown as a block diagram in 'suspension_simulator.slx' on Figure F.1 of Appendix F.3.

From the simulation, the spring force, $k(x_1 - x_2)$, at the time of a maximum value due to an abrupt change in the terrain's topography was considered a limiting factor to design and construct brackets and swing suspension arms that withstand that impact load. Thus, swing arms and brackets that comprise the main suspension components were designed considering this impact loading and the geometry of the shock absorbers and rubber bushings found in the ATV vehicles described previously. These components were made of different steel types, as detailed in Subsection 4.13.12.

For each wheel, a pair of swing arms in parallel with respect to a vertical plane was designed to maintain the same relative orientation between the gearbox (see

Subsection 4.3.1) and the bottom frame. Both swing arms were designed with the same dimensions fitting suspension requirements and the insertion of rubber bushings (see Subsection 4.3.6) at their ends, but for the superior swing arm, two triangular brackets were welded to assemble the shock absorber (see Subsection 4.3.5), being this arm was the most stressed with impact loading. Thus, an FEA was performed on the top swing arm, maintaining the mesh parameters of Section 4.1. The boundary conditions to perform the FEA were based on the assumption that the cylindrical internal surfaces of the bushing were rigidly fixed at both ends of the arm, while the load of the spring was applied to the bolt holes of the triangular brackets as shown in Figure 4.6. Details of the meshes used in the FEA for each scenario are shown in Table G.5 and Figure G.5.

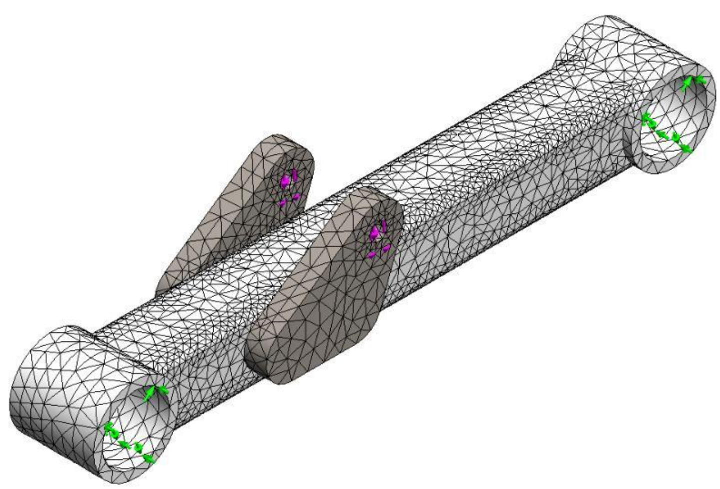

Figure 4.6 Boundary conditions of FEA on the top swing arm welded assembly. On green, all nodes of the internal cylindrical surfaces of rubber bushing inserts were fixed; while in magenta, all nodes of the cylindrical inner surfaces that pin-support the shock absorbers and are pulled down by an impact loading.

Additionally, for the superior swing arm, two more FEAs were performed in a single triangular bracket, due to a stress concentration location at a node in the weld intersection between the swing arm and the triangular plate. For both scenarios, the impact load was divided in two, assuming that only half of the spring force was applied down on the triangular bracket at the inner cylindrical surface of the hole where the shock absorbers were connected. In the first scenario, it was assumed that a welding surface 6.4 mm wide was only at the bottom planar surface of the bracket (Figure 4.7); while in the second scenario, the welding surface was assumed to have the same width of 6.4 mm, but applied to the planar bottom surface and their two contiguous cylindrical surfaces up to the end of the mating surface with the swing arm (Figure 4.8). Details of the meshes used in the FEA for each scenario are shown in Tables and Figures G.6 and G.7.

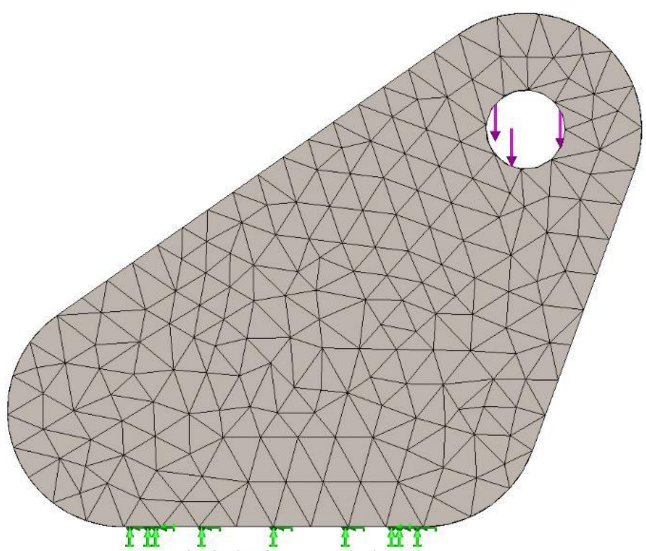

Figure 4.7 Boundary conditions of FEA of the first scenario on a triangular bracket of the top swing arm. On green, all nodes of half of the bottom planar surface; while in magenta, all nodes of the cylindrical inner surface that pin-support the shock absorber and are pulled down by a half of the impact loading.

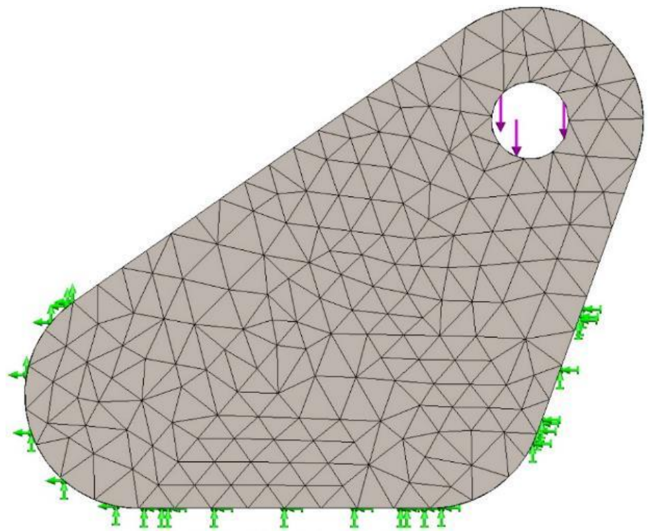

Figure 4.8 Boundary conditions of FEA of the second scenario on a triangular bracket of the top swing arm. On green, all nodes of half of the bottom planar surface and half of the contiguous cylindrical surfaces up to the end of the mating surface of the swing arm; while in magenta, all nodes of the cylindrical inner surface that pin-support the shock absorber and are pulled down by a half of the impact loading.

To hold and pin-connect the other end of each shock absorber, a pair of prismatic brackets of 12.7 mm thickness A36 steel plate were designed and tested under FEA, simulating the same impact loading, assuming each plate receives the half of the load. The FEA was performed setting the same mesh parameters of Section 4.1. Boundary conditions were set assuming that two holes are rigidly bolted with the bottom chassis (Figure 4.9), so the internal cylindrical faces were rigidly fixed, while a half of the spring force was transmitted to one plate through the internal cylindrical hole of the shock absorber pin. Details of the meshes used in the FEA are shown in Table G.8 and Figure G.8.

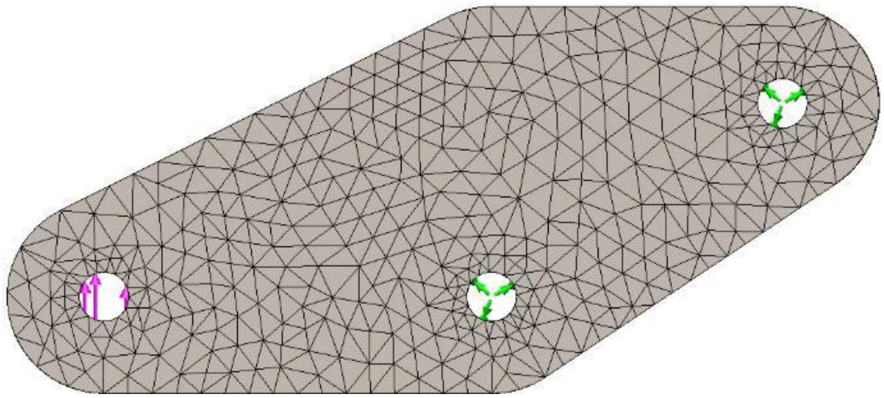

Figure 4.9 Boundary conditions of FEA of the prismatic bracket of the top swing arm. On green, all nodes of the cylindrical surfaces of the holes that are rigidly fixed with respect to the bottom chassis; while in magenta, all nodes of the cylindrical inner surface that pin-support the shock absorber and are pushed upward by a half of the impact loading.

Additionally, for each wheel, two pairs of triangular 9.4 mm thick A36 steel plate brackets were designed to hold the parallel swing arms. Due to the swing movement and the rubber bushings, no FEA was performed in these brackets due to an assumed low stress exerted on them. It was assumed that the brackets holding the shock absorbers, described previously, received the impact loadings.

4.1.3. Lateral Trusses and Bottom Chassis

Two side trusses and two bottom chasses were designed based on triangular shapes that are strong and lightweight (Hibbeler, 2004). Each side of the vehicle has a lateral truss connected to the top frame and a bottom chassis bolted to the truss. Two triangular plates of 12.7 mm thickness (Figure J.1) were added on top of each truss to provide a surface to bolt together the top structure. These bolts were selected to be high strength, Grade 5, and 12.7 mm (1/2 inch) in diameter (Subsection 4.3.13). To assemble each truss with each bottom chassis, a long horizontal plate of 9.5 mm (3/8 inch) in thickness was welded on the main bottom frame, and gussets of the same thickness were added to provide more strength. The assembly was bolted together with 9.5 mm (3/8 inch) diameter high strength bolts, Grade 5 (Subsection 4.3.13). Both structures were designed considering a maximum horizontal clearance of 72.6 cm between plants to avoid plant damage while moving along. The bottom chassis was designed to have enough space to hold and place batteries, electric motors and controllers, and other transmission components.

These structures were manufactured out of 51-mm aluminum square tubing as described in Subsection 4.3.12. Structural members were cut with a horizontal band saw and welded with a TIG/MIG aluminum-welding machine. Due to the size of the welding nozzle used, a distance of about 5 cm was left to allow for a weld bead over the vertex of the triangular shapes. The geometric design of the welds was carried out with SolidWorks Weldments® option, while the stress, strain and displacement analysis was performed with FEA in the SolidWorks Simulation® add-in, considering the same mesh parameters described in Section 4.1. Since both structures are assembled with bolts, it was assumed that internal cylindrical surfaces of critical points were prone to failure by a possible impact load due to a drastic change into the terrain, such as a bump or ditch around 30 cm. Thus, both structures were evaluated by FEA with the same impact loading used in the simulation previously described in Subsection 4.1.2.

For the lateral truss, it was assumed that a vehicle weight of 10,000 N (value rounded up after having more details about the components' weights) was transmitted to the other side to the other lateral truss, so the weight was assumed to be placed at the top planar surfaces of the truss, while the inner surfaces of the bolt holes that assemble it with the bottom chassis were rigidly fixed as shown in Figure 4.10. Details of the meshes used in the FEA are shown in Table and Figure G.9.

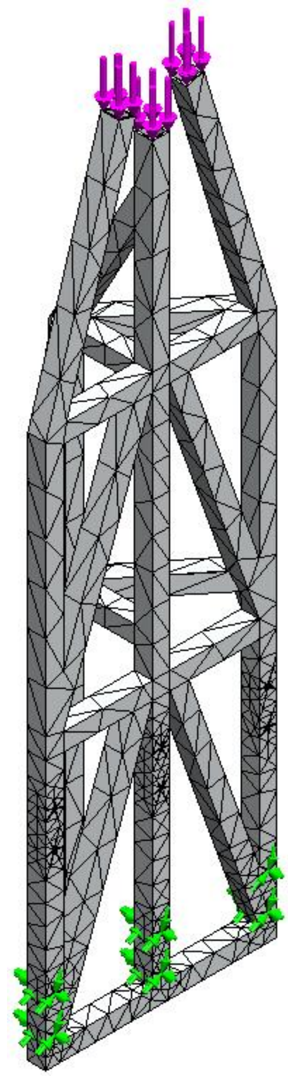

Figure 4.10 Boundary conditions of FEA of the truss. On green, all nodes of the twelve cylindrical inner surfaces that hold the truss with the bottom chassis through bolts; while in magenta, all nodes of the three top planar surfaces that are pushed down by the vehicle's weight transmitted from the other side of the vehicle.

For the bottom chassis, the FEA was performed considering the impact loading exerted by the spring of the shock absorber due to an abrupt change of 30 cm in the terrain (Subsections 4.1.2). The load was applied at the holes of the shock absorber brackets and is shown in magenta arrows pointing upward in Figure 4.11, while restraints were placed at the six holes of the other end of the bottom chassis.

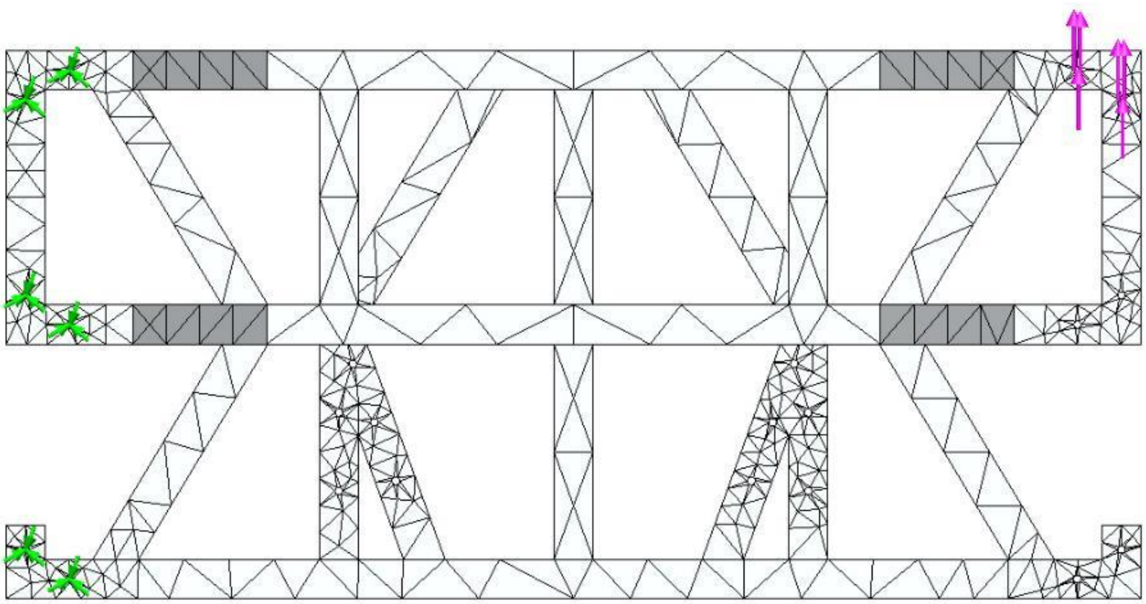

Figure 4.11 Boundary conditions of FEA of the bottom chassis. On green, all nodes of the twenty four cylindrical inner surfaces that hold the chassis with the suspension through bolts; while in magenta, all nodes of the holes that hold the shock absorber of the other side and are pushed up by the impact loading.

Two steel structures were constructed from steel to support the swivel wheels of Subsection 4.3.2, and they were attached to the front of the two bottom chasses described above. The design and construction were part of an expedited modification to the original all-wheel drive design in order to allow quicker field testing that was being delayed due to the lock up of electric motors and the unfinished synchronization controller for the four motors.

4.1.4. Transmission System

The transmission system was designed to be as narrow as possible, limited by a field furrow spacing of 76 cm, and it had to provide for a maximum vehicle speed of 8 km/h. The transmission was constructed from a center pivot irrigation-system transmission designed to work in agricultural conditions. The main component was the gearbox described in Subsection 4.3.1, which provides a gear ratio R = 52:1, and it is able to operate at speeds up to 2,000 rpm. With the selected gearbox and the tire model described in Subsections 4.3.1 and 4.3.2, and assuming no tire slippage, the maximum travel speed of the vehicle, v_{max}, was computed as follows.

$$v_{max} = R\, r_t\, \omega_{max},$$

where r_t is the nominal tire outside radius, and ω_{max} is the maximum angular speed of the gearbox input in radians per unit time.

The power supply was chosen based on the power to weight ratio of similar electric vehicles. An example is an electric golf cart, particularly the 2014 model EG202AK (Suzhou Eagle Electric Vehicle Manufacturing Co., Ltd., Guo Xiang Town, Suzhou, China), which has an electric motor rated at 5 kW maximum power and 270 kg maximum load, with a maximum speed of 40 km/h, (as specified in the data sheet of the Appendix E.1), providing a power to weight ratio of 18.5 W/kg. With the intended design to be around 1,000 kg, the need for power was estimated to be 10 kW, with the two 5-kW electric motors described in Subsection 4.3.3, providing a surplus of power due to the relatively low speed requirement of 8 km/h.

Two independent driving wheels were set at the rear of the EGPV and two swivel pneumatic wheels at the front. Thus, the steering of the vehicle was designed to be differential, such that varying the speed of each wheel independently would change the vehicle direction. This steering method allowed for design simplicity by avoiding a specific actuated steering mechanism. To transmit rotational energy from each motor to its corresponding gearbox, a steel keyed shaft was mounted along with flexible couplers and a mounted ball bearing and keys, as well as a custom-made drive shaft. Materials are described in Section 4.3.

The diameter of the keyed shaft was selected to be 25.4 mm to match the gearbox input size, and the mounted ball bearing was added to avoid directly stressing the motor shaft. The flexible coupler (mcmaster-carr.com) was added to absorb linear and angular misalignments, to fulfill the angular speed and torque requirements, and to match the 25.4 mm shaft diameter on one side and the 22.2 mm diameter of the electric motor shaft on the other side (see Appendix H.1). Two shaft keys (mcmaster-carr.com) were selected to match the cross-sectional dimensions of the shaft keyways, and their lengths were designed with the classical shear stress equation

$$\tau_{max} = \frac{V}{A},$$

where V is the shearing force at the cylindrical face of the shaft, and A is the shearing area of the key (Beer, *et al*, 2003).

The drive shafts described in Subsection 4.3.11 were custom made by Brazos Valley Drivelines Inc. after the other transmission components and suspension system had been assembled, at which point a full list of design parameters such as angular displacement and end-to-end shaft distances were known. See Appendix E.4 for the full list of design parameters.

Some transmission components were attached directly to the frame with ball bearing mounts through bolts or with sheet metal steel brackets 6.5 mm thick. These sheet metal brackets were designed with CAD and analyzed with FEA to hold the electric motors to the bottom chassis. Thus the maximum torque of the electric motor data sheet of 24 N-m was used as the torsion load applied to the internal cylindrical surface of the bracket, while the bolt holes were rigidly fixed, as shown in Figure 4.12. Mesh details are shown in Table G.11 and Figure G.11. These brackets were manufactured as described in Subsection (4.3.12).

Figure 4.12 Boundary conditions of FEA for motor bracket. On green, all nodes of the three cylindrical inner surfaces that hold the motor bracket with the bottom chassis through bolts; while in magenta, all nodes of the inner cylindrical surface where the motor fits and transmits a twisting force due to its maximum torque.

Two more brackets of 9.5 mm thick A36 steel plate were designed to hold and assemble the gearbox described in Subsection 4.3.1. The brackets were designed to match the bolt patterns of the rear and front part of the gearbox and to provide two pivoting points to assemble the suspension swing arms. The rear gearbox bracket was assumed to receive, in the worst case scenario, an impact force caused by a 30-cm bump in which the vehicle may pass while traveling. The impact loading was found by adding a 30-cm step function in the dynamic simulator described in Subsection 5.3.2. Thus, an FEA was performed, concentrating the impact load at the cylindrical surface of the top bolt hole that connects with the upper suspension swing arm, while rigidly fixing the four cylindrical surfaces of the bolt holes that assemble with the rear part of the gearbox as shown in Figure 4.13. The front gearbox, *plt-sus-05* (Figures K.4 and K.10), was added later to provide alignment to the suspension assembly, but no FEA was performed due to the fact that the rear gearbox bracket passed the FEA test by impact loading. Mesh details are shown in Table G.12 and Figure G.12.

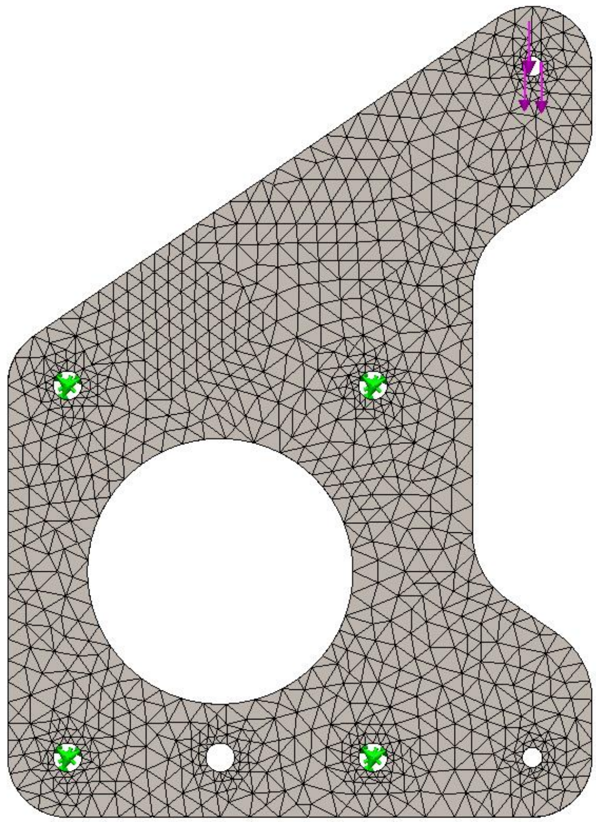

Figure 4.13 Boundary conditions of FEA for rear gearbox bracket. On green, all nodes of the four cylindrical inner surfaces that attach the bracket with the gearbox through bolts; while in magenta, all nodes of the top planar cylindrical surface that is pushed down by the impact loading.

4.2. Electric Ground Phenotyping Vehicle (EGPV) Materials

4.2.1. Gearboxes

Four irrigation-system VS-7000 gearboxes (Valmont Industries, Inc., Valley, NE, USA), model shown in Figure 4.14, were considered to attach eight-bolt-pattern agricultural wheels to the chassis of a 4-wheel drive vehicle. However, at the final stage of the design and to expedite field testing, only two gearboxes were used due to synchronization difficulties in the controlling system, changing the design such that it had two gearboxes at the rear and became a two-wheel drive vehicle. Each gearbox provides a 90º transmission direction change, obtained with a worm gear drivetrain, resulting in a gear ratio of 52:1, and is capable of working at input angular speeds up to 2,000 rpm. The compact gearbox enclosure and features make it suitable to fit between 76.2 cm crop rows.

Figure 4.14 VS-7000 irrigation gearbox (Valmont Industries, Inc., 2012).

4.2.2. Tires, Wheels, and Bolt Pattern Adapters

Two 12.5/70-16 BKT AT-621 All Terrain Traction Tires (BKT Tires USA Inc., Akron, OH, USA) and two aluminum wheels were selected as a lightweight wheel-tire combination for the EGPV's rear wheels. The gearbox bolt pattern was matched with bolt adapters (Figure 4.15). Tire datasheets are included in Appendix E.3.

Figure 4.15 Tire and wheel assembly, and bolt pattern adapters for wheel and gearbox attachment.

Two 63.5-cm (25-in), single-wheel, pneumatic swivel casters (Hamilton Caster, Hamilton OH, USA, model Heavy-Duty 7000) were used as driven front wheels, wheels (Figure 4.16). Steering was accomplished by the speed difference in the drive wheels previously described. The tire size for the caster wheels is 7.5/10, and the caster assembly is capable of withstanding a maximum load of 1,724 kg.

Figure 4.16 Heavy-Duty 7000 pneumatic swivel casters for the rear wheels of the EGPV (Hamilton Caster, 2020).

4.2.3. Electric Motors and Controllers

Two 48V-input, 5-kW power, fan-cooling electric motors (model HPM5000B Golden Motor Technology Co Ltd., Changzhou, Jiangsu, China) were used to propel the EGPV (Figure 4.17). This motor model has multiple applications in electric cars, golf carts, motorcycles, and boats. Its water resistant, lightweight design of 11 kg (aluminum case), customizable angular velocity from 2,000 to 6,000 rpm, and 91% efficiency make this motor suitable for the EGPV, mainly because it is compact to fit between sorghum rows, it is lightweight to not maintain a lighter vehicle that is intended to not to cause severe compaction of soils. The motor shaft has a 22.2 mm diameter with a keyway that is 5 mm wide and 43 mm long (more size and shape information is shown in Figure A.3).

Two 2.5-kg sine-wave controllers (model VEC300 Golden Motor Technology Co. Ltd., Changzhou, Jiangsu, China) were used to control each of the motors independently, as shown in Figure 4.6. According to the vendor, these motor controllers use a field-oriented control (FOC) technology to directly control torque, enabling reliable, highly efficient, smooth, and responsive performance, and configurable speed limit. These motor controllers receive an input voltage of 48V and a maximum current of 300A. The DC bus current can vary from 30A to 200A to provide output power from 1.0 kW to 10.0 kW.

Figure 4.17 Electric Motor and motor controller (Golden Motor Technology, Co., Ltd., 2016).

4.2.4. Batteries

Eight Trojan® T-1275 Master-Vent, 12V, deep-cycle, lead-acid batteries (Trojan Battery Company, Santa Fe Springs, CA, USA), were used to power the motors of the EGPV. Each battery can provide energy of 1.99 kWh and 150 Ah over 20 hours, or 120 Ah over 5 hours. The battery's has dimensions of 329 × 181 × 283 mm and weighs 39 kg. The selected batteries were the embedded low-profile terminal type in order to save height in the vehicle's chassis (see figures H.7 and H.8).

4.2.5. Shock Absorbers

Two shock absorbers (Kawasaki Motors Corp., Santa Ana, CA, USA, part number 45014-Y004-966) were used to absorb vibrations due to roughness and irregularities on the soil surface (Figure 4.18). The shock absorbers were selected based on the specifications of a 2016 Brute Force® 300 Kawasaki all-terrain vehicle (ATV), which is able to drive on very irregular dirt roads and absorb impacts with front and rear suspensions with wheel travels of 13.7 cm on average. The manufacturer did not include the spring rate in the specifications, so data were obtained from a similar spring model, a Kawasaki Brute Force® 650i, which has a spring rate between 46.4 and 53.6 kg/cm.

Figure 4.18 Shock absorber used in the UGPV suspension system (Kawasaki Motors Corp, 2020).

4.2.6. Rubber Bushings

In order to absorb random impacts from the oscillation of suspension arms due to terrain irregularities, eight rubber bushings (Suzuki Motor of America, Inc., Brea, CA, USA, part number 09319-10055) were used as shown in Figure 4.19. The selection was based on the bushings' ability to fit in the steel tubing of 34.9 mm inner diameter shown at the ends of the suspension arm of Figure 4.10.

Figure 4.19 Rubber bushing used in the swing arms of the EGPV suspension system. Measurement scale in inches (Partzilla, 2020).

4.2.7. Keyed Shafts

Two 1045 carbon steel, 25.4-mm diameter, 15.24-mm long, shafts were used as extensions to transmit power from the motor shafts to the u-joint drive shafts (described below). Each shaft has a full-length keyway with a cross section 3.18 mm deep by 6.35-mm wide (Part number 1497K144, McMaster-Carr). A full set of properties and dimensions can be found in Appendix I.1.

4.2.8. Flexible Couplings

Flexible couplings were used to absorb angular and offset misalignment between the motor shafts and keyed shafts. Each flexible coupling consists of three parts (Part numbers 6408K251, 6408K253, and 6408K75, respectively, McMaster-Carr): a hub (Figures I.3 and I.4) that fits a 22.2-mm shaft coming from the motor, a hub (Figures I.5 and I.6) for the 25.4-mm shaft of the mounted ball bearing, and a Buna-N rubber spider that absorbs vibrations and allows misalignments in the shafts at the connection (Figures I.7 and I.8). In Figure J.24, the whole transmission assembly is shown in exploded view including the flexible coupling components and shafts (item numbers 4 to 7 of Figure J.24).

4.2.9. Shaft Keys

Four 1095 spring steel, minimum hardness, Rockwell B91 keys of 6.4 × 6.4 × 12.7 mm were cut from a standard key stock of 6.35 × 6.35 × 304 mm in length (Part number 98535A150, McMaster-Carr; see Figure I.9) and used to hold the keyed shafts with the 25.4-mm coupling hubs and the CV joint drive shaft described below in Subsection 4.2.11.

Two other 5.0 × 5.0 × 12.7 mm keys (Part number 92288A725, McMaster-Carr) were cut to attach the motor shafts with the 22.2-mm coupling hubs (see Figures I.11 and I.12).

4.2.10. Mounted Ball Bearings

Two high-speed cast iron mounted steel ball bearings (Part numbers 2773T56 or 7728T56, McMaster-Carr), for 1-inch shaft diameter were used to diminish lateral loads on the motor shafts. These mounted bearings support the keyed shafts with two setscrews. These bearings are double sealed and lubricated with GoldPlex-HP grease. A full properties list and drawing is shown in figures I.13 and I.14 (Appendix I).

4.2.11. Drive Shafts

Two continuously variable joint (CVJ) drive shafts (Figure 4.20) were custom-manufactured by Brazos Valley Drivelines, Inc., Bryan, TX, USA, according to motor specifications including maximum torque of 24 N-m, angular velocity of 2,500 rpm, maximum offset distance between motor and gearbox shafts of 9 cm, maximum misalignment angle of 8 degrees due to the suspension travel, variable shaft length between 58 and 64 cm, and attachment ends to shafts of 25.4 mm diameter (see items 7 and 16 of Figure J.24). The manufacturer used industrial type shafts with Dana Spicer® series 1310 components for this specific application.

Figure 4.20 CVJ driveshaft for transmission between keyed shaft and gearbox.

4.2.12. Tubing and Plates for Chassis Construction

A 6061-T6 aluminum round tube 3.7 m long with 25.2 cm outer diameter and 12.7 mm wall thickness (Metals Depot International, Winchester, KY, USA, part number T3R6500) was used to construct two traverse structural members 152.4 and 203.2 cm long. These lengths were selected to provide two different working widths for the vehicle. According to the vendor, this round tube has yield and ultimate tensile strengths around 275 and 310

MPa, respectively, and a Brinell hardness value of 95. The tube also fulfills ASTM B221 and SAE QQA-200/8 standards.

Nine 6061-T6 aluminum square tubes 6 m long and 5.1 × 5.1 cm outer dimensions and 6.4 mm wall thickness (Metals Depot International, Winchester, KY, USA, part number T32214) were used to cut the required structural members to build the main frame of the vehicle. The vendor provided the same mechanical properties and adherence to standards as previously described for the round tube.

An ASTM A500 grade B steel square tube 4.6 m long with 5.1 × 5.1 cm outer dimensions and 4.8 mm wall thickness (Metals Depot International, Winchester, KY, USA, part number T122316) was used to fabricate five different structural members that were welded together to assemble two front frames that hold the swivel wheels at the front of the EGPV. The vendor provided values for yield strength as 317 MPa and ultimate tensile strength as 400 MPa. Additionally, an outside corner radius up to 3 times the wall thickness was specified.

Another ASTM A500 steel square tube, this one 1.3 m long with 3.8 × 3.8 cm outer dimensions and 6.4 mm wall thickness (Metals Depot International, Winchester, KY, USA, part number T1112250), was used to fabricate four 30.5 cm long swing arm members for suspension.

An ASTM A513 Type 5 steel round tube 41 cm long with 47.6 mm outside diameter and 34.9 mm inside diameter (Metals Depot International, Winchester, KY, USA, part number T21178250) was cut into eight members 49.2 mm long. The vendor specifies yield and ultimate tensile strengths around 483 and 552 MPa, respectively, and a Brinell hardness value of 80. This material fulfills the ASTM A513 Type 5, 1020/1026 mechanical grade standards. Each of these members was welded to an end of the above swing arm members, and a rubber bushing like those previously described was placed tightly inside each round tube as shown in Figure 4.21.

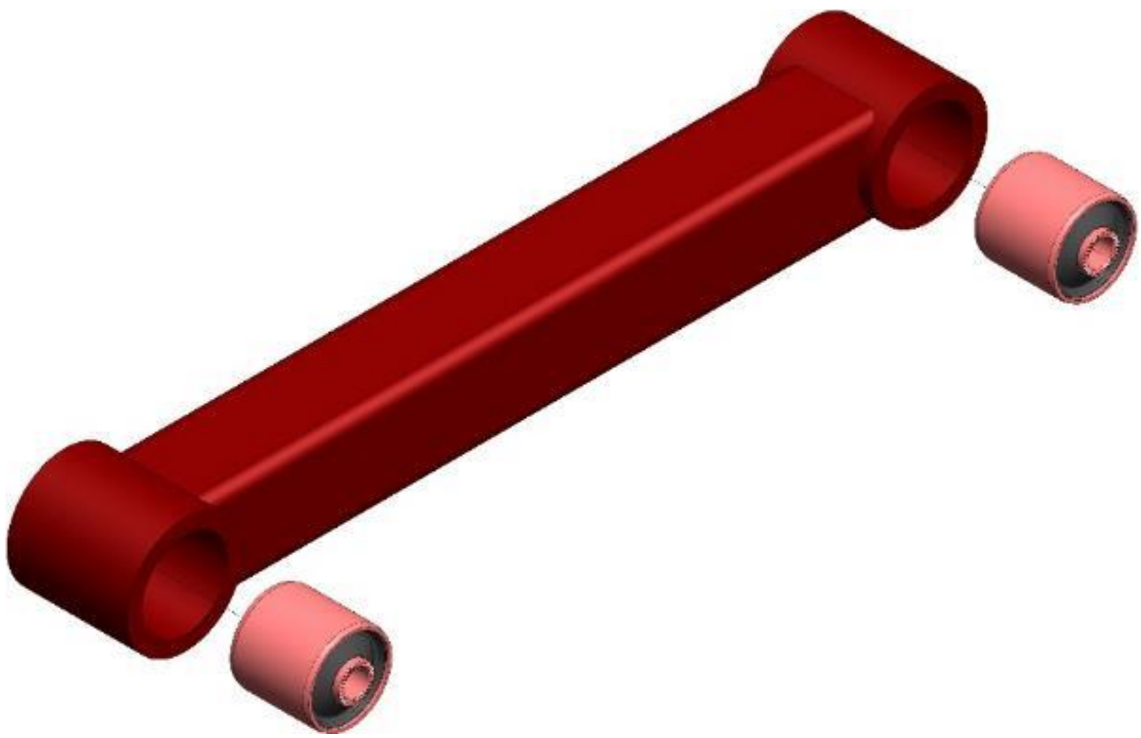

Figure 4.21 Suspension swing arm with rubber bushings.

Fifty 6061-T6 aluminum flat plates of several shapes were custom cut with water-jet by a local metal shop (Second Generation Arc ‘N Spark, Bryan, TX, USA). Plates of 12.7- and 9.7-mm thickness were welded to the structural tubing to strengthen the frame, most of the plates functioning as gussets. A different vendor supplied the aluminum plate material, but the same mechanical properties described previously for aluminum 6061-T6 tubing were assumed.

Additionally, forty-four ASTM A-36 steel plates were procured. Three thicknesses of 12.7, 9.7, and 6.4 mm were waterjet cut into different shapes and sizes, and two of them bent, by the same local metal shop. These plates were assembled with bolts to hold some components of the suspension and transmission system. The vendor did not specify mechanical properties, so some properties were assumed and taken from specifications on A-36 steel by Metals Depot (Metals Depot International, Winchester, KY, USA): yield and ultimate tensile strengths around 248 and 400 MPa and a Brinell hardness of 112.

4.2.13. Fasteners

All bolts, nuts, washers and spacers were procured from McMaster-Carr (www.mcmaster.com). The list of all fastener components and their quantities is included in Table 4.2.

Table 4.2 McMaster-Carr hardware BOM. The list includes the bolts, the washers, the nuts, and the spacers used in the EGPV assembly (prices updated on May 2017).

Subassembly	Part Number	Description	Qty	Price	Total	Also Used
Top Chassis (TC)	90128A367	Zinc-Plated Alloy Steel Socket Head Screw 3/8"-24 Thread Size, 1-1/4" Long	6	$0.57	$3.41	
	91104A033	Zinc Yellow-Chromate Plated Steel Split Lock Washer for 1/2" Screw Size, 0.512" ID, 0.869" OD	36	$0.12	$4.20	S
	91247A231	Medium-Strength Grade 5 Steel Hex Head Screw, Zinc-Plated, 3/8"-24 Thread Size, 3" Long, Partially Threaded	2	$0.50	$1.01	
	91247A368	Medium-Strength Grade 5 Steel Hex Head Screw, Zinc-Plated, 1/2"-20 Thread Size, 5" Long, Partially Threaded	16	$1.86	$29.70	
	95462A525	Medium-Strength Steel Hex Nut, Grade 5, Zinc-Plated, 1/2"-20 Thread Size	16	$0.15	$2.36	
	98023A118	Zinc Yellow-Chromate Plated Grade 8 Steel Washer with Material Certificate, 1/2" Screw Size, 0.531" ID, 1.062" OD	32	$0.37	$11.87	
Bottom Chassis	91104A031	Zinc Yellow-Chromate Plated Split Lock Washer, Grade 8 Steel, 3/8" Screw Size, 0.385" ID, 0.680" OD	150	$0.05	$8.12	S, T
	91247A234	Medium-Strength Grade 5 Steel Hex Head Screw, Zinc-Plated, 3/8"-24 Thread Size, 3-3/4" Long	60	$0.69	$41.58	
	91247A241	Medium-Strength Grade 5 Steel Hex Head Screw, Zinc-Plated, 3/8"-24 Thread Size, 5-1/2" Long	10	$1.26	$12.56	
	95462A515	Grade 5 Steel Hex Nut, Zinc Plated, 3/8"-24 Thread Size, 9/16" Wide, 21/64" High	92	$0.08	$7.62	T, TC
	98180A130	Grade 8 Steel Washer Zinc-Aluminum Coated, 3/8" Screw Size, 0.406" ID, 0.812" OD	170	$0.15	$25.98	T, S, TC
Suspension (S)	90128A716	Zinc-Plated Alloy Steel Socket Head Cap Screw, 1/2"-13 Thread, 1-1/2" Length	20	$1.04	$20.84	
	90201A333	Extreme-Strength Grade 9 Steel Cap Screw, 3/8"-16 Thread, 3-1/2" Long, Zinc-Plated	4	$2.10	$8.38	
	90201A336	Extreme-Strength Grade 9 Steel Cap Screw, 3/8"-16 Thread, 4" Long, Zinc-Plated	12	$2.88	$34.56	
	90850A200	Zinc Yellow-Chromate Plated Steel Flat Washer, Grade 9, 3/8" Screw Size, 0.411" ID, 0.827" OD	48	$0.28	$13.54	
	91117A222	Zinc-Plated Steel Oversized Flat Washer, 3/8" Screw Size, 0.406" ID, 0.235"-0.265" Thick	8	$1.86	$14.86	
	91257A650	High-Strength Grade 8 Steel Cap Screw, 3/8"-16 Thread, 7" Long, Zinc-Plated	8	$2.65	$21.20	
	91257A664	High-Strength Grade 8 Steel Cap Screw, 3/8"-24 Thread, 3-1/2" Long, Zinc-Plated	24	$1.23	$29.47	
	91280A638	Medium-Strength Zinc-Plated Steel Cap Screw - Class 8.8, M10 Fully Threaded, Pitch: 1.5, 40mm Long	20	$0.41	$8.19	
	92510A479	Aluminum Unthreaded Spacer, 3/4" OD, 2-1/2" Length, for 3/8" Screw Size	8	$7.56	$60.48	
	92510A491	Aluminum Unthreaded Spacer, 3/4" OD, 1/4" Length, for 3/8" Screw Size	40	$1.73	$69.20	
	93591A300	Grade 9 Steel Distorted-Thread Toplock Nut, Cadmium-Plated, 3/8"-16 Thread, 9/16" Wide, 13/32" High	24	$0.47	$11.28	
	94895A815	Zinc Yellow-Chromate Plated Steel Hex Nut, Grade 8, 3/8"-24 Thread Size, 9/16" Wide, 21/64" High, packs of 100	24	$0.07	$1.74	
Transmission (T)	91247A237	Medium-Strength Grade 5 Zinc-Plated Steel Cap Screw, 3/8"-24 Thread, 4-1/2" Long	8	$1.04	$8.28	
	91257A462	High-Strength Grade 8 Steel Cap Screw, 3/8"-24 Thread, 3-1/4" Long, Zinc-Plated	4	$0.89	$3.54	
	91290A428	Black-Oxide Class 12.9 Socket Head Cap Screw, Alloy Steel, M8 Thread, 22mm Length, 1.25mm Pitch	16	$0.17	$2.66	
	92510A808	Aluminum Unthreaded Spacer 3/4" OD, 1" Length, for 3/8" Screw Size	8	$2.88	$23.04	
	95615A150	Steel Nylon-Insert Locknut, Grade 5, Zinc-Plated, 3/8"- 24 Thread Size	4	$0.09	$0.36	
				Total:	**$480.02**	

4.3. Data Collection for the EGPV Testing

The phenotyping platform was tested in the field for functionality and its ability to enter in a single turn to a set of four furrows (vehicle working width) after a headland (2.29 m of turning radius for furrows of 76.2 cm, and 3.05 m of turning radius for furrows of 101.6 cm), for an average speed necessary to perform image recordings (2.9 km/h, estimated from the stereo vision experiment) and for a maximum speed for navigating in the roadway (6 km/h). Thus, the EGPV was tested for turning radius and speed. Tire pressure was maintained at 262 kPa (38 psi) for the rear driving wheels and 221 kPa (32 psi) for the front driven wheels for all tests, as recommended by the tire manufacturers.

4.3.1. Turning Radius

The turning radius was measured from a resting position. A marker was positioned on the ground, aligning it with the center of the EGPV. Turning was tested with the motors set to three different speeds of forward travel. The control voltage inputs in 8-bit digital values were 1200 (1.0V), 1600 (1.3V), and 2000 (1.6V). A turn was considered to be completed when the EGPV had turned to the opposite direction (180º). Then another marker was placed in the same position with respect to the EGPV center, as at the starting point. The turning radius was estimated by measuring the distance – perpendicular to the forward direction – between starting and ending markers and dividing it by 2. The experiment was performed to the left and right sides on tilled soil with crop residues in the TAMU Farm with three replications.

4.4. Data Analysis for the EGPV

4.4.1. Turning Radius Analysis

The average turning radius measured in the field was considered the radius required to allow the vehicle to enter to the next set of furrows. The EGPV was designed to cover a working width of four furrows. For a 101.6 cm distance between furrows, the target turning radius was set to be 3.05 m, while 2.29 m for a furrow offset configuration of 76.2 cm. These radii are the computed values assuming the machine will skip a working width and then enter to the next set of four furrows.

5. PART II: ELECTRIC GROUND PHENOTYPING VEHICLE: RESULTS OF MACHINE DESIGN

5.1. Top Structure

5.1.1. Analytical Solution on the Round Tubes

By substituting the radii of the aluminum tube (Figure J.1) into equation (4.3), the polar area moment of inertia was found as

$$J = \frac{\pi}{2}((0.0762 \text{ m})^4 - (0.0535 \text{ m})^4) = 2.7419 \times 10^{-5} \text{ m}^4.$$

Now, substituting the torque and polar area moment of inertia into equation (4.2), the maximum shear stress was

$$\tau_{max} = \frac{(4928.4 \text{ N} \cdot \text{m})(0.0762 \text{ m})}{2.7419 \times 10^{-5} \text{ m}^4} = 13.7 \text{ MPa}.$$

The shear modulus was found substituting the modulus of elasticity E = 68.9 GPa, and the Poisson ratio $\nu = 0.35$ for the material into equation (4.5) as

$$G = \frac{68.9 \text{ GPa}}{2(1 + 0.35)} = 25.5 \text{ GPa}.$$

Substituting this value, the assumed static torque T = 4928.4 N-m, the lengths of the short and long tubes $l_s = 1524$ mm and $l_l = 2013$ mm, and the value of $J = 2.7419 \times 10^{-5} \text{ m}^4$ into equation (4.4), the maximum angular deformation was found as

$$\phi_s = \frac{T(4928.4 \text{ N} \cdot \text{m})(1.524 \text{ m})}{(2.7419 \times 10^{-5} \text{ m}^4)(25.5 \times 10^9 \text{ N/m}^2)} = 0.0107 \text{ rad},$$

with a maximum linear displacement of

$$r_2 \sin \phi = (0.0762 \text{ m}) \sin 0.0107 = 0.8 \text{ mm},$$

and

$$\phi_l = \frac{T(4928.4 \text{ N} \cdot \text{m})(2.013 \text{ m})}{(2.7419 \times 10^{-5} \text{ m}^4)(25.5 \times 10^9 \text{ N/m}^2)} = 0.0143 \text{ rad},$$

with a maximum linear displacement of

$$r_2 \sin \phi = (0.0762 \text{ m}) \sin 0.0143 = 1.1 \text{ mm}.$$

By substituting $\tau_{max} = \tau_{xy} = \tau_{xz} = 13.7$ MPa, and G = 25.5 GPa in equation (4.6) the maximum shear strain was found as

$$\gamma_{xy} = \gamma_{xz} = \frac{13.7 \times 10^6 \text{ Pa}}{25.5 \times 10^9 \text{ Pa}} = 5.4 \times 10^{-4}$$

Now the FOS using the maximum-shear-stress theory was

$$FOS = \frac{\tau_{fail}}{\tau_{allow}} = \frac{Sy/2}{\tau_{max}} = \frac{275 \text{ MPa}/2}{13.7 \text{ MPa}} = 10.$$

All these analytical calculations were performed in the MATLAB® script called *torsion.m*, included in Appendix F.1.

5.1.2. Finite Element Analysis (FEA) on the Round Tubes

The round tubes with lengths of 1524 mm and 2013 mm were designed in CAD and denominated *tub-rnd-01.sldprt* and *tub-rnd-02.sldprt*, respectively. Their corresponding drawings are shown in Figures J.1 and J.2. Since FEA simulations for both tube lengths were very similar, besides displacement, only those results performed in the longest tube were considered to be displayed due to its higher likelihood of failure. Figure 5.1 shows the results of FEA performed in *tub-rnd-02.sldprt* for shear stress and its corresponding FOS. With this simulation it is possible to observe (Figure 5.1a) that the maximum shearing stress is 20.19 MPa, located at the annular nodes of the boundary conditions set at the simulated cylindrical surfaces located at the ends of the tube, where the welding seams were intended. In the same locations as the maximum shear stresses, the lowest FOS was located with a minimum value of 6.0, which is 40% smaller than the analytically computed value (see Figure 5.1b). However, this value is still conservative to withstand the assumed torsion load, (1) due to its high value, and (2) because the maximum-shear-stress failure theory is 15% more conservative when compared to the distortion energy (von Mises) failure theory (Budynas, 2015). Another FEA was performed on *tub-rnd-02.sldprt* with the distortion energy theory in order to compare results. Figure 5.2 shows the results for von Mises stress (Figure 2.2a) and its corresponding FOS (Figure 5.2b). In this case, the maximum von Mises stress was 39.5 MPa, with a minimum FOS of 7.0.

5.1.3. Analytical and FEA Comparison on the Round Tubes

In Table 5.1, a summary of the maximum and minimum values of FEA and analytical stresses, strains and displacements for each of the five mesh sizes is shown as a means of comparison. This table includes results for both CAD models: *tub-rnd-01.sldprt* and *tub-rnd-02.sldprt*. Additionally, an FEA run using the same size mesh number 5 was repeated, but its boundary conditions were changed to restrain the left annular planar surface of the tube (left surface nonvisible in Figures 5.1 and 5.2) when applying the torsional load at the other annular planar surface at the other end of the tube. This run was reported in Table 5.1 as Mesh 5RT. These restraints and torsional (RT) load boundary condition changes were only to compare and validate FEA with the analytical solution.

In Table 5.1 it is possible to see that maximum shear stresses, displacements, and shear strains simulated by FEA have greater absolute values than the analytical solutions, except for those of Mesh RT, which are closer to the analytical values. However, this last meshing was only performed to compare FEA with the analytical solution, but it is more realistic having restraints and the torque application in the cylindrical welding surfaces at the ends of the tubes (Figure J.1).

In general, the FEA for both tubes, *tub-rnd-01.sldprt* and *tub-rnd-02.sldprt*, showed numerical similarities (Table 5.1). The minimum FOS of 5.8 was computed for *tub-rnd-01.sldprt*, when this was simulated using Mesh 5 and using the maximum-shear-stress theory. This FOS is still a safe value and recommended to be equal to or higher than 4.0 for a machine element that has few input data, uncertainty about combined loading, welding processes and rough environmental conditions, especially at the beginning of the design process (R. L. Mott, 2004). Also, it is noticeable that the FOS = 6.7 when the von

Mises stress used corresponds to a 15% larger value than the FOS of maximum shear stress, validating what the theory says about this percentage (Budynas, 2015).

In terms of convergence, Table 5.2 shows the comparison of maximum shear stress and displacements for the five mesh sizes. Each convergence error is measured computing the absolute difference of the current mesh and the previous, relative to the current, and its value is expressed as a percentage. It is noticeable that for *tub-rnd-01.sldprt*, a convergence maximum shear stress value is found as 15.5 MPa, and a convergence displacement of 0.8 mm; while for *tub-rnd-02.sldprt*, a convergence maximum shear stress value of 14.9 MPa, and a convergence displacement of 1.0 mm. For those shear stresses, the corresponding FOS values are 8.2 for *tub-rnd-01.sldprt*, and 7.3 for *tub-rnd-02.sldprt*. For this case, only maximum shear stress theory was analyzed, because it is the recommended theory for ductile material biaxial stresses (R. L. Mott, 2014), considering that a torque produces shear stresses on plane *x*, in directions *y* and *z*.

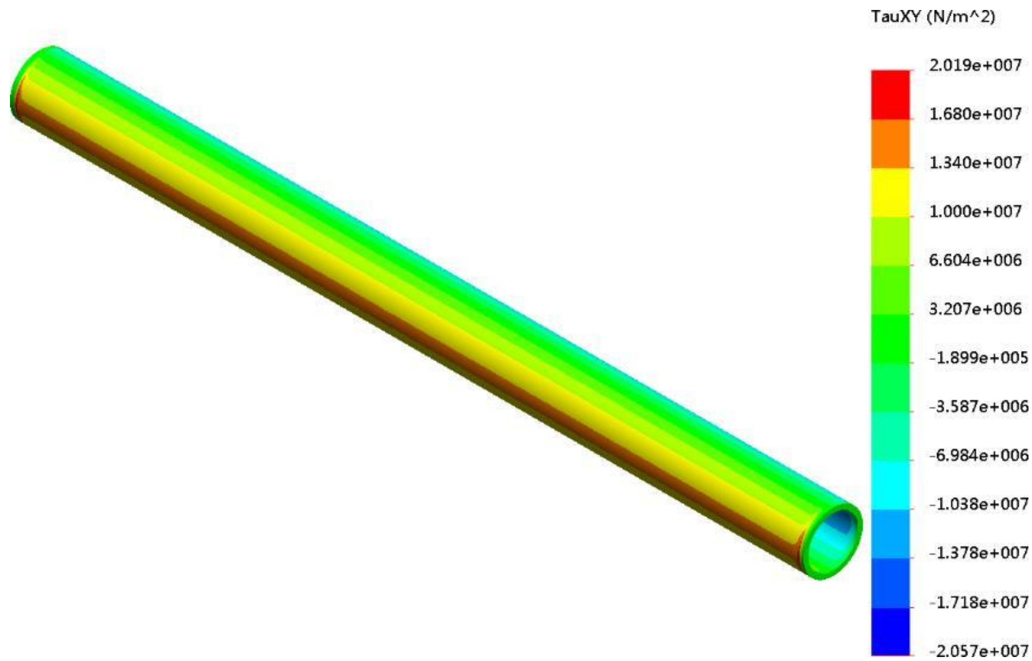

(a)

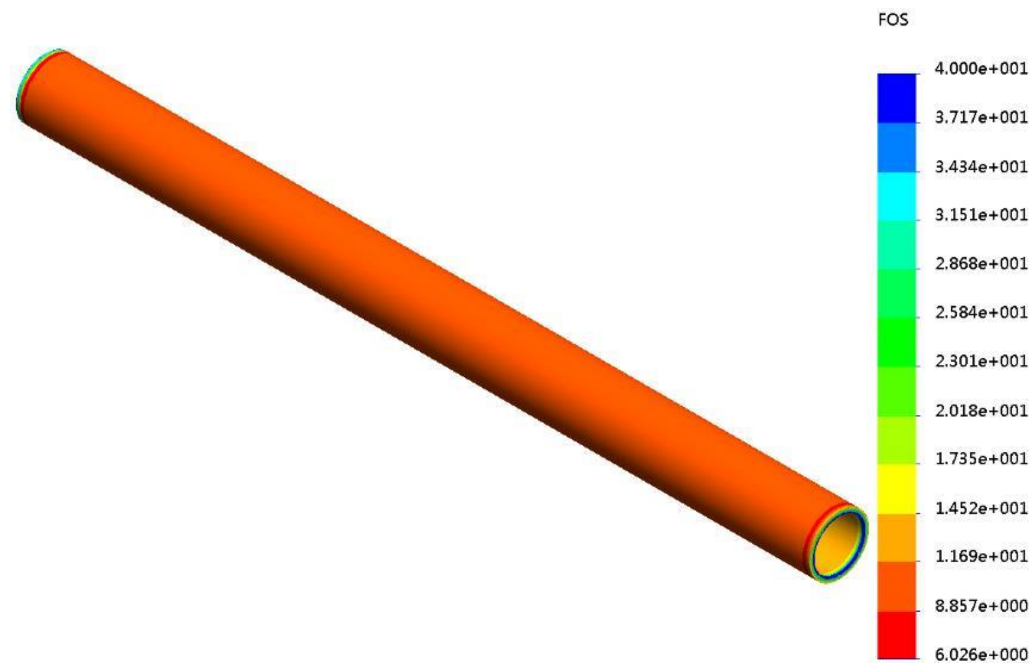

(b)

Figure 5.1 FEA results for shear stress and factor of safety on *tub-rnd-02.sldprt*. Fixture in the welding surface on the left hand side, with a torsion load of 4928.4 N·m applied on the other welding surface on the right hand side: (a) shear stress (τ_{xy}), and (b) factor of safety (FOS). The mesh number 5 was used for this analysis. The deformation scale applied was 1.

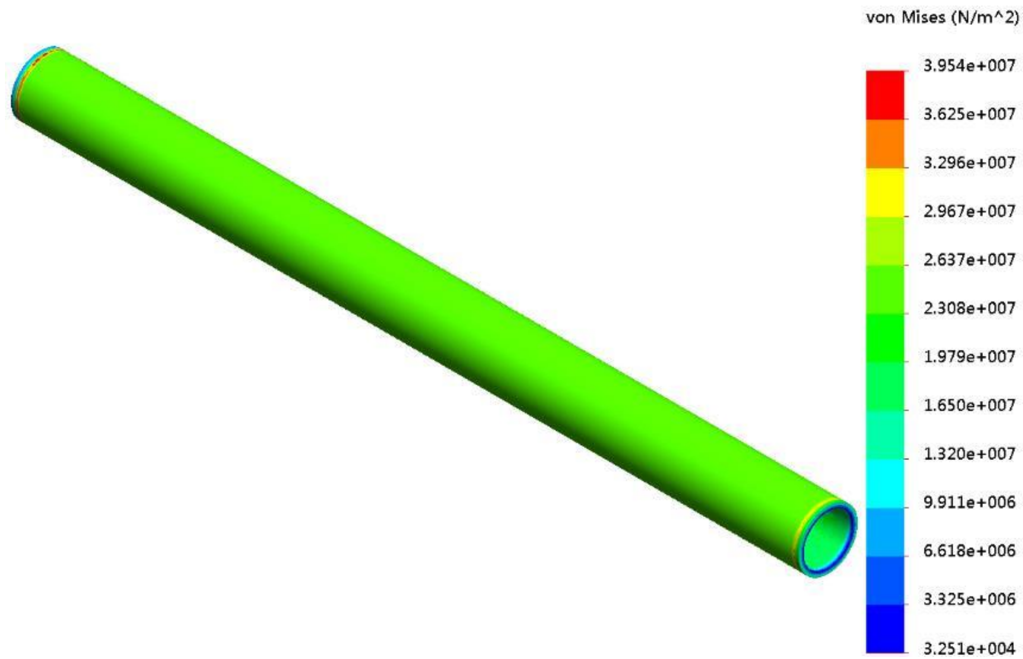

(a)

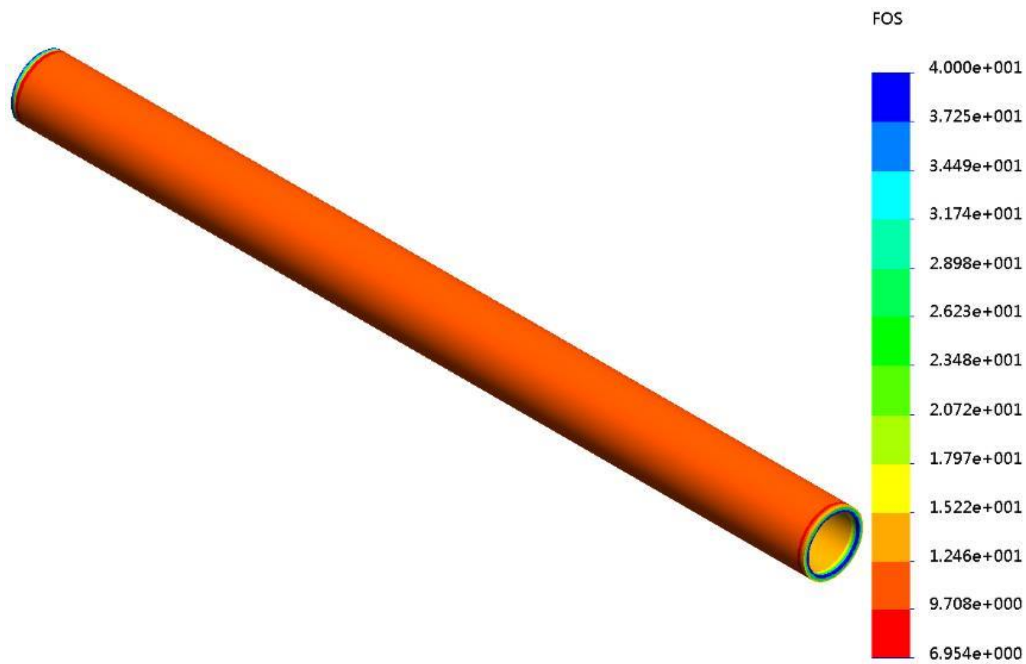

(b)

Figure 5.2 FEA results for von Mises stress and factor of safety on *tub-rnd-02.sldprt*. Fixture in the welding surface on the left hand side, with a torsion load of 4928.4 N·m applied on the other welding surface on the right hand side: (a) von Mises stress (σ_v), and (b) factor of safety (FOS). The mesh number 5 was used for this analysis. The deformation scale is 1.

Table 5.1 Summary of FEA results for torsion load on the top structure under five mesh sizes. The first half of the results corresponds to the 1,524 mm long tube (*tub-rnd-01.sldprt*), while the second half corresponds to 2,032 mm long tube (*tub-rnd-02.sldprt*). All the FEA boundary conditions (restraint and torque) were applied to the ends of the tubes in a 12.7 mm long external cylindrical surface, while restraint and torque in simulations "Mesh 5 RT" were applied the extreme planar annular surfaces.

Property	Mesh 1 (46 mm)		Mesh 2 (37 mm)		Mesh 3 (28 mm)		Mesh 4 (19 mm)		Mesh 5 (10 mm)		Mesh 5 RT (10 mm)		Analytical	
	Min	Max	Min	Max	Min	Max	Min	Max	Min	Max	Min	Max	Min	Max
σ_v (MPa)	7.8	28.9	1.2	27.9	0.8	29.1	0.3	32.2	0.1	41.0	19.6	23.9		
u_{res} (mm)	0.0	0.8	0.0	0.9	0.0	0.8	0.0	0.8	0.0	0.8	0.0	0.8		
ϵ_{eq} ($\times 10^{-4}$)	0.1	3.7	0.2	3.6	0.1	3.7	0.0	4.1	0.0	5.3	2.5	3.1		
τ_{xy} (MPa)	-14.3	14.0	-15.4	15.5	-15.6	15.5	-17.4	16.5	-20.5	19.1	-13.7	13.7	-13.7	13.7
τ_{xz} (MPa)	-14.2	15.4	-14.6	15.8	-15.7	15.8	-17.6	16.8	-21.8	21.3	-13.7	13.7	-13.7	13.7
τ_{yz} (MPa)	-9.8	10.3	-9.9	10.1	-10.4	11.2	-10.4	11.1	-17.5	17.0	-0.9	0.9	0.0	0.0
u_x (μm)	-3.9	3.6	-6.1	5.4	-5.9	7.1	-4.4	2.9	-1.6	1.5	-0.2	0.2	0.0	0.0
u_y (mm)	-0.8	0.8	-0.7	0.9	-0.8	0.8	-0.8	0.8	-0.8	0.8	-0.8	0.8	-0.8	0.8
u_z (mm)	-0.8	0.8	-0.9	0.8	-0.8	0.8	-0.8	0.8	-0.8	0.8	-0.8	0.8	-0.8	0.8
γ_{xy} ($\times 10^{-4}$)	-5.5	5.4	-5.9	6.0	-6.0	6.0	-6.7	6.0	-1.6	1.5	-5.3	5.3	-5.1	5.1
γ_{xz} ($\times 10^{-4}$)	-5.5	5.9	-5.6	6.1	-6.1	6.1	-6.1	6.5	-8.4	8.2	-5.3	5.3	-5.1	5.1
γ_{yz} ($\times 10^{-4}$)	-3.8	4.0	-3.8	3.9	-4.0	4.3	-4.0	4.3	-6.8	6.6	-0.3	0.3	0.0	0.0
FOS ($\sigma_{v\max}$)	9.5	353.1	9.9	230.7	9.5	352.8	8.5	923.7	6.7	3661.0	11.5	14.0		
FOS ($\tau_{\max}$)	8.2	305.8	8.5	199.9	8.2	319.9	7.4	800.0	5.8	3177.0	10.0	12.1	10.0	
σ_v (MPa)	0.9	29.9	1.1	28.4	1.2	32.6	0.4	30.9	0.0	39.5	19.7	23.8		
u_{res} (mm)	0.0	1.3	0.0	1.3	0.0	1.1	0.0	1.1	0.0	1.1	0.0	1.1		
ϵ_{eq} ($\times 10^{-4}$)	0.1	3.8	0.1	3.6	0.2	4.2	0.0	4.0	0.0	5.1	2.5	3.1		
τ_{xy} (MPa)	-14.7	15.7	-15.3	14.8	-15.0	14.9	-16.7	17.1	-20.6	20.2	-13.7	13.8	-13.7	13.7
τ_{xz} (MPa)	-14.5	14.4	-15.2	14.7	-16.1	16.5	-16.9	16.8	-21.1	20.3	-13.7	13.7	-13.7	13.7
τ_{yz} (MPa)	-9.7	9.8	-10.1	10.0	-11.6	11.0	-11.2	14.6	-15.8	16.5	-0.9	0.9	0.0	0.0
u_x (μm)	-13.5	13.0	-11.8	12.1	-0.9	0.9	-2.4	2.5	-0.2	0.1	-0.3	0.3	0.0	0.0
u_y (mm)	-1.1	1.1	-1.1	1.0	-1.1	1.1	-1.1	1.0	-1.1	1.1	-1.1	1.1	-1.0	1.0
u_z (mm)	-1.3	0.8	-0.9	1.3	-1.1	1.1	-1.0	1.1	-1.1	1.1	-1.1	1.1	-1.0	1.0
γ_{xy} ($\times 10^{-4}$)	-5.6	6.0	-5.9	5.7	-5.8	5.7	-6.4	6.6	-7.9	7.8	-5.3	5.3	-5.1	5.1
γ_{xz} ($\times 10^{-4}$)	-5.6	5.6	-5.9	5.7	-6.2	6.3	-6.5	6.5	-8.1	7.8	-5.3	5.3	-5.1	5.1
γ_{yz} ($\times 10^{-4}$)	-3.7	3.8	-3.9	3.8	-4.5	4.2	-4.3	5.6	-6.1	6.4	-0.4	0.4	0.0	0.0
FOS ($\sigma_{v\max}$)	9.2	319.3	9.7	249.1	8.4	235.4	8.9	733.5	7.0	8458.0	11.5	14.0		
FOS ($\tau_{\max}$)	8.0	276.6	8.4	236.0	7.3	205.5	7.7	645.7	6.0	7326.0	10.0	12.1	10.0	

Table 5.2 Percent of absolute relative convergence error (CE) for maximum von Mises and shear stress on face *x*, direction *y* and for displacement in *y* for five different mesh sizes. The first half of the table corresponds to results of FEA for the 1,524 mm long tube (*tub-rnd-01.sldprt*), while the second half corresponds to 2,032 mm long tube (*tub-rnd-02.sldprt*).

Mesh	Nodes	σ_v (MPa)	CE for σ_v (%)	τ_{xy} (MPa)	CE for τ_{xy} (%)	u_y (mm)	CE for u_y (%)
1	3613	28.9	Unknown	14.0	Unknown	0.8	Unknown
2	7285	27.9	3.5	15.5	9.4	0.9	3.5
3	12819	29.1	4.1	15.5	0.0	0.8	7.5
4	20893	32.2	9.6	16.5	6.1	0.8	0.0
5	123185	41.0	21.5	19.1	13.9	0.8	0.0
1	7538	29.9	Unknown	15.7	Unknown	1.1	Unknown
2	9041	28.4	5.3	14.8	5.6	1.0	8.3
3	13309	32.6	13.1	14.9	0.4	1.1	4.2
4	35268	30.9	5.6	17.1	13.0	1.0	3.3
5	219984	39.5	21.8	20.2	15.2	1.1	3.8

5.1.4. FEA on the Circular Plate

Since the top structure was designed to be a welded assembly, one of its two circular plates that connect to the round tubes was also evaluated with FEA, considering two possible boundary condition scenarios: first, a fixture in the welding annular planar surface was imposed, while the torque of 4928.4 N·m was applied over the external cylindrical surface of the plate; and second, the eight bolt holes were fixed while the torque was applied to the external cylindrical surface of the plate.

Figures 5.3 and 5.4 show the von Mises stress, resultant displacement, strain and FOS, performed on *plt-frm-01.sldprt*, considering the first scenario. In Figure 5.3a the maximum von Mises stress was found to be 49.8 MPa, located at some annular areas of the welding surface, especially at its outer radius. Similarly, the minimum FOS of 5.5 was located at this annular limit (Figure 5.3b). In terms of displacement, Figure 5.4a shows a maximum equivalent strain (ϵ_{eq}) of 0.00064 mm/mm and Figure 5.4b shows a maximum resultant displacement (u_{res}) of 0.015 mm.

For the second scenario, Figures 5.5 and 5.6 show the results of von Mises stress, resultant displacement, strain and FOS, performed on *plt-frm-01.sldprt*. In Figure 5.5a the maximum von Mises stress reached 40.6 MPa, located at some nodes of the inner cylindrical surfaces of the holes, where the fixtures resist clockwise twisting of the plate. For the stress value, these critical nodes present a minimum FOS of 6.8 as shown in Figure 5.5b. Figure 5.6a shows the results of strain, where the maximum value is 0.00052 mm/mm, located at the inner cylindrical surfaces of the bolts. Results for displacement are shown in Figure 5.6b, where the maximum resultant displacement (u_{res}) is 0.0094 mm, located in the nodes of the annular planar surface simulated for welding (see Figure 4.3b to refer to the annular planar surface).

In Table 5.3 a summary of FEA simulations shows the maximums and minimums values of von Mises and Maximum shear stresses, strains, displacements and FOS for different mesh sizes for the two previously mentioned scenarios. For the first scenario, the absolute maximum von Mises stress (σ_v) was found to be 49.8 MPa with a minimum FOS of 5.5, a maximum shear stress (τ_{xy}) of 22.9 MPa with a minimum FOS of 4.8, and a maximum displacement of 14.9 micrometers, all corresponding to the fifth mesh. However, in terms of mesh convergence, Table 5.4 shows that the minimum convergence error (CE) of 1.1% corresponds to a von Mises stress of 24.0 MPa (Mesh 2) with a corresponding FOS of 11.5, a CE of 6.4% to a maximum shear stress (τ_{yz}) of 13.4 MPa (Mesh 3) with its corresponding FOS of 8.1, and a CE of 0.9% for a maximum displacement of 12.6 micrometers (Mesh 2).

Similarly, for the second scenario the absolutes were as follows: the maximum von Mises stress (σ_v) was found to be 40.6 MPa with a minimum FOS of 6.8, a maximum shear stress (τ_{yz}) of 18.0 MPa with a minimum FOS of 5.9, and a maximum displacement of 9.4 micrometers. In terms of convergence, Table 5.4 shows that the minimum CE of 0.1% corresponds to a von Mises stress of 39.2 MPa (Mesh 4) with a corresponding FOS of 7.0, a CE of 3.8% to a maximum shear stress (τ_{yz}) of 15.0 MPa (Mesh 3) with its corresponding FOS of 6.1, and a CE of 0.0% for a maximum displacement of 9.3 micrometers (Mesh 4).

The first simulated scenario proved to be the more critical one, with an absolute minimum FOS of 4.8. This value is a conservative design choice, because established literature suggests a FOS of 4.0 for a machine element that has few input data and uncertainty about combined loading, welding processes and rough environmental conditions (R. L. Mott, 2004). Even with a high FOS, special care was taken to minimize the stress concentrations at the welding surfaces; a chamfered edge was created at the end of the tubes, promoting weld penetration and a consistent bead around the intersection between tubes and plates.

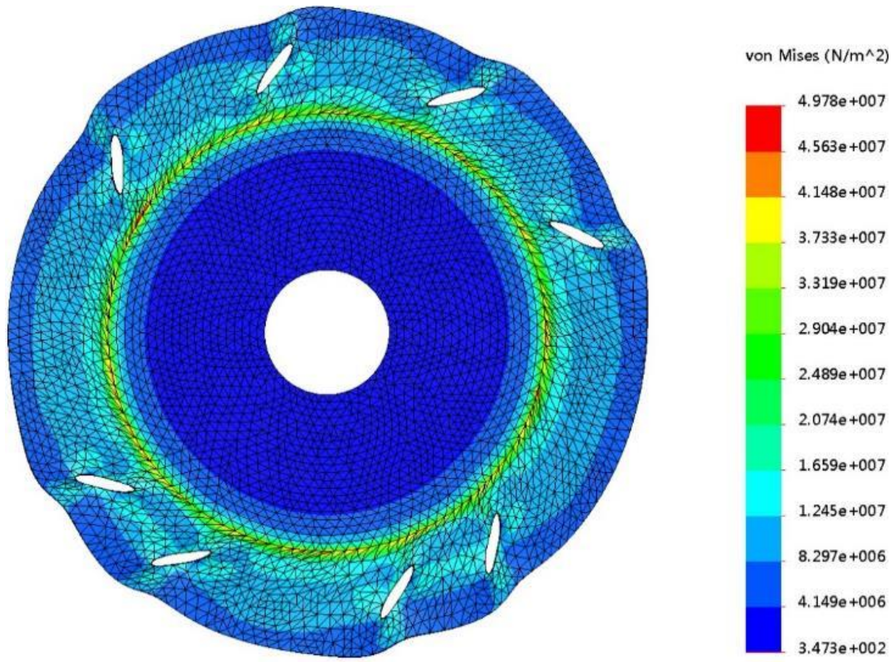

(a)

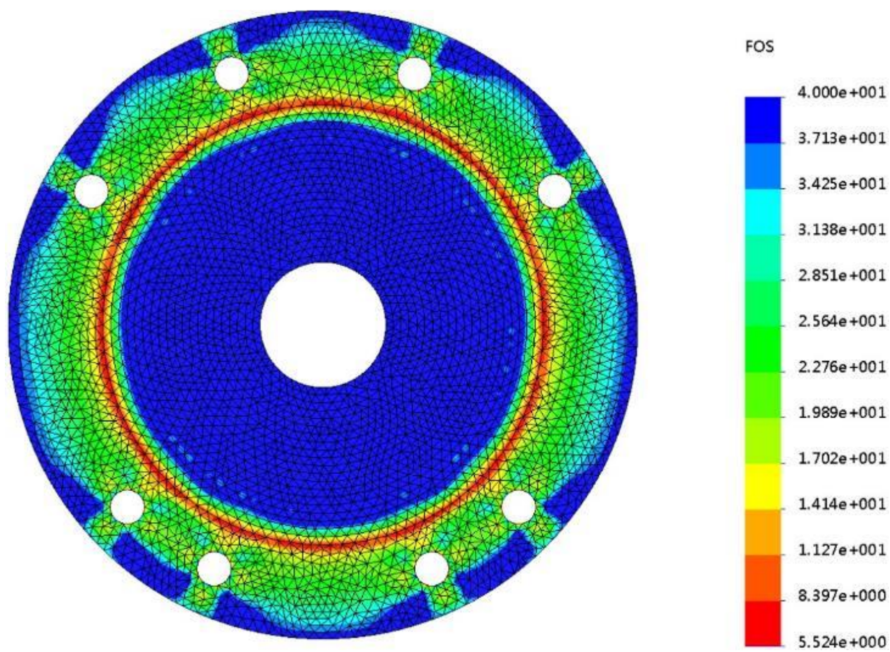

(b)

Figure 5.3 FEA results for von Mises stress and factor of safety on *plt-frm-01.sldprt* with fixture on the annular planar welding surface. Torsion load of 4928.4 N·m applied on the cylindrical external face. Models seen from the back, where the critical areas are visible for (a) von Mises stress (σ_v), with deformation scale of 2000; and (b) factor of safety (FOS) with no deformation.

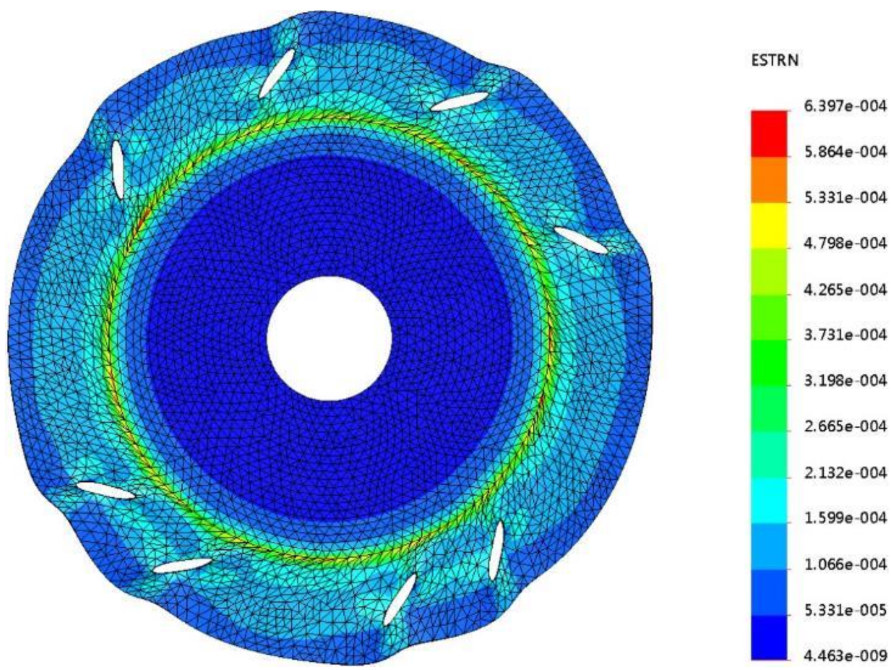

(a)

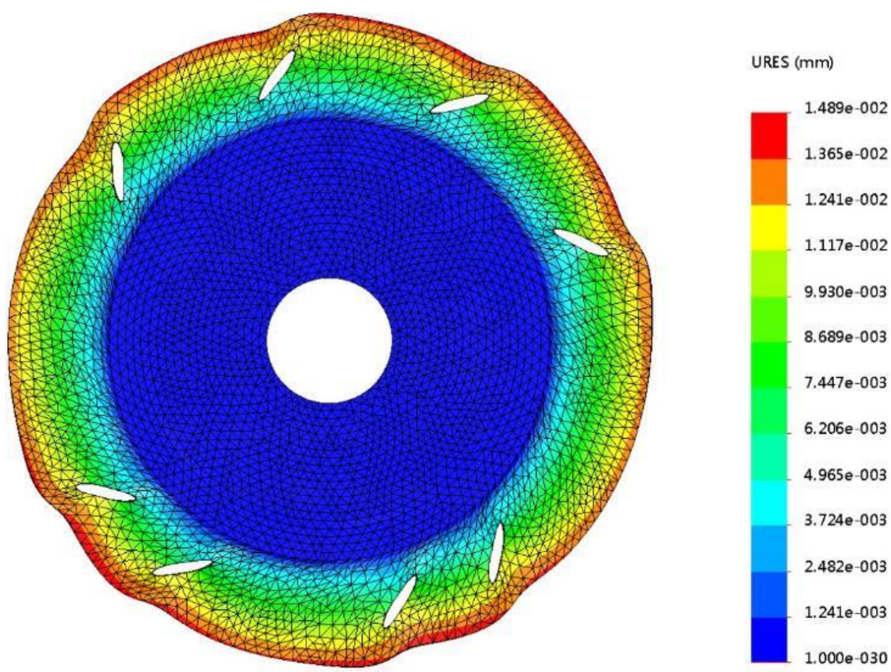

(b)

Figure 5.4 FEA results for equivalent strain and resultant displacement on *plt-frm-01.sldprt*, with fixture on the annular planar welding surface. Torsion load of 4928.4 N·m applied on the cylindrical external face. Models seen from the back, where the critical areas are visible for (a) equivalent strain (ϵ_{eq}); and (b) resultant displacement (u_{res}). The deformation scale is 2000.

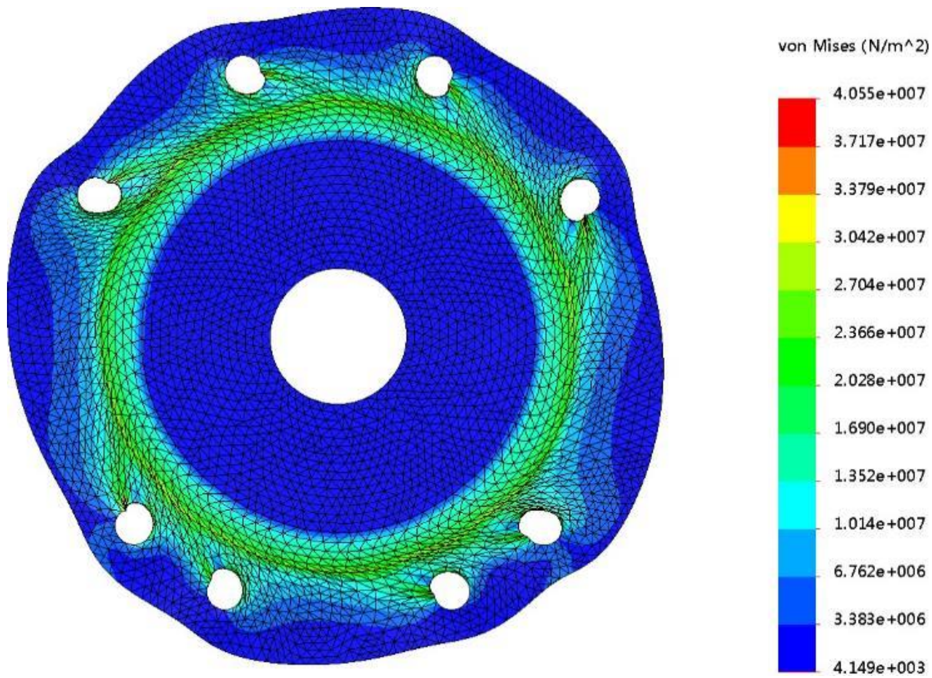

(a)

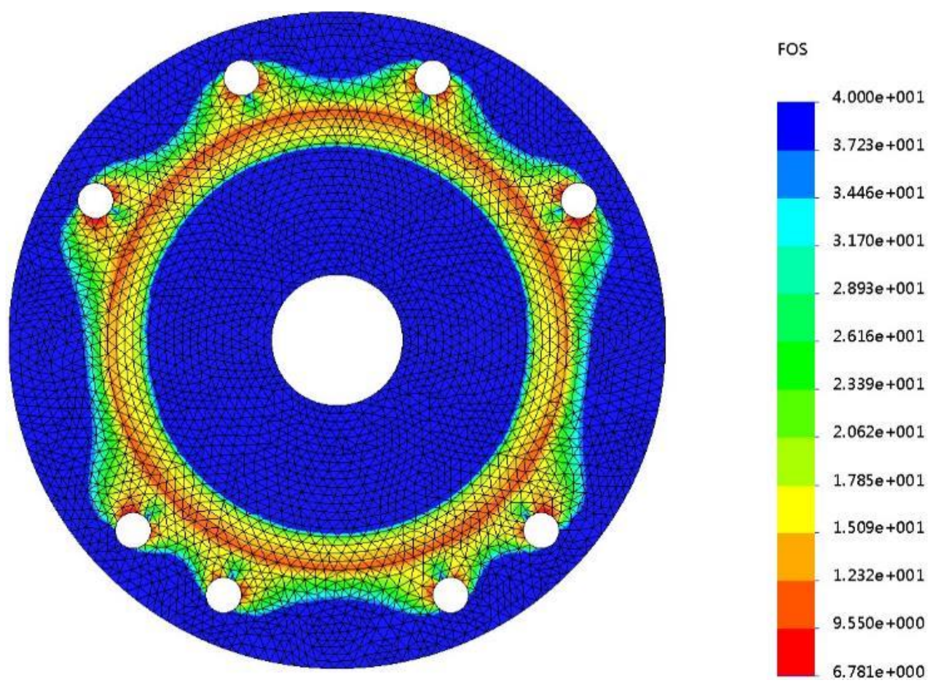

(b)

Figure 5.5 FEA results for von Mises stress and factor of safety on *plt-frm-01.sldprt*, with fixture on eight cylindrical surfaces of the boltholes. Torsion load of 4928.4 N·m applied on the annular planar welding surface. Models seen from the back, where the critical areas are visible for (a) von Mises stress (σ_v); and (b) factor of safety (FOS). The deformation scale is 3000.

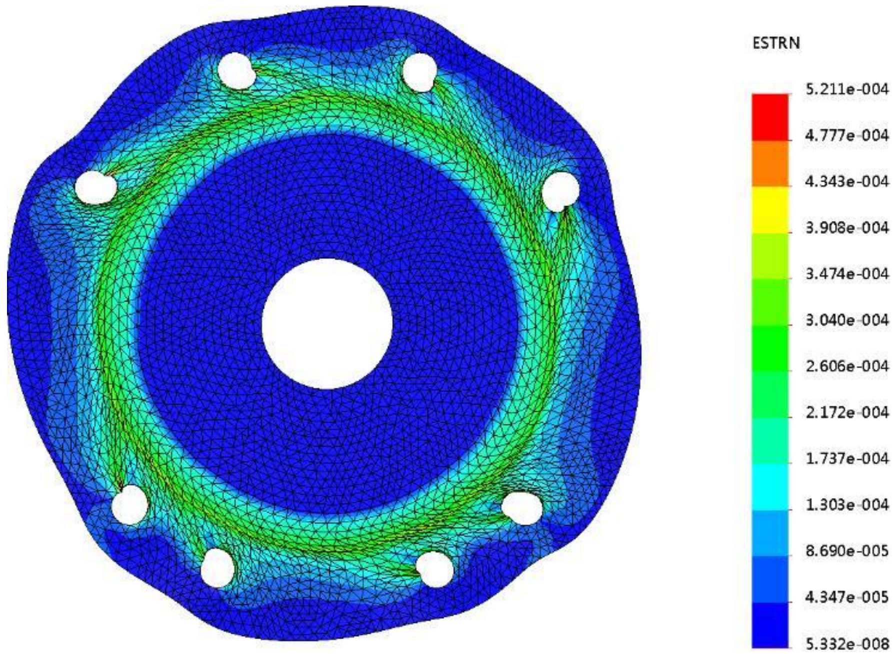

(a)

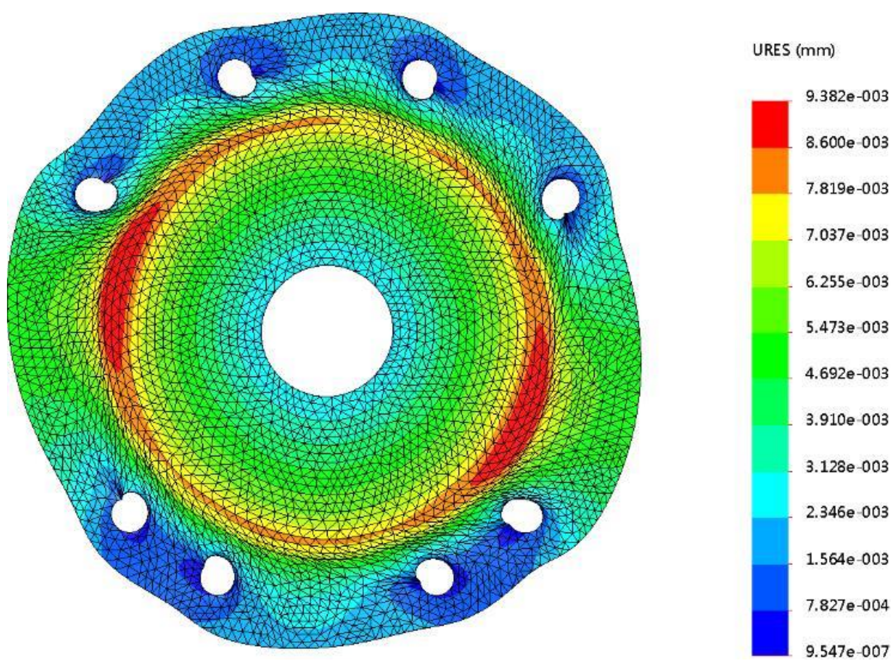

(b)

Figure 5.6 FEA results for equivalent strain and resultant displacement on *plt-frm-01.sldprt*, with on eight cylindrical surfaces of the boltholes. Torsion load of 4928.4 N·m applied on the annular planar welding surface: (a) equivalent strain (ϵ_{eq}) with deformation scale of 3000, and (b) resultant displacement (u_{res}) with no deformation. Models seen from the back, where the critical areas are visible.

Table 5.3 Summary of FEA results for torsion load on the circular plate, *plt-frm-01.sldprt*, with five different meshes. The first half corresponds to boundary conditions where the annular planar welding surface of 12.7 mm wide was fixed and the torque of 4928.4 N·m was applied at the outer cylindrical surface. The second half corresponds to the boundary conditions where the eight cylindrical surfaces of the boltholes were fixed and the torque was applied on the outer cylindrical surface.

Property	Mesh 1 (16 mm)		Mesh 2 (13 mm)		Mesh 3 (10 mm)		Mesh 4 (7 mm)		Mesh 5 (4 mm)	
	Min	Max	Min	Max	Min	Max	Min	Max	Min	Max
σ_v (MPa)	0.0	23.8	0.0	24.0	0.0	29.5	0.0	37.8	0.0	49.8
u_{res} (μm)	0.0	14.0	0.0	14.2	0.0	14.4	0.0	14.7	0.0	14.9
ϵ_{eq} ($\times 10^{-4}$)	0.0	3.1	0.0	3.1	0.0	3.8	0.0	4.9	0.0	6.4
τ_{xy} (MPa)	-7.7	7.8	-9.0	8.5	-12.2	12.0	-15.8	16.7	-21.2	22.9
τ_{xz} (MPa)	-7.6	9.3	-10.1	7.8	-12.7	13.2	-16.4	13.8	-20.5	19.7
τ_{yz} (MPa)	-10.4	9.6	-11.1	12.6	-12.7	13.4	-20.0	16.6	-24.8	22.3
u_x (μm)	-0.6	0.6	0.6	0.6	-0.7	0.6	-0.8	0.7	-0.8	0.8
u_y (μm)	-12.5	12.5	-12.6	12.6	-12.8	12.8	-13.0	13.0	-13.1	13.1
u_z (μm)	-13.2	13.1	-13.3	13.2	-13.5	13.4	-13.7	13.6	-13.9	13.8
γ_{xy} ($\times 10^{-4}$)	-3.0	3.0	-3.5	3.3	-4.7	4.6	-6.1	6.4	-8.2	8.8
γ_{xz} ($\times 10^{-4}$)	-2.9	3.6	-3.9	3.0	-4.9	5.1	-6.3	5.3	-7.9	7.6
γ_{yz} ($\times 10^{-4}$)	-4.0	3.7	-4.3	4.8	-4.9	5.2	-7.7	6.4	-9.5	8.6
FOS ($\sigma_{v\,\max}$)	11.6	76230.0	11.5	14230.0	9.3	106200.0	7.3	258800.0	5.5	791900.0
FOS ($\tau_{\max}$)	10.0	66450.0	9.9	123500.0	8.1	94750.0	6.3	234600.0	4.8	686500.0
σ_v (MPa)	0.0	35.2	0.0	35.1	0.0	39.1	0.0	39.2	0.0	40.6
u_{res} (μm)	0.0	0.0	0.0	9.3	0.0	9.4	0.0	9.4	0.0	9.4
ϵ_{eq} ($\times 10^{-4}$)	0.0	4.5	0.0	4.5	0.0	5.0	0.0	5.0	0.0	5.2
τ_{xy} (MPa)	-6.8	6.8	-7.5	7.8	-9.5	9.4	-9.7	9.7	-9.3	9.3
τ_{xz} (MPa)	-7.8	6.7	-7.7	7.9	-9.4	9.4	-9.6	9.8	-9.5	9.3
τ_{yz} (MPa)	-13.1	13.9	-15.8	15.6	-16.0	15.0	-17.6	17.1	-17.4	18.0
u_x (μm)	-0.3	0.3	-0.3	0.3	-0.3	0.3	-0.3	0.3	-0.3	0.3
u_y (μm)	-9.1	9.1	-9.1	9.3	-9.3	9.3	-9.3	9.3	-9.4	9.4
u_z (μm)	-7.4	7.6	-7.5	7.7	-7.7	7.8	-7.7	7.8	-7.8	7.9
γ_{xy} ($\times 10^{-4}$)	-2.6	2.6	-2.9	3.0	-3.7	3.6	-3.7	3.7	-3.6	3.6
γ_{xz} ($\times 10^{-4}$)	-3.0	2.6	-3.0	3.0	-3.6	3.6	-3.7	3.8	-3.6	3.6
γ_{yz} ($\times 10^{-4}$)	-5.0	5.4	-6.1	6.0	-6.2	5.8	-6.8	6.6	-6.7	6.9
FOS ($\sigma_{v\,\max}$)	7.8	12600.0	7.8	13780.0	7.0	11900.0	7.0	19710.0	6.8	66270.0
FOS ($\tau_{\max}$)	6.8	11250.0	6.8	12290.0	6.1	10430.0	6.2	18810.0	5.9	60420.0

Table 5.4 Percent of absolute relative convergence error (CE) for maximum von Mises and shear stress on face *y*, direction *z*, and for displacement in *y* for five different mesh sizes on *plt-frm-01.sldprt*. The first half of the table corresponds to results of FEA for circular plate with fixture on the welding annular surface and torque applied in its outer cylindrical surface, while the second half corresponds to fixture on the cylindrical surfaces of the eight bolt holes and a torque applied on the annular planar welding surface.

Mesh	Nodes	σ_v (MPa)	CE for σ_v (%)	τ_{yz} (MPa)	CE for τ_{yz} (%)	u_y (μm)	CE for u_y (%)
1	3829	23.8	Unknown	9.6	Unknown	12.5	Unknown
2	6027	24.0	1.1	12.6	23.3	12.6	0.9
3	11936	29.5	18.6	13.4	6.4	12.8	1.6
4	31503	37.8	22.1	16.6	19.3	13.0	1.5
5	137849	49.8	24.0	22.3	25.4	13.1	1.2
1	3921	35.2	Unknown	13.9	Unknown	9.1	Unknown
2	6024	35.1	0.4	15.6	11.0	9.3	1.9
3	11936	39.1	10.4	15.0	3.8	9.3	0.5
4	31510	39.2	0.1	17.1	12.1	9.3	0.0
5	137849	40.6	3.4	18.0	4.8	9.4	0.0

5.1.5. FEA on the Welded Assembly

An FEA was performed on the longer top structure welded assembly (*frm-w-02.sldasm*) to study global effects on the 2013-mm round tube (*tub-rnd-02.sldprt*) welded to two circular plates (*plt-frm-01.sldprt*). Only the longer welded assembly was considered because it had the same stress as the short assembly, but the greatest deformation (worst case scenario).

Figures 5.7 and 5.8 show the results of FEA performed in *frm-w-02.sldasm*. The boundary conditions were assumed in the scenario in which the cylindrical faces of the holes on the left circular plate were fixed, while the torque of 4928.4 N-m was applied at the external cylindrical surface of the circular plate on the right hand side. The critical values for maximum shear (Figure 5.7a) and von Mises (Figure 5.8a) stresses were

τ_{xy}=15.3 MPa and $\sigma_v = 38.1$ MPa with their corresponding minimum FOS of 6.3 (Figure 5.8a) and 7.2 (Figure 5.8b), respectively. Since the critical values were located at the holes of the left circular plate and at the welding zone of the intersection between the tube and plate, zoomed-in views were created to help the reader to visualize the values of the minimum FOS of maximum shear stress theory (Figure 5.9a) and minimum FOS for von Mises stress theory (Figure 5.9b).

Table 5.5 shows the summary of FEA results for the minimum and maximum values for stresses, displacements, strains and FOS on six different meshes. The first five meshes were created with the default element size generator, while Mesh 6 was created by refining the areas of the cylindrical holes of the fixtures (Figure J.4). Across all meshes, the absolute maximum shear stress found was $\tau_{yz} = 17.0$ MPa with a FOS of 6.3, the absolute von Mises was $\sigma_v = 38.1$ MPa with a FOS of 7.2, and the maximum displacement was 1.8 mm. These absolute maximums were found on Mesh 6, but the convergence analysis shown in Table 5.6 pointed out a maximum von Mises stress $\sigma_v = 30.2$ MPa with a FOS of 8.2 and a convergence error (CE) of 0.5% found in Mesh 5; a maximum shear stress $\tau_{xy} = 14.2$ MPa with a FOS of 7.6 and a CE of 1.4% found in Mesh 4; and a maximum displacement $u_y = 1.8$ mm with a CE of 0.3% found in Mesh 5.

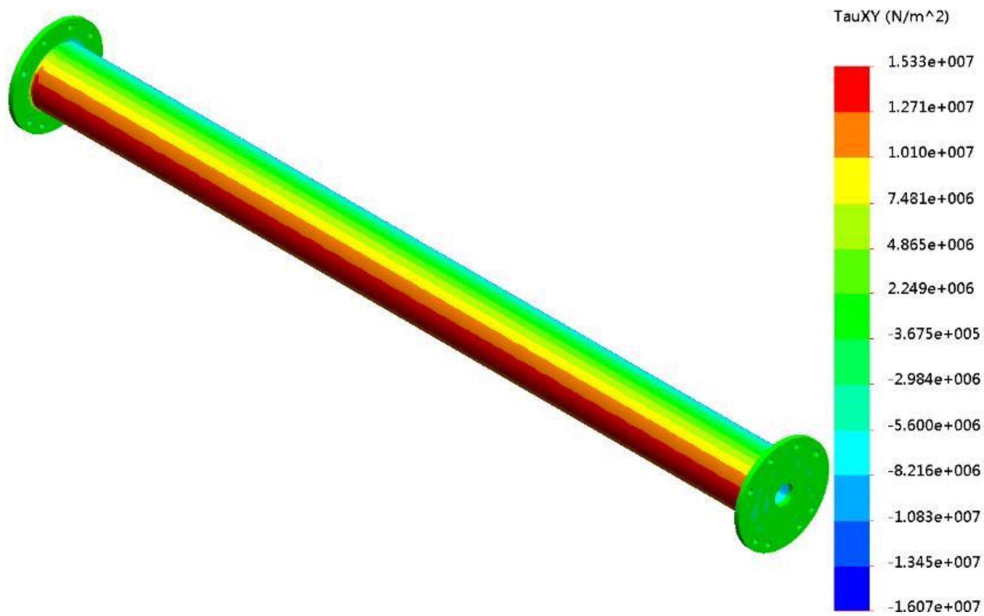

(a)

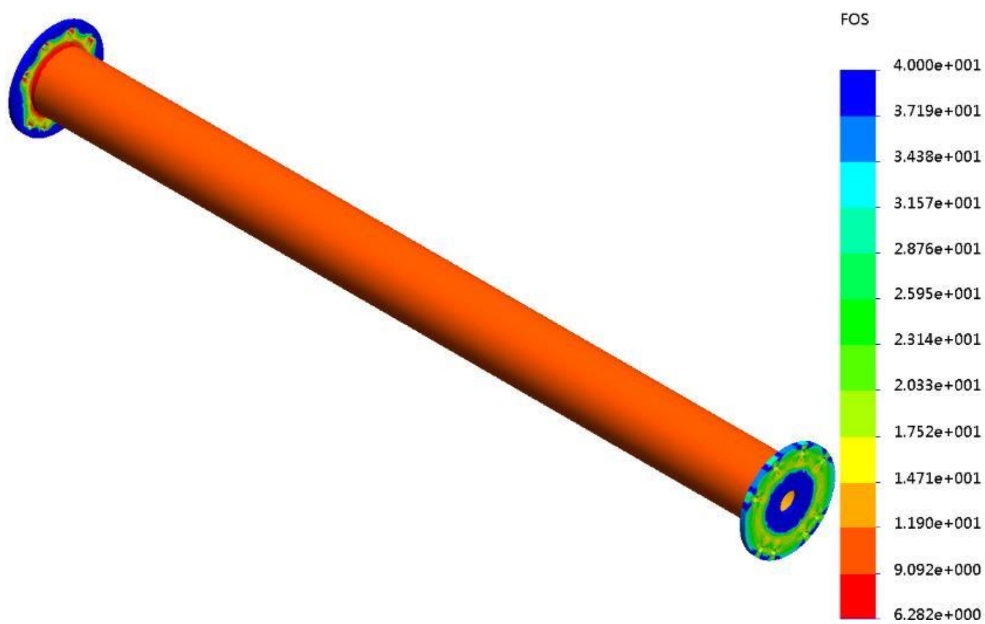

(b)

Figure 5.7 FEA results for shear stress and factor of safety on *frm-w-02.sldprt* with fixture in the eight cylindrical surfaces on the bolt holes on the left hand side. Torsion load of 4928.4 N·m applied on the outer cylindrical surface on the circular plate at the right hand side: (a) shear stress (τ_{xy}) and (b) factor of safety (FOS). The mesh number 6 was used for this analysis. The deformation scale applied was 1.

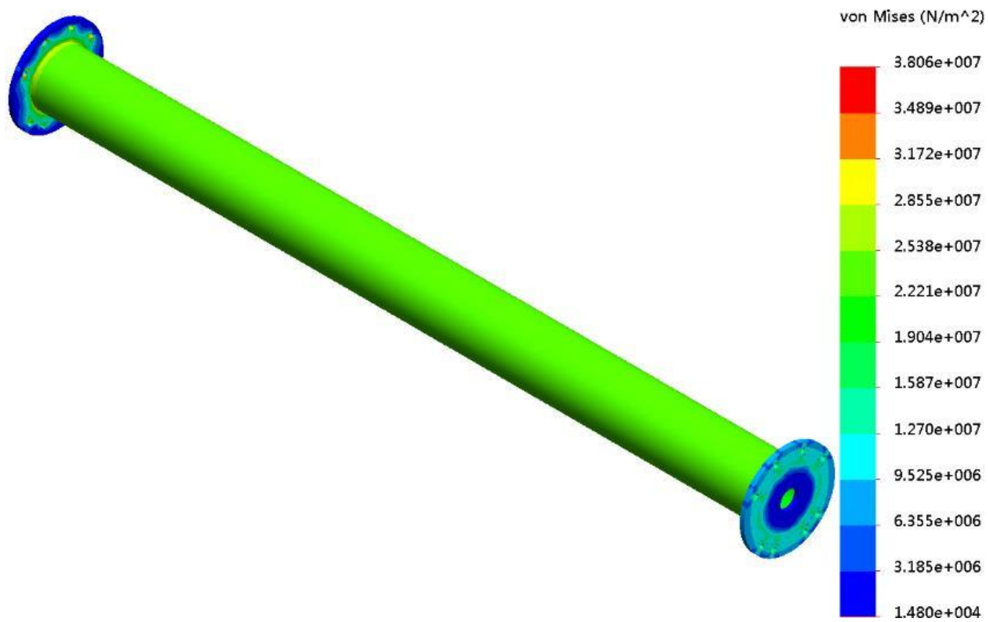

(a)

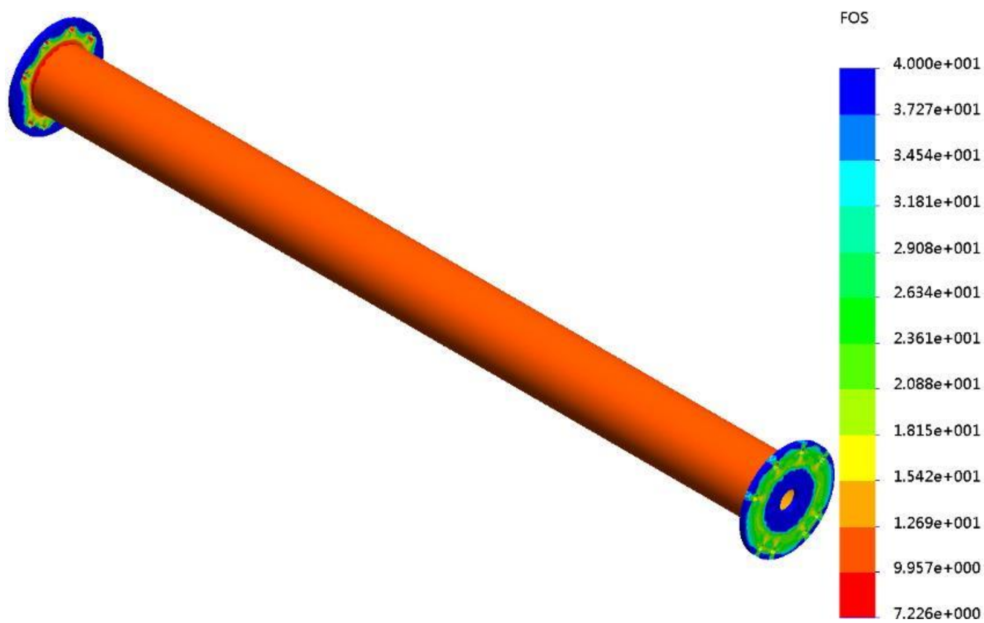

(b)

Figure 5.8 FEA results for von Mises stress and factor of safety on *frm-w-02.sldprt* with fixture in the eight cylindrical surfaces on the bolt holes on the left hand side. Torsion load of 4928.4 N·m applied on the outer cylindrical surface on the circular plate at the right hand side: (a) von Mises stress (σ_v) and (b) factor of safety (FOS). The mesh number 6 was used for this analysis. The deformation scale applied was 1.

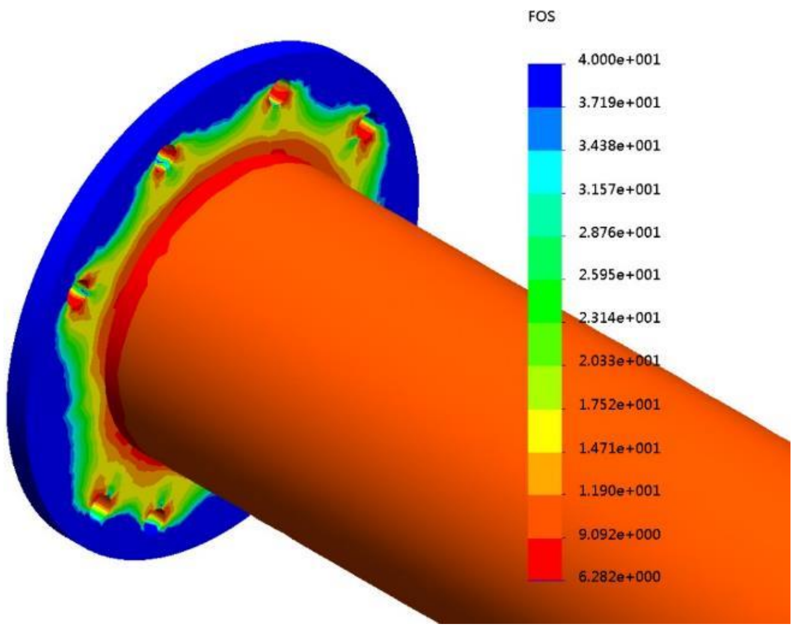

(a)

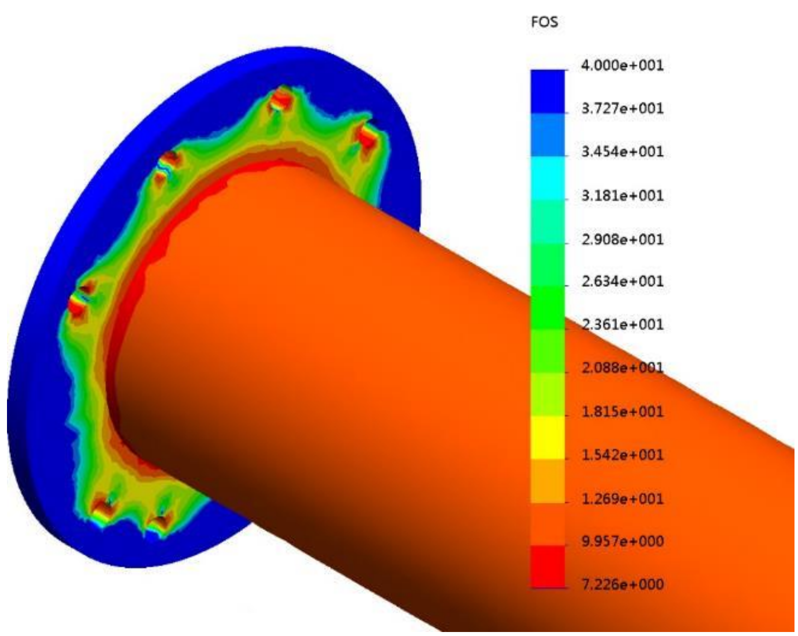

(b)

Figure 5.9 FEA results for factor of safety on *frm-w-02.sldprt* with fixture in the eight cylindrical surfaces on the bolt holes on the left hand side. Torsion load of 4928.4 N·m applied on the outer cylindrical surface on the circular plate at the right-hand side. Factors of safety for two different stresses: (a) for maximum shear, and (b) for von Mises. The mesh number 6 was used for this analysis. The deformation scale applied was 1.

Table 5.5 Summary of FEA results for torsion load on the welded top structure assembly, *str-w-02.sldprt*, with six different meshes. The boundary conditions were fixing the eight cylindrical surfaces of the plate boltholes on the left, while the torque of 4928.4 N·m was applied on the outer cylindrical surface of the plate on the right.

Property	Mesh 1 (112 mm)		Mesh 2 (91 mm)		Mesh 3 (70 mm)		Mesh 4 (49 mm)		Mesh 5 (28 mm)		Mesh 6 (28 and 5.6 mm)	
	Min	Max	Min	Max	Min	Max	Min	Max	Min	Max	Min	Max
σ_v (MPa)	0.0	32.0	0.2	29.4	0.2	35.4	0.3	30.0	0.0	30.2	0.0	38.1
u_{res} (mm)	0.0	1.8	0.0	1.8	0.0	1.9	0.0	1.8	0.0	1.8	0.0	1.8
ϵ_{eq} ($\times 10^{-4}$)	0.0	3.1	0.0	3.0	0.0	3.4	0.0	3.1	0.0	3.2	0.0	4.2
τ_{xy} (MPa)	-13.3	13.7	-14.2	14.2	14.1	14.4	-14.2	14.2	-14.9	14.6	-16.1	15.3
τ_{xz} (MPa)	-13.7	13.5	-14.0	14.1	13.9	14.0	-14.3	14.5	-14.6	15.1	-17.3	15.9
τ_{yz} (MPa)	-9.3	11.3	-10.6	10.2	-13.2	11.4	-14.7	10.3	-11.9	11.9	-17.1	17.0
u_x (μm)	-7.9	9.5	-4.2	2.4	-7.6	6.7	-3.0	3.1	-0.9	1.5	-0.9	0.9
u_y (mm)	-1.7	1.8	-1.8	1.8	-1.9	1.7	-1.8	1.8	-1.8	1.8	-1.8	1.8
u_z (mm)	-1.6	1.8	-1.8	1.8	-1.8	1.9	-1.8	1.8	-1.8	1.8	-1.8	1.8
γ_{xy} ($\times 10^{-4}$)	-5.1	5.3	-5.5	5.5	-5.4	5.6	-5.5	5.5	-5.7	5.6	-6.2	5.9
γ_{xz} ($\times 10^{-4}$)	-5.3	5.2	-5.4	5.4	-5.3	5.4	-5.5	5.6	-5.6	5.8	-6.7	6.1
γ_{yz} ($\times 10^{-4}$)	-3.6	4.4	-4.1	3.9	-5.1	4.4	-5.7	4.0	-4.6	4.6	-6.7	6.4
FOS ($\sigma_{v\,\max}$)	8.6	888.6	9.4	1221.0	7.8	12820.0	8.8	1065.0	8.2	11330.0	7.2	13510.0
FOS ($\tau_{\max}$)	7.6	769.6	8.5	1140.0	6.9	11.6	7.6	931.9	7.1	10130.0	6.3	13130.0

Table 5.6 Percent of absolute relative convergence error (CE) for maximum von Mises and shear stress on face *x*, direction *y*, and for displacement in *y* for six different mesh sizes on *frm-w-02.sldasm*.

Mesh	Nodes	σ_v (MPa)	CE for σ_v (%)	τ_{xy} (MPa)	CE for τ_{xy} (%)	u_y (mm)	CE for u_y (%)
1	3792	32.0	Unknown	13.7	Unknown	1.8	Unknown
2	5404	29.4	8.7	14.2	3.1	1.8	0.5
3	5631	35.4	16.9	14.4	1.8	1.7	3.6
4	7248	30.0	17.9	14.2	1.4	1.8	5.3
5	16054	30.2	0.5	14.6	2.8	1.8	0.3
6	28852	38.1	20.8	15.3	4.6	1.8	0.6

5.1.6. Design and Construction Considerations

The FEA on both tubes with the two different boundary conditions, the circular plate with the two different boundary conditions, and the whole top structure assembly showed FOS greater than 4.0, which is a design FOS recommended for static elements or structures under dynamic loads, with uncertainty about material, stresses or environment (Mott, 2004). Finally, the drawing specifications (Figures J.1 to J.3) were sent to manufacturer.

5.2. Suspension System

5.2.1. Mathematical Model of a Quarter Suspension System

A dynamic simulation was run in MATLAB® to understand the behavior of the suspension system and determine the critical force in order to perform FEA on key suspension components. The simulation followed the methodology presented in Subsection 4.1.2 and focused on the quarter suspension model of Figure 5.10, represented in equations (5.1) and (5.2).

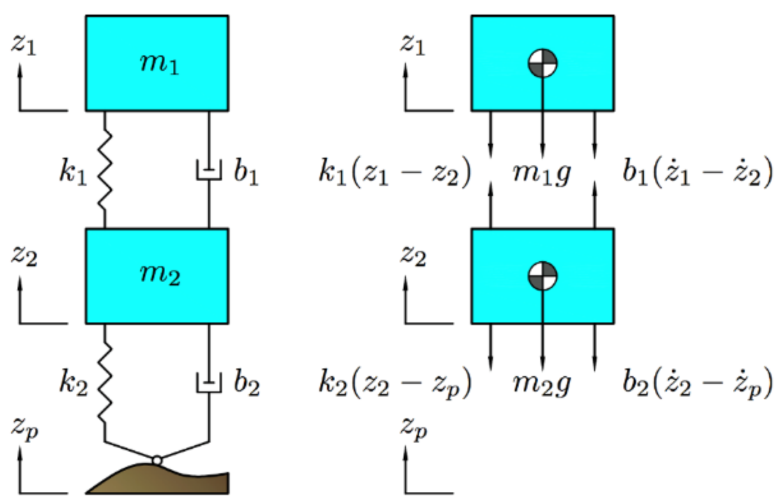

Figure 5.10 One-quarter-suspension model with its free body diagrams.

$$m_1\ddot{z}_1 = -k_1(z_1 - z_2) - b_1(\dot{z}_1 - \dot{z}_2) - m_1 g, \tag{5.1}$$

$$m_2\ddot{z}_2 = k_1(z_1 - z_2) + b_1(\dot{z}_1 - \dot{z}_2) - k_2(z_2 - z_p) - b_2(\dot{z}_2 - \dot{z}_p) - m_2 g, \tag{5.2}$$

5.2.2. Dynamic Simulations of a Quarter Suspension System

A dynamic simulator built in MATLAB® & Simulink® (Figure 5.11) was programmed to simulate a quarter suspension system. The block diagram simulator shows two inputs as green blocks: a step function simulating a 30-cm bump due to a furrow and a uniform random function to simulate soil clods. For design purposes, the road profile step function was the only input considered because it was a drastic condition. The outputs of the simulator are variables plotted over time such as position, spring compression, relative velocity, inertial force, spring force, and kinetic energy, all presented as light green blocks. All the constant suspension parameters were introduced in orange blocks, previously loaded in a MATLAB® script (Appendix F.2) as $m_1 = 165.6$ kg, $m_2 = 116$ kg, $k_1 = 49$ kN/m, $k_2 = 210$ kN/m, $b_1 = 4.6$ kNs/m, and $b_2 = 458$ Ns/m. Integrators and differentiators were presented in blue blocks, adding or subtracting operators in red blocks, and power operators in magenta blocks.

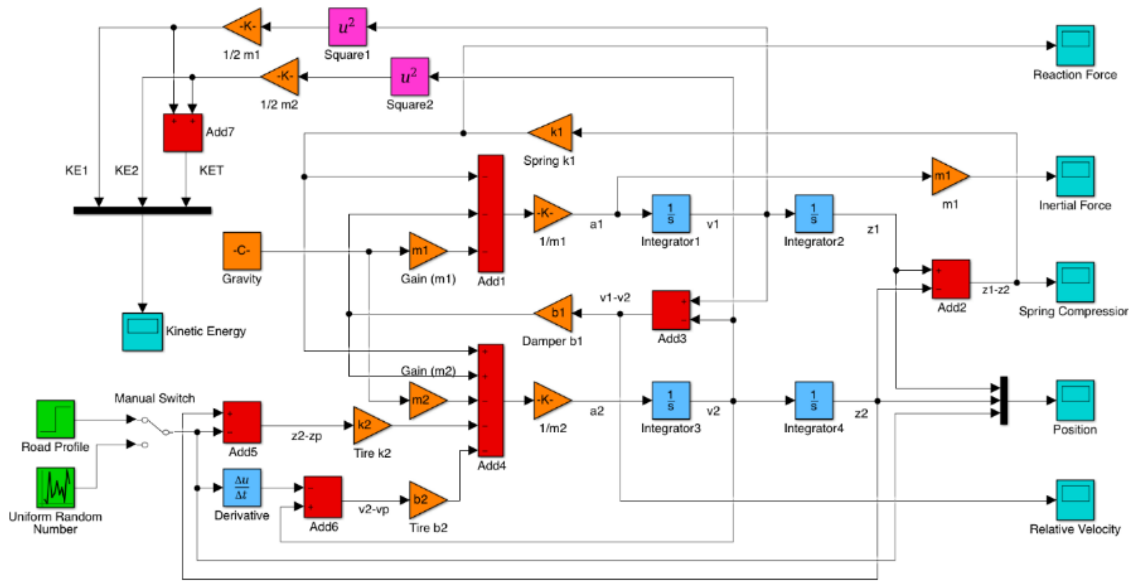

Figure 5.11 Dynamic simulator of a quarter suspension system. Road conditions are shown in green block diagrams, constant parameters in orange, adding operators in red, integrators and differentiators in blue, square operators in magenta, and the output graphs in aqua blue.

Two simulations with different initial conditions were performed during 1.0 s, because this was the time to see the stabilization of the dynamic system. Figures 5.12 and 5.13 show the results of the first simulation, in which all initial conditions of positions and velocities were set to zero as if the vehicle were released on the ground and the spring was compressed due to the vehicle's own weight. In general, the simulations showed that all dynamic performance finished after 0.5 seconds.

Figure 5.12 shows that, after spring and damper effects, position z_1 of the vehicle's chassis went down about 4.6 cm, while the tire position $z_2$went down about 1.3 cm. According to Figure 5.12, the maximum spring force computed was 1.7 kN going downwards, while the maximum inertial force due to falling of the chassis by gravity was around 900 N. Spring compression was, then, around 33 mm according to Figure 5.13, with a maximum relative compressive velocity of 0.34 m/s. Position values were computed (Figure 5.12) as a reference to show that the suspension system corresponded to the behavior of like vehicles.

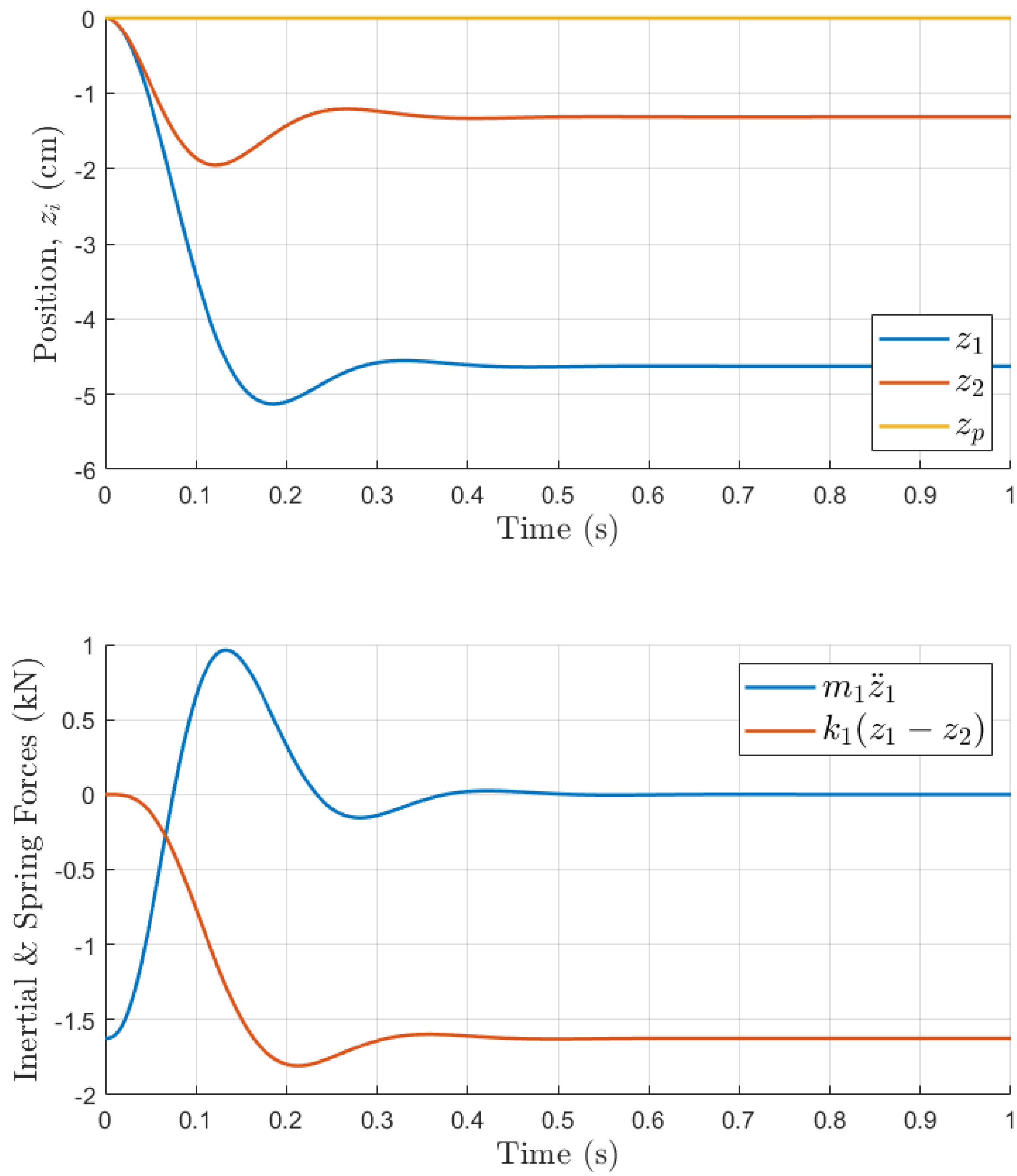

Figure 5.12 Position, and inertial and spring forces, for the quarter suspension system at resting conditions. Initial conditions: all positions and velocities at zero.

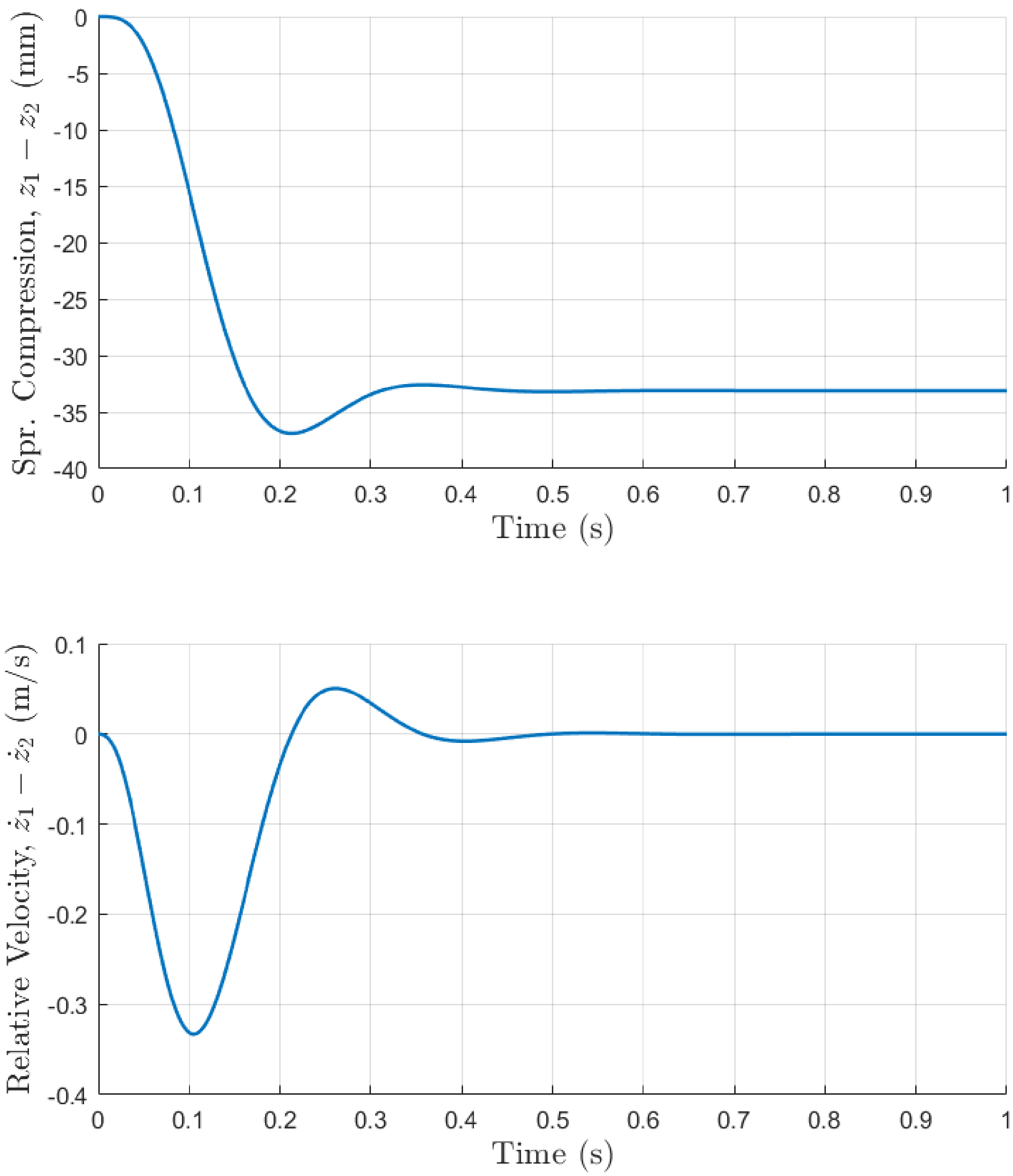

Figure 5.13 Spring compression and damping relative velocity for the quarter suspension system at resting conditions. Initial conditions: all positions and velocities at zero.

For design purposes, the values used were those of the simulation with a drastic change in the terrain profile. On Figure 5.14, positions of the chassis and the wheel assembly started at z_1 = -4.6 cm, and z_2 = -1.3 cm, respectively (see Figure 5.12 where these values were obtained), while a starting step-shape of 25 cm for the terrain profile was set and the dynamic behavior was simulated. The position plot shows that a bump of 25 cm caused both chassis and wheel assemblies to go upwards with maximum values of 35.1 and 35.6 cm from the ground in about 0.1 s, and they reached a steady state at 20.4 cm and 23.7 cm after 0.5 s, respectively. For the spring force, as shown in Figure 5.14, a maximum value of 8.2 kN was reached at 0.05 s and used as the extreme impact force to design suspension components.

Figure 5.15 shows that the maximum spring compression was about 169 mm at 0.05 s, and it reached a steady compression around 33 mm after 0.5 s, with a maximum relative velocity of 4.0 m/s.

Figure 5.15 shows the kinetic energy obtained for each mass body and the total energy for the two simulation scenarios. Figure 5.14a shows that for the initial conditions of all positions to be zero, the maximum kinetic energies for bodies 1 and 2 were 18 and 4 N-m, respectively. Figure 5.14b shows the simulation scenario in which the 25-cm step bump due to a furrow caused maximum kinetic energy values for mass bodies 1 and 2 of 2.1 and 2.3 kN-m, respectively, and a maximum total energy of 3.6 kN-m.

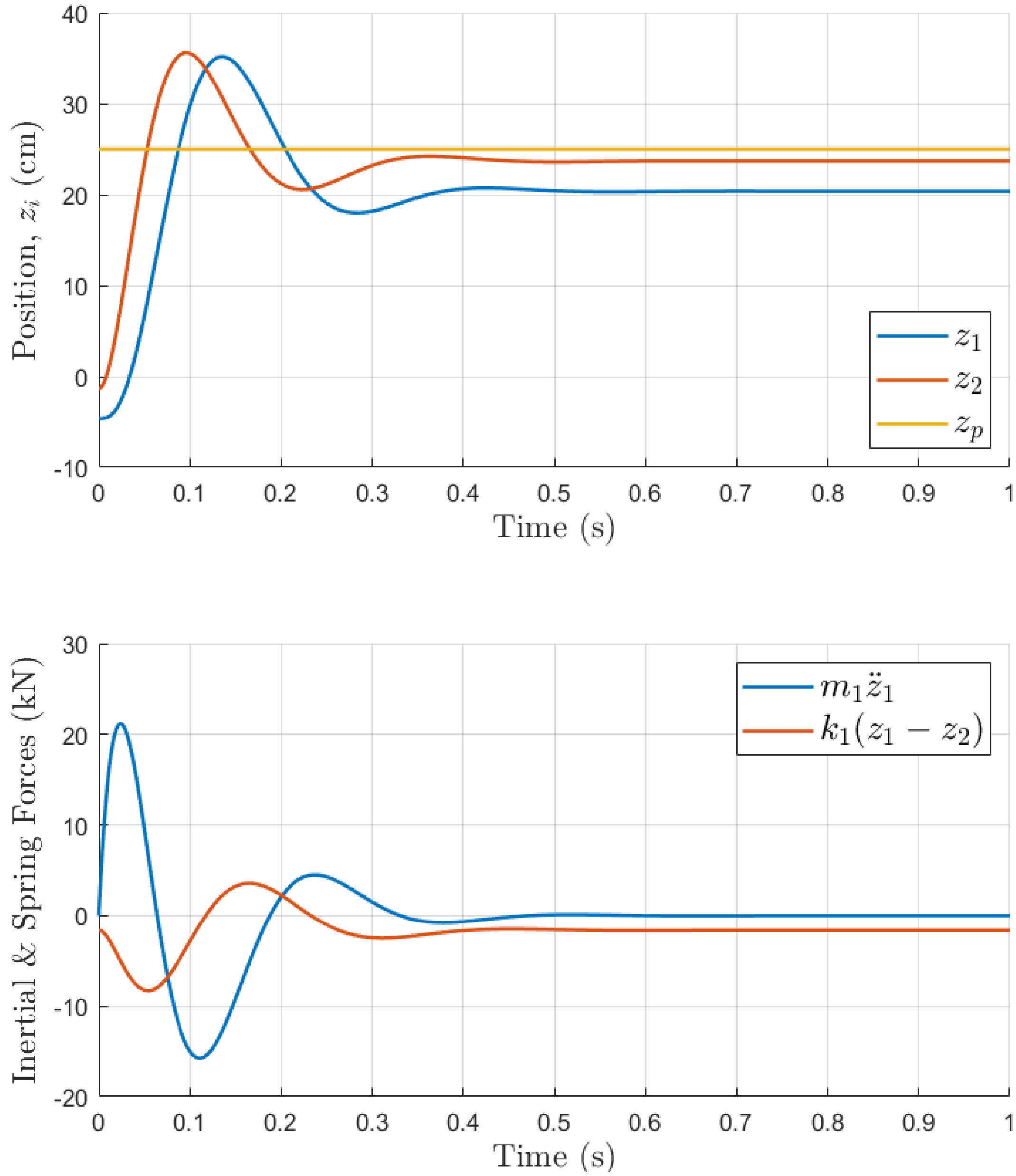

Figure 5.14 Position, and inertial and spring forces for the quarter suspension system at impact conditions. Initial conditions: z_1 = -4.6 cm, z_2 = -1.3 cm and z_p = 25 cm, and all velocities at zero.

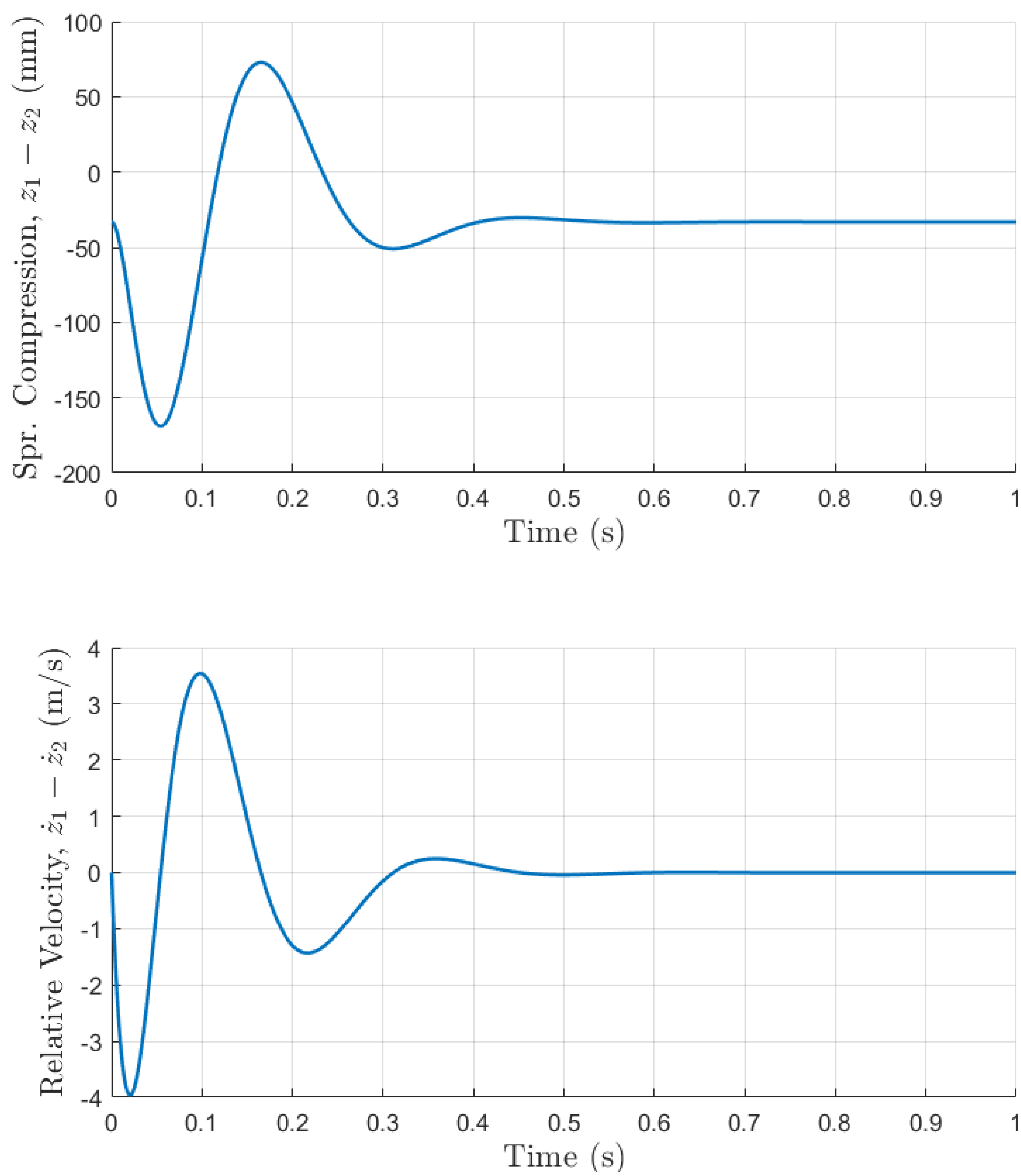

Figure 5.15 Spring compression and damping relative velocity for the quarter suspension system at impact conditions. Initial conditions: z_1 = -4.6 cm and z_2 = -1.3 cm, and z_p = 25 cm, and all velocities at zero.

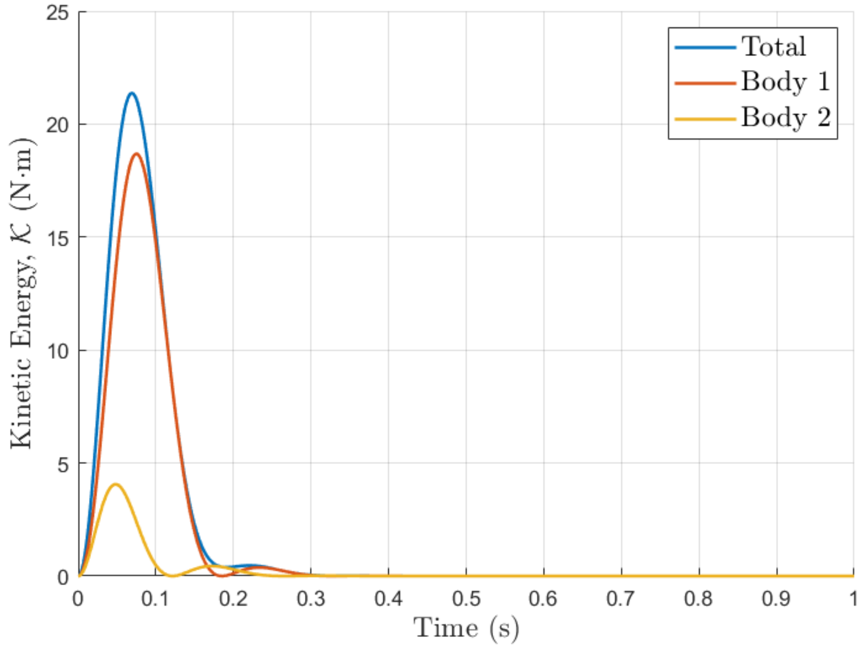

(a)

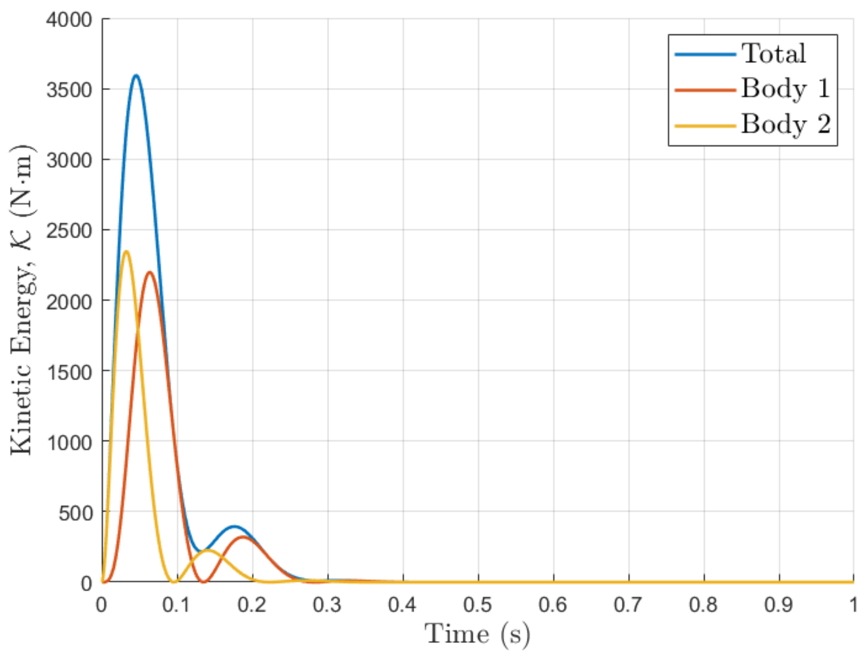

(b)

Figure 5.16 Kinetic energy of the two bodies and their total kinetic energy for the two simulation conditions. (a) All positions and velocities at zero; and (b) z_1 = -4.6 cm, z_2 = -1.3 cm, and z_p = 25 cm, and all velocities at zero.

5.2.3. FEA on Chassis Bracket for Shock Absorber

Two chassis brackets, denominated *plt-sus-02.sldprt*, were designed to be mounted on the bottom chassis and to assemble with each shock absorber. Thus, each bracket was simulated with FEA, assuming that the maximum spring load of 4.1 kN was pointing upwards on the inner cylindrical surface of the left-most hole, while the two cylindrical surfaces were fixed at the right (Figure 4.9) as bolted through the chassis. On Figure 5.15, the maximum von Mises stresses of 64.5 MPa are located at the support cylindrical surfaces with corresponding minimum FOS of 3.9. On Figure 5.16, the results of a maximum resultant displacement of 35.7 μm located at the left side of the bracket is shown, while the maximum strain value of 0.00027 mm/mm was shown for the pin holes. Except for resultant displacement, all simulations showed critical locations at the cylindrical holes that support the bracket, and at some extent at the cylindrical surface where the force was applied.

A summary of the FEA results for five different mesh sizes is shown in Table 5.7. The most critical values were obtained with the finest mesh number, 5, especially the FOS of 3.5 when using the maximum shear stress theory. However, the convergence results of Table 5.8 showed a von Mises stress of 60.2 MPa with a relative CE of 1.5% for a corresponding FOS of 4.2 obtained in Mesh 3, and a maximum equivalent displacement of 35.7 μm converging in all meshes with null CE.

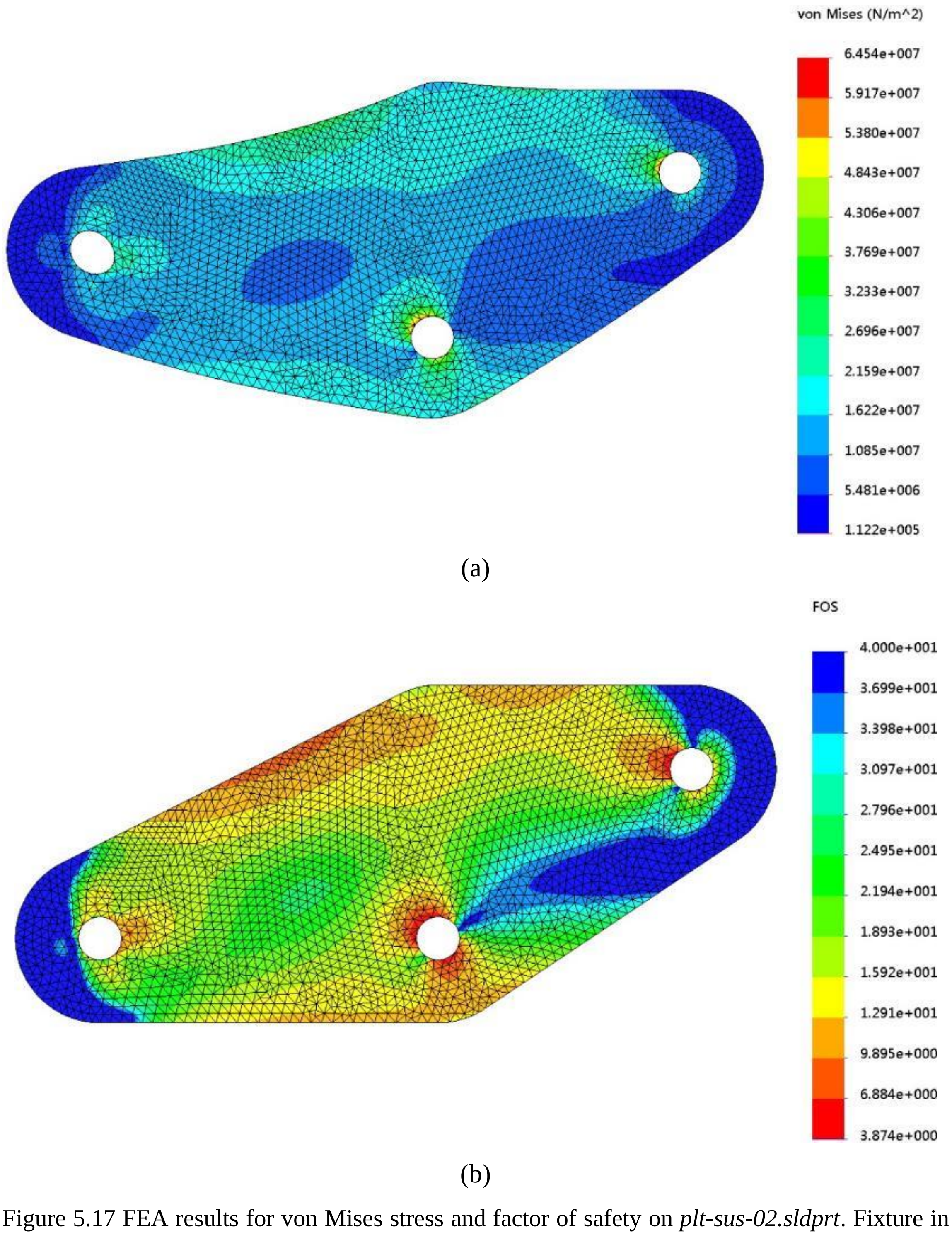

Figure 5.17 FEA results for von Mises stress and factor of safety on *plt-sus-02.sldprt*. Fixture in the two cylindrical surfaces on the bolt holes on the right hand side. Upward load of 4.1 kN applied on the internal cylindrical surface on bolt hole at the left hand side: (a) von Mises (σ_v) with deformation scale of 700, and (b) factor of safety (FOS) with no deformation scale.

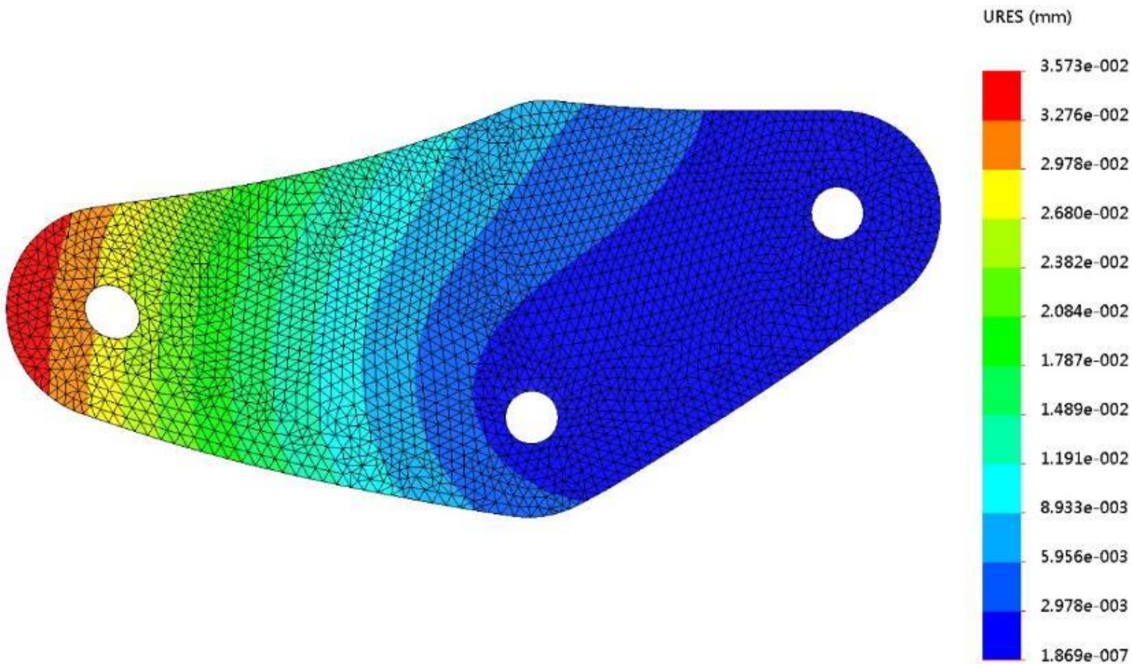

(a)

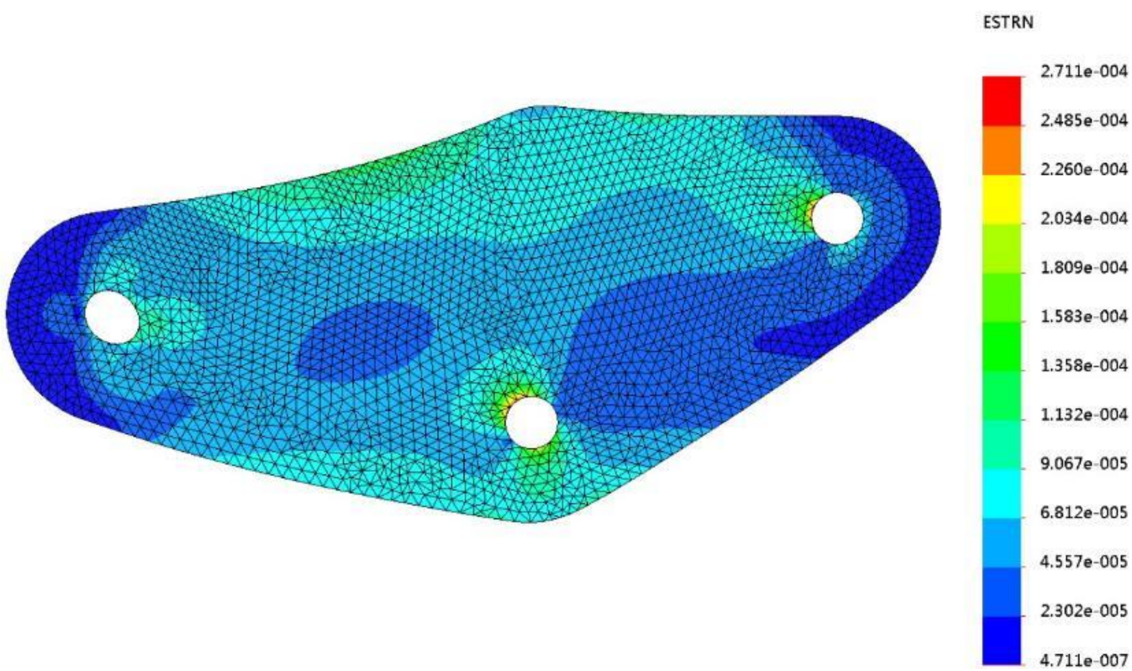

(b)

Figure 5.18 FEA results for equivalent strain and resultant displacement on *plt-sus-02.sldprt*. Fixture in the two cylindrical surfaces on the bolt holes on the right hand side. Upward load of 4.1 kN applied on the internal cylindrical surface on bolt hole at the left hand side: (a) equivalent strain (ϵ_{eq}) and (b) resultant displacement (u_{res}). The deformation scales applied were 700.

Table 5.7 Summary of FEA results for impact loading on the chassis bracket for shock absorber, *plt-sus-02.sldprt*, with five different meshes. The boundary conditions were fixing the two cylindrical surfaces of the plate bolt holes on the right, while the half of the impact load of 4.1 kN was applied upwards on the cylindrical surface of the bolt hole on the left.

Property	Mesh 1 (10 and 3.33 mm)		Mesh 2 (8 mm)		Mesh 3 (6 and 1.99 mm)		Mesh 4 (4 and 1.33 mm)		Mesh 5 (2 and 0.66 mm)	
	Min	Max	Min	Max	Min	Max	Min	Max	Min	Max
σ_v (MPa)	0.6	57.0	0.4	61.1	0.1	60.2	0.2	58.6	0.1	64.5
u_{res} (μm)	0.0	35.7	0.0	35.7	0.0	35.7	0.3	35.7	0.0	35.7
ϵ_{eq} ($\times 10^{-4}$)	0.0	2.4	0.0	2.6	0.0	2.5	0.0	2.5	0.0	2.7
FOS ($\sigma_{v\,\text{max}}$)	4.4	386.8	4.1	668.2	4.2	1770.0	4.3	1595.0	3.9	2229.0
FOS (τ_{max})	3.9	337.1	3.7	616.0	3.7	1580.0	3.8	1433.0	3.5	1977.0

Table 5.8 Percent of absolute relative convergence error (CE) for maximum von Mises and resultant displacement for five different mesh sizes on *plt-sus-02.sldprt*.

Mesh	Nodes	σ_v (MPa)	CE for σ_v (%)	u_{res} (μm)	CE for u_{res} (%)
1	3613	57.0	Unknown	35.7	Unknown
2	7285	61.1	6.7	35.7	0.0
3	12819	60.2	1.5	35.7	0.0
4	20893	58.6	2.8	35.7	0.0
5	123185	64.5	9.2	35.7	0.0

5.2.4. FEA on Swing Arm Bracket for Shock Absorber

Two swing arm brackets, denominated *plt-sus-03-sldprt,* were designed to be welded on each shock absorber swing arm, to assemble the shocks with the arms. This bracket was simulated with FEA, assuming that the maximum spring load of 4.1 kN was pointing downwards on the inner cylindrical surface of the pin hole. For the restraints, there were two scenarios: (1) fixing the bottom planar surface (Figure 4.7), and (2) fixing a portion of the bottom surface that mates with the swing arm (Figure 4.8).

For the first scenario, Figure 5.17 shows a maximum von Mises stress of 163 MPa with a corresponding FOS of 1.5. In both cases, the critical area is shown at the right side of the bottom planar surface of the bracket. On Figure 5.18, a maximum resultant displacement of 15.5 μm was found at the outer top right portion of the bracket, while the critical value for strain was 0.00068 mm/mm.

For the second scenario, Figure 5.19 shows a maximum von Mises stress of 172 Mpa with a corresponding FOS of 1.4, located at the corner of the simulated welding surface. The maximum resultant displacement was found to be 6.0 μm, located at the left top portion of the bracket, while the maximum strain was 0.00072 mm/mm.

A summary of the FEA results for both fixture scenarios and for five different mesh sizes is shown in Table 5.9. The most critical values were obtained with the finest mesh number 5 on the second scenario, especially the FOS of 1.3 when using the maximum shear stress theory. However, the convergence results of Table 5.10 show, for the first scenario, a von Mises stress of 81 Mpa with a relative CE of 8.2% for a corresponding FOS of 3.1, and a maximum resultant displacement of 15.0 μm with a relative CE of 0.6%, both found in mesh 3. For the second scenario, Table 5.10 shows a maximum von Mises stress of 68.3 Mpa with an associated CE of 14.3%, with a corresponding FOS of 3.7 found in Mesh 2, and a maximum displacement of 5.7 μm with a relative CE of 1.7% found in Mesh 3. According to Norton (2014), the increasing stresses associated with iterated mesh refinement suggest that there are high probabilities of node singularities with stress values that diverge to infinity due to the effect of boundary conditions associated to local stresses. Using the SolidWorks® Stress Hot Spot tool, there were singularities found for both scenarios at the node where the stresses are higher. Thus, disregarding the red areas where these stresses are located, the upper limit can be taken with FOS of 4.3 (Figure 5.17) in the first scenario, and a FOS of 4.6 (Figure 5.19) for the second scenario.

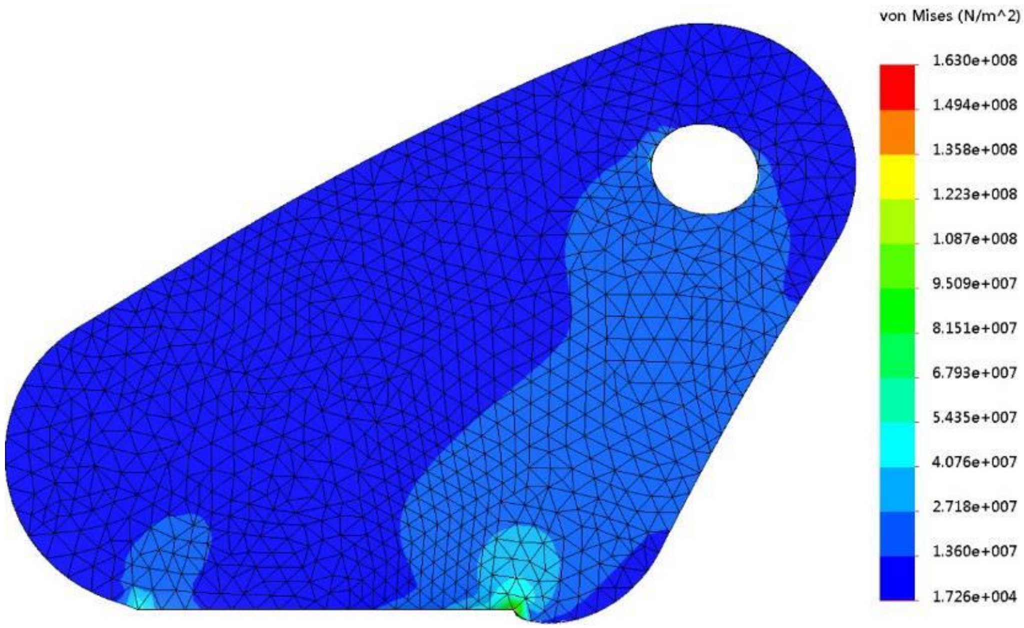

(a)

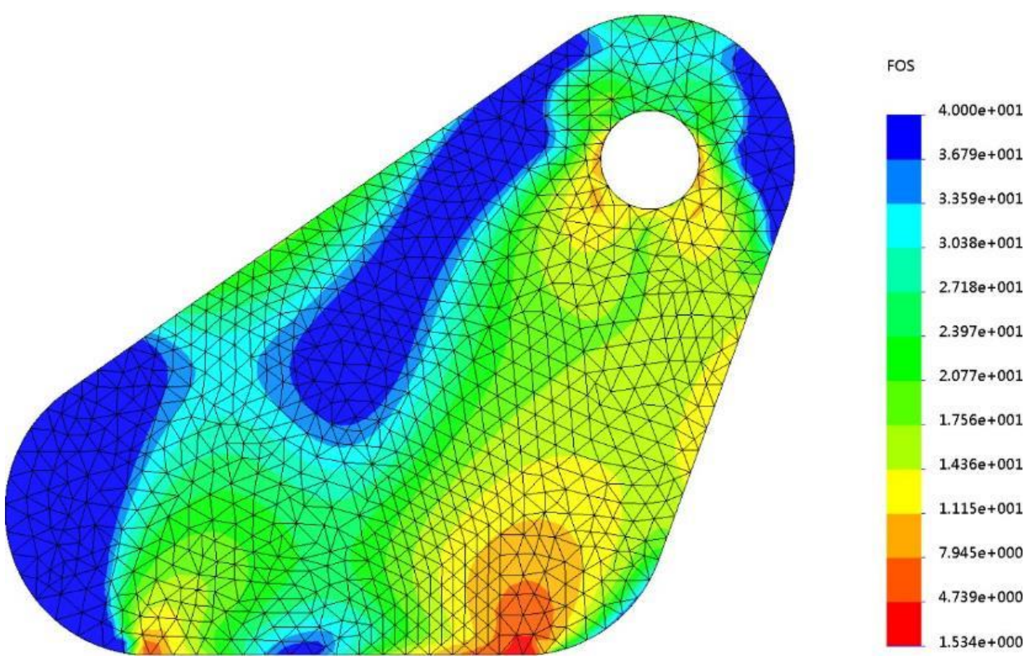

(b)

Figure 5.19 FEA results for von Mises stress and factor of safety on *plt-sus-03.sldprt*. Fixture in the planar surface at the bottom. Downward load of 4.1 kN applied on the internal cylindrical surface on bolt hole at the top right side: (a) von Mises (σ_v) with deformation scale of 700, and (b) factor of safety (FOS) with no deformation scale.

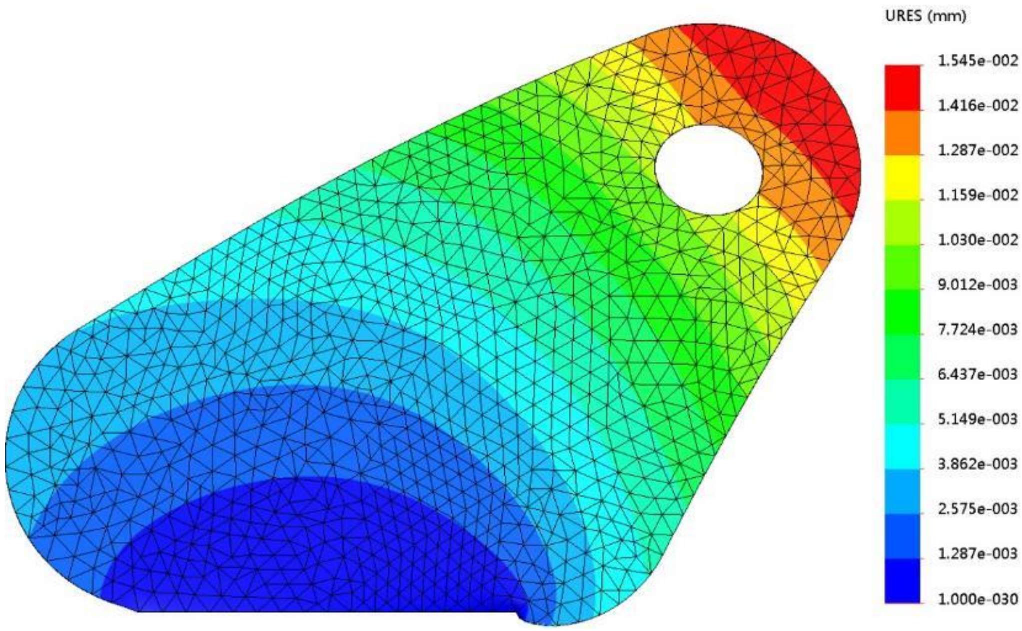

(a)

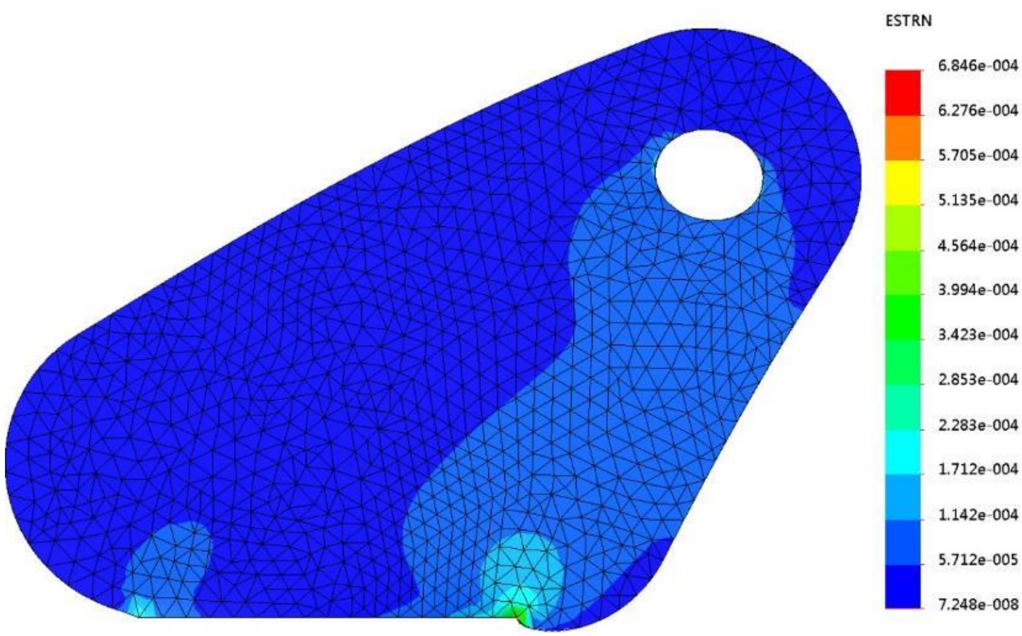

(b)

Figure 5.20 FEA results for equivalent strain and resultant displacement on *plt-sus-03.sldprt*. Fixture in the planar surface at the bottom. Downward load of 4.1 kN applied on the internal cylindrical surface on bolt hole at the top right side: (a) equivalent strain (ϵ_{eq}), and (b) resultant displacement (u_{res}). The deformation scale applied was 700.

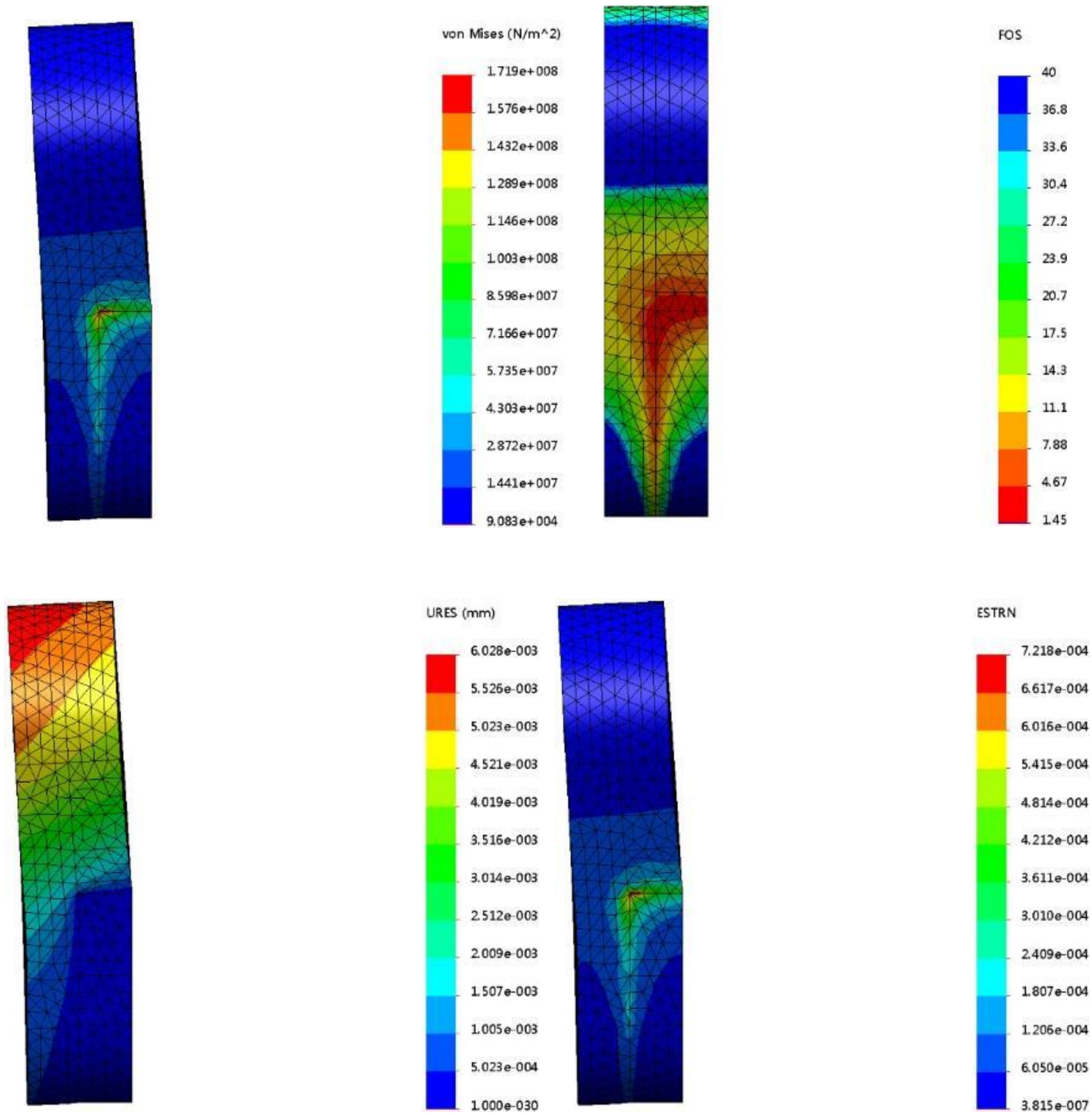

Figure 5.21 FEA results for von Mises (σ_v) stress, factor of safety (FOS), equivalent strain (ϵ_{eq}) and resultant displacement (u_{res}) on *plt-sus-03.sldprt*. Fixture in the simulated welding surface that mates with the swing arm, with a downward load of 4.1 kN applied on the internal cylindrical surface on bolt hole at the top right side. The deformation scale applied was 700, and 1 for the FOS figure.

Table 5.9 Summary of FEA results for impact loading on the swing arm bracket for shock absorber, *plt-sus-03.sldprt*, with five different meshes. The first half of the table corresponds to results of FEA for the bracket with fixture on the bottom planar surface, while the second half corresponds to fixture on the simulated welding surface that mates with the swing arm. Both cases with the force applied downwards to the cylindrical surface of the hole.

Property	Mesh 1 (7 mm)		Mesh 2 (5.75 mm)		Mesh 3 (4.5 mm)		Mesh 4 (3.25 mm)		Mesh 5 (2 mm)	
	Min	Max	Min	Max	Min	Max	Min	Max	Min	Max
σ_v (MPa)	0.1	55.9	0.0	74.4	0.0	81.0	0.0	111.7	0.0	164.4
u_{res} (μm)	0.0	15.0	0.0	15.1	0.0	15.0	0.0	15.3	0.0	15.4
ϵ_{eq} ($\times 10^{-4}$)	0.0	2.3	0.0	3.1	0.0	3.4	0.0	4.6	0.0	6.9
FOS ($\sigma_{v\,\text{max}}$)	4.5	4076.0	3.4	6503.0	3.1	5838.0	2.2	8871.0	1.5	10090.0
FOS (τ_{max})	4.3	3575.0	3.2	5652.0	3.1	5108.0	2.1	7693.0	1.5	9153.0
σ_v (MPa)	0.3	58.5	0.2	68.3	0.2	80.8	0.1	119.0	0.1	171.9
u_{res} (μm)	0.0	5.4	0.0	5.6	0.0	5.7	0.0	5.9	0.0	6.0
ϵ_{eq} ($\times 10^{-4}$)	0.0	2.5	0.0	2.9	0.0	3.4	0.0	5.0	0.0	7.2
FOS ($\sigma_{v\,\text{max}}$)	4.3	928.2	3.7	1335.0	3.1	1219.0	2.1	1841.0	1.5	2752.0
FOS (τ_{max})	4.1	890.9	3.3	1158.0	2.8	1068.0	1.9	1689.0	1.3	2527.0

Table 5.10 Percent of absolute relative convergence error (CE) for maximum von Mises and resultant displacement for five different mesh sizes on *plt-sus-03.sldprt*.

Mesh	Nodes	σ_v (MPa)	CE for σ_v (%)	u_{res} (μm)	CE for u_{res} (%)
1	3647	55.9	Unknown	15.0	Unknown
2	3682	74.4	24.9	15.1	0.8
3	7464	81.0	8.2	15.0	0.6
4	16267	111.7	27.4	15.3	1.6
5	65173	163.0	31.5	15.5	1.3
1	3711	58.5	Unknown	5.4	Unknown
2	3794	68.3	14.3	5.6	3.7
3	7703	80.8	15.5	5.7	1.7
4	16901	119.0	32.1	5.9	3.9
5	62519	171.9	30.8	6.0	2.0

5.2.5. FEA on Swing Arm Welded Assembly for Shock Absorber

Once the whole assembly of the swing arm was conceived, an FEA was performed. The results of von Mises stress and FOS for *sus-04-sldasm* are shown in Figures 5.20. The maximum stress was 318 MPa and the corresponding FOS was 0.6. Figure 5.21 shows the resultant displacement and strain with their maximum values as 0.194 mm and 0.00133 mm/mm, respectively. However, in Figure 5.22, a closer inspection of the results shows that the high stress value is likely to be a stress singularity of the FEA due to its presence on a sharp edge (Norton, 2014), and confirmed with singularity using SolidWorks® Stress Hot Spot tool. Therefore, the upper limit of the FOS can be taken as 3.8 as shown in Figures 5.20 and 5.22 for the critical areas in red color.

Table 5.11 shows a summary of the FEA results for five different mesh sizes. Critical values were obtained with the second finest mesh number, 4, especially the FOS of 0.51 with the maximum shear stress theory. However, the convergence results of Table 5.12 show a von Mises stress of 318 MPa with a relative CE of 12% for a corresponding FOS of 0.57, and a maximum resultant displacement of 194.3 μm with a relative CE of 0.15%, both found with mesh 5. Even though the FOS values for the simulations are less than 1.0, closer inspection of the stress locations shown in Figure 5.22 shows that the maximum stress is located at the corners of the shock absorber brackets with the intersection of the mating swing arm planar surface. Thus, the values are likely to be nodes with near zero area causing erroneous stress values (Norton, 2014). A more likely scenario is that of considering the stress values near the vicinity of the critical node, then from Figure 5.22 the values for maximum stress range between 80 MPa and 106 MPa, shown in cyan color, with a minimum FOS around 3.9, shown in orange color.

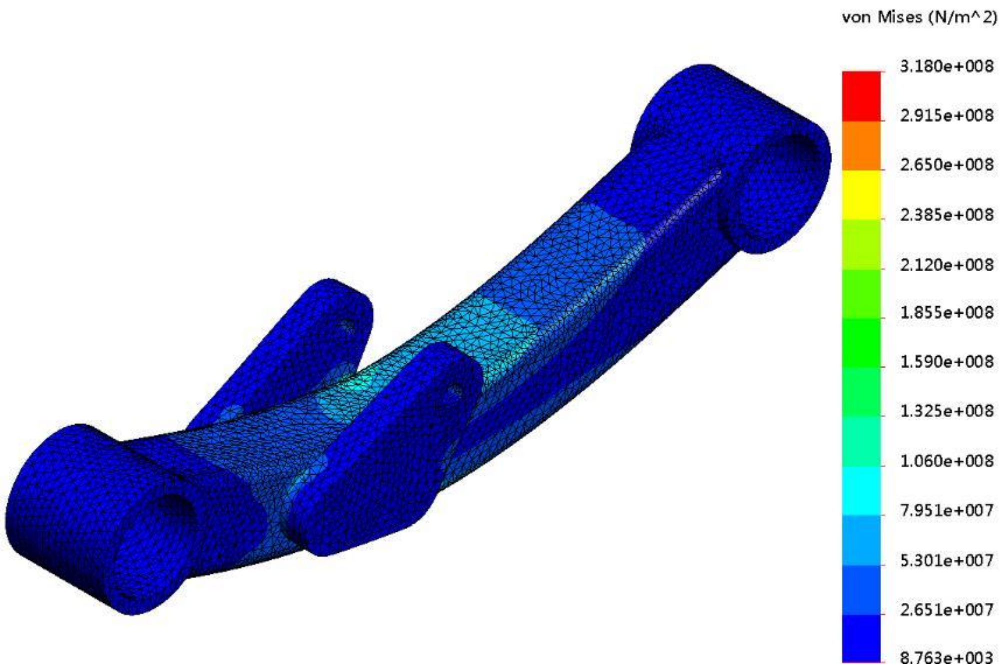

(a)

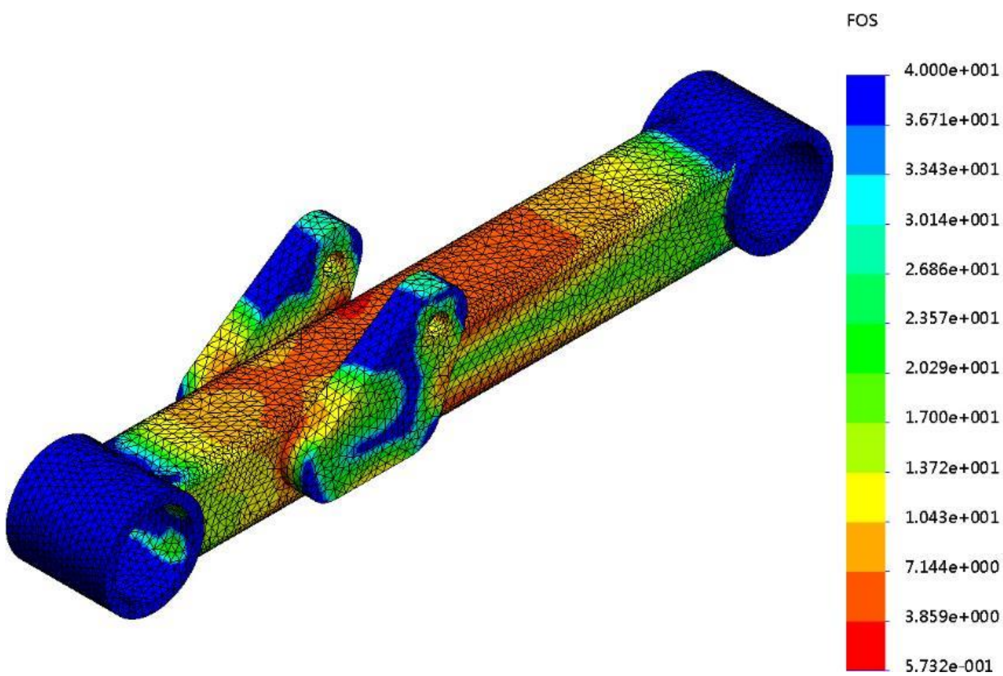

(b)

Figure 5.22 FEA results for von Mises stress and factor of safety on *sus-04.sldasm*. Fixture in the two cylindrical inner surfaces at the ends of the arm, with an downward load of 8.2 kN applied on the two internal cylindrical surfaces on bolt hole at the top: (a) von Mises stress (σ_v) with deformation scale of 200, and (b) factor of safety (FOS) with no deformation scale.

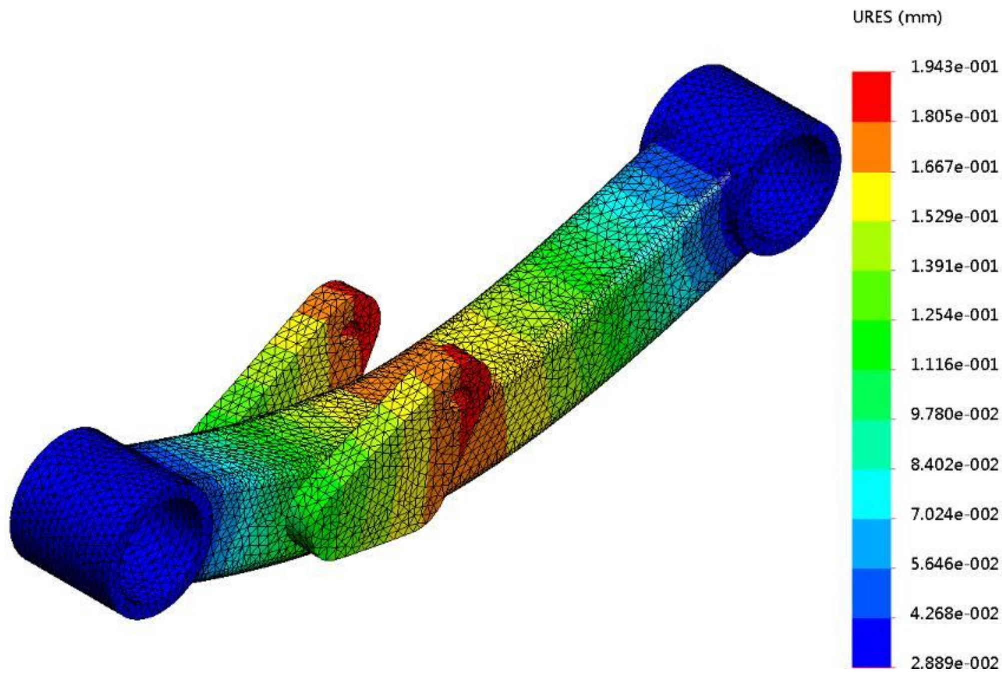

(a)

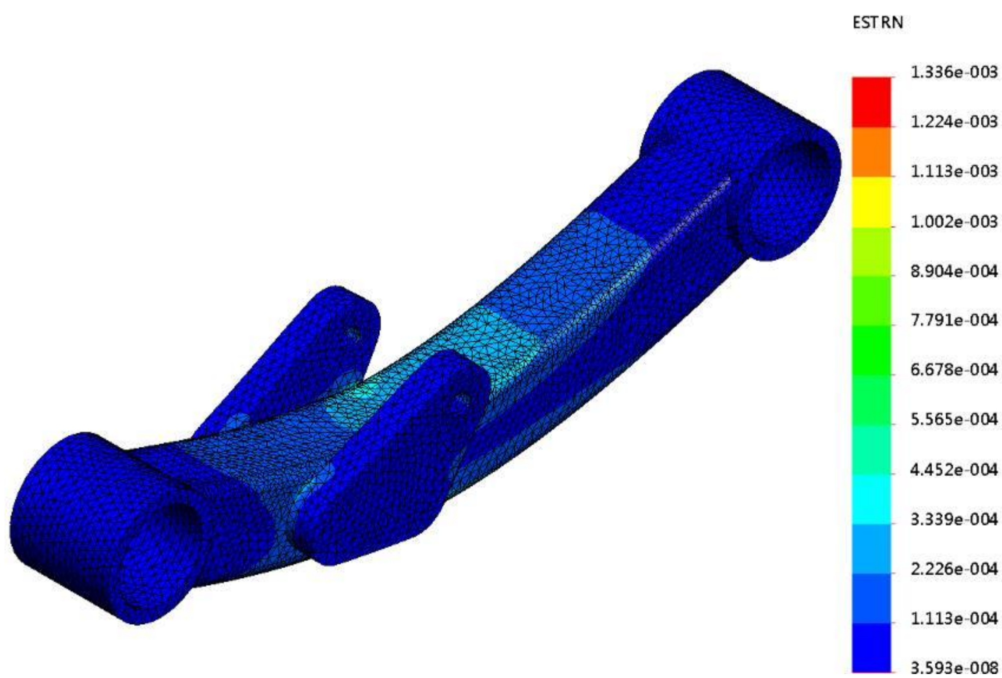

(b)

Figure 5.23 FEA results for resultant displacement and equivalent strain on *sus-04.sldasm*. Fixture in the two cylindrical inner surfaces at the ends of the arm, with an downward load of 8.2 kN applied on the two internal cylindrical surfaces on bolt hole at the top: (a) resultant displacement (u_{res}), and (b) equivalent strain (ϵ_{eq}). The deformation scale applied was 200.

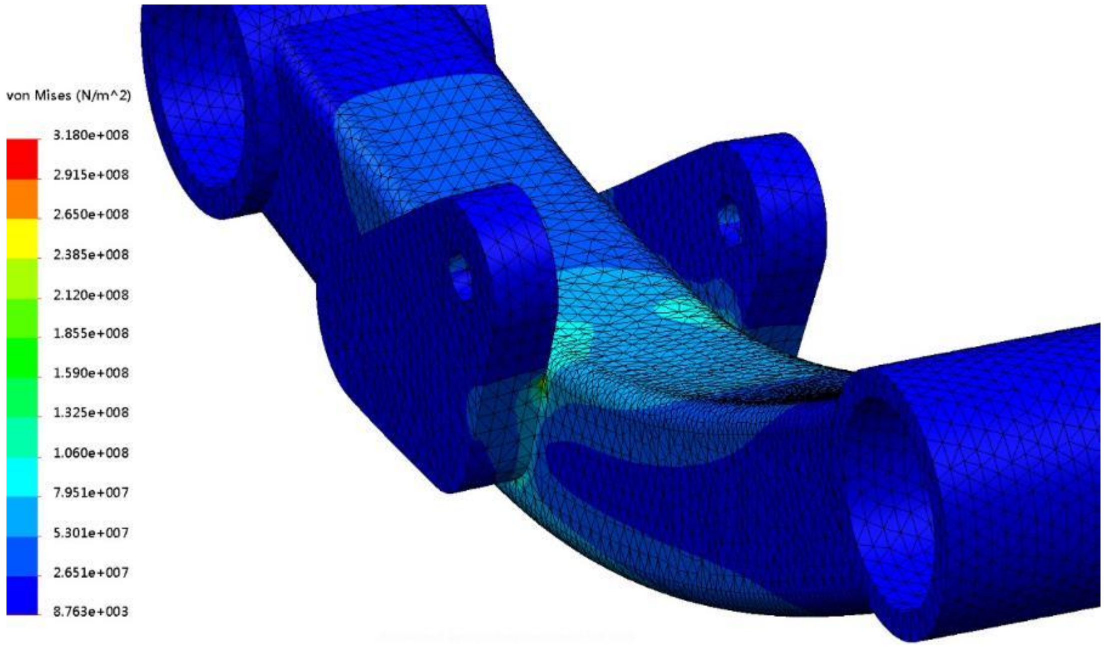

(a)

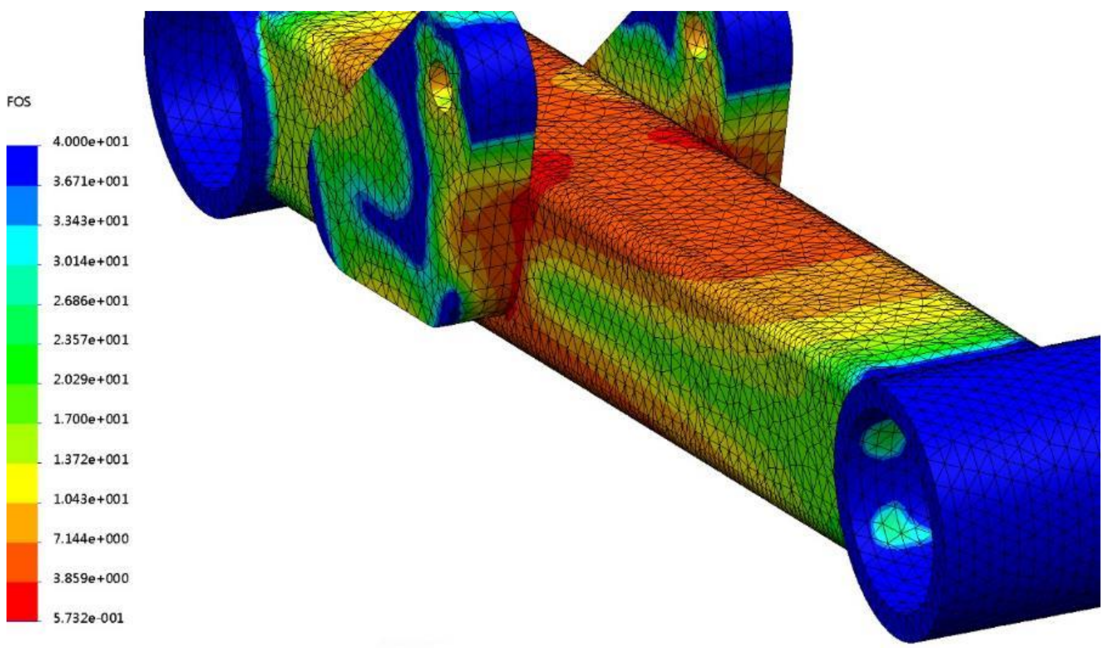

(b)

Figure 5.24 Augmented rear view of FEA results on *sus-04.sldasm*. Fixture in the two cylindrical inner surfaces at the ends of the arm, with an downward load of 8.2 kN applied on the two internal cylindrical surfaces on bolt hole at the top: (a) von Mises stress (σ_v) with deformation scale of 200, and (b) factor of safety (FOS) with no deformation scale.

Table 5.11 Summary of FEA results for impact loading on the top swing arm welded assembly for shock absorber, *sus-04.sldasm*, with five different meshes. The boundary conditions were established by fixing the internal cylindrical surfaces of the ends of the arm, while applying a load of 8.2 kN downwards on the internal cylindrical surfaces of the two small holes on the top.

Property	Mesh 1 (14 and 4.66 mm)		Mesh 2 (11.5 and 3.83mm)		Mesh 3 (9 and 3 mm)		Mesh 4 (6.5 and 2.16 mm)		Mesh 5 (4 and 1.33 mm)	
	Min	Max	Min	Max	Min	Max	Min	Max	Min	Max
σ_v (MPa)	0.0	161.8	0.03	187.6	0.01	271.7	0.01	356.1	0.01	318.0
u_{res} (μm)	28.8	192.6	28.8	192.9	28.9	193.4	28.9	194.0	28.9	194.3
ϵ_{eq} ($\times 10^{-4}$)	0.0	6.8	0.00	7.9	0.00	11.4	0.00	15.0	0.00	13.4
FOS ($\sigma_{v\,\text{max}}$)	1.2	11770.0	0.93	11780.0	0.78	26050.0	0.57	32460.0	0.57	36190.0
FOS (τ_{max})	1.1	10200.0	0.85	10220.0	0.70	22770.0	0.51	28410.0	0.52	35320.0

Table 5.12 Percent of absolute relative convergence error (CE) for maximum von Mises and resultant displacement for five different mesh sizes on *sus-04.sldasm*.

Mesh	Nodes	σ_v (MPa)	CE for σ_v (%)	u_{res} (μm)	CE for u_{res} (%)
1	14580	161.8	Unknown	192.6	Unknown
2	17871	187.6	13.8	192.9	0.2
3	27488	271.7	31.0	193.4	0.3
4	51587	356.1	23.7	194.0	0.3
5	108792	318.0	12.0	194.3	0.2

5.2.6. FEA on Gearbox Plate for Shock Absorber

Another element receiving the impact loading due to the shock absorber is the plate where the gearbox attaches, so an FEA was performed on *plt-sus-04.sldprt*. Figure 5.23 shows the maximum stress with a value of 76.8 MPa with a corresponding FOS of 3.3. On Figure 5.24 the resultant displacement and strain are shown with maximum values of 0.0696 mm and 0.00032 mm/mm, respectively.

Table 5.13 summarizes the FEA results for five different mesh sizes. A maximum shear stress value of 76.8 MPa, corresponding to a FOS of 3.3 was obtained with the finest mesh number, 5. However, the convergence results of Table 5.14 show a von Mises stress of 74.8 MPa with a relative CE of 0.1% for a corresponding FOS of 3.3, and a maximum resultant displacement of 69.6 μm with a relative CE of 0.01%, found in meshes 4 and 5. It is important to mention that the 8.2 kN force applied was considered before an addition of a parallel plate for the gearbox, called *plt-sus-05.sldprt* of item 14 of Figure J.4 that would reduce the load in half (4.1 kN). Thus, the FOS for plates *plt-sus-04* and *plt-sus-05* would be similar and greater than 4.0. This was an expedite change to keep the suspension system aligned with respect to the swing arms.

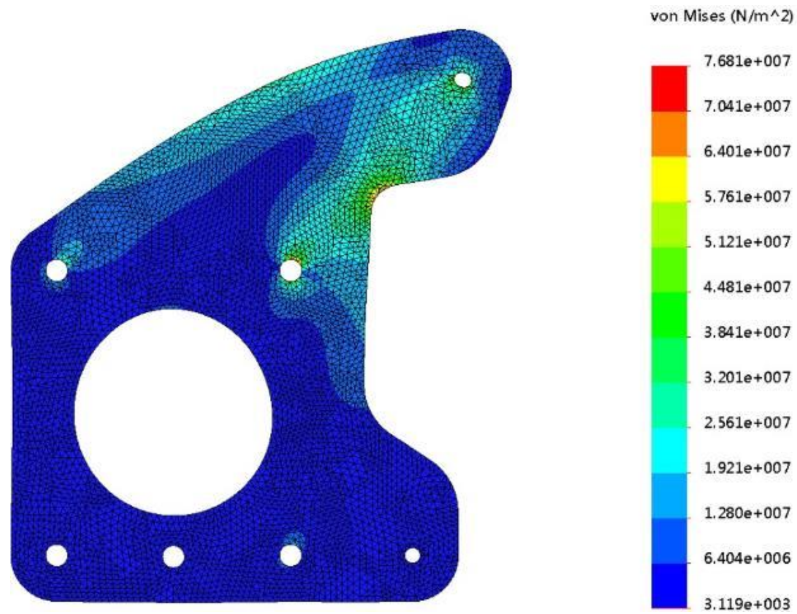

(a)

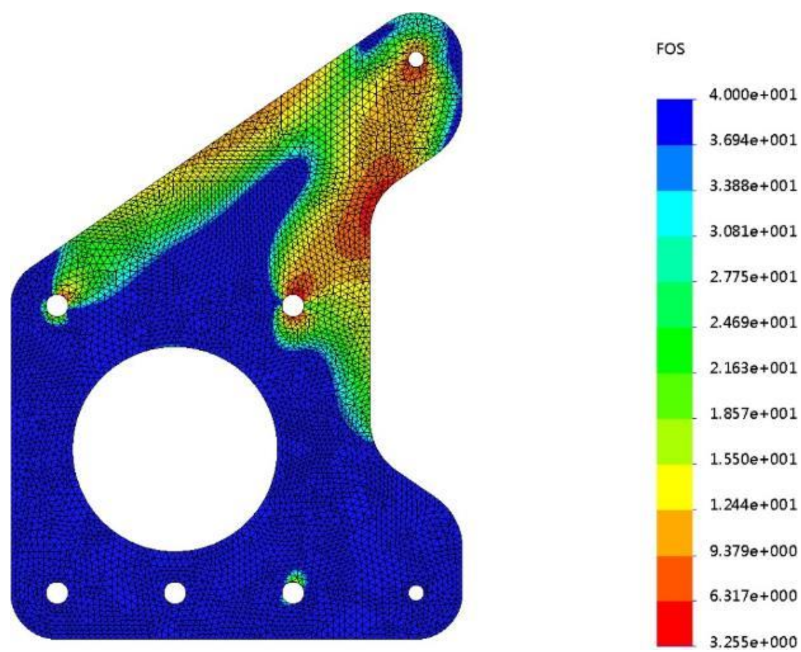

(b)

Figure 5.25 FEA results for von Mises stress and factor of safety on *plt-sus-04.sldprt*. Fixture in four cylindrical inner surfaces of the bolts arranged in a rectangle, with an downward load of 8.2 kN applied on the top internal cylindrical surface: (a) von Mises stress (σ_v) with deformation scale of 800, and (b) factor of safety (FOS) with no deformation scale.

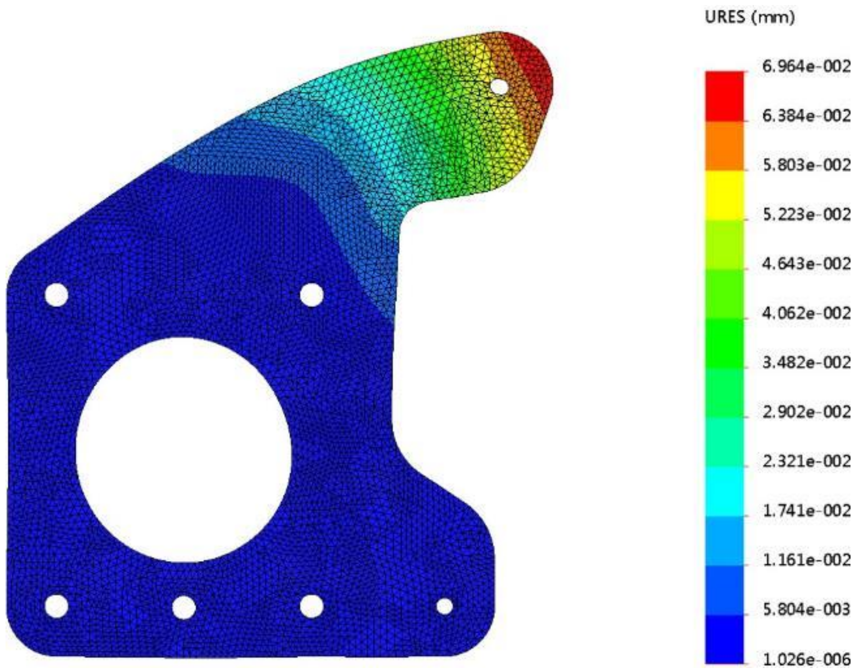

(a)

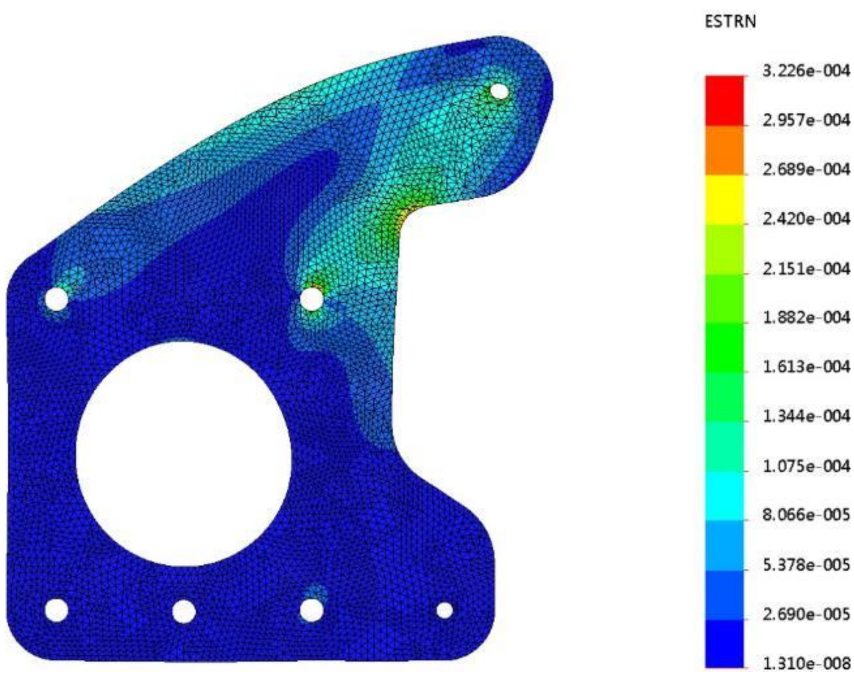

(b)

Figure 5.26 FEA results for resultant displacement and equivalent strain on *plt-sus-04.sldprt*. Fixture in four cylindrical inner surfaces of the bolts arranged in a rectangle, with an downward load of 8.2 kN applied on the top internal cylindrical surface: (a) resultant displacement (u_{res}), and (b) equivalent strain (ϵ_{eq}). The deformation scale applied was 800.

Table 5.13 Summary of FEA results for impact loading on the gearbox plate for shock absorber, *plt-sus-04.sldprt*, with five different meshes. The boundary conditions were established by fixing the internal cylindrical surfaces of the four cylindrical bolt holes that form a rectangle, while applying a load of 8.2 kN downwards on the internal cylindrical surfaces of the small hole on the top.

Property	Mesh 1 (16 and 5.33 mm)		Mesh 2 (13 and 4.33mm)		Mesh 3 (10 and 3.33 mm)		Mesh 4 (7 and 2.33 mm)		Mesh 5 (4 and 1.33 mm)	
	Min	Max	Min	Max	Min	Max	Min	Max	Min	Max
σ_v (MPa)	0.0	74.9	0.0	74.7	0.0	74.8	0.0	74.0	0.0	76.8
u_{res} (μm)	0.0	69.6	0.0	69.6	0.0	69.6	0.0	69.6	0.0	69.6
ϵ_{eq} ($\times 10^{-4}$)	0.0	3.1	0.0	3.1	0.0	3.1	0.0	3.1	0.0	3.2
FOS ($\sigma_{v\max}$)	3.3	8346.0	3.3	10320.0	3.3	9719.0	3.4	47250.0	3.3	80150.0
FOS ($\tau_{\max}$)	2.9	7705.0	3.0	9326.0	3.0	8457.0	3.0	45400.0	2.9	71070.0

Table 5.14 Percent of absolute relative convergence error (CE) for maximum von Mises stress and resultant displacement for five different mesh sizes on *plt-sus-04.sldprt*.

Mesh	Nodes	σ_v (MPa)	CE for σ_v (%)	u_{res} (μm)	CE for u_{res} (%)
1	7842	74.9	Unknown	69.6	Unknown
2	11707	74.7	0.3	69.6	0.04
3	18510	74.8	0.1	69.6	0.04
4	37209	74.0	1.0	69.6	0.01
5	145919	76.8	3.6	69.6	0.01

5.2.7. Design and Construction Considerations

All the suspension components were designed considering the whole assembly shown in Figure J.4. The lengths of swing arms and the position of the brackets were designed iteratively until all the components fit without exceeding the machine's general dimensions. In terms of strength, the values of FEA were accepted because FOS were near or greater than 3.0. The lowest FOS of 3.9 found in the swing arm was considered appropriate since a FOS ranging from 2.5 to 4.0 is still suggested for static elements under uncertain dynamic loads, material properties and stresses (Mott, 2004). Even with the appropriate FOS, the selection of steel for the suspension components (*plt-sus-01*, *plt-sus-02*, *sus-05*, *str-03*, *plt-sus-04*, and *plt-sus-05*) was mainly due to its capacity to withstand dynamic loads presenting deformation before fracture, relative to aluminum. Thus, these brackets were sent to manufacture with the specifications shown in the drawings of Appendix J.2.

5.3. Lateral Structures

Two lateral structures were designed to provide the vehicle a clearance of roughly three meters from the ground. The lateral trusses are symmetrical with respect to its vertical middle axis and were composed mainly of 50 by 50 mm square tubing, with two planar triangular plates at the top section in order to provide a bolted-through attachment with any of the two top structures (*frm-w-01.sldasm* and *frm-w-01.sldasm*) previously described in Section 5.2.

5.3.1. FEA on the Lateral Truss

On Figures 5.25 and 5.26, the FEA results for *str-01-sldprt* show that the maximum von Mises stress was 49.8 MPa, located at the red-colored areas of the inner planar surfaces of the two top diagonal structural square tubing members. The maximum stresses corresponded to a minimum FOS of 5.5. In the FOS image, the red-colored areas were indicated in a larger total area, especially at the inner and outer planar surfaces of the two top diagonal members, but also at the two intersections of these members with the horizontal ones.

On Figure 5.27, the results of FEA for resultant displacement and strain on *str-01-sldprt* showed that given the boundary conditions, the maximum resultant displacement of 5.1 mm would occur, as expected, at the top ends of the diagonal square tubing members with maximum strain values of 0.00064 mm/mm, located where the maximum stresses occurred (Figure 5.24).

Table 5.15 shows a summary of the FEA performed on *str-01-sldprt* with five different mesh sizes. The maximum von Mises stress was 49.8 MPa, with a corresponding minimum FOS of 5.5 found in Mesh 5, the finest. However, the convergence summary of Table 5.16 showed that 39.4 MPa was the maximum von Mises stress with a relative CE of 4.9%, with a corresponding FOS of 7.0 found in Mesh 3. For displacement, the convergence table showed a maximum resultant displacement of 4.1 mm with a relative CE of 1.2% found in Mesh 2.

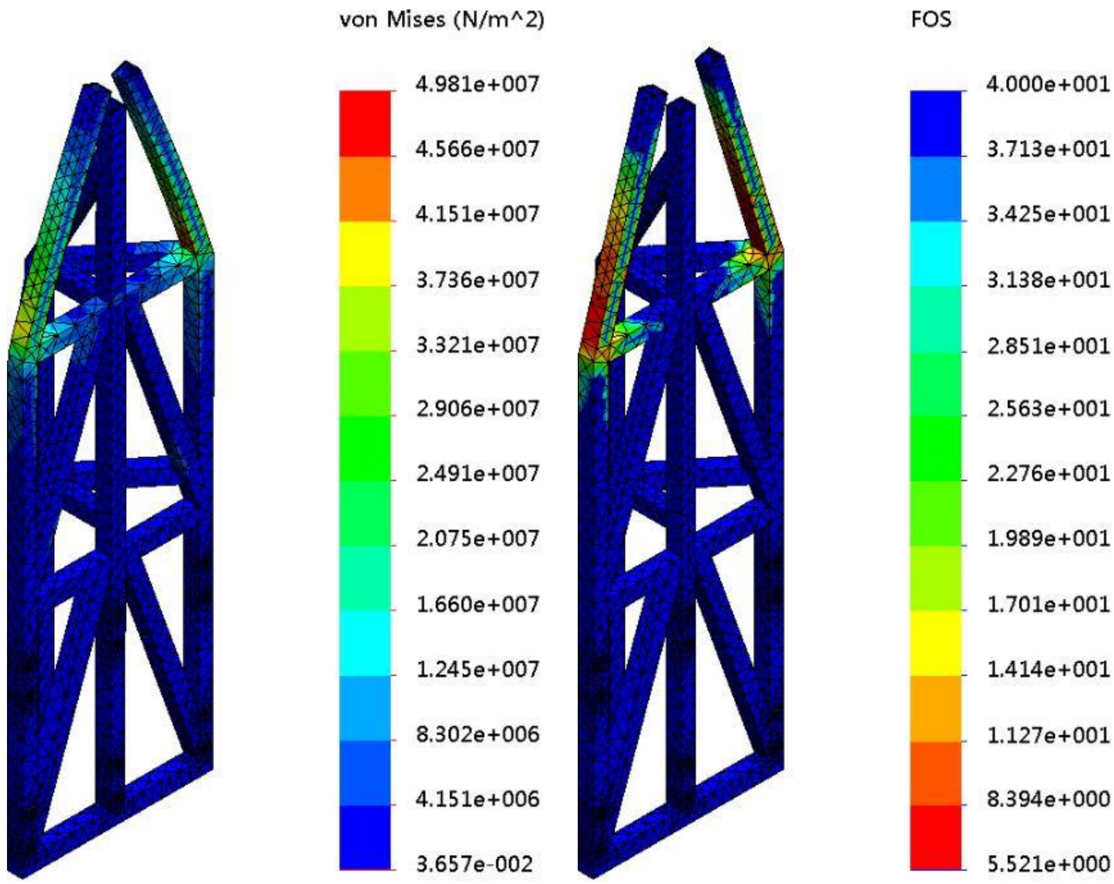

Figure 5.27 FEA results for von Mises (σ_v) and factor of safety (FOS) on *str-01.sldprt*. Fixture in the twelve cylindrical inner surfaces of the bolts at the bottom of the structure, with a downward load of 10 kN applied on the top three planar surfaces of the cross-section square tubing. The deformation scale applied was 10 and 1.

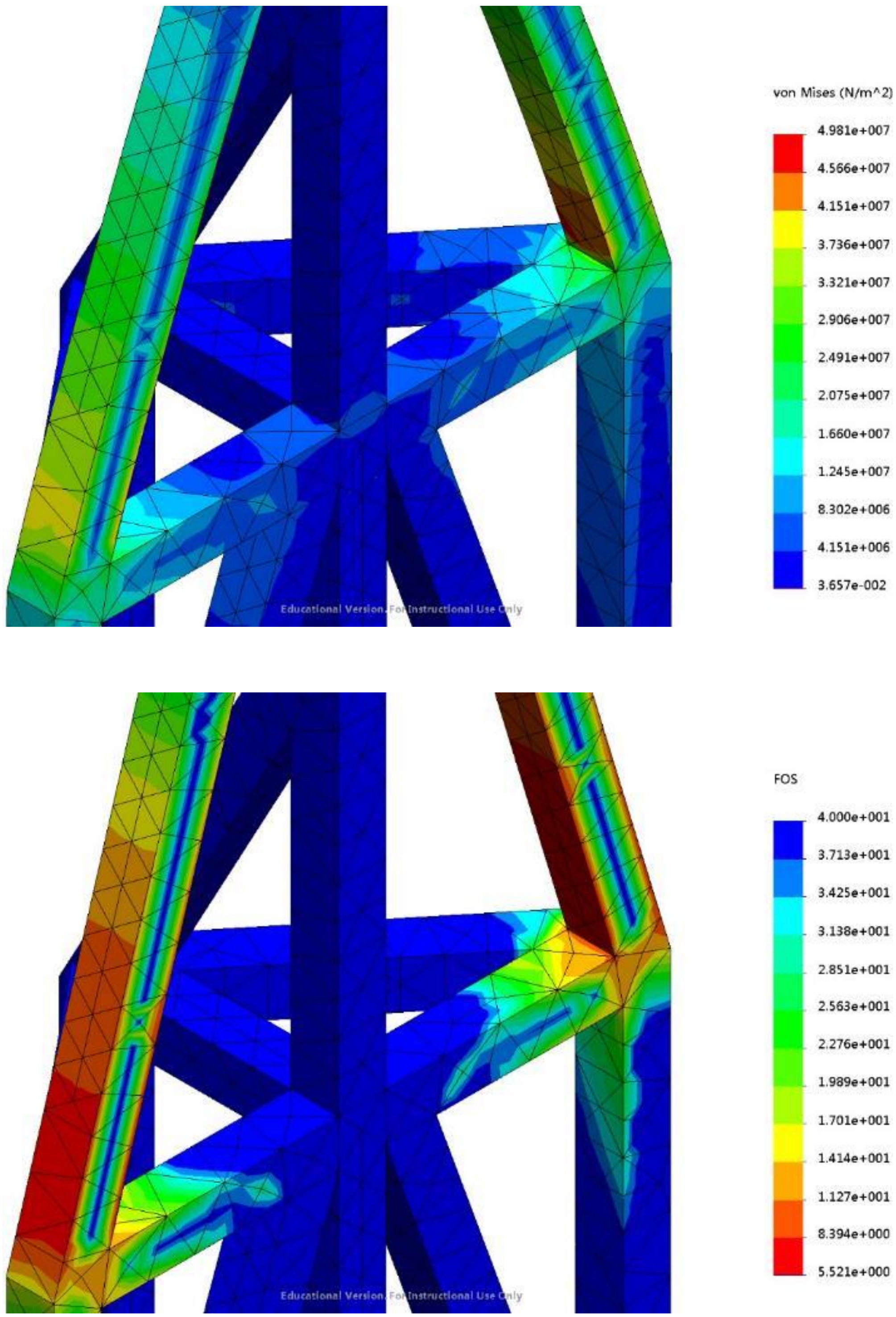

Figure 5.28 Critical areas of the FEA results for von Mises (σ_v) and factor of safety (FOS) on *str-01.sldprt*. Fixture in the twelve cylindrical inner surfaces of the bolts at the bottom of the structure, with a downward load of 10 kN applied on the top three planar surfaces of the cross-section square tubing. The deformation scale applied was 10 and 1.

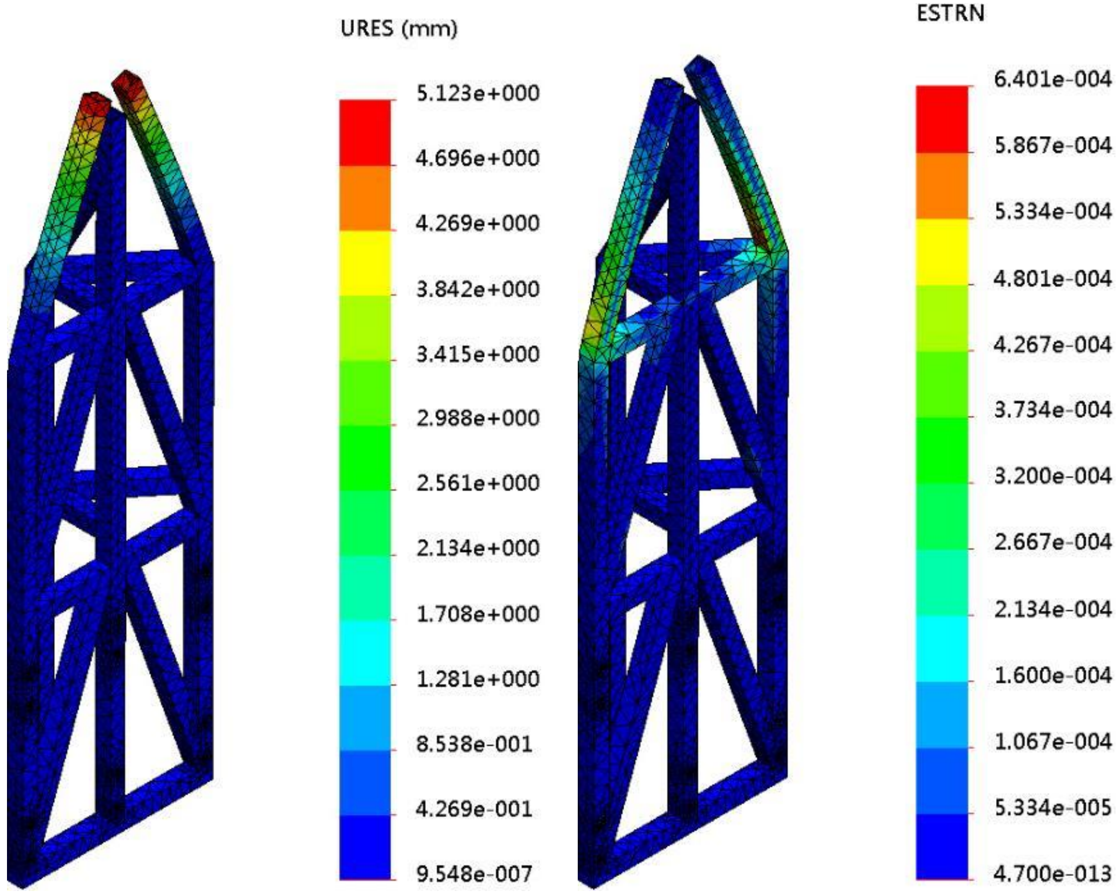

Figure 5.29 FEA results for displacement (u_{res}) and equivalent strain (ϵ_{eq}) on *str-01.sldprt*. Fixture in the twelve cylindrical inner surfaces of the bolts at the bottom of the structure, with an downward load of 10 kN applied on the top three planar surfaces of the cross-section square tubing. The deformation scale applied was 10.

Table 5.15 Summary of FEA results for impact loading on the lateral truss, *str-01.sldprt*, with five different meshes. The boundary conditions were established by fixing the twelve internal cylindrical surfaces of the bolt holes at the bottom, while applying a weight of 10 kN downwards on the three cross-sectional planar surfaces of the square tubes.

Property	Mesh 1 (180 and 36 mm)		Mesh 2 (146 and 29.2 mm)		Mesh 3 (112 and 22.4 mm)		Mesh 4 (78 and 15.6 mm)		Mesh 5 (44 and 8.8 mm)	
	Min	Max	Min	Max	Min	Max	Min	Max	Min	Max
σ_v (MPa)	0.0	44.8	0.0	41.3	0.0	39.4	0.0	41.8	0.0	49.8
u_{res} (mm)	0.0	4.1	0.0	4.1	0.0	4.6	0.0	4.8	0.0	5.1
ϵ_{eq} ($\times 10^{-4}$)	0.0	5.8	0.0	5.3	0.0	5.1	0.0	5.4	0.0	6.4
FOS ($\sigma_{v\,\max}$)	6.1	> 1000	6.7	> 1000	7.0	> 1000	6.6	> 1000	5.5	> 1000
FOS ($\tau_{\max}$)	5.4	> 1000	5.8	> 1000	6.7	> 1000	6.5	> 1000	5.3	> 1000

Table 5.16 Percent of absolute relative convergence error (CE) for maximum von Mises and resultant displacement for five different mesh sizes on *str-01.sldprt*.

Mesh	Nodes	σ_v (MPa)	CE for σ_v (%)	u_{res} (mm)	CE for u_{res} (%)
1	10347	44.8	Unknown	4.1	Unknown
2	11501	41.3	8.3	4.1	1.2
3	13969	39.4	4.9	4.6	10.5
4	18613	41.8	5.6	4.8	5.5
5	35216	49.8	16.2	5.1	5.7

5.3.2. Design and Construction Considerations

The minimum FOS of 5.5 located at the intersections of the top diagonal members with the other horizontal members was considered appropriate for a machine structure under dynamic loads with uncertainty about the complexity of the combination of loads such as weight, impact loadings, and vibrations, especially under field conditions (Mott, 2004). Additionally, special care was put into the welding process at the critical locations, but also the addition of two triangular top plates per truss (*plt-str-01.sldprt*) was intended to reduce the stresses and displacements, which were around a half centimeter. Thus, the corresponding detailed drawings of Appendix J.3 were created and sent to manufacture.

5.4. Bottom Chassis

Two symmetric bottom chassis were designed mainly to support and connect the wheels and the two lateral trusses previously described, but also to carry the electric motors, motor controllers, and batteries. These chassis were designed to clear the ground with at least the same clearance between the gearboxes and the ground. As with the trusses, the chassis were manufactured of 50 by 50 mm aluminum square tubing in order to be lightweight.

Plates and gussets were welded to the tubing to provide strength and a means of attachment to assemble the lateral trusses (*frm-w-03.sldasm*) with bolts.

5.4.1. FEA on the Bottom Chassis

Figure 5.28 shows the FEA general results of the von Mises stress and FOS on the bottom chassis (*str-02.sldprt*). The maximum stress of 103 MPa and its corresponding FOS of 2.7 were computed and highlighted with a red color at the top and bottom holes of the vicinity with their cylindrical surfaces as shown in the two zoomed-in FEA images of Figures 5.30 and 5.31 especially at the bottom hole. Figure 5.29 shows resultant displacement and strain with critical values of 1.3 mm of maximum displacement and 0.001326 mm/mm, respectively. In both cases the critical values are shown in red. As expected, in the top right portion of the structure, where the upward spring load was applied, was the maximum resultant displacement, while the maximum strain values were located in the vicinity of the fixed holes, where deformation was critical.

Table 5.17 shows a summary of the FEA performed with five different meshes. The critical values, as expected, were found in the finest mesh number, 5, with the same values previously presented for Figures 5.28 to 5.30. In terms of convergence, the maximum von Mises stress of 70.9 MPa with a corresponding FOS of 3.9 and a relative CE of 16.35% was found in Mesh 3, while a maximum resultant displacement of 1.1 mm with a relative CE of 2.2% was found in Mesh 4.

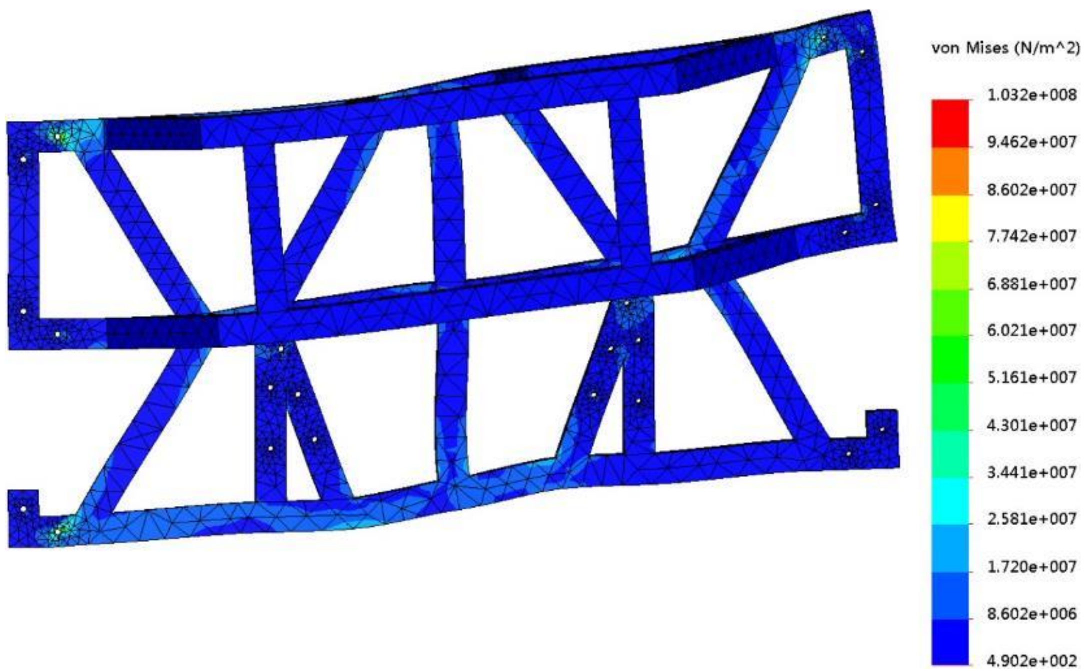

(a)

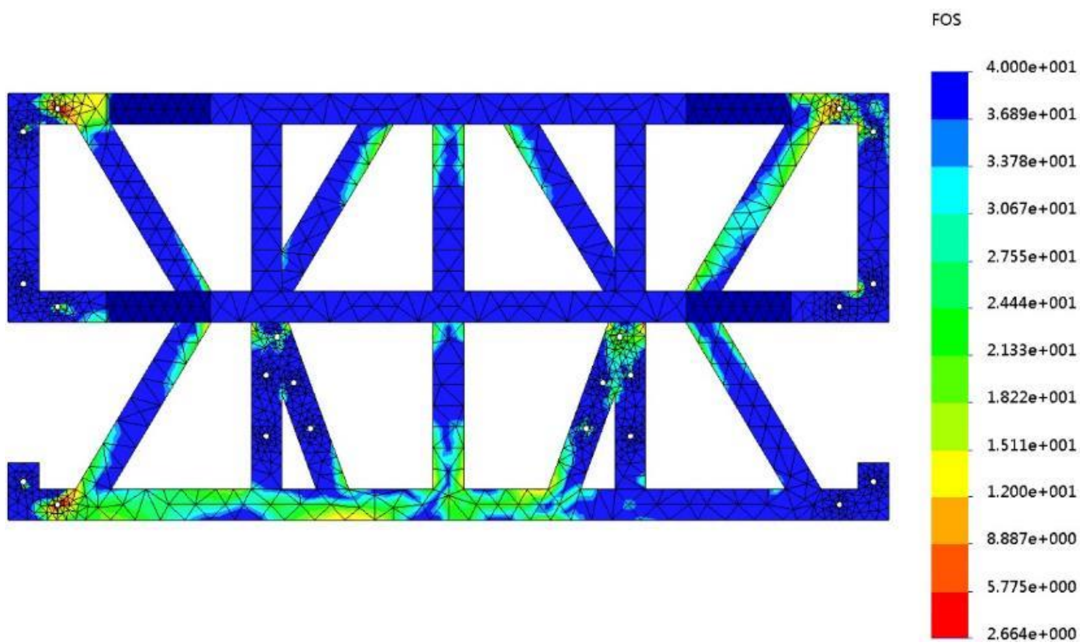

(b)

Figure 5.30 FEA results for von Mises stress and factor of safety on *str-02.sldprt*. Fixture in the twelve cylindrical inner surfaces of the bolts at the left of the structure, with an upward load of 8.2 kN applied on the top four cylindrical surfaces that attach to the shock absorber brackets: (a) von Mises stress (σ_v) with deformation scale of 150, and (b) factor of safety (FOS) with no deformation scale.

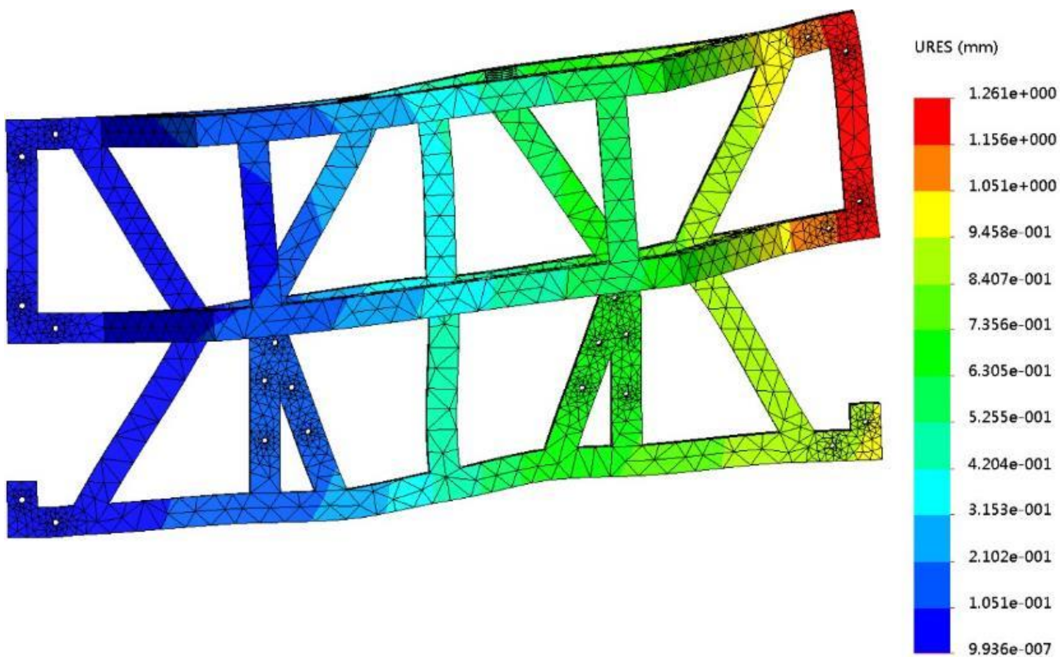

(a)

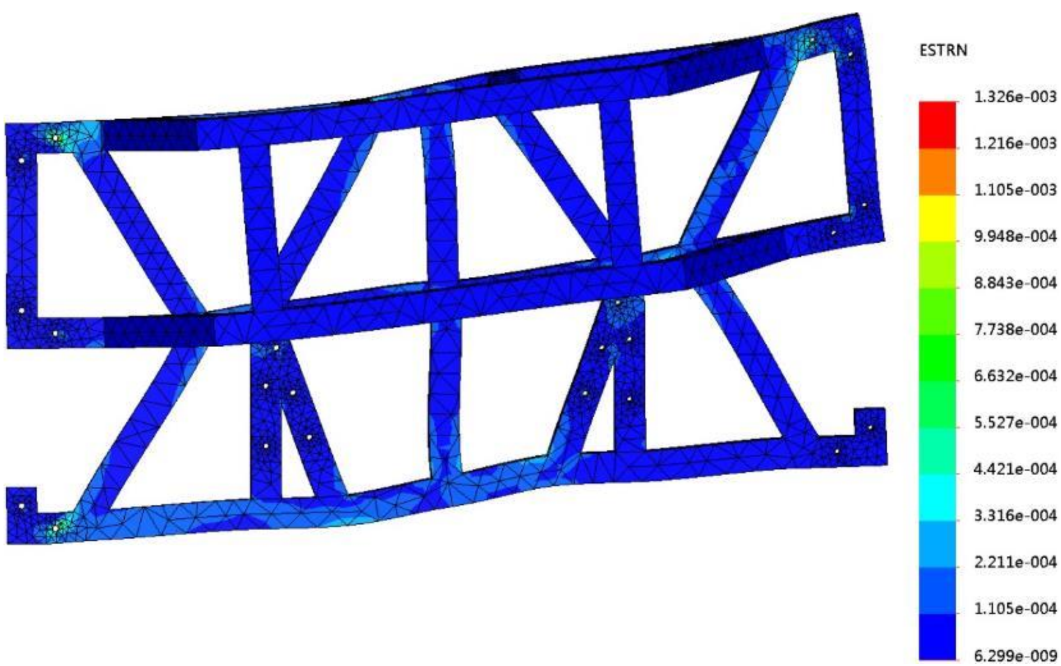

(b)

Figure 5.31 FEA results for resultant displacement and equivalent strain on *str-02.sldprt*. Fixture in the twelve cylindrical inner surfaces of the bolts at the left of the structure, with an upward load of 8.2 kN applied on the top four cylindrical surfaces that attach to the shock absorber brackets: (a) resultant displacement (u_{res}), and (b) equivalent strain. The deformation scale applied was 150.

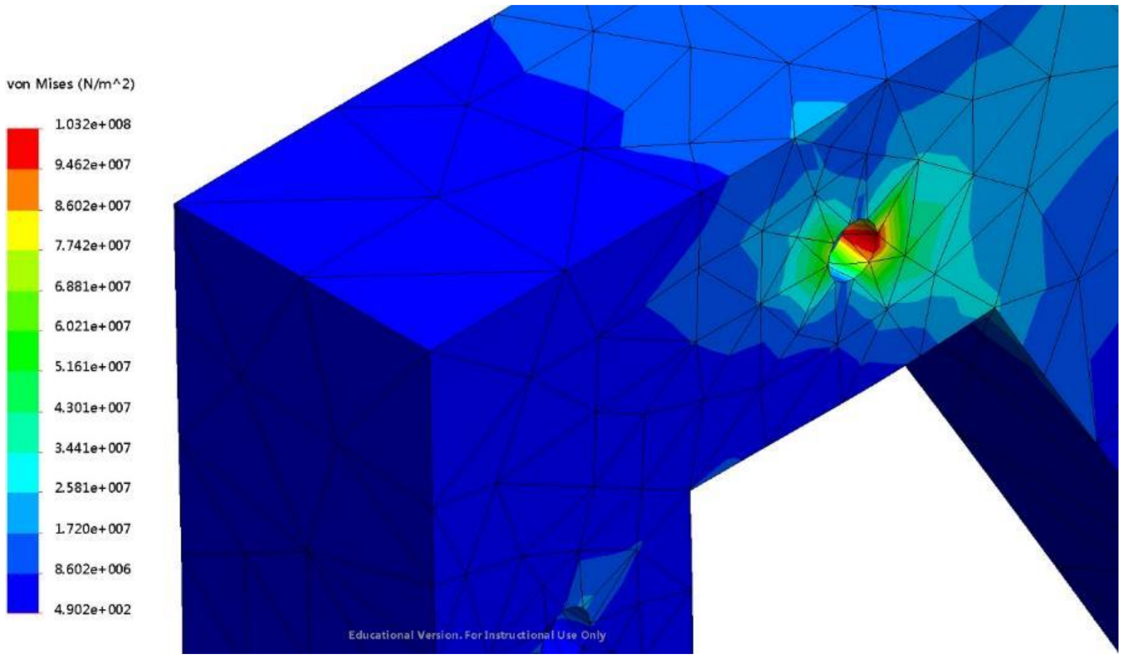

(a)

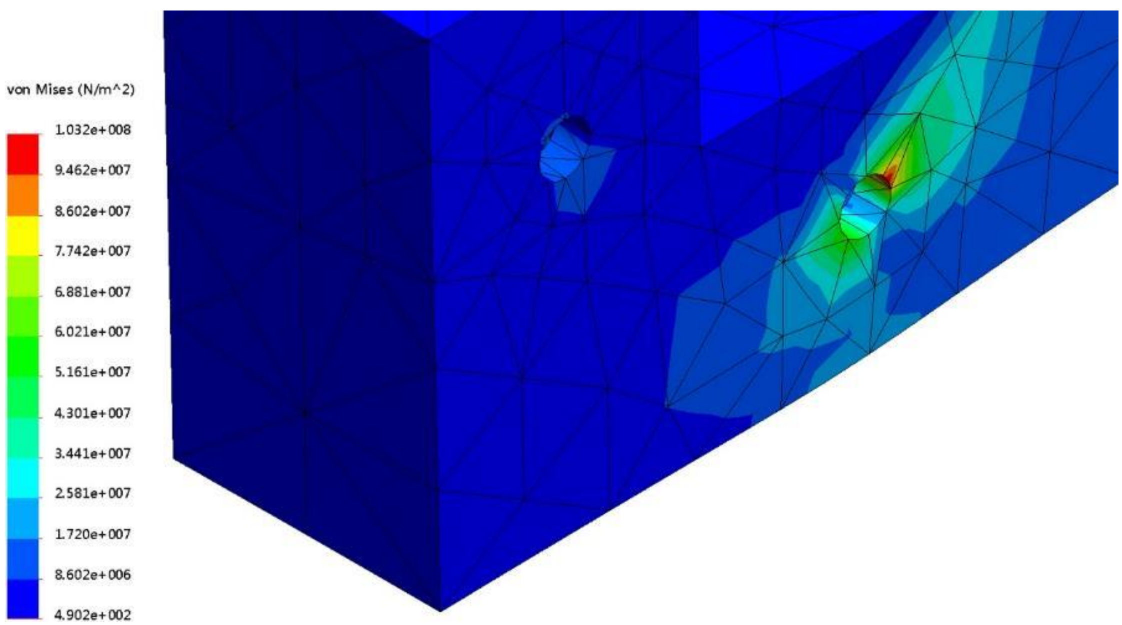

(b)

Figure 5.32 Critical FEA results for von Mises stress (σ_v) on *str-02.sldprt*. Fixture in the twelve cylindrical inner surfaces of the bolts at the left of the structure, with an upward load of 8.2 kN applied on the top four cylindrical surfaces that attach to the shock absorber brackets: (a) zoom-in on top holes, and (b) zoom-in on bottom holes. The deformation scale applied was 1.

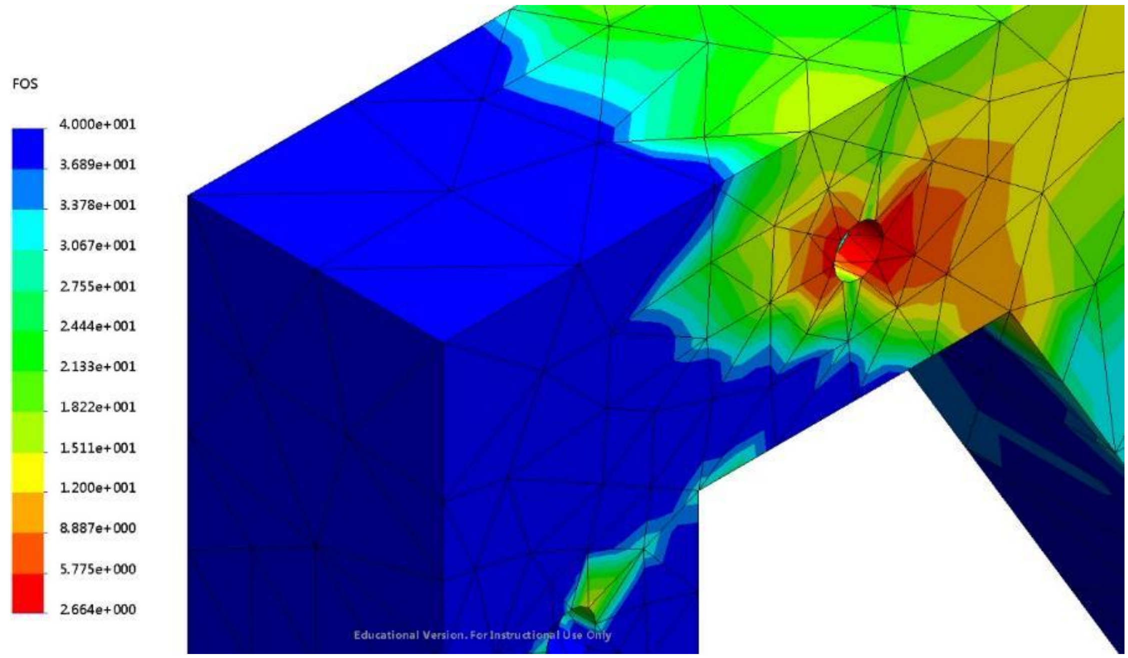

(a)

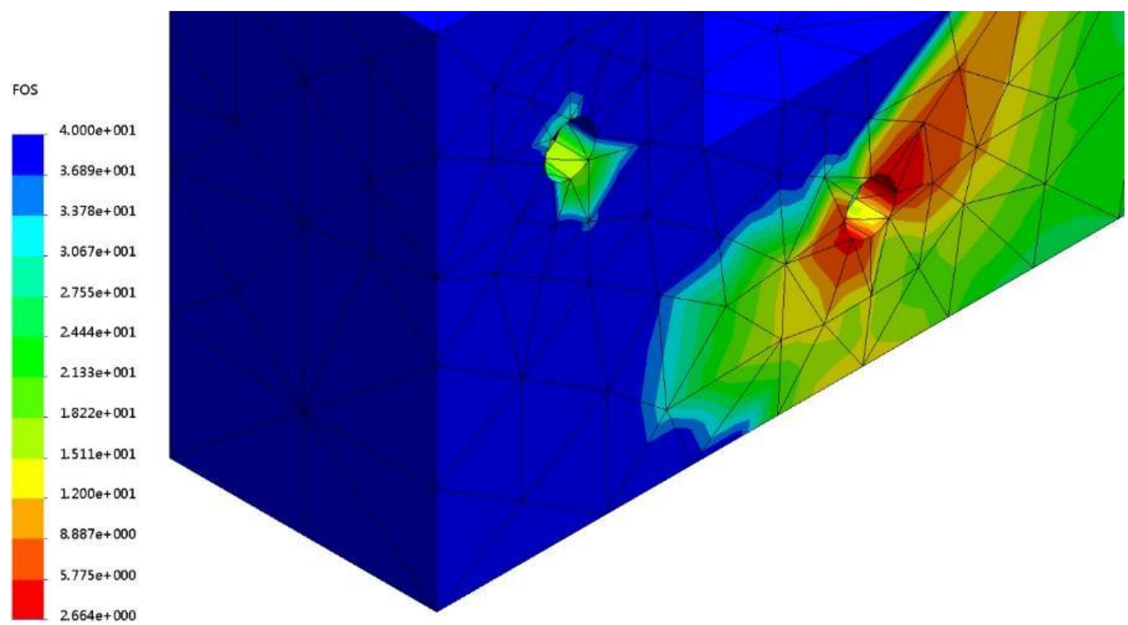

(b)

Figure 5.33 Critical FEA results for FOS on *str-02.sldprt*. Fixture in the twelve cylindrical inner surfaces of the bolts at the left of the structure, with an upward load of 8.2 kN applied on the top four cylindrical surfaces that attach to the shock absorber brackets: (a) fixed top holes and (b) fixed bottom holes The deformation scale applied was 1.

Table 5.17 Summary of FEA results for impact loading on the bottom chassis structure, *str-02.sldprt*, with five different meshes. The boundary conditions were established by fixing the twelve internal cylindrical surfaces of the bolt holes at the left, while applying a load of 8.2 kN upwards on the eight cylindrical surfaces of the boltholes that assemble the shock absorber bracket (*plt-sus-02.sldprt*).

Property	Mesh 1 (165 and 33 mm)		Mesh 2 (134 and 26.8 mm)		Mesh 3 (102 and 20.4 mm)		Mesh 4 (71 and 14.2 mm)		Mesh 5 (40 and 8 mm)	
	Min	Max	Min	Max	Min	Max	Min	Max	Min	Max
σ_v (MPa)	0.0	76.0	0.0	58.5	0.0	70.9	0.0	84.8	0.0	103.2
u_{res} (mm)	0.0	0.9	0.0	1.0	0.0	1.1	0.0	1.1	0.0	1.3
ϵ_{eq} ($\times 10^{-4}$)	0.0	9.8	0.0	7.5	0.0	9.1	0.0	10.9	0.0	13.3
FOS ($\sigma_{v\max}$)	3.6	> 1000	4.7	> 1000	3.9	> 1000	3.2	> 1000	2.7	> 1000
FOS ($\tau_{\max}$)	3.3	> 1000	4.1	> 1000	3.4	> 1000	2.8	> 1000	2.3	> 1000

Table 5.18 Percent of absolute relative convergence error (CE) for maximum von Mises and resultant displacement for five different mesh sizes on *str-02.sldprt*.

Mesh	Nodes	σ_v (MPa)	CE for σ_v (%)	u_{res} (mm)	CE for u_{res} (%)
1	11921	76.0	Unknown	0.9	Unknown
2	13885	58.5	29.84	1.0	3.17
3	17633	70.9	17.50	1.1	12.13
4	22768	84.8	16.35	1.1	2.20
5	43365	103.2	17.85	1.3	9.91

5.4.2. Design and Construction Considerations

As stated in Mott, (2004), a minimum FOS of 3.9 was an appropriate design value for a machine structure under dynamic loads with uncertainty about the complexity of the combination of loads such as weight, impact loadings, and vibrations. This minimum FOS value was located at the bottom hole of the left side of the structure and corresponds to the scenario in which the structure was fixed in such a way that the stress reaches the critical value. However, since at the bottom holes, there is attached a swing arm, the stress would be reduced significantly. Additionally, the possible maximum stresses would be reduced by the friction of the brackets that will hold the swing arm in place with the bottom chassis. Thus, two identical chassis were constructed according to the drawings of Figure J.13.

Since the bottom chassis needed to carry the batteries and to assemble with the lateral trusses and the suspension system, additional aluminum plates and gussets were sent to manufacture and welded to it. Figure J.15 shows in context these plates and gussets, and their dimensions are shown in Figures J.16 to J.23. The additional plates, as a logical conclusion, add extra strength, reducing global deformation of the bottom chassis, but they were left out of the chassis FEA due to difficulties in meshing types of elements: structural members of the chassis (trusses) with solid bodies (plates) in SolidWorks®.

5.5. Transmission System

5.5.1. Gearbox Output Angular Speed and Torque, and Vehicle's Maximum Speed

The required maximum linear velocity of the EGPV was 8 km/h. Thus, a gearbox, wheel and tire, and electric motor with the appropriate specifications were procured in order the achieve the maximum required speed. From Subsections 4.2.1 and 4.2.2, a summary of the parameters to compute wheels' output angular velocity and vehicle's linear velocity were gearbox ratio of 52:1, maximum recommended angular velocity of 2,000 rpm, and tire radius of 428 mm. Thus, the output angular velocity was found as

$$n_{out} = e\, n_{in}$$

where n_{out} is the output angular speed of the gearbox shaft connected to the wheel and tire, e is the train value or gear ratio, and n_{in} is the input angular speed of the driveshaft connected to the electric motor. Substituting the datasheet values into the previous equation, the output speed obtained was

$$n_{out} = \left(\frac{1}{52}\right) 2000 = 38.5\, rpm,$$

corresponding to an output angular velocity denoted as $\omega_{out} = 4$ rad/s.

The output torque was computed as

$$T_{out} = \left(\frac{1}{e}\right) T_{in} = (52)(24\, N \cdot m) = 1248\, N \cdot m,$$

where T_{out} is the output torque at the wheel's shaft and T_{in} is the input maximum torque of the electric motor.

The maximum linear speed of the vehicle (v_{max}) was then computed substituting values into the following equation.

$$v_{max} = r_t\, \omega_{out} = (0.428\, m)\left(4 \frac{rad}{s}\right) = 1.72 \frac{m}{s},$$

which corresponds to 6.2 km/h. Since the gearbox manufacturer recommended a maximum angular velocity of 2,000 rpm, the EGPV could travel at 6.2 km/h, and the requirement of 8 km/h will not be fulfilled. However, the speed of 8 km/h was a design requirement for the EGPV to travel from the farmstead to field, but for phenotyping activities the speed of 6.2 km/h is enough when compared to the travel speed estimated of 2.9 km/h for the phenotyping experiment of the field, where the sorghum plants were grown up to 3 m and a higher speed might damage them.

5.5.2. FEA on Motor Bracket

Figure 5.32 shows the FEA results of von Mises stress and FOS on the motor bracket, *sht-frm-01.sldprt*. Assuming that the maximum electric motor torque of 24 N-m was applied in the large inner cylindrical surface of the bracket, the maximum stress of 53 MPa with a corresponding minimum FOS of 4.7 was located at the top hole of the three supporting holes that were set as fixed in the FEA. Both values are indicated in red in the figure.

The maximum resultant displacement and strain are shown in Figure 5.33. The critical displacement of 0.2 mm was located at the top right section of the bracket, while the maximum strain of 0.00022 mm/mm was located at the top supporting hole where the bracket assembles with the bottom chassis.

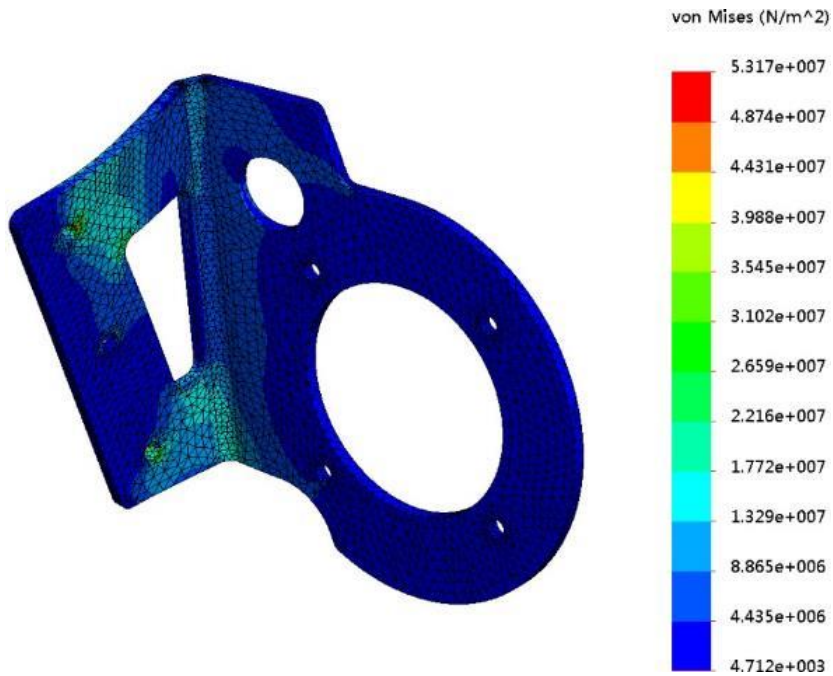

(a)

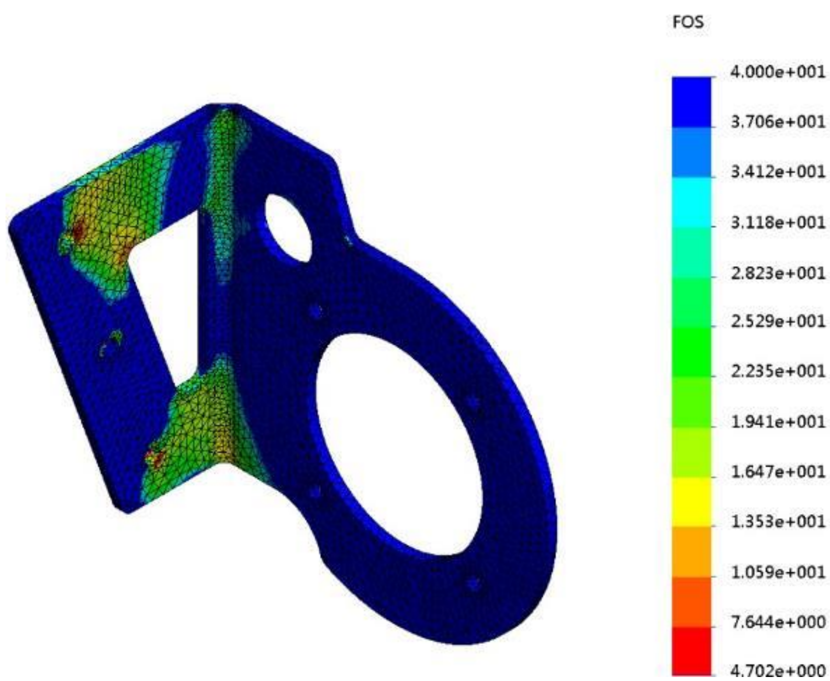

(b)

Figure 5.34 FEA results for von Mises stress and factor of safety on *sht-frm-01.sldprt*. Fixture in the three cylindrical inner surfaces of the bolts at the left of the sheet metal, with torsion load of 24 N-m applied on the big inner cylindrical surface: (a) von Mises stress (σ_v) with deformation scale of 200, and (b) factor of safety (FOS) with no deformation scale.

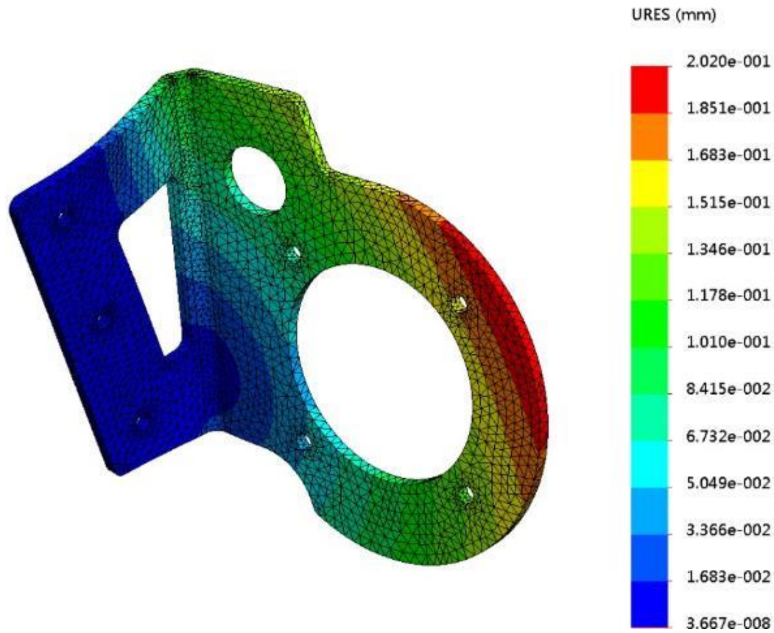

(a)

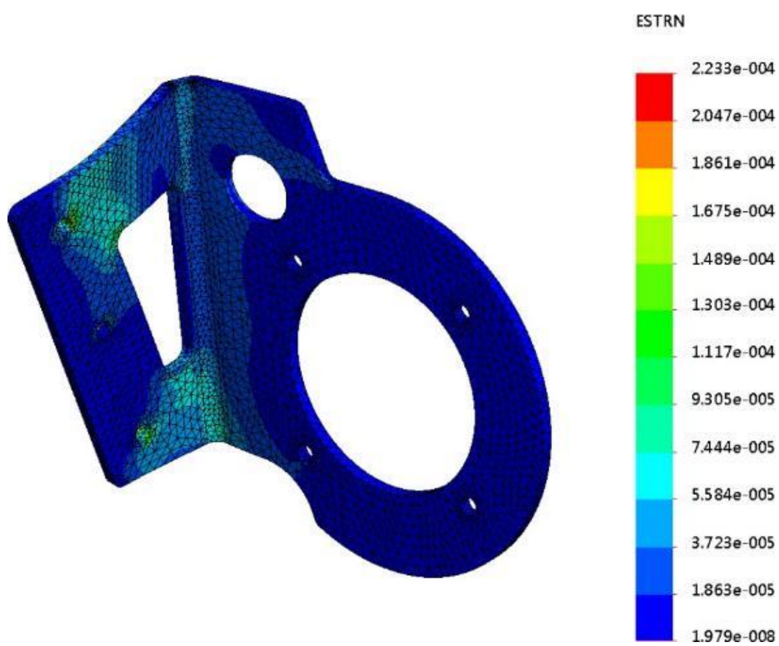

(b)

Figure 5.35 FEA results for resultant displacement and equivalent strain on *sht-frm-01.sldprt*. Fixture in the three cylindrical inner surfaces of the bolts at the left of the sheet metal, with torsion load of 24 N-m applied on the big inner cylindrical surface: (a) resultant displacement (u_{res}), and (b) equivalent strain. The deformation scale was 200.

Table 5.19 Summary of FEA results for torsion loading on the motor bracket, *sht-str-01.sldprt*, with five different meshes. The boundary conditions were established by fixing the three internal cylindrical surfaces of the bolt holes at the left, while applying a torsion load of 25 N-m counterclockwise on internal cylindrical surface of the motor hole.

Property	Mesh 1 (26 and 5.2 mm)		Mesh 2 (21 and 4.2 mm)		Mesh 3 (16 and 3.2 mm)		Mesh 4 (11 and 2.2 mm)		Mesh 5 (6 and 1.2 mm)	
	Min	Max	Min	Max	Min	Max	Min	Max	Min	Max
σ_v (MPa)	0.0	41.3	0.0	46.7	0.0	52.8	0.0	58.8	0.0	53.2
u_{res} (μm)	0.0	198.6	0.0	200.0	0.0	200.9	0.0	201.2	0.0	202.0
ϵ_{eq} ($\times 10^{-4}$)	0.0	1.7	0.0	2.0	0.0	2.2	0.0	2.5	0.0	2.2
FOS ($\sigma_{v\,\text{max}}$)	6.1	19750.0	5.4	7816.0	4.7	9304.0	4.3	9517.0	4.7	53050.0
FOS (τ_{max})	5.7	17140.0	5.3	6.8	4.5	8151.0	4.1	8253.0	4.5	48190.0

Table 5.20 Percent of absolute relative convergence error (CE) for maximum von Mises and resultant displacement for five different mesh sizes on *sht-str-01.sldprt*.

Mesh	Nodes	σ_v (MPa)	Ce for σ_v (%)	u_{res} (μm)	CE for u_{res} (%)
1	9729	41.3	Unknown	198.6	Unknown
2	12991	46.7	11.6	200.0	0.7
3	18962	52.8	11.6	200.9	0.4
4	21152	58.8	10.2	201.2	0.1
5	34335	53.2	10.6	202.0	0.4

Table 5.19 shows the summary data from the FEA performed on the motor bracket under five different mesh sizes. The table shows a critical von Mises stress of 58.8 MPa with a minimum FOS of 4.3 found for Mesh 4, and a maximum resultant displacement of 202 μm found in Mesh 5. The convergence analysis of Table 5.20 shows that the von Mises stress of 58.8 MPa has the minimum relative CE of 10.2%, while the maximum resultant displacement of 201 μm has a relative CE of 0.1%, both for Mesh 4.

5.5.3. Design and Construction Considerations

It was noted that the theoretical maximum traveling speed of 6 km/h was within the average range of the speeds (5 to 9 km/h) of the majority of tillage, cultivation, seeding, and harvesting operations (Hunt, 2001). Also, it was estimated from the video taken and the plots measured (Subsections 2.2.2 and 2.5.7) that the maximum average GPV's speed was 2.9 km/h while recording video. The canopy of the sorghum plants limited this speed value at the stage data collection with the GPV (Figures 2.7 and 2.14). However, at less dense canopy stages, the speed can be increased. When traveling from the farmstead to the field, the maximum speed of 6.2 km/h might not be fast enough, and if battery drainage is considered, operating time in the field will be reduced.

Since only one bracket model to hold the electric motor was designed of steel sheet metal, the FEA minimum FOS of 4.3 was appropriate for a member that is designed with some degree of uncertainty and that will operate under field conditions. All the other elements of the transmission systems were procured based on the requirements of the EGPV, and these are shown in the exploded view of the drawing of Figure J.24. The specific dimensions of the motor bracket are shown in Figure J.25 in a flat pattern view that was bent after cutting. The sheet metal bracket included internal cuts to be lighter, and the manufacturing processes of waterjet cutting and bending were performed by a local manufacturer (Second Generation Arc 'N Spark, Bryan, TX, USA).

5.6. Results of the EGPV Testing

Tests of functionality and reliability of the EGPV were performed in collaboration with Zikun Guo (Master of Engineering student in Biological and Agricultural Engineering at Texas A&M University), as part of his research project related to the development and testing of the electronics and control of an autonomous navigation system for the EGPV. During tests of the navigation system, the EGPV was tested about 20 times in the paved open space behind the Price Hobgood building at TAMU, during the tests, functionality of transmission system and structure worked according to the intended design. Once the previously described tests were performed, the EGPV was taken out to the field at the TAMU Farm. During nearly 5 field tests, the machine was able to navigate and turn with the specifics described in the following Subsection.

5.6.1. Turning Radius

Results of turning radius in the field was measured to be 3.0 m, under the controlling navigation system, and the mechanical capabilities of the driving wheels and driven casters. Skipping a working width of four furrows, this turning radius value was considered appropriate for the requirement of 3.05 m to enter a set of four furrows of 101.6 cm of separation between them, and higher as compared to the requirement of 2.29 m to enter a similar set of furrows of 76.2 cm of separation between them. Even though the minimum turning radius to enter in a closed turn to the next headland was not fulfilled for furrow offset of 76.2 cm, the machine and the controlling system still could be programmed to turn with a wider radius, occupying more space after a headland, or to maneuver by turning gradually, going forward and backward as needed until entering the next set of furrows. Another potential solution is incorporating a four-wheel drive system to use differential drive, as in the original design. The wheels of one side rotating forward while the wheels of the opposite side spinning backward, could make the vehicle to rotate on its own vertical axis.

6. CONCLUSIONS

6.1. RGB and Depth Camera System

A first semiautomated stalk thickness estimation system was developed for the controlled conditions of a greenhouse. The system consisted of a 3D camera with an RGB sensor and a time-of-flight (ToF) sensor that recorded images in a computer to be later processed and analyzed. The classification algorithms were supervised methods of minimum distance and *k*-means, with two methods of stalk-edge identification by the user. Of the four methods, the most accurate was *k*-means “single-window” (KMS) with a coefficient of determination, R^2 = 0.70, accounting for a 70% of the variability of the caliper measurements. Individual stalk estimates were found to have a mean bias of 1.32 mm relative to the average caliper measurement of 27.81 mm, and the 95% confidence interval was 29.14±6.54 mm. Variety A had a mean value estimated with the KMS of 30.82 mm, with a mean bias of 1.41 mm relative to the mean caliper measurement of 29.41 mm; while variety B was estimated with a mean of 27.45 mm, with a bias of 1.24 mm relative to the mean caliper value of 26.21 mm. The 95% confidence intervals were 30.82±5.96 mm for variety A and 27.46±7.98 mm for variety B.

For a sorghum breeder, the KMS estimations can be used as the basis to discriminate varieties that do not present thick stalks and identify those with higher potential. In this study variety A was found to be thicker than variety B, for the KMS method and for the caliper measurements.

6.1.1. Limitations

The imaging system as developed had some limitations. It required potted plants to be manually placed in an isolation chamber, and the camera was triggered by hand. The two image classification methods are supervised, requiring training sampling from the user's knowledge, and the measurement location is identified by the user. The ToF camera requires that the direct sunlight does not interfere with the sensor, potentially causing erroneous images.

6.1.2. Recommendations

Some plants in their early stages (6^{th} and 7^{th} week) presented leaves at their stalk base, occluding the stalk. Thus, if understanding growth patterns is desired, it is preferable to start recording images once the stalks are clear and well defined (by roughly the 8^{th} week). However, if biomass content is to be measured, the measurements could be made once prior to harvesting, when occluding leaves is unlikely to be a problem.

When using the ToF camera, times and viewing angles at which sunlight or lamps can interfere with the infrared sensor should be avoided.

6.1.3. Future Work

Future research should involve implementing double-window image classification algorithms for RGB images and/or integrating the depth infrared band with the RGB bands to get a four-band image. Doing so would provide additional important information for classification with supervised and unsupervised algorithms. Additionally, as mentioned in

Jiang and Li (2020), state-of-the-art deep convolutional neural networks could be used to recognize stalks automatically, avoiding the need for a user to select where to take the measurements.

The work on stereo vision reported in this document showed it to be accurate and to not require an isolation chamber, which potentially makes the stereo camera a convenient option to perform stalk thickness estimations for greenhouse conditions as well.

A fully automated system would require research and implementation of other image recognition algorithms, such as artificial intelligence for the identification of stalks and their measuring points in order to avoid having the user pinpoint them manually.

6.2. Stereo Vision System

A second semiautomated stalk thickness estimation system was developed with a stereo camera mounted on a ground phenotyping vehicle (GPV), with an on-board computer to record video. The video was then processed to compute depth maps and estimate the real *xyz*-coordinate system components for each pixel of an image. The data from stalk thickness estimations with the stereo vision system had a coefficient of determination, R^2 = 0.81, accounting for 81% of the variability in the caliper data. Individual stalk estimates were found to have a mean bias of 0.98 mm, relative to the average caliper measurements (25.36 mm), and a 95% confidence interval of 24.34±3.74 mm. The stereo imaging system had better accuracy than the RGB and ToF system presented; thus, the stereo system also can help a breeder in stalk thickness estimation of sorghum plants as a tool to discriminate the cultivars with thinner stalks.

For the conditions of the experiments, the stereo vision system presented time-saving advantages over the RGB system since it did not require (1) an isolation chamber for individual pots, (2) moving pots manually to the chamber, and (3) triggering the camera manually. Required operations with the RGB system resulted in measurements on around a plant per minute, whereas field operations with the stereo system were much faster. A noticeable overall phenotyping time advantage exists with the stereo vision system mounted on the GPV, which could travel at 2.9 km/h with a corresponding rate of 115 tagged plants per minute, and an estimated potential to record more than 230 plants per minute.

Additionally, the RGB system required image classification algorithms to differentiate plants and background in the scene, while the stereo images need the user to only verify that the pixels selected to measure the stalk thickness were close to the distance between the stereo camera and the plants (38 cm) for both measuring points of a stalk.

6.2.1. Limitations

The stereo imaging system must be mounted on a GPV, and a high clearance vehicle is required to work in tall crop plants like sorghum. A significant disadvantage of this system is that the videos recorded occupy a large amount of computer storage. For example, recording 1:46 minutes at 15 fps with a resolution of 752 × 430 pixels required 1.2 GB of memory, for a total of 1,590 images. Another major limitation is that the user (breeder) must select two points manually with the mouse to compute the stalk thickness in each image.

6.2.2. Recommendations

Since the stereo system requires a computer for recording and storage, there is a need to provide a place in the GPV to carry it. Also, the computer should have a large storage drive (approximately 185 GB per hectare of sorghum with a furrow spacing of 76.2 cm and at a driving speed of 2.3 km/h) on it due to the memory required to record a video or a set of videos. This storage space would provide for approximately 4.4 hours of video at 15 fps with a resolution of 752 × 430 pixels.

When selecting the points from disparity maps, a convenient method to reduce the likelihood of selecting an erroneous depth value would be to take the average or median of the neighboring pixels of those selected. For example, if one of the pixel at a point selected with the mouse cursor will have eight contiguous neighbors in a square window of 3 by 3 pixels. Similarly, the average or median of a 5 by 5, 7 by 7, or larger window could be considered.

6.2.3. Future Work

An RGB stereo camera system to record color stereo images and combine depth images with color should be considered to better differentiate plants from background. Create a fully automated system that can search for the edges of the stalks based on depth changes withing a range of depth values, or also with the potential implementation of artificial intelligence methods like deep convolutional neural networks (Jiang and Li, 2020) for the identification of stalks and their measuring points in order to eliminate the need for a user to pinpoint them manually.

As explained at the end of Subsection 2.5.8, from a 3D scene of stereo vision, leaf angle can be computed, opening the option to use the system as a tool to estimate plant leaf angle, a trait that influence the amount of solar radiation that plants receive. Thus, an experiment should be conducted to compare the stereo vision system against ground truth data and estimate the system accuracy.

6.3. Electric Ground Phenotyping Vehicle (EGPV)

The EGPV was developed as a high-clearance electrical mobile platform to carry sensors to obtain information on plants that grow up to 3.15-m tall (Figure 4.1), fulfilling the requirement to clear mature sorghum or corn plants planted in offset furrows of 76.2 cm or 101.6 cm. The trusses and chassis structures were designed with square tubing that can be used as attachments for camera sensors as those used in the imaging systems of Part I (see drawing specifications on Appendices J.3 and J.4). The designed EGPV can carry sensors and cameras on its structure to gather data and images on stalk thickness from several angles. Ultrasonic sensors to measure plant height, vegetation indices, canopy cover, etc. can be placed on the top structure as shown in Figure 4.1.

The design factor of safety was set to be greater than 4.0, corresponding to the “design of static structures or machine elements under dynamic loading with uncertainty about some combination of loads, material properties, stress analysis, or the environment”

(Mott, 2004). Thus, the FEA performed on the critical components was satisfied once the factor of safety was around 4.0. Exceptions to the expectation of FOS greater than or equal to 4.0 were the case of the swing arm of the suspension system, which had a FOS of 3.9 (see Section 5.2.5). However, according to Mott (2004), a design factor between 2.5 and 4.0 is still appropriate for normal operation conditions of the components. Additionally, these suspension components were simulated to be rigidly attached to ground, but in the reality the swing arms with rubber bushings would absorb part of the impact, increasing the FOS.

6.3.1. Limitations

The EGPV was first conceived as a 4WD system, but it required an expedited modification for field testing. The problem was assumed to be a motor-controller synchronization that caused two motors of the left side (or the right side) to oppose to each other and lock up, stopping the vehicle. The new settings were a rear wheel drive and caster wheels in the front with a turning radius of 3 m, which will require the EGPV to maneuver at the end of the headland to enter the next four contiguous furrows that require 152.4 cm or 203.2 cm of turning radius. The caster wheel supports were fabricated based on experience, but no FEA was performed for these components.

6.3.2. Recommendations

Guards should be added for the drive shafts and guides or guards to avoid damaging plants when the vehicle enters the crop, especially for the planting settings of 76-cm furrows.

6.3.3. Future Work

The weight to power ratio of the machine should be reduced by selecting smaller gearboxes or batteries that allow an overall lighter weight structure. Also, a narrower chassis should be design and constructed such that interference with plants is minimized to avoid plant damage.

An onboard location to carry a computer (laptop) should be considered in order to store images of the plants. This location has to be able to protect the computer form physical damage, dust, moisture, and heat.

Both imaging systems, the RGB system with image classification and the stereo vision system, as well as the electric ground phenotyping vehicle (EGPV), have been part of a larger project for sorghum and maize high-throughput phenotyping that has the objective of phenotyping a large quantity of plants, helping breeders to increase biomass by detecting the plant genotypes with wider stalks.

REFERENCES

Atefi, A.; Ge, Y.; Pitla, S.; Schnable, J. (2020). Robotic Detection and Grasp of Maize and Sorghum: Stem Measurement with Contact. *Robotics* (9)58, 1-14.

Andrade-Sanchez, P.; Gore, M. A.; Heun, J. T.; Thorp, K. R.; Carmo-Silva, A. E.; French, A. N.; White, J. W. (2014). Development and evaluation of a field-based high-throughput phenotyping platform. *Functional Plant Biology*, 41, 68-79.

AnnRose, J.; Seldev, C. C. (2014). Performance analysis of minimum distance classifier and clustering algorithm in CBIR. *Applied Mechanics & Materials*, (626), 14-19.

Bai, G.; Ge, Y.; Hussain, W; Baenziger, P. S.; Graef, G. (2016). A multi-sensor system for high throughput field phenotyping in soybean and wheat breeding. *Computers and Electronics in Agriculture*, (128), 181–192.

Bai, G.; Ge, Y.; Scoby, D.; Leavitt, B.; Stoerger, V.; Kirchgessner, N.; Irmak, S.; Graef, G.; Schnable, J.; Awada, T. (2019). NU-Spidercam: A large-scale, cable-driven, integrated sensing and robotic system for advanced phenotyping, remote sensing, and agronomic research. *Computers and Electronics in Agriculture*, 160, 71-81.

Barker III, J.; Zhang, N.; Sharon, J.; Steeves, R.; Wang, X.; Wei, Y.; Poland, J. (2016, February). Development of a field-based high-throughput mobile phenotyping platform. *Computers & Electronics in Agriculture*, 122, 74-85.

Batz, J.; Méndez-Dorado, M. A.; Thomasson J. A. Imaging for High-Throughput Phenotyping in Energy Sorghum. MDPI: *Journal of Imaging*, 2(1), 1–12, 2016.

Bedford, A.; Fowler, W. L. (2005). *Engineering Mechanics: Statics & Dynamics* (Fourth ed.). Pearson/Prentice Hall, Upper Saddle River, New Jersey, U.S.A.

Beer, F. P.; Jhonston E. R.; DeWolf J. T. (2003). *Mechanics of Materials* (Fourth ed.). McGraw-Hill, New York, U.S.A.

Bortolamedi, M. (2015, November). Accounting for hidden energy dependency: The impact of energy embodied in traded goods on cross-country energy security assessments. *Energy*, 93, 1361-1372.

Brase, T. A. (2006). *Precision Agriculture*. Thomson Delmar Learning, Clifton Park, New York.

Budynas, Richard G. (2015). *Shigley's Mechanical Engineering Design* (8th ed.). New York, NY: McGraw- Hill.

Busemeyer, L.; Mentrup, D.; Moller, K.; Wunder, E.; Alheit, K.; Hahn, V.; Ruckelshausen, A. (2013, February). Breedvision—a multi-sensor platform for non-destructive field-based phenotyping in plant breeding. *Sensors*, 13(3), 2830-2847.

CACYSSF (Committee on Assessing Crop Yield-Site-Specific Farming, Information Systems, and Research Opportunities). Board on Agriculture & National Research Council. (1997). *Precision agriculture in the 21st century: geospatial and information technologies in crop management*. National Academy Press, Washington, D.C.

Campbell, James B. and Wynne, Randolph H. *Introduction to Remote Sensing*, Fifth Edition, Guilford, 2011.

Chapman, S. C.; Chakraborty, S.; Dreccer, M. F.; Howden, S. M. (2012, May). Plant adaptation to climate change—opportunities and priorities in breeding. *Crop and Pasture Science*, 63(3), 251-268.

Cline, D. *Statistical Analysis; STAT 601 Class Notes*; Texas A&M University: College Station, TX, USA, 2015.

Cobb, J. N.; DeClerck, G.; Greenberg, A.; Clark, R.; McCouch, S. (2013, March). Next-generation phenotyping: requirements and strategies for enhancing our understanding of genotype—phenotype relationships and its relevance to crop improvement. *Theoretical and Applied Genetics*, 126(4), 867-887.

Code Laboratories Inc. (2018). DUO MC ultra-compact camera (photograph). Henderson, Nevada, USA. Available online: https://duo3d.com/product/duo-mc-lv1 (accessed on 16 November 2020).

Comar, A.; Burger, P.; De Solan, B.; Baret, F.; Daumard, F.; Hanocq, J.F. (2012, August). A semi-automatic system for high throughput phenotyping wheat cultivars in-field conditions: description and first results. *Functional Plant Biology*, 39(11), 914-924.

Constant, K.; Nourry, C.; Seegmuller, T. (2014). Population growth in polluting industrialization. *Resource and Energy Economics*, 36(1), 229-247.

Corke, P. *Robotics, Vision and Control: Fundamental Algorithms in MATLAB*; Springer Science & Business Media: Berlin, Germany, 2011; Volume 73.

Crain, J. L.; Wei, Y.; Barker III, J.; Thompson, S. M.; Alderman, P. D.; Reynolds, M.; Poland, J. (2016, May). Development and deployment of a portable field phenotyping platform. *Crop Science*, 56(3), 965-975.

Creative Technology Ltd. (2020) Creative Senz3D web camera, product details and photo. Milpitas, California, USA. Available online: https://support.creative.com/Products/ProductDetails.aspx (accessed on 16 November 2020).

Epting, R. (Biological & Agricultural Engineering, Texas A&M University, College Station, TX, USA) Suspension system design. Personal communication, 2016.

Furbank, R. T.; Tester, M. (2011, December). Phenomics—technologies to relieve the phenotyping bottleneck. *Trends in Plant Science*, 16(12), 635-644.

Gerland, P.; Raftery, A. E.; Sevcikova, H.; Li, N.; Gu, D.; Spoorenberg, T.; ... Wilmoth, J. (2014, October 10th). World population stabilization unlikely this century. *Science*, 346(6206), 234-237.

Ghimire, S.; Wang, H. Classification of image pixels based on minimum distance and hypothesis testing. *Comput. Stat. Data Anal.* 2012, *56*, 2273–2287.

Golden Motor Technology Co., Ltd. (2016). 5-kW BLDC electric motor, controller and wiring diagram (pictures and specs). Changzhou, Jiangsu, China. Available online: https://www.goldenmotor.com/ (accessed on 17 November 2020).

Hamilton Caster (2020). Pneumatic Casters 7000 Series, Cush-N-Aire Casters. Hamilton Ohio, USA, Available online: https://www.hamiltoncaster.com/Casters/Pneumatic-Semi-Solid-Pneumatic-/Pneumatic-Casters/Pneumatic-Casters-7000-Series (accessed on 18 November 2020).

Hayashi, A.; Akimoto, K.; Tomoda, T.; Kii, M. (2013). Global evaluation of the effects of agriculture and water management adaptations on the water-stressed population. *Mitigation & Adaptation Strategies for Global Change*, 18(5), 591-618.

Heiberger, R. M.; Holland B. Statistics Concepts in *Statistical Analysis and Data Display. An Intermediate Course with Examples in R*, 2nd ed.; DeVeaux, R.; Fienberg S. E.; Olkin, I., Eds.; Springer Science & Business Media: New York, USA, 2015; pp. 29-84.

Hibbeler, R. C. (2004) *Engineering Mechanics, Statics*, tenth edition, Pearson, Prentice Hall, Upper Saddle River, New Jersey, U.S.A.

Hibbeler, R. C. (2014) *Mechanics of Materials*, nineth edition, Pearson, Prentice Hall, Upper Saddle River, New Jersey, U.S.A.

Hunt, Donnell (2001). *Farm Power and Machinery Management* (10th ed.). Long Grove, IL: Waveland Press, Inc.

Jiang, Y.; Li, C. (2020). Convolutional Neural Networks for Image-Based High-

Throughput Plant Phenotyping: A Review. *Plant Phenomics*, (2020), 1-22.

Johannsen, W. (1911, March). The genotype conception of heredity. *The American Naturalist*, 45(531), 129-159.

Kawasaki Motors Corp. (2020). Shock absorber front green, model 45014-Y004-966, for Brute Force 300, model year 2016. Santa Ana, California, USA. Available online: https://www.kawasaki.com/en-us/shop/vehicle-accessories/atv/kvf300cgf (accessed on 17 November 2020).

Kurowski, P. M. (2004). *Finite element analysis for design engineers*. SAE International, Warrendale, PA, U.S.A.

Laihanen, M.; Karhunen, A.; Ranta, T. (2016). The role of local renewable energy sources in regional energy production: The case of southeast Finland. *International Journal of Energy & Environment*, 7(1), 89-96.

Lan, Y.; Zhang, H.; Lacey, R.; Hoffmann, W. C.; Wu, W. (2009, April). Development of an integrated sensor and instrumentation system for measuring crop conditions. *CIGR ejournal*, 11, 1-16.

Lee, H.-H. (2014). *Mechanics of materials labs with Solidworks simulation 2014*. Huei-Huang Lee. Mission, KS: SDC Publications.

Li, L. (2015). Energy security and energy risk management. *Journal of International Affairs*, 69(1), 86-97.

Maimaitijiang, M.; Sagan, V.; Erkbol, H.; Adrian, J.; Newcomb, M.; LeBauer, D.; Pauli, D.; Shakoor, N.; Mockler, T. C. (2020). UAV-based sorghum growth monitoring: a comparative analysis of lidar and photogrammetry. Remote Sensing and Spatial Information Sciences, *2020 XXIV ISPRS Congress*, 3, 489-497.

Malambo, L.; Popescu, S. C.; Murray, S. C.; Putman, E.; Pugh, N. A.; Horne, D. W.; Richardson, G.; Sheridan, R.; Rooney, W. L.; Avant, R.; Vidrine, M.; McCutchen, B.; Baltensperger, D.; Bishop, M. (2018). Multitemporal field-based plant height estimation using 3D point clouds generated from small unmanned aerial systems high-resolution imagery. *Int J Appl Earth Obs Geoinformation*, 64, 31–42.

McCarthy, C.; Hancock, N.; Raine, S. (2010). Apparatus and infield evaluations of a prototype machine vision system for cotton plant internode length measurement. *The Journal of Cotton Science*, 14(4), 221-232.

Mei, X.; Feng, Z.; He, R.; Gao, Y.; Dai, Y. (2015, July). Further understanding of the food safety problem. *Asian Agricultural Research*, 7(7), 81-84.

Milliken, W. F.; Milliken, D. L. (1995). *Race car vehicle dynamics*. SAE International, Warrendale, PA, U.S.A.

Montes, J. M.; Melchinger, A. E.; Reif, J. C. (2007, August). Novel throughput phenotyping platforms in plant genetic studies. *Trends in Plant Science*, 12(10), 433-436.

Montes, J. M.; Technow, F.; Dhillon, B. S.; Mauch, F.; Melchinger, A. E. (2011). High-throughput non-destructive biomass determination during early plant development in maize under field conditions. *Field Crops Research*, 121(2), 268-273.

Mott, Robert. L. (2004.) *Machine Elements in Mechanical Design* (4th ed.). Upper Saddle River, NJ: Pearson-Prentice Hall.

Mullet, J.; Morishige, D.; McCormick, R.; Truong, S.; Hilley, J.; McKinley B.; Anderson, R.; Olson, S. N.; Rooney, W. (2014) Energy Sorghum—a genetic model for the design of C4 grass bioenergy crops. *Journal of Experimental Botany*, Volume 65, Number 13, 3479–3489. doi:10.1093/jxb/eru229

Munns, R.; James, R. A.; Sirault, X. R. R.; Furbank, R. T.; Jones, H. G. (2010, July). New phenotyping methods for screening wheat and barley for beneficial responses to water deficit. *Journal of Experimental Botany*, 61(13), 3499-3507.

Murphy, D.J.; Beppler, D.C. and Sommer, H.J. (1985). Tractor stability indicator. *Applied Ergonomics*, 16(3), 187-191.

Nature. (2010, July, 29th). How to feed a hungry world. *Nature*, 466(7306), 531-532.

Neter, J.; Kutner, M.H.; Nachtsheim, C.J.; Wasserman, W. *Applied Linear Statistical Models*, 4th ed.; McGraw-Hill: Boston, MA, USA, 1996.

Norton, R. L. (2014). *Machine design: an integrated approach* (Fifth ed.). Prentice Hall, Boston, USA.

Otsuka, K. (2013, November). Food insecurity, income inequality, and the changing comparative advantage in world agriculture. *Agricultural Economics*, 44, 7-18.

Partzilla (2020). Suzuki rubber bushing, part number 09319-10055. Albany, Georgia, USA. Available online: https://www.partzilla.com/product/suzuki/09319-10055 (accessed on 17 November 2020).

Passioura, J. B. (2012, September). Phenotyping for drought tolerance in grain crops: when is it useful to breeders? *Functional Plant Biology*, 39, 851- 859.

Poorter, H.; Fiorani, F.; Pieruschka, R.; Wojciechowski, T.; van der Putten, W. H.; Kleyer, M.; Schurr, U.; Postma, J. (2016). Pampered inside, pestered outside? Differences and similarities between plants growing in controlled conditions and in the field. *New Phytologist*, 212, 838–855.

Preda, I. (2016, 01/13). Model based algorithm for the study of the vehicle suspension. *Applied Mechanics & Materials, 823*, 247-252.

Roitsch, T.; Cabrera-Bosquet, L.; Fournier, A.; Ghamkhar, K.; Jiménez-Berni, J.; Pinto, F.; Oberg, E. S. (2019). Review: New sensors and data-driven approaches—A path to next generation phenomics. *Plant Science*, 282, 2–10.

Rooney, W. L.; Blumenthal, J.; Bean, B.; Mullet, J. E. (2007, July). Designing sorghum as a dedicated bioenergy feedstock. *Biofuels, Bioproducts & Biorefining*, 1(2), 147-157.

Rooney, W.L. (Soil and Crop Science Professor, Texas A&M University, College Station, TX, USA) Stalk diameter measure location in energy sorghum. Personal communication, 2015.

Sabater, N, Morel, J.-M.; Almansa, A. (2011). How Accurate Can Block Matches Be in Stereo Vision? *Society for Industrial and Applied Mathematics,* Vol. 4, No. 1, pp. 472–500.

Salas Fernandez, M. G.; Bao, Y.; Tang, L.; Schnable, P. S. (2017). A High-Throughput, Field-Based Phenotyping Technology for Tall Biomass Crops. *Plant Physiology*, 174, 2008-2022.

Shane, M.; Teigen, L.; Gehlhar, M.; Roe, T. (2000, June). Economic growth and world food insecurity: a parametric approach. *Food Policy,* 25 (3), 297-315.

Shetty, P. (2015, August 10th). From food security to food and nutrition security: role of agriculture and farming systems for nutrition. *Current Science*, 109(3), 456-461.

Svensgaard, J.; Roitsch, T.; Christensen, S. (2014, July, 1st). Development of a mobile multispectral imaging platform for precise field phenotyping. *Agronomy*, 4(3), 322-336.

Tâtar, A.; Popescu, G. (2015, December). Primary energy resources. Annals of Constantin Brâncuşi University of Târgu Jiu. *Engineering Series* (4), 56-58.

United Nations, Department of Economic and Social Affairs, Population Division (2019). World Population Prospects 2019, Volume II: *Demographic Profiles* (ST/ESA/SER.A/427). Available online: https://population.un.org/wpp/Publications/Files/WPP2019_Volume-II-Demographic-Profiles.pdf (accessed on 17 May 2020).

USDA, NSF. (2011, March-April). Phenomics: Genotype to phenotype. A report of the phenomics workshop sponsored by the USDA and NSF (Tech. Rep.). USDA-NFS.

Valmont Industries, Inc. (2012). VS Irrigation Gearbox (picture), Valley, Nebraska, USA. Available online: http://az276019.vo.msecnd.net/valmontstaging/valleyirrigation-com---usa---brochures/valleyirrigation_drivetrain.pdf?sfvrsn=2 (accessed on 16 November 2020).

Virlet, N.; Sabermanesh, K.; Sadeghi-Tehran, P.; Hawkesford, M. J. (2017). Field Scanalyzer: An automated robotic field phenotyping platform for detailed crop monitoring. *Functional Plant Biology*, 44, 143-453.

von Mogel, K. H. (2013, March). Taking the phenomics revolution into the field. *CSA News*, 4-10.

White, J. W.; Andrade-Sanchez, P.; Gore, M. A.; Bronson, K. F.; Coffelt, T. A.; Conley, M. M.; Wang, G. (2012). Field-based phenomics for plant genetics research. *Field Crops Research*, 133, 101-112.

White, J. W.; Conley, M. M. (2013, June, 4th). A flexible, low-cost cart for proximal sensing. *Crop Science*, 53, 1646-1649.

Xianga, L.; Bao, Y.; Tang, L.; Ortiz, D.; Salas-Fernandez, M. G. (2019). Automated morphological traits extraction for sorghum plants via 3D point cloud data analysis. *Computers and Electronics in Agriculture*, 162, 951-961.

Yang, W.; Li, Y.; Fang, Z.; He, K. (2014, 07/23). Simulation and analysis of ride comfort of 4wd electric vehicle. *Applied Mechanics & Materials* (574), 287-291.

Yuan, J. S.; Tiller, K. H.; Al-Ahmad, H.; Stewart, N. R.; Stewart Jr., C. N. (2008, July). Plants to power: bioenergy to fuel the future. *Trends in Plant Science*, 13(8), 421-429.

Wildcat Manufacturing (2015). Ground Phenotyping Vehicle photographed at their facilities. Tahoka, Texas, USA. Website available online: https://www.wildcatmfg.net/ (accessed on 16 November 2020).

APPENDIX A

EXAMPLE OF MINIMUM DISTANCE CLASSIFICATION

A.1. Simplified Example

This appendix presents a simplified example of an RGB minimum distance classification using only two samples with three points each in RB coordinates, excluding green color (G). The simplification explains how an image pixel would be classified by the algorithm. The values are supposed to range from 0 to 255 as in an 8-bit image.

Table A.1. Sample points for the two example classes, with their means and standard deviations. The maximum values of the standard deviations are marked in bold.

Point	**Red Sample**		**Blue Sample**	
	R	**B**	**R**	**B**
R1/B1	100	110	75	135
R2/B2	140	90	30	140
R3/B3	110	70	40	100
Mean	116.7	90.0	48.3	125.0
STD	**17.0**	16.3	**19.3**	17.8

On Table A.1, two samples of three points with their cartesian RB coordinates are listed, and their means and standard deviation were computed by column. The two classes were defined as Red and Blue since one is more like the red color, and the other to the blue color. Graphically, in Figure A.1, the sample points are plotted with asterisks in red or blue, according to their sample class. The mean (center) of each class was identified with a square point and a label. Then, the mean of the Red sample, expressed with coordinates is R (116, 90), while the mean of Blue is B (48, 125).

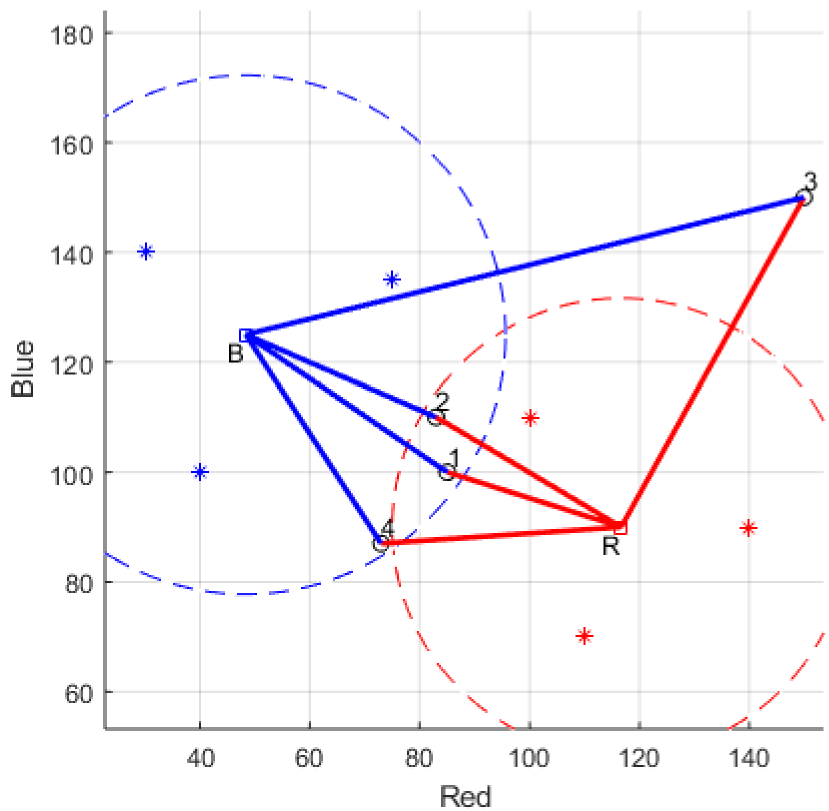

Figure A.1. Distance lines from each point to be classified to each sample mean.

Now, if the four points (pixels) of Table A.2 were to be classified, their corresponding Euclidian distances from each to each center class should be computed and then compared to find the minimum distance and classified to the corresponding class. However, if the minimum distance of a classifying point (pixel) is larger than a stablished threshold, then that point will be classified as unknown. In this minimum distance classification, a threshold of two times the maximum value of the standard deviations was selected and plotted in Figure A.1 as a circle for each class.

In Figure A.1, it is easy to see that points 1 and 2 fall inside the threshold of both categories, but point 1 is closer to the red center, while point 2 is closer to the blue center. In the case of point 3, the minimum distance was registered to be to the red center, but since it does not fall within the threshold, it is classified as "Unknown". For point 4, it is computed that it is closer to the red center, but it does not fall into the red threshold. Thus, point 4 was classified Blue since it falls within the blue threshold.

Table A.2 Four points to be classified with their computed distances to each cluster center (mean) and their classification label. Minimum distances are shown in bold font.

Point	R	B	Distance to Red	Distance to Blue	Classification
1	85	100	**33.2**	44.4	Red
2	83	110	39.2	**37.8**	Blue
3	150	150	**68.6**	104.7	Unknown
4	73	87	**43.8**	45.3	Blue

A.2. Script of the Example

```
%MINIMUM_DISTANCE_EXAMPLE  Plot sample points of two classes and points to
%   classify.
%
%   Given two sets of sample points, distances from point P to the means of
%   sample are computed. The script plots the sample points, the mean of
%   each sample, the points "to be classified", and straight lines from the
%   classification points to each sample mean. Additionally, a threshold
%   for each class is defined as 2 times the maximum value of the standard
%   deviation of the sample class.
%   The classes S1 and S2 are exemplified by three asterisk points each.
%   The mean coordinates of each class are plotted in a square. The
%   thresholds are represented by circles of radii = thresholds. The points
%   to classify are represented in small black circles, and the distance
%   lines are plotted form each point to each mean.
%
% Script created by Mario Mendez. 10 May 2019.

% Red sample coordinates
SR = [100, 110;
      140, 90;
      110, 70];
% Statistics of the red sample
R_mean = mean(SR);
R_std = std(SR);

% Blue sample coordinates
SB = [75, 135;
```

```
      30, 140;
      40, 100];

% Statistics of the blue sample
B_mean = mean(SB);
B_std = std(SB);

% Classification
P = [85 100;
     83 110
     150 150;
     73 87];

% Distances form point(i) to R_mean and B_mean (matrix of R B columns)
m = length(P);
Dist = zeros(m,2);
for i = 1:m
    Dist(i,1) = norm(R_mean - P(i,:)); % Distance of point(i) to red mean
    Dist(i,2) = norm(B_mean - P(i,:)); % Distance of point(i) to blue mean
end

clf
% Plot of points (*) and means (square)
plot(SR(:,1),SR(:,2),'r*'), hold on
plot(R_mean(1),R_mean(2),'rs'), hold on
plot(SB(:,1),SB(:,2),'b*'), hold on
plot(B_mean(1),B_mean(2),'bs'), hold on
text([R_mean(1); B_mean(1)], [R_mean(2); B_mean(2)],{'R' 'B'},...
    'VerticalAlignment','top','HorizontalAlignment','right')

% Plot thresholds circles
viscircles(R_mean, 2*max(R_std), 'Color', 'r', 'LineWidth', 0.5,...
    'LineStyle', '--'); hold on
viscircles(B_mean, 2*max(B_std), 'Color', 'b', 'LineWidth', 0.5,...
    'LineStyle', '--'); hold on

% Create labels in a string
labels = strings(1,m);
for i = 1:m
    labels(i) = mat2str(i);
end

% Plot points to classify
plot(P(:,1), P(:,2), 'ko'), hold on
text(P(:,1), P(:,2), labels, 'VerticalAlignment','bottom',...
    'HorizontalAlignment','left')

% Plot distance lines
for i = 1:m
    plot([P(i,1) R_mean(1)], [P(i,2) R_mean(2)], 'r-',...
        'LineWidth', 2), hold on % R Lines
    plot([P(i,1) B_mean(1)], [P(i,2) B_mean(2)], 'b-',...
        'LineWidth', 2), hold on % B Lines
end
axis([0 255 0 255]), grid on, box off
axis square
xlabel('Red')
ylabel('Blue')

D = floor(Dist)
```

APPENDIX B

MATLAB® SCRIPTS FOR THE VISION SYSTEMS

B.1. Plotting Individual Histograms of Image Samples

```
function [hSr, hSg, hSb] = histogram_sample(S,xrange,size,location,value)
%HISTOGRAM_SAMPLE  Plots the histograms of an RGB image sample.
%
%   HISTOGRAM_SAMPLE(S,XRANGE,SIZE,LOCATION,VALUE), where S in N-by-3
%   dimension is class sample of an image in RGB; XRANGE is the range of
%   the x-axis; SIZE is a scalar that indicated the number of bins; and
%   LOCATION and VALUE are strings that indicate where the plot legend will
%   be placed.
%
% Function created by Mario Mendez. 31 August 2015.

Means = mean(S);
sdev = std(S);

subplot(3,1,1)
hSr = histogram(S(:,1),size, 'FaceColor','r'); grid on, box off
xlim(xrange)
y_lim = get(gca,'ylim');
hold on
plot([Means(1) Means(1)],y_lim,'-k','LineWidth',2)
plot([Means(1)+sdev(1) Means(1)+sdev(1)], y_lim,'--k','LineWidth',2)
plot([Means(1)-sdev(1) Means(1)-sdev(1)], y_lim,'--k','LineWidth',2)
legend('Frequency','Mean','Std Dev (+)','Std Dev (-)',location,value)
xlabel('Red intensity')
ylabel('Frequency')

subplot(3,1,2)
hSg = histogram(S(:,2),size, 'FaceColor','g'); grid on, box off
xlim(xrange)
y_lim = get(gca,'ylim');
hold on
plot([Means(2) Means(2)],y_lim,'-k','LineWidth',2)
plot([Means(2)+sdev(2) Means(2)+sdev(2)], y_lim,'--k','LineWidth',2)
plot([Means(2)-sdev(2) Means(2)-sdev(2)], y_lim,'--k','LineWidth',2)
legend('Frequency','Mean','Std Dev (+)','Std Dev (-)',location,value)
xlabel('Green intensity')
ylabel('Frequency')

subplot(3,1,3)
hSb = histogram(S(:,3),size, 'FaceColor','b'); grid on, box off
xlim(xrange)
y_lim = get(gca,'ylim');
hold on
plot([Means(3) Means(3)],y_lim,'-k','LineWidth',2)
plot([Means(3)+sdev(3) Means(3)+sdev(3)], y_lim,'--k','LineWidth',2)
plot([Means(3)-sdev(3) Means(3)-sdev(3)], y_lim,'--k','LineWidth',2)
legend('Frequency','Mean','Std Dev (+)','Std Dev (-)',location,value)
xlabel('Blue intensity')
ylabel('Frequency')
end
```

B.2. Sampling for Minimum Distance

```
%SAMPLIG_ANALYSIS  Image Samplig Analysis for Minimum Distance.
%
%   Given an input image of sorghum plant taken in the greenhouse, the user
%   has to select three rectangles per class, for a total of four classes.
%   The samples of all four classes will be stored in the 'samples.mat',
%   along with their means in the file 'means.mat'. The maximum per class
%   of the RGB standard deviations is used and stored in 'thresh.mat' file
%   to be used in the Minimum Distance classification.
%
%   Script created by Mario Mendez. 2 August 2015.


s1 = sampling_rectangle(Im);
s2 = sampling_rectangle(Im);
s3 = sampling_rectangle(Im);
C1 = [s1;s2;s3];

s4 = sampling_rectangle(Im);
s5 = sampling_rectangle(Im);
s6 = sampling_rectangle(Im);
C2 = [s4;s5;s6];

s7 = sampling_rectangle(Im);
s8 = sampling_rectangle(Im);
s9 = sampling_rectangle(Im);
C3 = [s7;s8;s9];

s10 = sampling_rectangle(Im);
s11 = sampling_rectangle(Im);
s12 = sampling_rectangle(Im);
C4 = [s10;s11;s12];

save('samples.mat','C1','C2','C3','C4')
load('samples.mat')

m1 = mean(C1); % Mean of sample 1
m2 = mean(C2); % Mean of the green plant sample
m3 = mean(C3); % Mean of the yellow plant sample
m4 = mean(C4); % Mean of the white board sample
means = [m1; m2; m3; m4];
save('means.mat', 'means')
%csvwrite('means.csv', means)

std1 = std(C1);
std2 = std(C2);
std3 = std(C3);
std4 = std(C4);

t1 = max(std1);
t2 = max(std2);
t3 = max(std3);
t4 = max(std4);

thresh = [t1;t2;t3;t4];
save('thresh.mat','thresh')
%csvwrite('thresh.csv',thresh)

% plotting the samples for separability visualization
% 1e4 is for scaling the point units and show a "cluster" of pixels

figure
histogram_sample(C1,[0 1],33,'Location','NorthEast');
figure
histogram_sample(C2,[0 1],33,'Location','NorthWest');
```

```
figure
histogram_sample(C3,[0 1],33,'Location','NorthWest');
figure
histogram_sample(C4,[0 1],33,'Location','NorthWest');
```

B.3. Minimum Distance Classification

```
function ImClass = minimum_distance(ImInput,Means,thresh)
%MINIMUM_DISTANCE  Performs a minimum distance clssification on an image.
%
%   MINIMUM_DISTANCE(IMINPUT,MEANS,THRESH) for an RGB image, a matrix of N
%   means (3-by-N), and a vector of thresholds, one per class. This
%   function gives a gray scale image with values in (0,1]. If the minimum
%   distances is bigger than the corresponding threshold, the pixel value
%   to classify becomes a 0.
%
% Function created by Mario Mendez. 2 August 2015.

[m,n,~] = size(ImInput);
classNum = length(Means(:,1));
ImClass = zeros(m,n);
for i = 1:m
    for j = 1:n
        for t = 1:length(thresh)       % number of thresholds, 1/class
            minDist = thresh(t);       % variable thresholds
            for k = 1:classNum
                if norm(Means(k,:) - [ImInput(i,j,1) ImInput(i,j,2)...
                        ImInput(i,j,3)]) < minDist
                    minDist = norm(Means(k,:) - [ImInput(i,j,1)...
                        ImInput(i,j,2) ImInput(i,j,3)]);
                    ImClass(i,j) = k/classNum; % assign values in [0, 1]
                end
            end
        end
    end
end

end
```

B.4. Conversion Factor from Camera to Object

B.4.1. Script

```
%CONVERSION_FACTOR  Estimation of the conversion factor of depth distance.
%
%   Given a set of depth distances (cm) and a set of widths of the object
%   of interest (pixels), the script computes a linear regression model and
%   plots the original data. Regression previously done in Excel (by
%   November 2015).
%
%   Script created by Mario Mendez. 10 July 2017.

% Diameter of PVC pipe
d_p = 47.625; % (mm) (1.875 in)

% RGB Image Data
% distance to from camera to the PVC pipe
dis = [20, 30, 40 , 50, 60, 70, 80, 90]; % (cm)

% Number of pixels according to distance
pix = [230, 155, 117, 95, 80, 70, 61, 52];

% Conversion factor in mm/pixel
cf = d_p ./ pix;

% Linear regression
LM = fitlm(dis,cf)

% Linear model
m = 0.009813;
y1 = 0.0096558;
x = 0:100;
y = m * x + y1;

plot(dis,cf,'*'), hold on
plot(x,y), grid
xlabel('Distance from camera to object (cm)')
ylabel('Conversion factor (mm/pixel)')
```

B.4.2. Output

```
Linear regression model:
    y ~ 1 + x1

Estimated Coefficients:
                   Estimate        SE          tStat       pValue
                   _________    __________    _______    __________

    (Intercept)    0.0096558      0.012072    0.79983        0.4543
    x1              0.009813    0.00020262     48.431    5.1957e-09


Number of observations: 8, Error degrees of freedom: 6
Root Mean Squared Error: 0.0131
R-squared: 0.997, Adjusted R-Squared 0.997
F-statistic vs. constant model: 2.35e+03, p-value = 5.2e-09
```

B.5. Linear Regression for Depth Distances

B.5.1. Script

```
%DEPTHS_MANUAL_CAMERA  Linear regression of manual vs camera depth
%   measurements.
%
%   This script reads the distances between the camera and the sorghum
%   stalks of the greenhouse experiment. The script reads manual and IR
%   distances from the file 'distance_comparison.csv' and computed its
%   correlation.
%
%   Script created by Mario Mendez. 12 July 2017.

% Read the CSV file skipping the first row.
depths = csvread('distance_comparison.csv',1);

% Linear model all data
lm1 = fitlm(depths(:,2),depths(:,1))

x = 30:80;
y1 = -0.58747 + 0.91689 * x;

% Plots
figure(1)
plot(depths(:,2),depths(:,1),'*'), hold on
plot(x,y1), box off, grid on
h = xlabel('Depth Camera (cm)');
j = ylabel('Manual Measurements (cm)');

% Linear model no outliers
lm2 = fitlm(depths(1:36,4),depths(1:36,3))

y2 = -0.68192 + 0.90852 * x;

% Plots
figure(2)
plot(depths(1:46,4),depths(1:46,3),'*'), hold on
plot(x,y2), box off, grid on
h = xlabel('Depth Camera (cm)');
j = ylabel('Manual Measurements (cm)');
```

B.5.2. Output 1

```
Linear regression model:
    y ~ 1 + x1

Estimated Coefficients:
                   Estimate       SE        tStat       pValue
                   ________    ________    ________    __________

    (Intercept)    -0.58747      2.4209    -0.24266       0.80935
    x1              0.91689    0.050212       18.26    1.0428e-22


Number of observations: 48, Error degrees of freedom: 46
Root Mean Squared Error: 4.53
R-squared: 0.879, Adjusted R-Squared 0.876
F-statistic vs. constant model: 333, p-value = 1.04e-22
```

B.5.3. Output 2

```
Linear regression model:
    y ~ 1 + x1

Estimated Coefficients:
                   Estimate       SE        tStat       pValue
                   ________    ________    ________    __________

    (Intercept)    -0.68192       1.173    -0.58136       0.56484
    x1              0.90852    0.023173      39.206    6.8751e-30


Number of observations: 36, Error degrees of freedom: 34
Root Mean Squared Error: 1.97
R-squared: 0.978, Adjusted R-Squared 0.978
F-statistic vs. constant model: 1.54e+03, p-value = 6.88e-30
```

B.6. Statistical Analysis for Caliper vs KMS

B.6.1. Script

```
%CAL_KMS_NO_OUTLIERS Linear regression of manual vs k-means single-window
%   measurements.
%
%   This script reads the stalk thickness of CAL and KMS measurements
%   ('cal_kms.csv') for the greenhouse experiment. The script computes the
%   correlation of both variables. It plots histograms and residuals
%   scatterplots, to later transform the variables to fulfill normality, and
%   then compute the studentized residuals bigger than 2.0. Finally, it
%   plots the original data without outliers.
%
%   Script created by Mario Mendez. 6 September 2017.

% Read the CSV file skipping the first row.
thick = csvread('cal_kms_no_outliers.csv',1);

CAL = thick(:,1);
KMS = thick(:,2);

figure(1) % Plot CAL histogram
histfit(CAL), box off, grid on
xlabel('CAL (mm)')
ylabel('Counts')

figure(2) % Plot KMS histogram
histfit(KMS), box off, grid on
xlabel('KMS (mm)')
ylabel('Counts')

% Linear model of the original data
lm1 = fitlm(KMS,CAL)

x1 = 15:50;
y1 = 9.4461 + 0.65707 * x1;

% Scatter plot and linear regression of original data
figure(3)
plot(KMS,CAL,'*'), hold on
plot(x1,y1), box off, grid on
xlabel('KMS (mm)');
ylabel('CAL (mm)');

figure(4) % Plot residuals of first linear fit
plot(CAL, CAL - (9.4461 + 0.65707 * KMS),'*'), hold on
plot([15,50],[0,0]), box off, grid on
xlabel('CAL (mm)')
ylabel('Residuals (mm)')

figure(5) % Histogram of residuals of first linear fit
histfit(CAL - (9.4461 + 0.65707 * KMS)), box off, grid on
xlabel('Residuals (mm)')
ylabel('Counts')

figure(6) % Plot LOG(CAL) histogram
histfit(log(CAL)), box off, grid on
xlabel('Log CAL (mm)')
ylabel('Counts')

figure(7) % Plot LOG(KMS) histogram
histfit(log(KMS)), box off, grid on
xlabel('Log KMS (mm)')
ylabel('Counts')
```

```
% Linear regression of the Log-transformed data
lm2 = fitlm(log(KMS),log(CAL))

x2 = 2.6:0.2:4;
y2 = 1.0235 + 0.68621 * x2;

% Scatter plot and linear regression of the Log-transformed data
figure(8)
plot(log(KMS),log(CAL),'*'), hold on
plot(x2,y2), box off, grid on
xlabel('KMS (mm)');
ylabel('CAL (mm)');

figure(9) % Plot residuals of transformed linear fit
plot(CAL,log(CAL) - (1.0235 + 0.68621 * log(KMS)),'*'), hold on
plot([15,50],[0,0]), box off, grid on
xlabel('CAL (mm)')
ylabel('Residuals of the Transformed Data (mm)')

figure(10) % Histogram of residuals of transformed linear fit
histfit(log(CAL) - (1.0235 + 0.68621 * log(KMS))), box off, grid on
xlabel('Residuals of Transformed Data (mm)')
ylabel('Counts')

% Studentized residuals
st_r = studentized(log(CAL), 1.0235 + 0.68621 * log(KMS));

% Find outliers
outliers = find(abs(st_r) >= 2.0)'

% Add the erroneous plants
erroneous_plants = [10 11 12 13];

% Append outliers
outliers_extended = [erroneous_plants, outliers];

% Exclude outliers from the original data set
DATA = [CAL,KMS];
DATA(outliers_extended,:) = [];

% Rename CAL and KMS with no outliers
CAL2 = DATA(:,1);
KMS2 = DATA(:,2);

% Compute a linear regression of the new data set (no outliers)
lm3 = fitlm(KMS2,CAL2)

% Create new variables
x3 = 15:50;
y3 = 1.8801 + 0.90177 * x3;

figure(12) % Plot a scatterplot and a linear regression of CAL and KMA
plot(KMS2,CAL2,'*'), hold on
plot(x3,y3), box off, grid on
xlabel('KMS (mm)');
ylabel('CAL (mm)');

figure(13) % Plot residuals of transformed linear fit
plot(CAL2, CAL2 - KMS2,'*'), hold on
plot([15,45],[0,0]), box off, grid on
xlabel('CAL (mm)')
ylabel('Residuals (mm)')
```

B.6.2. Output 1

```
Linear regression model:
    y ~ 1 + x1

Estimated Coefficients:
                   Estimate      SE       tStat       pValue
                   ________    _______    ______    __________

    (Intercept)     9.4461      4.6788    2.0189      0.049344
    x1             0.65707     0.15377    4.2731    9.5921e-05


Number of observations: 48, Error degrees of freedom: 46
Root Mean Squared Error: 6.27
R-squared: 0.284, Adjusted R-Squared 0.269
F-statistic vs. constant model: 18.3, p-value = 9.59e-05
```

B.6.3. Output 2

```
Linear regression model:
    y ~ 1 + x1

Estimated Coefficients:
                   Estimate      SE       tStat       pValue
                   ________    _______    ______    __________

    (Intercept)     1.0235      0.4773    2.1443      0.037327
    x1             0.68621     0.14111    4.8628    1.3909e-05


Number of observations: 48, Error degrees of freedom: 46
Root Mean Squared Error: 0.197
R-squared: 0.34, Adjusted R-Squared 0.325
F-statistic vs. constant model: 23.6, p-value = 1.39e-05
```

B.6.4. Output 3

```
Linear regression model:
    y ~ 1 + x1

Estimated Coefficients:
                   Estimate       SE        tStat       pValue
                   ________    ________    ______    __________

    (Intercept)     3.4314       2.6592    1.2904       0.20471
    x1             0.83677     0.089603    9.3387    2.2071e-11


Number of observations: 40, Error degrees of freedom: 38
Root Mean Squared Error: 3.19
R-squared: 0.697,  Adjusted R-Squared 0.689
F-statistic vs. constant model: 87.2, p-value = 2.21e-11
```

B.7. Studentized Residuals

```
function t = studentized(Y1,Y2)
%STUDENTIZED   Computes the studentized error.
%
% Function written by Mario Mendez, 16 March 2017.

e = Y1 - Y2;

X = [ones(length(Y1),1), Y2];
H = X * inv(X'*X) * X';

t = zeros(length(Y1),1);
for i = 1:length(Y1)
    t(i) = e(i) / std(e) / sqrt(1-H(i,i));
end

end
```

B.8. Video Reader for Stereo Vision

```
%VIDEO_READER  Reads a recorded video.
%   This script uses the VIDEOREADER('filename') function to store a video
%   object containing the appropriate video formats that can be read by
%   MATLAB. Type 'help VIDEOREADER' to see more details.
%
%   Then, the video is stored in a structure data type for further
%   manipulation in MATLAB.
%
%   Requirements:
%   1) Computer Vision System Toolbox
%   2) Run 'video_reader.m'
%
%   Script Created by Mario A. Mendez. 30 November 2016.

% Original video files recorded (current uncommented):
% file = 'DUOCapture-05-08-2016-12-29-24-499.avi'; % Variety A
file = 'DUOCapture-05-08-2016-12-56-15-194.avi'; % Variety B
% file = 'DUOCapture-13-12-2016-11-03-34-361.avi'; % Office for angle

% Read the video and store it in a video object
vidObj = VideoReader(file);

% Extract and assign height and width of the video
H = vidObj.Height;
W = vidObj.Width;

% Create a structure data type of zeros
s = struct('cdata',zeros(H,W,'uint8'));

% Replace the zeros of the structure with pixel values
k = 1;
while hasFrame(vidObj)
    s(k).cdata = readFrame(vidObj);
    k = k+1;
end
```

B.9. World Coordinate System Mapping

```
function WC = wcsys(DM,f,POI)
%WCSYS   World coordinate system mapping.
%   WC = WCSYS(DM,F,POI) maps a set of points of interest (POI) into the
%   world coordinate system. Its inputs are a Depth Map (DM), the camera's
%   focal length (F), and the POI.
%
%   WC is an R-by-3 matrix, containing R XYZ points, expressed in the
%   world coordinate system. Each row of WC represents a point in the
%   "world".
%
%   POI is an R-by-2 matrix, containing a list of (u,v) = (x,y) image
%   points. Each row of POI represents a point in the left image in pixels.
%
%   DM is an M-by-N matrix containing the estimated depth values of a
%   disparity map. Its calculation is DM = B * F ./ disparityMap, where B
%   is the baseline in world units between two cameras in a stereo system.
%
%   F is a scalar value of the focal length, expressed in pixels.
%
%   Function created by Mario Mendez. 30 November 2016.

[m,n] = size(DM); % Depth Map matrix dimensions M-by-N.
[mp,~] = size(POI); % Depth Map matrix dimensions M-by-N.

cch = n/2;        % Camera horizontal center (pixels).
ccv = m/2;        % Camera vertical center (pixels).

%% World Coordinates
WC = zeros(mp,3);
for i = 1:mp
    WC(i,3) = DM(ceil(POI(i,2)),ceil(POI(i,1))); % Zi = DM(i,j) = DM(y,x)
    WC(i,1) = WC(i,3) * ( POI(i,1) - cch ) / f;  % Xi = Zi(xi - cch)/f
    WC(i,2) = WC(i,3) * ( POI(i,2) - ccv ) / f;  % Yi = Zi(yi - ccv)/f
end

end
```

B.10. Euclidean Distance

```
function d = euclidean(P1,P2)
%EUCLIDEAN   Euclidean distance between pairs of N-dimensional coordinates.
%   D = EUCLIDEAN(P1,P2) is the Euclidean distance between points P1 and
%   P2. P1 and P2 must have the same dimension and be of the form
%   [X1,X2,...,Xn] to get a scalar output. If P1 and P2 are matrices of
%   dimension M-by-N, then the output D is a M-by-1 column vector,
%   containing a set of distances.
%
%   Example:
%       P1 = [2 3 5;1 5 7];
%       P2 = [1 3 2;2 7 3];
%       d = euclidean(P1,P2)

%   Function created by Mario Mendez. 1 December 2016.

[m1,n1] = size(P1);
[m2,n2] = size(P2);

if m1 ~= m2 || n1 ~= n2
    error('Input arguments must have the same dimension.')
end

m = m2;
n = n1;

sq_diffs = zeros(1,n);
d = zeros(m,1);
for i = 1:m
    for j = 1:n
        sq_diffs(j) = ( P2(i,j) - P1(i,j) )^2;
    end
    d(i) = sqrt( sum(sq_diffs) );
end

end
```

B.11. Display Diameter on the Left Image

```
function IM = imagediam(frame_number,s,W,p)
%IMAGEDIAM   Image diameter, or Image length.
%   IM=IMAGEDIAM(FRAME_NUMBER,S,W,P) computes the Euclidian distance of
%   two image points, but the distance is computed from the converted image
%   points into world coordinates, expressed in the left image of the frame
%   of the a stereo video stored in a structure data type S, at a specific
%   FRAME_NUMBER. Then, the results are shown in an image, and stored in
%   the variable IM.
%
%   The points P are stored in a 2-by-2 matrix, where the first column
%   contains the X coordinates and the second column contains the Y
%   coordinates. So the first row is the first point and the second row has
%   the second point; both in pixel coordinates.
%
%   The width (pixels) of the stereo video is stored in a variable W at the
%   time of running 'video_reader.m'.
%
%   Requirements:
%   1) Computer Vision System Toolbox; 2) Run 'video_reader.m'
%
%   Function created by Mario A. Mendez, February 2017.

% Parameters
camera_height = 690; % distance from the ground.
f = 350;             % Focal length in pixels (2.1 mm)

A = s(frame_number).cdata(:,1:W/2);
D = depthmap(frame_number,s,W);
WC = wcsys(D,f,p);

x1 = p(1,1);
x2 = p(2,1);
y1 = p(1,2);
y2 = p(2,2);
d = euclidean(WC(1,:),WC(2,:));
A_line = insertShape(A,'Line',[x1 y1 x2 y2],...
    'LineWidth',3,'Opacity',1.0);
A_mark = insertMarker(A_line,[x1 y1; x2 y2],...
    'x','size',5,'color',[0,0,0]);

% Offset text coordinates
p1_str = ['P1 = (' num2str(ceil(x1)) ',' num2str(ceil(y1)) ')'];
p2_str = ['P2 = (' num2str(ceil(x2)) ',' num2str(ceil(y2)) ')'];

P1_str = ['(' num2str(WC(1,1),'%.1f\n') ','...
    num2str(WC(1,2),'%.1f\n') ',' num2str(WC(1,3),'%.1f\n') ')'];
P2_str = ['(' num2str(WC(2,1),'%.1f\n') ','...
    num2str(WC(2,2),'%.1f\n') ',' num2str(WC(2,3),'%.1f\n') ')'];

dist_str = ['Distance = ' num2str(d,'%.1f\n')];

h1_str = ['H1 =', num2str(camera_height - WC(1,2),'%.1f\n')];
h2_str = ['H2 =', num2str(camera_height - WC(2,2),'%.1f\n')];

box_color = {'green','green','green','green','green','green',...
    'green','green','green','green'};

text_pos = [0 0; 0 40; 0 70; 0 110; 0 140; 0 180; 0 220; 0 250;
    x1-40 y1-30; x2+10 y2-30];
frame_str = ['Frame: ',num2str(frame_number)];

IM = insertText(A_mark,text_pos,...
{frame_str,p1_str,P1_str,p2_str,P2_str,dist_str,h1_str,h2_str,...
'P1','P2'},'BoxColor',box_color,...
```

```
'FontSize',16,'Font','LucidaSansDemiBold');

imshow(IM)
end
```

B.12. Point Identification GUI

```
%POINT_IDENTIFICATION_GUI  Identifies and stores hand-selected points for
%   stalk diameter, internode lenght, or angle estimation.
%
%   STEPS:
%   1. Run 'video_reader.m' script to load the video.
%   2. Define (type) a frame number where a clear stalk is shown.
%   3. Define (type) the plant variety to add a tag to the output file.
%   4. Select two points to estimate stalk diameter or internode length, or
%      select three points to estimate leaf angle.
%   5. Decide whether or not to store the values in the output files
%      'results_diameter.txt' or 'results_angle.txt', according to the
%      question prompt.
%   6. Type the next frame number to estimate diameter, length, or angle;
%      and repeat steps 2 to 5.
%   7. Open the output files 'results_diameter.txt' or 'results_angle.txt'
%      to copy and paste or read the results in another software like
%      Excel. Once the coordinates are stored, these can be used by the
%      script 'depth_maps_saving.m' to save the depth maps, and result
%      images.
%
%   The output file 'results_diameter.txt' records 7 columns: Plant ID (ID);
%   Frame Number (FRM); the pixel coordinates of the two points: X_1, Y_1,
%   X_2, and Y_2; and DIAMETER.
%
%   The output file 'results_angle.txt' records 11 columns: Plant ID (ID);
%   Frame Number (FRM); the pixel coordinates of the three points: X_1,
%   Y_1, X_2, Y_2, X_3, Y_3; Length of line 1 (LENG1), Length of line 2
%   (LENG2), and ANGLE.
%
%   Requirements:
%   1) Computer Vision System Toolbox
%   2) Run 'video_reader.m'
%   3) Run 'point_identification_gui.m'
%
%   Script Created by Mario A. Mendez. 30 November 2016.

frame_number = 238;
plant_variety = 'A';
camera_height = 690; % Distance from the ground (mm)

A = s(frame_number).cdata(:,1:W/2);     % Left image
B = s(frame_number).cdata(:,W/2+1:W);   % Right image

%disparityMap = disparity(A,B,'Method','BlockMatching');

f = 350; % Focal length in pixels (2.1 mm)
b = 30;  % Base line (mm)

% Estimated depth map in world coordinates
%D = b * f ./ disparityMap;      % Depth map in world Z units (mm)

%D_im = mat2gray(D, [190,570]); % Convert matrix to gray image
%C = imfuse(A,D_im);            % Fusion between the left and depth images

figure(1)
imshow(A)

% User Interface to Collect Points in the Image
```

```
[x,y] = ginput(3); % Number of points to collect
p = [x,y];
[mp,~] = size(p);  % Number of rows in 'p'
%WC = wcsys(D,f,p); % Estimate the world coordinates

if mp == 2
    RGB = imagediam(frame_number,s,W,p);
    d = euclidean(WC(1,:),WC(2,:));
    usr_input = input('Do you want to write the values? Y/N [N]: ','s');
    if isempty(usr_input)
        usr_input = 'N';
    end
    if usr_input == 'n' || usr_input == 'N'
        error('You need to start over');
    end
    if usr_input == 'y' || usr_input == 'Y'
        var_num = input('Type the plant number: ');
        % Rounding up
        line = [var_num frame_number ceil(p(1,1)) ceil(p(1,2))...
        ceil(p(2,1)) ceil(p(2,2)) d];
        fileID = fopen('points_diameter.txt','a');
        fmt = [plant_variety '%d %d %d %d %d %d %3.2f \n'];
        fprintf(fileID,fmt,line);
        fclose(fileID);
    else
        error('You need to start over');
    end
end

if mp == 3
    RGB = imageangle(frame_number,s,W,p);
    d1 = euclidean(WC(1,:),WC(2,:));
    d2 = euclidean(WC(3,:),WC(2,:));
    theta = angle3(WC(1,:),WC(2,:),WC(3,:));
    usr_input = input('Do you want to write the values? Y/N [N]: ','s');
    if isempty(usr_input)
        usr_input = 'N';
    end
    if usr_input == 'n' || usr_input == 'N'
        error('You need to start over');
    end
    if usr_input == 'y' || usr_input == 'Y'
        var_num = input('Type the plant number: ');
        % Rounding up
        line = [var_num frame_number ceil(p(1,1)) ceil(p(1,2))...
        ceil(p(2,1)) ceil(p(2,2)) ceil(p(3,1)) ceil(p(3,2)) d1 d2 theta];
        fileID = fopen('points_angle.txt','a');
        fmt = [plant_variety '%d %d %d %d %d %d %d %d %3.1f %3.1f %3.1f \n'];
        fprintf(fileID,fmt,line);
        fclose(fileID);
    else
        error('You need to start over');
    end
end
```

B.13. Results Images

```
%RESULTS_IMAGES   Saves the results on a set of images.
%   RESULTS_IMAGES is an script that uses 'measurements.csv' file to read
%   and load data in a matrix form. The CSV file contains lines with the
%   frame number, and positions X1 Y1 X2 Y2 that were previusly identify as
%   suitable locations to estimate diameter at each frame.
%
%   A MAT file is stored under the name '.mat'

data = csvread('measurements.csv',2,0); % Skips the first 3 rows.

method = 'BM_BS19';  % check method in the function DEPTHMAP.
directory = ['/Users/dorado/Documents/MATLAB/Images','_',method];

frame_number = data(:,1);

f = 350; % Focal length in pixels (2.1 mm)

n = length(frame_number);

DM = cell(n); % list of matrices
for i = 1:n
   A = s(frame_number(i)).cdata(:,1:W/2);
   DM{i} = depthmap(frame_number(i),s,W);   % Check the appropriate method
   out_name = ['A',num2str(i),'_',num2str(frame_number(i))];
   imwrite(A,fullfile(directory,[out_name,'_left.jpg']),'jpg');
   imagesc(DM{i},[0,700])
   axis image
   colormap jet
   axis off
   saveas(gcf,fullfile(directory,[out_name,'_',method]),'epsc')
   saveas(gcf,fullfile(directory,[out_name,'_',method]),'jpg')
   colorbar
   saveas(gcf,fullfile(directory,[out_name,'_bar','_',method]),'epsc')
   saveas(gcf,fullfile(directory,[out_name,'_bar','_',method]),'jpg')
   axis on
   saveas(gcf,fullfile(directory,[out_name,'_bar_axis','_',method]),'epsc')
   saveas(gcf,fullfile(directory,[out_name,'_bar_axis','_',method]),'jpg')

   % Read each row of collected data: (frame, x1, y1, z2, y2)
   p = reshape(data(i,2:5),2,2)';
   RGB = imagediam(frame_number(i),s,W,p);
   imwrite(RGB,[fullfile(directory,...
       [out_name,'_',method]),'_diameter.jpg'],'jpg')
   WC = wcsys(DM{i},f,p); % Estimate the world coordinates
   d = euclidean(WC(1,:),WC(2,:));
   line = [i frame_number(i) ceil(p(1,1)) ceil(p(1,2))...
   ceil(p(2,1)) ceil(p(2,2)) d];
   fileID = fopen(['results_diameter','_',method,'.txt'],'a');
   fmt = '%d %d %d %d %d %d %3.2f\n';
   fprintf(fileID,fmt,line);
   fclose(fileID);
end

save(['DepthMaps',method],'DM')
```

B.14. Angle Between Two Lines Formed by Three Points

```
function theta = angle3(P1,P2,P3)
%ANGLE3   Angle between two straight lines formed by three points.
%   theta = ANGLE3(P1,P2,P3) computes the angle (degree) between the two
%   straight lines that intersect at P2. So the first line starts at P2 and
%   ends at P1, while the second line starts at P2 and end at P3. Imagine
%   that the ends of lines have arrow heads indicating the sense of
%   direction.
%
%   P1, P2, and P3 must have the same dimension of the form [X1,X2,...,Xn],
%   if they are row vectors, but they can also be M-by-N arrays in which
%   case the output is an M-by-1 column vector, containing a set of angles.
%
%   Example:
%       P1 = [2 3 5;1 5 7];
%       P2 = [1 2 2;2 7 3];
%       P3 = [4 3 2;1 6 3];
%       theta = angle3(P1,P2,P3)

%   Function created by Mario Mendez. 1 December 2016.

[m1,n1] = size(P1);
[m2,n2] = size(P2);
[m3,n3] = size(P3);

if m1 ~= m2 || n1 ~= n2
    error('Input arguments must have the same dimension.')
end

if m1 ~= m3 || n1 ~= n3
    error('Input arguments must have the same dimension.')
end

m = m2;

theta = zeros(m,1);
for i = 1:m
    v1 = P1(i,:) - P2(i,:);
    v2 = P3(i,:) - P2(i,:);
    theta(i) = acosd( dot(v1,v2) / ( norm(v1) * norm(v2) ));
end
```

B.15. Image Angle

```
function RGB = imageangle(frame_number,s,W,p)
%IMAGEDIAM   Image angle between two lines or leaf angle.
%   IM=IMAGEDIAM(FRAME_NUMBER,S,W,P) computes the angle in degrees between
%   two straight lines defined by tree image points, but the angle is
%   computed from the converted image points into world coordinates,
%   expressed in the left image of the frame of the a stereo video stored
%   in a structure data type S, at a specific FRAME_NUMBER. Then, the
%   results are shown in an image, and stored in the variable IM.
%
%   The points P are stored in a 3-by-2 matrix, where the first column
%   contains the X coordinates and the second column contains the Y
%   coordinates. So the first row is the first point and the second row has
%   the second point, and the third row has the third point, all
%   expressed in pixel coordinates.
%
%   The width (pixels) of the stereo video is stored in a variable W at the
%   time of running 'video_reader.m'.
%
%   Requirements:
%   1) Computer Vision System Toolbox
%   2) Run 'video_reader.m'
%
%   Created by Mario A. Mendez, February 2017.

% Parameters
camera_height = 690; % distance from the ground.
f = 350;      % Focal length in pixels (2.1 mm)

A = s(frame_number).cdata(:,1:W/2);
D = depthmap(frame_number,s,W);
WC = wcsys(D,f,p);

x1 = p(1,1);
x2 = p(2,1);
x3 = p(3,1);
y1 = p(1,2);
y2 = p(2,2);
y3 = p(3,2);


d1 = euclidean(WC(1,:),WC(2,:));
d2 = euclidean(WC(3,:),WC(2,:));
theta = angle3(WC(1,:),WC(2,:),WC(3,:));
A_line = insertShape(A,'Line',[x1 y1 x2 y2;...
    x2 y2 x3 y3],'LineWidth',3,'Opacity',1.0);
A_mark = insertMarker(A_line,[x1 y1; x2 y2;...
    x3 y3],'x','size',5,'color',[0,0,0]);

% Offset text coordinates
p1_str = ['P1 = (' num2str(ceil(x1)) ',' num2str(ceil(y1)) ')'];
p2_str = ['P2 = (' num2str(ceil(x2)) ',' num2str(ceil(y2)) ')'];
p3_str = ['P3 = (' num2str(ceil(x3)) ',' num2str(ceil(y3)) ')'];

P1_str = ['(' num2str(WC(1,1),'%.1f\n') ','...
num2str(WC(1,2),'%.1f\n') ',' num2str(WC(1,3),'%.1f\n') ')'];
P2_str = ['(' num2str(WC(2,1),'%.1f\n') ','...
num2str(WC(2,2),'%.1f\n') ',' num2str(WC(2,3),'%.1f\n') ')'];
P3_str = ['(' num2str(WC(3,1),'%.1f\n') ','...
num2str(WC(3,2),'%.1f\n') ',' num2str(WC(3,3),'%.1f\n') ')'];

dist1_str = ['Distance 1 = ' num2str(d1,'%.1f\n')];
dist2_str = ['Distance 2 = ' num2str(d2,'%.1f\n')];
ang_str = ['Angle = ' num2str(theta,'%.1f\n') char(176)];
```

```
h1_str = ['H1 =', num2str(camera_height - WC(1,2),'%.1f\n')];
h2_str = ['H2 =', num2str(camera_height - WC(2,2),'%.1f\n')];
h3_str = ['H3 =', num2str(camera_height - WC(3,2),'%.1f\n')];

box_color = {'green','green','green','green','green','green',...
    'green','green','green','green','green','green','green',...
    'green','green','green'};

frame_str = ['Frame: ',num2str(frame_number)];

text_pos = [0 0; 0 40; 0 70; 0 110; 0 140; 0 180; 0, 210; 0 250; 0 280;...
        0 310; 0 350; 0 380; 0 410;...
        x1-50 y1-10; x2+10 y2; x3+20 y3-10];

RGB = insertText(A_mark,text_pos,...
    {frame_str,p1_str,P1_str,p2_str,P2_str,p3_str,P3_str,dist1_str,...
    dist2_str,ang_str,h1_str,h2_str,h3_str,'P1','P2','P3'},...
    'BoxColor',box_color,'FontSize',16,'Font','LucidaSansDemiBold');

% Printing on the image
out_name = [num2str(frame_number) '_angle'];
imshow(RGB)
imwrite(RGB,out_name,'jpg')

end
```

B.16. Linear Regression for Stereo Stalk Thickness Estimations

B.16.1. Script

```
%STATISTICS_STEREO Linear regression of manual vs stereo vision
%   measurements.
%
%   This script reads the stalk thikness of CAL and STEREO measurements
%   ('tickness_results_rep_2_statitics.csv') for the field experiment.
%   The script computes the correlation of both variables. It plots histograms and
%   residuals scaterplots, to later compute the studentized residuals
%   bigger or equal than 2.5. Finally, it
%   plots the original data without ouliers.
%
%   Script created by Mario Mendez. 21 March 2018.
%   Modified 8 September 2020.

clear all
clc
% Read the CSV file skipping the first row and column.
thickness_data = csvread('tickness_results_rep_2_statitics_good.csv',1,1);
stereo = thickness_data(:,1);
caliper = thickness_data(:,2);

figure(1) % Plot caliper histogram
histfit(caliper), box off
xlabel('Thickness (mm)')
ylabel('Counts')

figure(2) % Plot stereo estimations histogram
histfit(stereo), box off
xlabel('Thickness (mm)')
ylabel('Counts')

figure(3) % Plot raw error histogram
plot(caliper - stereo,'*'), box off
line([0 100],[0 0],'Color','k')
xlabel('Data number')
```

```
ylabel('Raw error (mm)')

% Compute the Linear Fit
lm_1 = fitlm(stereo, caliper);

% Compute Studentized residuals and remove those equal or greater
%  or equal than 2.5.
studentized_residuals = studentized(caliper, lm_1.Coefficients.Estimate(1)...
    + lm_1.Coefficients.Estimate(2) * stereo);
filtered_data = [(1:length(studentized_residuals))', caliper, stereo, ...
    studentized_residuals];
index_del = find(abs(filtered_data(:,4)) >= 2.5);
filtered_data(index_del,:) = [];

figure(4) % Plot raw error with no outliers
plot(filtered_data(:,2) - filtered_data(:,3), '*'), box off
line([0 100],[0 0], 'Color', 'k')
xlabel('Data number')
ylabel('Raw error (mm)')

figure(5) % Plot raw error histogram with no outliers
histfit(filtered_data(:,2) - filtered_data(:,3)), box off
xlabel('Raw error (mm)')
ylabel('Counts')

% Compute the two linear regression lines
x = 12:37;
lm_2 = fitlm(filtered_data(:,2), filtered_data(:,3));

estimations_1 = lm_1.Coefficients.Estimate(1) ...
    + lm_1.Coefficients.Estimate(2) * x;

estimations_2 = lm_2.Coefficients.Estimate(1) ...
    + lm_2.Coefficients.Estimate(2) * x;
%
figure(6) % Plot scatterplot and linear fit
plot(stereo, caliper, '*'), hold on
plot(x, estimations_1), box off, grid on
xlabel('Stereo-imaging estimates (mm)')
ylabel('Caliper measurements (mm)')
xlim([10 40])
ylim([10 40])
axis equal

figure(7) % Plot scatterplot and linear fit without outliers
plot(filtered_data(:,3), filtered_data(:,2), '*'), hold on
plot(x, estimations_2), box off, grid on
xlabel('Stereo-imaging estimates (mm)')
ylabel('Caliper measurements (mm)')
xlim([10 40])
ylim([10 40])
axis equal

figure(8) % Plot residuals
plot(caliper, caliper - (lm_1.Coefficients.Estimate(1)...
    + lm_1.Coefficients.Estimate(2) * stereo),'*'), hold on
plot([15,50],[0,0]), box off, grid on
xlabel('Caliper measurements (mm)')
ylabel('Residuals (mm)')
xlim([15 35])

figure(9) % Plot residuals
plot(filtered_data(:,2), filtered_data(:,2)...
    - (lm_2.Coefficients.Estimate(1) +...
    lm_2.Coefficients.Estimate(2) * filtered_data(:,3)),'*'), hold on
plot([15,50],[0,0]), box off, grid on
xlabel('Caliper measurements (mm)')
```

```
ylabel('Residuals (mm)')
xlim([15 35])

index_outliers_boxplot = [10, 44, 51, 84];

filtered_data_2 = [caliper, stereo];

figure(10)
histfit(filtered_data_2(:,1) - filtered_data_2(:,2)), box off
xlabel('CAL - STR (mm)')
ylabel('Counts')

% Fist column is CAL and second column is STR
filtered_data_2(index_outliers_boxplot,:) = [];

figure(11)
subplot(1,2,1);
boxplot(caliper - stereo,'Labels', 'All Data')
ylabel('CAL - STR (mm)')
subplot(1,2,2);
boxplot(filtered_data_2(:,1) - filtered_data_2(:,2), 'Labels', 'No Outliers')
ylabel('CAL - STR (mm)')

figure(12)
histfit(filtered_data_2(:,1) - filtered_data_2(:,2)), box off
xlabel('CAL - STR (mm)')
ylabel('Counts')

% Fist column is CAL and second column is STR
CAL_no_outliers = filtered_data_2(:,1);
STR_no_outliers = filtered_data_2(:,2);

% Test of normality
[h_normal, p_normal] = adtest(CAL_no_outliers - STR_no_outliers);

average_CAL_no_outliers = mean(filtered_data_2(:,1));
average_STR_no_outliers = mean(filtered_data_2(:,2));

raw_average_bias = average_STR_no_outliers - average_CAL_no_outliers;
predicted_average = predict(lm_2, mean(average_STR_no_outliers));
predicted_average_bias = predicted_average - average_CAL_no_outliers;

% Standard error at x = any value;
x = average_STR_no_outliers;
standard_error = lm_2.RMSE * sqrt( 1 / lm_2.NumObservations + ...
    (x - average_STR_no_outliers)^2 / ( (lm_2.NumObservations - 1) * ...
    var(STR_no_outliers) ) );

% t-statistic for alpha = 0.05/2 with n - 2 dof (dof of error)
alpha = 0.05;
t_stat = tinv(1 - alpha/2, lm_2.DFE);

plus_minus_error = t_stat * sqrt(lm_2.RMSE^2 + standard_error^2); %Cline pp. 147
```

B.16.2. Output 1

```
Linear regression model:
    y ~ 1 + x1

Estimated Coefficients:
                   Estimate      SE       tStat       pValue
                   ________   ________   ______   __________
```

```
    (Intercept)     5.2695       1.2572    4.1914    6.4681e-05
    x1             0.80512     0.049281    16.337    1.1511e-28


Number of observations: 92, Error degrees of freedom: 90
Root Mean Squared Error: 2.07
R-squared: 0.748,  Adjusted R-Squared: 0.745
F-statistic vs. constant model: 267, p-value = 1.15e-28
```

B.16.3. Output 2

```
Linear regression model:
    y ~ 1 + x1

Estimated Coefficients:
                   Estimate       SE        tStat       pValue  
                   ________    ________    _______    __________

    (Intercept)     1.1402       1.2483    0.91343       0.36354
    x1             0.93638     0.048462     19.322    3.1654e-33


Number of observations: 89, Error degrees of freedom: 87
Root Mean Squared Error: 1.87
R-squared: 0.811,  Adjusted R-Squared: 0.809
F-statistic vs. constant model: 373, p-value = 3.17e-33
```

B.17. MATLAB® Print from the Help of the Disparity Map Function

```
disparity Compute disparity map.

  disparity is not recommended. Use disparityBM or disparitySGM instead.

    disparityMap = disparity(I1,I2) returns the disparity map for a pair of
    stereo images, I1 and I2. I1 and I2 must have the same size and must be
    rectified such that the corresponding points are located on the same
    rows. This rectification can be performed using the rectifyStereoImages
    function. The returned disparity map has the same size as I1 and
    I2.

    The disparity function implements two different algorithms: Block
    Matching and Semi-Global Block Matching. These algorithms consist of
    the following steps:

     (1) Compute a measure of contrast of the image by using the Sobel
         filter.

     (2) Compute the disparity for each pixel in I1.

     (3) Mark the elements of d for which disparity was not computed
         reliably with -REALMAX('single').

    disparityMap = disparity(...,Name,Value) specifies additional
    name-value pairs described below:

    'Method'               'BlockMatching' for basic Block Matching or
                           'SemiGlobal' for Semi-Global Block Matching. In
                           the Block Matching method the function computes
                           disparity by comparing the sum of absolute
                           differences (SAD) of each block of pixels in the
                           image. In the Semi-Global Block Matching method
                           the function additionally forces similar
                           disparity on neighboring blocks. This additional
                           constraint results in a more complete disparity
                           estimate than in Block Matching.

                           Default: 'SemiGlobal'

    'DisparityRange'       A two-element vector,
                           [MinDisparity MaxDisparity], defining the range
                           of disparity. MinDisparity and MaxDisparity must
                           be integers and their difference must be
                           divisible by 16.

                           Default: [0 64]

    'BlockSize'            An odd integer, 5 <= BlockSize <= 255. The width
                           of each square block of pixels used for
                           comparison between I1 and I2.

                           Default: 15

    'ContrastThreshold'    A scalar value, 0 < ContrastThreshold <= 1,
                           defining the acceptable range of contrast
                           values. Increasing this parameter results in
                           fewer pixels being marked as unreliable.

                           Default: 0.5

    'UniquenessThreshold'  A non-negative integer defining the minimum
                           value of uniqueness. If a pixel is less unique,
                           the disparity computed for it is less reliable.
```

```
                         Increasing this parameter will result in marking
                         more pixels unreliable. You can set this
                         parameter to 0 to disable it.

                         Default: 15

  'DistanceThreshold'    A non-negative integer defining the maximum
                         distance for left-right checking.Increasing this
                         parameter results in fewer pixels being marked
                         as unreliable. You can also set this parameter
                         to an empty matrix [] to disable it.

                         Default: [] (disabled)

  'TextureThreshold'     A scalar value, 0 <= TextureThreshold < 1,
                         defining the minimum texture. If a block of
                         pixels is less textured, the computed disparity
                         is less reliable. Increasing this parameter
                         results in more pixels being marked as
                         unreliable. Set this parameter to 0 to disable
                         it.

                         This parameter is used only with the
                         'BlockMatching' method.

                         Default: 0.0002

  Class Support
  -------------
  All inputs must be real, finite, and nonsparse. I1 and I2 must have the
  same class and must be uint8, uint16, int16, single, or double.

  Example
  -------
  % Load the images.
  I1 = imread('scene_left.png');
  I2 = imread('scene_right.png');

  % Show the stereo anaglyph. You can view the image in 3-D using
  % red-cyan stereo glasses.
  figure
  imshow(stereoAnaglyph(I1,I2))
  title('Red-cyan composite view of the stereo images')

  % Compute the disparity map.
  range = [-6 10];
  disparityMap = disparity(rgb2gray(I1), rgb2gray(I2), ...
     'BlockSize', 15, 'DisparityRange', range);

  % Show the disparity map. For better visualization use the disparity
  % range as the display range for imshow.
  figure
  imshow(disparityMap, range)
  title('Disparity Map')
  colormap jet
  colorbar

See also rectifyStereoImages, reconstructScene,
estimateCameraParameters, estimateUncalibratedRectification

  Reference page for disparity
```

APPENDIX C

IMAGE CLASSIFICATION BY MINUIMUM DISTANCE

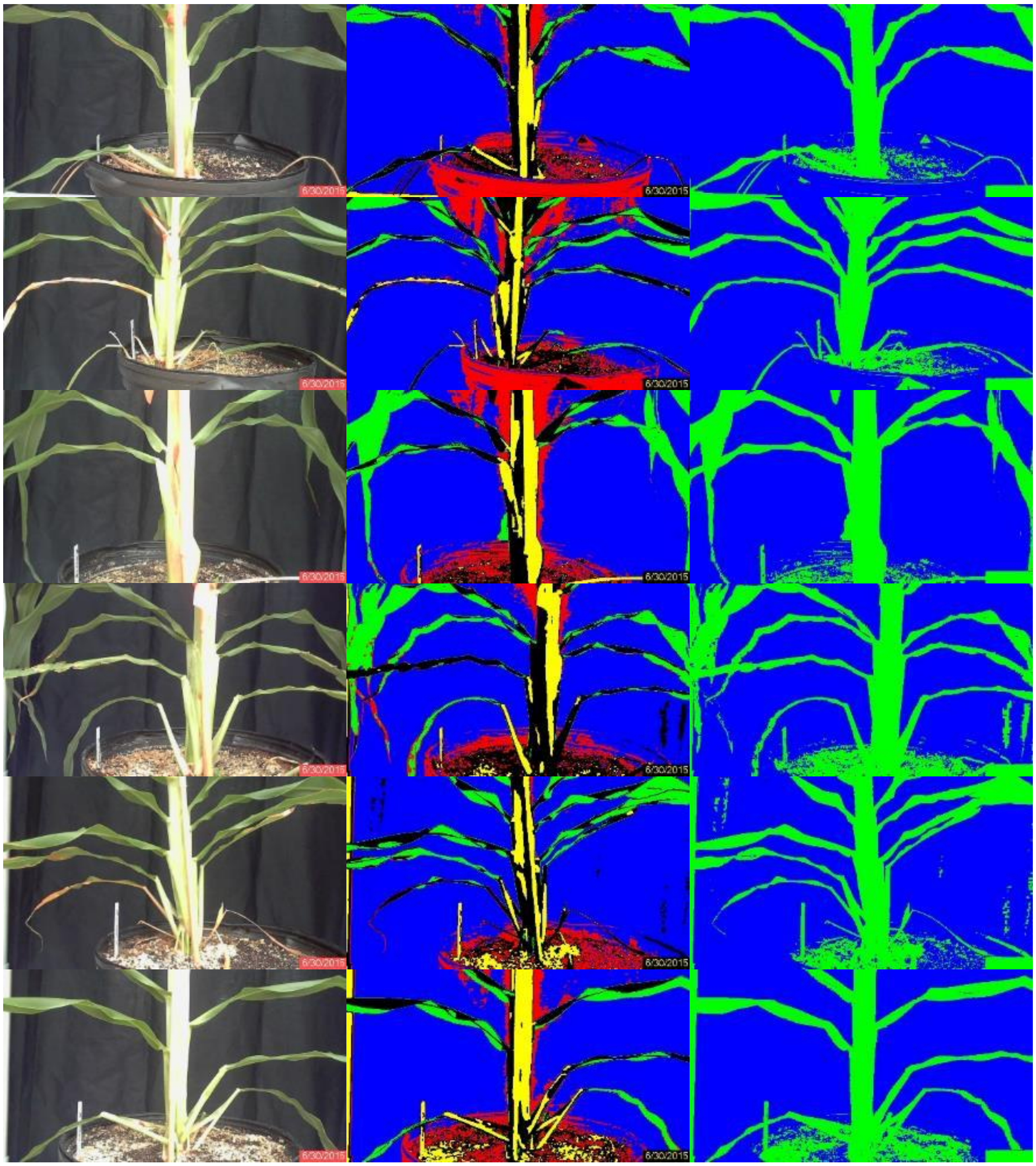

Figure C.1. From left to right, RGB, classified, and binary images. From top to bottom, plants 1A, 2A, 3A, 4A, 2B, and 3B, corresponding to 30 June 2015.

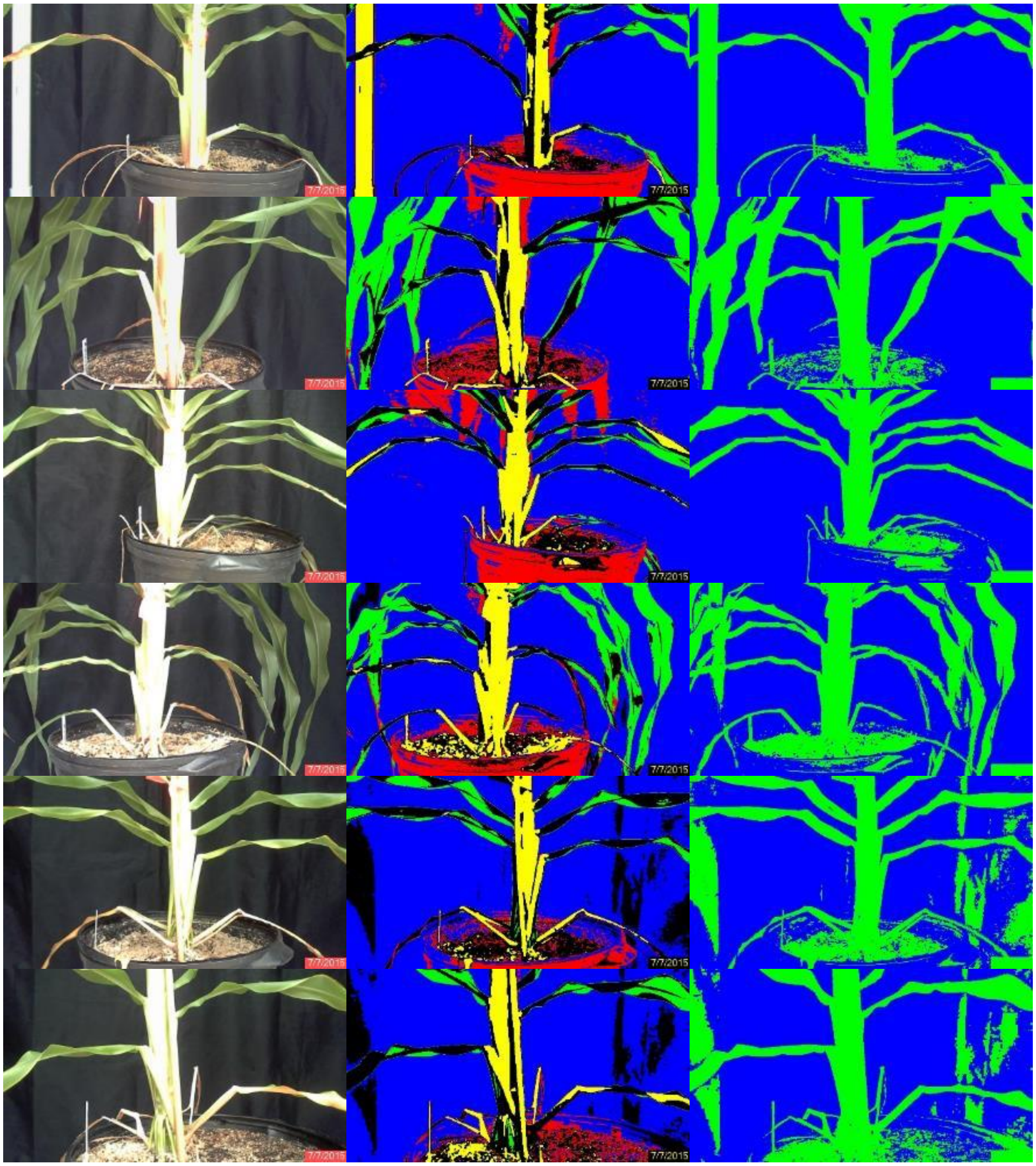

Figure C.2. From left to right, RGB, classified, and binary images. From top to bottom, plants 1A, 2A, 3A, 4A, 1B, and 2B, corresponding to 7 July 2015.

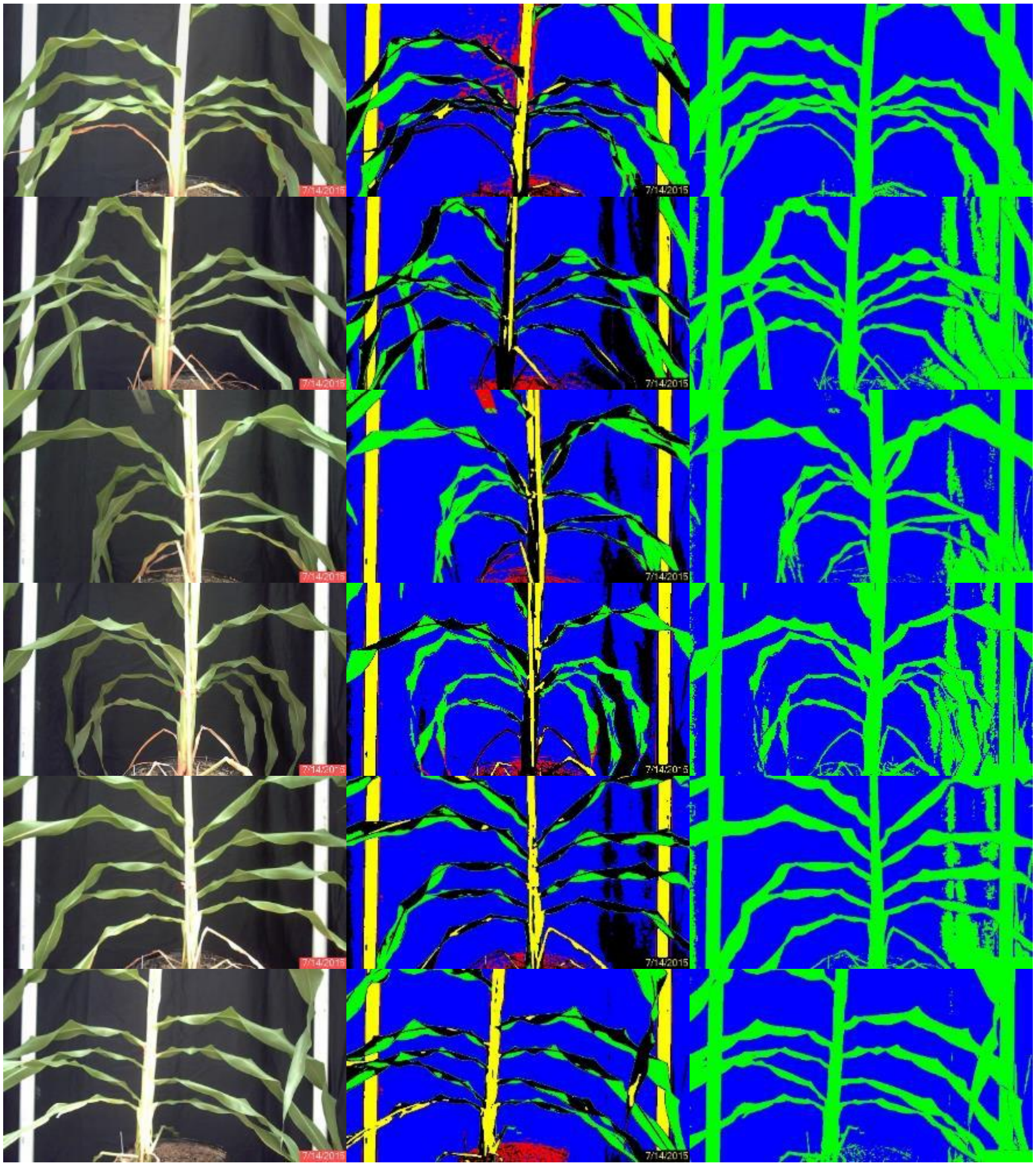

Figure C.3. From left to right, RGB, classified, and binary images. From top to bottom, plants 1A, 2A, 3A, 4A, 1B, and 4B, corresponding to 14 July 2015.

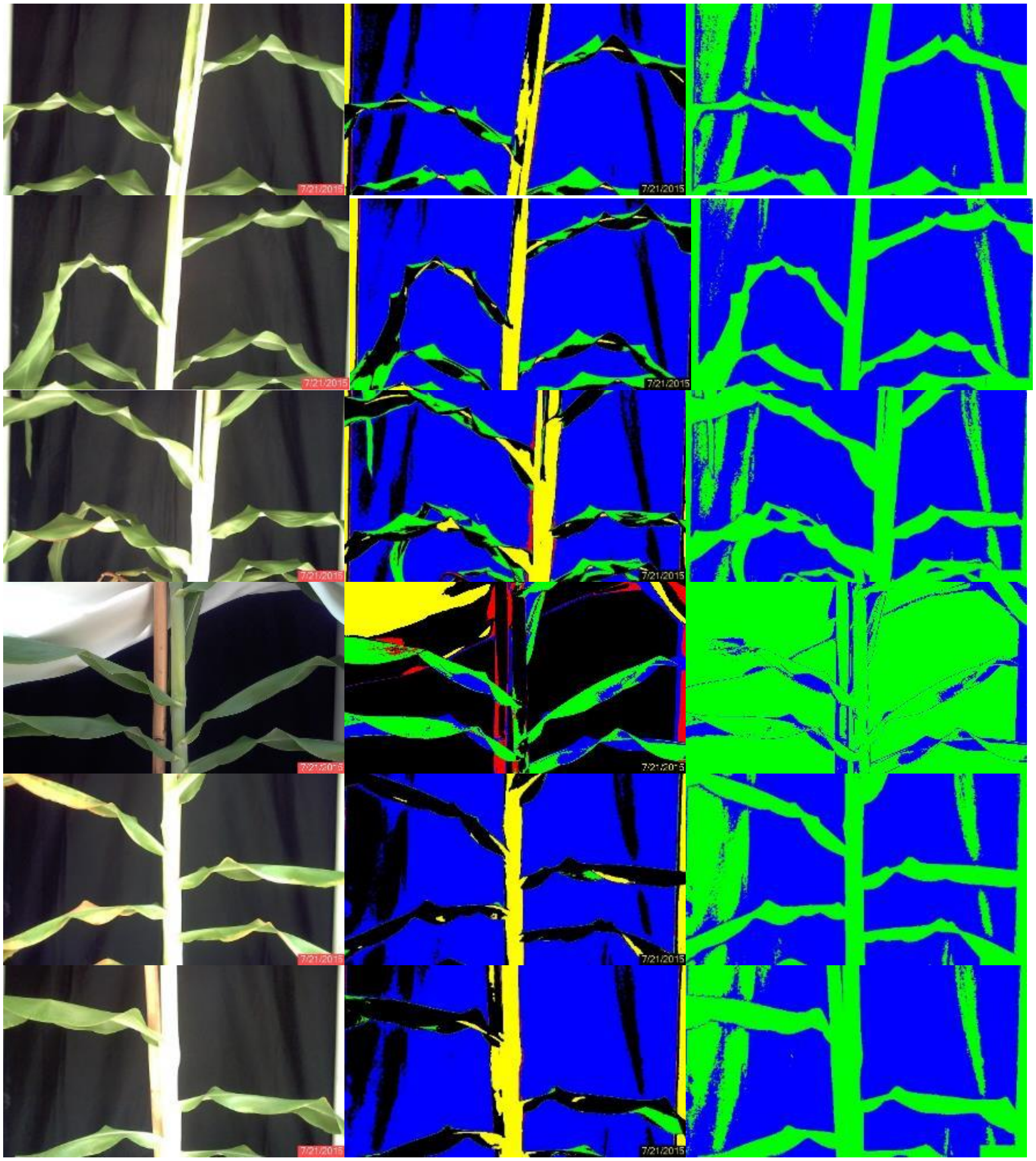

Figure C.4. From left to right, RGB, classified, and binary images. From top to bottom, plants 1A, 2A, 4A, 1B, 2B, and 4B, corresponding to 21 July 2015.

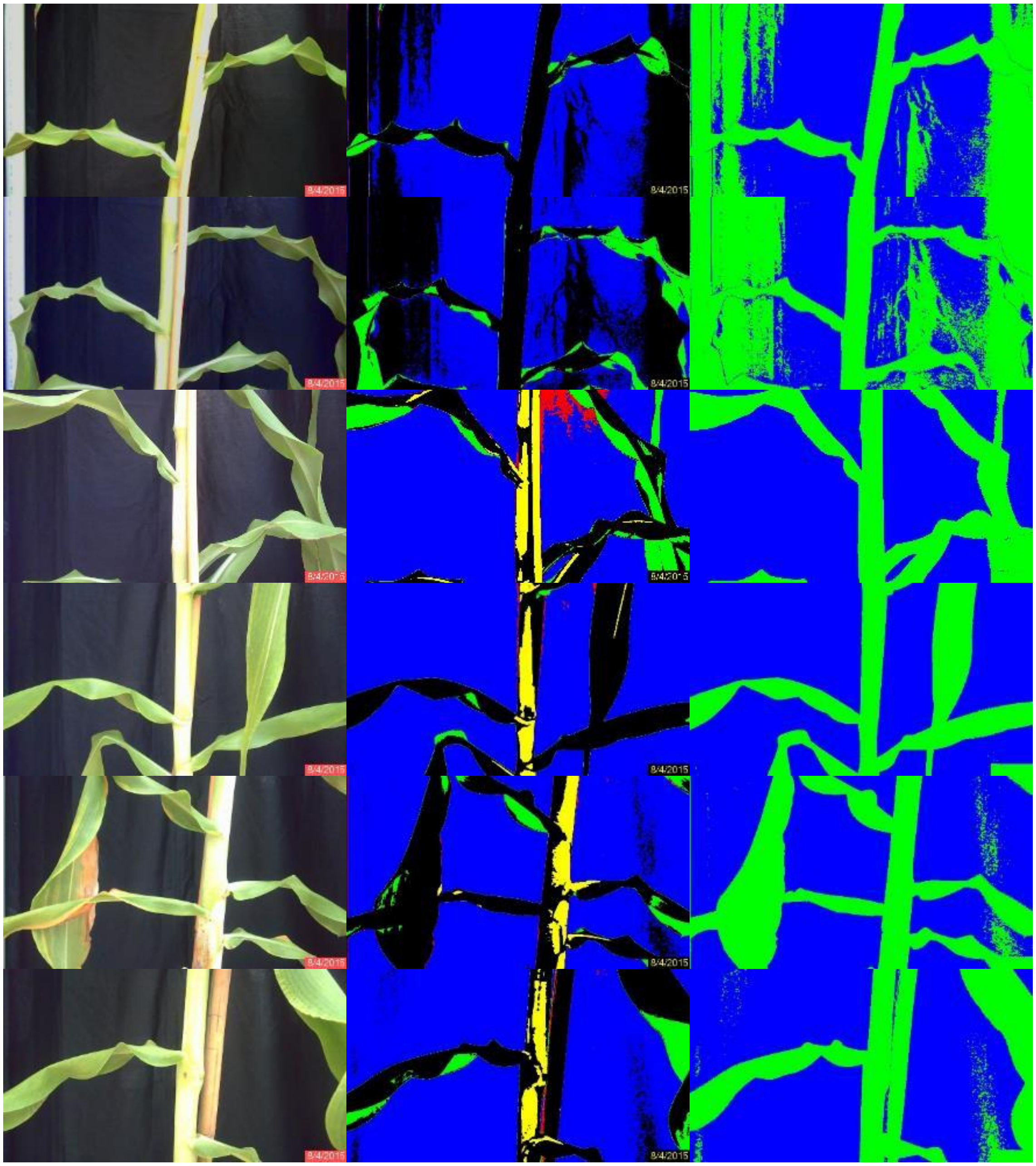

Figure C.5. From left to right, RGB, classified, and binary images. From top to bottom, plants 1A, 2A, 3A, 1B, 3B, and 4B, corresponding to 4 August 2015.

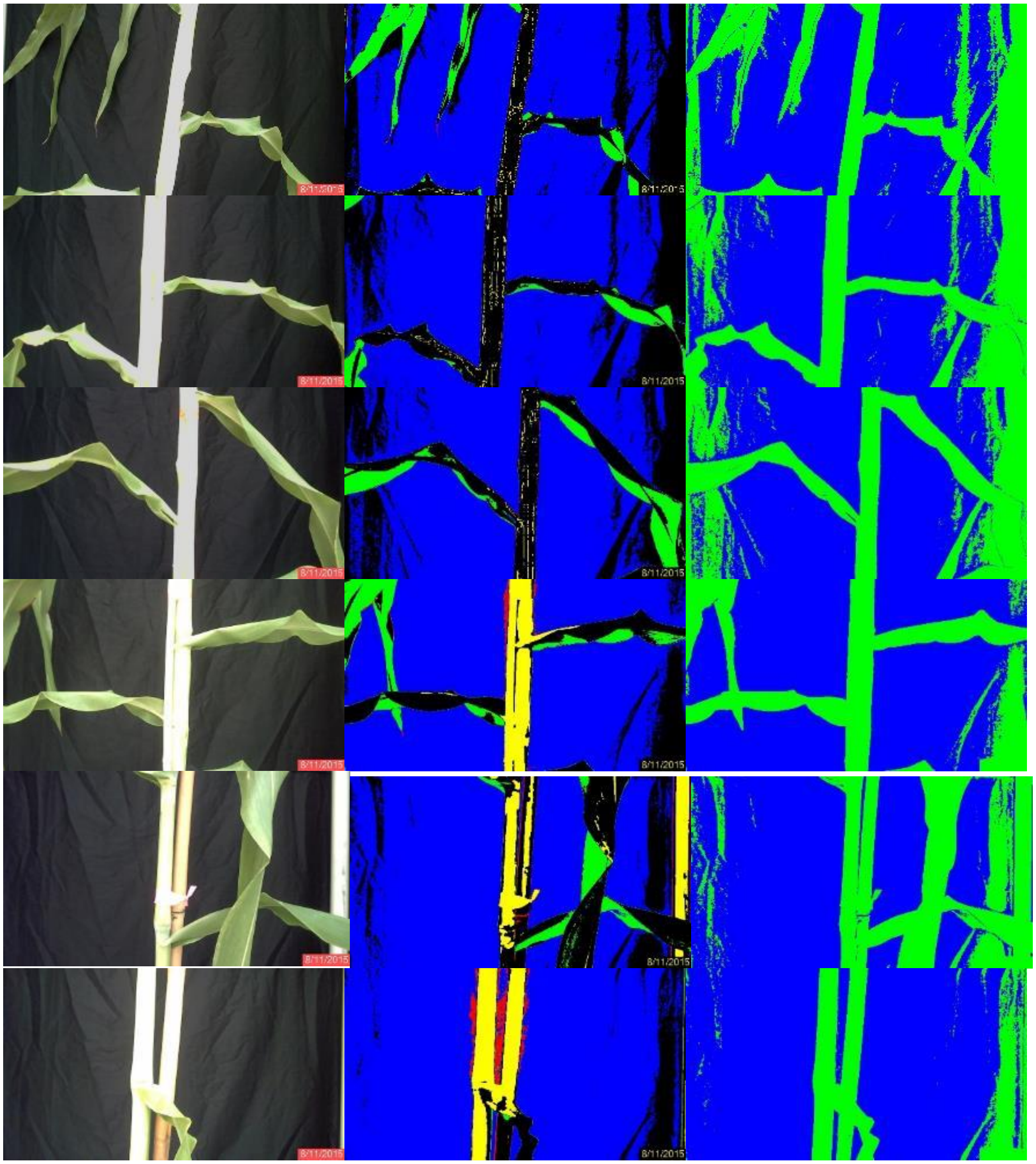

Figure C.6. From left to right, RGB, classified, and binary images. From top to bottom, plants 1A, 2A, 3A, 4A, 1B, and 4B, corresponding to 11 August 2015.

APPENDIX D

STALK THICKNESS AND DEPTH MAPS

This appendix shows the results of stalk thickness estimations. On gray scale, the left-hand side images of the stereo camera; overlaying frame number, pixel and world coordinates of the two points (P1, P2), distance (stalk thickness) between the two points, and their height from the ground (H1, H2). On color, the corresponding depth maps with a scale bar in millimeters.

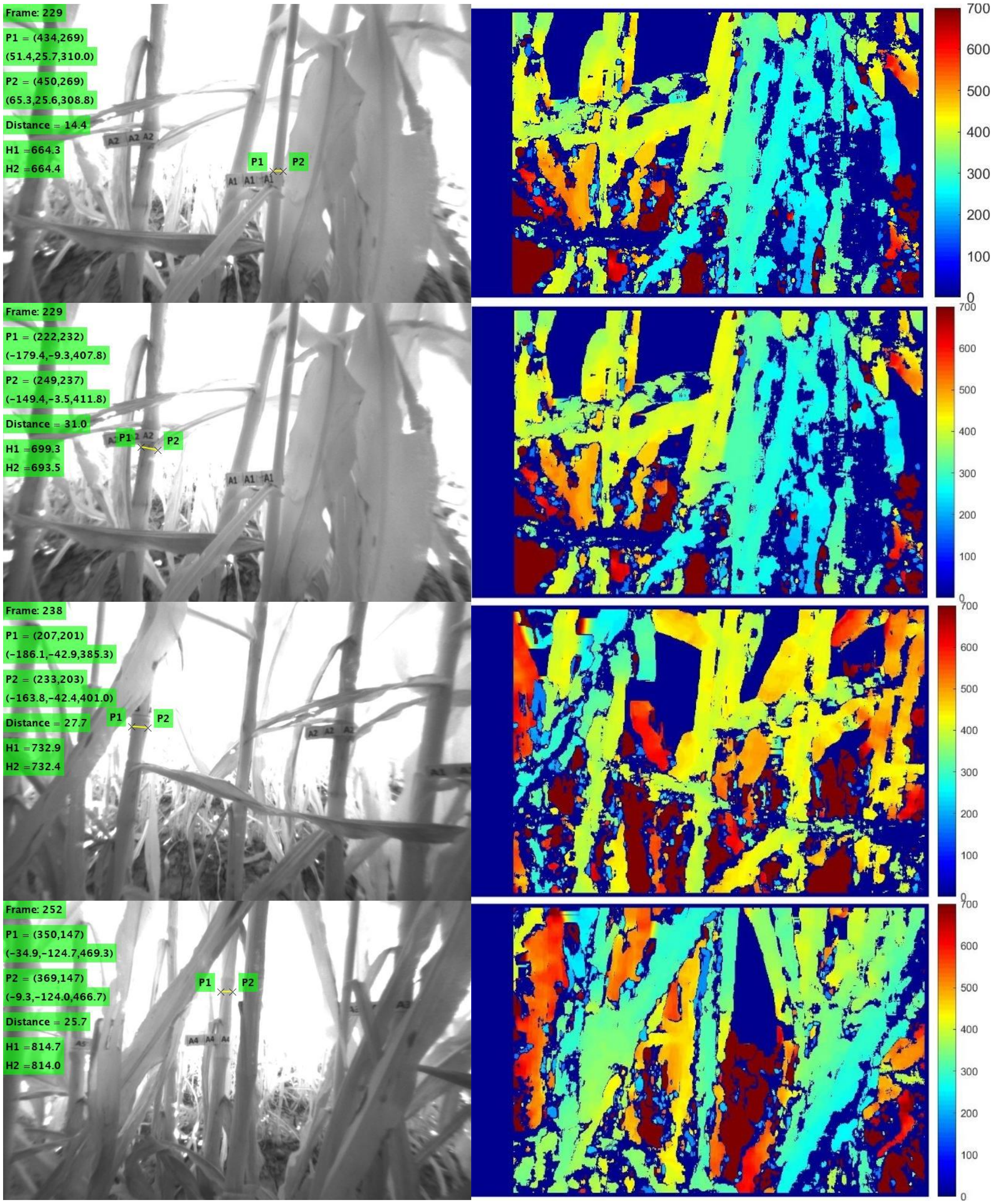

Figure D.1. Stalk thickness estimations using stereovision for plants A1 to A4.

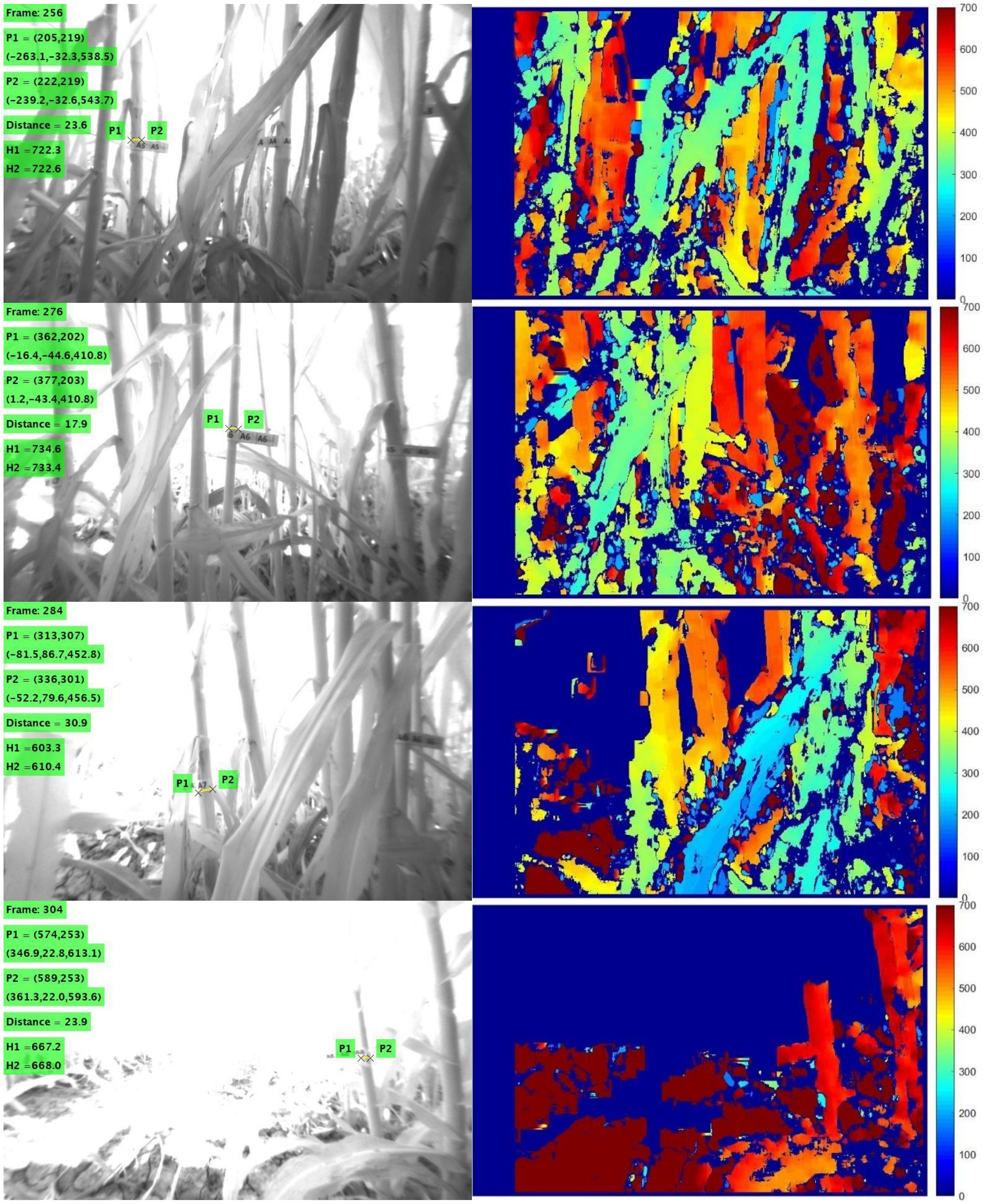

Figure D.2. Stalk thickness estimations using stereovision for plants A5 to A8

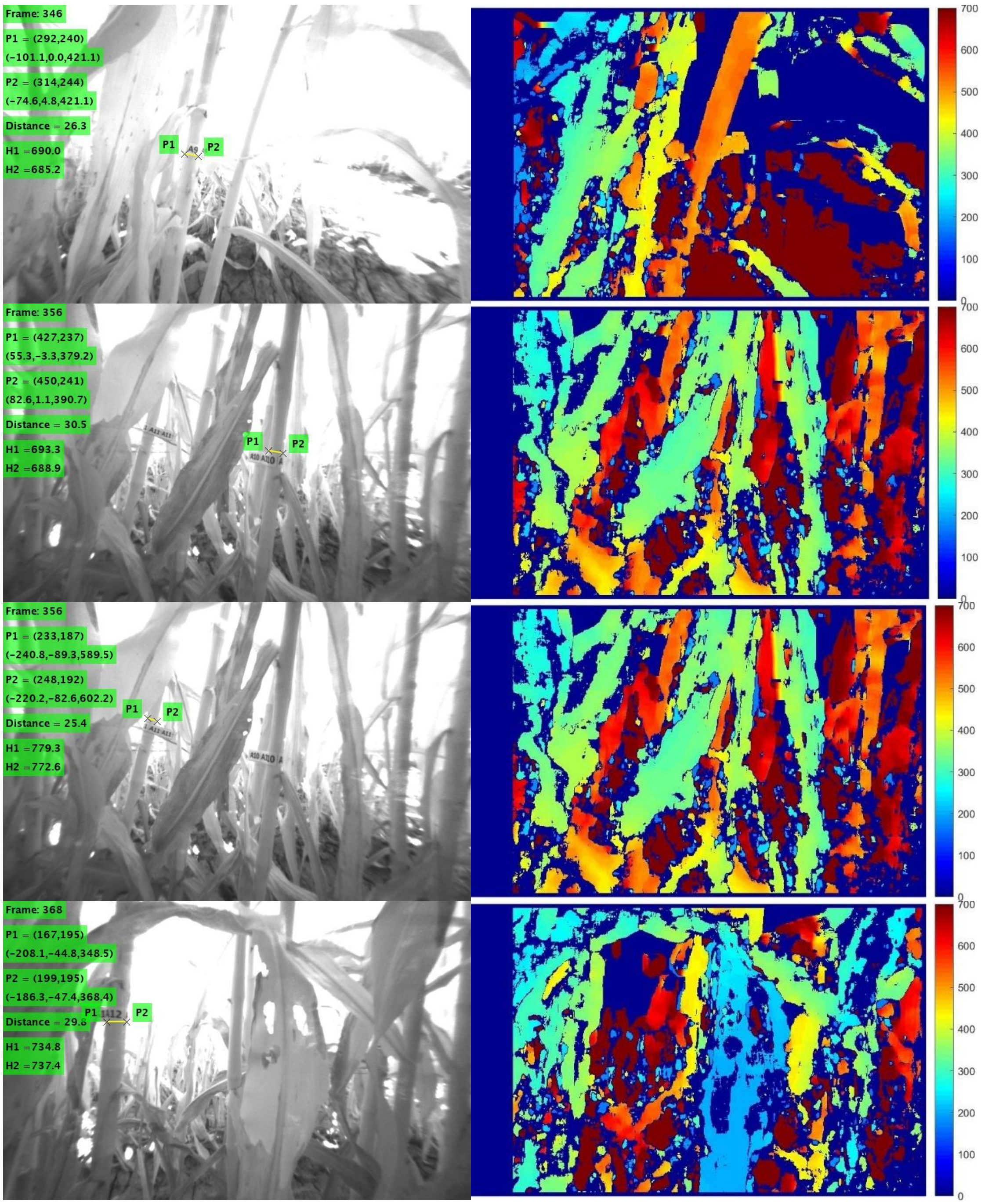

Figure D.3. Stalk thickness estimations using stereovision for plants A9 to A12.

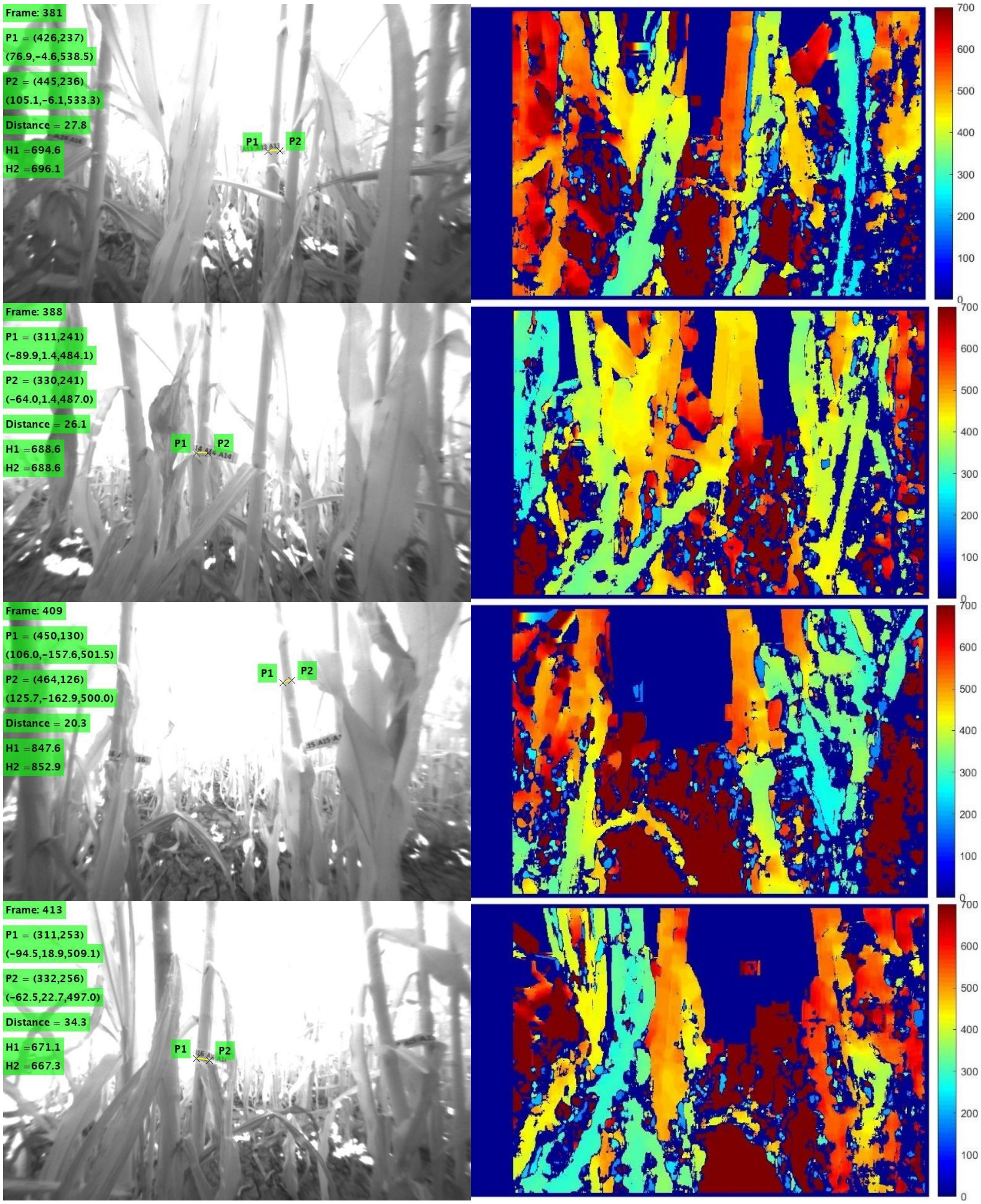

Figure D.4. Stalk thickness estimations using stereovision for plants A13 to A16.

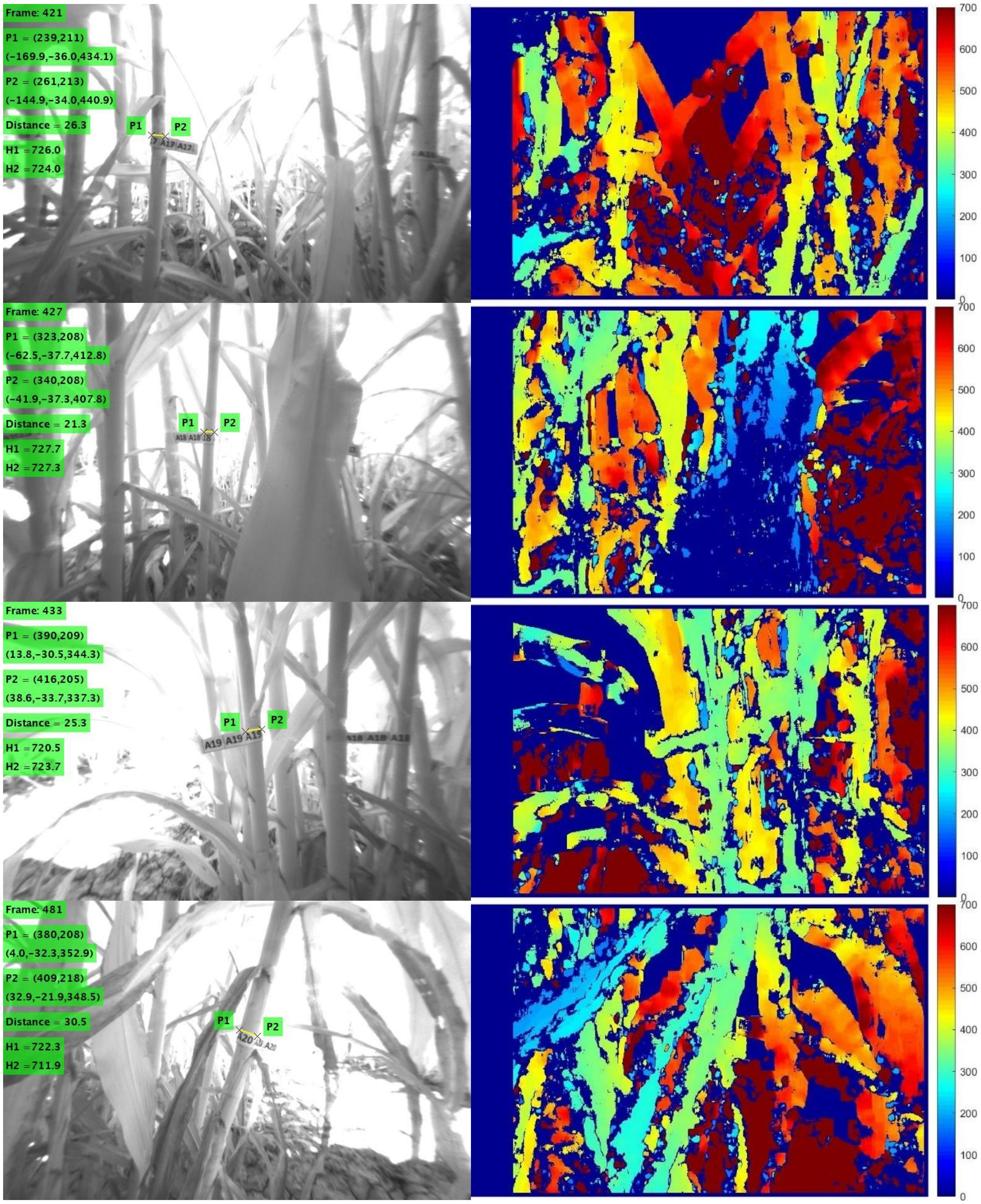

Figure D.5. Stalk thickness estimations using stereovision for plants A17 to A20.

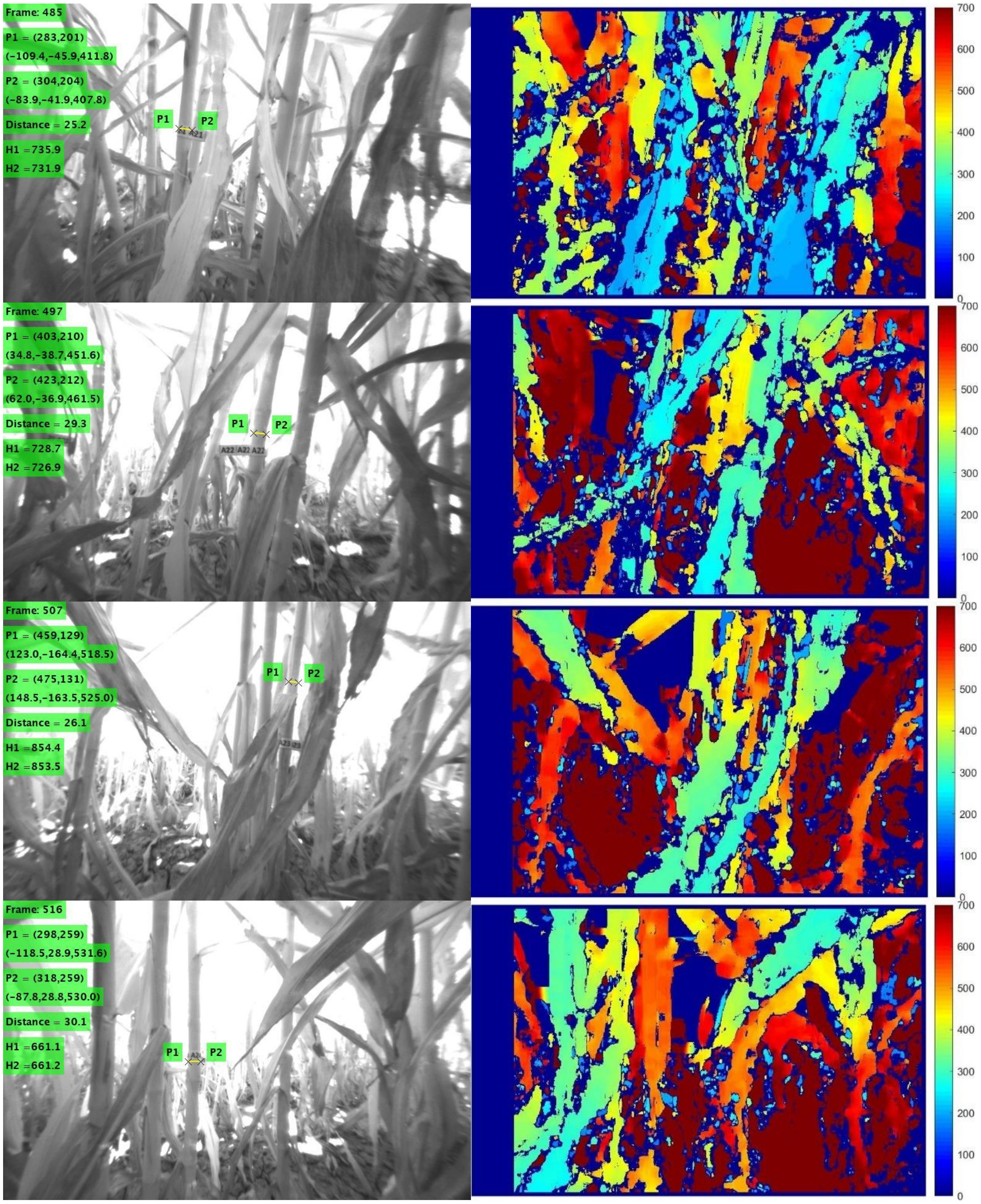

Figure D.6. Stalk thickness estimations using stereovision for plants A21 to A24.

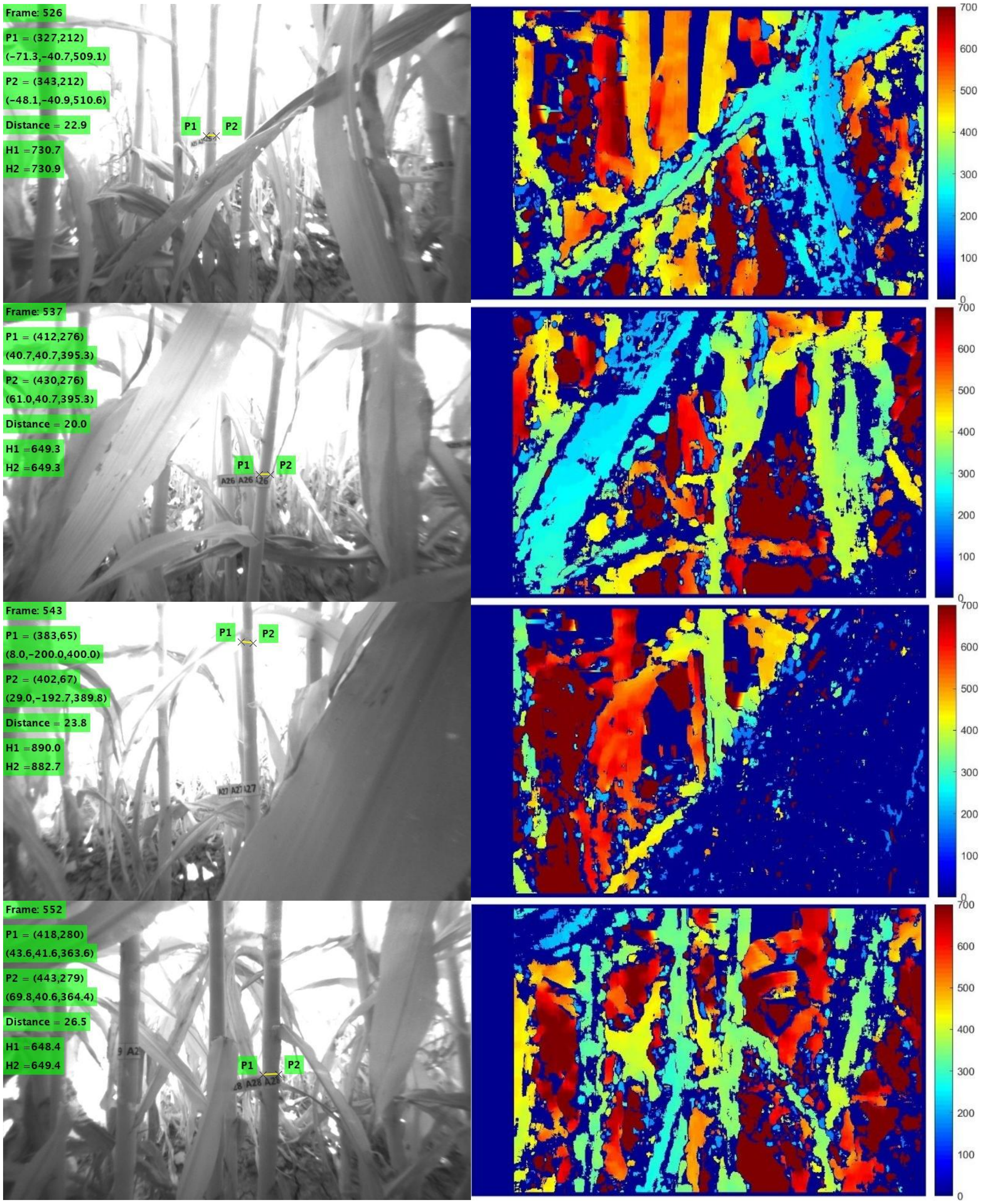

Figure D.7. Stalk thickness estimations using stereovision for plants A25 to A28.

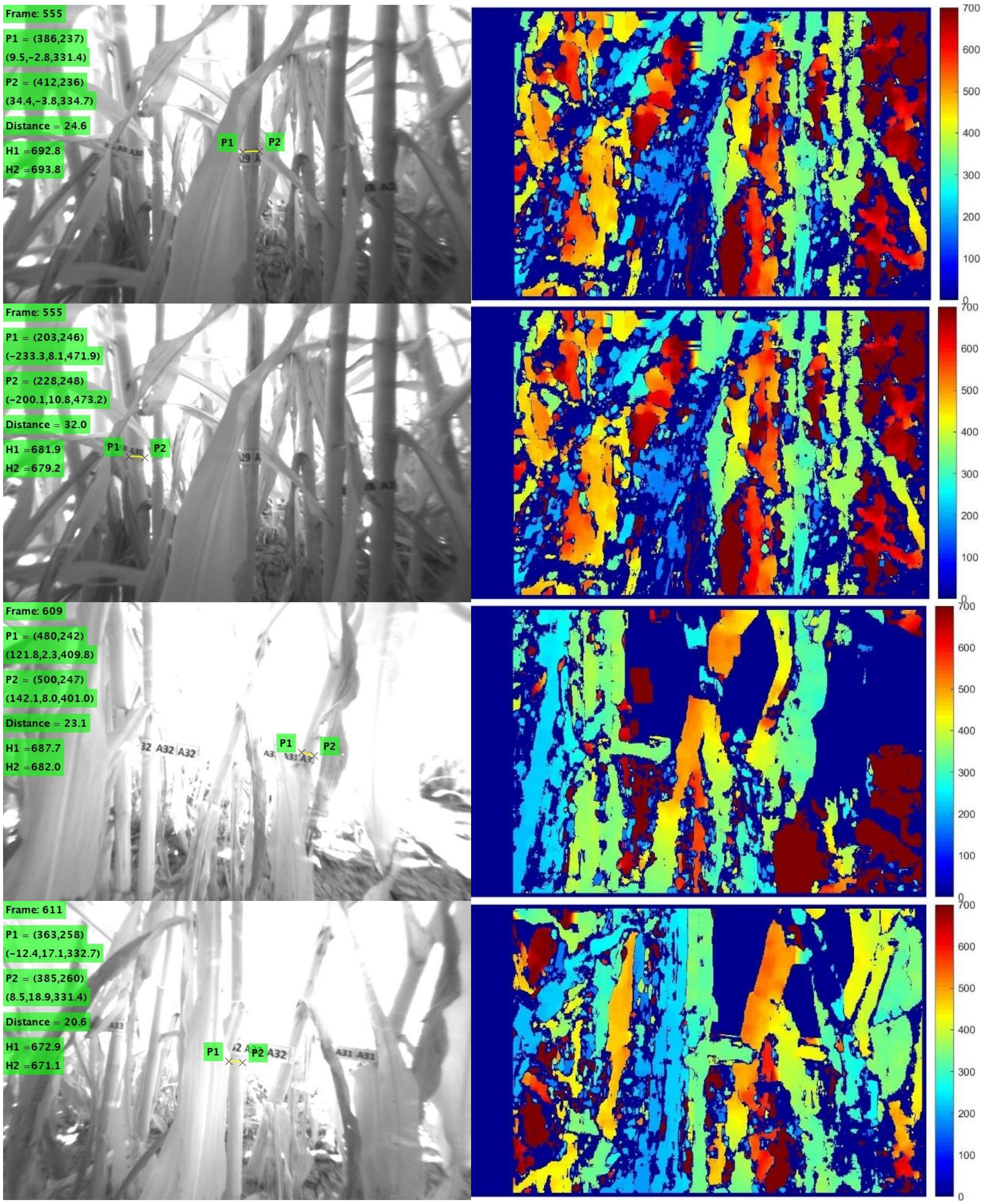

Figure D.8. Stalk thickness estimations using stereovision for plants A29 to A32.

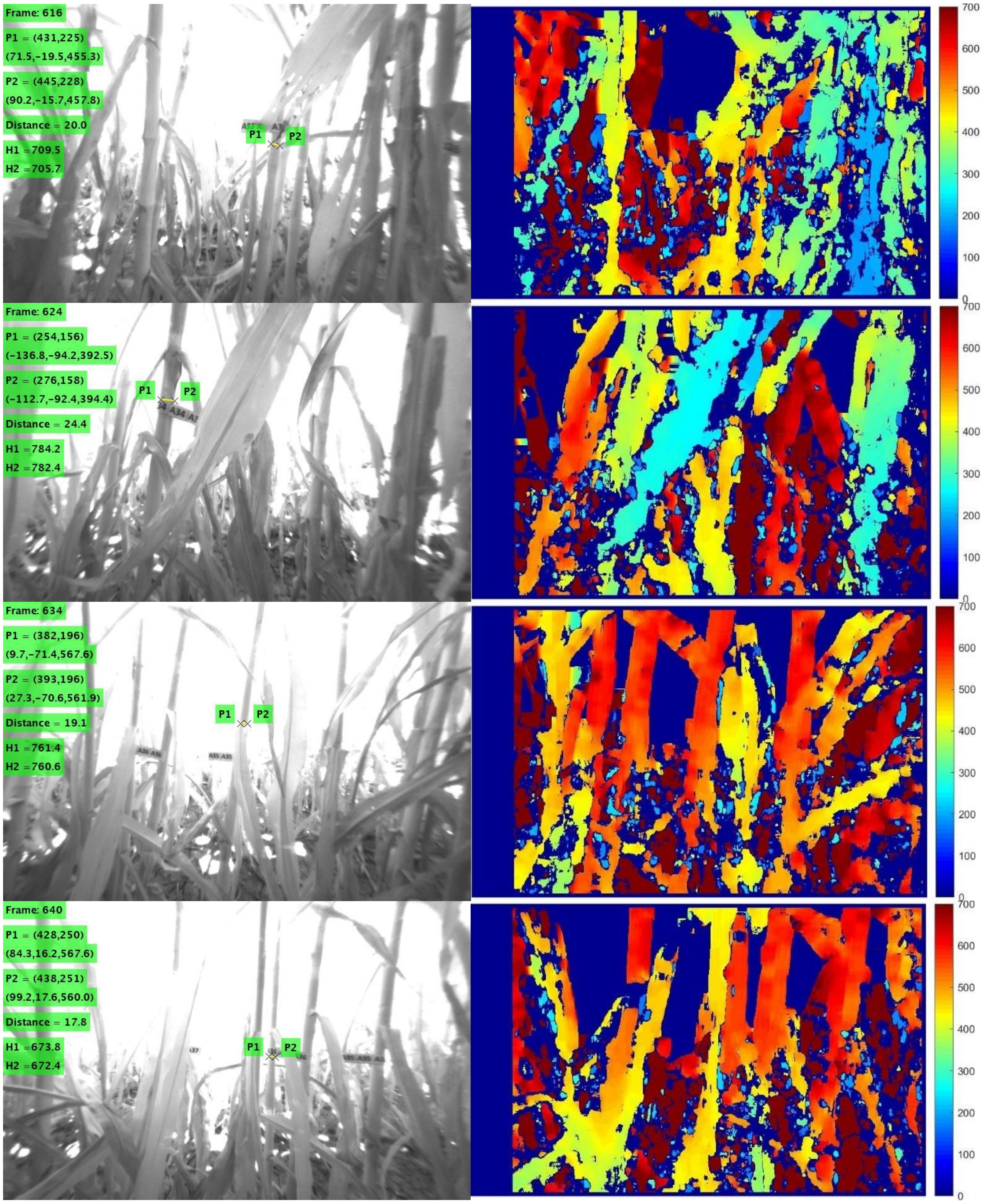

Figure D.9. Stalk thickness estimations using stereovision for plants A33 to A36.

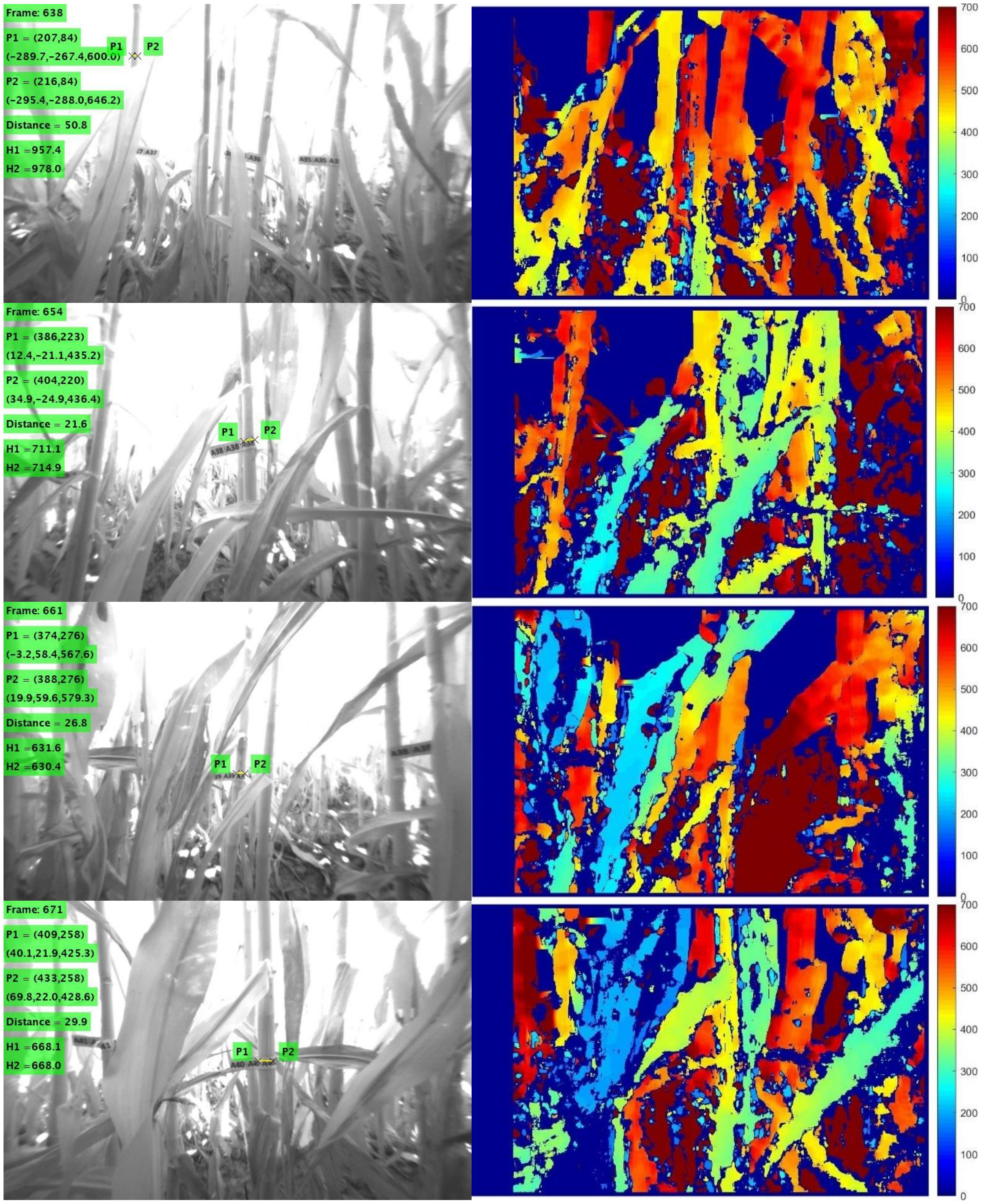

Figure D.10. Stalk thickness estimations using stereovision for plants A37 to A40.

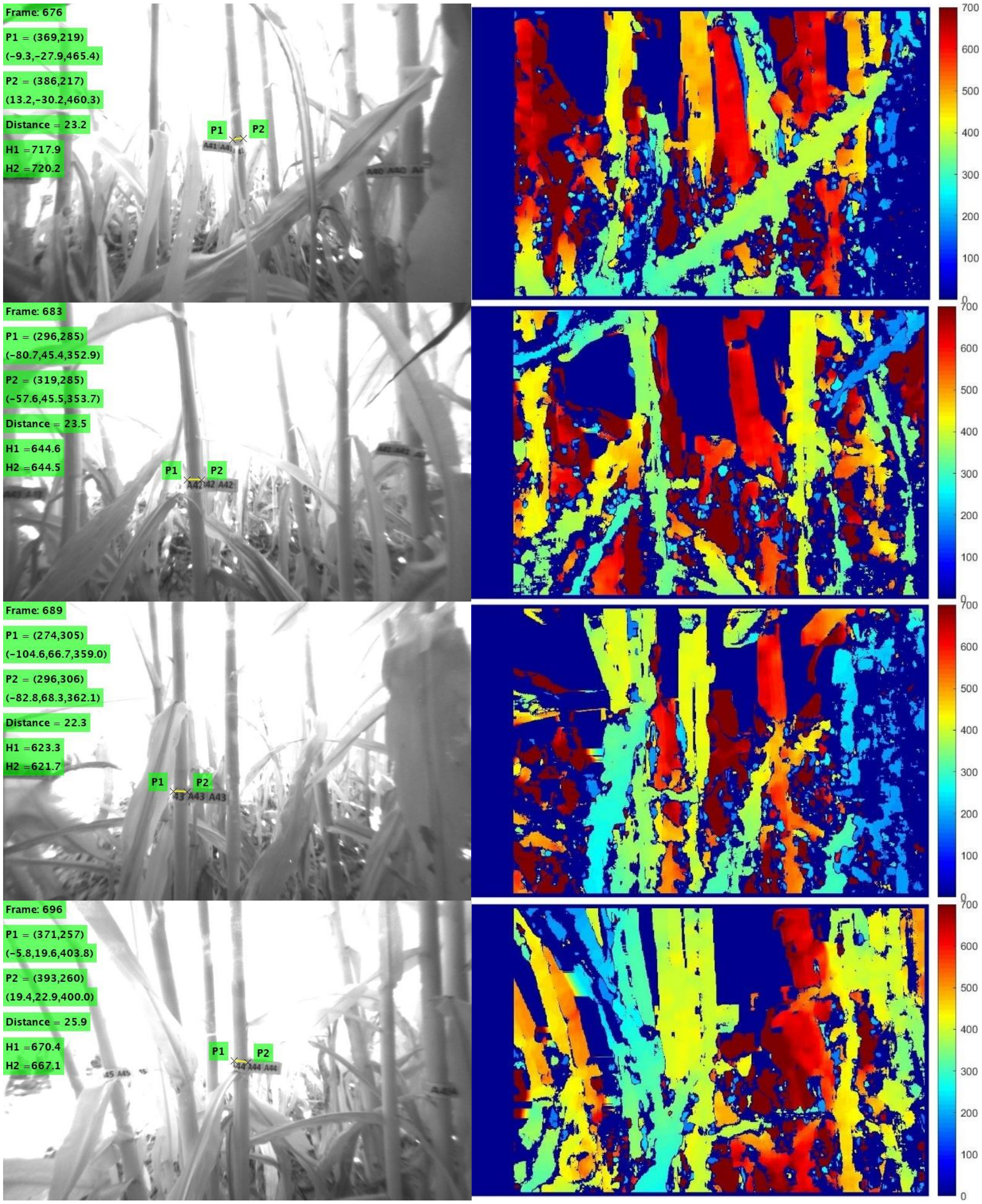

Figure D.11. Stalk thickness estimations using stereovision for plants A41 to A44.

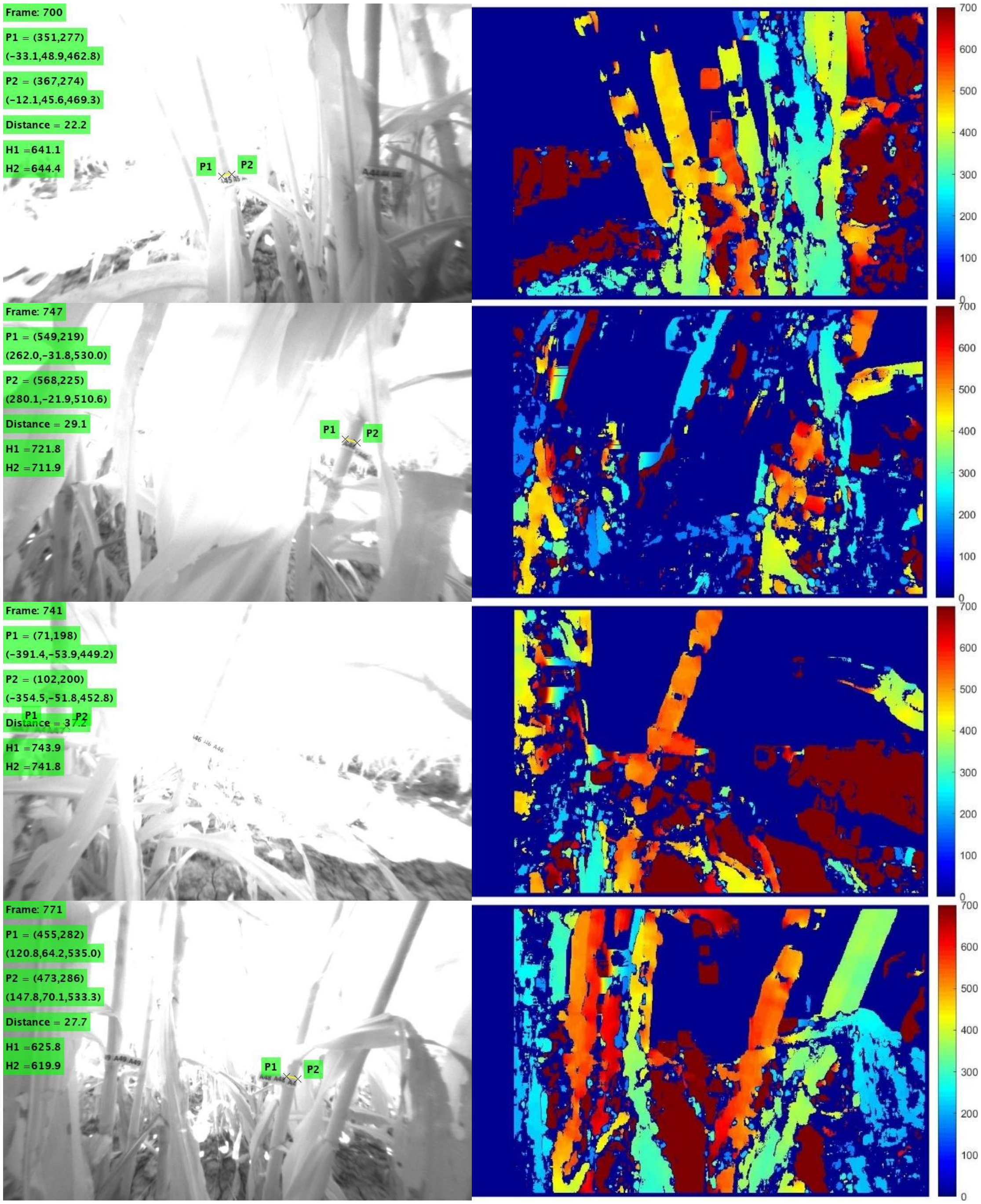

Figure D.12. Stalk thickness estimations using stereovision for plants A45 to A48.

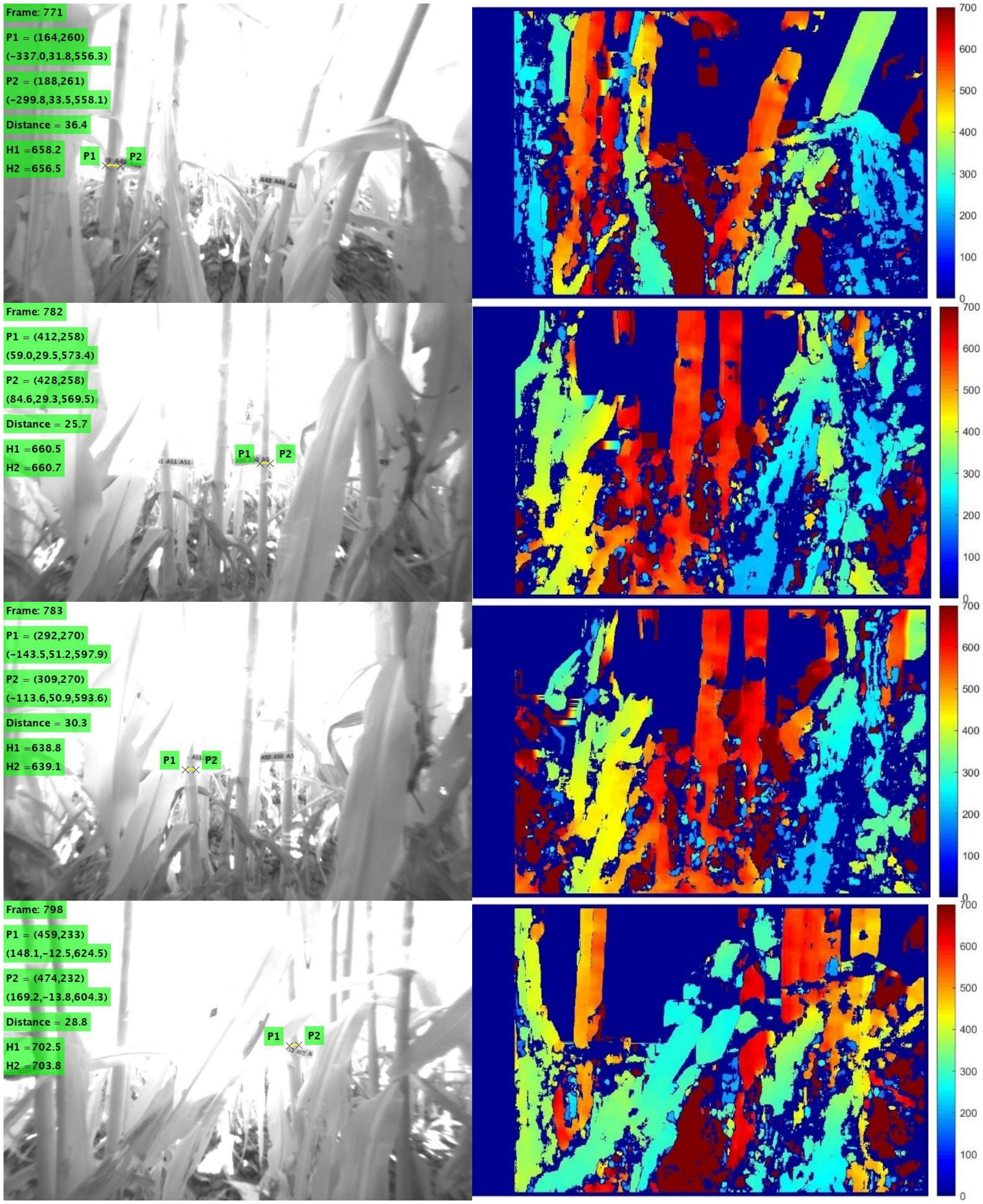

Figure D.13. Stalk thickness estimations using stereovision for plants A49 to A52.

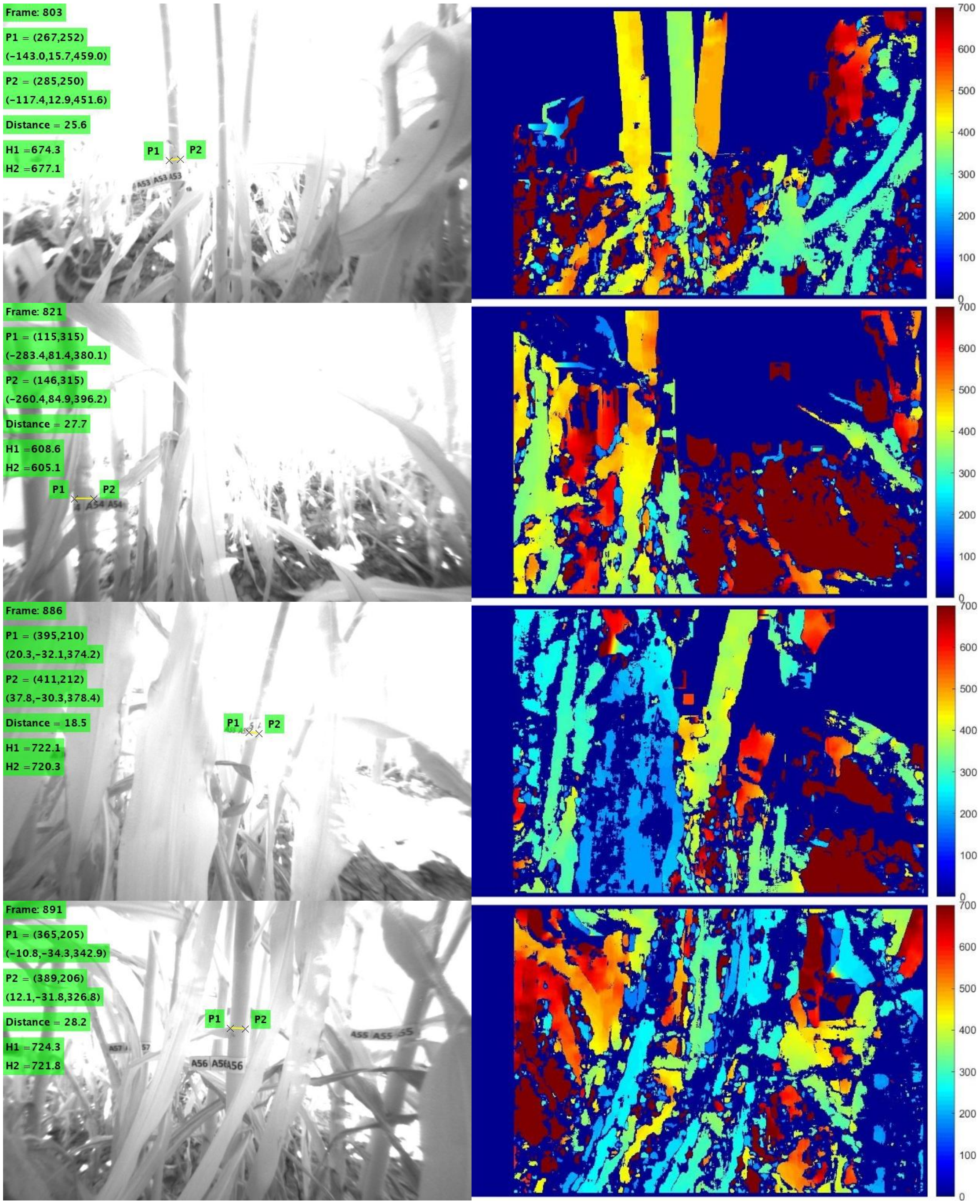

Figure D.14. Stalk thickness estimations using stereovision for plants A53 to A56.

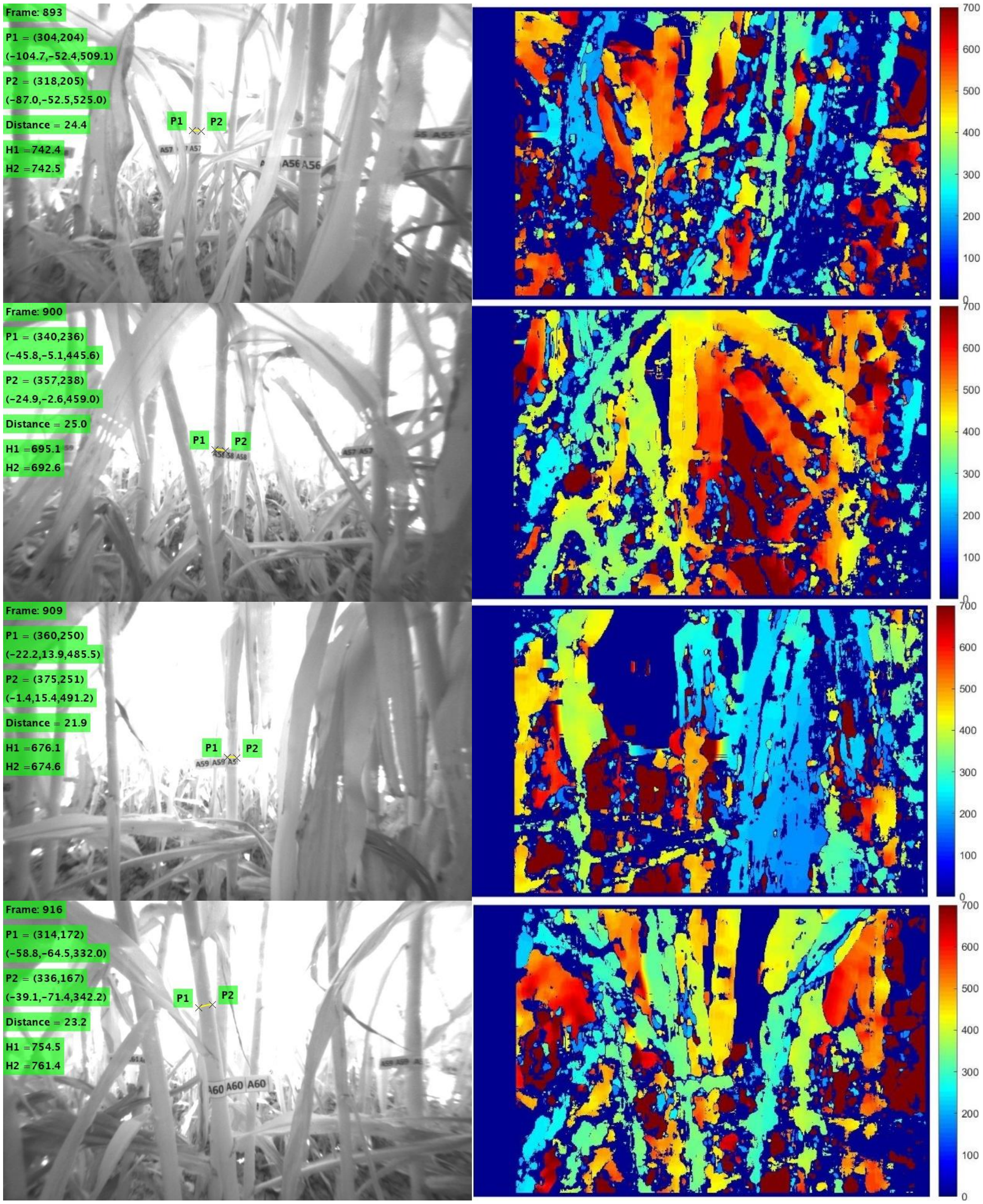

Figure D.15. Stalk thickness estimations using stereovision for plants A57 to A60.

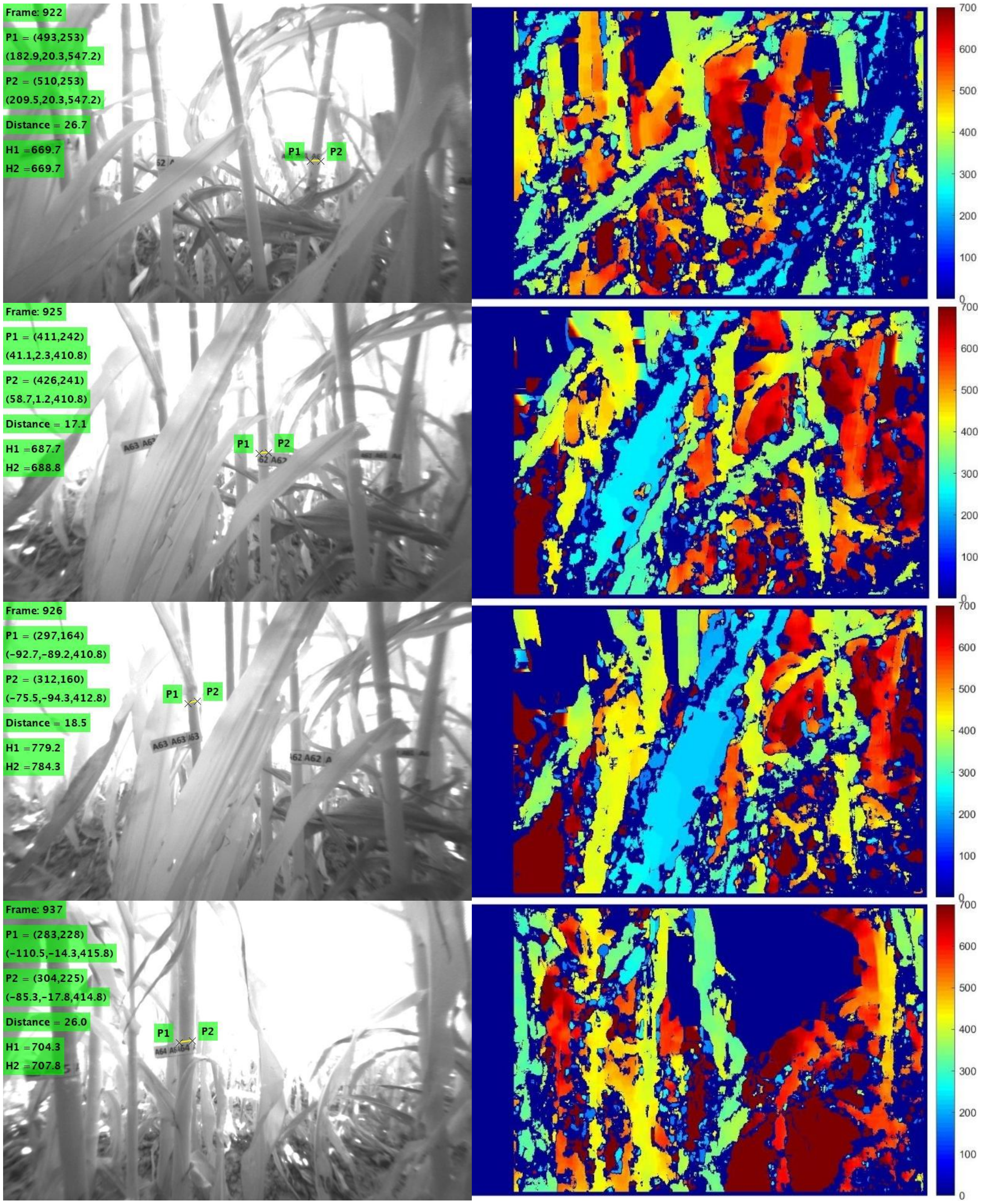

Figure D.16. Stalk thickness estimations using stereovision for plants A61 to A64.

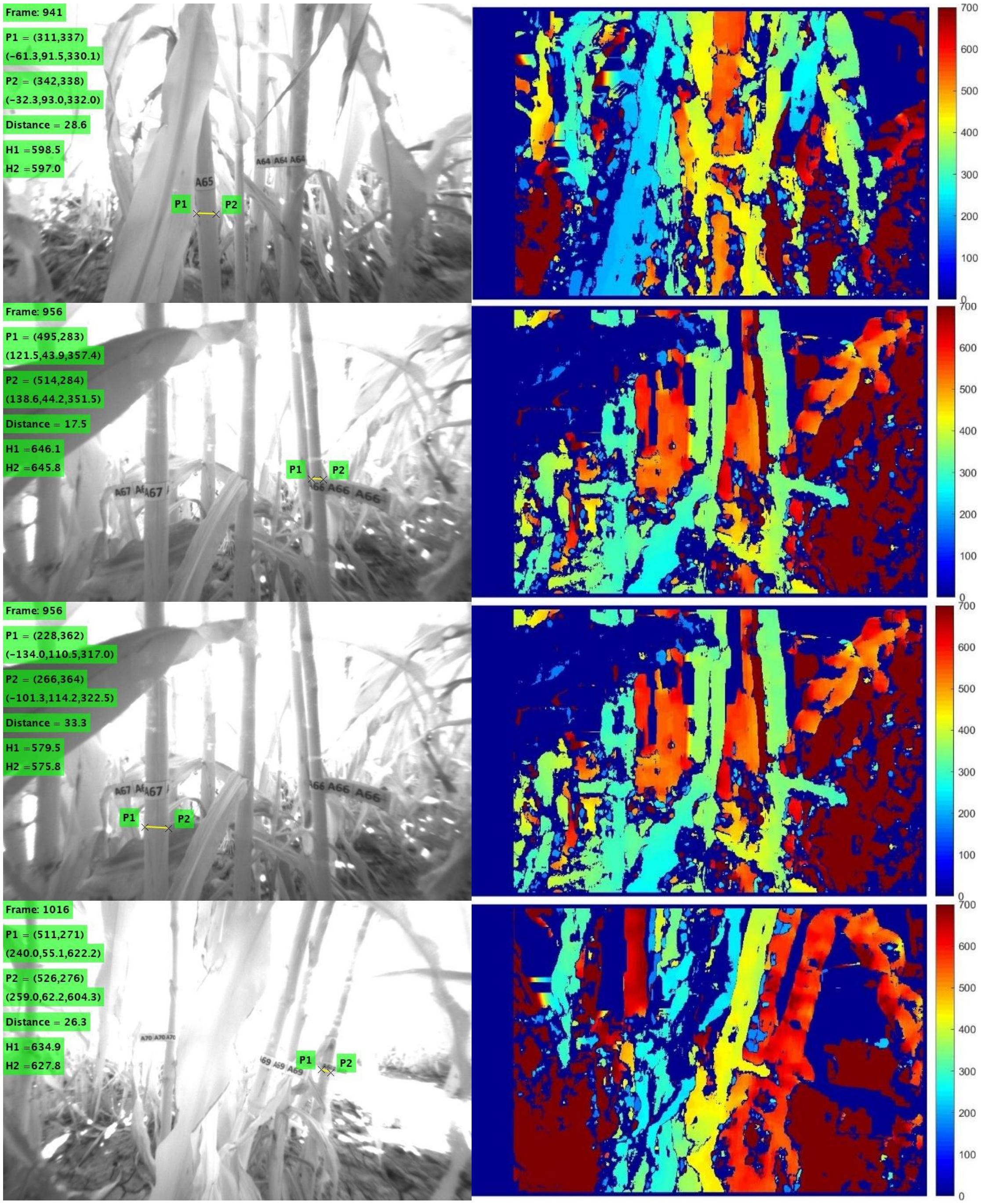

Figure D.17. Stalk thickness estimations using stereovision for plants A65 to A68.

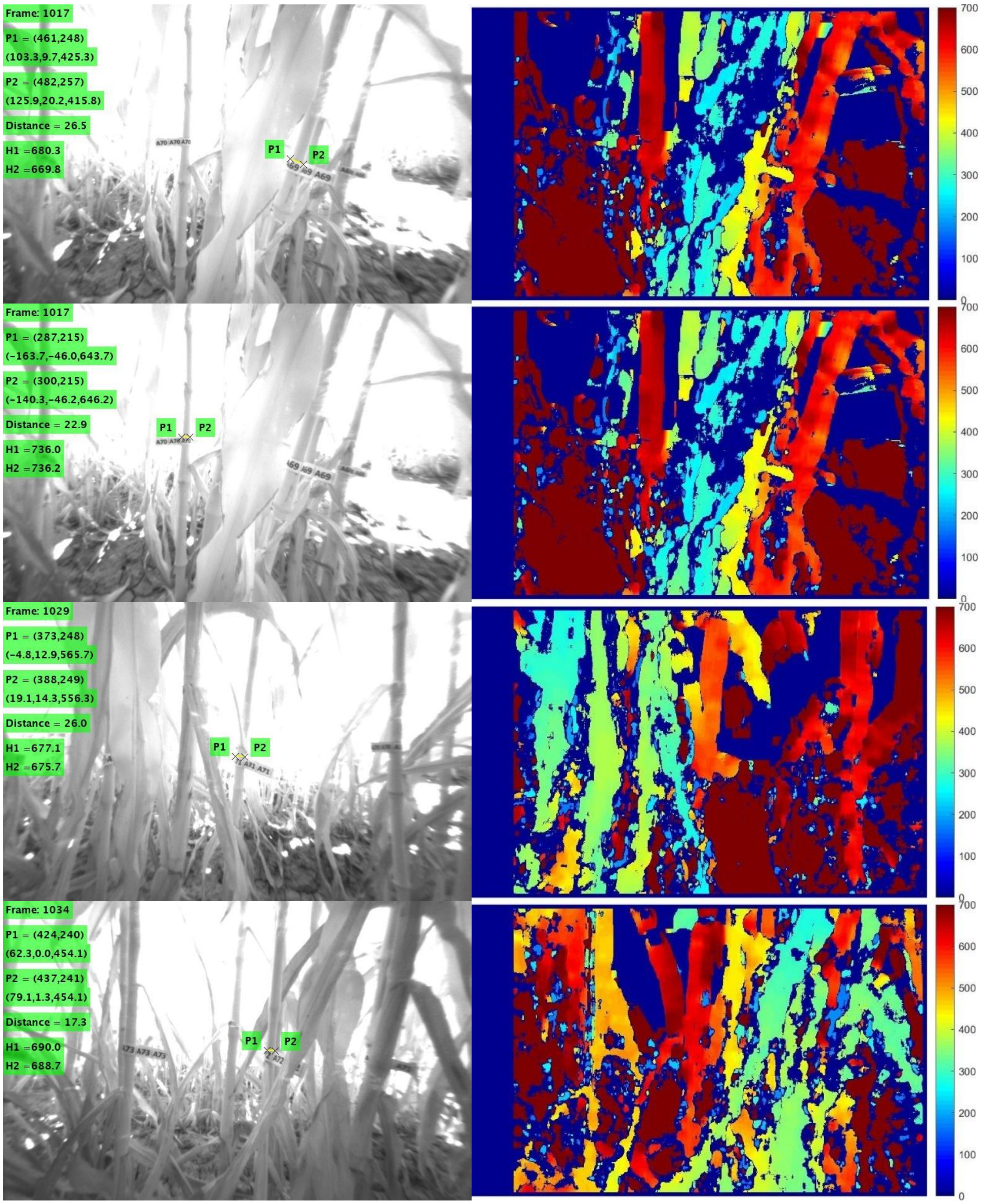

Figure D.18. Stalk thickness estimations using stereovision for plants A69 to A72.

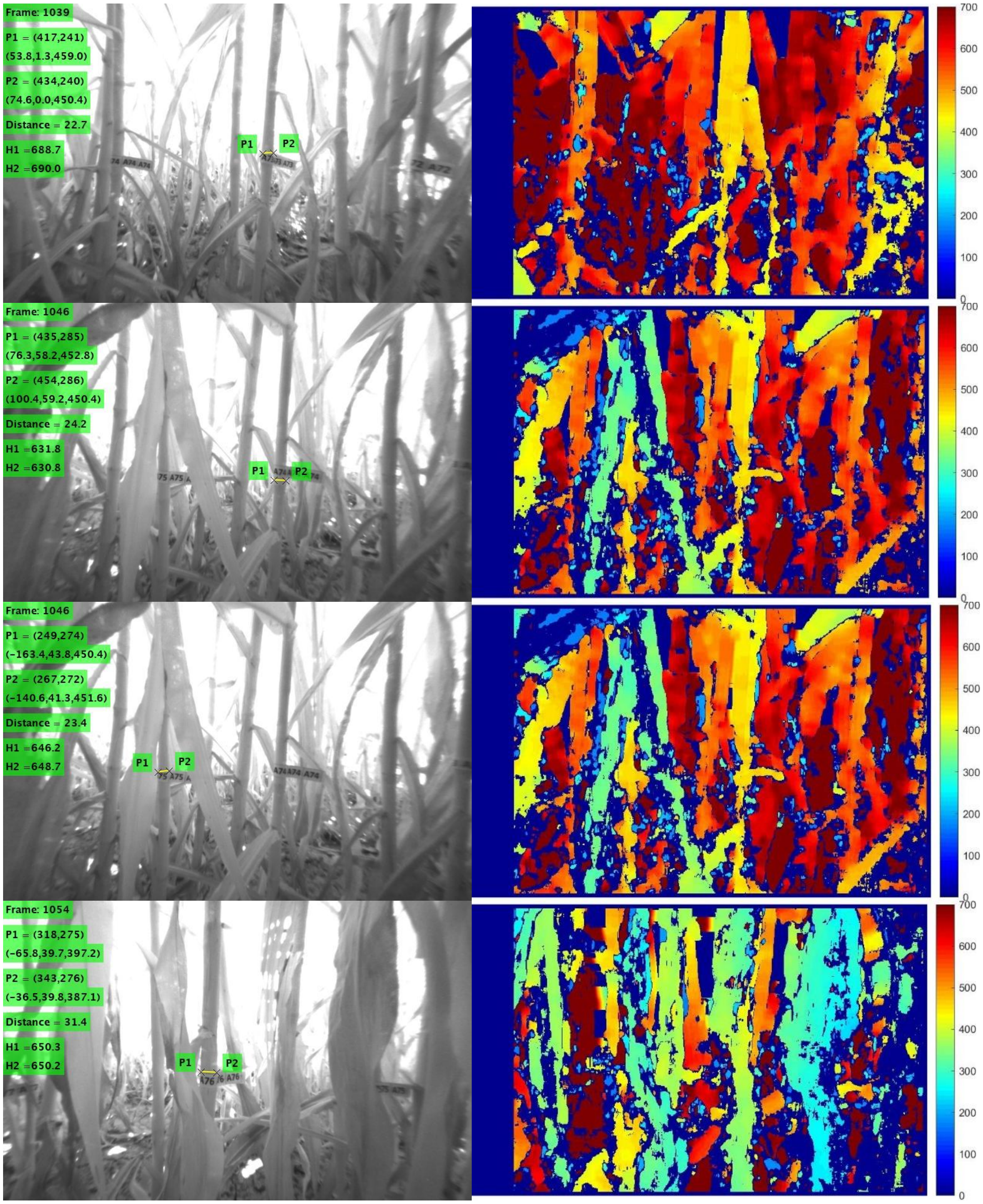

Figure D.19. Stalk thickness estimations using stereovision for plants A73 to A76.

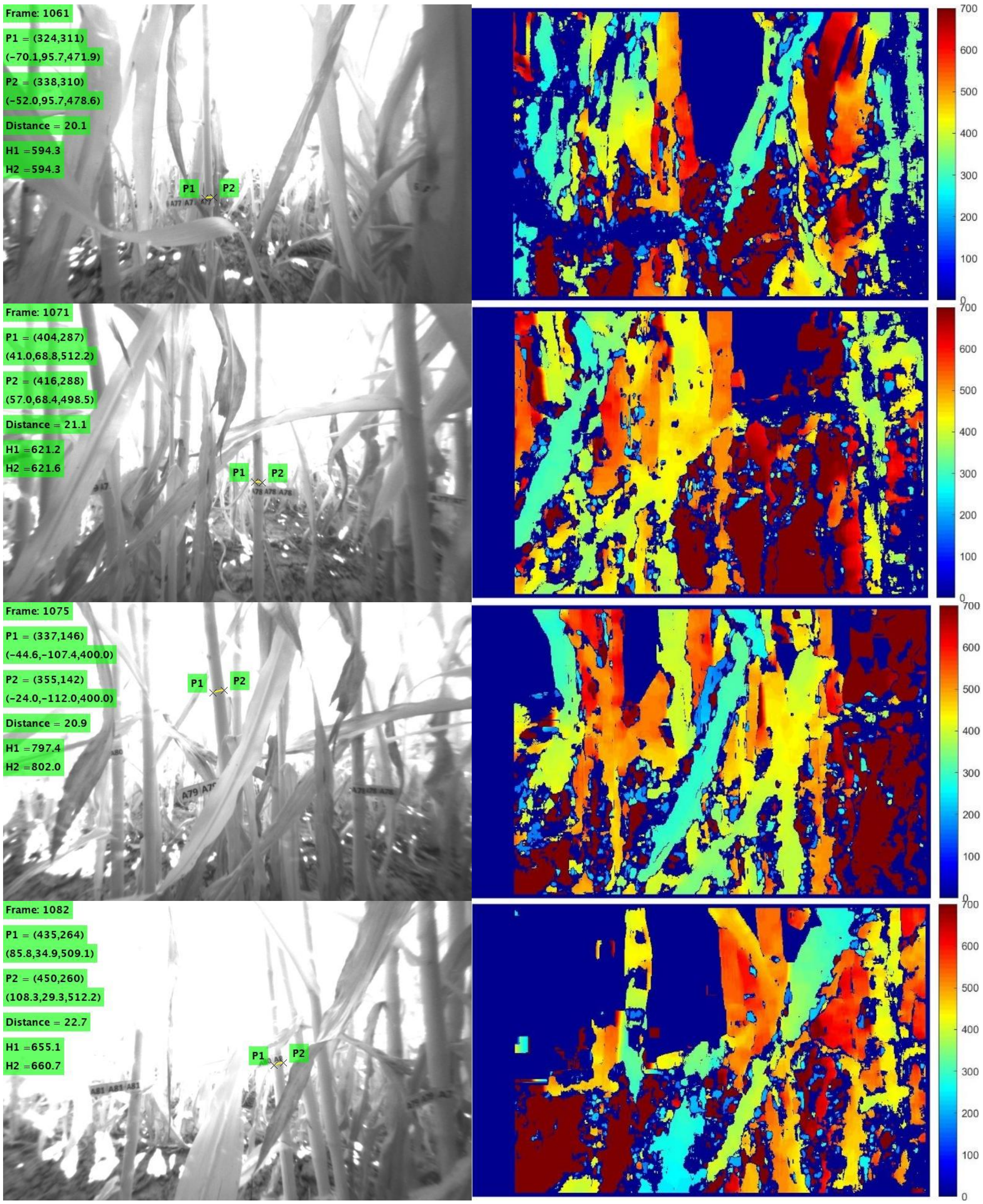

Figure D.20. Stalk thickness estimations using stereovision for plants A77 to A80.

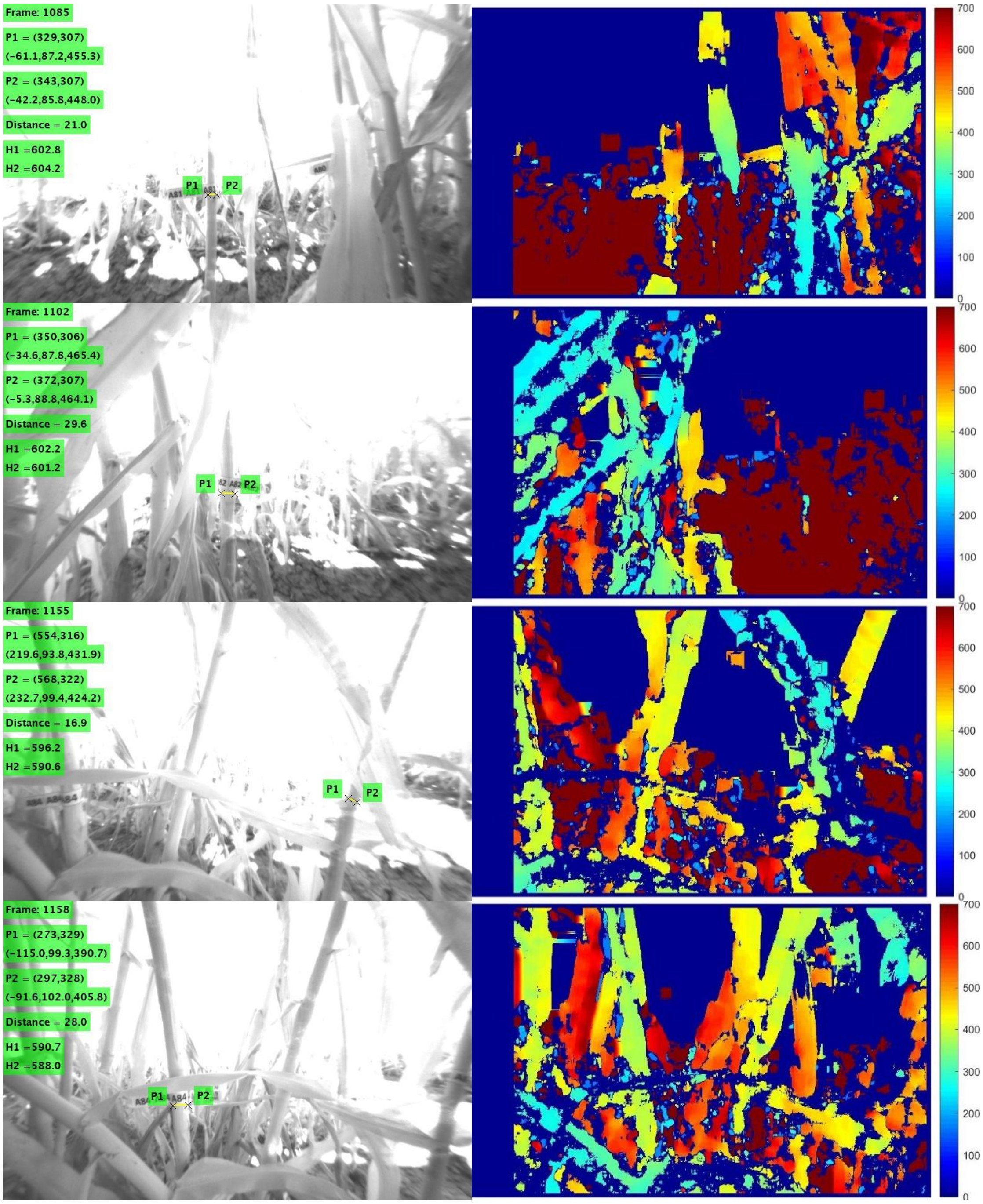

Figure D.21. Stalk thickness estimations using stereovision for plants A81 to A84.

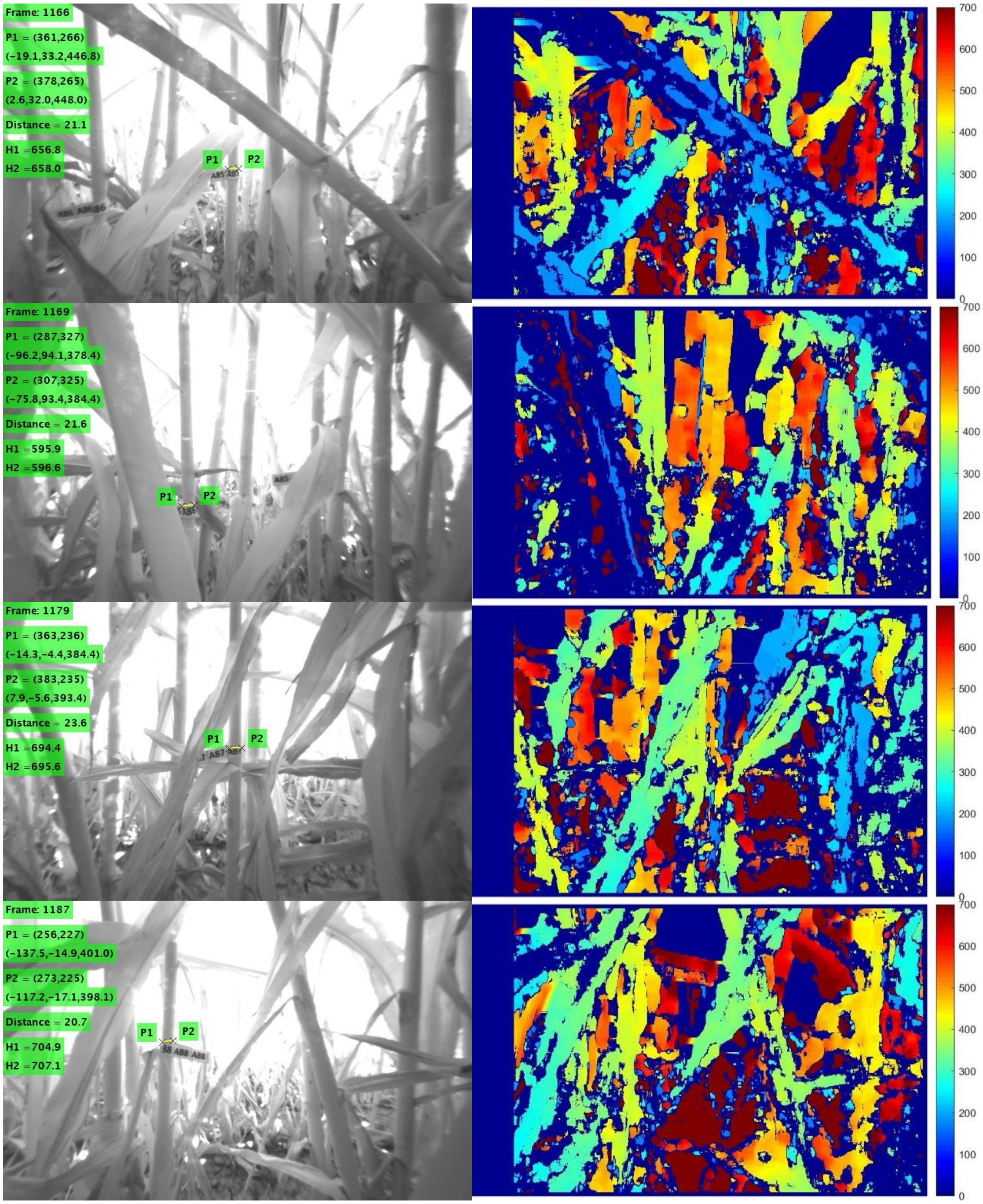

Figure D.22. Stalk thickness estimations using stereovision for plants A85 to A88.

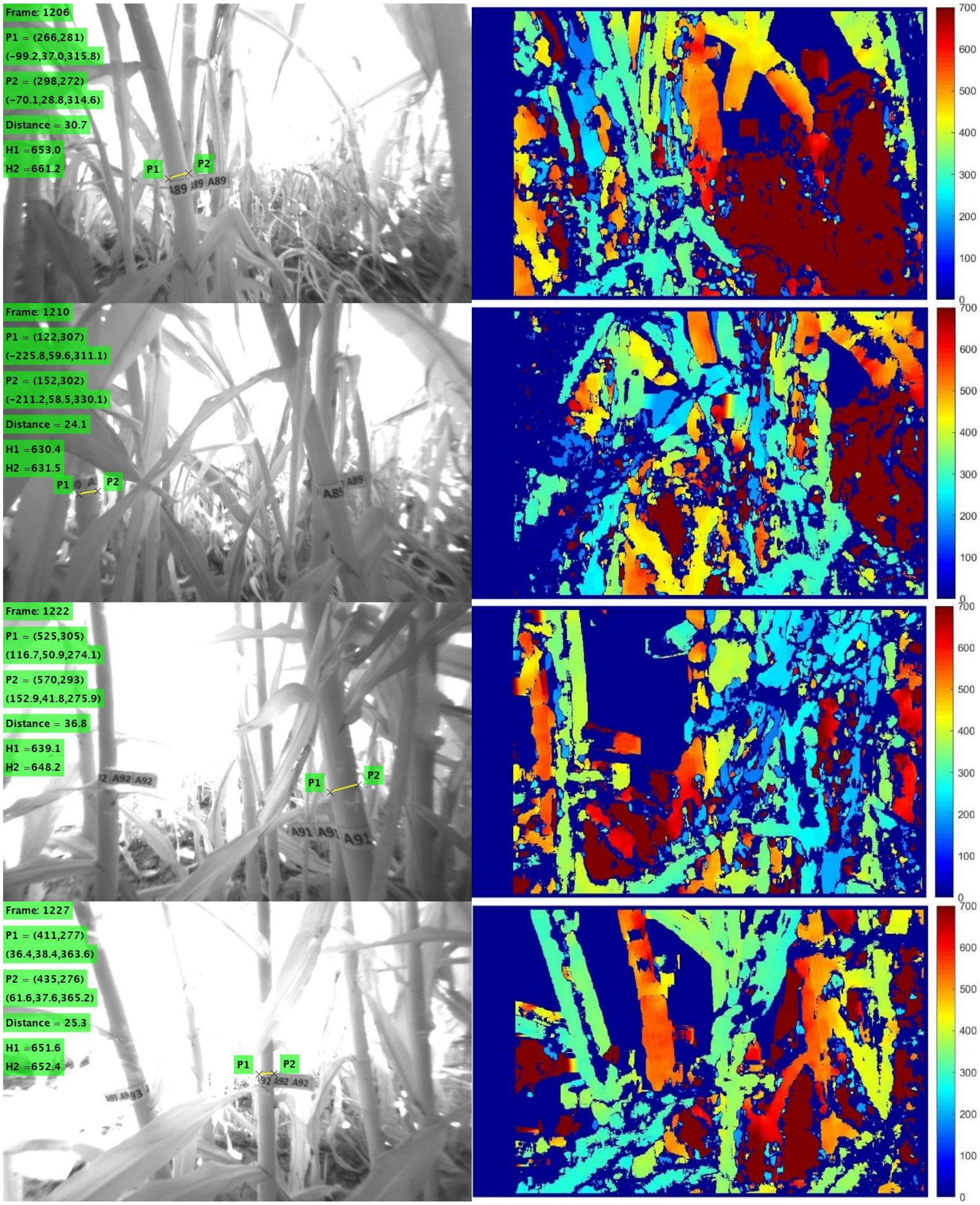

Figure D.23. Stalk thickness estimations using stereovision for plants A89 to A92.

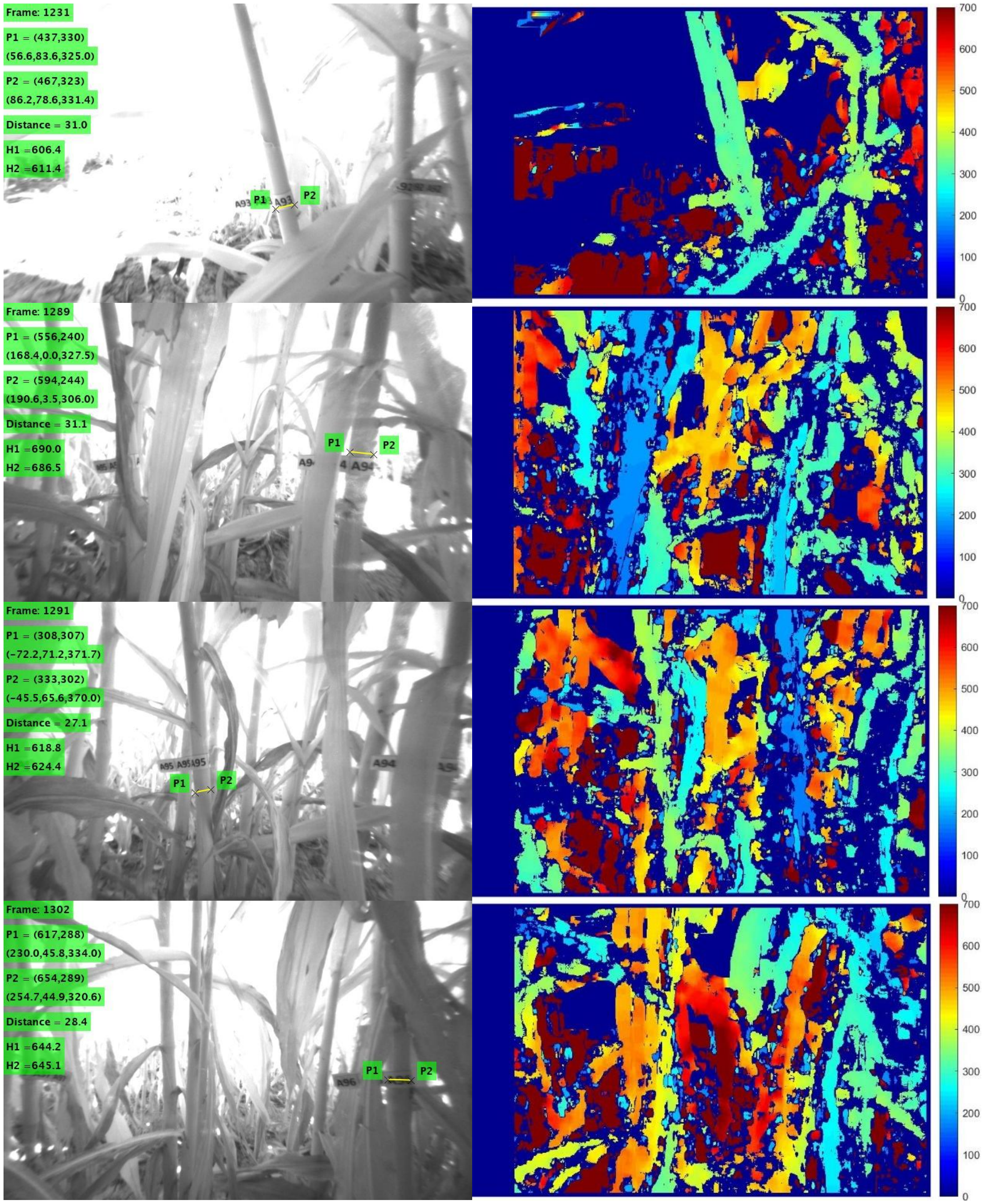

Figure D.24. Stalk thickness estimations using stereovision for plants A93 to A96.

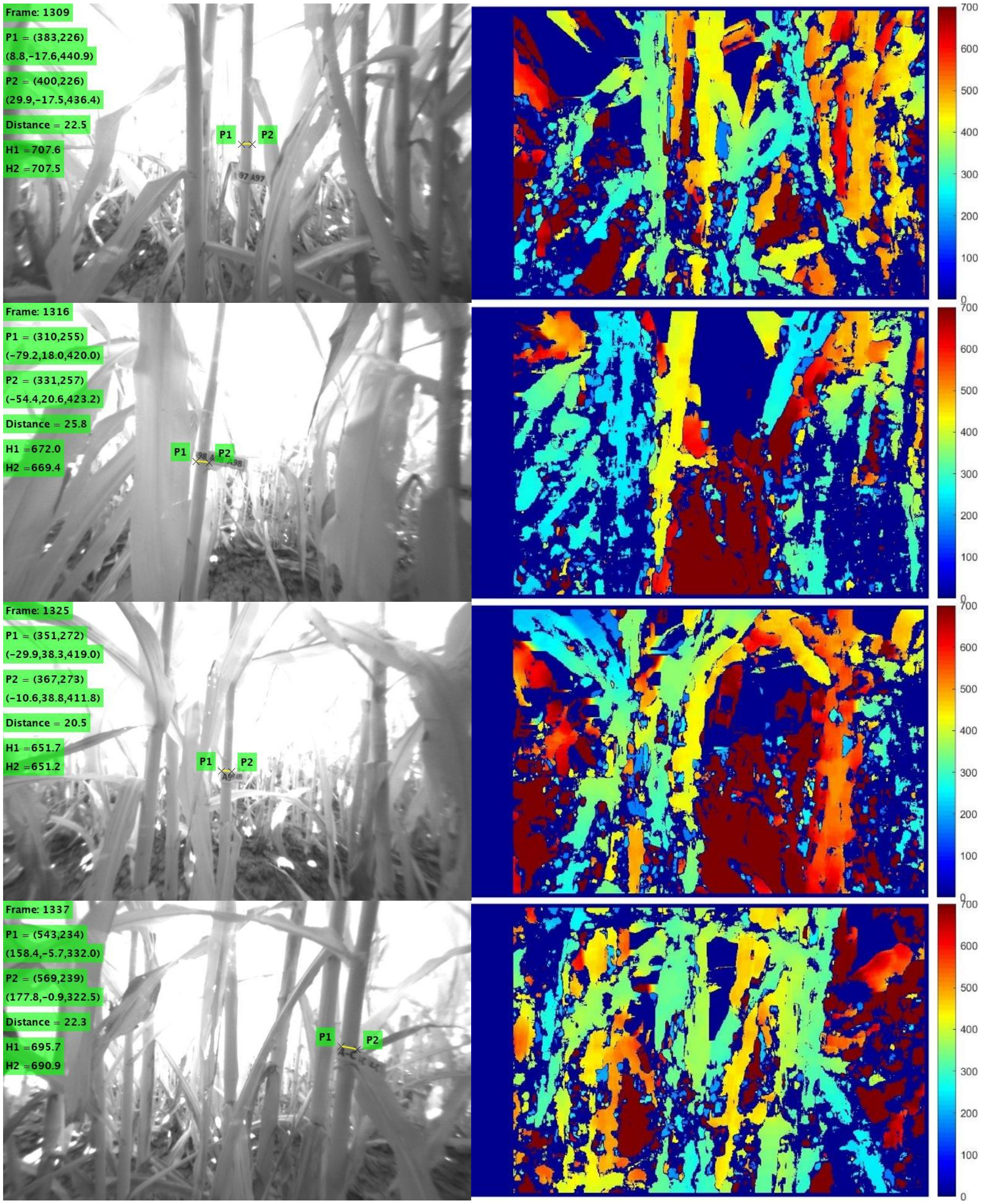

Figure D.25. Stalk thickness estimations using stereovision for plants A97 to A100.

APPENDIX E

SUSPENSION AND TRANSMISSION PARAMETERS

E.1. Eagle Golf Cart as Reference for Power Supply

2014 new golf carts, 2 seats, aluminum frame,EG202AK - Eagle Electric Vehicle Manufacturing Co., Ltd. 7/24/17, 18)42

EAGLE

export@eg-ev.com | skype | Inquiry Basket(0) | FAQ

Search

Home | Electric Vehicles | Accessaries | Testimonials | Resources | News | About Us | Contact Us

Home > Electric Vehicles > Electric Golf Carts > 2014 new electric golf utility cart, EG202AK

2014 new electric golf utility cart, EG202AK

Description:

EG202AK is Suzhou Eagle's 2014 new golf carts. It has many features like aluminum chassis, front independent suspension, EM brake, LED lights, etc.

Send Inquiry Now

Add To Inquiry List

Product Details | Inquiry Now

Key Components

Item	Description
Controller	Curtis controller, 275A-400A, imported from USA directly
Motor	Rated 3KW-5KW (4.08HP-6.8HP), ADC brand or Chinese brand Both DC motor and AC motor are available
Battery	Trojan battery, T875 or T105+, imported from USA directly
Charger	High Frequency onboard charger (input 90V-265V, 47-63HZ, output 48V/22A, 36V/25A)

Performance

Item	Description
Passenger Capacity	2
Range (loaded) (km)*	up to 100
Max.speed (km/h)	up to 40
Min.turning radius (m)	3
Max.climbing ability(loaded)	up to 25%

You May Also Like

2 seats golf cart, EG2028K

Electric golf buggies, 6 s...

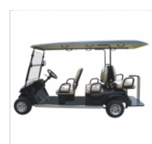

Electric golf cars, 6 seat...

golf cars for sale,6 seats...

Electric ambulance, EG2...

http://www.eagle-ev.com/index.php?route=product/product&path=17_24&product_id=135 Page 1 of 4

Figure E.1. 2014 golf utility cart, model EG202AK specs (page 1/2) (reprinted form Eagle, 2017).

Max. movement after brake at speed of 20km/h	≤4m
Max.loading weight (kgs)	270
Charging time (hour)	8-10
Battery lifespan (cycles)	750

* 1) based on the test conditions: 20km/h speed, flat and straight concrete road, wind speed less than 5m/s, temperature of 25 Celsius degree;

2) Range will vary depending on temperature, grade, payload and driving style.

Dimensions

Item	Description
Overall dimensions (mm)	2410x1180x1800 (LxWxH)
Min.ground clearance (mm)	120
Wheelbase (mm)	1680
Front wheel tread (mm)	1010
Rear wheel tread (mm)	1010

Body and Frame

Item	Description
Frame & Chassis	Aluminum alloy beam, bended
Body	PP plastic front and rear body cover, injected
Roof	Plastic
Windshield	One-piece organic glass (PMMA)
Roof supports	Aluminum with black powder coating
Cushion	Reborn sponge with artificial leather and plastic bottom cover
Backrest	Reborn sponge with artificial leather and plastic cover
Armrest	Plastic, black texture finish
Floor mat	Skidproof rubber
Centre sweater basket	Plastic, large volume
Golf bag holder	Plastic support with nylon strap
Dashboard	Black plastic, with F/R switch, battery power indicator, ignition key on it
Beverage holders	4 cups holders, 2 each side
Side trim	Plastic, black
Score card holder	On the steering wheel

Electric System

Item	Description
Lights	12V, headlight (with hight/low beam), front turning light, LED front position light, LED taillights (includes brake lights and turning light),
Horn	Electric horn, 12V

Figure E.2. 2014 golf utility cart, model EG202AK specs (page 2/2) (reprinted form Eagle, 2017).

E.2. Kawasaki Brute Force© ATV as Reference for Suspension

SPECIFICATIONS

2016 BRUTE FORCE® 300

POWER	
Engine	4-stroke, 1-cylinder, SOHC
Displacement	271cc
Bore x Stroke	72.7 x 65.2mm
Compression ratio	11.0:1
Fuel System	Keihin CVK32 Carburetor
Ignition	DC-CDI
Transmission	2-Speed automatic, reverse
Final Drive	2WD, Shaft

CAPABILITY	
Front Suspension / Wheel Travel	Double wishbone/5.2 in
Rear Suspension / Wheel Travel	Swingarm/5.6 in
Front Tire Size	AT 22 x 7-10 Maxxis® tubeless
Rear Tire Size	AT 22 x 10-10 Maxxis® tubeless
Front Brakes	Dual 180mm discs
Rear Brakes	Single 180mm disc
Ground Clearance	6.1 in
Starting System	Electrical with recoil backup
Fuel Capacity	3.2 gal
Turning Radius	9.2 ft
Towing Capacity	500 lb
Total Rack Capacity	110 lb
Rack Capacity, Front / Rear	44 lb/66 lb
Lighting	(2) 35W headlights, 5W taillight and 21W stoplight

DETAILS	
Frame Type	Double cradle, steel
Track Front/Rear	33.5/32.7 in
Overall Length	75.4 in
Overall Width	42.5 in
Overall Height	46.1 in
Seat Height	33.3 in
Curb Weight	535.8 lb**
Wheelbase	45.9 in
Instruments	Speedometer, odometer, clock, fuel gauge and coolant temp light
Color Choices	Super Black, Bright White
Warranty	12 Month Limited Warranty
Kawasaki Protection Plus™ (optional)	12, 24, 36, or 48 months

**Curb weight includes all necessary materials and fluids to operate correctly, full tank of fuel (more than 90 percent capacity) and tool kit (if supplied).

Kawasaki KAWASAKI.COM

Figure E.3. Datasheet of the reference vehicle to design the suspension system. Main features are curb weight of 243 kg, and an estimated average passenger weight of 91 kg, for a total of 334 kg (reprinted from Kawasaki, 2016).

E.3. Datasheets for Different Tire Models

sat-ii-23 3/16/16, 4:08 PM

(/EN-US/INDEX.HTML)

PRODUCTS

SOLUTIONS

TECHNOLOGY

RESOURCES

PROGRAMS

FIND A DEALER

OUR HERITAGE (/EN-US/ABOUT-US.HTML)

CONTACT US (/EN-US/CONTACT-US.HTML)

SEARCH

CONTACT US

1-844-64-TIRES

(1-844-648-4737)

(TEL:+18446484737)

SUPER ALL TRACTION II 23°

[R-1] Modern tread design to maximize traction and improve ride.

OVERVIEW

- Increased footprint to minimize soil compaction
- Increased number of lugs vs. Traction Field and Road for better wear and ride
- More lugs than our Traction Field & Road for better road wear and ride

APPLICATION

- Agricultural

RESOURCES

- LOAD & INFLATION - TABLE E (/CONTENT/DAM/BCS-SITES/FIRESTONE/AG/LOAD-INFLATION-TABLES/MAR2015/LOAD AND INFLATION - TABLE E.PDF)
- LOAD & INFLATION - TABLE F3 (/CONTENT/DAM/BCS-SITES/FIRESTONE/AG/LOAD-INFLATION-TABLES/MAR2015/LOAD AND INFLATION - TABLE F3.PDF)
- AGRICULTURAL BIAS TIRE WARRANTY (/CONTENT/DAM/BCS-SITES/FIRESTONE/AG/WARRANTIES/MAR2015/BIAS-WARRANTY.PDF)
- AGRICULTURAL TIRE WARRANTY - CANADA (/CONTENT/DAM/BCS-SITES/FIRESTONE/AG/WARRANTIES/MAR2015/CANADIAN-

SPECIFICATIONS

Size(Ply/Star Rating)

250/85D16.5

Unit

STANDARD METRIC

APPLICATION	AGRICULTURAL
TECHNOLOGY	BIAS 23° TREAD BAR ADVANTAGE
ARTICLE NUMBER	365401
TIRE SIZE	250/85D16.5
LOAD INDEX	92
PLY/STAR RATING	
MEAS. RIM (IN.)	8.25
OVERALL WIDTH (MM)	249
OVERALL DIAMETER (MM)	838
STATIC LOADED RADIUS (MM)	378
ROLLING CIRCUMFERENCE (MM)	2515
ROLLING CIRCUMFERENCE INDEX	0
TREAD DEPTH (MM)	31.8
FLAT PLATE (CM^2)	445
MAX. SPEED (KPH)	0

http://commercial.firestone.com/en/agriculture/product/sat-ii-23 Page 1 of 3

Figure E.4. Specifications of the Firestone Super All Traction 23º tire model (page 1/3) (reprinted from Bridgestone Americas, 2020).

WARRANTY.PDF)

FIND A DEALER

DOWNLOAD SPEC SHEET

(/CONTENT/DAM/BCS-SITES/FIRESTONE/AG/PRODUCT-BROCHURES/NEW2015/MAR2015/BIAS BROCHURE_D-118 (03-15).PDF)

MINIMUM DUAL SPACING (MM)	0
MAX. TIRE LOAD (KG)	850
INFLATION PRESSURE (KPA)	159
LOAD INFLATION TABLE	TABLE E (/CONTENT/DAM/BCS-SITES/FIRESTONE/AG/LOAD-INFLATION-TABLES/MAR2015/LOAD AND INFLATION - TABLE E.PDF)

(/EN-US/SOLUTIONS/OFF-THE-ROAD/PRODUCT-SEARCH.HTML)

(HTTP://WWW.BRIDGESTONENATIONALFLEET.COM) ... TECHNOLOGY/AD2.HTML)

CONSTRUCTION TIRES

Firestone construction tires are designed and tested for specific equipment and environments to meet performance needs.

FOR FLEETS

No two fleets are alike. That's why we refuse to provide generic products, services, answers. Instead, we listen and create solutions specific to your needs.

AD² FARM TIRE TECHNOLOGY

Firestone's AD² technology can carry the same load at lower pressures – available in both IF and VF designations.

OFF-THE-ROAD (/EN-US/SOLUTIONS/OFF-THE-ROAD.HTML)

TRUCK & BUS (/EN-US/SOLUTIONS/TRUCK-AND-BUS.HTML)

AGRICULTURE (/EN-US/SOLUTIONS/AGRICULTURE

OFF-THE-ROAD

- Backhoe (/En-Us/Off-The-Road/Backhoe-Tires)
- Container Handler (/En-Us/Off-The-Road/Container-Handler-Tires)
- Dump Truck - Rigid (/En-Us/Off-The-Road/Rigid-Dump-Truck-Tires)
- Grader (/En-Us/Off-The-Road/Grader-Tires)
- Loader/Dozer (/En-Us/Off-The-Road/Loader-Tires)
- Scraper (/En-Us/Off-The-Road/Scraper-Tires)
- Skid Steer (/En-Us/Off-The-Road/Skid-Steer-Tires)
- Specialty (/En-Us/Off-The-Road/Specialty-Tires)
- Straddle Carrier (/En-Us/Off-The-Road/Straddler-Tires)

PRODUCTS

SOLUTIONS

TECHNOLOGY

RESOURCES

PROGRAMS

OUR HERITAGE (/EN-US/ABOUT-US.HTML)

FIND A DEALER

AG DEALER (HTTP://DEALERSUPPORT.FI

THE TREAD (HTTP://WWW.THETREAD.C(

PASSENGER TIRES (HTTP://WWW.FIRESTONETI

FIRESTONE AG:

Figure E.5. Specifications of the Firestone Super All Traction 23º tire model (page 2/3) (reprinted from Bridgestone Americas, 2020).

TRACTORS

MICHELIN Multibib™ (XM108) Technical Data

320/65 R16 107A8/104B TL XM108™

MSPN : 46787 **CAI : 123896**

See notes on page 14 for guidance on correct application of these load / pressure tables.

Load per tire				
30 mph 50 km/h	25 mph 40 km/h	20 mph 30 km/h	6 mph 10 km/h	Pressure
		820 lbs	840 lbs	6 psi
		370 kgs	380 kgs	0.4 bar
900 lbs	970 lbs	1,040 lbs	1,110 lbs	7 psi
410 kgs	440 kgs	470 kgs	505 kgs	0.5 bar
1,100 lbs	1,190 lbs	1,260 lbs	1,390 lbs	9 psi
500 kgs	540 kgs	570 kgs	630 kgs	0.6 bar
1,280 lbs	1,390 lbs	1,470 lbs	1,680 lbs	12 psi
580 kgs	630 kgs	665 kgs	760 kgs	0.8 bar
1,460 lbs	1,580 lbs	1,680 lbs	1,950 lbs	15 psi
660 kgs	715 kgs	760 kgs	885 kgs	1.0 bar
1,630 lbs	1,760 lbs	1,880 lbs	2,240 lbs	17 psi
740 kgs	800 kgs	855 kgs	1,015 kgs	1.2 bar
1,810 lbs	1,960 lbs	2,090 lbs	2,510 lbs	20 psi
820 kgs	890 kgs	950 kgs	1,140 kgs	1.4 bar
1,980 lbs	2,160 lbs	2,290 lbs	2,800 lbs	23 psi
900 kgs	980 kgs	1,040 kgs	1,270 kgs	1.6 bar
			3,080 lbs	26 psi
			1,395 kgs	1.8 bar
			3,220 lbs	28 psi
			1,460 kgs	1.9 bar

Tire Technical Data				Rims (preferred in bold)
Unloaded Dimensions		Loaded Dimensions		
Overall Width	Overall Diameter	Loaded Radius	Rolling Circumference	**W8** W8L W9 W10L
12.2 in	33.2 in	14.8 in	98.5 in	
309 mm	844 mm	375 mm	2,501 mm	

Rolling Circumference Index	Number of Lugs	Tube MSPN	Tube CAI
	17 x 2	03500	813635

Gross Flat Plate	100% Tire Volume	Tread Depth	Minimum Dual/Triple Spacing
101 sq in	22.7 gals	35/32nd	16.5 in
649 sq cm	86 liters	28 mm	420 mm

420/65 R24 126A8/126B TL XM108™

MSPN : 77842 **CAI : 122712**

See notes on page 14 for guidance on correct application of these load / pressure tables.

Load per tire				
30 mph 50 km/h	25 mph 40 km/h	20 mph 30 km/h	6 mph 10 km/h	Pressure
		1,740 lbs	2,180 lbs	6 psi
		790 kgs	990 kgs	0.4 bar
1,870 lbs	1,870 lbs	2,090 lbs	2,580 lbs	7 psi
850 kgs	850 kgs	950 kgs	1,170 kgs	0.5 bar
2,290 lbs	2,290 lbs	2,450 lbs	2,980 lbs	9 psi
1,040 kgs	1,040 kgs	1,110 kgs	1,350 kgs	0.6 bar
2,540 lbs	2,660 lbs	2,840 lbs	3,460 lbs	12 psi
1,150 kgs	1,205 kgs	1,290 kgs	1,570 kgs	0.8 bar
2,780 lbs	3,020 lbs	3,230 lbs	3,940 lbs	15 psi
1,260 kgs	1,370 kgs	1,465 kgs	1,785 kgs	1.0 bar
3,020 lbs	3,380 lbs	3,620 lbs	4,420 lbs	17 psi
1,370 kgs	1,535 kgs	1,640 kgs	2,005 kgs	1.2 bar
3,260 lbs	3,750 lbs	4,010 lbs	4,910 lbs	20 psi
1,480 kgs	1,700 kgs	1,820 kgs	2,225 kgs	1.4 bar
3,510 lbs			5,380 lbs	23 psi
1,590 kgs			2,440 kgs	1.6 bar
3,630 lbs			5,620 lbs	25 psi
1,645 kgs			2,550 kgs	1.7 bar
3,750 lbs				26 psi
1,700 kgs				1.8 bar

Tire Technical Data				Rims (preferred in bold)
Unloaded Dimensions		Loaded Dimensions		
Overall Width	Overall Diameter	Loaded Radius	Rolling Circumference	**W11** W10 W12
15.6 in	45.7 in	20.0 in	134.8 in	
395 mm	1,160 mm	507 mm	3,425 mm	

Rolling Circumference Index	Number of Lugs	Tube MSPN	Tube CAI
37	20 x 2	89251	170039

Gross Flat Plate	100% Tire Volume	Tread Depth	Minimum Dual/Triple Spacing
214 sq in	52.8 gals	47/32nd	20.7 in
1,382 sq cm	200 liters	37 mm	527 mm

Figure E.6. Technical data for Michelin Multibib, model XM108 (reprinted from Michelin, 2020).

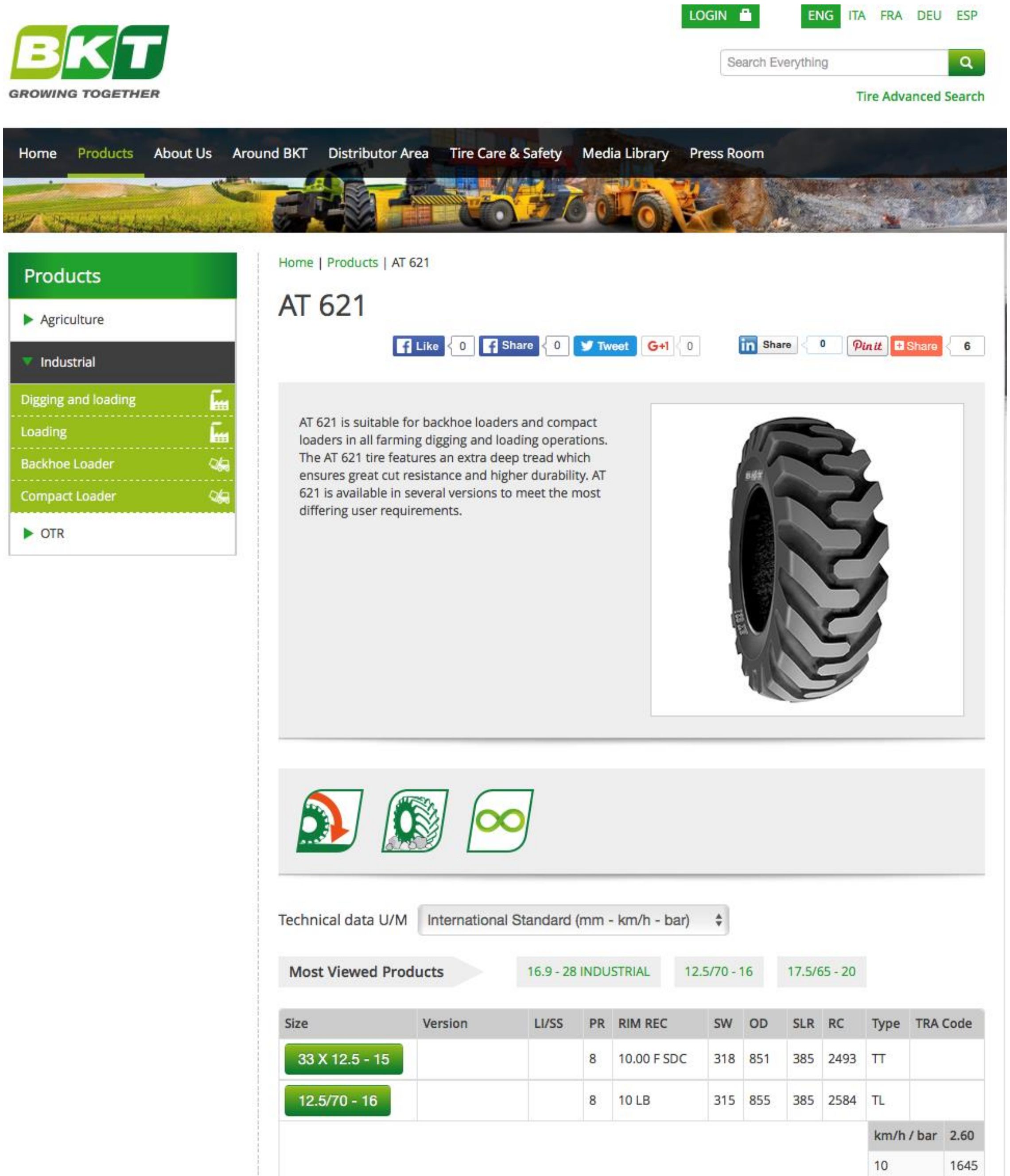
LOGIN
ENG ITA FRA DEU ESP
Search Everything
Tire Advanced Search
Home Products About Us Around BKT Distributor Area Tire Care & Safety Media Library Press Room
Products
Agriculture
Industrial
Digging and loading
Loading
Backhoe Loader
Compact Loader
OTR
Home | Products | AT 621
AT 621
Like 0 Share 0 Tweet G+1 0 Share 0 Pin it Share 6
AT 621 is suitable for backhoe loaders and compact loaders in all farming digging and loading operations. The AT 621 tire features an extra deep tread which ensures great cut resistance and higher durability. AT 621 is available in several versions to meet the most differing user requirements.
Technical data U/M International Standard (mm - km/h - bar)
Most Viewed Products 16.9 - 28 INDUSTRIAL 12.5/70 - 16 17.5/65 - 20

Size	Version	LI/SS	PR	RIM REC	SW	OD	SLR	RC	Type	TRA Code
33 X 12.5 - 15			8	10.00 F SDC	318	851	385	2493	TT	
12.5/70 - 16			8	10 LB	315	855	385	2584	TL	

km/h / bar	2.60
10	1645

Figure E.7. Technical data for BKT, model AT 621 (reprinted from BKT, 2019).

E.4. Driveshaft Specs Requirements

Brazos Valley Drivelines, Inc.

840 N. Harvey Mitchell Pkwy.
Bryan, Texas 77807

(979) 775-3535

[Fax: 979-775-0105]

October 21, 2016

Mario A. Mendez
Graduate Student
Biological & Agricultural Engineering
Texas A&M University
229 Scoates Hall
College Station, TX 77843

Re: Quotation on supplying one driveshaft.
Mr. Mendez,

We are able to supply one new driveshaft to fit the application you detailed:

1. Gearbox shaft dia: 1.0 in (up to 2.2 in long).
2. Gearbox shaft pin hole: 3/8 in at 1.0 in, after shaft end (center).
3. Motor shaft dia: 1.0 in, keyway 1/4x1/8, up to 2.2 in long.
4. End-to-end shafts distances: 23 25 in.
5. Distance between shaft centers: 1.5 3.5 in.
6. Distance between driveshaft ends: 23 25 in
7. Angle: 4.4 - 7.9 degrees
8. RPM: 2,500
9. Max torque: 22 lb-ft (30 N-m)

Our price for the complete unit is $644.00.
We can have this complete and ready to pick up within 2 days of receiving the order.
Our payment terms are “net 30 days”, we will accept a purchase order number. We will not add sales tax to the invoice.

Thanks for allowing us to quote.

Bill Averyt

Bill Averyt
(president)

Figure E.8. Full list of design parameters for the drive shaft, and quote.

References of Appendix E

Eagle (2017). Electric Golf Utility Cart, model EG202AK, 2014. Suzhou Eagle Electric Vehicle Manufacturing Co., Ltd. Suzhou, Jiangsu, China. Available online: https://www.eagleev.com/index.php?route=product/product&path=17_24&product_id=135 (accessed on 18 November 2020).

BKT (2019). AT 621 Agricultural Tire. Balkrishna Industries Limited. Mumbai, India. Available online: https://www.bkt-tires.com/ww/en/at-621 (accessed on 18 November 2020).

Bridgestone Americas (2020). Super All Traction II 23° Agricultural Tire. Bridgestone Americas Tire Operations LLC. Nashville, Tennessee, USA. Available online: https://commercial.firestone.com/en/agriculture/product/sat-ii-23# (accessed on 18 November 2020).

Kawasaki Motors Corp. (2020). ATV Brute Force 300, model year 2016. Santa Ana, California, USA. Available online: https://www.kawasaki.com/en-us/atv/atv-utility-recreation/utility-recreation/brute-force-300/2021-brute-force-300?cm_re=MPP-_-BRUTEFORCE%C2%AE300:MODELS-_-VIEWSPECSDETAILS (accessed on 17 November 2020).

Michelin (2020). Michelin Multibib XM108 Agricultural Tire. Michelin North America, Inc. Greenville, South Carolina, USA. Available online: https://agricultural.michelinman.com/us/Our-Tires/Tractor/US-MULTIBIB (accessed on 18 November 2020).

APPENDIX F

MATLAB® SCRIPTS AND SIMULATOR FOR THE EGPV

F.1. Torsion in Top Structure

```
%TORSION Maximum Shear Stress Calculation on the 6" Round Tube

% Script created by Mario Mendez. 11 April 2016.

% Input parameters:
m = 2000;              % Vehicle mass (kg).
v = 2.22;              % Vehicle speed (m/s).
D1 = 5;                % Minor diameter (in).
D2 = 6;                % Major diameter (in).
L = 60;                % Round tube length (in).
sigma_y = 275e+06;     % Yield strength (Pa), from www.metalsdepot.com.
E = 68.9e+09;          % Modulus of elasticity (Pa), from Hibbeler (2014).
nu = 0.35;             % Poisson's ratio.

% Conversions of diameters to radii, and length from inches to meters:
r1 = D1 * 0.0254 / 2; % Minor radius (m).
r2 = D2 * 0.0254 / 2; % Mayor radius (m).
l = L * 0.0254;        % Round tube length (m).

% Kinetic energy (N-m)
K = 0.5 * m * v^2;

% Torque (N-m)
T = K;

% Polar moment of area (m^4)
J = pi / 2 * ( r2^4 - r1^4);

% Shear stress at radius r (Pa)
tau_max = T * r2 / J;

% Modulus of rigidity
G = E / ( 2*(1+nu) );

% Angular deflection (rad)
phi = T * l / (J * G);

% Linear displacement (mm)
u_y = r2 * sin(phi);

% Shear strain
gamma_xy = tau_max / G;

% Factor of safety
FOS = sigma_y / 2 / tau_max;
```

F.2. Suspension Parameters

```
%SUSPENSION_PARAMETERS  Mass parameters for the dynamic simulation of the
% quarter suspension model.
%
% Script created by Mario Mendez. 15 March 2016.

mtf = 135.127;   % top frame
mbf = 72.304*2;  % bottom frame (frm-b-04)
ms  = 4.334*4;   % suspension (sus-03)
mmdf = 32.853*2; % motor and drive shafts
mel  = 75.825*2; % electric mass
msb = 4*37;      % suspension brackets
%%%%
msm = 13.308;    % suspension mobile parts (sus-01)
mgb = 51.015;    % gearbox
mwt = 51.797;    % wheel and tire

mv = mtf + mbf + ms + mmdf + mel + msb; % vehicle

% masses
m1 = mv/4;
m2 = msm + mgb + mwt;

% stiffness
k1 = 49035;
k2 = 209943;

% friction
b1 = 4576;
b2 = 458;
```

F.3. Quarter Suspension Simulator

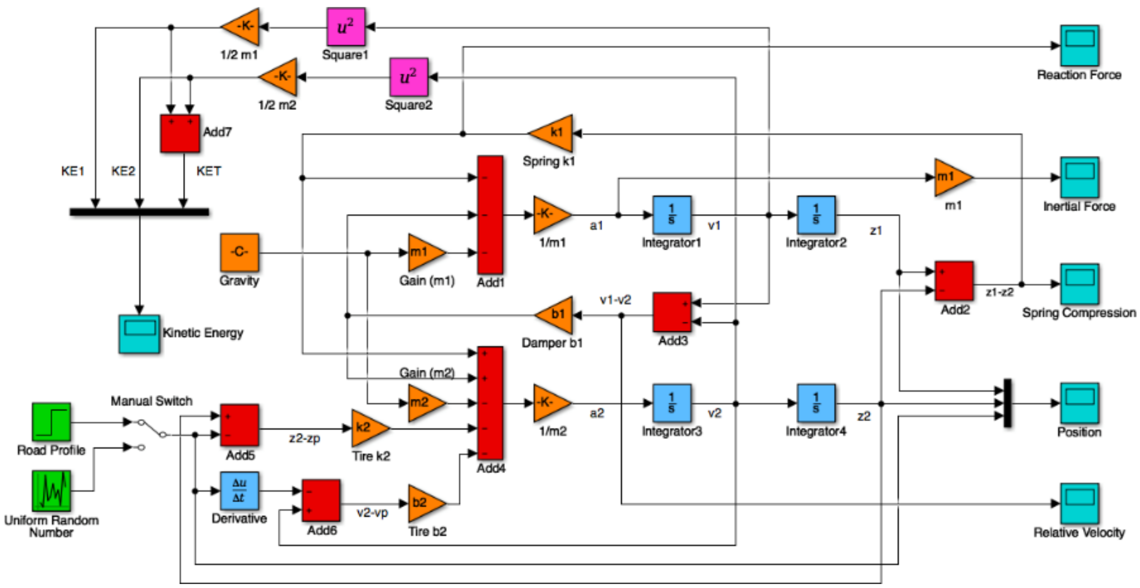

Figure F.1. Numerical block diagram suspension simulator. File name suspension_simulator.slx (Simulink).

APPENDIX G

MESH DETAILS FOR FEA

Table G.1. Mesh details for torsion simulation in part tub-rnd.sldprt.

	Mesh 1	Mesh 2	Mesh 3	Mesh 4	Mesh 5
Study name	Torsion (-FEA-)	Torsion (-FEA-)	Torsion (-FEA-)	Torsion (-FEA-)	Torsion (-FEA-)
Mesh type	Solid Mesh	Solid Mesh	Solid Mesh	Solid Mesh	Solid Mesh
Mesher Used	Curvature based	Curvature based	Curvature based	Curvature based	Curvature based
Jacobian points	4 points	4 points	4 points	4 points	4 points
Max Element Size	46 mm	37 mm	28 mm	19 mm	10 mm
Min Element Size	46 mm	37 mm	28 mm	19 mm	10 mm
Mesh quality	High	High	High	High	High
Total nodes	3613	7285	12819	20893	123185
Total elements	1774	3637	6367	10447	71826
Maximum Aspect Ratio	9.0897	7.3436	5.1152	4.8273	4.0736
Percentage of elements with Aspect Ratio < 3	30.8	53.2	98.5	98.7	99.5
Percentage of elements with Aspect Ratio > 10	0	0	0	0	0
Percentage of distorted elements (Jacobian)	0	0	0	0	0
Time to complete mesh (hh:mm:ss)	0:00:01	0:00:01	0:00:02	0:00:03	0:00:08
Computer name	R-APP-001	R-APP-001	R-APP-001	R-APP-001	R-APP-001

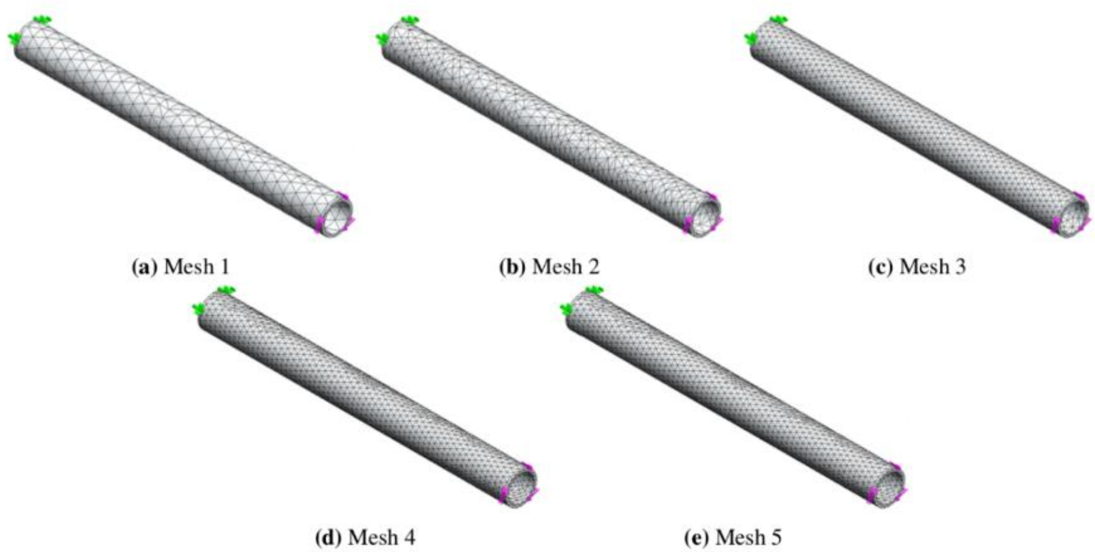

(a) Mesh 1 **(b)** Mesh 2 **(c)** Mesh 3

(d) Mesh 4 **(e)** Mesh 5

Figure G.1. Five different meshes for FEA in tub-rnd-01.sldprt.

Table G.2. Mesh details for torsion simulation in part plt-frm-01.sldprt with fixture in the weld annular surface.

	Mesh 1	Mesh 2	Mesh 3	Mesh 4	Mesh 5
Study name	Torsion Weld	Torsion Weld	Torsion Weld	Torsion Weld	Torsion Weld
Mesh type	Solid Mesh	Solid Mesh	Solid Mesh	Solid Mesh	Solid Mesh
Mesher Used	Curvature based	Curvature based	Curvature based	Curvature based	Curvature based
Jacobian points	4 points	4 points	4 points	4 points	4 points
Max Element Size	16 mm	13 mm	10 mm	7 mm	4 mm
Min Element Size	16 mm	13 mm	10 mm	7 mm	4 mm
Mesh quality	High	High	High	High	High
Total nodes	3829	6027	11936	31503	137849
Total elements	1847	3121	6755	19139	90345
Maximum Aspect Ratio	6.168	7.5621	4.3279	5.1269	5.0086
Percentage of elements with Aspect Ratio < 3	90.1	95.5	99.4	99.7	99.8
Percentage of elements with Aspect Ratio > 10	0	0	0	0	0
Percentage of distorted elements (Jacobian)	0	0	0	0	0
Time to complete mesh (hh:mm:ss)	0:00:01	0:00:02	0:00:01	0:00:02	0:00:06
Computer name	R-APP-096	R-APP-096	R-APP-096	R-APP-096	R-APP-096

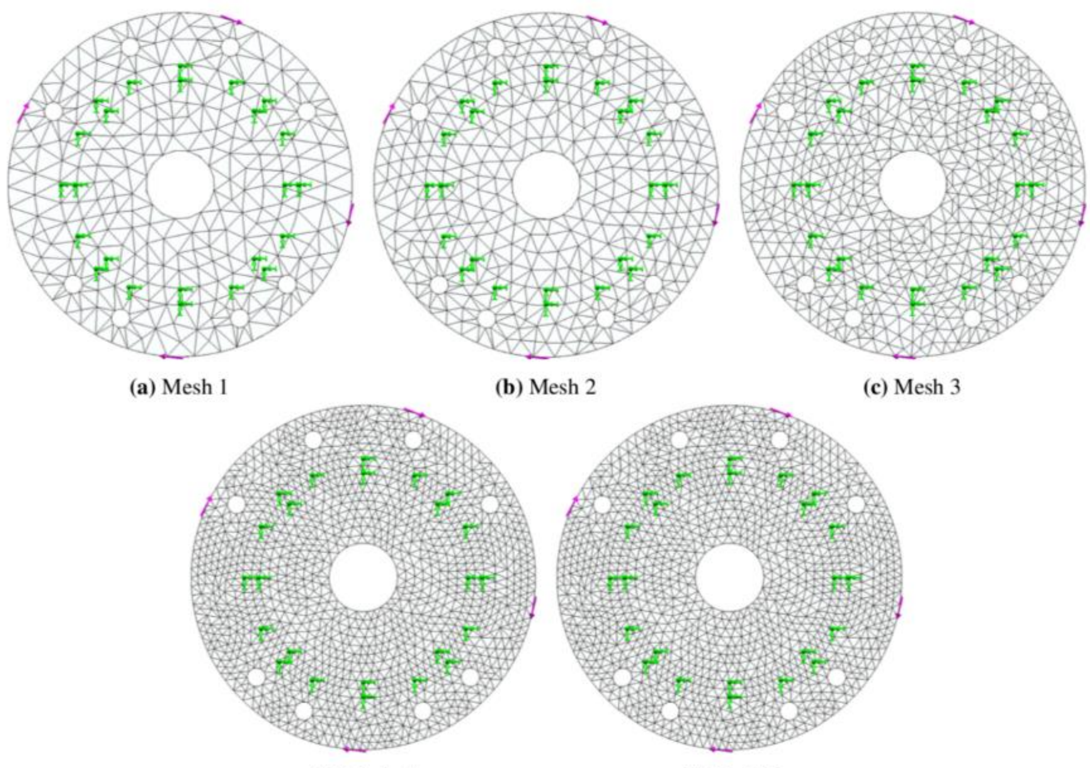

(a) Mesh 1 **(b)** Mesh 2 **(c)** Mesh 3

(d) Mesh 4 **(e)** Mesh 5

Figure G.2. Five different meshes for FEA of plt-frm-01.sldprt.

Table G.3: Mesh details for torsion simulation in part plt-frm-01.sldprt with fixture in bolts.

	Mesh 1	Mesh 2	Mesh 3	Mesh 4	Mesh 5
Study name	Torsion Bolts	Torsion Bolts	Torsion Bolts	Torsion Bolts	Torsion Bolts
Mesh type	Solid Mesh	Solid Mesh	Solid Mesh	Solid Mesh	Solid Mesh
Mesher Used	Curvature based	Curvature based	Curvature based	Curvature based	Curvature based
Jacobian points	4 points	4 points	4 points	4 points	4 points
Max Element Size	16 mm	13 mm	10 mm	7 mm	4 mm
Min Element Size	16 mm	13 mm	10 mm	7 mm	4 mm
Mesh quality	High	High	High	High	High
Total nodes	3921	6024	11936	31510	137849
Total elements	1909	3118	6755	19146	90345
Maximum Aspect Ratio	5.1843	7.5621	4.3279	5.1279	5.0086
Percentage of elements with Aspect Ratio < 3	90.8	95.5	99.4	99.8	99.8
Percentage of elements with Aspect Ratio > 10	0	0	0	0	0
Percentage of distorted elements (Jacobian)	0	0	0	0	0
Time to complete mesh (hh:mm:ss)	0:00:01	0:00:02	0:00:01	0:00:04	0:00:07
Computer name	R-APP-096	R-APP-096	R-APP-096	R-APP-096	R-APP-096

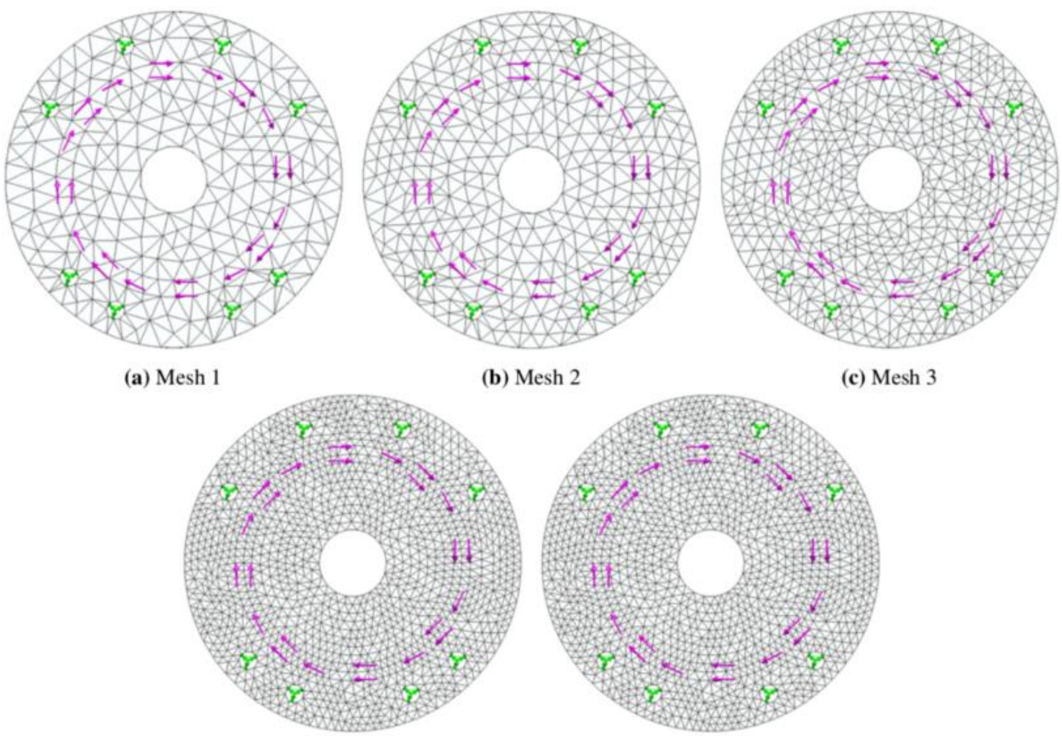

(a) Mesh 1 **(b)** Mesh 2 **(c)** Mesh 3

(d) Mesh 4 **(e)** Mesh 5

Figure G.3. Five different meshes for FEA of plt-frm-01.sldprt with fixture in the cylindrical surfaces of the bolts and torque applied on the external cylindrical face.

Table G.4. Mesh details for torsion simulation in assembly frm-w-02.sldasm.

	Mesh 1	Mesh 2	Mesh 3	Mesh 4	Mesh 5	Mesh 6
Study name	Torsion Bolts	Torsion Bolts	Torsion Bolts	Torsion Bolts	Torsion Bolts	Torsion Bolts
Mesh type	Solid Mesh	Solid Mesh	Solid Mesh	Solid Mesh	Solid Mesh	Solid Mesh
Mesher Used	Curvature based	Curvature based	Curvature based	Curvature based	Curvature based	Curvature based
Jacobian points	4 points	4 points	4 points	4 points	4 points	4 points
Max Element Size	112 mm	91mm	70 mm	49 mm	28 mm	28 mm
Min Element Size	112 mm	91mm	70 mm	49 mm	28 mm	5.6 mm
Mesh quality	High	High	High	High	High	High
Total nodes	3792	5404	5631	7248	16054	28852
Total elements	1727	2546	2641	3459	7866	15172
Maximum Aspect Ratio	37.887	22.85	35.44	16.052	12.597	5.7081
Percentage of elements with Aspect Ratio < 3	7.93	11.2	8.9	17.2	90.4	97.5
Percentage of elements with Aspect Ratio > 10	20.4	2.91	4.09	0.983	0.0381	0
Percentage of distorted elements (Jacobian)	0	0	0	0	0	0
Remesh failed parts with incompatible mesh	Off	Off	Off	Off	Off	Off
Time to complete mesh (hh:mm:ss)	0:00:01	0:00:01	0:00:01	0:00:01	0:00:02	0:00:02
Computer name	SCTS213-LAB12	SCTS213-LAB12	SCTS213-LAB12	SCTS213-LAB12	SCTS213-LAB12	SCTS213-LAB12

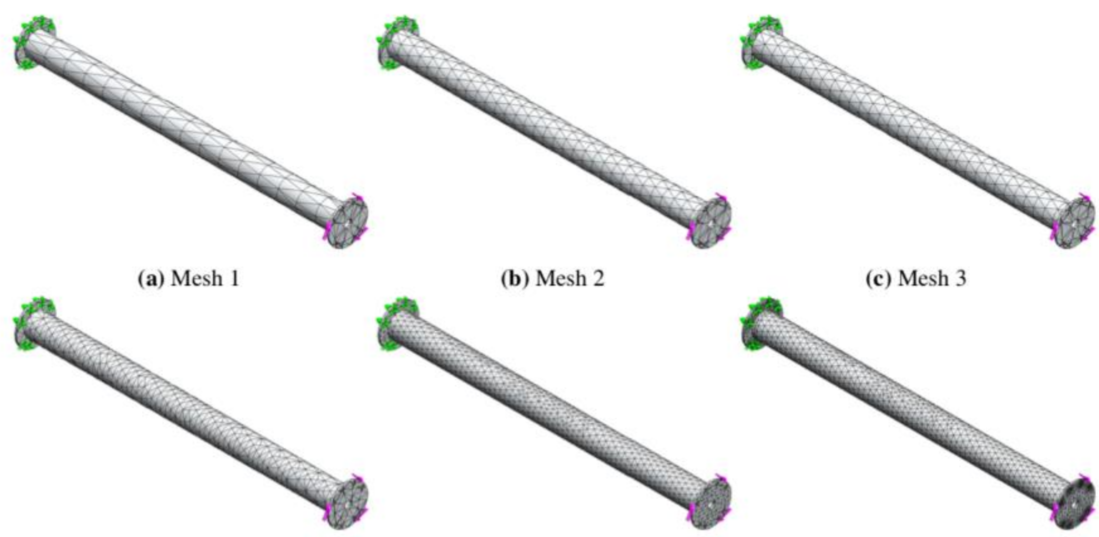

(a) Mesh 1 **(b)** Mesh 2 **(c)** Mesh 3

(d) Mesh 4 **(e)** Mesh 5 **(f)** Mesh 6

Figure G.4. Six different meshes for FEA of frm-w-02.sldasm.

Table G.5. Mesh details for impact loading FEA in assembly sus-04.sldasm.

	Mesh 1	Mesh 2	Mesh 3	Mesh 4	Mesh 5
Study name	Impact	Impact	Impact	Impact	Impact
Mesh type	Solid Mesh	Solid Mesh	Solid Mesh	Solid Mesh	Solid Mesh
Mesher Used	Curvature based	Curvature based	Curvature based	Curvature based	Curvature based
Jacobian points	4 points	4 points	4 points	4 points	4 points
Max Element Size	14 mm	11.5 mm	9 mm	6.5 mm	4 mm
Min Element Size	4.66 mm	3.83329 mm	2.99997 mm	2.16664 mm	1.33332 mm
Mesh quality	High	High	High	High	High
Total nodes	14580	17871	27488	51587	108792
Total elements	7462	9209	14450	29598	67059
Maximum Aspect Ratio	8.6647	12.924	8.2326	9.2443	4.6989
Percentage of elements with Aspect Ratio < 3	85.9	90.1	85.7	97.1	99.8
Percentage of elements with Aspect Ratio > 10	0	0.0434	0	0	0
Percentage of distorted elements (Jacobian)	0	0	0	0	0
Remesh failed parts with incompatible mesh	Off	Off	Off	Off	Off
Time to complete mesh (hh:mm:ss)	0:00:02	0:00:02	0:00:02	0:00:03	0:00:04
Computer name	SCTS213-LAB09	SCTS213-LAB09	SCTS213-LAB09	SCTS213-LAB09	SCTS213-LAB09

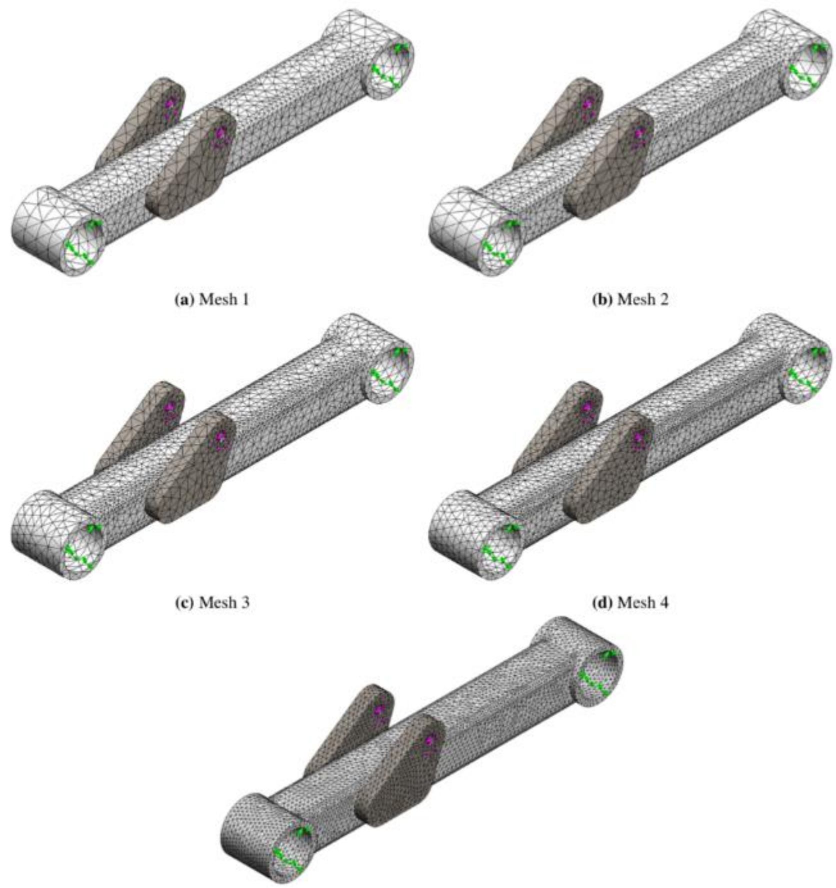

(a) Mesh 1 **(b)** Mesh 2

(c) Mesh 3 **(d)** Mesh 4

Figure G.5. Five different meshes for FEA of sus-04.sldasm with fixture in the cylindrical surfaces of the rubber bushing holes, and impact load of 8.2 kN applied on the cylindrical surfaces of the two top right holes.

Table G.6. Mesh details for impact loading in part plt-sus-03.sldprt with flat surface restraint.

	Mesh 1	Mesh 2	Mesh 3	Mesh 4	Mesh 5
Study name	Impact Flat	Impact Flat	Impact Flat	Impact Flat	Impact Flat
Mesh type	Solid Mesh	Solid Mesh	Solid Mesh	Solid Mesh	Solid Mesh
Mesher Used	Curvature based	Curvature based	Curvature based	Curvature based	Curvature based
Jacobian points	4 points	4 points	4 points	4 points	4 points
Max Element Size	7 mm	5.75 mm	4.5 mm	3.25 mm	2 mm
Min Element Size	2.33 mm	5.75 mm	4.5 mm	3.25 mm	2 mm
Mesh quality	High	High	High	High	High
Total nodes	3647	3682	7464	16267	65173
Total elements	2169	2194	4649	10543	44521
Maximum Aspect Ratio	3.545	4.3492	3.6975	4.2804	3.642
Percentage of elements with Aspect Ratio < 3	99.1	98.9	99.7	99.7	99.9
Percentage of elements with Aspect Ratio > 10	0	0	0	0	0
Percentage of distorted elements (Jacobian)	0	0	0	0	0
Time to complete mesh (hh:mm:ss)	0:00:00	0:00:00	0:00:01	0:00:01	0:00:03
Computer name	SCTS213-LAB01	SCTS213-LAB01	SCTS213-LAB01	SCTS213-LAB01	SCTS213-LAB13

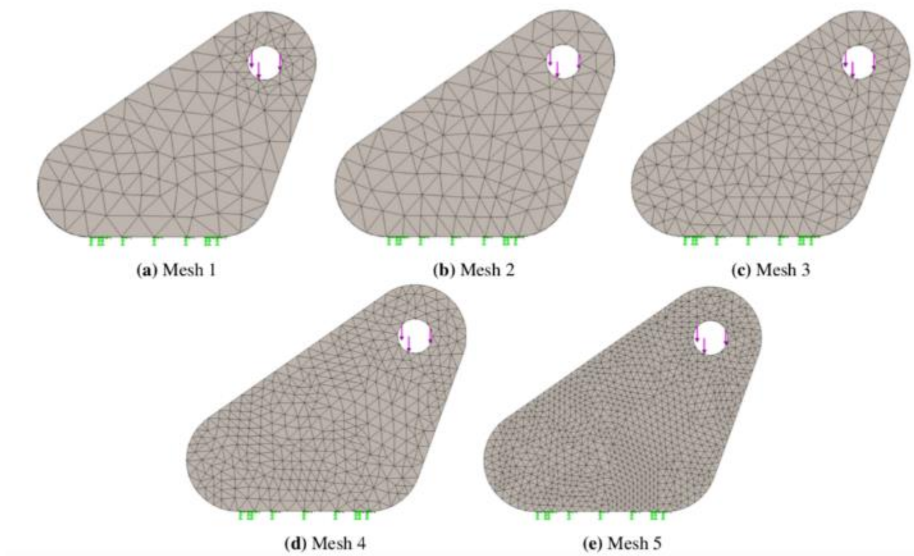

Figure G.6. Five different meshes for FEA in plt-sus-03 flat.sldprt with flat surface. The green arrows on the flat bottom surface represent a rigid restraint. The magenta arrows represent the impact loading of 4.1 kN applied downward on the hole's cylindrical surface. See Table A.8 for meshes details.

Table G.7. Mesh details for impact loading in part plt-sus-03.sldprt with welding edge (see Figure A.9).

	Mesh 1	Mesh 2	Mesh 3	Mesh 4	Mesh 5
Study name	Impact Weld	Impact Weld	Impact Weld	Impact Weld	Impact Weld
Mesh type	Solid Mesh	Solid Mesh	Solid Mesh	Solid Mesh	Solid Mesh
Mesher Used	Curvature based	Curvature based	Curvature based	Curvature based	Curvature based
Jacobian points	4 points	4 points	4 points	4 points	4 points
Max Element Size	7 mm	5.75 mm	4.5 mm	3.25 mm	2 mm
Min Element Size	2.33 mm	5.75 mm	4.5 mm	3.25 mm	2 mm
Mesh quality	High	High	High	High	High
Total nodes	3711	3794	7703	16901	62519
Total elements	2178	2269	4815	10970	42652
Maximum Aspect Ratio	6.5938	5.4452	5.0636	4.8681	3.5748
Percentage of elements with Aspect Ratio < 3	98.5	99.6	99.2	99.4	99.8
Percentage of elements with Aspect Ratio > 10	0	0	0	0	0
Percentage of distorted elements (Jacobian)	0	0	0	0	0
Time to complete mesh (hh:mm:ss)	0:00:01	0:00:00	0:00:01	0:00:01	0:00:03
Computer name	SCTS213-LAB01	SCTS213-LAB01	SCTS213-LAB01	SCTS213-LAB01	SCTS213-LAB01

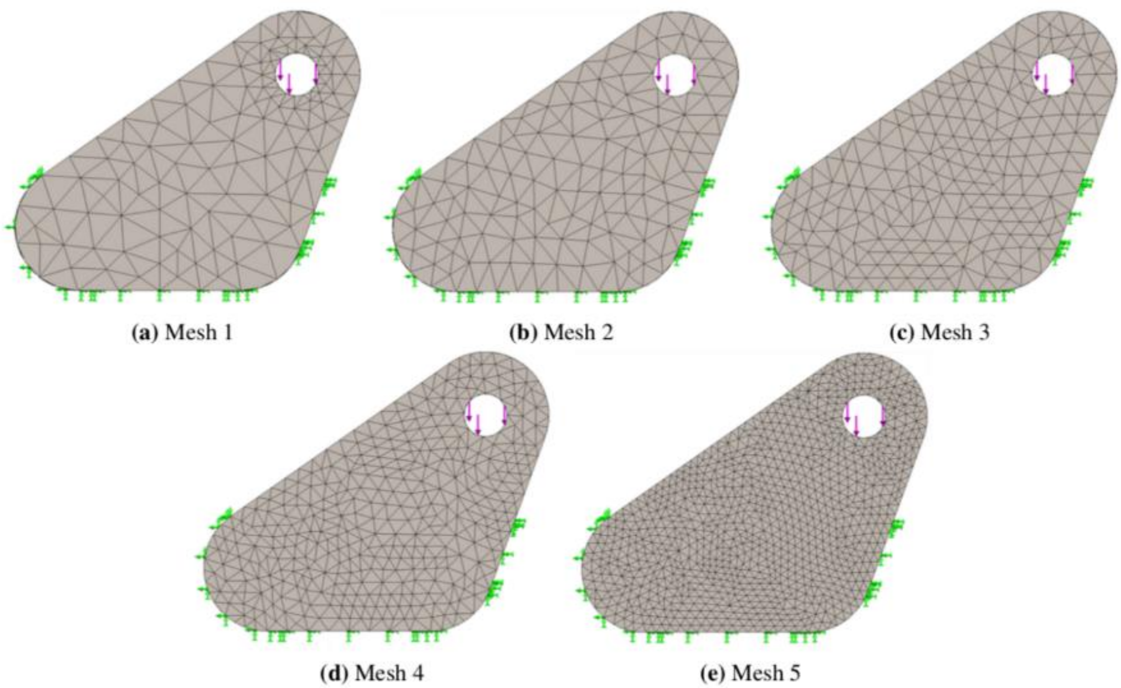

Figure G.7. Five different meshes for FEA in plt-sus-03.sldprt with welding surface. The green arrows sur- rounding the bottom surfaces represent a rigid welding seam of 5.35 mm of thickness. The magenta arrows represent the impact loading of 4.1 kN applied downward on the hole's cylindrical surface. See Table A.9 for meshes details.

Table G.8. Mesh details for impact loading in part plt-sus-02.sldprt.

	Mesh 1	Mesh 2	Mesh 3	Mesh 4	Mesh 5
Study name	Impact (-Default-)	Impact (-Default-)	Impact (-Default-)	Impact (-Default-)	Impact (-Default-)
Mesh type	Solid Mesh	Solid Mesh	Solid Mesh	Solid Mesh	Solid Mesh
Mesher Used	Curvature based	Curvature based	Curvature based	Curvature based	Curvature based
Jacobian points	4 points	4 points	4 points	4 points	4 points
Max Element Size	10 mm	8 mm	6 mm	4 mm	2 mm
Min Element Size	3.33 mm	2.66 mm	1.99 mm	1.33 mm	0.66 mm
Mesh quality	High	High	High	High	High
Total nodes	5594	8492	13266	29017	169122
Total elements	3244	5086	8135	18643	116133
Maximum Aspect Ratio	3.9468	6.1514	6.0317	5.2299	4.0752
Percentage of elements with Aspect Ratio < 3	99	98.3	99.3	99.6	99.8
Percentage of elements with Aspect Ratio > 10	0	0	0	0	0
Percentage of distorted elements (Jacobian)	0	0	0	0	0
Time to complete mesh (hh:mm:ss)	0:00:02	0:00:00	0:00:02	0:00:01	0:00:05
Computer name	SCTS213-LAB14	SCTS213-LAB14	SCTS213-LAB14	SCTS213-LAB14	SCTS213-LAB14

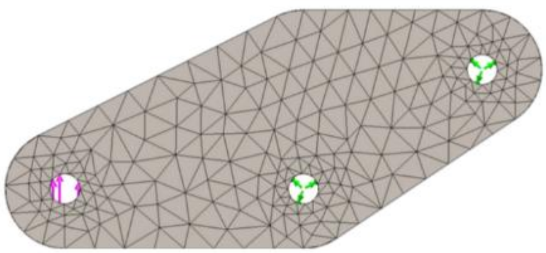

(a) Mesh 1

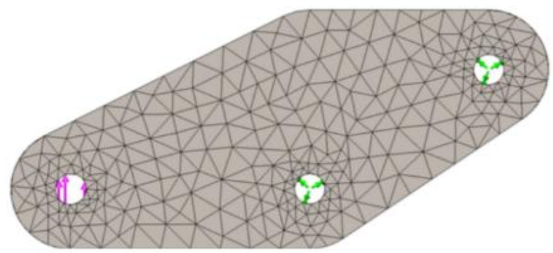

(b) Mesh 2

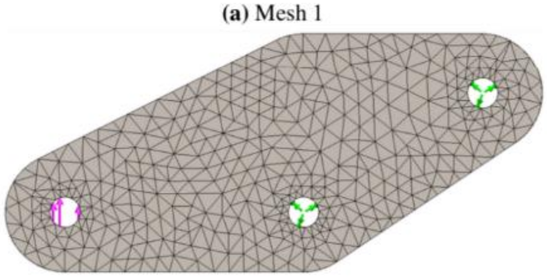

(c) Mesh 3

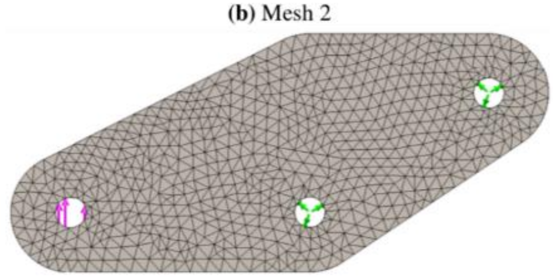

(d) Mesh 4

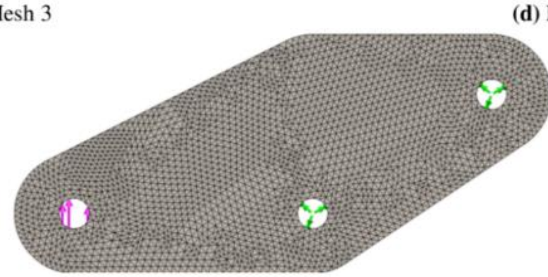

(e) Mesh 5

Figure G.8. Five different meshes for FEA of plt-sus-02.sldprt with fixed hinges supports in the two right holes and a load o 4.1 kN applied upward.

Table G.9. Mesh details for weight simulation in welded assembly str-01.sldprt.

	Mesh 1	Mesh 2	Mesh 3	Mesh 4	Mesh 5
Study name	Weight	Weight	Weight	Weight	Weight
Mesh type	Solid Mesh	Solid Mesh	Solid Mesh	Solid Mesh	Solid Mesh
Mesher Used	Curvature based	Curvature based	Curvature based	Curvature based	Curvature based
Jacobian points	4 points	4 points	4 points	4 points	4 points
Max Element Size	180 mm	146 mm	112 mm	78 mm	44 mm
Min Element Size	36 mm	29.2 mm	22.4 mm	15.6 mm	8.8 mm
Mesh quality	High	High	High	High	High
Total nodes	10347	11501	13969	18613	35216
Total elements	5258	5820	7039	9354	17713
Maximum Aspect Ratio	231.28	213.94	85.227	92.317	37.096
Percentage of elements with Aspect Ratio < 3	1.39	1.24	2.73	8.86	25.4
Percentage of elements with Aspect Ratio > 10	53	47.9	44.5	31.1	1.62
Percentage of distorted elements (Jacobian)	0	0	0	0	0
Time to complete mesh (hh:mm:ss)	0:00:03	0:00:02	0:00:02	0:00:02	0:00:03
Computer name	SCTS213-LAB09	SCTS213-LAB09	SCTS213-LAB09	SCTS213-LAB09	SCTS213-LAB09

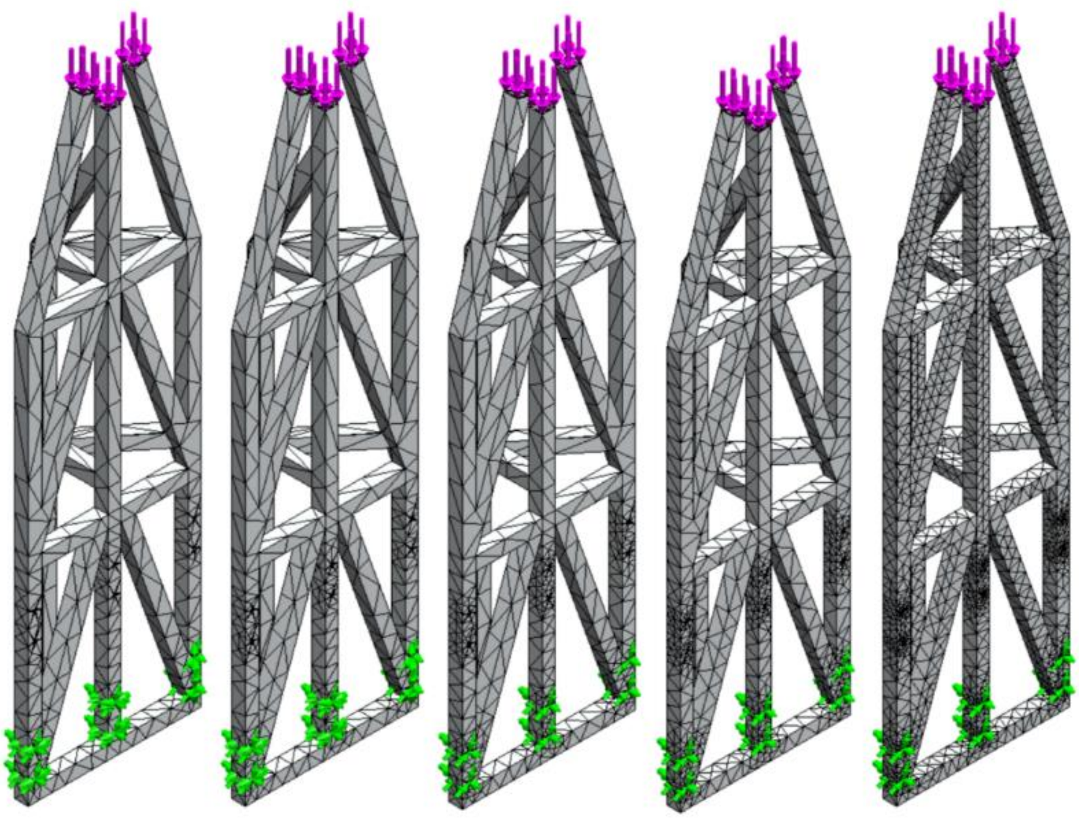

(a) Mesh 1 **(b)** Mesh 2 **(c)** Mesh 3 **(d)** Mesh 4 **(e)** Mesh 5

Figure G.9. Five different meshes for FEA in str-01.sldprt. Green arrows with cylindrical hole faces, and magenta arrows with a weight loading of 10 kN.

Table G.10. Mesh details for impact loading in part str-02 comb.sldprt.

	Mesh 1	Mesh 2	Mesh 3	Mesh 4	Mesh 5
Study name	Impact	Impact	Impact	Impact	Impact
Mesh type	Solid Mesh	Solid Mesh	Solid Mesh	Solid Mesh	Solid Mesh
Mesher Used	Curvature based	Curvature based	Curvature based	Curvature based	Curvature based
Jacobian points	4 points	4 points	4 points	4 points	4 points
Max Element Size	165 mm	134 mm	102 mm	71 mm	40 mm
Min Element Size	33 mm	26.8 mm	20.4 mm	14.2 mm	8 mm
Mesh quality	High	High	High	High	High
Total nodes	11921	13885	17633	22768	43365
Total elements	5906	6871	8763	11307	21685
Maximum Aspect Ratio	201.55	133.37	133.37	154.06	57.914
Percentage of elements with Aspect Ratio < 3	1.35	2.33	6.05	20.8	43.2
Percentage of elements with Aspect Ratio > 10	41	35.7	26.2	20.6	0.812
Percentage of distorted elements (Jacobian)	0	0	0	0	0
Time to complete mesh (hh:mm:ss)	0:00:02	0:00:03	0:00:02	0:00:02	0:00:03
Computer name	SCTS213-LAB13	SCTS213-LAB13	SCTS213-LAB13	SCTS213-LAB13	SCTS213-LAB13

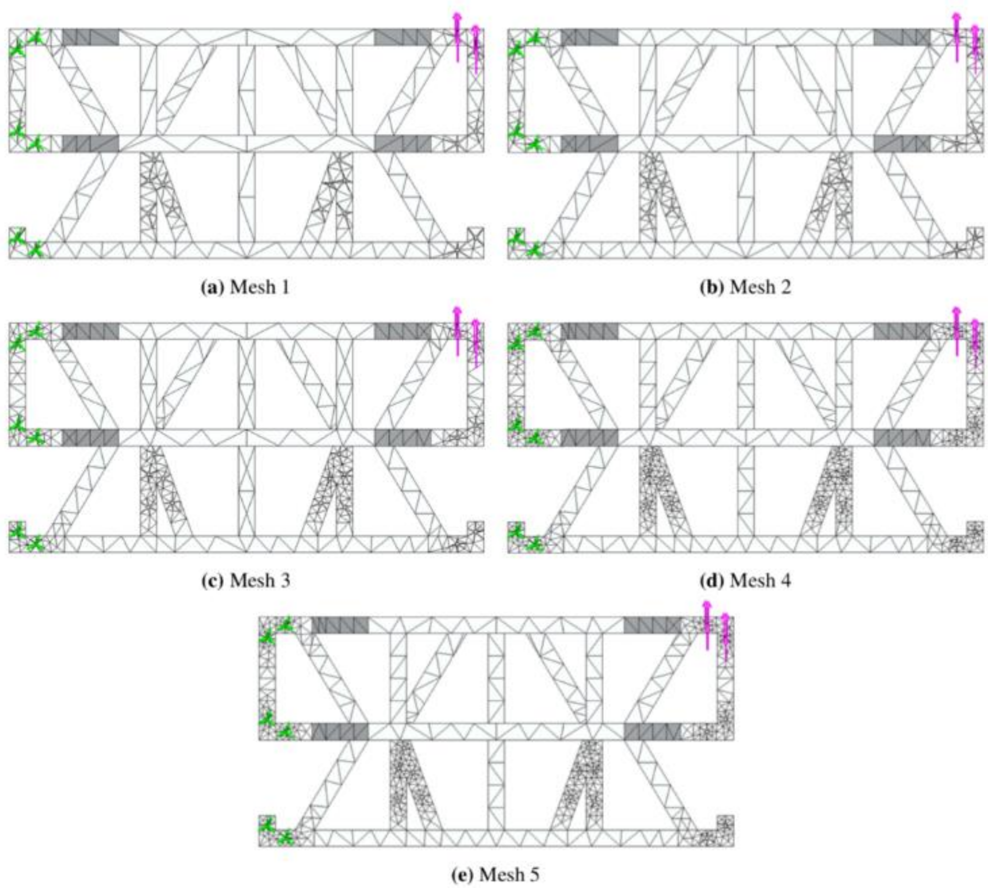

(a) Mesh 1

(b) Mesh 2

(c) Mesh 3

(d) Mesh 4

(e) Mesh 5

Figure G.10. Five different meshes for FEA of str-02 comb.sldprt with fixture in the cylindrical surfaces of the six left holes, and impact load of 8.2 kN applied on the cylindrical surfaces of the two top right holes.

Table G.11. Mesh details for impact loading in part sht-frm-01.sldprt with welding edge.

	Mesh 1	Mesh 2	Mesh 3	Mesh 4	Mesh 5
Study name	Torsion	Torsion	Torsion	Torsion	Torsion
Mesh type	Solid Mesh	Solid Mesh	Solid Mesh	Solid Mesh	Solid Mesh
Mesher Used	Curvature based	Curvature based	Curvature based	Curvature based	Curvature based
Jacobian points	4 points	4 points	4 points	4 points	4 points
Max Element Size	26 mm	21 mm	16 mm	11 mm	6 mm
Min Element Size	5.2 mm	4.2 mm	3.2 mm	2.2 mm	1.2 mm
Mesh quality	High	High	High	High	High
Total nodes	9729	12991	18962	21152	34335
Total elements	4826	6610	10042	11325	19014
Maximum Aspect Ratio	39.262	39.477	29.482	29.39	29.444
Percentage of elements with Aspect Ratio < 3	95.7	95.1	95.6	97	99.1
Percentage of elements with Aspect Ratio > 10	0.145	0.197	0.139	0.124	0.0841
Percentage of distorted elements (Jacobian)	0	0	0	0	0
Time to complete mesh (hh:mm:ss)	0:00:01	0:00:01	0:00:01	0:00:01	0:00:01
Computer name	SCTS213-LAB09	SCTS213-LAB09	SCTS213-LAB09	SCTS213-LAB09	SCTS213-LAB09

(a) Mesh 1 **(b)** Mesh 2 **(c)** Mesh 3 **(d)** Mesh 4 **(e)** Mesh 5

Figure G.11. Five different meshes for FEA in sht-frm-01.sldprt. The green arrows in the back holes are fixed hinges boundary conditions. The magenta arrows represent the maximum torque of 25 N·m applied on the inner cylindrical surface.

Table G.12. Mesh details for impact loading in part plt-sus-04.sldprt.

	Mesh 1	Mesh 2	Mesh 3	Mesh 4	Mesh 5
Study name	Impact	Impact	Impact	Impact	Impact
Mesh type	Solid Mesh	Solid Mesh	Solid Mesh	Solid Mesh	Solid Mesh
Mesher Used	Curvature based	Curvature based	Curvature based	Curvature based	Curvature based
Jacobian points	4 points	4 points	4 points	4 points	4 points
Max Element Size	16 mm	13 mm	10 mm	7 mm	4 mm
Min Element Size	5.33 mm	4.33 mm	3.33 mm	2.33 mm	1.33 mm
Mesh quality	High	High	High	High	High
Total nodes	7842	11707	18510	37209	145919
Total elements	3954	6141	10186	21523	92347
Maximum Aspect Ratio	4.8127	5.552	4.4719	3.8818	4.0672
Percentage of elements with Aspect Ratio < 3	97.7	97.9	98.8	99.9	99.9
Percentage of elements with Aspect Ratio > 10	0	0	0	0	0
Percentage of distorted elements (Jacobian)	0	0	0	0	0
Time to complete mesh (hh:mm:ss)	0:00:01	0:00:01	0:00:01	0:00:01	0:00:05
Computer name	SCTS213-LAB11	SCTS213-LAB11	SCTS213-LAB11	SCTS213-LAB11	SCTS213-LAB11

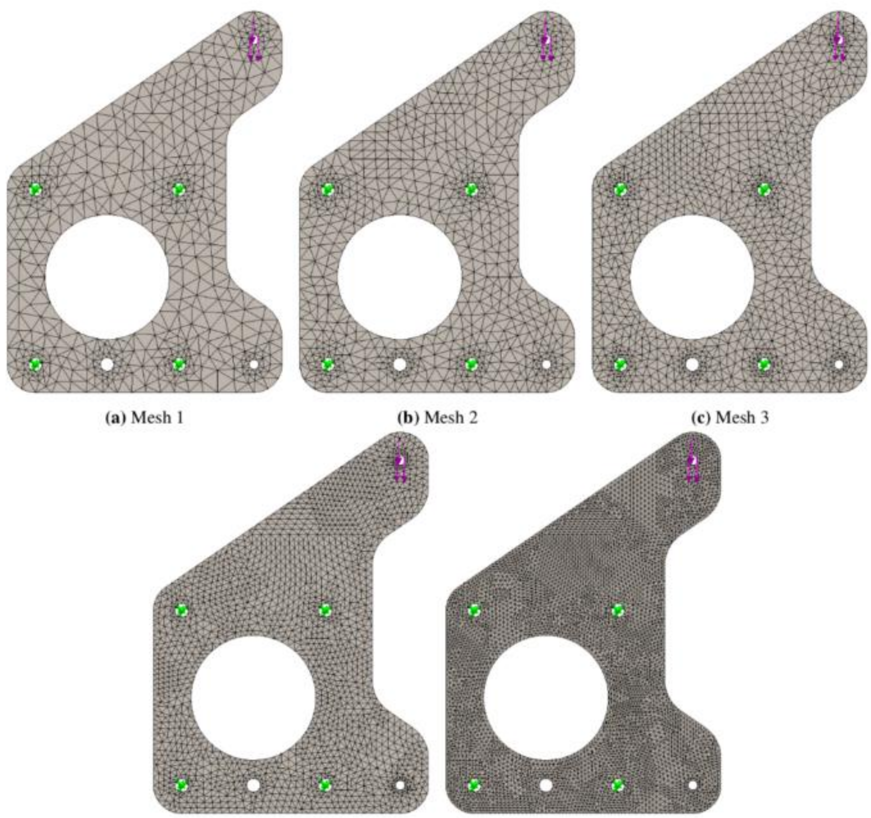

(a) Mesh 1 **(b)** Mesh 2 **(c)** Mesh 3 **(d)** Mesh 4 **(e)** Mesh 5

Figure G.12. Five different meshes for FEA in plt-sus-04.sldprt. The magenta arrows represent the impact loading of 8.2 kN applied downward on the top hole's cylindrical surface.

APPENDIX H

ELECTRIC MATERIAL DATASHEETS

H.1. Motor and Controllers Datasheets

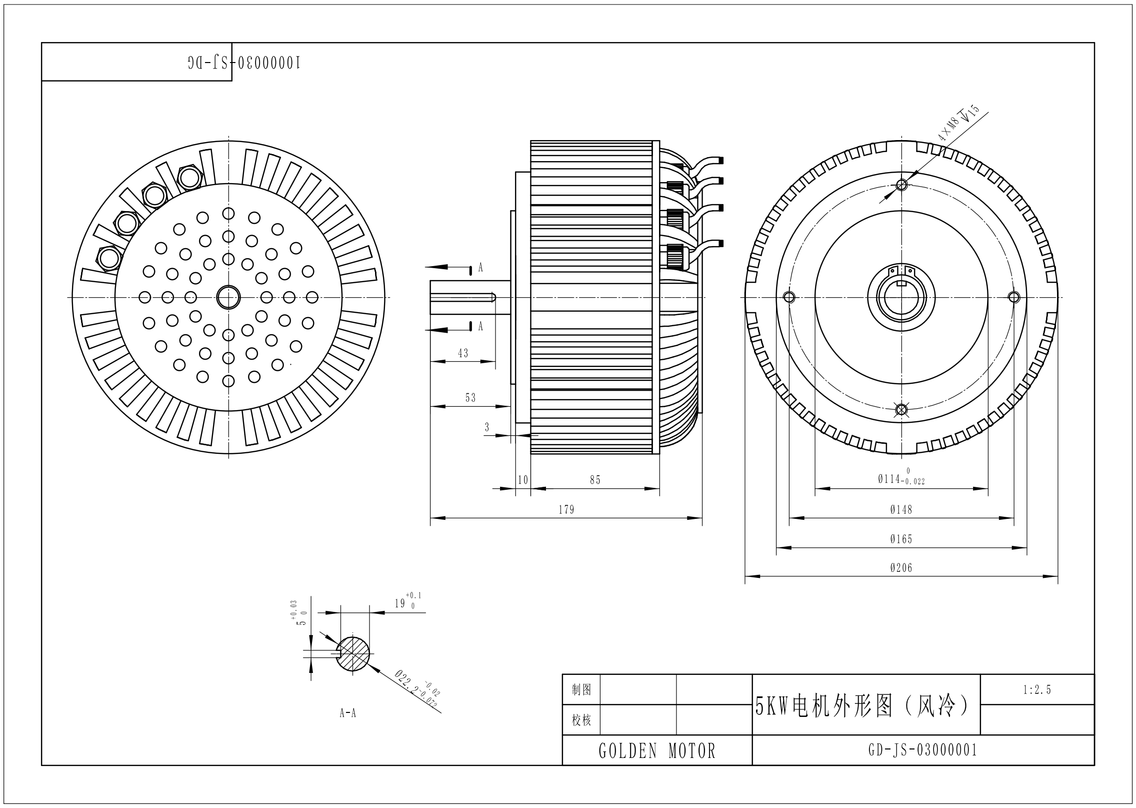

Figure H.1. Golden Motor HPM5000B electric motor main drawing dimensions (reprinted from Golden Motor Technology Co., Ltd., 2016).

type: HPM48-5000 NO.: G20130514008 operator: 001 date: 2013-5-14

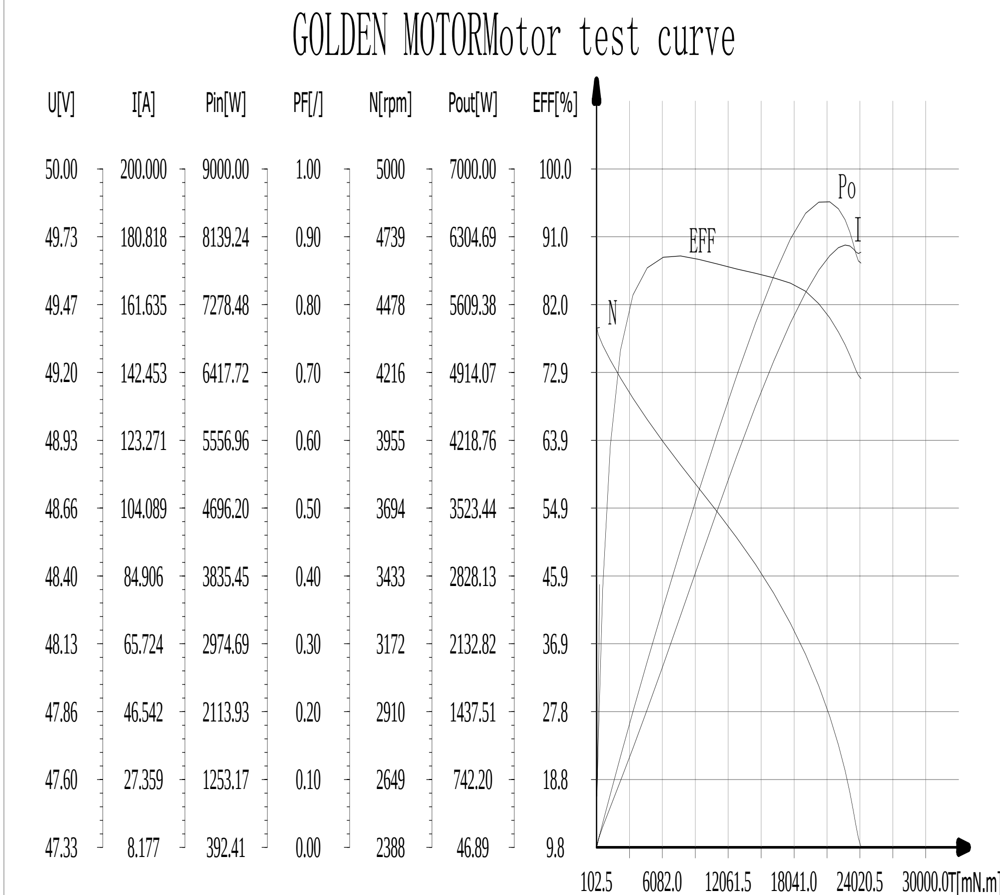

Description	voltage(V)	current(A)	P. input(W)	torque(mN.m)	rotate(RPM)	P. output(W)	eff(%)
Upload point	47.99	8.177	392.41	360.0	4389	165.45	42.2
Most efficiency point	47.57	73.689	3500.65	7728.8	3861	3096.05	88.4
Max Po. point	47.34	175.436	8307.60	21276.9	2892	6661.91	80.2
Max torque point	47.42	176.418	8366.97	24117.9	2389	6033.82	72.1
End point	47.42	176.430	8367.19	24122.5	2388	6031.89	72.1
Rated rotate point	47.38	132.885	6296.72	14540.5	3476	5421.21	86.1

Figure H.2. Golden Motor HPM5000B Electric motor test curves (reprinted from Golden Motor Technology Co., Ltd., 2016).

Dynamic Test

company:	GOLDEN MOTOR		
Type:	HPM48-5000	rated U:	48 V
No.:	G20130514008	rated I:	120 A
Operator:	001	rated P.:	5000 W
Date:	2013-5-14	rated N:	3500 RPM

Items NO.	voltage V	current A	P. input W	P. factor PF	frequency Hz	torque mN.m	rotate rpm	P. output W	efficiency %
1	47.99	8.177	392.41	1.000	0.00	360.0	4389	165.45	42.2
2	47.98	8.538	409.70	1.000	0.00	242.5	4384	111.32	27.2
3	47.98	9.967	478.17	1.000	0.00	102.5	4369	46.89	9.8
4	47.95	13.222	633.99	1.000	0.00	577.5	4335	262.14	41.4
5	47.91	18.686	895.30	1.000	0.00	1412.5	4279	632.89	70.7
6	47.86	26.320	1259.60	1.000	0.00	2415.0	4204	1063.11	84.4
7	47.80	35.715	1707.06	1.000	0.00	3552.5	4116	1531.11	89.7
8	47.72	46.523	2219.96	1.000	0.00	4812.5	4021	2026.29	91.3
9	47.63	58.475	2785.48	1.000	0.00	6182.5	3923	2539.68	91.2
10	47.55	71.460	3397.57	1.000	0.00	7680.0	3826	3076.83	90.6
11	47.46	85.414	4053.55	1.000	0.00	9262.5	3734	3621.59	89.3
12	47.38	100.283	4751.16	1.000	0.00	10920.0	3647	4170.18	87.8
13	47.40	116.273	5511.32	1.000	0.00	12647.5	3573	4731.89	85.9
14	47.41	132.690	6291.16	1.000	0.00	14387.5	3501	5274.41	83.8
15	47.39	149.915	7104.47	1.000	0.00	16157.5	3429	5801.47	81.7
16	47.37	167.085	7915.23	1.000	0.00	17950.0	3350	6296.60	79.5
17	47.33	174.525	8260.27	1.000	0.00	19495.0	3206	6544.60	79.2
18	47.33	174.870	8277.47	1.000	0.00	20797.5	2994	6520.18	78.8
19	47.34	175.082	8287.97	1.000	0.00	21697.5	2827	6422.91	77.5
20	47.33	175.240	8294.11	1.000	0.00	22292.5	2705	6314.26	76.1
21	47.34	175.500	8309.05	1.000	0.00	22735.0	2625	6249.15	75.2
22	47.39	175.840	8333.50	1.000	0.00	23087.5	2563	6196.15	74.3
23	47.40	175.953	8339.27	1.000	0.00	23382.5	2512	6150.45	73.8
24	47.41	176.173	8352.78	1.000	0.00	23657.5	2466	6108.84	73.1
25	47.42	176.292	8360.23	1.000	0.00	23887.5	2427	6070.68	72.6
26	47.42	176.430	8367.19	1.000	0.00	24122.5	2388	6031.89	72.1

Client :　　　　　　　　　　　　　　　　　　　　　　　　P: 1

Figure H.3. Golden Motor HPM5000B electric motor dynamic test table (reprinted from Golden Motor Technology Co., Ltd., 2016).

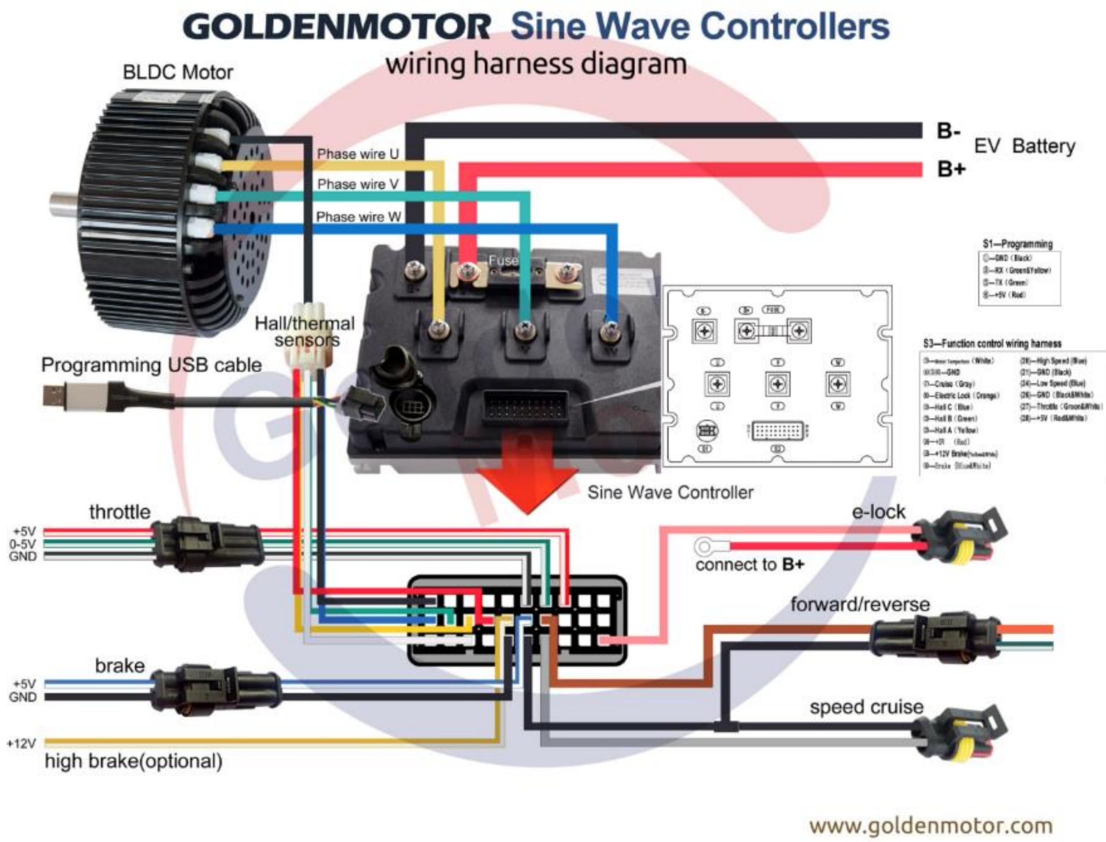

Figure H.4. VEC300 motor controller diagram for 5-kW electric motor (reprinted from Golden Motor Technology Co., Ltd., 2016).

H.2. Battery Datasheet

Trojan BATTERY COMPANY

DATA SHEET

T-1275

MODEL	**T-1275 with Master Vent**
VOLTAGE	**12**
MATERIAL	**Polypropylene**
DIMENSIONS	**Inches (mm)**
BATTERY	**Deep-Cycle Flooded/Wet Lead-Acid Battery**
COLOR	**Maroon**
WATERING	**HydroLink™ Watering System**

12V

PRODUCT + PHYSICAL SPECIFICATIONS

BCI Group Size	Type	Voltage	Cell(s)	Terminal Type [G]	Dimensions [C] Inches (mm)			Weight Lbs. (kg)
					Length	Width	Height [F]	
GC12	T-1275	12	6	1, 2	12.96 (329)	7.13 (181)	11.13 (283)	85 (39)

ELECTRICAL SPECIFICATIONS

Cranking Performance		Capacity [A] Minutes			Capacity [B] Amp-Hours (AH)				Energy (kWh)	Internal Resistance (mΩ)	Short Circuit Current (amps)
C.C.A.[D] @ 0°F (-18°C)	C.A.[E] @ 32°F (0°C)	@ 25 Amps	@ 56 Amps	@ 75 Amps	5-Hr	10-Hr	20-Hr	100-Hr	100-Hr		
—	—	280	102	70	120	134	150	166	1.99	—	—

CHARGING INSTRUCTIONS

Charger Voltage Settings (at 77°F/25°C)				
System Voltage	12V	24V	36V	48V
Bulk Charge	14.82	29.64	44.46	59.28
Float Charge	13.50	27.00	40.50	54.00
Equalize Charge	16.20	32.40	48.60	64.80

Do not install or charge batteries in a sealed or non-ventilated compartment. Constant under or overcharging will damage the battery and shorten its life as with any battery.

CHARGING TEMPERATURE COMPENSATION

Add	Subtract
0.005 volt per cell for every 1°C below 25°C 0.0028 volt per cell for every 1°F below 77°F	0.005 volt per cell for every 1°C above 25°C 0.0028 volt per cell for every 1°F above 77°F

OPERATIONAL DATA

Operating Temperature	Self Discharge
-4°F to 113°F (-20°C to +45°C). At temperatures below 32°F (0°C) maintain a state of charge greater than 60%.	5 – 15% per month depending on storage temperature conditions.

STATE OF CHARGE MEASURE OF OPEN-CIRCUIT VOLTAGE

Percentage Charge	Specific Gravity	Cell	12 Volt
100	1.277	2.122	12.73
90	1.258	2.103	12.62
80	1.238	2.083	12.50
70	1.217	2.062	12.37
60	1.195	2.040	12.24
50	1.172	2.017	12.10
40	1.148	1.993	11.96
30	1.124	1.969	11.81
20	1.098	1.943	11.66

Figure H.5. Trojan T-1275 led acid battery (Sheet 1) (reprinted from Trojan Battery Company, 2020).

TERMINAL CONFIGURATIONS[G]

1	ELPT	Embedded Low Profile Terminal
		**Terminal Height Inches (mm)** 1.22 (31) **Torque Values in-lb (Nm)** 95 – 105 (11 – 12) **Bolt** 5/16"

2	EHPT	Embedded High Profile Terminal
		**Terminal Height Inches (mm)** 1.50 (38) **Torque Values in-lb (Nm)** 95 – 105 (11 – 12) **Bolt** 5/16"

BATTERY DIMENSIONS (shown with EHPT)

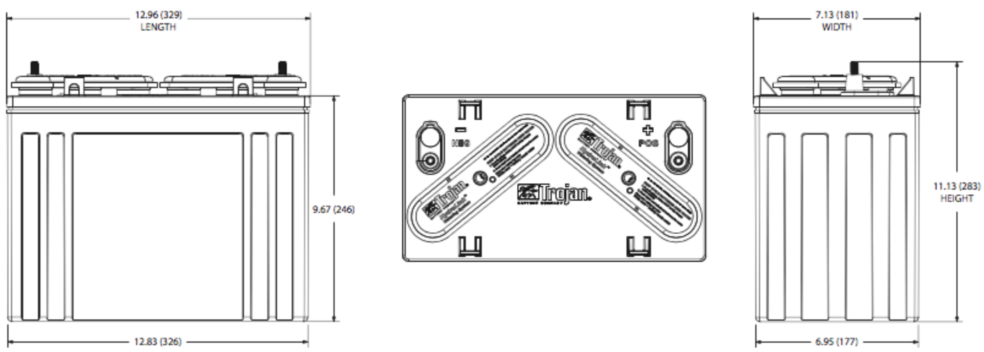

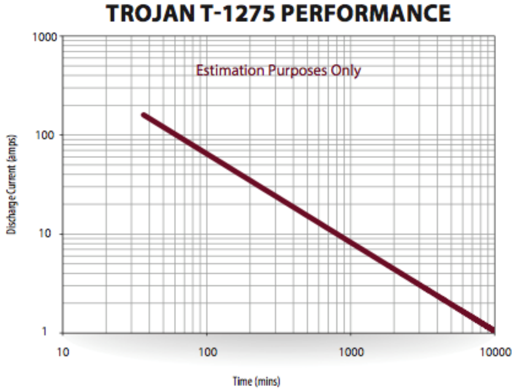

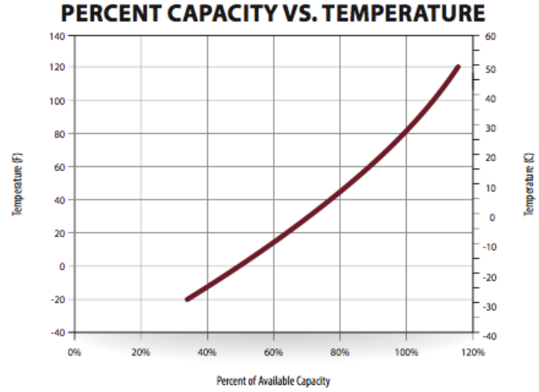

A. The number of minutes a battery can deliver when discharged at a constant rate at 80°F (27°C) and maintain a voltage above 1.75 V/cell. Capacities are based on peak performance.
B. The amount of amp-hours (AH) a battery can deliver when discharged at a constant rate at 80°F (27°C) and maintain a voltage above 1.75 V/cell. Capacities are based on peak performance.
C. Dimensions may vary depending on type of handle or terminal. Batteries should be mounted with 0.5 inches (12.7 mm) spacing minimum.
D. C.C.A. (Cold Cranking Amps) - the discharge load in amperes which a new, fully charged battery can maintain for 30 seconds at 0°F (-18°C) at a voltage above 1.2 V/cell.
E. C.A. (Cranking Amps) - the discharge load in amperes which a new, fully charged battery can maintain for 30 seconds at 32°F (0°C) at a voltage above 1.2 V/cell. This is sometimes referred to as marine cranking amps @ 32°F or M.C.A. @ 32°F.
F. Height taken from bottom of the battery to the highest point on the battery. Heights may vary depending on type of terminal.
G. Terminal images are representative only.

Trojan BATTERY COMPANY

800.423.6569 / +1.562.236.3000 / trojanbattery.com

T-1275 DS 2016_0826

Figure H.6. Trojan T-1275 led acid battery (Sheet 2) (reprinted from Trojan Battery Company, 2020).

H.3. Battery Maintenance

English 简体中文 Español

Search

About Us | Applications | Products | Where to Buy | Technical Support | Resources | News Room | Partners

Battery Maintenance

Trojan Battery Company has been manufacturing deep-cycle, flooded batteries for more than three generations.

Our experience has shown that the key factor to achieving optimum performance and long battery life is to follow a regular care and maintenance program.

While reviewing our battery maintenance tips, please keep in mind that all battery systems are unique. Battery type, charger technology, equipment loads, cable size, climate, and other factors can all vary. Slight or significant, these differences will require battery maintenance to be adjusted accordingly. These are only guidelines to follow for proper battery care. Each particular system will always require a degree of customized attention.

To view a complete list of our User's Guides

Trojan Tips Educational Videos

Before Getting Started

Achieving Optimum Performance and Long Battery Life

Before Getting Started

- Make sure you know your system voltage, battery compartment size (length, width and height) and your energy needs.
- Determine whether you want to use a deep-cycle flooded, AGM or gel battery.

Step 1: Determine Your Battery Voltage And How Many Batteries To Use

1-1 Based on your system voltage, you must first decide which battery is needed and how many to use in order to meet your requirements. For example, you may connect a series of eight 6V batteries, six 8V batteries or four 12V batteries for a 48-volt system. The size of your battery compartment, your performance requirements and costs may limit your options.

1-2 Make sure there is enough space between batteries to allow for minor battery expansion that occurs during use and to allow proper airflow to keep battery temperature down in hot environments.

TIP

Connecting batteries in series does not increase the capacity of the batteries; it simply increases the overall voltage to meet your system requirements. Once your voltage requirements are met, and if space allows, you can double the batteries in a parallel connection — thereby doubling your battery capacity. See diagrams below.

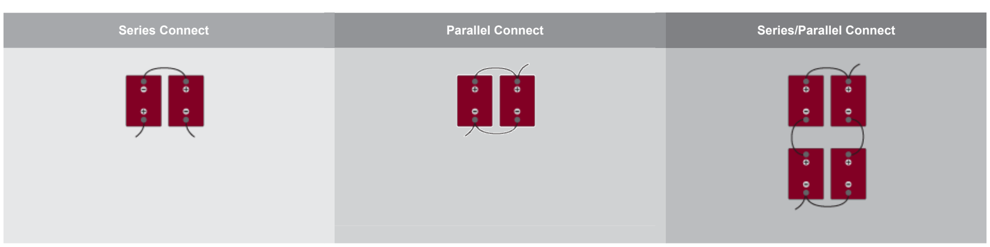

Figure H.7. Trojan Battery Maintenance (page 1/10) (reprinted from Trojan Battery Company, 2020).

To increase voltage, connect batteries in series. This will not increase the system capacity. **Example** Two T-105, 6V Batteries rated at 225AH Connected in Series **System Voltage** 6V + 6V = 12VSystem Capacity = 225AH To increase voltage, connect batteries in series.	**To increase capacity, connect batteries in parallel. This will not increase the system voltage.** **Example** Two T-105, 6V Batteries rated at 225AH Connected in Parallel **System Voltage** 6VSystem Capacity = 225AH + 225AH = 450AH To increase amp-hour capacity, connect batteries in parallel.	**To increase both voltage and capacity, connect additional batteries in series and parallel.** **Example** Four T-105, 6V Batteries rated at 225AH Connected in Series/Parallel **System Voltage** 6V + 6V = 12VSystem Capacity = 225AH + 225AH = 450AH To increase both voltage and amp-hour capacity, connect batteries in series/parallel.

Step 2: Choose Your Best Battery Model

2-1 When choosing your battery model, first consider your battery compartment space, as this may limit your options. Within your size restrictions you may have several battery options to choose from. For example, you can use a T-605, T-105 or T-125 in the same space, as they are the exact same physical size. The difference between these batteries is the amount of energy they offer.

2-2 Next consider your energy needs. If replacing an existing battery, use it as a reference point. If your old battery provided enough energy, it can be replaced with a similar capacity battery. If you need more energy you can size up, or if you need less energy you can size down.

TIP

If you do not know what battery to use, contact your equipment manufacturer for their recommended battery specification. Trojan Battery also offers outstanding technical support provided by full-time applications engineers to help you select your ideal batteries.

Step 3: Select Your Best Terminal

3-1 Finally determine which terminal option best meets your needs based on the type of cable connections you plan to use. Look for the terminal(s) available for the battery you have selected.

TIP

Make sure you use the proper cable size when connecting your batteries so the connections do not overheat. For information regarding correct wire sizes you can refer to the National Electric Code, Trojan Battery User's Guide, or contact Trojan's live technical support at 800.423.6569.

BACK TO TOP

Battery Type

Lead acid batteries are generally classified by application (what they are used for) and by construction (how they are made). Deep-cycle batteries are used for various types of applications specific such as RV, golf cars, renewable energy, and marine.

There are two popular construction types: flooded batteries (wet) and VRLA batteries (Valve Regulated Lead Acid). In the flooded types, the electrolyte is a solution of sulfuric acid and water that can spill out if the battery is tipped over. In VRLA batteries, the electrolyte is suspended in a gel or a fiberglass-mat (AGM technology), allowing these batteries to be mounted in a variety of positions.

Before getting started, be sure to identify the type of battery involved. This section addresses the charging and maintenance for both deep-cycle flooded and VRLA batteries.

BACK TO TOP

Inspection

There are many tools that may help in properly caring for and maintaining batteries. Below is a list of basic items that Trojan recommends for this task:

Recommended Equipment			
Baking Soda	Distilled Water	Goggles & Gloves	Hydrometer
Post Cleaner	Vaseline	Voltmeter	Wrench

CAUTION: Always wear protective clothing, gloves and goggles, when handling batteries, electrolyte, and charging your battery.

Batteries should be carefully inspected on a regular basis in order to detect and correct potential problems before they can do harm. It is a great idea to start this routine when you

Figure H.8. Trojan Battery Maintenance (page 2/10) (reprinted from Trojan Battery Company, 2020).

first receive the batteries are first received.

Inspection Guidelines

1. Examine the outside appearance of the battery.

- Look for cracks in the container.
- The top of the battery, posts, and connections should be clean, free of dirt, fluids, and corrosion. If batteries are dirty, refer to the Cleaning section for the proper cleaning procedure.
- Repair or replace any damaged batteries.

2. Any fluids on or around the battery may be an indication that electrolyte is spilling, leaching, or leaking out.

- Leaking batteries must be repaired or replaced.

3. Check all battery cables and their connections.

- Look closely for loose or damaged parts.
- Battery cables should be intact; broken or frayed cables can be extremely hazardous.
- Replace any cable that looks suspicious.

4. Tighten all wiring connections to the proper specification (see below). Make certain there is good contact with the terminals.

Proper Torque Values for Connection Hardware			
Flooded		**VRLA**	
Automotive	50 – 70 in-lbs	Button	90 – 100 in-lbs
Side	70 – 90 in-lbs	LT	100 – 120 in-lbs
Wingnut	95 – 105 in-lbs		
LPT	95 – 105 in-lbs		
Stud	120 – 180 in-lbs		
LT	100 – 120 in-lbs		

WARNING: Do not overtighten terminals. Doing so can result in post breakage, post meltdown, or fire.

BACK TO TOP

Testing

Visual inspection alone is not sufficient to determine the overall health of the battery.

Both open-circuit voltage and specific gravity readings can give a good indication of the battery's charge level, age, and health. Routine voltage and gravity checks will not only show the state of charge but also help spot signs of improper care, such as undercharging and over-watering, and possibly even locate a bad or weak battery. The following steps outline how to properly perform routine voltage and specific gravity testing on batteries.

I. Specific Gravity Test (Flooded batteries only)

1. Do not add water at this time.
2. Fill and drain the hydrometer 2 to 4 times before pulling out a sample.
3. There should be enough sample electrolyte in the hydrometer to completely support the float.
4. Take a reading, record it, and return the electrolyte back to the cell.
5. To check another cell, repeat the 3 steps above.
6. Check all cells in the battery.
7. Replace the vent caps and wipe off any electrolyte that might have been spilled.
8. Correct the readings to 80º F (26.6º C):
   • Add 0.004 to readings for every 10º F (5.6º C) above 80º F (26.6º C)

Figure H.9. Trojan Battery Maintenance (page 3/10) (reprinted from Trojan Battery Company, 2020).

- Subtract 0.004 for every 10º (5.6º C) below 80º F (26.6º C)

9. Compare the readings.
10. Check the state of charge using Table 1 below.

The readings should be at or above the factory specification of 1.277 +/- 0.007. If any specific gravity readings register low, then follow the steps below.

1. Check and record voltage level(s).
2. Put battery(s) on a complete charge.
3. Take specific gravity readings again.

If any specific gravity readings still register low then follow the steps below.

1. Check voltage level(s).
2. Perform equalization charge. Refer to the Equalizing section for the proper procedure.
3. Take specific gravity readings again.

If any specific gravity reading still registers lower than the factory specification of 1.277+/- 0.007 then one or more of the following conditions may exist:

1. The battery is old and approaching the end of its life.
2. The battery was left in a state of discharge too long.
3. Electrolyte was lost due to spillage or overflow.
4. A weak or bad cell is developing.
5. Battery was watered excessively previous to testing.

Batteries in conditions 1 – 4 should be taken to a specialist for further evaluation or retired from service.

II. Open-Circuit Voltage Test

For accurate voltage readings, batteries must remain idle (no charging, no discharging) for at least 6 hrs, preferably 24 hrs.

1. Disconnect all loads from the batteries.
2. Measure the voltage using a DC voltmeter.
3. Check the state of charge with Table 1 below.
4. Charge the battery if it registers 0% to 70% charged.

If battery registers below the Table 1 values, the following conditions may exist:

1. The battery was left in a state of discharge too long.
2. The battery has a bad cell.

Batteries in these conditions should be taken to a specialist for further evaluation or retired from service.

TABLE 1

State of Charge as Related to Specific Gravity and Open Circuit Voltage

Percentage of Charge	Specific Gravity Corrected To	Open-Circuit Voltage					
		6v	8v	12v	24v	36v	48v
100	1.277	6.37	8.49	12.73	25.46	38.20	50.93
90	1.258	6.31	8.41	12.62	25.24	37.85	50.47
80	1.238	6.25	8.33	12.50	25.00	37.49	49.99
70	1.217	6.19	8.25	12.37	24.74	37.12	49.49
60	1.195	6.12	8.16	12.27	24.48	36.72	48.96
50	1.172	6.02	8.07	12.10	24.20	36.31	48.41
40	1.148	5.98	7.97	11.89	23.92	35.87	47.83
30	1.124	5.91	7.88	11.81	23.63	35.44	47.26
20	1.098	5.83	7.77	11.66	23.32	34.97	46.63
10	1.073	5.75	7.67	11.51	23.02	34.52	46.03

Figure H.10. Trojan Battery Maintenance (page 4/10) (reprinted from Trojan Battery Company, 2020).

BACK TO TOP

Watering

FLOODED BATTERIES ONLY

Flooded batteries need water.

More importantly, watering must be done at the right time and in the right amount or the battery's performance and longevity suffers.

Water should always be added after fully charging the battery. Prior to charging, there should be enough water to cover the plates. If the battery has been discharged (partially or fully), the water level should also be above the plates. Keeping the water at the correct level after a full charge will prevent having to worry about the water level at a different state of charge.

Depending on the local climate, charging methods, application, etc., Trojan recommends that batteries be checked once a month until you get a feel for how often your batteries are need watering.

Important Things to Remember

1. Do not let the plates get exposed to air. This will damage (corrode) the plates.
2. Do not fill the water level in the filling well to the cap. This most likely will cause the battery to overflow acid, consequently losing capacity and causing a corrosive mess.
3. Do not use water with a high mineral content. Use distilled or deionized water only.

CAUTION: The electrolyte is a solution of acid and water so skin contact should be avoided.

Step-By-Step Watering Procedure

1. Open the vent caps and look inside the fill wells.
2. Check electrolyte level; the minimum level is at the top of the plates.
3. If necessary add just enough water to cover the plates at this time.
4. Put batteries on a complete charge before adding any additional water (refer to the Charging section).
5. Once charging is completed, open the vent caps and look inside the fill wells.
6. Add water until the electrolyte level is 1/8″ below the bottom of the fill well.
7. A piece of rubber can be used safely as a dipstick to help determine this level.
8. Clean, replace, and tighten all vent caps.

WARNING: Never add acid to a battery.

BACK TO TOP

Cleaning

Batteries seem to attract dust, dirt, and grime. Keeping them clean will help spot signs of trouble when they appear and avoid problems associated with grime.

1. Check that all vent caps are tightly in place.
2. Clean the battery top with a cloth or brush and a solution of baking soda and water.
   - When cleaning, do not allow any cleaning solution or other foreign matter to get inside the battery.
3. Rinse with water and dry with a clean cloth.
4. Clean battery terminals and the inside of cable clamps using a post and clamp cleaner.
   - Clean terminals will have a bright metallic shine.
5. Reconnect the clamps to the terminals and thinly coat them with an anti-corrosive spray or silicon gel.
6. Keep the area around batteries clean and dry.

BACK TO TOP

Figure H.11. Trojan Battery Maintenance (page 5/10) (reprinted from Trojan Battery Company, 2020).

Storage

Periods of inactivity can be extremely harmful to lead acid batteries. When placing a battery into storage, follow the recommendations below to ensure that the battery remains healthy and ready for use.

NOTE: Storing, charging or operating batteries on concrete is perfectly OK.

The Most Important Things to Avoid

1. Freezing. Avoid locations where freezing temperature are expected. Keeping a battery at a high state of charge will also prevent freezing. Freezing results in irreparable damage to a battery's plates and container.
2. Heat. Avoid direct exposure to heat sources, such as radiators or space heaters. Temperatures above 80° F (26.6° C) accelerate the battery's self-discharge characteristics.

Step-By-Step Storage Procedure

1. Completely charge the battery before storing.
2. Store the battery in a cool, dry location, protected from the elements.
3. During storage, monitor the specific gravity (flooded) or voltage. Batteries in storage should be given a boost charge when they show a 70% charge or less. See Table 1 in the Testing Section.
4. Completely charge the battery before re-activating.
5. For optimum performance, equalize the batteries (flooded) before putting them back into service. Refer to the Equalizing section for this procedure.

BACK TO TOP

Charger Selection

Most deep-cycle applications have some sort of charging system already installed for battery charging (e.g. solar panels, inverter, golf car charger, alternator, etc.). However, there are still systems with deep-cycle batteries where an individual charger must be selected. The following will help in making a proper selection.

There are many types of chargers available today. They are usually rated by their start rate, the rate in amperes that the charger will supply at the beginning of the charge cycle. When selecting a charger, the charge rate should be between 10% and 13% of the battery's 20-hour AH capacity. For example, a battery with a 20-hour capacity rating of 225 AH will use a charger rated between approximately 23 and 30 amps (for multiple battery charging use the AH rating of the entire bank). Chargers with lower ratings can be used but the charging time will be increased.

Trojan recommends using a 3-stage charger. Also called "automatic", "smart" or "IEI" chargers, which prolong battery life with their programmed charging profile. These chargers usually have three distinct charging stages: bulk, acceptance, and float.

BACK TO TOP

Charging

Charging batteries properly requires administering the right amount of current at the right voltage. Most charging equipment automatically regulates these values. Some chargers allow the user to set these values. Both automatic and manual equipment can present difficulties in charging. Tables 2 & 3 list most of the necessary voltage settings one might need to program a charger. In either case the original instructions for your charging equipment should also be referenced for proper charging. Here is list of helpful items to remember when charging.

1. Become familiar with and follow the instructions issued by the charger manufacturer.
2. Batteries should be charged after each period of use.
3. Lead acid batteries do not develop a memory and do need not be fully discharged before recharging.
4. Charge only in well-ventilated areas. Keep sparks or flames away from a charging battery.
5. Verify charger voltage settings are correct (Table 2).
6. Correct the charging voltage to compensate for temperatures above and below 80° F (26.6°C). (Add .028 volt per cell for every 10° below 80° F (26.6°C) and subtract 0.028 volt per cell for every 10° F (12.2°C) above 80° F (26.6° C))
7. Check water level (see the Watering section).
8. Tighten all vent caps before charging.
9. Prevent overcharging the batteries. Overcharging causes excessive gassing (water breakdown), heat buildup, and battery aging.
10. Prevent undercharging the batteries. Undercharging causes stratification which can lead to premature battery failure.

Figure H.12. Trojan Battery Maintenance (page 6/10) (reprinted from Trojan Battery Company, 2020).

11. Do not charge a frozen battery.
12. Avoid charging at temperatures above 120° F (48.8° C).

Table 2					
Charger Voltage Settings for Flooded Batteries	System Voltage				
Charger Voltage Setting	6v	12v	24v	36v	48v
Bulk Charge	7.4	14.8	29.6	44.5	59.3
Float Charge	6.7	13.5	27	40.5	54
Equalize Charge	8.1	16.2	32.4	48.6	64.8

Table 3				
Charger Voltage Settings for VRLA Batteries	**System Voltage**			
Charger Voltage Setting	12v	24v	36v	48v
Bulk Charge	14.4	28.8	43.2	57.6
Float Charge	13.5	27	40.5	54

Additional VRLA Charging Instructions:

1. Become familiar with and follow the instructions issued by the charger manufacturer.
2. Verify charger has necessary VRLA setting.
3. Set charger to VRLA voltage settings (Table 3).
4. Do not overcharge VRLA batteries. Overcharging will dry out the electrolyte and damage battery.

BACK TO TOP

Equalizing

FLOODED BATTERIES ONLY

Equalizing is an overcharge performed on flooded lead acid batteries after they have been fully charged.

It reverses the buildup of negative chemical effects like stratification, a condition where acid concentration is greater at the bottom of the battery than at the top. Equalizing also helps to remove sulfate crystals that might have built up on the plates. If left unchecked, this condition, called sulfation, will reduce the overall capacity of the battery.

Many experts recommend that batteries be equalized periodically, ranging anywhere from once a month to once or twice per year. However, Trojan only recommends equalizing when low or wide ranging specific gravity (>0.030) are detected after fully charging a battery.

Step-By-Step Equalizing

1. Verify the battery(s) are flooded type.
2. Remove all loads from the batteries.
3. Connect battery charger.
4. Set charger for the equalizing voltage *(See Table 2 in the Charging section)*. If your charger doesn't have an equalization mode, you can unplug the charger and re-plug it back in. This also will conduct the equalization charge.
5. Start charging batteries.
6. Batteries will begin gassing and bubbling vigorously.
7. Take specific gravity readings every hour.
8. Equalization is complete when specific gravity values no longer rise during the gassing stage.

BACK TO TOP

Figure H.13. Trojan Battery Maintenance (page 7/10) (reprinted from Trojan Battery Company, 2020).

Discharging

Discharging batteries is entirely a function of your particular application.

However, below is list of helpful items:

1. Shallow discharges will result in a longer battery life.
2. 50% (or less) discharges are recommended.
3. 80% discharge is the maximum safe discharge.
4. Do not fully discharge flooded batteries (80% or more). This will damage (or kill) the battery.
5. Many experts recommend operating batteries only between the 50% to 85% of full charge range. A periodic equalization charge is a must when using this practice.
6. Do not leave batteries deeply discharged for any length of time.
7. Lead acid batteries do not develop a memory and do not need to be fully discharged before recharging.
8. Batteries should be charged after each period of use.
9. Batteries that charge up but cannot support a load are most likely bad and should be tested. Refer to the Testing section for proper procedure.

% Discharged					
100	80	60	40	20	0
0	20	40	60	80	100

BACK TO TOP

Watering Diagram

Flooded batteries need water.

But more importantly, watering must be done at the right time and in the right amount or the battery's performance and longevity suffers.

General Watering Instructions:

- Add water, never acid, to cells *(distilled water recommended)*
- DO NOT OVERWATER
- For fully charged standard deep-cycle batteries, add water to the level of 1/8 below bottom of vent well *(see diagram A below)*
- For fully charged Plus Series batteries, add water to the maximum water level indicator *(see diagram B below)*
- If the batteries are discharged, only add water if the plates are exposed. Add just enough water to cover the plates, then charge the batteries. Once fully charged, add water to the proper level indicated above
- After watering, secure vent caps on batteries

Diagram A **Diagram B**

Figure H.14. Trojan Battery Maintenance (page 8/10) (reprinted from Trojan Battery Company, 2020).

Add water to 0.125″ below bottom of the vent well.

Add water to the maximum water level indicator.

BACK TO TOP

Tips For Maximizing Your Battery Life

FOR SOLAR APPLICATION

Store and operate your batteries in a cool, dry place.
For every 18° F (10° C) rise above room temperature (77° F or 25° C), battery life decreases by 50%.

Charge your batteries fully after each period of use.
Allowing your batteries to sit in a low state of charge for extended periods will decrease their capacity and life.

If you store your batteries for an extended period of time, be sure to charge them fully every 3 to 6 months. Lead acid batteries will self-discharge 5% to 15% per month, depending on the temperature of the storage conditions.

Monitor battery voltage and specific gravity of the electrolyte regularly to verify full recharging. As a general rule of thumb, the total amps from your PV panels should be sized between 10% and 20% of the total amp-hours (Ah) of the battery pack.

Many charge controllers have equalization settings that you can set to help ensure the health of your batteries. Equalize your batteries at least once per month for 2 to 4 hours, longer if your batteries have been consistently undercharged.

System Voltage					
Voltage Settings	6V	12V	24V	36V	48V
Daily Charge	7.4	14.8	29.6	44.5	59.3
Float Charge	6.7	13.5	27	40.5	54
Equalize Charge	8.1	16.2	32.4	48.6	64.8

Water your batteries regularly.
Flooded, or wet cell batteries require watering periodically. Check your batteries once a month after installation to determine the proper watering schedule. Add water after fully charging the battery and use distilled water.

For procedures on watering, checking battery voltage and other maintenance instructions, refer to our battery maintenance section for more details.

BACK TO TOP

Figure H.15. Trojan Battery Maintenance (page 9/10) (reprinted from Trojan Battery Company, 2020).

Renewable Energy Brochure
Transportation Brochure
HydroLink Data Sheet
Trojan iPad App

Events
Our Mission
Privacy Policy
Legal

BLUE HEART CAMPAIGN

CALIFORNIA TRANSPARENCY ACT

Request MORE INFORMATION

Site Map

Figure H.16. Trojan Battery Maintenance (page 10/10) (reprinted from Trojan Battery Company, 2020).

References of Appendix H

Golden Motor Technology Co., Ltd. (2016). 5-kW BLDC electric motor, controller and wiring diagram (pictures and specs). Changzhou, Jiangsu, China. Available online: https://www.goldenmotor.com/ (accessed on 17 November 2020).

Trojan Battery Company (2020). Data Sheet of Battery, model T-1275. Available online: https://www.trojanbattery.com/pdf/datasheets/T1275_Trojan_Data_Sheets.pdf (accessed on 18 November 2020).

APPENDIX I

MCMASTER-CARR MATERIALS*

I.1. Keyed Rotary Shaft Datasheet

McMaster-Carr - Keyed Rotary Shaft, 1045 Carbon Steel, 1" Diameter, 6" Long 5/13/17, 17(37

McMASTER-CARR®

Keyed Rotary Shaft
1045 Carbon Steel, 1" Diameter, 6" Long

In stock
$17.12 Each
1497K144

Material	1045 Carbon Steel
Diameter	1"
Length	6"
Keyway	
Width	1/4"
Depth	1/8"
Length	6"
ANSI Keys Included	No
Diameter Tolerance	-0.0025" to -0.001"
Straightness Tolerance	0.012" per ft.
Length Tolerance	-0.0313" to 0.0313"
End Shape	Chamfered
Hardness Rating	Medium
Hardness	Rockwell B95
Yield Strength	75,000 psi
For Motion Type	Rotary
Shaft Type	Keyed
End Type	Straight
RoHS	Compliant

Made of carbon steel, these shafts are stronger than aluminum and stainless steel shafts. For a secure hold in high-torque applications, an ANSI keyway runs along the length of the shaft (keys not included; see our selection of key stock). Commonly known as drive shafts, rotary shafts are often used with gears, sprockets, rotary bearings and other power transmission components.

https://www.mcmaster.com/#1497k144/=17m2z6r Page 1 of 2

Figure I.1. Keyed rotary shaft specs (reprinted from McMaster-Carr, 2016).

* All figures on this Appendix were reprinted form McMaster-Carr (2016). McMaster-Carr Supply Company catalog. Atlanta, Georgia, USA. Available online: https://www.mcmaster.com/ (accessed on 17 November 2020).

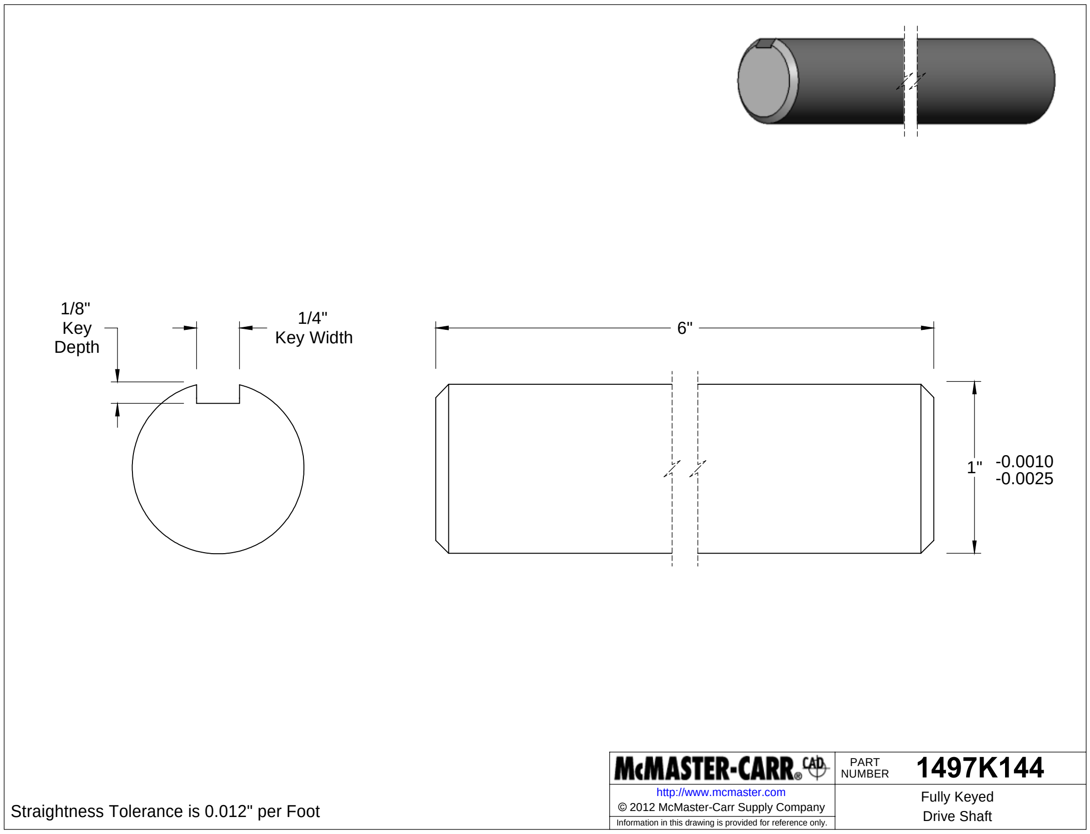

Figure I.2. Keyed rotary shaft drawing (reprinted from McMaster-Carr, 2016).

I.2. Coupling Hubs and Rubber Spider Datasheets

McMaster-Carr - Flexible Shaft Coupling, Iron Hub for 1/4" to 1" & 12mm to 24mm Diameter Shaft 5/13/17, 18)44

McMASTER-CARR®

Flexible Shaft Coupling

Iron Hub for 1/4" to 1" & 12mm to 24mm Diameter Shaft

In stock
$10.37 Each
6408K14

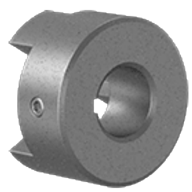

Hubs and Spider Shown Assembled

Overall Length	2 5/32"
OD	2 7/64"
Keyway	
Width	3/16"
Depth	3/32"
For Shaft Type	Keyed
For Shaft Misalignment Type	Parallel, Angular
For Motion Type	Forward/Reverse, Start/Stop
Shaft Coupling Type	Flexible
Construction	Multipiece
Shaft Mount Type	Set Screw
Set Screw	
Type	Hex Socket
Material	Steel
Number Included	1
Component	Hub
Material	Iron
For Shaft Dia.	7/8"
RoHS	Compliant
Related Products	Buna-N Rubber Spiders
	Hytrel Rubber Spiders
	Polyurethane Split Spiders
	347 Stainless Steel Retaining Rings
	Polyurethane Spiders

Each hub includes a set screw, which bites into your shaft to hold the coupling in place. Also known as Lovejoy couplings, these three-piece couplings have a spider-shaped cushion between two hubs to reduce shock and handle minor shaft misalignment.

A complete coupling consists of two hubs and one spider, or two hubs, one split spider, and one retaining ring (all components sold separately). Split spiders are easier to install and replace than standard spiders because there's no need for tools or removing your hubs. Twist-lock them in place using a retaining ring.

Hubs for 1/2" shaft dia. and above (unless noted) and all metric sizes have a keyway.

https://www.mcmaster.com/#6408k14/=17m44h9 Page 1 of 2

Figure I.3. Flexible shaft coupling hub for 22.2-mm shaft specs (reprinted from McMaster-Carr, 2016).

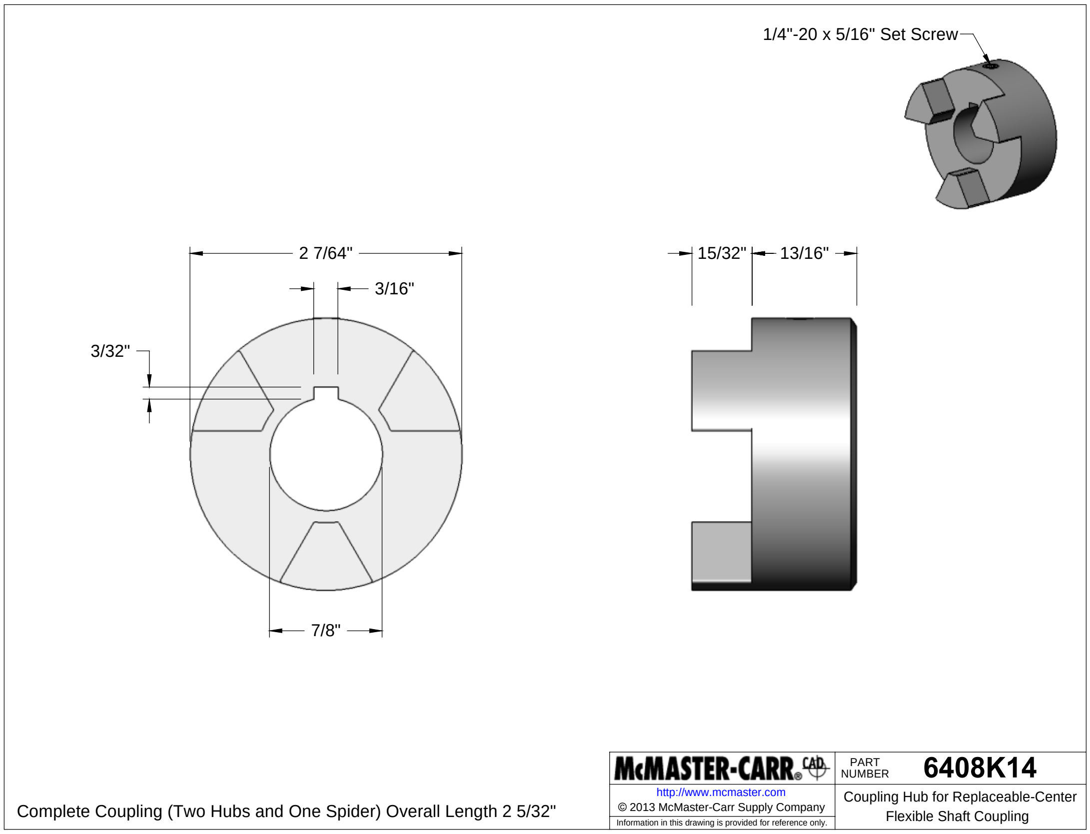

Figure I.4. Flexible shaft coupling hub for 22.2-mm shaft drawing (reprinted from McMaster-Carr, 2016).

McMASTER-CARR®

Flexible Shaft Coupling Iron Hub
with Set Screw, 2-5/32" Overall Length, 2-7/64" OD

In stock
$10.37 Each
6408K14

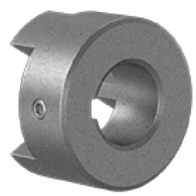

Hubs and Spider Shown Assembled

Overall Length	2 5/32"
OD	2 7/64"
Keyway	
Width	1/4"
Depth	1/8"
For Shaft Type	Keyed
For Shaft Misalignment Type	Parallel, Angular
For Motion Type	Forward/Reverse, Start/Stop
Shaft Coupling Type	Flexible
Construction	Multipiece
Shaft Mount Type	Set Screw
Set Screw	
Type	Hex Socket
Material	Steel
Number Included	1
Component	Hub
Material	Iron
For Shaft Dia.	1"
RoHS	Compliant
Related Products	Buna-N Rubber Spiders
	Hytrel Rubber Spiders
	Polyurethane Split Spiders
	347 Stainless Steel Retaining Rings
	Polyurethane Spiders

Each hub includes a set screw, which bites into your shaft to hold the coupling in place. Also known as Lovejoy couplings, these three-piece couplings have a spider-shaped cushion between two hubs to reduce shock and handle minor shaft misalignment.

A complete coupling consists of two hubs and one spider, or two hubs, one split spider, and one retaining ring (all components sold separately). Split spiders are easier to install and replace than standard spiders because there's no need for tools or removing your hubs. Twist-lock them in place using a retaining ring.

Hubs for 1/2" shaft dia. and above (unless noted) and all metric sizes have a keyway.

Figure I.5. Flexible shaft coupling hub for 25.4-mm shaft specs (reprinted from McMaster-Carr, 2016).

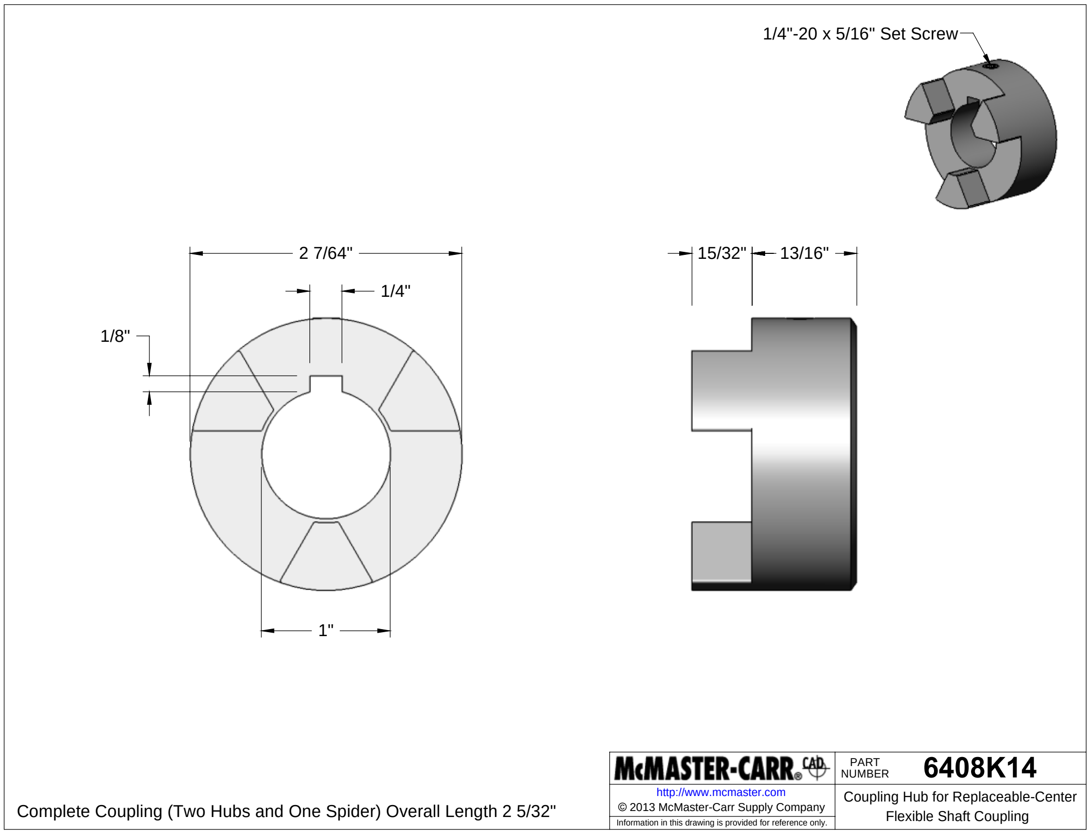

Figure I.6. Flexible shaft coupling hub for 25.4-mm shaft drawing (reprinted from McMaster-Carr, 2016).

MCMASTER-CARR®

Buna-N Spider for 2-7/64" Outside Diameter Flexible Shaft Coupling

In stock
$7.72 Each
6408K75

Component	Spider
Material	Buna-N Rubber
Maximum Speed	9,000 rpm
Maximum Torque	140 in.-lbs.
Misalignment Capability	
Parallel	0.015"
Angular	1°
Temperature Range	-40° to 212° F
RoHS	Compliant

Figure I.7. Buna-N spider for shaft coupling hubs specs (reprinted from McMaster-Carr, 2016).

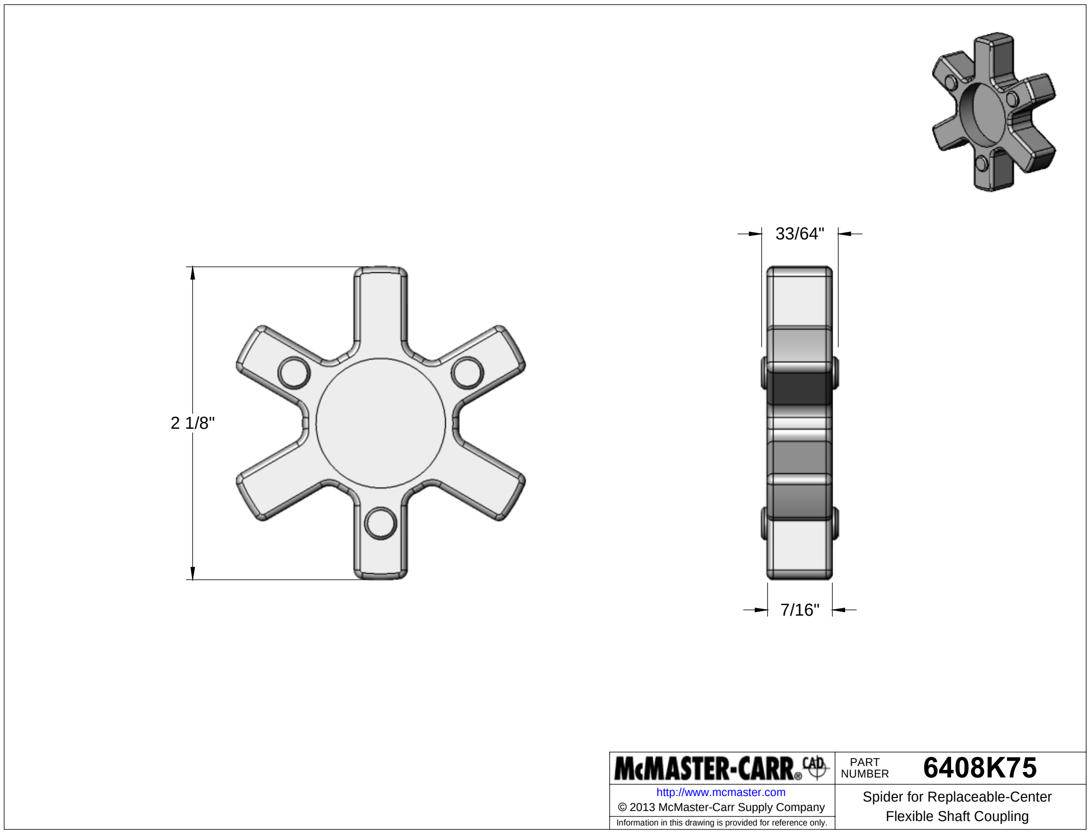

Figure I.8. Buna-N spider for shaft coupling hubs drawing (reprinted from McMaster-Carr, 2016).

I.3. Shaft Standard and Metric Key Stock Datasheets

McMASTER-CARR®

1095 Spring Steel Machine Key Stock
1/4" x 1/4", 12" Long

In stock
$3.23 Each
98535A150

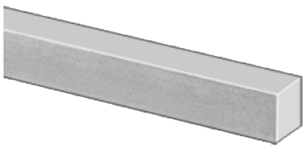

Material	1095 Spring Steel
Size	1/4" × 1/4"
Length	12"
Tolerance	
Size	-0.015" to 0.015"
Length	-0.125" to 0"
Tolerance Rating	Standard
Minimum Hardness	Rockwell B91
Key Type	Straight
System of Measurement	Inch
RoHS	Compliant

Made from 1095 steel, this stock is annealed for easy machining and can be heat treated for strength. Ready to cut with very little filing needed, it may be slightly larger or smaller than the size listed in the table. Use it to create a machine key at the length you need.

Figure I.9. Standard spring steel machine key stock specs (reprinted from McMaster-Carr, 2016).

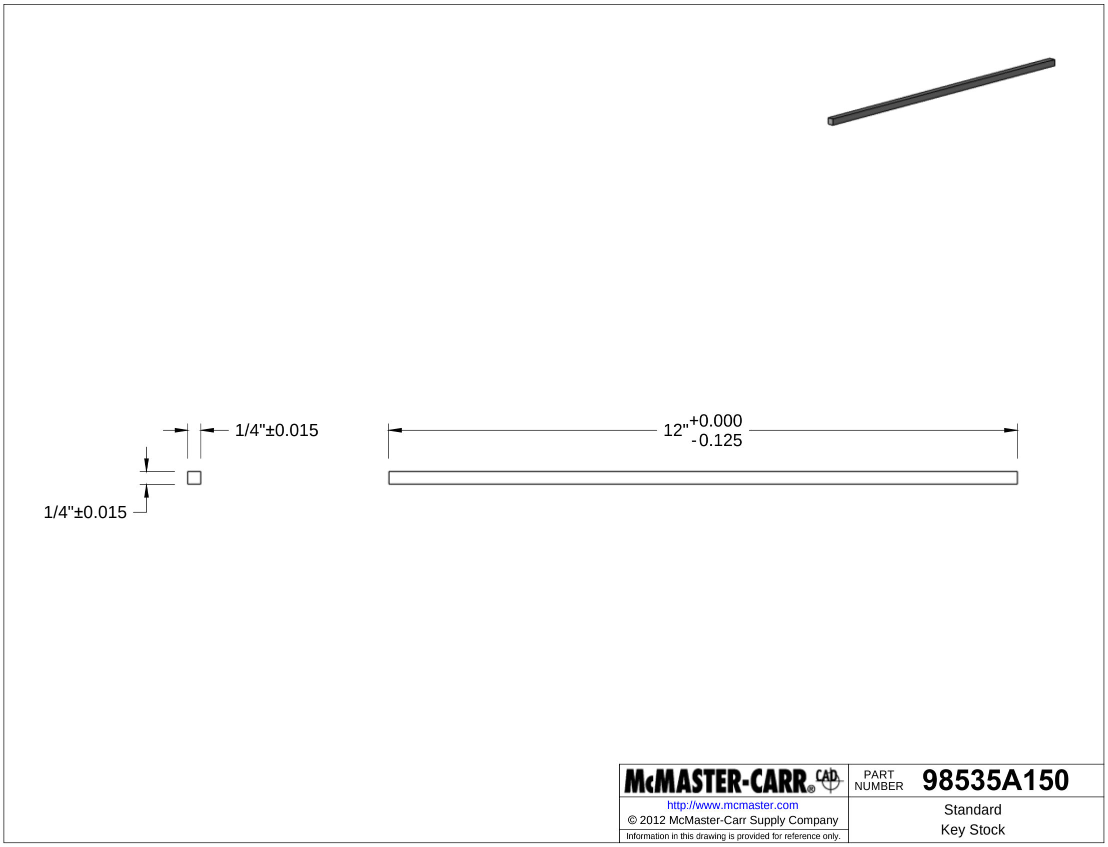

Figure I.10. Standard spring steel machine key stock drawing (reprinted from McMaster-Carr, 2016).

McMASTER-CARR®

Metric Steel Machine Key Stock

Undersized, 5 x 5 mm, 12" Long

In stock
$2.38 Each
92288A725

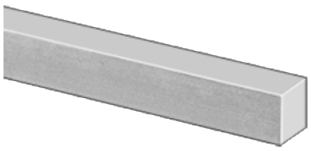

Material	Steel
Size	5 × 5 mm
Length	12"
Tolerance	
Size	-0.075 to 0 mm
Length	-0.125" to 0"
Tolerance Rating	Undersized
Minimum Hardness	Not Rated
Specifications Met	DIN 6880
Key Type	Straight
System of Measurement	Metric
RoHS	Compliant

Slightly smaller than the size listed in the table, this metric stock is the choice when you need a slightly looser fit or when you have an inconsistent keyway. Made of steel, it is economical with high strength. Use it to create a machine key at the length you need.

Figure I.11. Metric steel machine key stock specs (reprinted from McMaster-Carr, 2016).

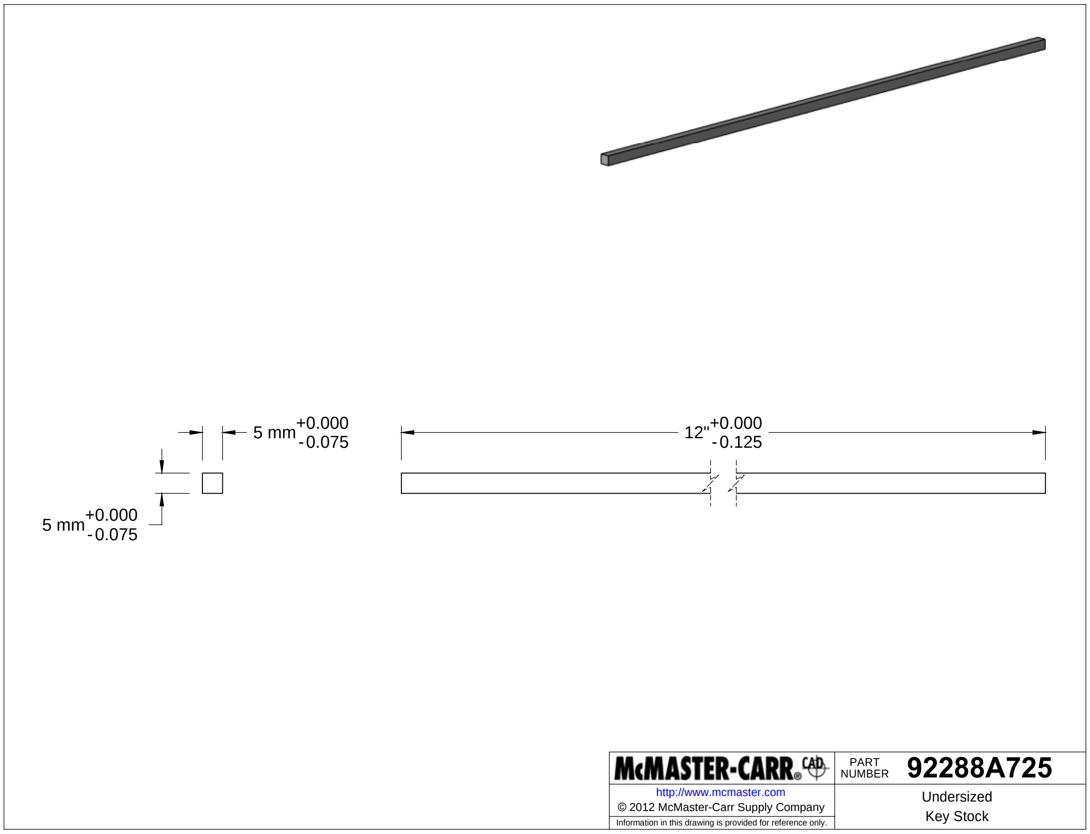

Figure I.12. Metric steel machine key stock drawing (reprinted from McMaster-Carr, 2016).

I.4. Mounted Ball Bearing Datasheet

McMASTER-CARR®

Mounted Ball Bearing with Cast Iron Housing
for 1" Shaft Diameter, with Set Screw

In stock
$81.00 Each
7728T56

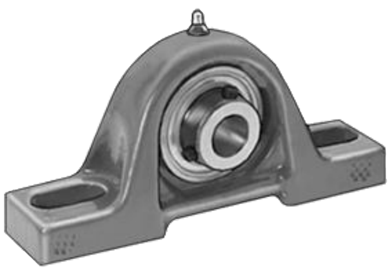

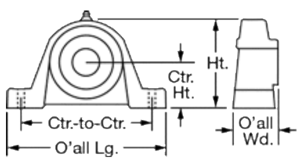

Mounted Bearing Component	Complete Unit
Bearing Type	Ball
For Load Direction	Radial
Mounted Bearing Type	Base Mount
Base Mount Type	Solid
Shaft Mount Type	Set Screw
Number of Set Screws	2
Seal Type	Double Sealed
For Shaft Diameter	1"
ID	1.000"
ID Tolerance	0.0002" to 0.0007"
Center Height	1 7/16"
Width	1 3/8"
Height	2 13/16"
Overall	
Height	3 3/16"
Length	5 1/2"
Width	1 3/8"
Material	
Bearing	52100 Steel
Housing	Cast Iron
Lubrication	Lubricated
Lubrication Method	Filled
Lubricant Type	Grease
Lubricant	GoldPlex-HP
Lubrication Port	Grease Fitting
Dynamic Radial Load Capacity	2,801 lbs.
Maximum Speed	6,350 rpm
Temperature Range	0° to 220° F
ABEC Rating	ABEC-1
Alignment Style	Self Aligning
Misalignment Capability	2°
Mounting Hole Size	3/8"
Mounting Holes Center-to-	4 1/8"

Figure I.13. Mounted ball bearing specs (reprinted from McMaster-Carr, 2016).

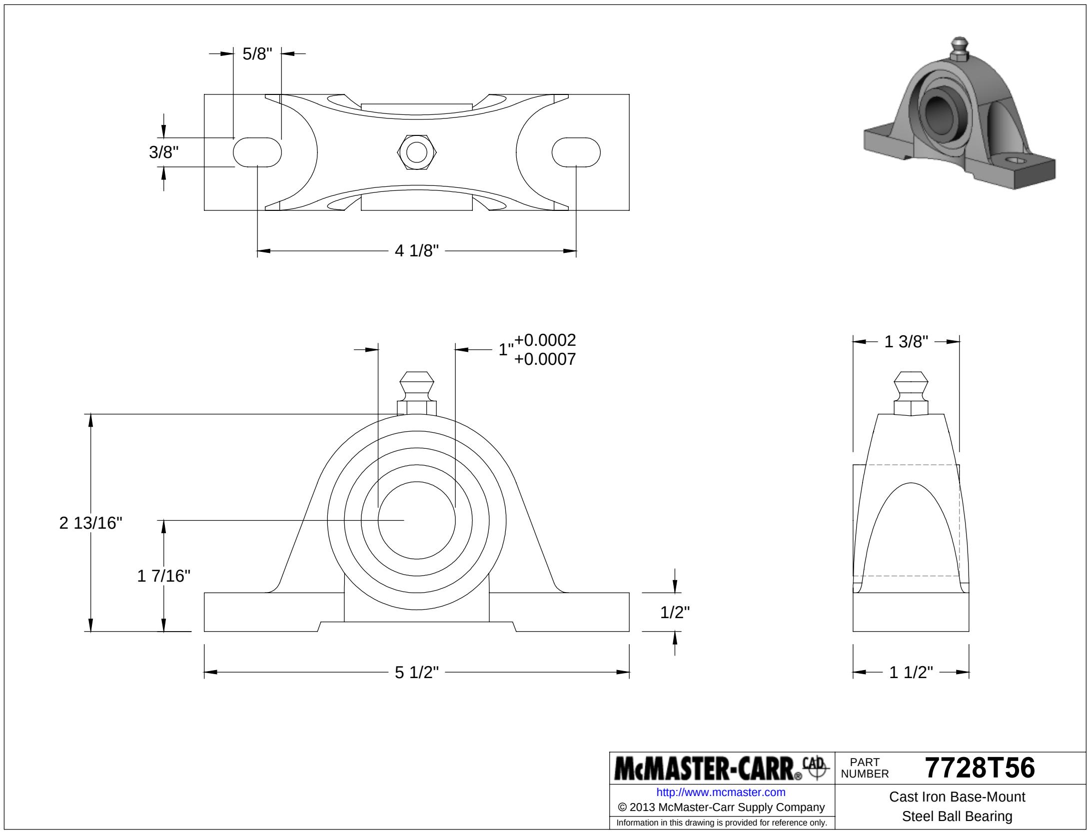

Figure I.14. Mounted ball bearing drawing (reprinted from McMaster-Carr, 2016).

I.5. Fasteners for the Top Chassis Subassembly

McMaster-Carr - Zinc-Plated Alloy Steel Socket Head Screw, 3/8"-24 Thread Size, 1-1/4" Long 5/27/17, 18)20

McMASTER-CARR®

Zinc-Plated Alloy Steel Socket Head Screw
3/8"-24 Thread Size, 1-1/4" Long

In stock
$5.68 per pack of 10
90128A367

Thread Size	3/8"-24
Length	1 1/4"
Threading	Fully Threaded
Head Diameter	0.563"
Head Height	0.375"
Drive Size	5/16"
Material	Zinc-Plated Alloy Steel
Hardness	Rockwell C37
Tensile Strength	170,000 psi
Screw Size Decimal Equivalent	0.375"
Thread Type	UNF
Thread Spacing	Fine
Thread Fit	Class 3A
Thread Direction	Right Hand
Head Type	Socket
Socket Head Profile	Standard
Drive Style	Hex
Specifications Met	ASTM A574
System of Measurement	Inch
RoHS	Compliant

These screws are made from an alloy steel that's stronger than Grade 8 steel. Length is measured from under the head.

Zinc-plated steel screws are more corrosion resistant than black-oxide screws for use in wet environments.

https://www.mcmaster.com/#90128a367/=17tb3fw Page 1 of 2

Figure I.15. Zinc-plated alloy steel socket head screw specs (part number 90128A367) (reprinted from McMaster-Carr, 2016).

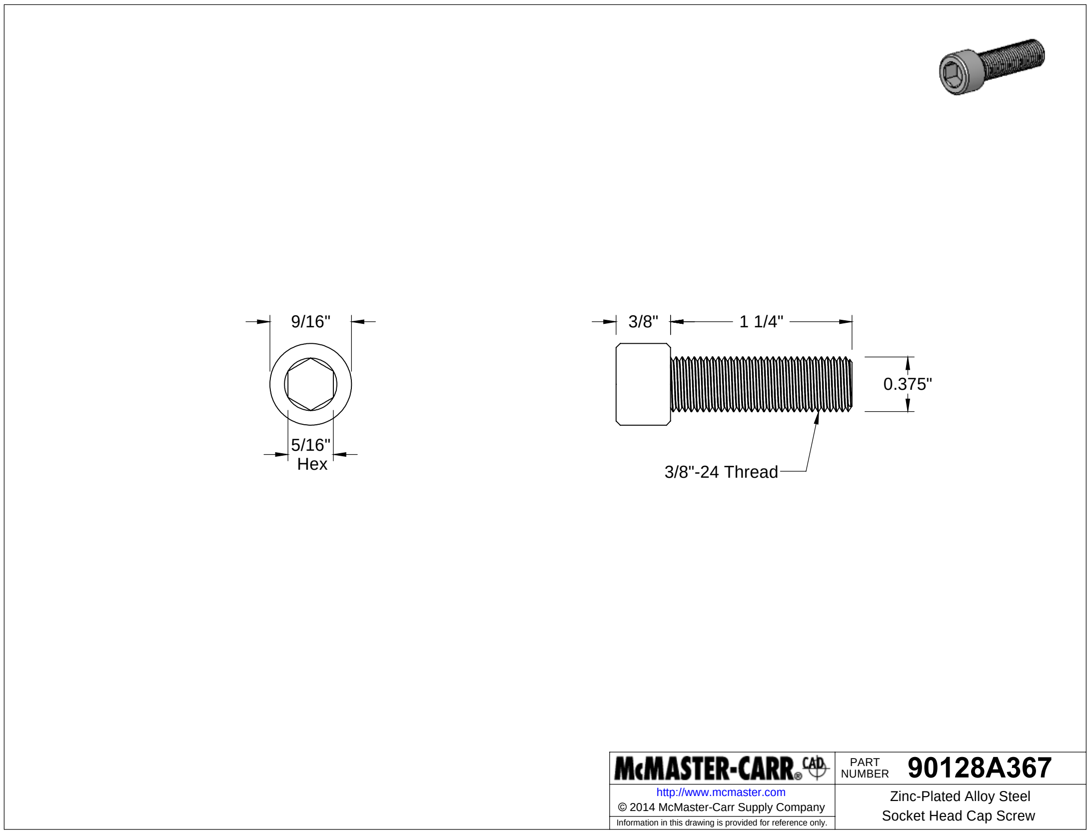

Figure I.16. Zinc-plated alloy steel socket head screw drawing (part number 90128A367) (reprinted from McMaster-Carr, 2016).

McMASTER-CARR®

Zinc Yellow-Chromate Plated Steel Split Lock Washer
for 1/2" Screw Size, 0.512" ID, 0.869" OD

In stock
$11.67 per pack of 100
91104A033

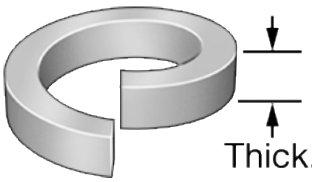

Material	Zinc Yellow-Chromate Plated Steel
Fastener Strength Grade/Class	Grade 8
For Screw Size	1/2"
ID	0.512"
OD	0.869"
Thickness	0.125"
Washer Type	Split Lock
System of Measurement	Inch
Hardness	Rockwell C38
Specifications Met	ASME B18.21.1
RoHS	Not Compliant

As a screw is tightened, these washers flatten to add tension to the joint and prevent loosening from small amounts of vibration.

Zinc- and zinc yellow-chromate plated steel washers are corrosion resistant in wet environments.

Figure I.17. Zinc yellow-chromate plated steel split lock washer specs (part number 91104A033) (reprinted from McMaster-Carr, 2016).

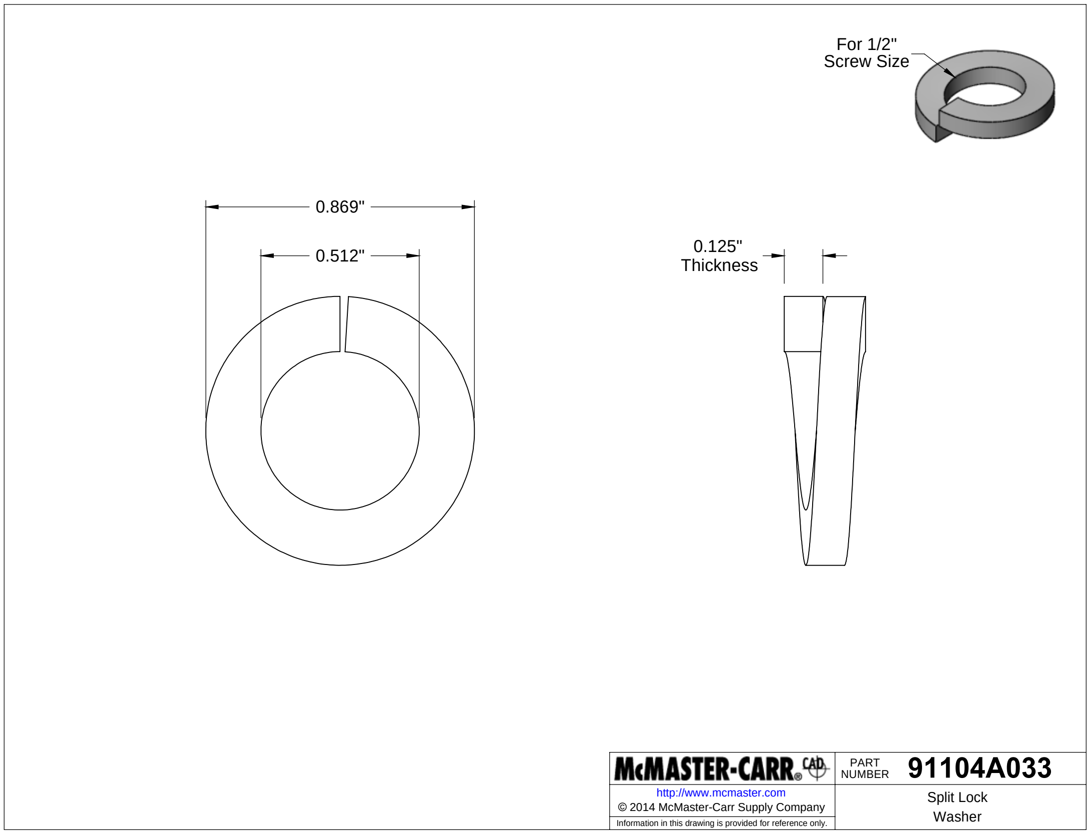

Figure I.18. Zinc yellow-chromate plated steel split lock washer drawing (part number 91104A033) (reprinted from McMaster-Carr, 2016).

McMASTER-CARR®

Medium-Strength Grade 5 Steel Hex Head Screw

Zinc-Plated, 3/8"-24 Thread Size, 3" Long, Partially Threaded

In stock
$12.59 per pack of 25
91247A231

Thread Size	3/8"-24
Length	3"
Threading	Partially Threaded
Minimum Thread Length	1"
Head Width	9/16"
Head Height	1/4"
Material	Zinc-Plated Steel
Fastener Strength Grade/Class	Grade 5
Hardness	Rockwell C25
Tensile Strength	120,000 psi
Screw Size Decimal Equivalent	0.375"
Thread Type	UNF
Thread Spacing	Fine
Thread Fit	Class 2A
Thread Direction	Right Hand
Head Type	Hex
Hex Head Profile	Standard
Drive Style	External Hex
Specifications Met	ASME B18.2.1, SAE J429
System of Measurement	Inch
RoHS	Compliant

These screws are suitable for fastening most machinery and equipment. Length is measured from under the head.

Zinc-plated steel screws resist corrosion in wet environments.

Figure I.19. Medium-strength grade 5 steel hex head screw specs (part number 91247A231) (reprinted from McMaster-Carr, 2016).

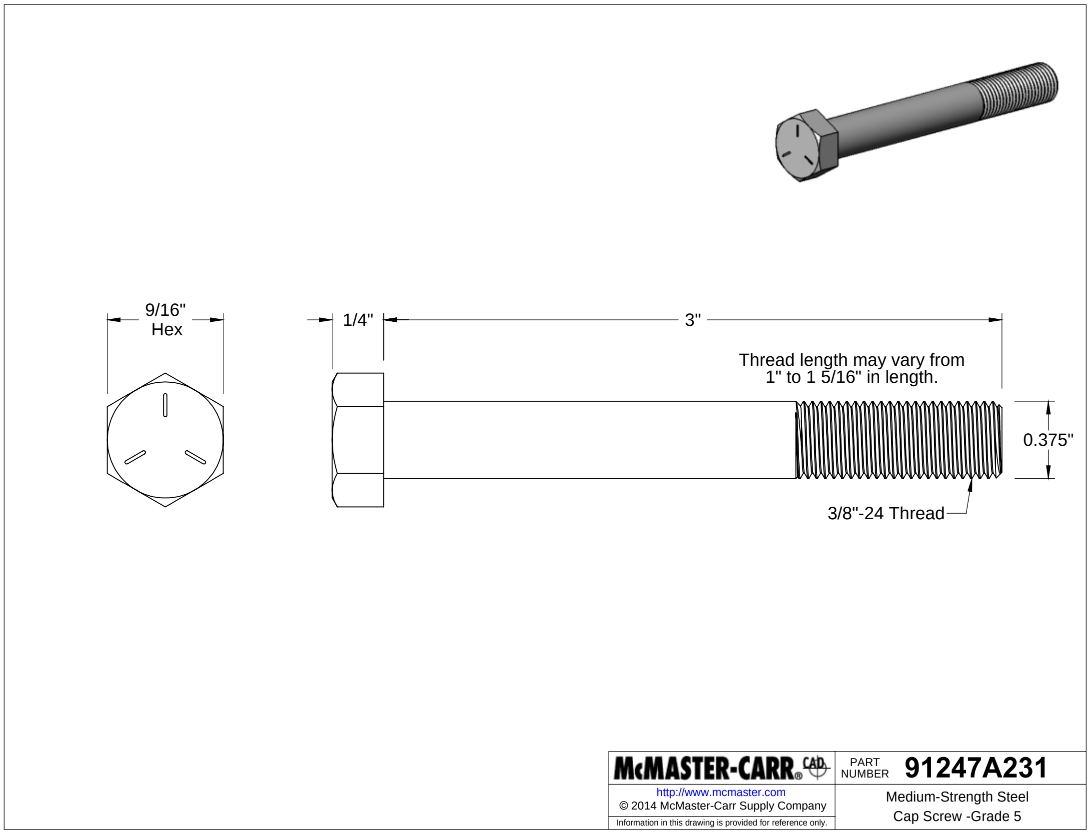

Figure I.20. Medium-strength grade 5 steel hex head screw drawing (part number 91247A231) (reprinted from McMaster-Carr, 2016).

McMASTER-CARR®

Medium-Strength Grade 5 Steel Hex Head Screw

Zinc-Plated, 1/2"-20 Thread Size, 5" Long, Partially Threaded

In stock
$9.28 per pack of 5
91247A368

Thread Size	1/2"-20
Length	5"
Threading	Partially Threaded
Minimum Thread Length	1 1/4"
Head Width	3/4"
Head Height	11/32"
Material	Zinc-Plated Steel
Fastener Strength Grade/Class	Grade 5
Hardness	Rockwell C25
Tensile Strength	120,000 psi
Screw Size Decimal Equivalent	0.500"
Thread Type	UNF
Thread Spacing	Fine
Thread Fit	Class 2A
Thread Direction	Right Hand
Head Type	Hex
Hex Head Profile	Standard
Drive Style	External Hex
Specifications Met	ASME B18.2.1, SAE J429
System of Measurement	Inch
RoHS	Compliant

These screws are suitable for fastening most machinery and equipment. Length is measured from under the head.

Zinc-plated steel screws resist corrosion in wet environments.

Figure I.21. Medium-strength grade 5 steel hex head screw specs (part number 91247A368) (reprinted from McMaster-Carr, 2016).

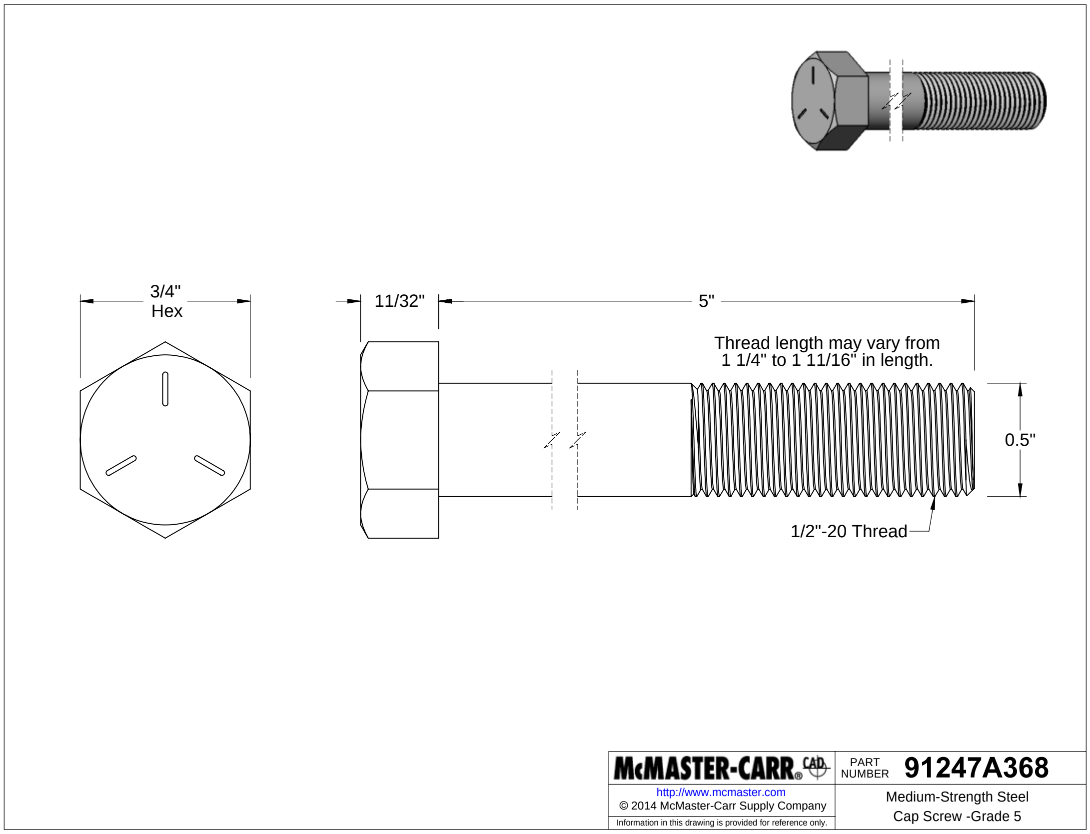

Figure I.22. Medium-strength grade 5 steel hex head screw drawing (part number 91247A368) (reprinted from McMaster-Carr, 2016).

MCMASTER-CARR®

Medium-Strength Steel Hex Nut
Grade 5, Zinc-Plated, 1/2"-20 Thread Size

In stock
$14.76 per pack of 100
95462A525

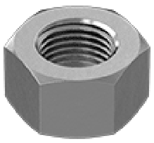

Material	Zinc-Plated Steel
Fastener Strength Grade/Class	Grade 5
Thread Size	1/2"-20
Thread Type	UNF
Thread Spacing	Fine
Thread Fit	Class 2B
Thread Direction	Right Hand
Width	3/4"
Height	7/16"
Drive Style	External Hex
Nut Type	Hex
Hex Nut Profile	Standard
System of Measurement	Inch
RoHS	Compliant

These nuts are suitable for fastening most machinery and equipment.

Zinc-plated steel nuts resist corrosion in wet environments.

Figure I.23. Medium-strength steel hex nut specs (part number 95462A525) (reprinted from McMaster-Carr, 2016).

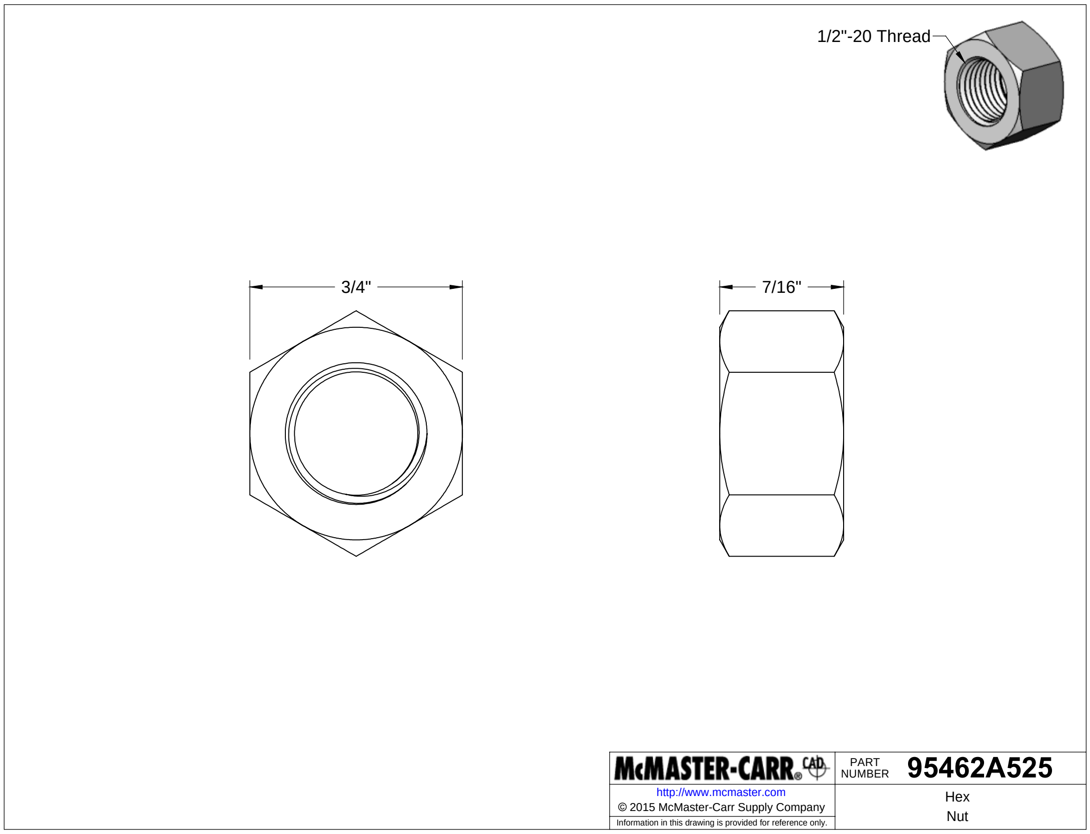

Figure I.24. Medium-strength steel hex nut drawing (part number 95462A525) (reprinted from McMaster-Carr, 2016).

McMaster-Carr - Zinc Yellow-Chromate Plated Grade 8 Steel Washer, with Material Certificate, 1/2" Screw Size, 0.531" ID, 1.062" OD 5/27/17, 18)41

MCMASTER-CARR®

Zinc Yellow-Chromate Plated Grade 8 Steel Washer

with Material Certificate, 1/2" Screw Size, 0.531" ID, 1.062" OD

In stock
$9.27 per pack of 25
98023A118

Material	Zinc Yellow-Chromate Plated Steel
Fastener Strength Grade/Class	Grade 8
For Screw Size	1/2"
ID	0.531"
OD	1.062"
Thickness	0.074"-0.121"
Washer Type	Flat
System of Measurement	Inch
Hardness	Rockwell C38
Certification	Material Certificate with Traceable Lot Number and Test Report
Specifications Met	ASME B18.21.1
RoHS	Compliant

These washers come with a traceable lot number and a physical and chemical test report. They're zinc yellow-chromate plated for corrosion resistance in wet environments.

https://www.mcmaster.com/#98023a118/=17tbd4i Page 1 of 2

Figure I.25. Zinc yellow-chromate plated grade 8 steel washer specs (part number 98023A118) (reprinted from McMaster-Carr, 2016).

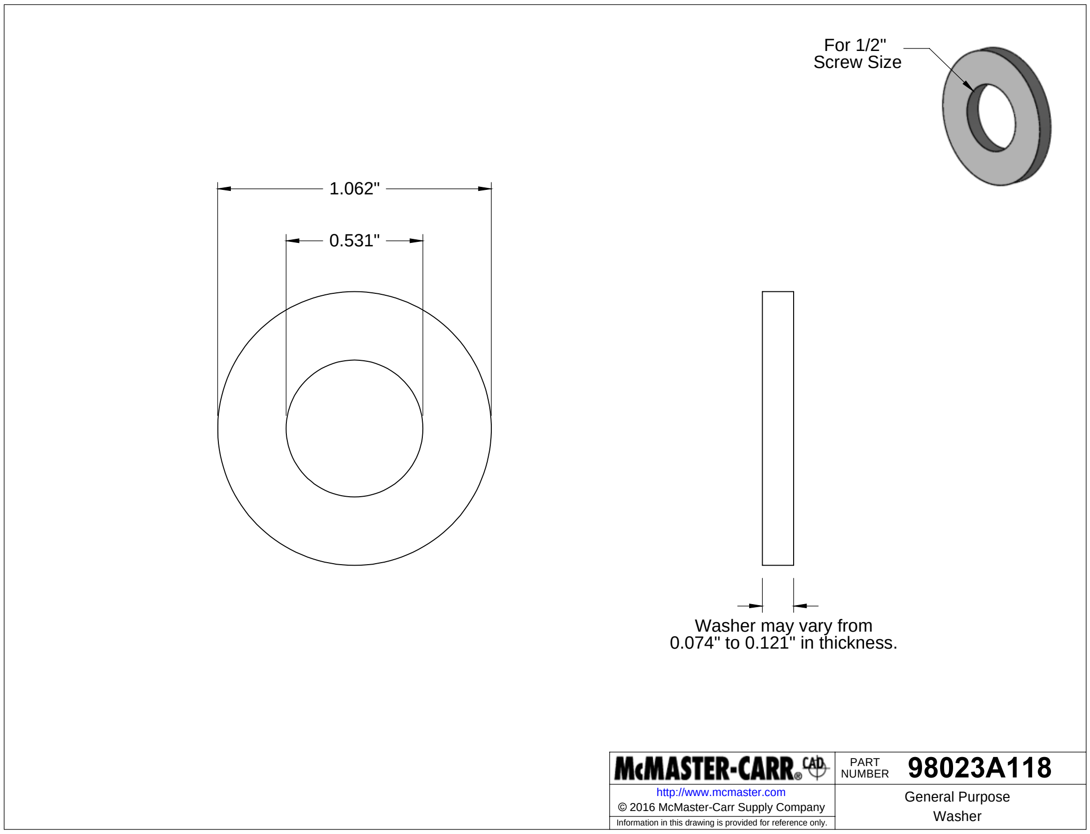

Figure I.26. Zinc yellow-chromate plated grade 8 steel washer drawing (part number 98023A118) (reprinted from McMaster-Carr, 2016).

I.6. Fasteners for the Bottom Chassis Subassembly

McMaster-Carr - Zinc Yellow-Chromate Plated Steel Split Lock Washer, for 3/8" Screw Size, 0.385" ID, 0.68" OD 5/30/17, 18*05

McMASTER-CARR®

Zinc Yellow-Chromate Plated Steel Split Lock Washer
for 3/8" Screw Size, 0.385" ID, 0.68" OD

In stock
$5.41 per pack of 100
91104A031

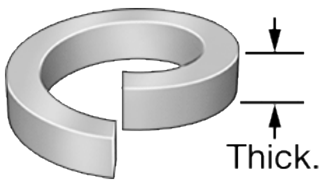

Material	Zinc Yellow-Chromate Plated Steel
Fastener Strength Grade/Class	Grade 8
For Screw Size	3/8"
ID	0.385"
OD	0.680"
Thickness	0.094"
Washer Type	Split Lock
System of Measurement	Inch
Hardness	Rockwell C38
Specifications Met	ASME B18.21.1
RoHS	Not Compliant

As a screw is tightened, these washers flatten to add tension to the joint and prevent loosening from small amounts of vibration.

Zinc- and zinc yellow-chromate plated steel washers are corrosion resistant in wet environments.

https://www.mcmaster.com/#91104a031/=17uugiv Page 1 of 2

Figure I.27. Zinc yellow-chromate plated steel split lock washer specs (part number 91104A031) (reprinted from McMaster-Carr, 2016).

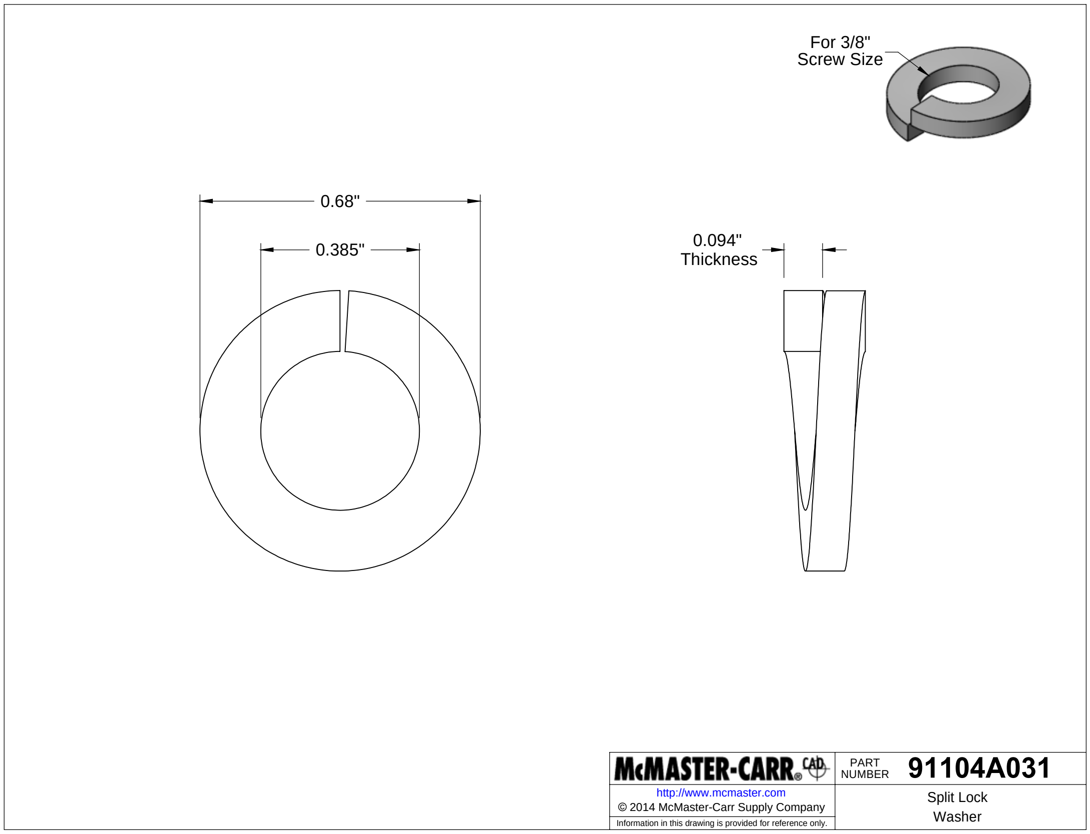

Figure I.28. Zinc yellow-chromate plated steel split lock washer drawing (part number 91104A031) (reprinted from McMaster-Carr, 2016).

McMASTER-CARR®

Medium-Strength Grade 5 Steel Hex Head Screw

Zinc-Plated, 3/8"-24 Thread Size, 3-3/4" Long

In stock
$6.93 per pack of 10
91247A234

Thread Size	3/8"-24
Length	3 3/4"
Threading	Partially Threaded
Minimum Thread Length	1"
Head Width	9/16"
Head Height	1/4"
Material	Zinc-Plated Steel
Fastener Strength Grade/Class	Grade 5
Hardness	Rockwell C25
Tensile Strength	120,000 psi
Screw Size Decimal Equivalent	0.375"
Thread Type	UNF
Thread Spacing	Fine
Thread Fit	Class 2A
Thread Direction	Right Hand
Head Type	Hex
Hex Head Profile	Standard
Drive Style	External Hex
Specifications Met	ASME B18.2.1, SAE J429
System of Measurement	Inch
RoHS	Compliant

These screws are suitable for fastening most machinery and equipment. Length is measured from under the head.

Zinc-plated steel screws resist corrosion in wet environments.

Figure I.29. Medium strength grade 5 steel hex head screw specs (part number 91247A234) (reprinted from McMaster-Carr, 2016).

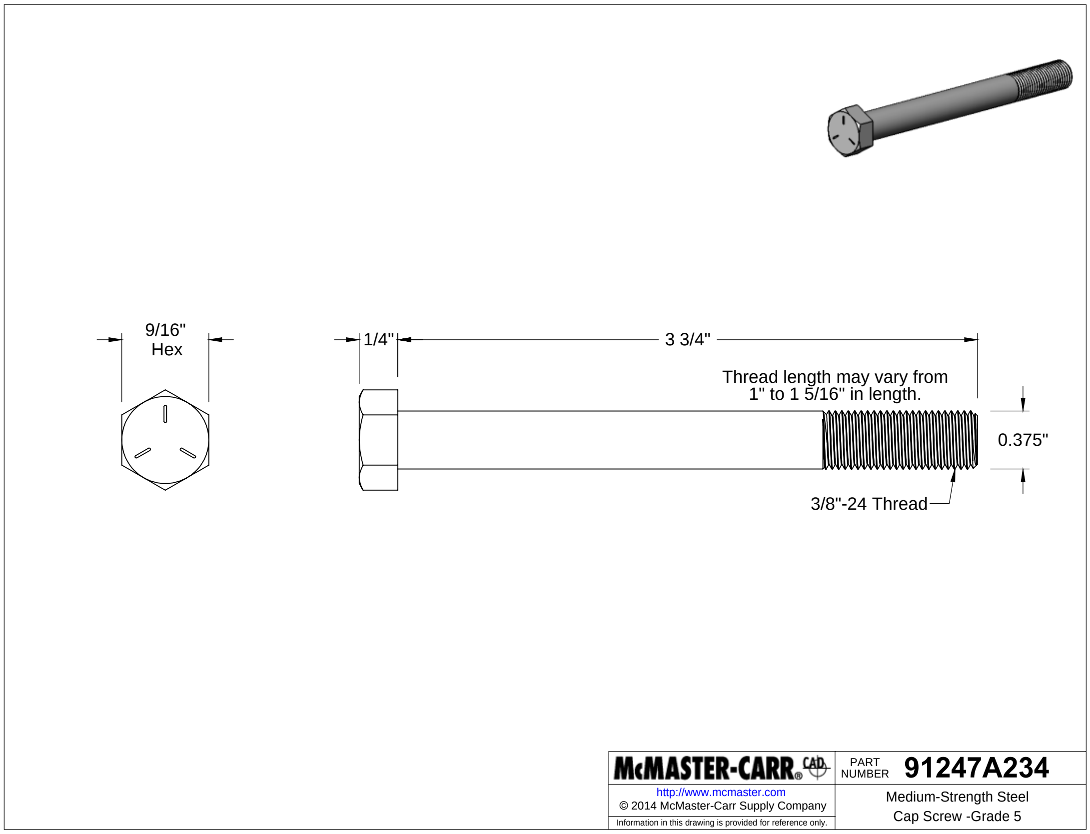

Figure I.30. Medium strength grade 5 steel hex head screw drawing (part number 91247A234) (reprinted from McMaster-Carr, 2016).

McMASTER-CARR®

Medium-Strength Grade 5 Steel Hex Head Screw

Zinc-Plated, 3/8"-24 Thread Size, 5-1/2" Long

In stock
$12.56 per pack of 10
91247A241

Thread Size	3/8"-24
Length	5 1/2"
Threading	Partially Threaded
Minimum Thread Length	1"
Head Width	9/16"
Head Height	1/4"
Material	Zinc-Plated Steel
Fastener Strength Grade/Class	Grade 5
Hardness	Rockwell C25
Tensile Strength	120,000 psi
Screw Size Decimal Equivalent	0.375"
Thread Type	UNF
Thread Spacing	Fine
Thread Fit	Class 2A
Thread Direction	Right Hand
Head Type	Hex
Hex Head Profile	Standard
Drive Style	External Hex
Specifications Met	ASME B18.2.1, SAE J429
System of Measurement	Inch
RoHS	Compliant

These screws are suitable for fastening most machinery and equipment. Length is measured from under the head.

Zinc-plated steel screws resist corrosion in wet environments.

Figure I.31. Medium strength grade 5 steel hex head screw specs (part number 91247A241) (reprinted from McMaster-Carr, 2016).

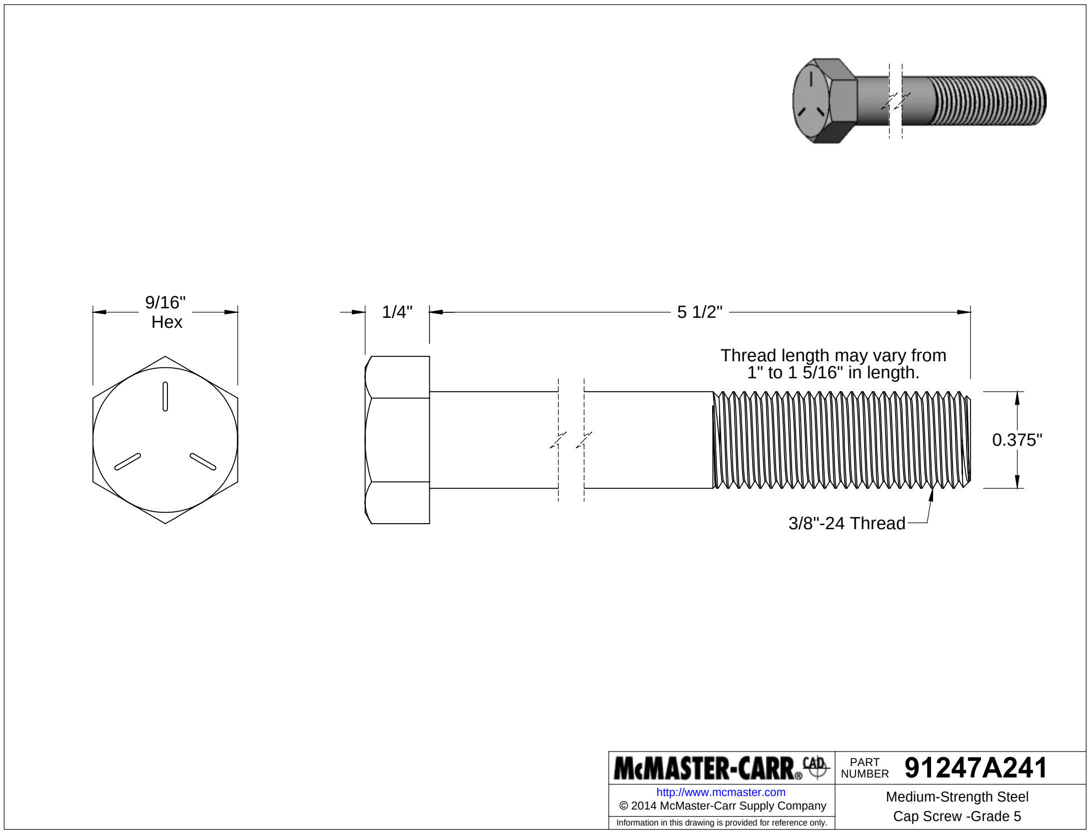

Figure I.32. Medium strength grade 5 steel hex head screw drawing (part number 91247A241) (reprinted from McMaster-Carr, 2016).

MCMASTER-CARR®

Medium-Strength Steel Hex Nut

Grade 5, Zinc-Plated, 3/8"-24 Thread Size

In stock
$8.28 per pack of 100
95462A515

Material	Zinc-Plated Steel
Fastener Strength Grade/Class	Grade 5
Thread Size	3/8"-24
Thread Type	UNF
Thread Spacing	Fine
Thread Fit	Class 2B
Thread Direction	Right Hand
Width	9/16"
Height	21/64"
Drive Style	External Hex
Nut Type	Hex
Hex Nut Profile	Standard
System of Measurement	Inch
RoHS	Compliant

These nuts are suitable for fastening most machinery and equipment.

Zinc-plated steel nuts resist corrosion in wet environments.

Figure I.33. Medium strength steel hex nut specs (part number 95462A515) (reprinted from McMaster-Carr, 2016).

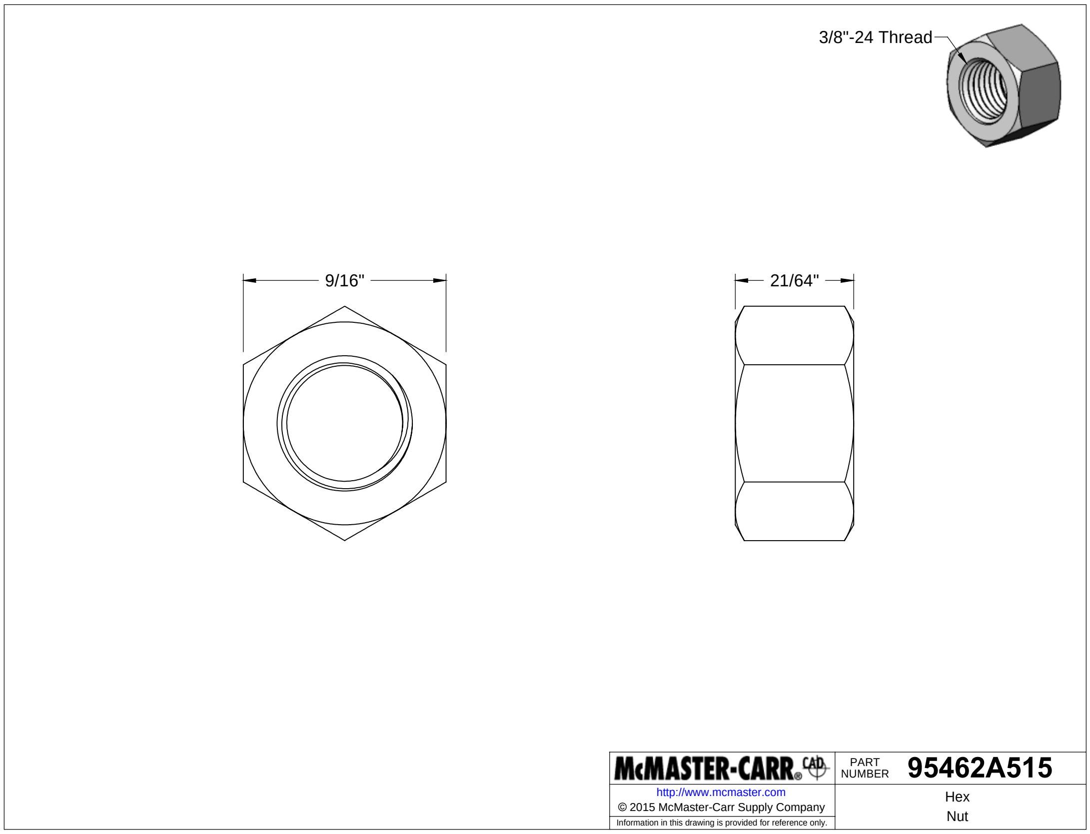

Figure I.34. Medium strength steel hex nut drawing (part number 95462A515) (reprinted from McMaster-Carr, 2016).

McMaster-Carr - Grade 8 Steel Washer, Zinc-Aluminum Coated, 3/8" Screw Size, 0.406" ID, 0.812" OD 5/27/17, 18)18

McMASTER-CARR®

Grade 8 Steel Washer

Zinc-Aluminum Coated, 3/8" Screw Size, 0.406" ID, 0.812" OD

In stock
$7.64 per pack of 50
98180A130

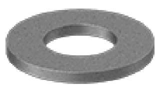

Material	Zinc-Aluminum Coated Steel
Fastener Strength Grade/Class	Grade 8
For Screw Size	3/8"
ID	0.406"
OD	0.812"
Thickness	0.055"-0.065"
Washer Type	Flat
System of Measurement	Inch
Hardness	Rockwell C38
Specifications Met	ASME B18.21.1, SAE Standards
RoHS	Compliant

Zinc-aluminum coated and black ultra-corrosion-resistant coated steel washers resist chemicals and withstand 1,000 hours of salt spray.

https://www.mcmaster.com/#98180a130/=17tb1xq Page 1 of 2

Figure I.35. Grade 8 steel washer specs (part number 98180A130) (reprinted from McMaster-Carr, 2016).

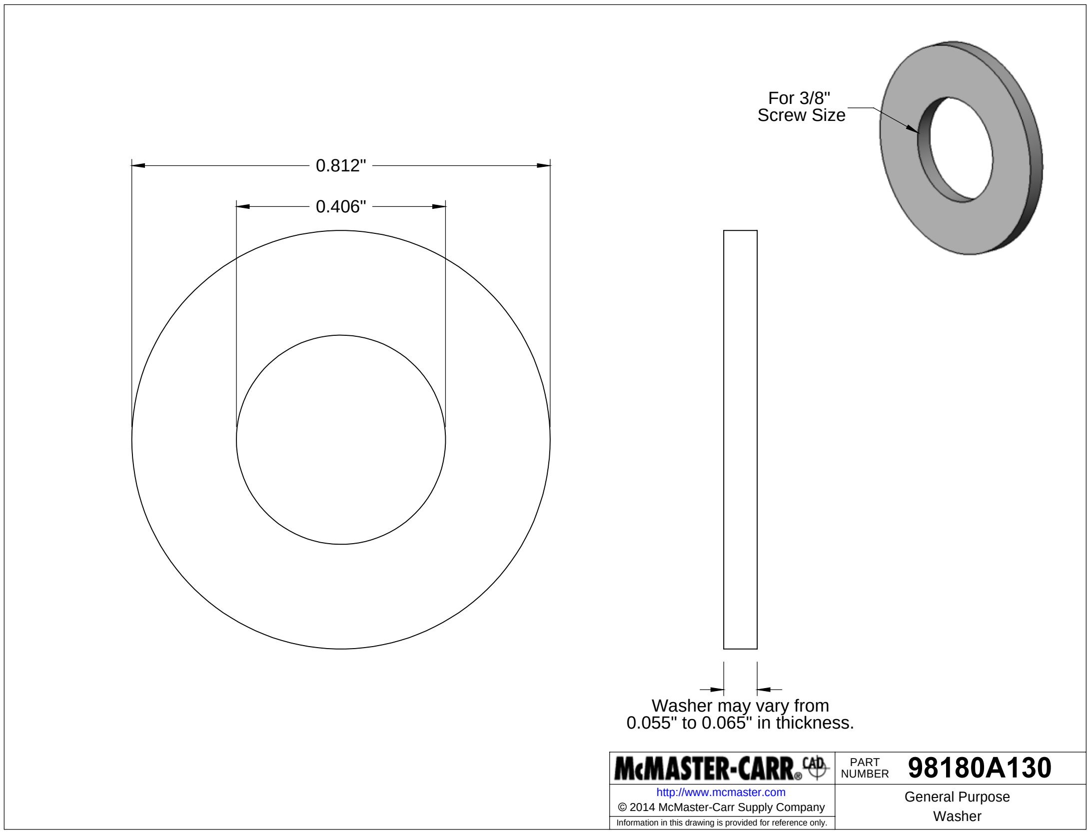

Figure I.36. Grade 8 steel washer drawing (part number 98180A130) (reprinted from McMaster-Carr, 2016).

I.7. Fasteners for the Suspension System Subassembly

McMaster-Carr - Zinc-Plated Alloy Steel Socket Head Screw, 1/2"-13 Thread Size, 1-1/2" Long 5/31/17, 12)48

MCMASTER-CARR®

Zinc-Plated Alloy Steel Socket Head Screw
1/2"-13 Thread Size, 1-1/2" Long

In stock
$5.21 per pack of 5
90128A716

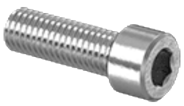

Thread Size	1/2"-13
Length	1 1/2"
Threading	Fully Threaded
Head Diameter	0.75"
Head Height	0.5"
Drive Size	3/8"
Material	Zinc-Plated Alloy Steel
Hardness	Rockwell C37
Tensile Strength	170,000 psi
Screw Size Decimal Equivalent	0.500"
Thread Type	UNC
Thread Spacing	Coarse
Thread Fit	Class 3A
Thread Direction	Right Hand
Head Type	Socket
Socket Head Profile	Standard
Drive Style	Hex
Specifications Met	ASTM A574
System of Measurement	Inch
RoHS	Compliant

These screws are made from an alloy steel that's stronger than Grade 8 steel. Length is measured from under the head.

Zinc-plated steel screws are more corrosion resistant than black-oxide screws for use in wet environments.

https://www.mcmaster.com/#90128a716/=17v8wn3 Page 1 of 2

Figure I.37. Zinc-plated alloy steel socket head screw specs (part number 90128A716) (reprinted from McMaster-Carr, 2016).

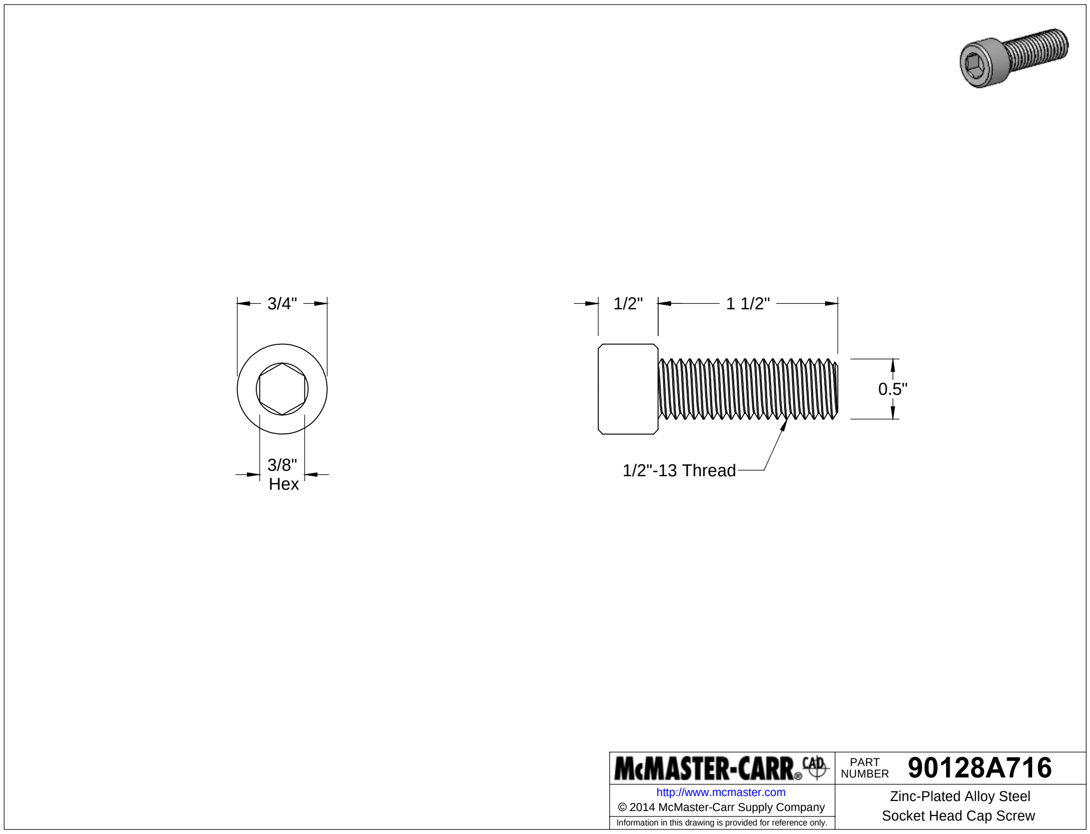

Figure I.38. Zinc-plated alloy steel socket head screw drawing (part number 90128A716) (reprinted from McMaster-Carr, 2016).

McMaster-Carr - Extreme-Strength Grade 9 Steel Hex Head Screw, 3/8"-16 Thread Size, 3-1/2" Long 5/31/17, 12)42

McMASTER-CARR®

Extreme-Strength Grade 9 Steel Hex Head Screw
3/8"-16 Thread Size, 3-1/2" Long

In stock
$10.48 per pack of 5
90201A333

Thread Size	3/8"-16
Length	3 1/2"
Threading	Partially Threaded
Minimum Thread Length	1"
Head Width	9/16"
Head Height	9/32"
Material	Zinc Yellow-Chromate Plated Steel
Fastener Strength Grade/Class	Grade 9
Hardness	Rockwell C38
Tensile Strength	180,000 psi
Screw Size Decimal Equivalent	0.375"
Thread Type	UNC
Thread Spacing	Coarse
Thread Fit	Class 2A
Thread Direction	Right Hand
Head Type	Hex
Hex Head Profile	Standard
Drive Style	External Hex
System of Measurement	Inch
RoHS	Not Compliant

Our strongest screws, these are about 20% stronger than high-strength steel screws and often used in heavy duty applications such as stamping. The zinc yellow-chromate plating provides corrosion resistance in wet environments. Length is measured from under the head. Use with Grade 9 nuts and washers.

https://www.mcmaster.com/#90201a333/=17v8tp0 Page 1 of 2

Figure I.39. Extreme-strength grade 9 steel hex head screw specs (part number 90201A333) (reprinted from McMaster-Carr, 2016).

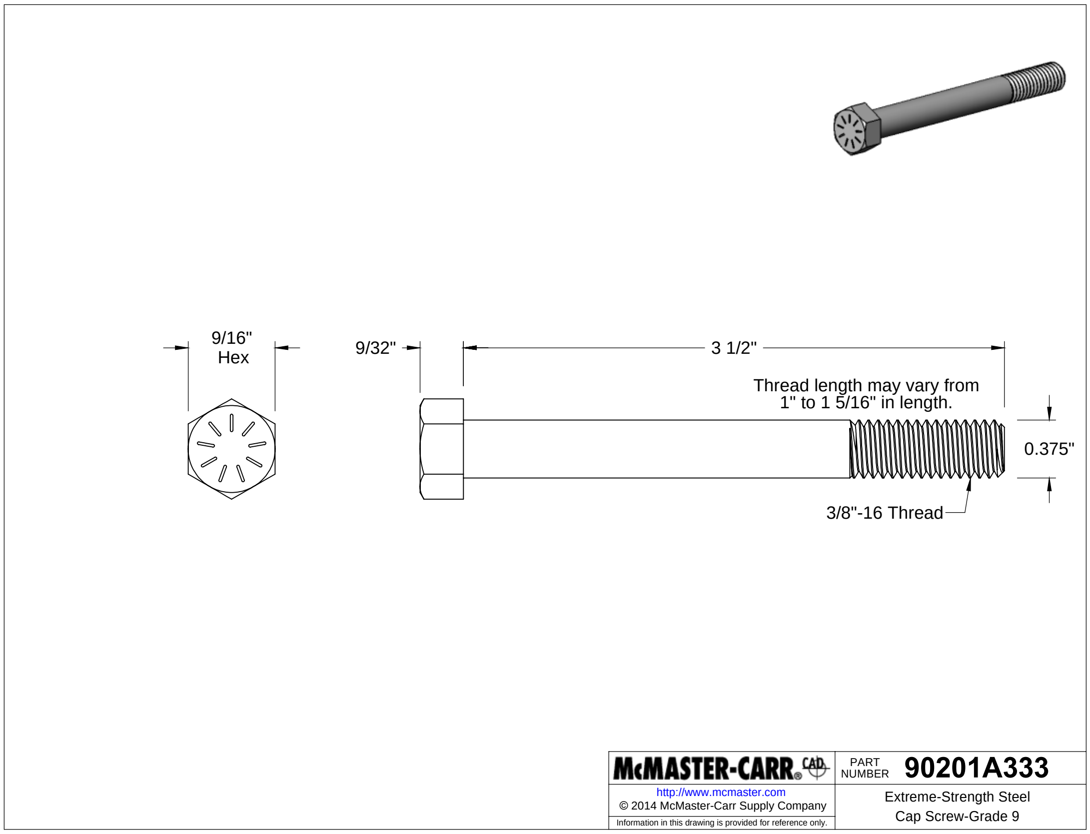

Figure I.40. Extreme-strength grade 9 steel hex head screw drawing (part number 90201A333) (reprinted from McMaster-Carr, 2016).

McMaster-Carr - Extreme-Strength Grade 9 Steel Hex Head Screw, 3/8"-16 Thread Size, 4" Long 5/30/17, 18*17

McMASTER-CARR®

Extreme-Strength Grade 9 Steel Hex Head Screw
3/8"-16 Thread Size, 4" Long

In stock
$2.88 per pack of 1
90201A336

Thread Size	3/8"-16
Length	4"
Threading	Partially Threaded
Minimum Thread Length	1"
Head Width	9/16"
Head Height	9/32"
Material	Zinc Yellow-Chromate Plated Steel
Fastener Strength Grade/Class	Grade 9
Hardness	Rockwell C38
Tensile Strength	180,000 psi
Screw Size Decimal Equivalent	0.375"
Thread Type	UNC
Thread Spacing	Coarse
Thread Fit	Class 2A
Thread Direction	Right Hand
Head Type	Hex
Hex Head Profile	Standard
Drive Style	External Hex
System of Measurement	Inch
RoHS	Not Compliant

Our strongest screws, these are about 20% stronger than high-strength steel screws and often used in heavy duty applications such as stamping. The zinc yellow-chromate plating provides corrosion resistance in wet environments. Length is measured from under the head. Use with Grade 9 nuts and washers.

https://www.mcmaster.com/#90201a336/=17uumcp Page 1 of 2

Figure I.41. Extreme-strength grade 9 steel hex head screw specs (part number 90201A336) (reprinted from McMaster-Carr, 2016).

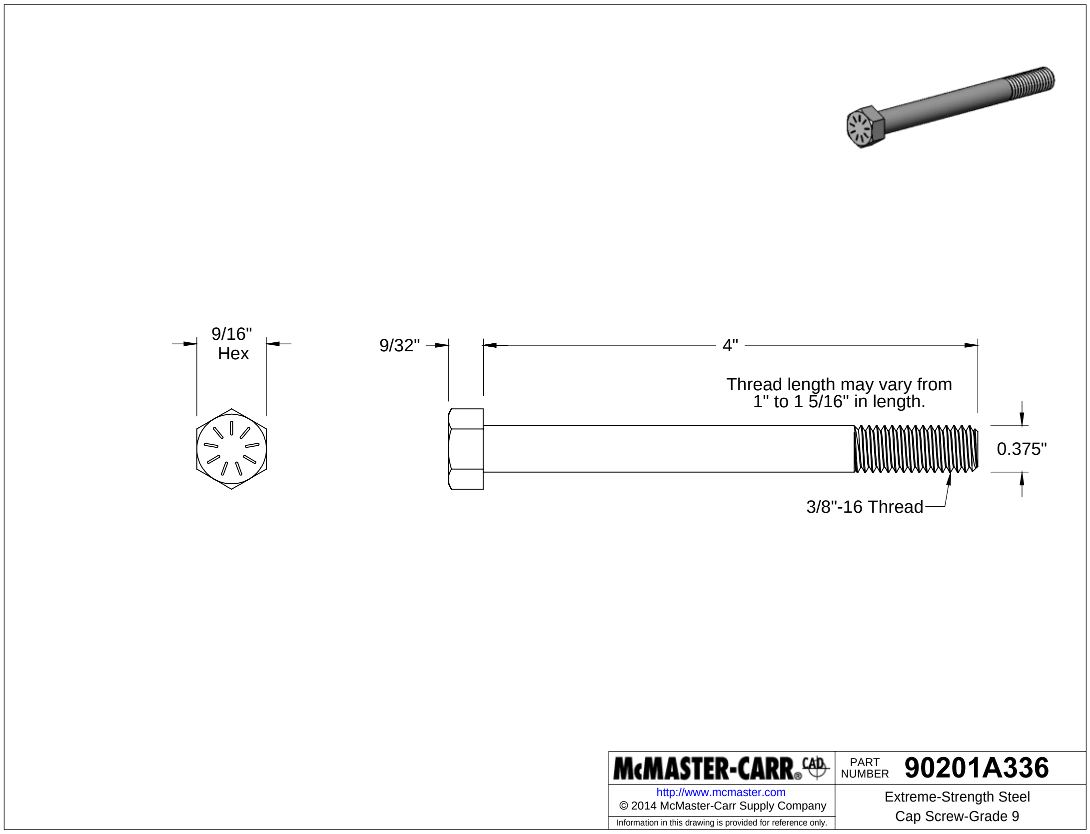

Figure I.42. Extreme-strength grade 9 steel hex head screw drawing (part number 90201A336) (reprinted from McMaster-Carr, 2016).

Grade 9 Steel Washer

Zinc Yellow-Chromate Plated, 3/8" Screw Size, 0.827" OD

In stock
$7.05 per pack of 25
90850A200

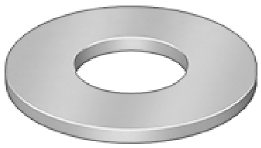

Material	Zinc Yellow-Chromate Plated Steel
Fastener Strength Grade/Class	Grade 9
For Screw Size	3/8"
ID	0.411"
OD	0.827"
Thickness	0.090"-0.112"
Washer Type	Flat
System of Measurement	Inch
Hardness	Rockwell C40
RoHS	Not Compliant

Zinc yellow-chromate and chrome-plated steel washers are corrosion resistant in wet environments.

Figure I.43. Extreme-strength grade 9 steel hex head screw specs (part number 90850A200) (reprinted from McMaster-Carr, 2016).

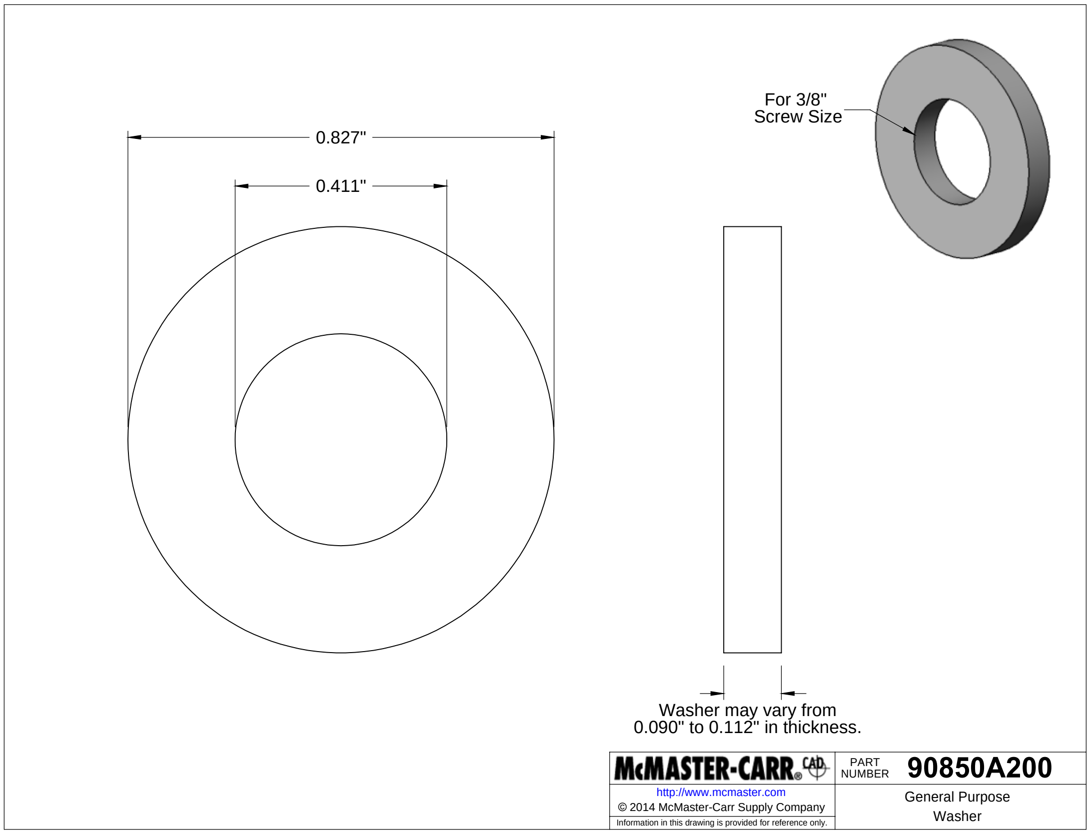

Figure I.44. Extreme-strength grade 9 steel hex head screw drawing (part number 90850A200) (reprinted from McMaster-Carr, 2016).

McMASTER-CARR®

Zinc-Plated Steel Oversized Washer

for 3/8" Screw Size, 0.406" ID, 2" OD, 0.235"- 0.265" Thickness

In stock
$9.29 per pack of 5
91117A222

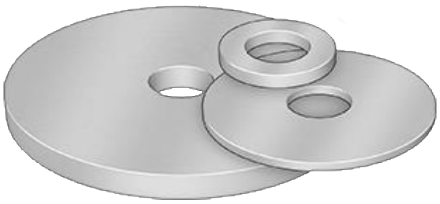

Material	Zinc-Plated Steel
For Screw Size	3/8"
ID	0.406"
OD	2.000"
Thickness	0.235"-0.265"
Washer Type	Flat
System of Measurement	Inch
Hardness	Rockwell B40
RoHS	Not Compliant

Compared to our general purpose washers, these have exaggerated diameters and/or thicknesses for covering oversized holes or for use as spacers and levelers.

Zinc- and zinc yellow-chromate plated steel washers are corrosion resistant in wet environments.

Figure I.45. Zinc-plated steel oversized washer specs (part number 91117A222) (reprinted from McMaster-Carr, 2016).

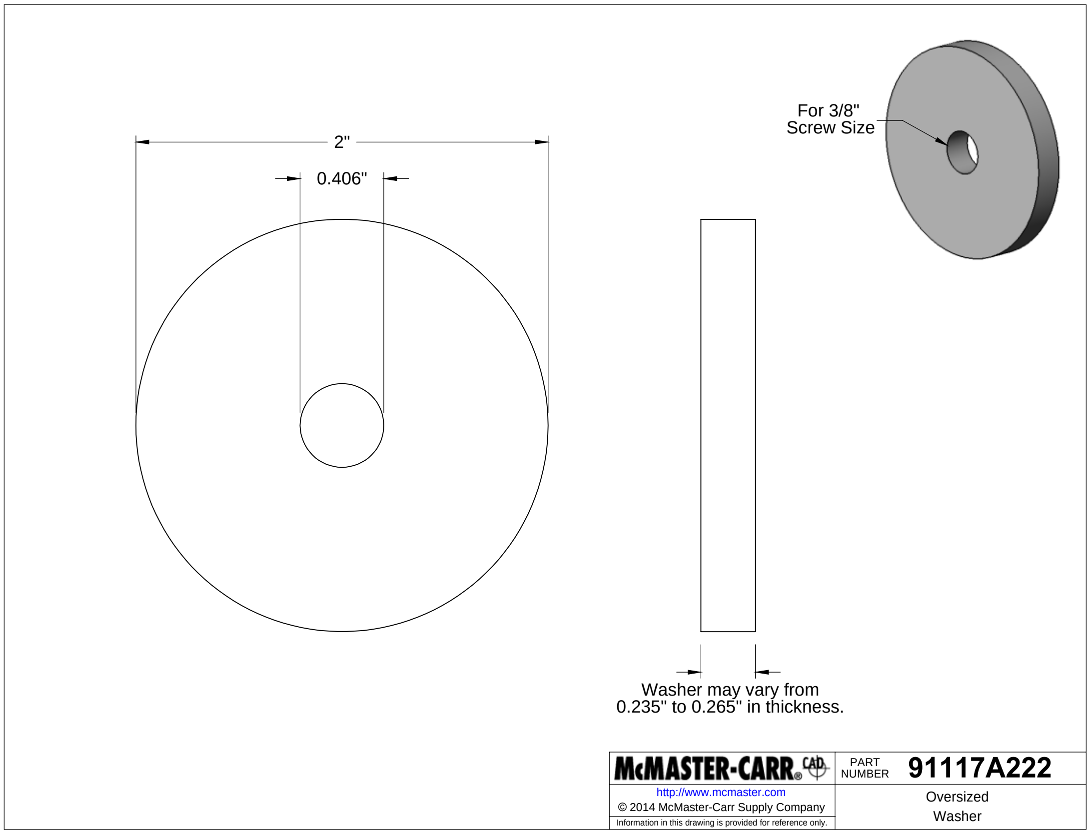

Figure I.46. Zinc-plated steel oversized washer drawing (part number 91117A222) (reprinted from McMaster-Carr, 2016).

McMASTER-CARR®

Zinc Yellow-Chromate Plated Hex Head Screw

Grade 8 Steel, 3/8"-16 Thread Size, 7" Long

In stock
$13.25 per pack of 5
91257A650

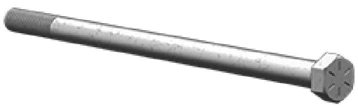

Thread Size	3/8"-16
Length	7"
Threading	Partially Threaded
Minimum Thread Length	1 1/4"
Head Width	9/16"
Head Height	1/4"
Material	Zinc Yellow-Chromate Plated Steel
Fastener Strength Grade/Class	Grade 8
Hardness	Rockwell C33
Tensile Strength	150,000 psi
Screw Size Decimal Equivalent	0.375"
Thread Type	UNC
Thread Spacing	Coarse
Thread Fit	Class 2A
Thread Direction	Right Hand
Head Type	Hex
Hex Head Profile	Standard
Drive Style	External Hex
Specifications Met	ASME B18.2.1, SAE J429
System of Measurement	Inch
RoHS	Not Compliant

Good for demanding applications such as suspension systems, these screws are at least 25% stronger than medium-strength steel screws. Length is measured from under the head.

Zinc yellow-chromate plated steel screws resist corrosion in wet environments.

Figure I.47. Zinc Yellow-chromate plated hex head screw specs (part number 91257A650) (reprinted from McMaster-Carr, 2016).

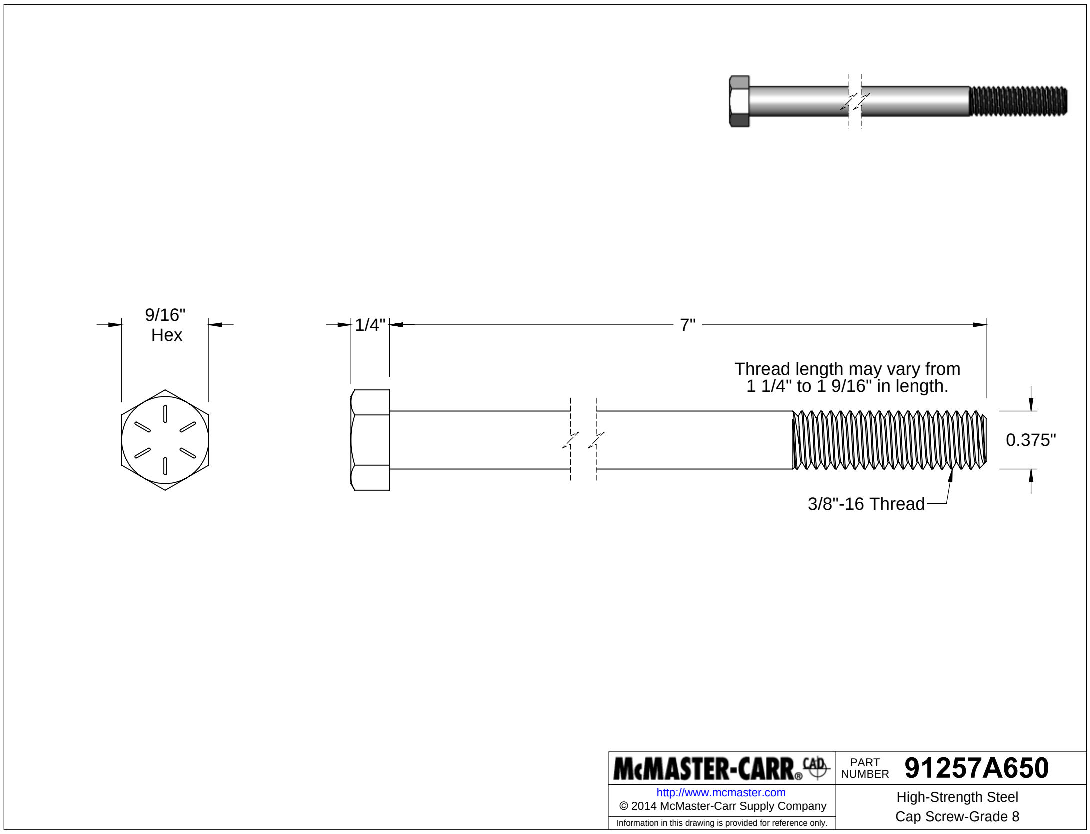

Figure I.48. Zinc Yellow-chromate plated hex head screw drawing (part number 91257A650) (reprinted from McMaster-Carr, 2016).

McMaster-Carr - Zinc Yellow-Chromate Plated Hex Head Screw, Grade 8 Steel, 3/8"-24 Thread, 3-1/2" Long, Partially Threaded 5/31/17, 13(03

McMASTER-CARR®

Zinc Yellow-Chromate Plated Hex Head Screw

Grade 8 Steel, 3/8"-24 Thread, 3-1/2" Long, Partially Threaded

In stock
$12.28 per pack of 10
91257A664

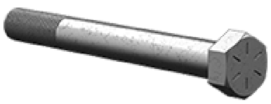

Thread Size	3/8"-24
Length	3 1/2"
Threading	Partially Threaded
Minimum Thread Length	1"
Head Width	9/16"
Head Height	1/4"
Material	Zinc Yellow-Chromate Plated Steel
Fastener Strength Grade/Class	Grade 8
Hardness	Rockwell C33
Tensile Strength	150,000 psi
Screw Size Decimal Equivalent	0.375"
Thread Type	UNF
Thread Spacing	Fine
Thread Fit	Class 2A
Thread Direction	Right Hand
Head Type	Hex
Hex Head Profile	Standard
Drive Style	External Hex
Specifications Met	ASME B18.2.1, SAE J429
System of Measurement	Inch
RoHS	Not Compliant

Good for demanding applications such as suspension systems, these screws are at least 25% stronger than medium-strength steel screws. Length is measured from under the head.

Zinc yellow-chromate plated steel screws resist corrosion in wet environments.

https://www.mcmaster.com/#91257a664/=17v93at Page 1 of 2

Figure I.49. Zinc Yellow-chromate plated hex head screw specs (part number 91257A664) (reprinted from McMaster-Carr, 2016).

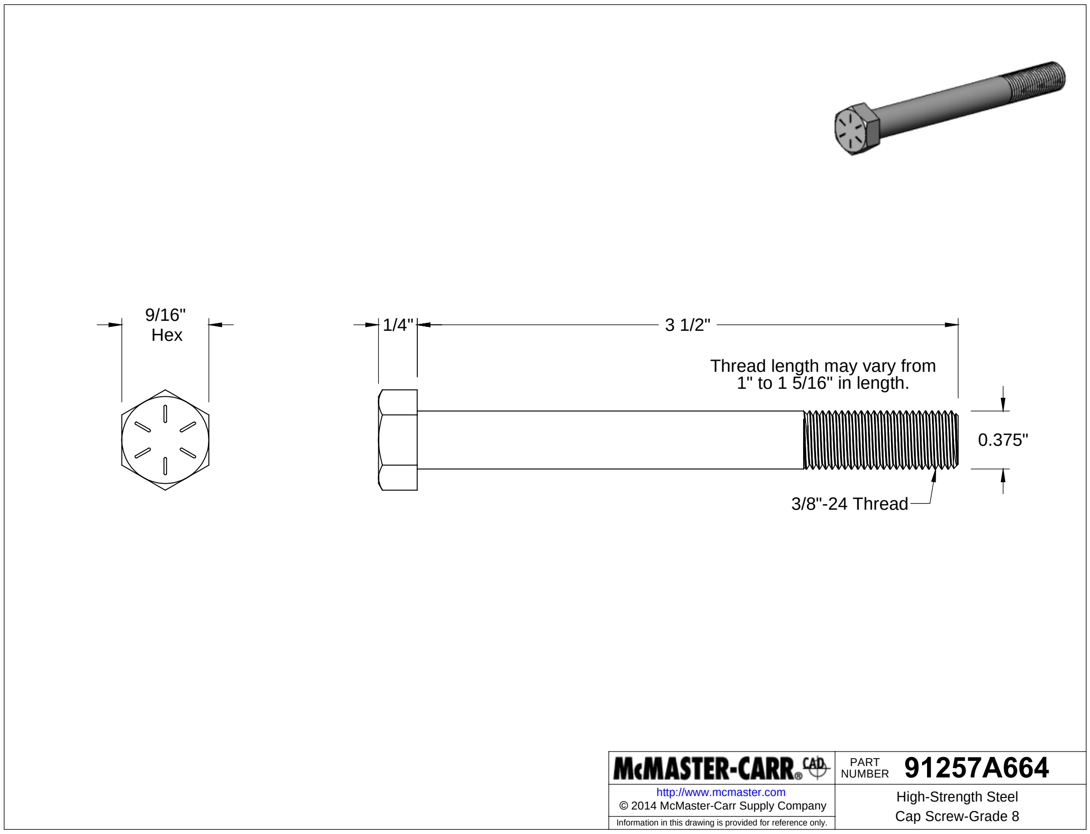

Figure I.50. Zinc Yellow-chromate plated hex head screw drawing (part number 91257A664) (reprinted from McMaster-Carr, 2016).

MCMASTER-CARR®

Medium-Strength Class 8.8 Steel Hex Head Screw

Zinc-Plated, M10 x 1.5 mm Thread, 40 mm Long

In stock
$10.24 per pack of 25
91280A638

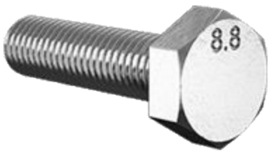

Thread Size	M10
Thread Pitch	1.5 mm
Length	40 mm
Threading	Fully Threaded
Head Width	17 mm
Head Height	6.4 mm
Material	Zinc-Plated Steel
Fastener Strength Grade/Class	Class 8.8
Hardness	Rockwell C21
Tensile Strength	110,000 psi
Thread Type	Metric
Thread Spacing	Coarse
Thread Fit	Class 6h
Thread Direction	Right Hand
Head Type	Hex
Hex Head Profile	Standard
Drive Style	External Hex
Specifications Met	DIN 933
System of Measurement	Metric
RoHS	Compliant

These screws are suitable for fastening most machinery and equipment. Length is measured from under the head.

Zinc-plated steel screws resist corrosion in wet environments.

Figure I.51. Medium-strength class 8.8 steel hex head screw specs (part number 91280A638) (reprinted from McMaster-Carr, 2016).

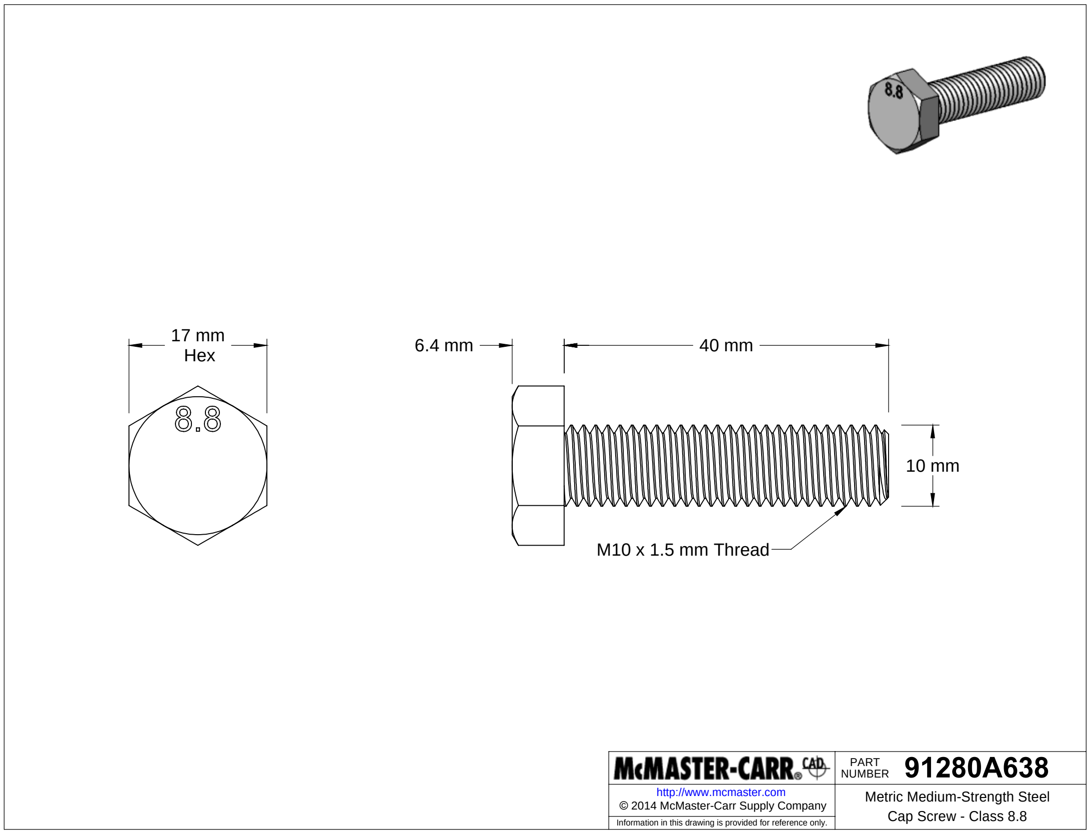

Figure I.52. Medium-strength class 8.8 steel hex head screw drawing (part number 91280A638) (reprinted from McMaster-Carr, 2016).

McMASTER-CARR®

Aluminum Unthreaded Spacer

3/4" OD, 2-1/2" Length, for 3/8" Screw Size

In stock
1-9 Each $7.56
10 or more $6.41
92510A479

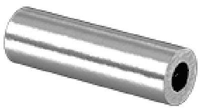

OD	3/4"
OD Tolerance	-0.005" to 0.005"
Length	2 1/2"
For Screw Size	3/8"
ID	0.380"
ID Tolerance	0" to 0.01"
Length Tolerance	-0.005" to 0.005"
Shape	Round
Tensile Strength	45,000 psi
Hardness	Rockwell B50
Material	2011 Aluminum
RoHS	Compliant

These spacers are also known as clearance spacers.

Aluminum and black-anodized aluminum are lightweight and have mild corrosion resistance.

Figure I.53. Aluminum unthreaded spacer specs (part number 92510A479) (reprinted from McMaster-Carr, 2016).

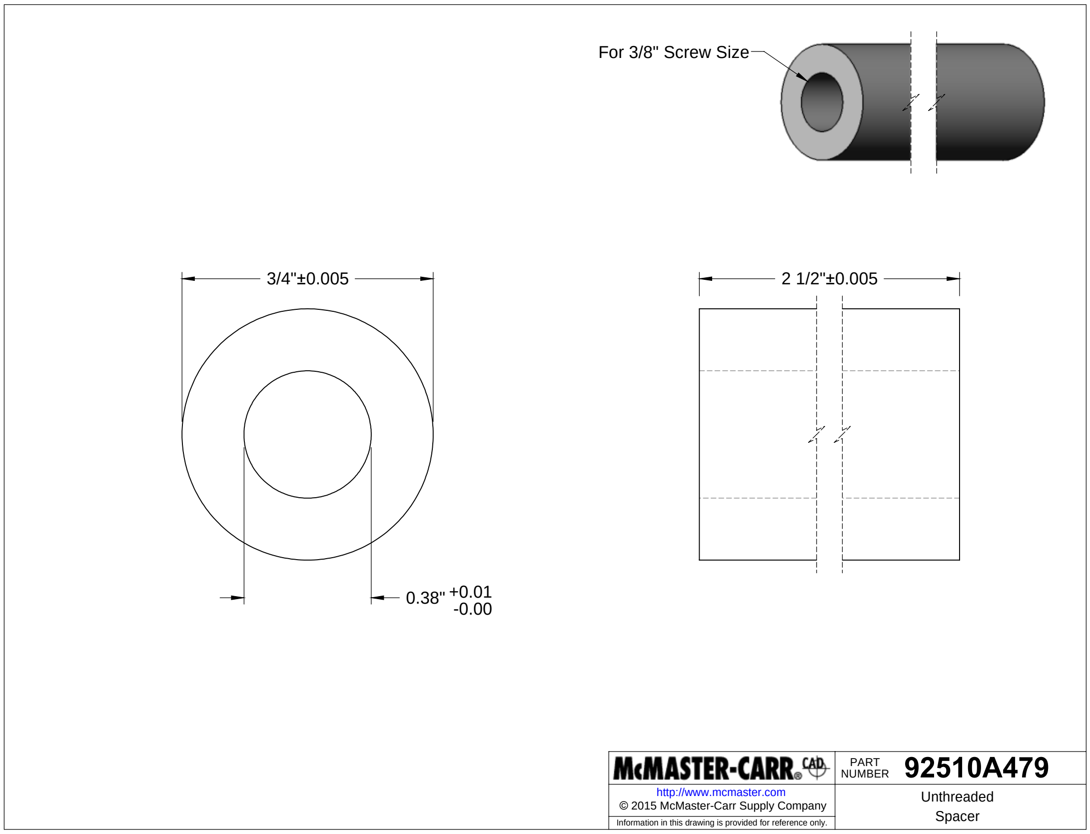

Figure I.54. Aluminum unthreaded spacer drawing (part number 92510A479) (reprinted from McMaster-Carr, 2016).

McMaster-Carr - Aluminum Unthreaded Spacer, 3/4" OD, 1/4" Length, for 3/8" Screw Size 5/31/17, 12)45

McMASTER-CARR®

Aluminum Unthreaded Spacer
3/4" OD, 1/4" Length, for 3/8" Screw Size

In stock
1-9 Each $2.05
10 or more $1.73
92510A491

OD	3/4"
OD Tolerance	-0.005" to 0.005"
Length	1/4"
For Screw Size	3/8"
ID	0.380"
ID Tolerance	0" to 0.01"
Length Tolerance	-0.005" to 0.005"
Shape	Round
Tensile Strength	45,000 psi
Hardness	Rockwell B50
Material	2011 Aluminum
RoHS	Compliant

These spacers are also known as clearance spacers.

Aluminum and black-anodized aluminum are lightweight and have mild corrosion resistance.

https://www.mcmaster.com/#92510a491/=17v8v9b Page 1 of 2

Figure I.55. Aluminum unthreaded spacer specs (part number 92510A491) (reprinted from McMaster-Carr, 2016).

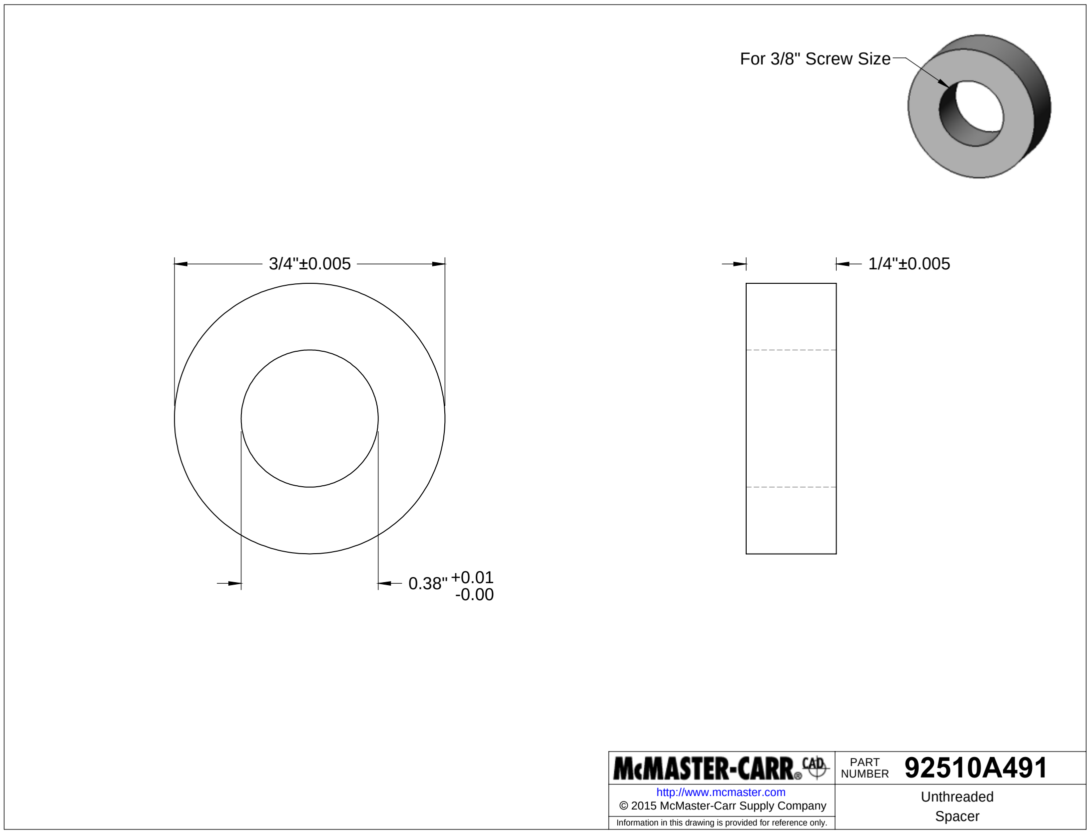

Figure I.56. Aluminum unthreaded spacer drawing (part number 92510A491) (reprinted from McMaster-Carr, 2016).

McMASTER-CARR®

Top-Lock Distorted-Thread Locknut

Extreme-Strength Steel, Grade 9, 3/8"-16 Thread Size

In stock
$4.70 per pack of 10
93591A300

Material	Cadmium-Plated Steel
Fastener Strength Grade/Class	Grade 9
Thread Size	3/8"-16
Thread Type	UNC
Thread Spacing	Coarse
Thread Fit	Class 2B
Thread Direction	Right Hand
Width	9/16"
Height	25/64"
Drive Style	External Hex
Nut Type	Locknut
Hex Nut Profile	Standard
Locking Type	Distorted Thread
Distorted Thread Type	Top Lock
System of Measurement	Inch
RoHS	Not Compliant

These locknuts have an irregularly shaped thread at the top of the nut that grips the bolt for a stronger hold than nylon-insert locknuts. They thread on from the bottom of the nut, allowing more threads to engage the bolt before tightening for easier installation than center-lock distorted thread locknuts. The strength of the bolt should match the strength of the nut to prevent damaging threads. They're not reusable. About 20% stronger than high-strength steel locknuts, they're often used in heavy machinery, such as earth-moving equipment. A cadmium plating provides corrosion resistance in wet environments and adds lubricity so they thread on smoothly.

Figure I.57. Top-lock distorted-thread locknut specs (part number 93591A300) (reprinted from McMaster-Carr, 2016).

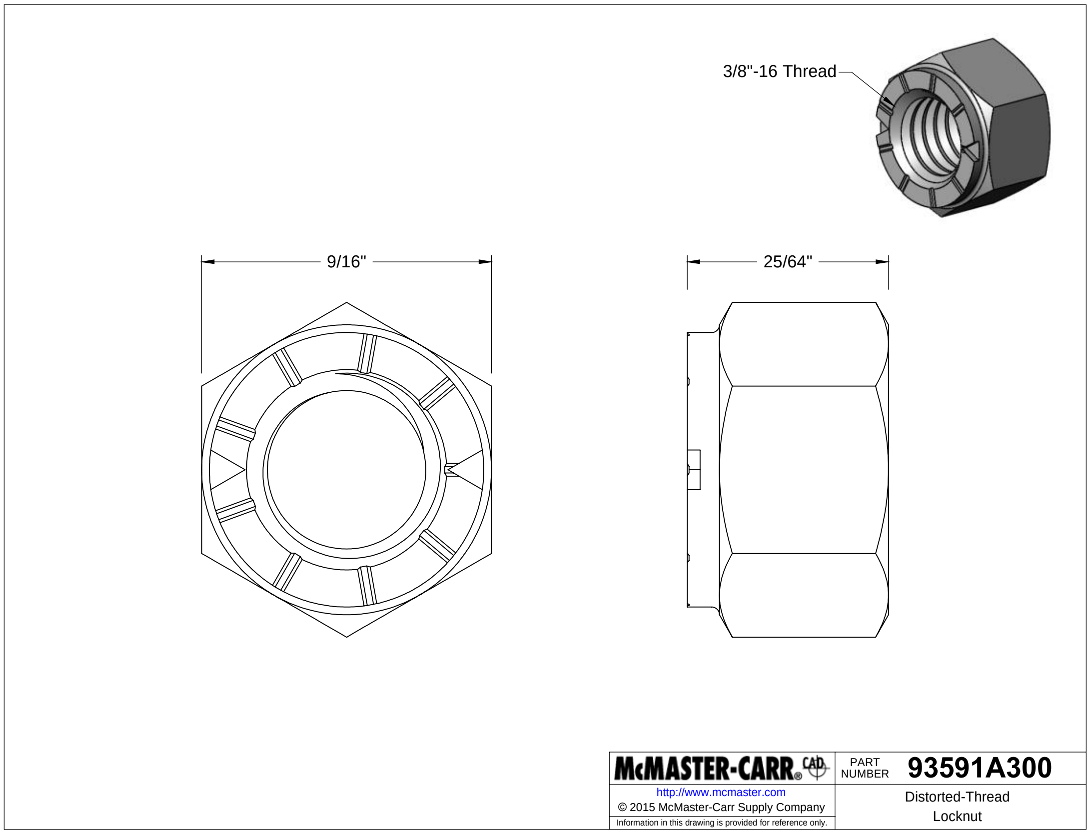

Figure I.58. Top-lock distorted-thread locknut drawing (part number 93591A300) (reprinted from McMaster-Carr, 2016).

McMASTER-CARR®

High-Strength Steel Hex Nut

Grade 8, Zinc Yellow-Chromate Plated, 3/8"-24 Thread Size

In stock
$7.24 per pack of 100
94895A815

Material	Zinc Yellow-Chromate Plated Steel
Fastener Strength Grade/Class	Grade 8
Thread Size	3/8"-24
Thread Type	UNF
Thread Spacing	Fine
Thread Fit	Class 2B
Thread Direction	Right Hand
Width	9/16"
Height	21/64"
Drive Style	External Hex
Nut Type	Hex
Hex Nut Profile	Standard
System of Measurement	Inch
RoHS	Not Compliant

These nuts are about 25% stronger than medium-strength steel nuts.

Zinc yellow-chromate plated steel nuts resist corrosion in wet environments.

Figure I.59. High-strength steel hex nut specs (part number 94895A815) (reprinted from McMaster-Carr, 2016).

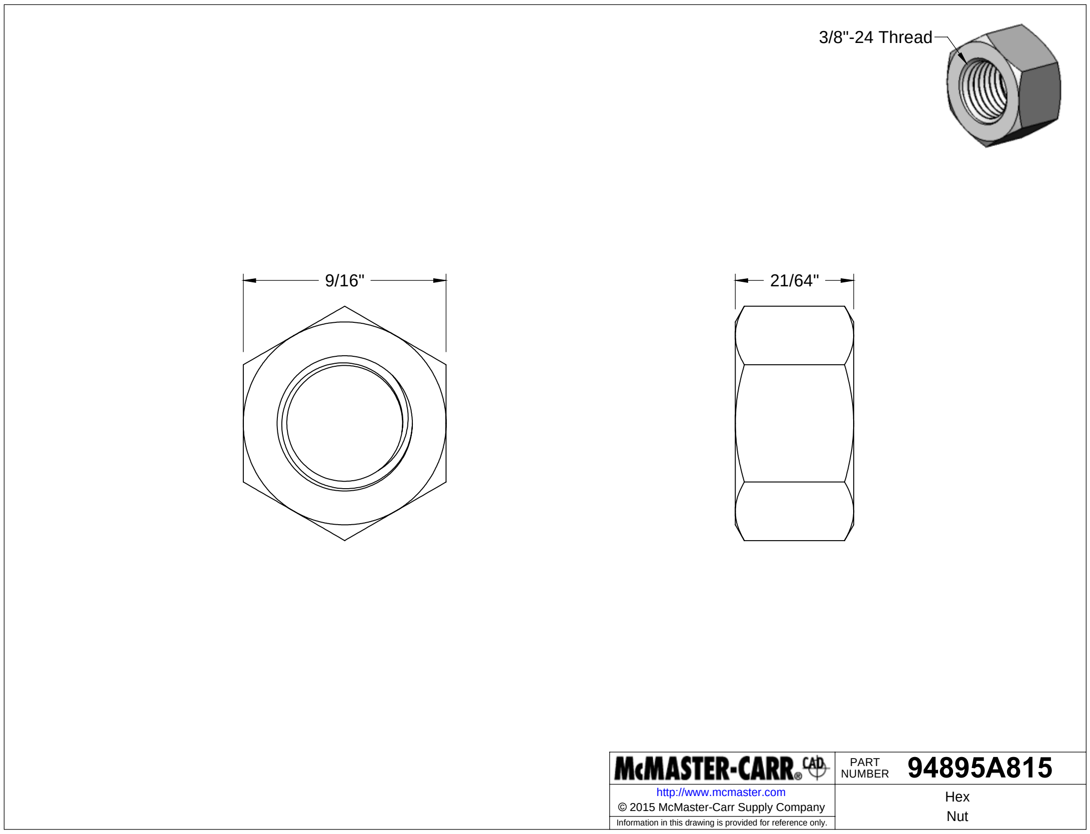

Figure I.60. High-strength steel hex nut drawing (part number 94895A815) (reprinted from McMaster-Carr, 2016).

I.8. Fasteners for the Transmission System Subassembly

McMaster-Carr - Medium-Strength Grade 5 Steel Hex Head Screw, Zinc-Plated, 3/8"-24 Thread Size, 4-1/2" Long, Partially Threaded 5/31/17, 13(18

McMASTER-CARR®

Medium-Strength Grade 5 Steel Hex Head Screw
Zinc-Plated, 3/8"-24 Thread Size, 4-1/2" Long, Partially Threaded

In stock
$10.35 per pack of 10
91247A237

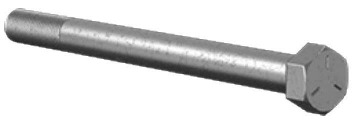

Thread Size	3/8"-24
Length	4 1/2"
Threading	Partially Threaded
Minimum Thread Length	1"
Head Width	9/16"
Head Height	1/4"
Material	Zinc-Plated Steel
Fastener Strength Grade/Class	Grade 5
Hardness	Rockwell C25
Tensile Strength	120,000 psi
Screw Size Decimal Equivalent	0.375"
Thread Type	UNF
Thread Spacing	Fine
Thread Fit	Class 2A
Thread Direction	Right Hand
Head Type	Hex
Hex Head Profile	Standard
Drive Style	External Hex
Specifications Met	ASME B18.2.1, SAE J429
System of Measurement	Inch
RoHS	Compliant

These screws are suitable for fastening most machinery and equipment. Length is measured from under the head.

Zinc-plated steel screws resist corrosion in wet environments.

https://www.mcmaster.com/#91247a237/=17v9a52 Page 1 of 2

Figure I.61. Medium-strength grade 5 steel hex head screw specs (part number 91247A237) (reprinted from McMaster-Carr, 2016).

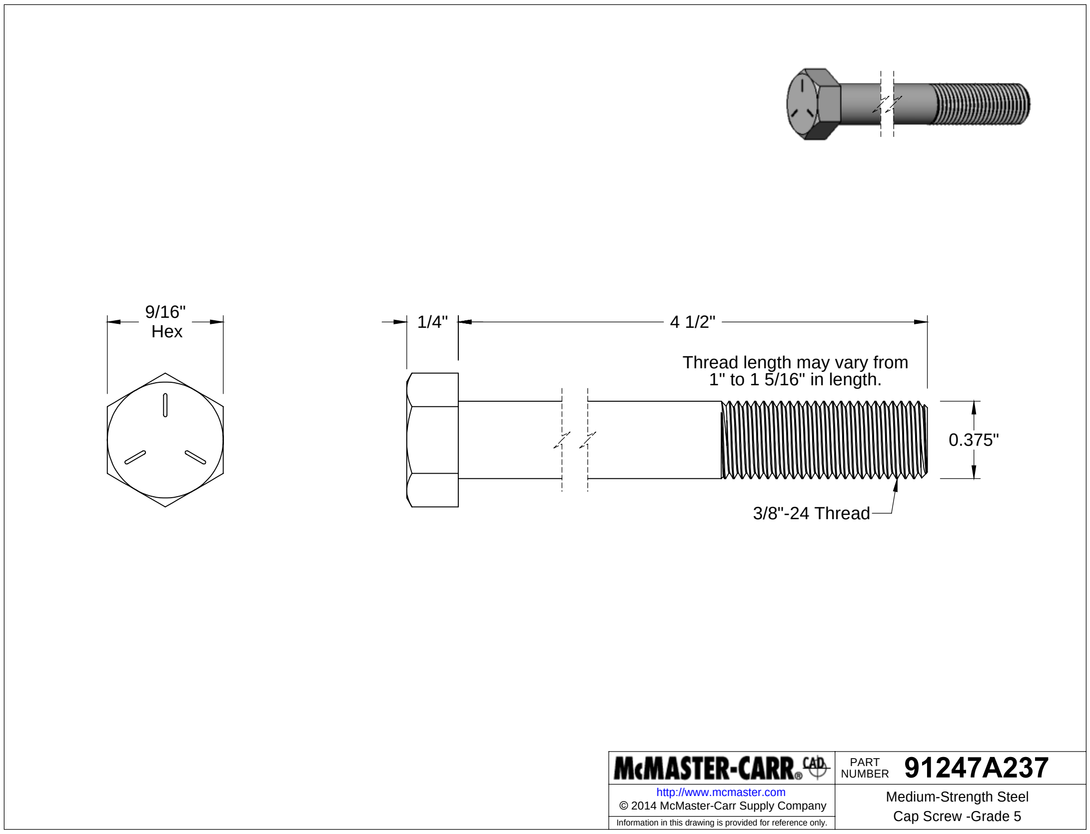

Figure I.62. Medium-strength grade 5 steel hex head screw drawing (part number 91247A237) (reprinted from McMaster-Carr, 2016).

Zinc Yellow-Chromate Plated Hex Head Screw

Grade 8 Steel, 3/8"-24 Thread Size, 3-1/4" Long

In stock
$8.85 per pack of 10
91257A462

Thread Size	3/8"-24
Length	3 1/4"
Threading	Partially Threaded
Minimum Thread Length	1"
Head Width	9/16"
Head Height	1/4"
Material	Zinc Yellow-Chromate Plated Steel
Fastener Strength Grade/Class	Grade 8
Hardness	Rockwell C33
Tensile Strength	150,000 psi
Screw Size Decimal Equivalent	0.375"
Thread Type	UNF
Thread Spacing	Fine
Thread Fit	Class 2A
Thread Direction	Right Hand
Head Type	Hex
Hex Head Profile	Standard
Drive Style	External Hex
Specifications Met	ASME B18.2.1, SAE J429
System of Measurement	Inch
RoHS	Compliant

Good for demanding applications such as suspension systems, these screws are at least 25% stronger than medium-strength steel screws. Length is measured from under the head.

Zinc yellow-chromate plated steel screws resist corrosion in wet environments.

Figure I.63. Zinc Yellow-chromate plated hex head screw specs (part number 91257A462) (reprinted from McMaster-Carr, 2016).

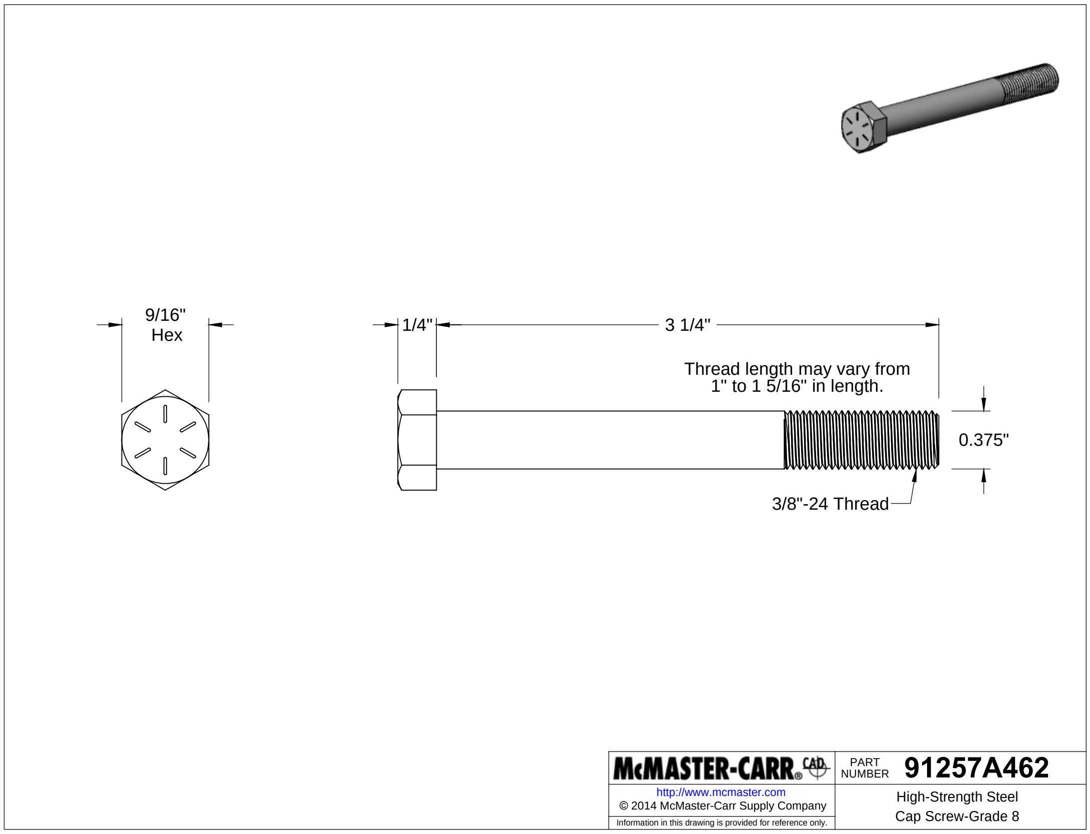

Figure I.64. Zinc Yellow-chromate plated hex head screw drawing (part number 91257A462) (reprinted from McMaster-Carr, 2016).

McMASTER-CARR®

Black-Oxide Alloy Steel Socket Head Screw

M8 x 1.25 mm Thread, 22 mm Long

In stock
$8.31 per pack of 50
91290A428

Thread Size	M8
Thread Pitch	1.25 mm
Length	22 mm
Threading	Fully Threaded
Head Diameter	13 mm
Head Height	8 mm
Drive Size	6 mm
Material	Black-Oxide Alloy Steel
Fastener Strength Grade/Class	Class 12.9
Hardness	Rockwell C37
Tensile Strength	170,000 psi
Thread Type	Metric
Thread Spacing	Coarse
Thread Fit	Class 5g6g
Thread Direction	Right Hand
Head Type	Socket
Socket Head Profile	Standard
Drive Style	Hex
Specifications Met	DIN 912, ISO 4762
System of Measurement	Metric
RoHS	Not Compliant

These screws are made from an alloy steel that's stronger than Grade 8 steel. Length is measured from under the head.

Black-oxide steel screws are mildly corrosion resistant in dry environments.

Figure I.65. Black-oxide alloy steel socket head screw specs (part number 91290A428) (reprinted from McMaster-Carr, 2016).

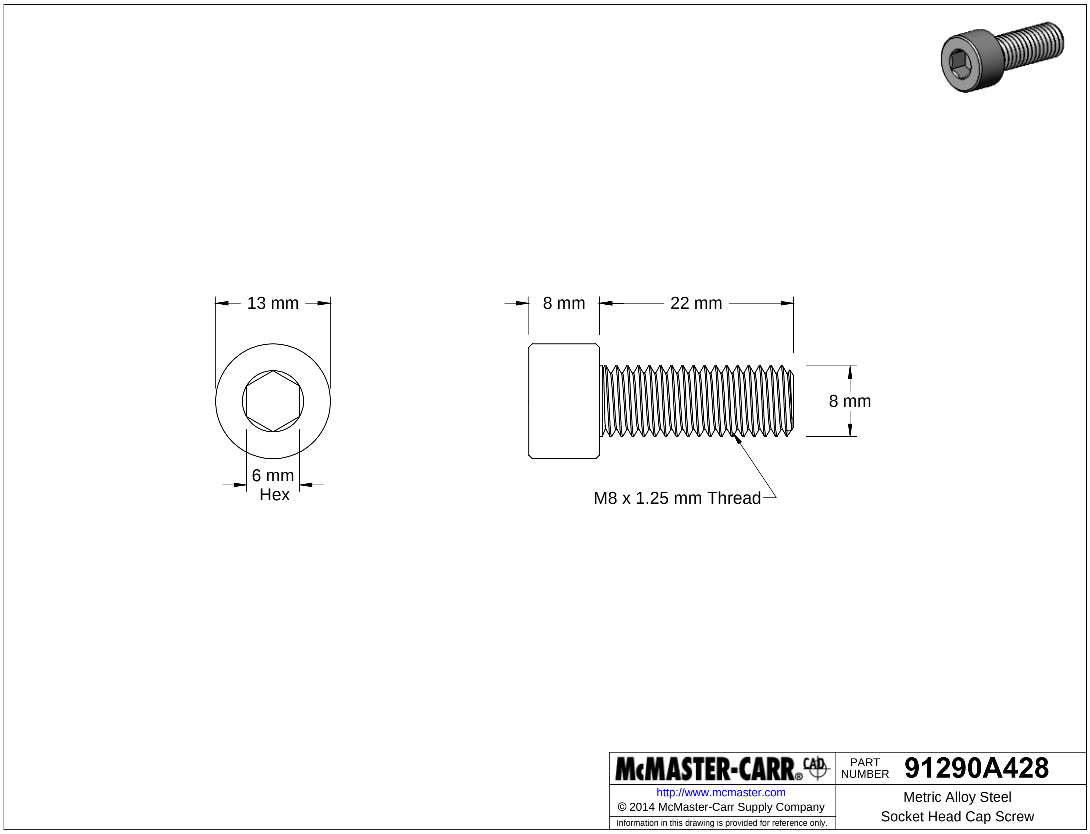

Figure I.66. Black-oxide alloy steel socket head screw drawing (part number 91290A428) (reprinted from McMaster-Carr, 2016).

MCMASTER-CARR®

Aluminum Unthreaded Spacer

3/4" OD, 1" Length, for 3/8" Screw Size

In stock
1-9 Each $2.88
10 or more $2.46
92510A808

OD	3/4"
OD Tolerance	-0.005" to 0.005"
Length	1"
For Screw Size	3/8"
ID	0.380"
ID Tolerance	0" to 0.01"
Length Tolerance	-0.005" to 0.005"
Shape	Round
Tensile Strength	45,000 psi
Hardness	Rockwell B50
Material	2011 Aluminum
RoHS	Compliant

These spacers are also known as clearance spacers.

Aluminum and black-anodized aluminum are lightweight and have mild corrosion resistance.

Figure I.67. Aluminum unthreaded spacer specs (part number 92510A808) (reprinted from McMaster-Carr, 2016).

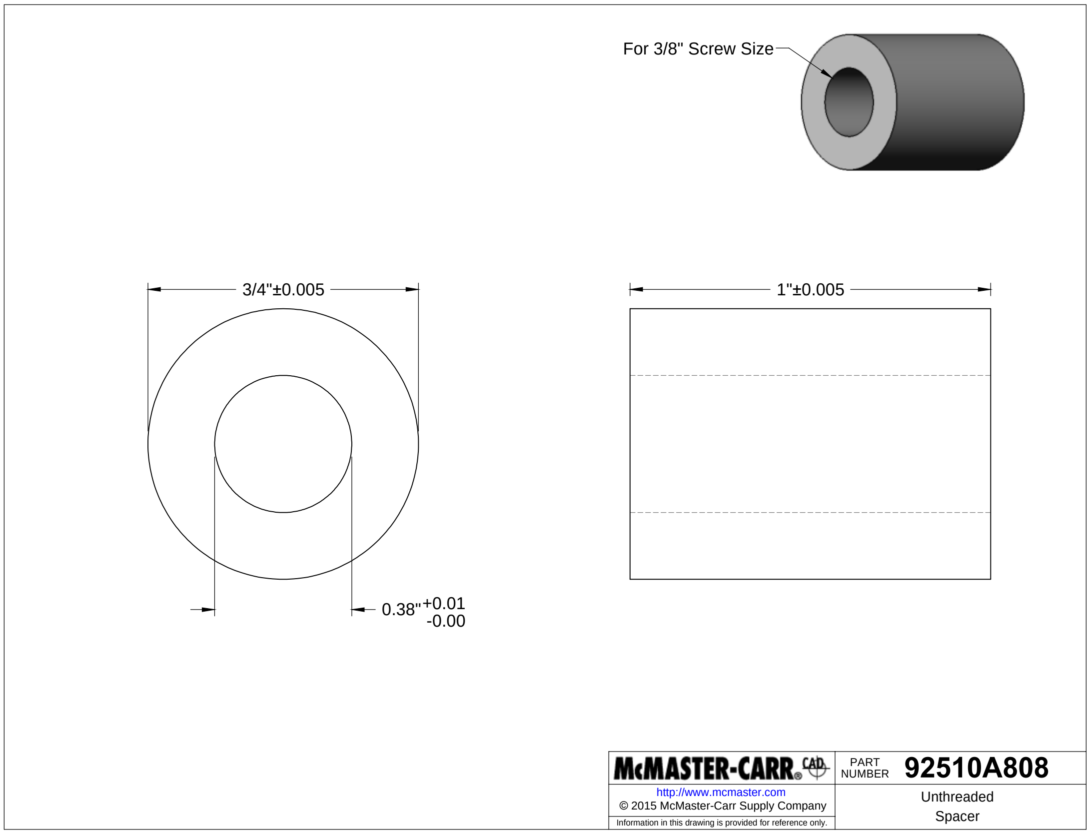

Figure I.68. Aluminum unthreaded spacer drawing (part number 92510A808) (reprinted from McMaster-Carr, 2016).

McMASTER-CARR®

Medium-Strength Steel Nylon-Insert Locknut
Grade 5, Zinc-Plated, 3/8"-24 Thread Size

In stock
$9.08 per pack of 100
95615A150

Material	Zinc-Plated Steel
Fastener Strength Grade/Class	Grade 5
Thread Size	3/8"-24
Thread Type	UNF
Thread Spacing	Fine
Thread Fit	Class 2B
Thread Direction	Right Hand
Width	9/16"
Height	29/64"
Insert Maximum Temperature	220° F
Drive Style	External Hex
Nut Type	Locknut
Hex Nut Profile	Standard
Locking Type	Nylon Insert
System of Measurement	Inch
RoHS	Compliant

A nylon insert grips the bolt to resist loosening without damaging threads. These locknuts are reusable, but their holding power lessens with each use. They are suitable for fastening most machinery and equipment. A zinc plating provides corrosion resistance in wet environments.

Figure I.69. Medium-strength steel nylon-insert locknut specs (part number 95615A150) (reprinted from McMaster-Carr, 2016).

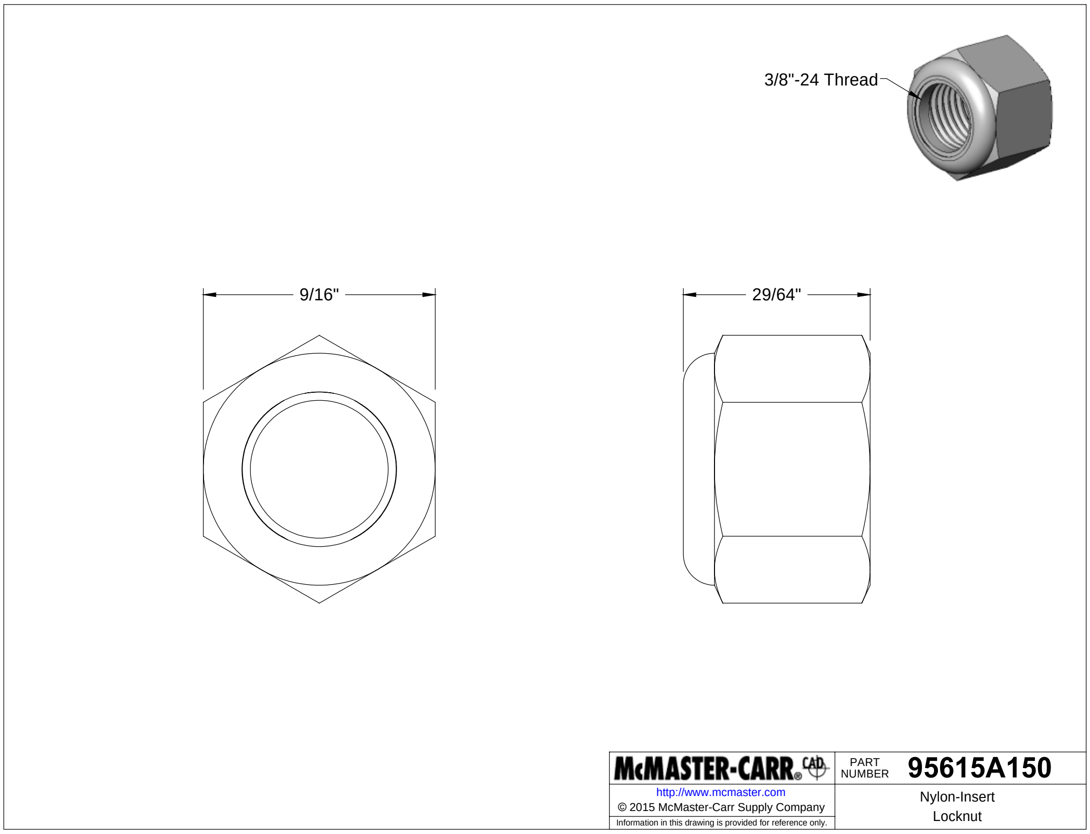

Figure I.70. Medium-strength steel nylon-insert locknut drawing (part number 95615A150) (reprinted from McMaster-Carr, 2016).

APPENDIX J

CAD DRAWINGS

J.1. Top Structure

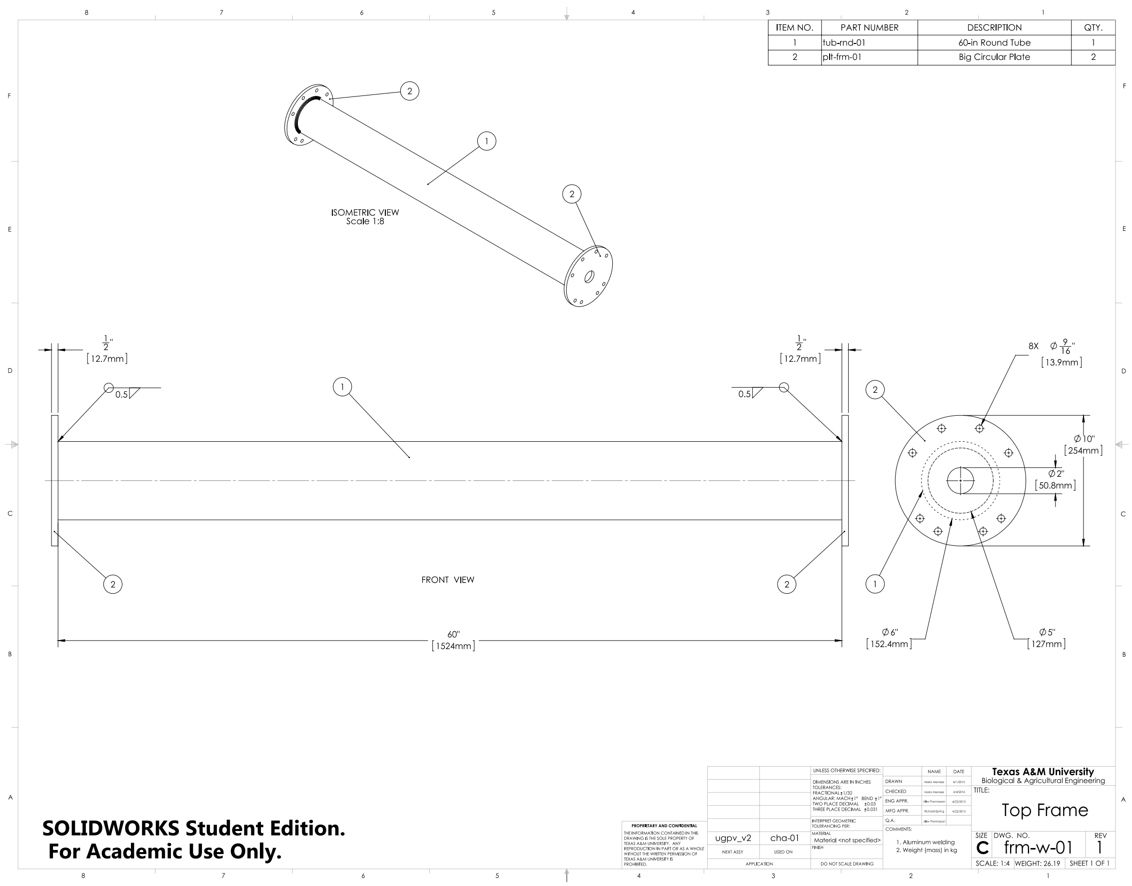

Figure J.1. Drawing of the short top structure (frame) welded assembly, *frm-w-01.sldasm*.

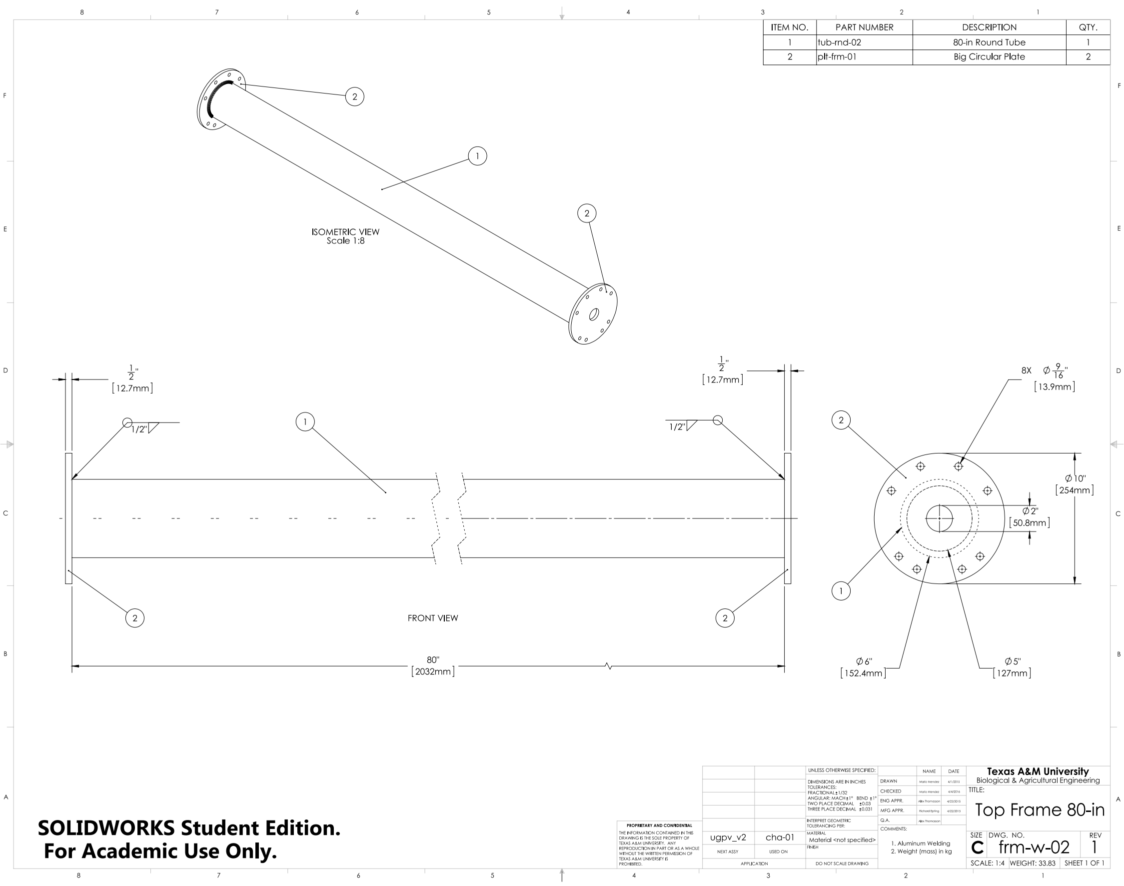

Figure J.2. Drawing of the long top structure (frame) welded assembly, *frm-w-02.sldasm*.

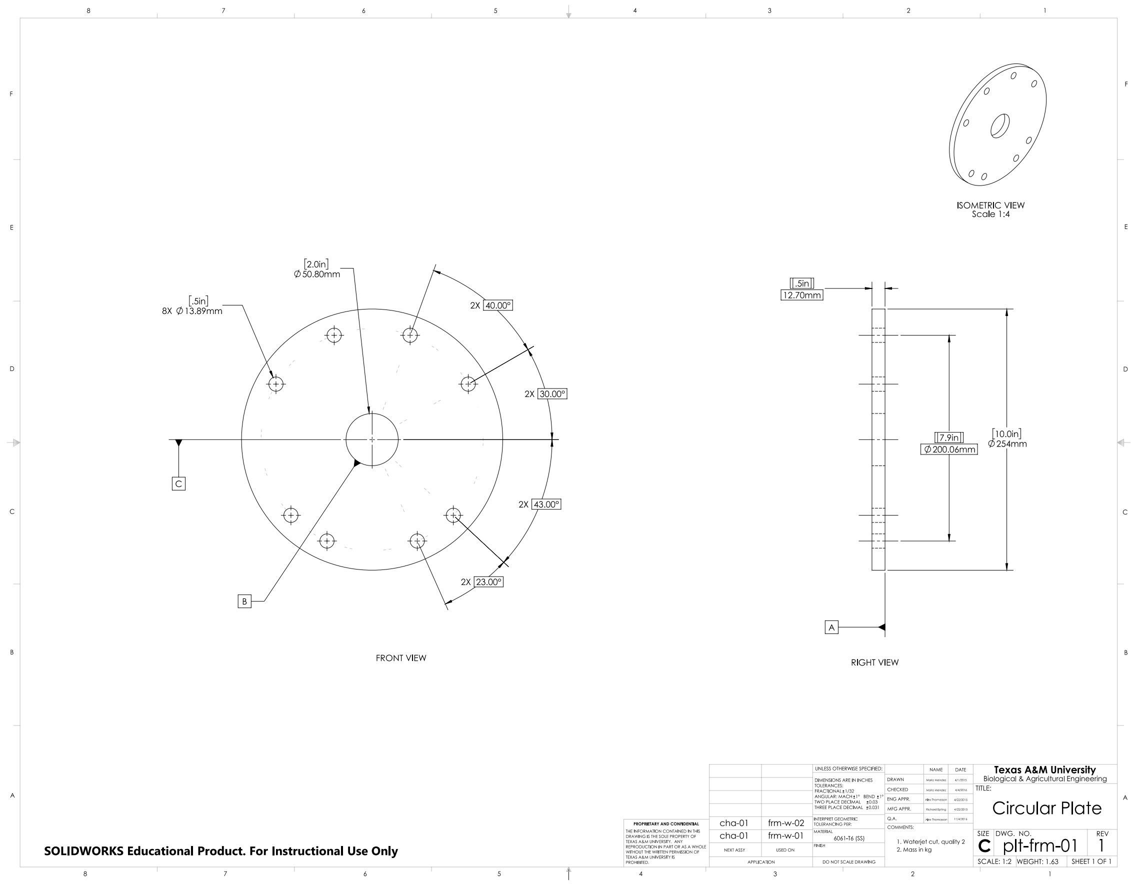

Figure J.3. Drawing of the circular plate, *plt-frm-01.sldprt*.

J.2. Suspension System

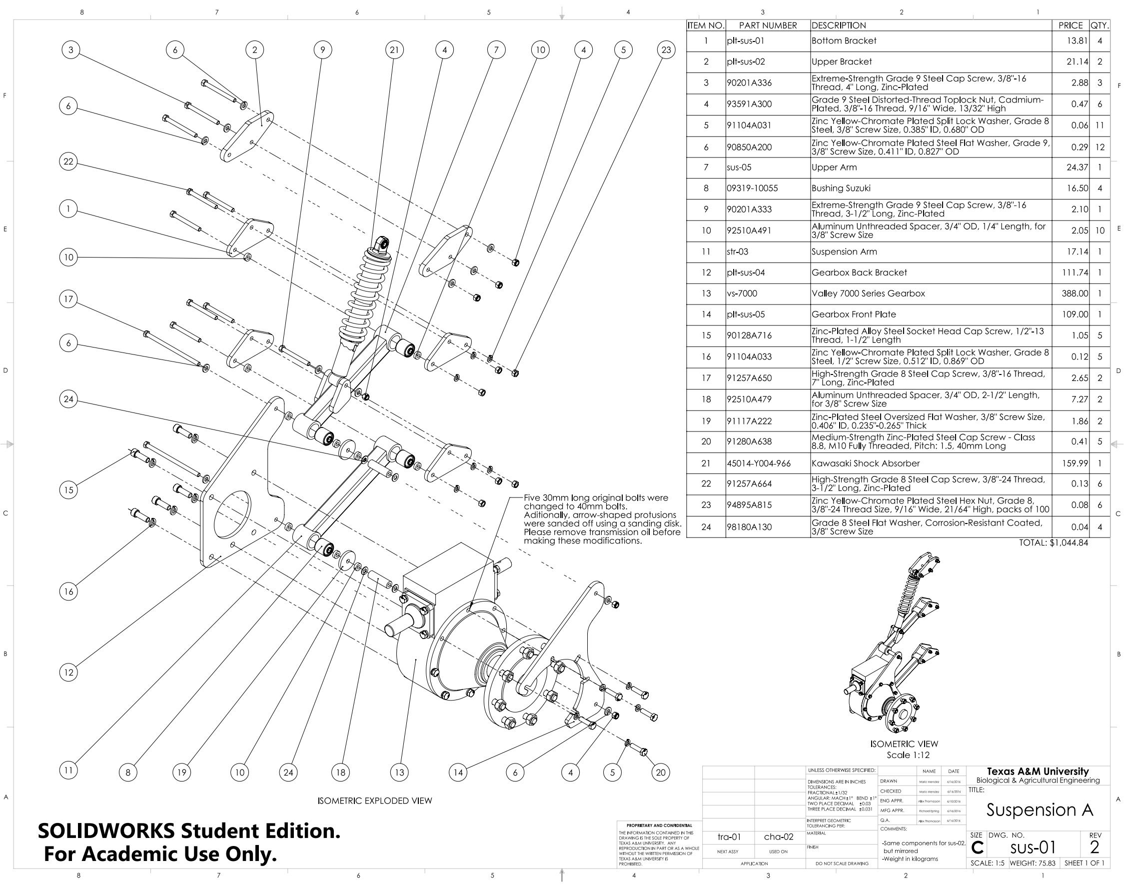

ITEM NO.	PART NUMBER	DESCRIPTION	PRICE	QTY.
1	plt-sus-01	Bottom Bracket	13.81	4
2	plt-sus-02	Upper Bracket	21.14	2
3	90201A336	Extreme-Strength Grade 9 Steel Cap Screw, 3/8"-16 Thread, 4" Long, Zinc-Plated	2.88	3
4	93591A300	Grade 9 Steel Distorted-Thread Toplock Nut, Cadmium-Plated, 3/8"-16 Thread, 9/16" Wide, 13/32" High	0.47	6
5	91104A031	Zinc Yellow-Chromate Plated Split Lock Washer, Grade 8 Steel, 3/8" Screw Size, 0.385" ID, 0.680" OD	0.06	11
6	90850A200	Zinc Yellow-Chromate Plated Steel Flat Washer, Grade 9, 3/8" Screw Size, 0.411" ID, 0.827" OD	0.29	12
7	sus-05	Upper Arm	24.37	1
8	09319-10055	Bushing Suzuki	16.50	4
9	90201A333	Extreme-Strength Grade 9 Steel Cap Screw, 3/8"-16 Thread, 3-1/2" Long, Zinc-Plated	2.10	1
10	92510A491	Aluminum Unthreaded Spacer, 3/4" OD, 1/4" Length, for 3/8" Screw Size	2.05	10
11	str-03	Suspension Arm	17.14	1
12	plt-sus-04	Gearbox Back Bracket	111.74	1
13	vs-7000	Valley 7000 Series Gearbox	388.00	1
14	plt-sus-05	Gearbox Front Plate	109.00	1
15	90128A716	Zinc-Plated Alloy Steel Socket Head Cap Screw, 1/2"-13 Thread, 1-1/2" Length	1.05	5
16	91104A033	Zinc Yellow-Chromate Plated Split Lock Washer, Grade 8 Steel, 1/2" Screw Size, 0.512" ID, 0.869" OD	0.12	5
17	91257A650	High-Strength Grade 8 Steel Cap Screw, 3/8"-16 Thread, 7" Long, Zinc-Plated	2.65	2
18	92510A479	Aluminum Unthreaded Spacer, 3/4" OD, 2-1/2" Length, for 3/8" Screw Size	7.27	2
19	91117A222	Zinc-Plated Steel Oversized Flat Washer, 3/8" Screw Size, 0.406" ID, 0.235"-0.265" Thick	1.86	2
20	91280A638	Medium-Strength Zinc-Plated Steel Cap Screw - Class 8.8, M10 Fully Threaded, Pitch: 1.5, 40mm Long	0.41	5
21	45014-Y004-966	Kawasaki Shock Absorber	159.99	1
22	91257A664	High-Strength Grade 8 Steel Cap Screw, 3/8"-24 Thread, 3-1/2" Long, Zinc-Plated	0.13	6
23	94895A815	Zinc Yellow-Chromate Plated Steel Hex Nut, Grade 8, 3/8"-24 Thread Size, 9/16" Wide, 21/64" High, packs of 100	0.08	6
24	98180A130	Grade 8 Steel Flat Washer, Corrosion-Resistant Coated, 3/8" Screw Size	0.04	4

TOTAL: $1,044.84

Figure J.4. Drawing of the exploded isometric view of the quarter suspension system, *sus-01.sld.asm*, with its corresponding BOM table.

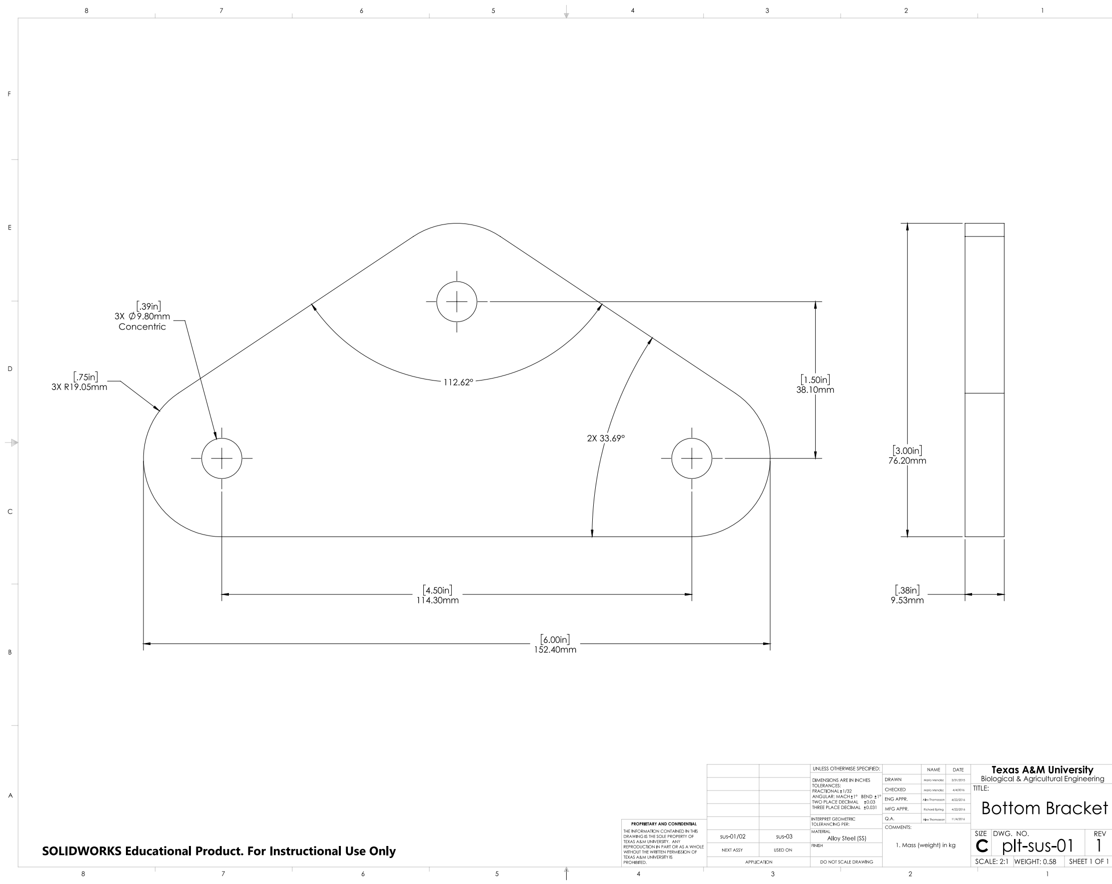

Figure J.5. Drawing of the bracket for the bottom swing arm, *plt-sus-01.sldprt*.

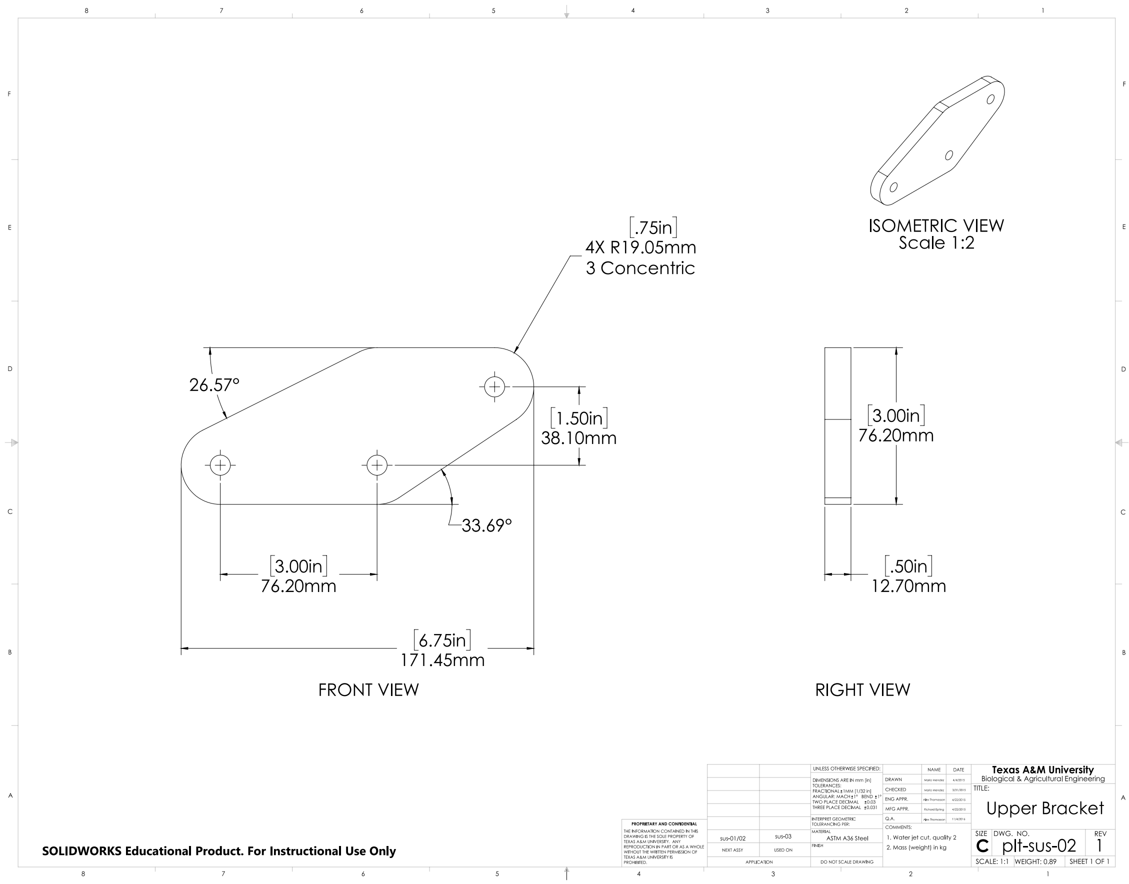

Figure J.6. Drawing of the bracket for the shock absorber swing arm, *plt-sus-02.sldprt*.

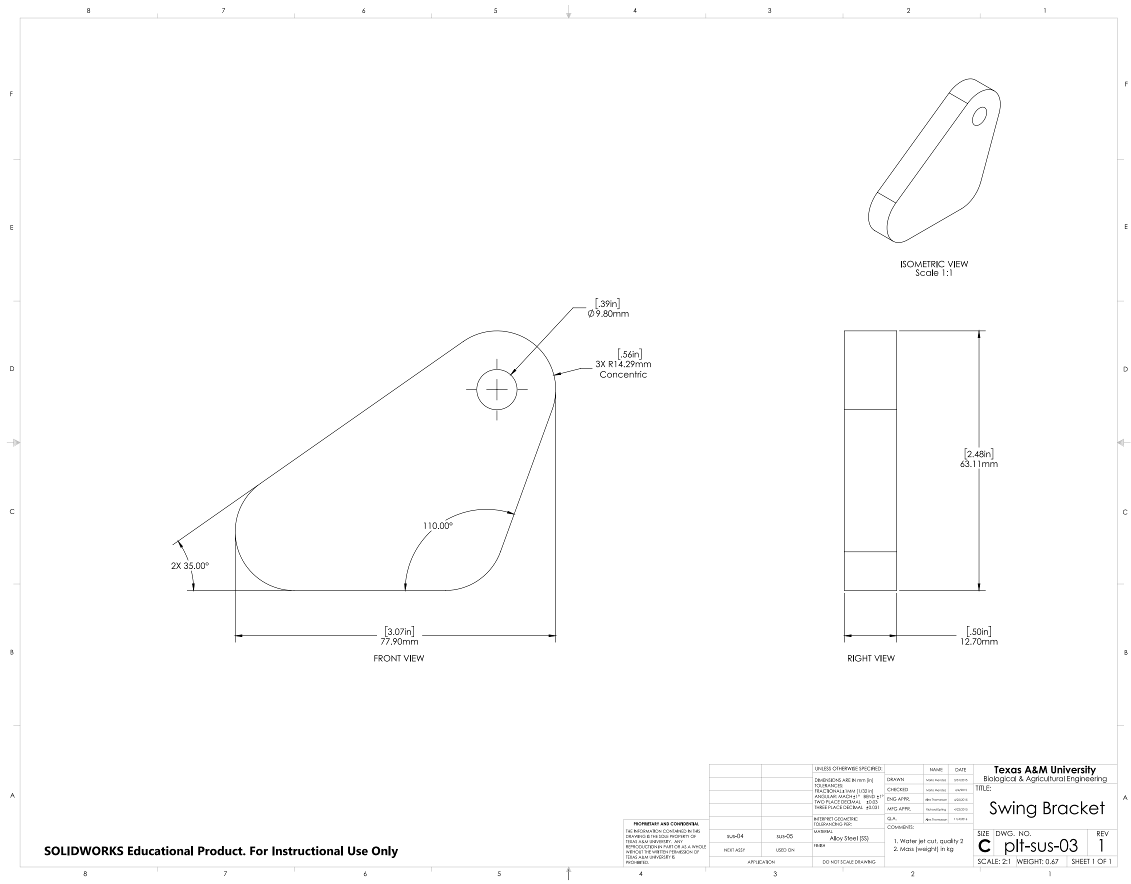

Figure J.7. Drawing of the swing arm bracket for shock absorber, *plt-sus-03.sldprt*.

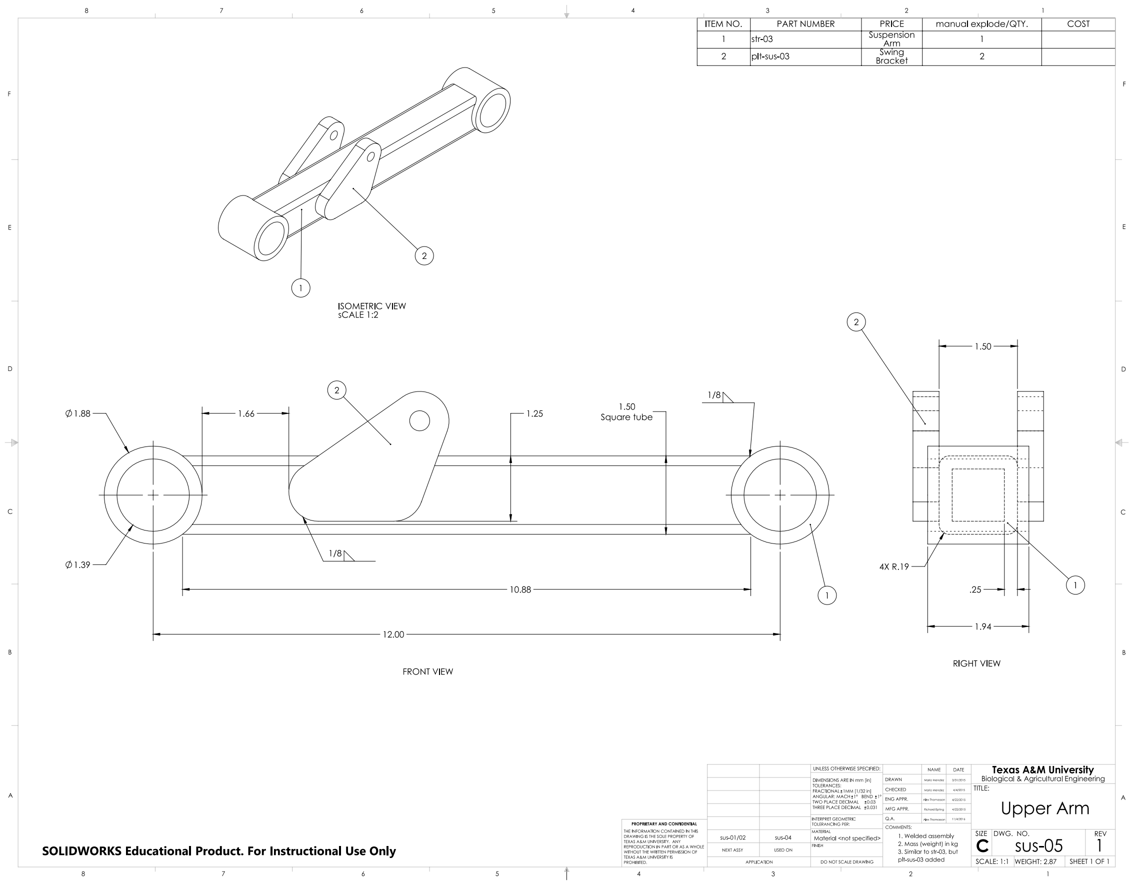

Figure J.8. Drawing of the swing arm for shock absorber, *sus-05.sldasm*.

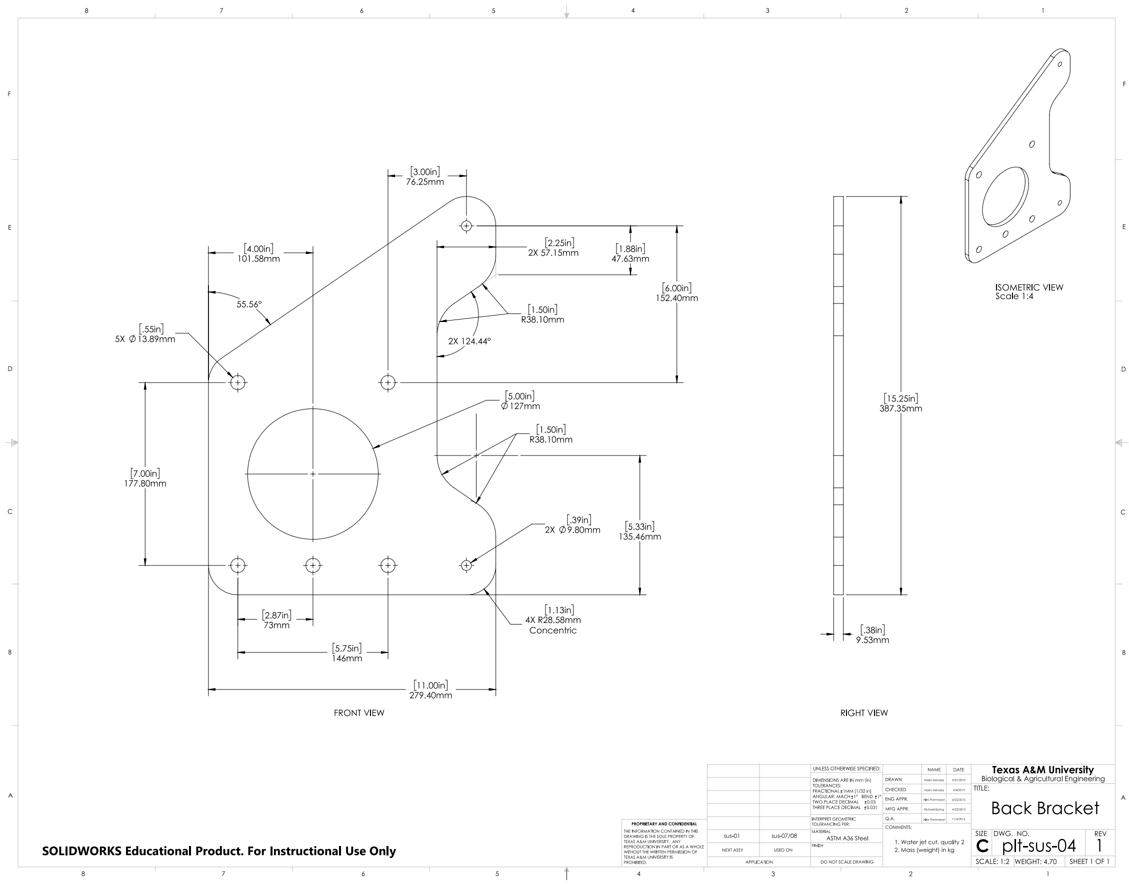

Figure J.9. Drawing of the gearbox inside bracket, *plt-sus-04.sldprt*.

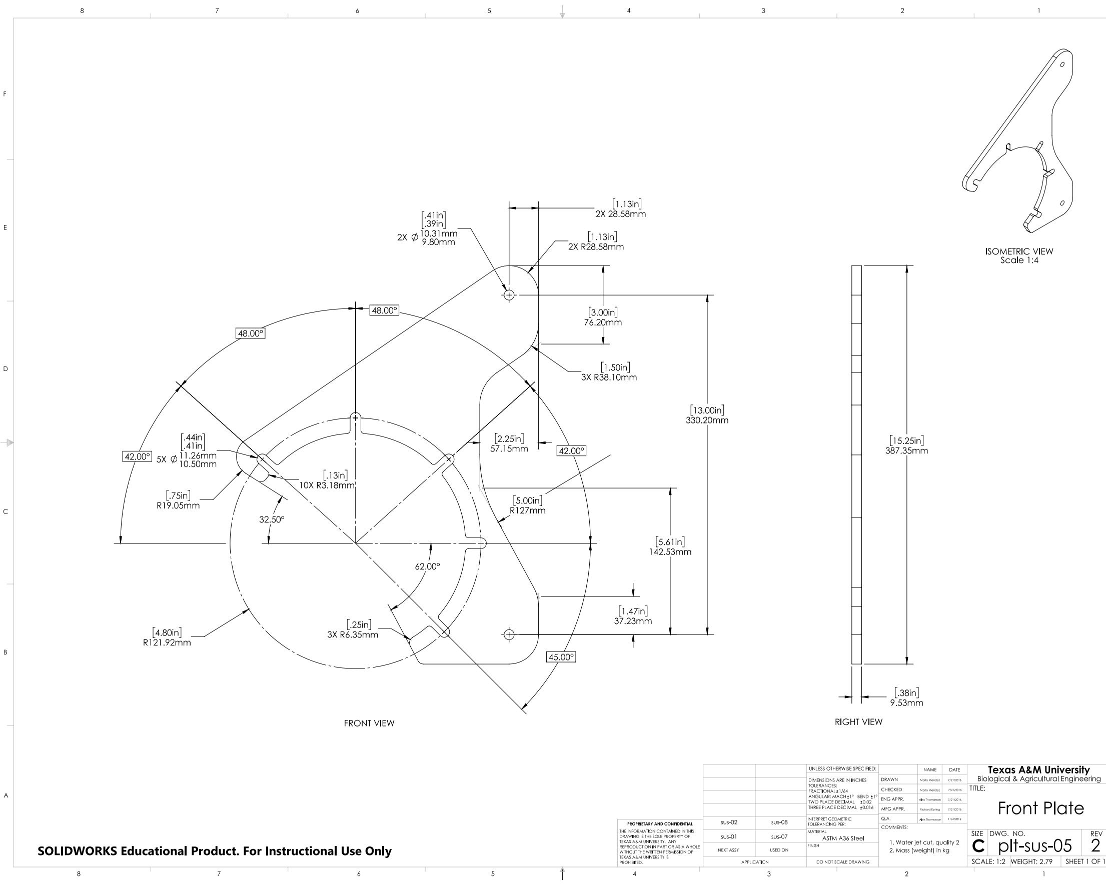

Figure J.10. Drawing of the gearbox outside bracket, *plt-sus-05.sldprt*.

J.3. Lateral Truss

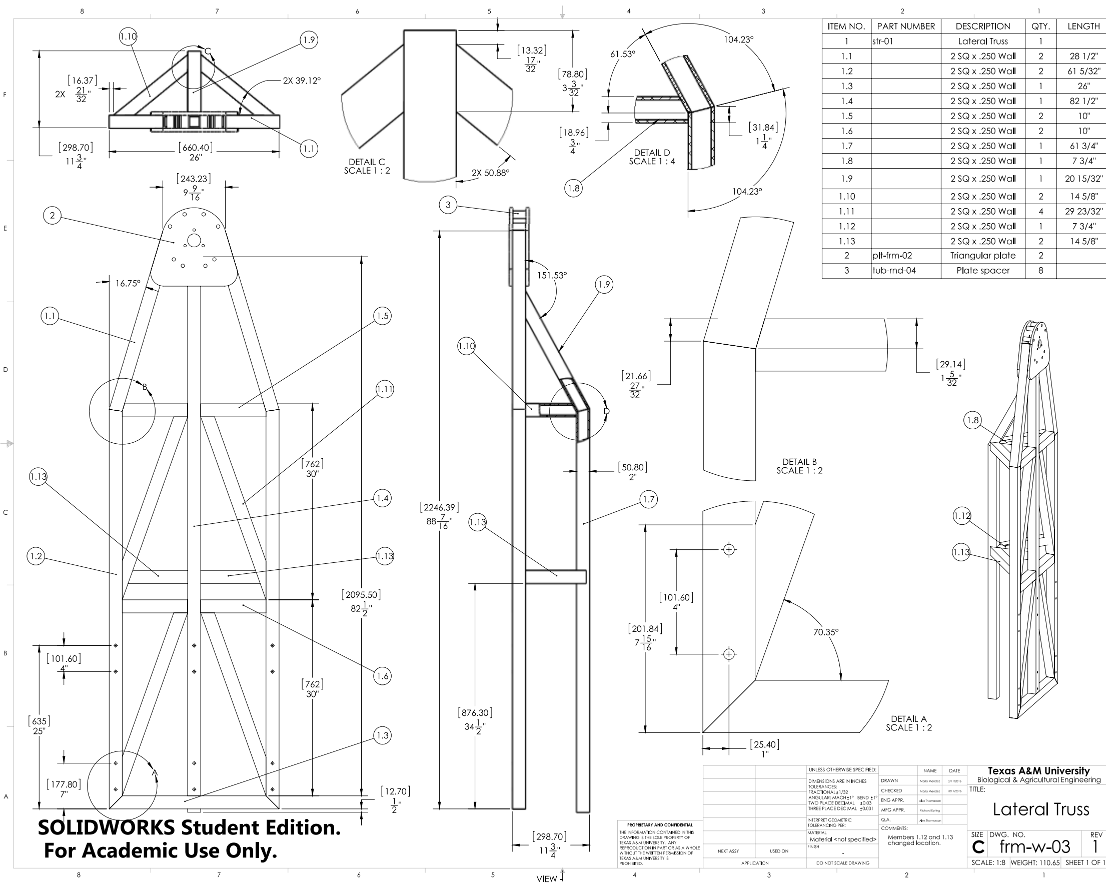

Figure J.11. Drawing of the lateral truss assembly, *frm-w-03.sldasm*.

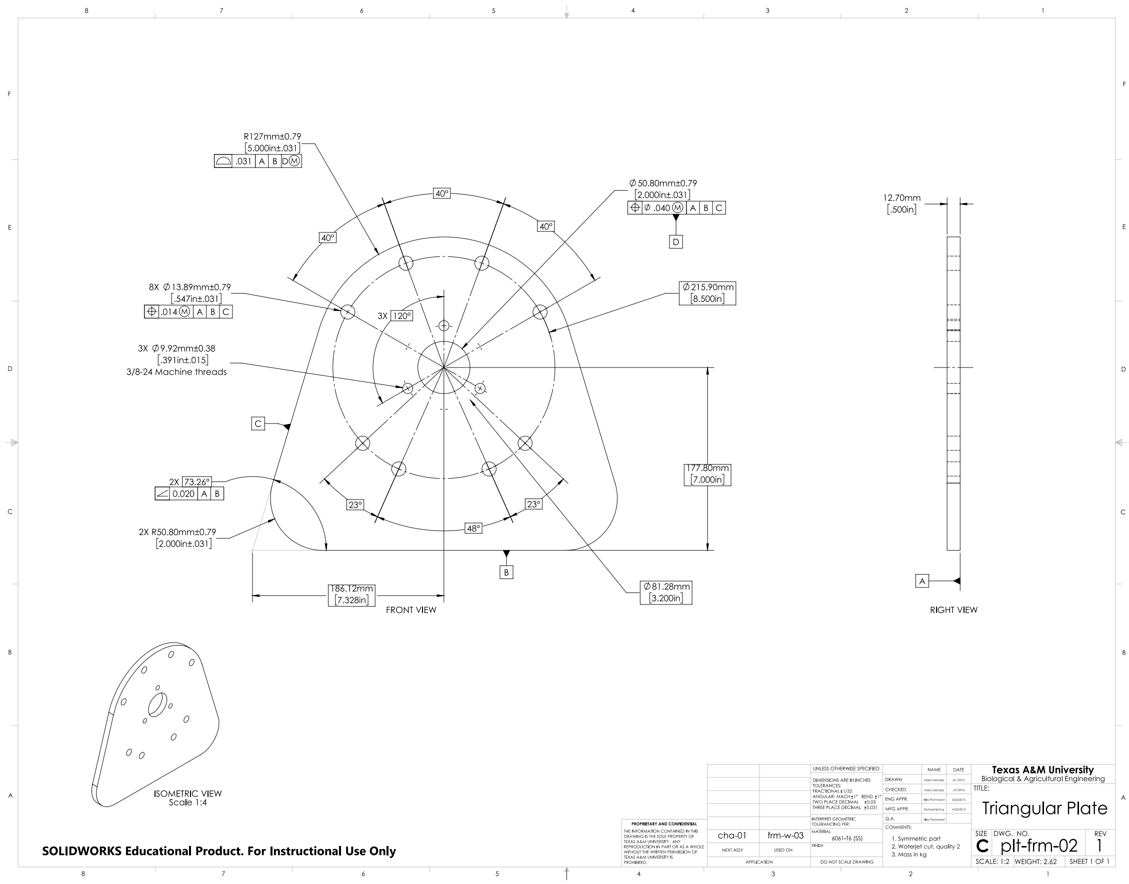

Figure J.12. Drawing of the top triangular plate, *plt-frm-02.sldprt*.

J.4. Bottom Chassis

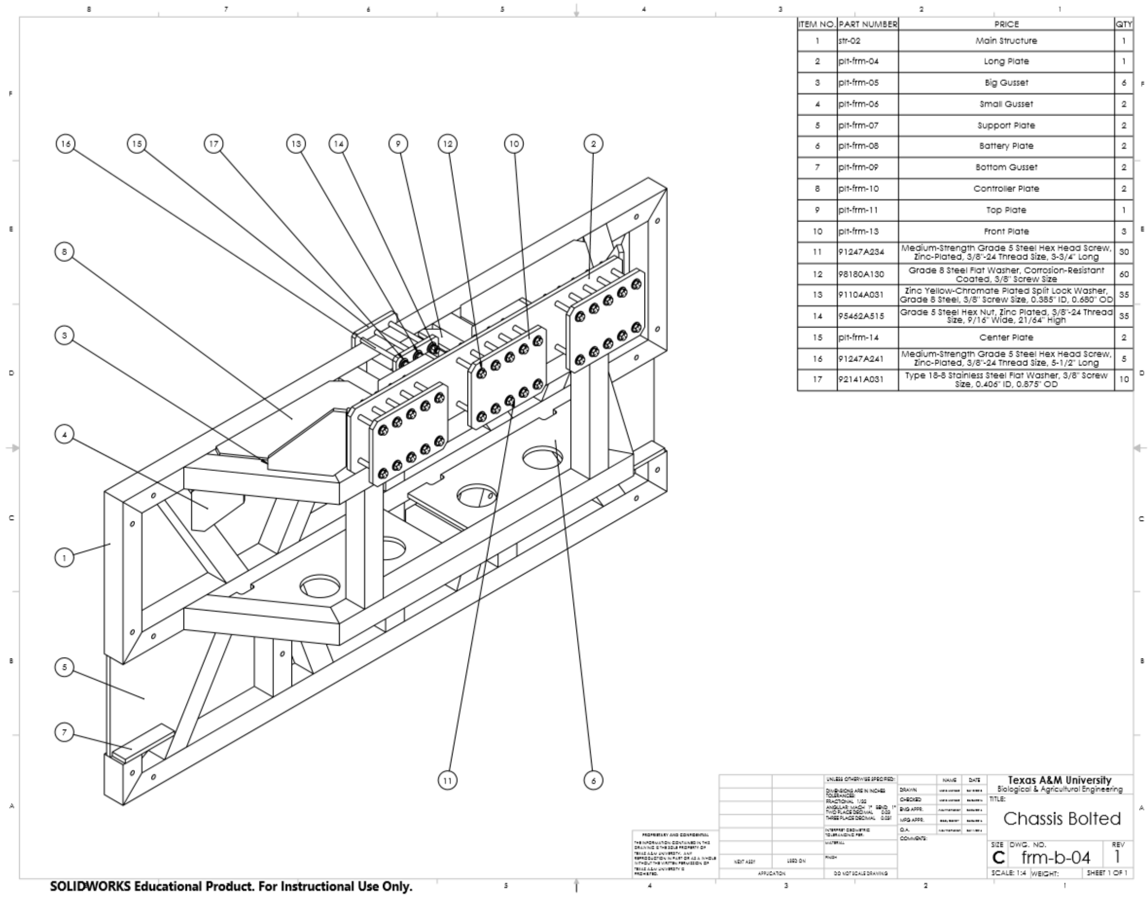

ITEM NO.	PART NUMBER	PRICE	QTY
1	str-02	Main Structure	1
2	plt-frm-04	Long Plate	1
3	plt-frm-05	Big Gusset	6
4	plt-frm-06	Small Gusset	2
5	plt-frm-07	Support Plate	2
6	plt-frm-08	Battery Plate	2
7	plt-frm-09	Bottom Gusset	2
8	plt-frm-10	Controller Plate	2
9	plt-frm-11	Top Plate	1
10	plt-frm-13	Front Plate	3
11	91247A234	Medium-Strength Grade 5 Steel Hex Head Screw, Zinc-Plated, 3/8"-24 Thread Size, 3-3/4" Long	30
12	98180A130	Grade 8 Steel Flat Washer, Corrosion-Resistant Coated, 3/8" Screw Size	60
13	91104A031	Zinc Yellow-Chromate Plated Split Lock Washer, Grade 8 Steel, 3/8" Screw Size, 0.385" ID, 0.680" OD	35
14	95462A515	Grade 5 Steel Hex Nut, Zinc Plated, 3/8"-24 Thread Size, 9/16" Wide, 21/64" High	35
15	plt-frm-14	Center Plate	2
16	91247A241	Medium-Strength Grade 5 Steel Hex Head Screw, Zinc-Plated, 3/8"-24 Thread Size, 5-1/2" Long	5
17	92141A031	Type 18-8 Stainless Steel Flat Washer, 3/8" Screw Size, 0.406" ID, 0.875" OD	10

Figure J.13. Drawing of the bolted bottom chassis assembly, *frm-b-04.sldasm*.

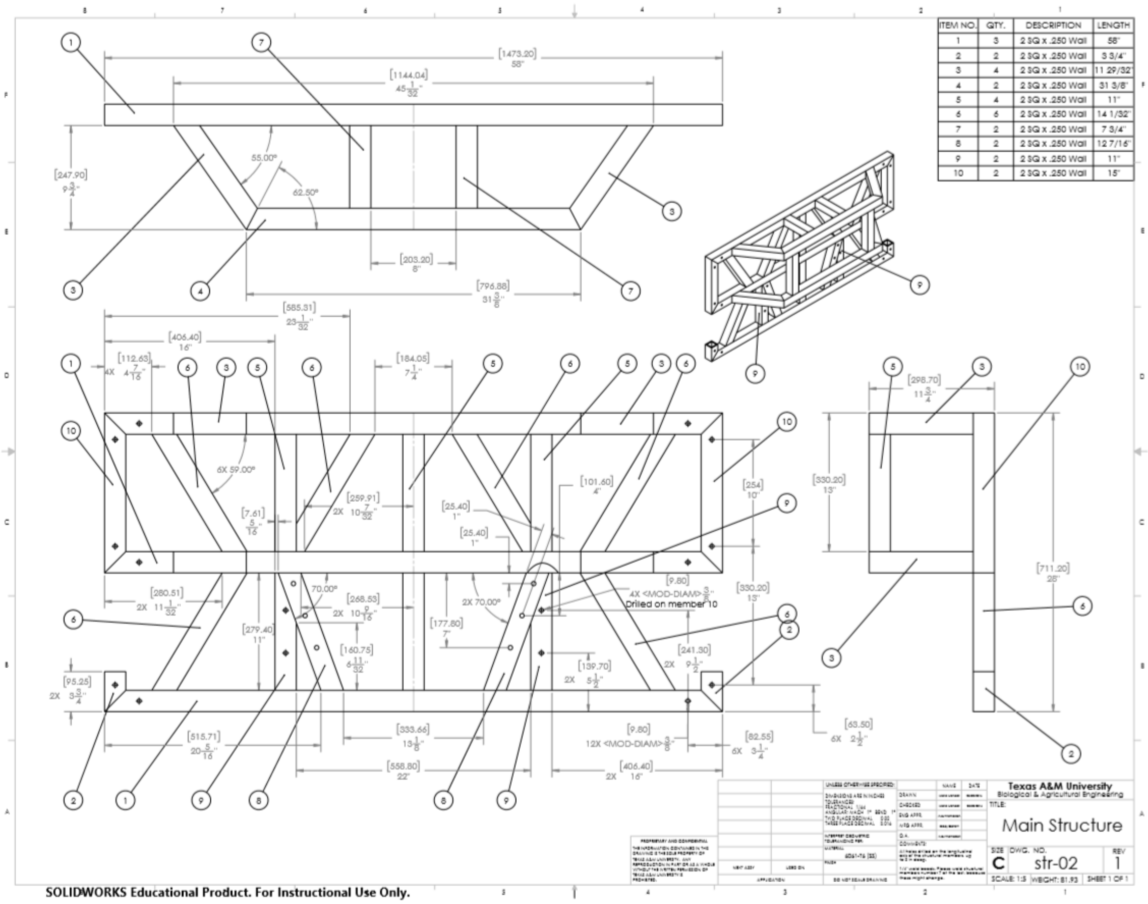

Figure J.14. Drawing of the main structure of the bottom chassis, *str-02.sldprt*.

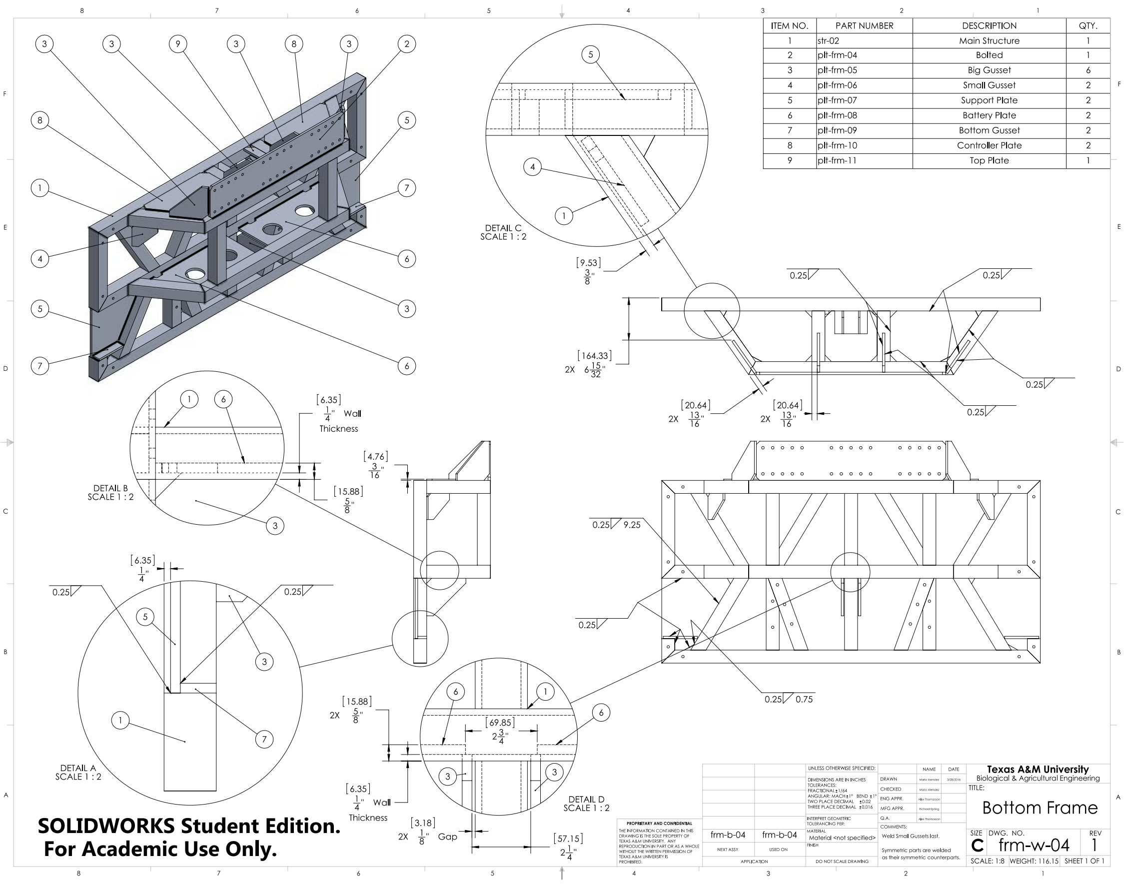

Figure J.15. Drawing of the welded bottom chassis assembly, *frm-w-04.sldasm*.

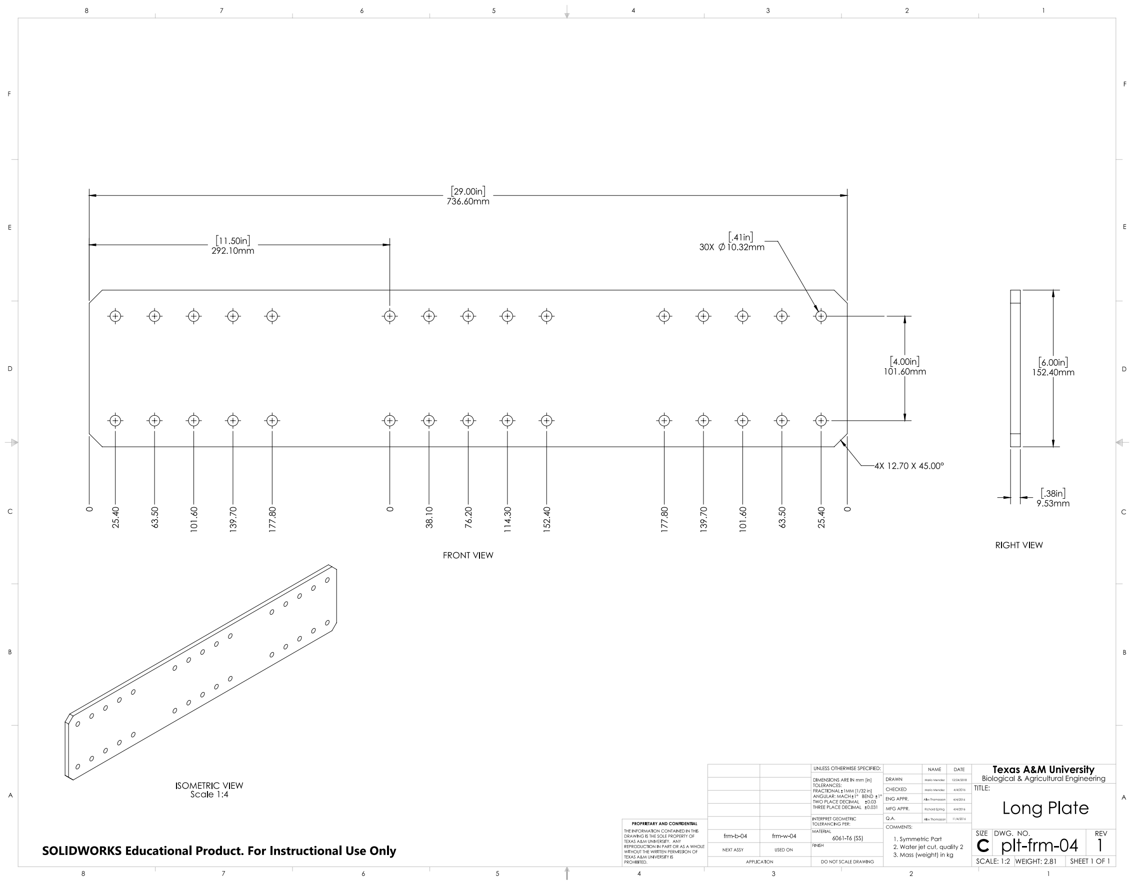

Figure J.16. Drawing of the top long plate for bolting, *plt-frm-04.sldprt*.

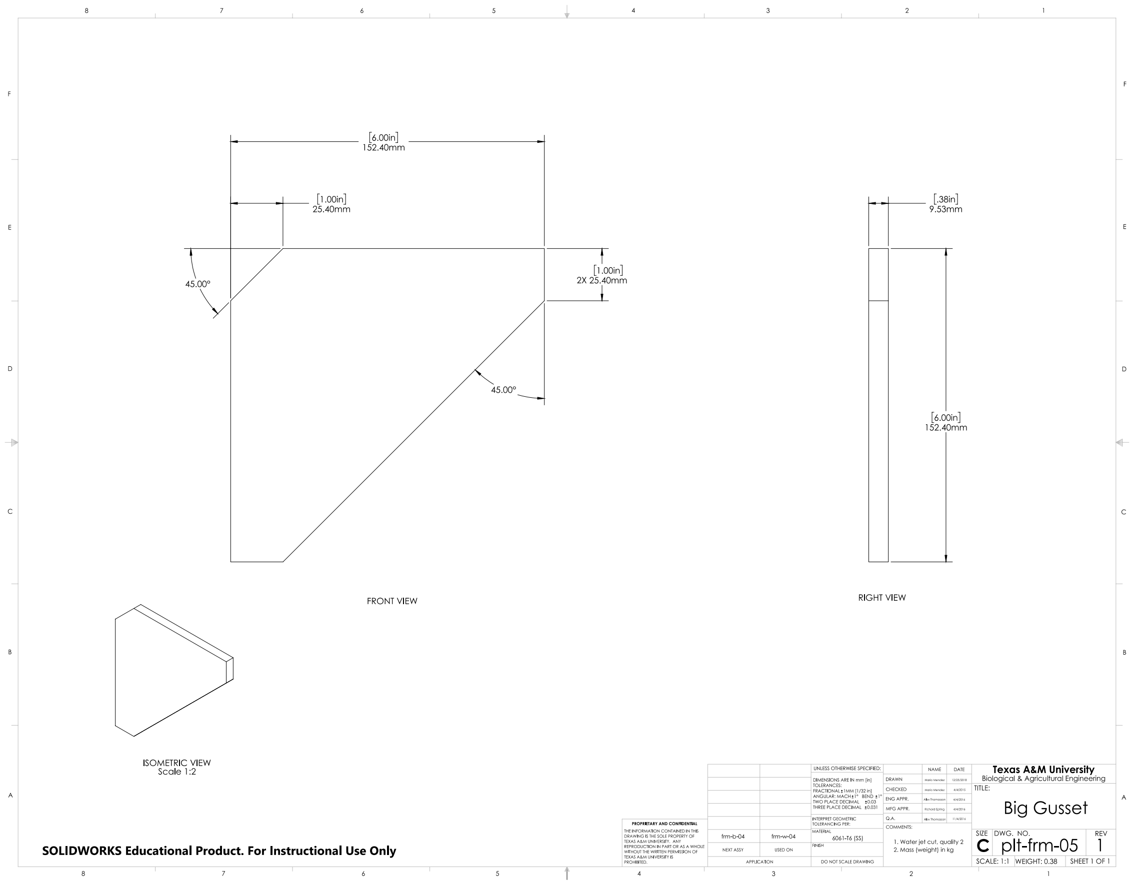

Figure J.17. Drawing of the big gusset, *plt-frm-05.sldprt*.

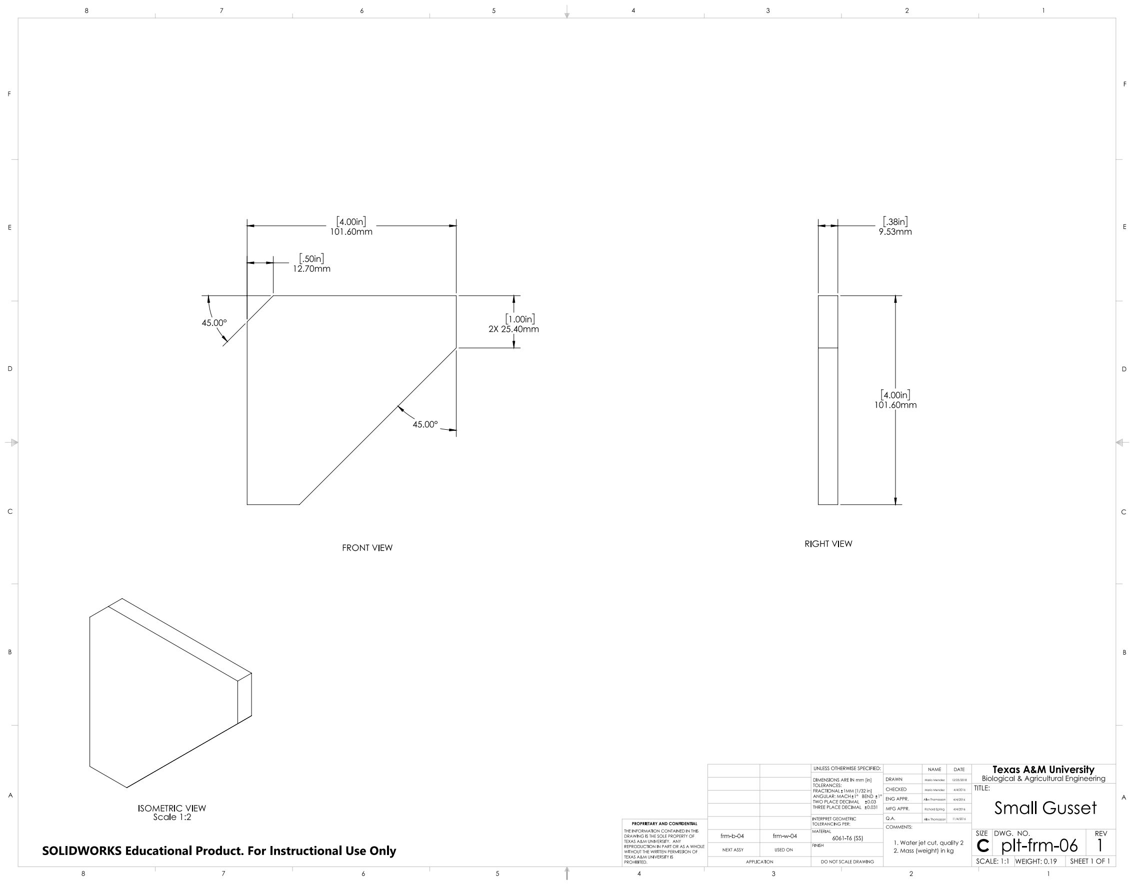

Figure J.18. Drawing of the small gusset, *plt-frm-06.sldprt*.

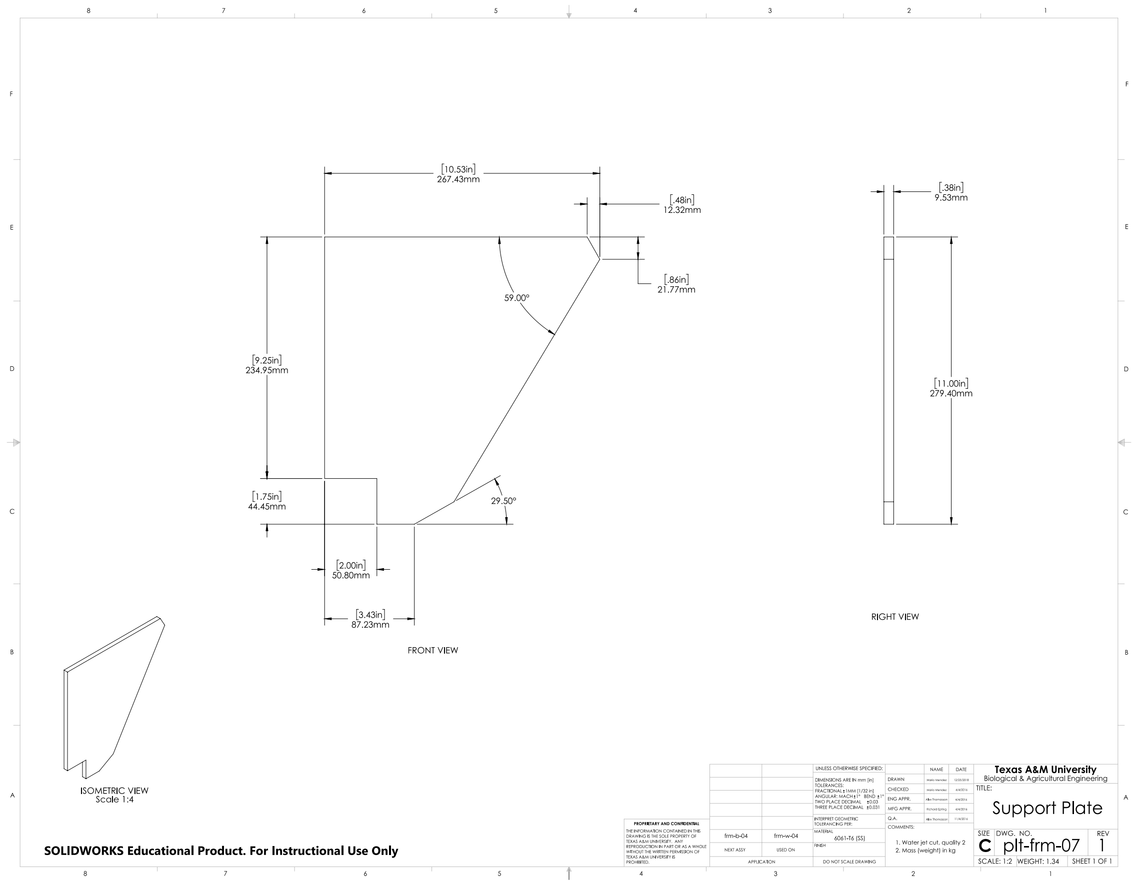

Figure J.19. Drawing of the lateral support plate, *plt-frm-07.sldprt*.

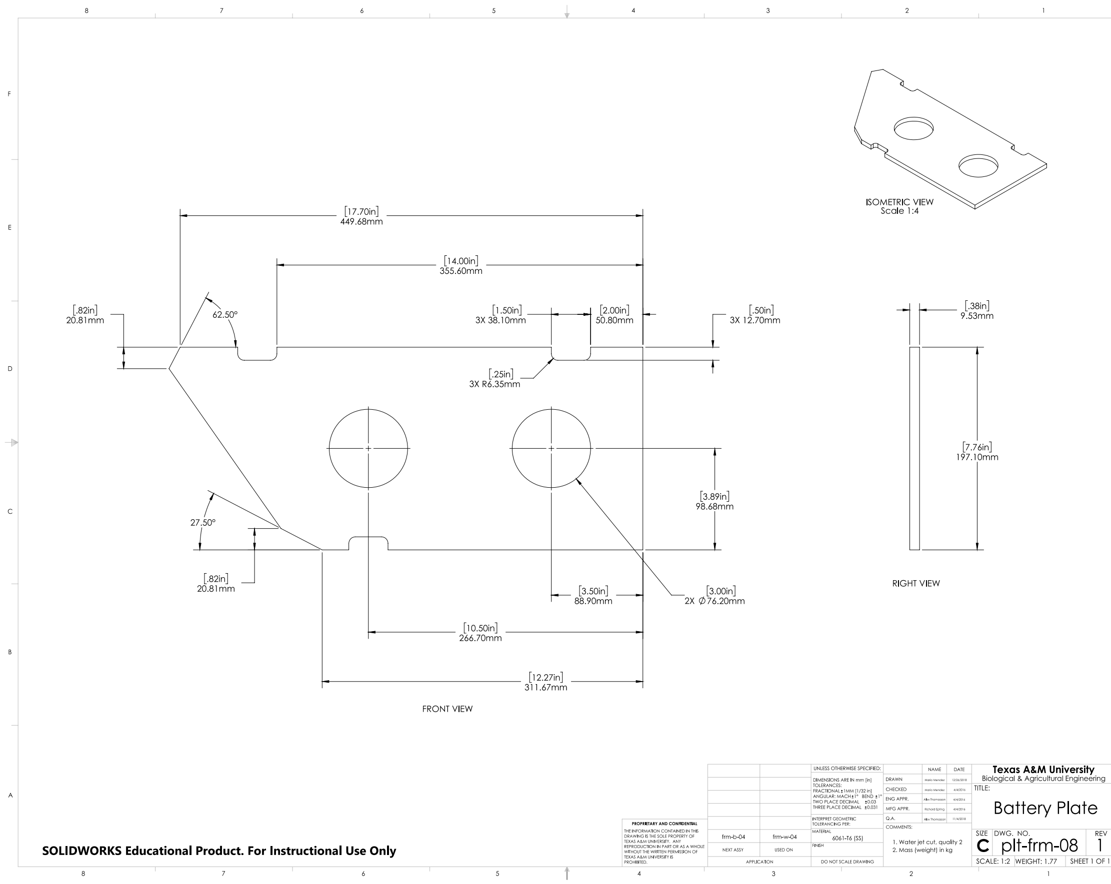

Figure J.20. Drawing of the battery plate, *plt-frm-08.sldprt*.

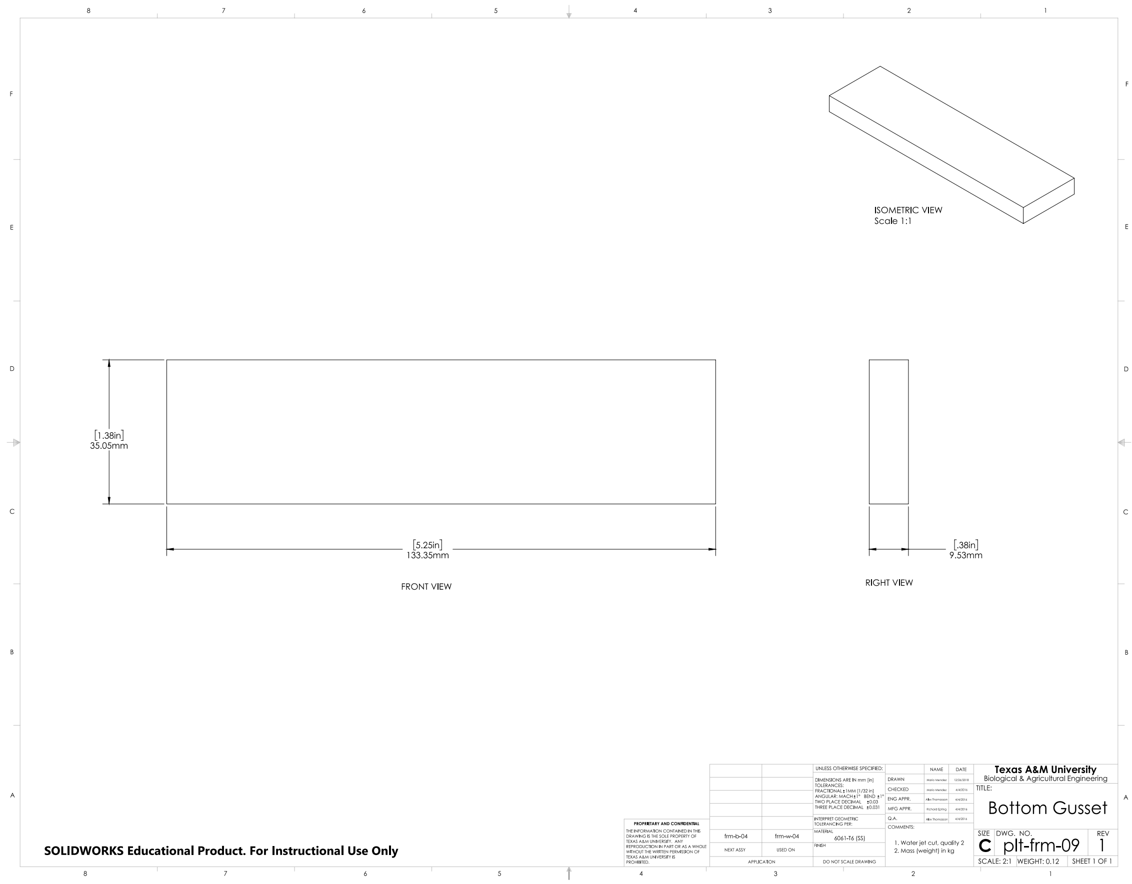

Figure J.21. Drawing of the bottom gusset, *plt-frm-09.sldprt*.

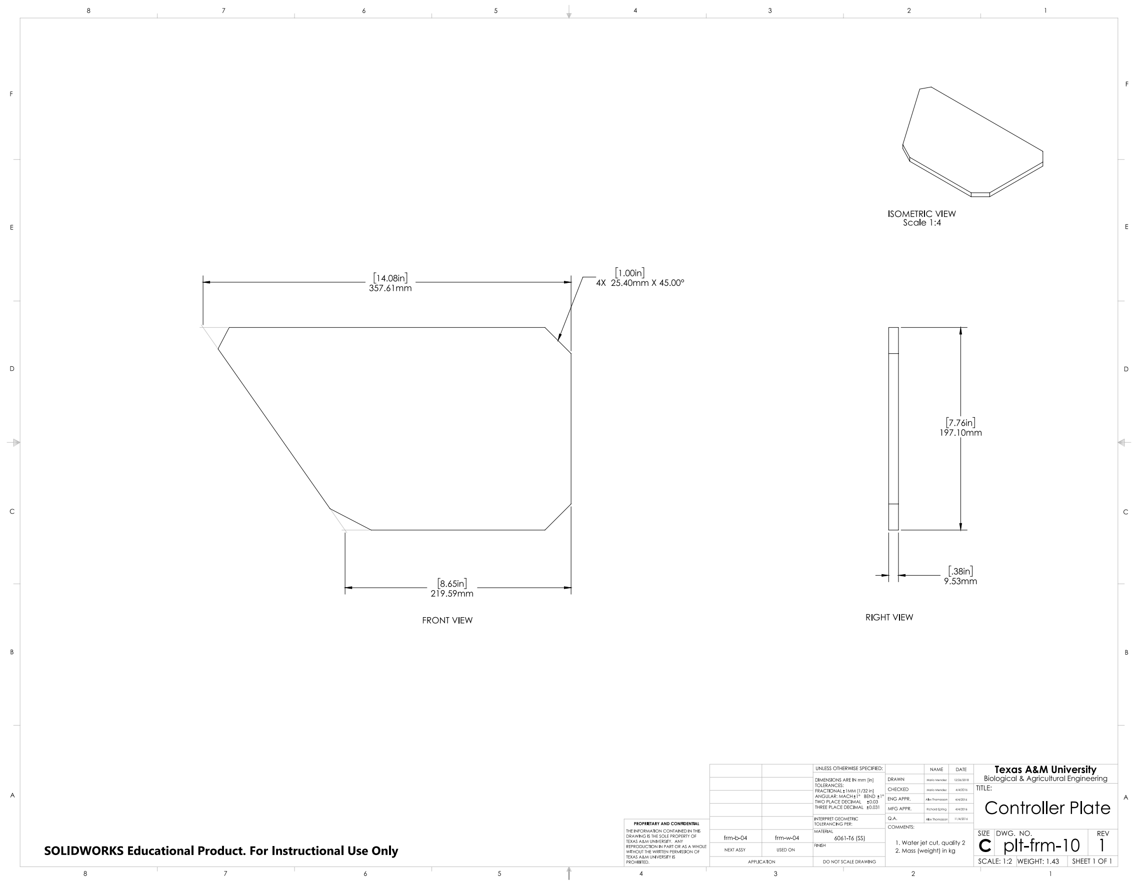

Figure J.22. Drawing of the motor controller plate, *plt-frm-10.sldprt*.

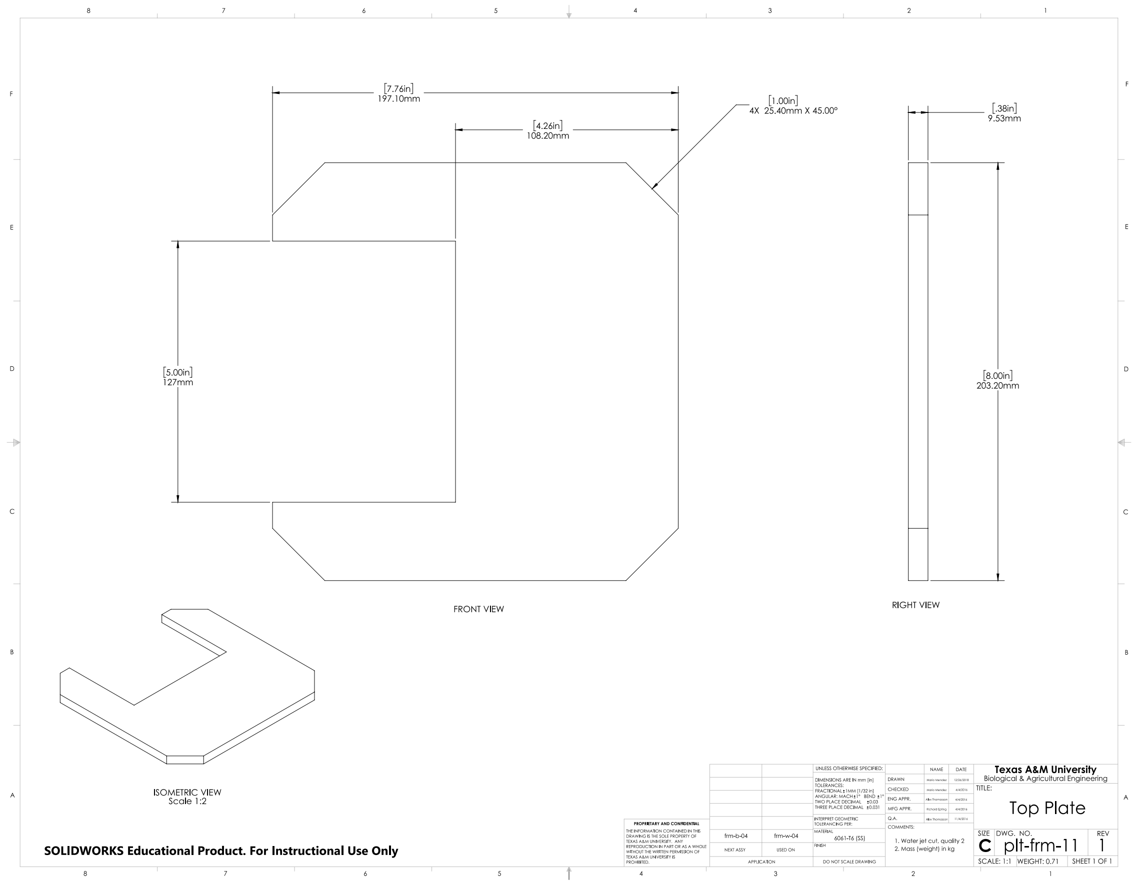

Figure J.23. Drawing of the top plate, *plt-frm-11.sldprt*.

J.5. Transmission System

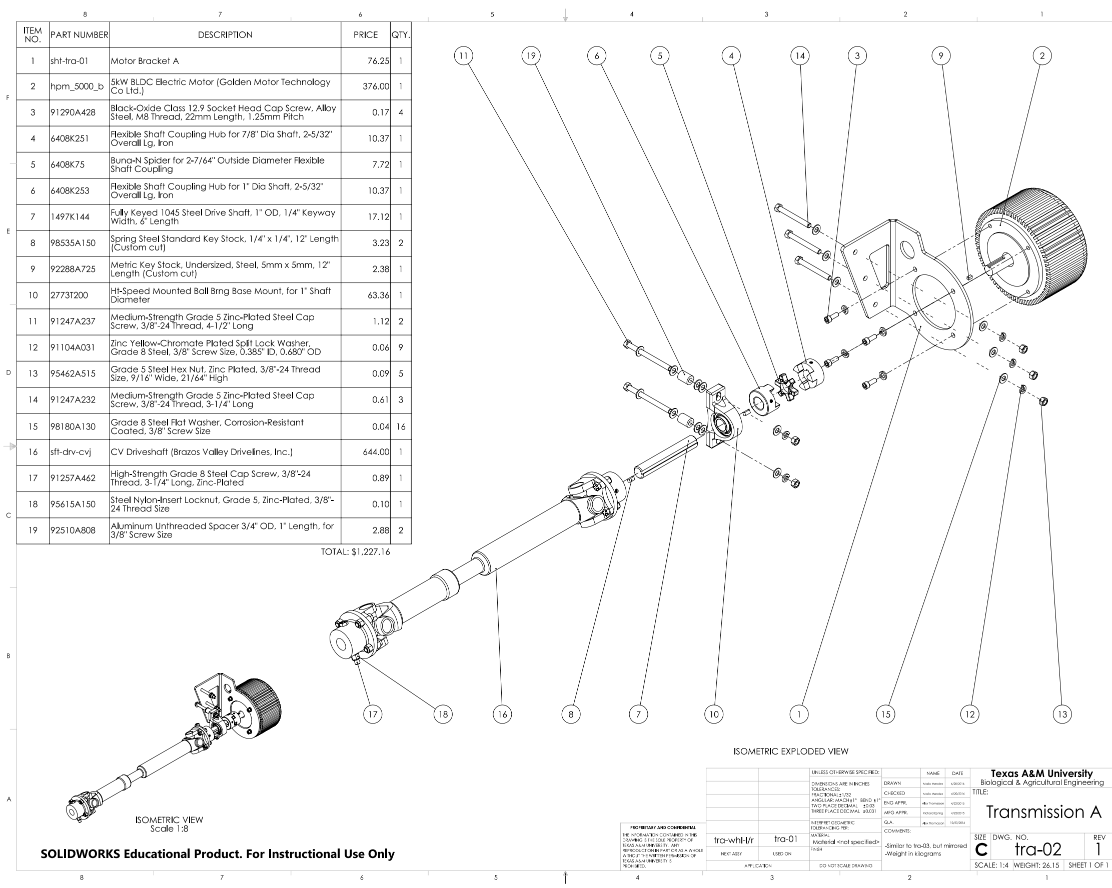

Figure J.24. Drawing of the isometric exploded view of the transmission system, *tra-02.sldasm*.

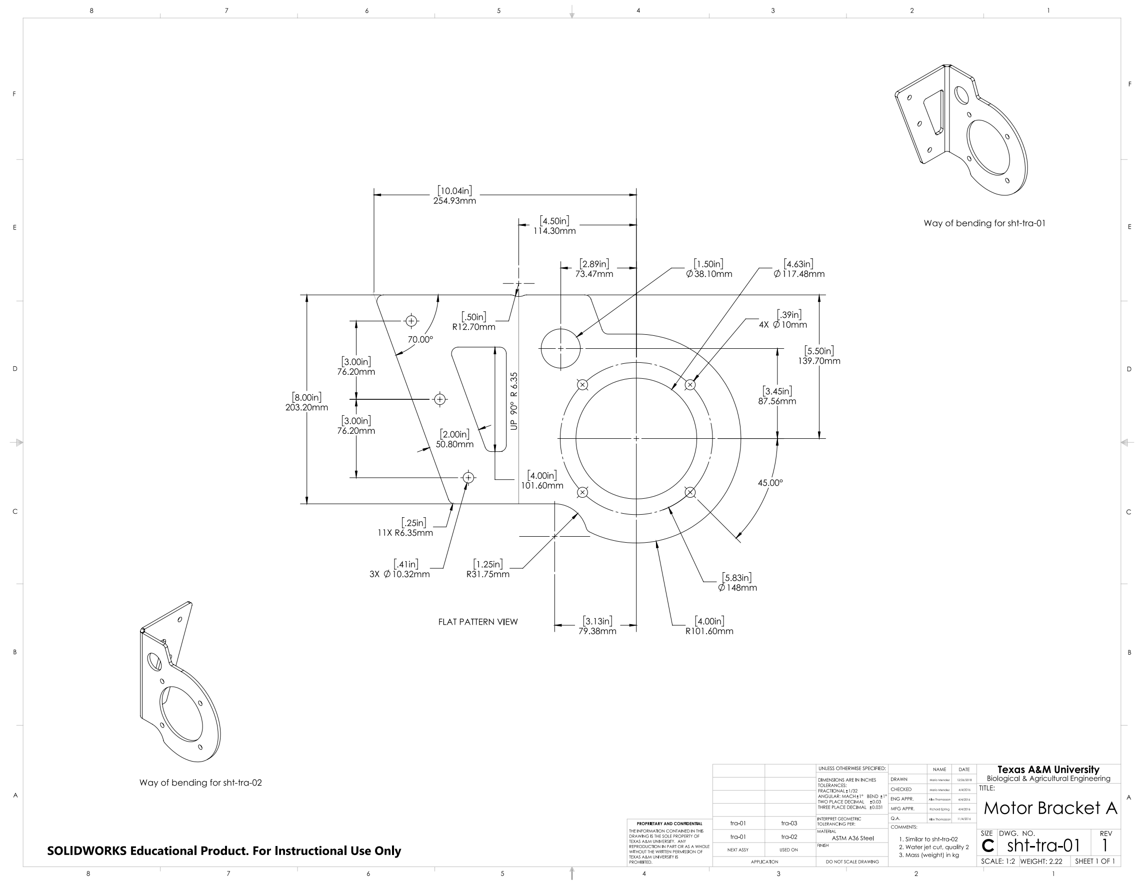

Figure J.25. Drawing of the sheet metal motor bracket, *sht-tra-01.sldprt*.

J.6. Stereo Camera Holder

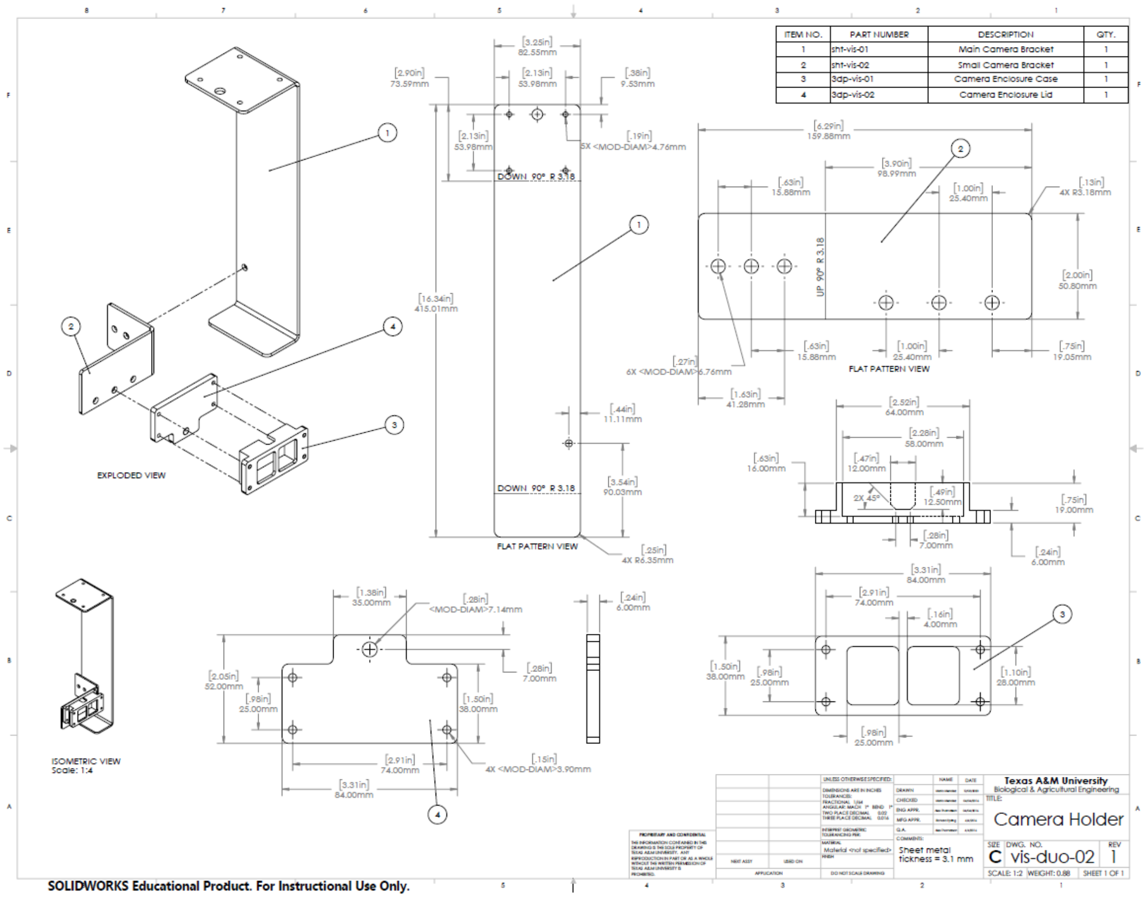

Figure J.26. Drawing camera holder, *vis-duo-02.sldasm* and individual components.